QA: QA

MDL-MGR-GS-000005 REV 01

November 2004

NOTICE OF OPEN CHANGE DOCUMENTS - THIS DOCUMENT IS IMPACTED BY THE LISTED CHANGE DOCUMENT AND CANNOT BE USED WITHOUT IT.

---

1) ACN-001, DATED 06/23/2005

Dike/Drift Interactions

Prepared for:
U.S. Department of Energy
Office of Civilian Radioactive Waste Management
Office of Repository Development
1551 Hillshire Drive
Las Vegas, Nevada 89134-6321

Prepared by:
Bechtel SAIC Company, LLC
1180 Town Center Drive
Las Vegas, Nevada 89144

Under Contract Number
DE-AC28-01RW12101

DISCLAIMER

This report was prepared as an account of work sponsored by an agency of the United States Government. Neither the United States Government nor any agency thereof, nor any of their employees, nor any of their contractors, subcontractors or their employees, makes any warranty, express or implied, or assumes any legal liability or responsibility for the accuracy, completeness, or any third party's use or the results of such use of any information, apparatus, product, or process disclosed, or represents that its use would not infringe privately owned rights. Reference herein to any specific commercial product, process, or service by trade name, trademark, manufacturer, or otherwise, does not necessarily constitute or imply its endorsement, recommendation, or favoring by the United States Government or any agency thereof or its contractors or subcontractors. The views and opinions of authors expressed herein do not necessarily state or reflect those of the United States Government or any agency thereof.

QA: QA

Dike/Drift Interactions

MDL-MGR-GS-000005 REV 01

November 2004

OCRWM	MODEL SIGNATURE PAGE/CHANGE HISTORY	Page: iii 1. Total Pages: 416

2. Type of Mathematical Model

X Process Model ☐ Abstraction Model ☐ System Model

Describe Intended Use of Model

3. Title

Dike/Drift Interactions

4. DI (Including Rev. No., if applicable):

MDL-MGR-GS-000005 REV 01

5. Total Appendices	6. No. of Pages in Each Appendix
A, B, C, D, E, F, G	A-18, B-10, C-10, D-18, E-4, F-14, G-12, H-6

	Printed Name	Signature	Date
7. Originator	E.S. Gaffney		23 Nov 04
8. Independent Technical Reviewer	R.W. Andrews		11/23/04
9. Checker	Christine Stockman, Terje Brandshaug, Gordon Kearny		11/23/04 11/23/04 11/23/04
10. QER	K. Gilkerson		11/23/04
11. Responsible Manager/Lead	E.S. Gaffney		23 Nov 04
12. Responsible Manager	K.M. Cline	K.M. Cline	11/23/04

13. Remarks

Supporting authors: B. Damjanac, E. Sonnenthal, Daniel Bilbrey, Douglas Alde, Stephen Nelson, and Patricia Bernot.

TER-02-0100 has been addressed by including a summary of this AMR's outputs and output DTNs in Section 8 of this report.

All software is currently qualified. UDEC and FLAC3D underwent further validation because of a CR. The software was validated. The RIT Action Items List indicates UDEC as Action FLI-061604-133032-96, CR 2779B, and FLAC 3D as FLI-060804-150155-35, CR 2781B.

Change History

14. Revision No.	15. Description of Change
00	Original issue
01	Documents new analyses for dike propagation and the "dog-leg" scenario, incorporates revised text for transparency and traceability, and incorporates relevant text (magma cooling, models) related to igneous activity post-emplacement phenomena from model report *Igneous Intrusion Impacts to Waste Package and Waste Form*, REV 01 (MDL-EBS-GS-000002). This model report is being archived and all relevant information will be contained in *Dike Drift Interactions* REV 01. This document is a complete revision and no change bars are provided.

INTENTIONALLY LEFT BLANK

CONTENTS

Page

ACRONYMS AND ABBREVIATIONS xix

1. PURPOSE 1-1
   1.1 SCOPE OF WORK 1-1
   1.2 DIKE/DRIFT CONCEPTUAL MODEL 1-4
      1.2.1 Dike Intrusion Submodel 1-4
      1.2.2 Eruption Stage 1-5
      1.2.3 Post-Intrusion Submodel 1-5
   1.3 BACKGROUND 1-5
      1.3.1 Previous Reports 1-7
      1.3.2 Conceptual Model for Igneous Processes 1-7
   1.4 LIMITATIONS OF MODELS AND ANALYSES 1-9
      1.4.1 Analysis of Natural and Thermal Stresses 1-9
      1.4.2 Dike Propagation Model 1-9
      1.4.3 Analysis of Magma Flow 1-10
      1.4.4 Secondary Dike Analysis 1-11
      1.4.5 Drift Scale Gas Flow Analysis 1-11
      1.4.6 Basalt Cooling and Solidification Model 1-11
      1.4.7 Basalt/Water Seepage Model 1-12

2. QUALITY ASSURANCE 2-1

3. USE OF SOFTWARE 3-1
   3.1 SOFTWARE TRACKED BY CONFIGURATION MANAGEMENT 3-1
   3.2 EXEMPT SOFTWARE 3-2
   3.3 USE OF UNQUALIFIED SOFTWARE 3-2

4. INPUTS 4-1
   4.1 DATA, PARAMETERS, AND OTHER MODEL INPUTS 4-1
      4.1.1 Data and Parameters 4-1
         4.1.1.1 Inputs to Thermal Calculations 4-4
         4.1.1.2 Inputs Into Seepage Chemistry Calculations 4-5
            4.1.1.2.1 Inputs for EQ6 Simulation of Water/Basalt Reaction Hydrochemistry 4-6
            4.1.1.2.2 Composition of Intruded Basalt Material 4-6
            4.1.1.2.3 Dissolution Rates of Basalt Minerals 4-7
            4.1.1.2.4 Composition and Flow Rate of Incoming Water 4-10
         4.1.1.3 Sensitivity Cases 4-12
         4.1.1.4 General EQ6 Inputs That Apply to All EQ6 Cases in This Model 4-12
            4.1.1.4.1 Thermodynamic Database 4-12
            4.1.1.4.2 Atomic Weights 4-13

CONTENTS (Continued)

Page

4.2 CRITERIA 4-13
4.3 CODES, STANDARDS, AND REGULATIONS 4-13

5. ASSUMPTIONS 5-1
5.1 DIKE PROPAGATION FROM DEPTH 5-1
5.2 MAGMA FLOW INTO DRIFTS FOR EFFUSIVE FLOW 5-1
5.3 DRIFT-SCALE GAS FLOW 5-2
5.4 COOLING OF BASALT-FILLED DRIFTS 5-2
5.4.1 Permeability of Metamorphic Aureole and Cooled Basalt 5-2
5.4.2 Fracturing of Basalt and Block Size 5-3
5.4.3 Thermal Properties of the Magma 5-4

6. MODELS AND ANALYSES 6-1
6.1 FEATURES, EVENTS, AND PROCESSES ADDRESSED BY THE DIKE/DRIFT INTERACTION MODEL 6-2
6.2 ANALYSIS OF NATURAL AND INDUCED STRESSES AT THE REPOSITORY 6-4
6.2.1 Inputs for Topographic and Thermal Effects 6-4
6.2.2 Stress Due to Natural Topography 6-5
6.2.3 Stresses Due to Excavation of the Drift 6-7
6.2.4 Thermal Stresses Induced by Radioactive Decay of Waste 6-8
6.2.5 Summary 6-10
6.3 DIKE PROPAGATION FROM DEPTH MODEL 6-10
6.3.1 Model Description 6-11
6.3.1.1 Background 6-11
6.3.1.2 Implementation 6-12
6.3.2 Assumptions and Simplifications 6-14
6.3.3 Mathematical Description 6-18
6.3.3.1 Governing Equations 6-19
6.3.3.2 Scaling and Dimensionless Formulation 6-21
6.3.3.3 Simplifications in the Case of the Dike Problem 6-24
6.3.3.4 Self-Similar Problem of a Deep Dike 6-25
6.3.4 Model Uncertainties and Limitations 6-27
6.3.5 Model Inputs 6-29
6.3.6 Boundary and Initial Conditions 6-31
6.3.7 Model Results 6-32
6.3.7.1 Base Case 6-34
6.3.7.2 Effect of Pressure Inside the Tip Cavity 6-44
6.3.7.3 Effect of Thermally Induced Increased Horizontal Stress 6-49
6.3.8 Alternative Models for Dike Propagation 6-66
6.3.8.1 Analytic Solutions of the Hydraulic-Fracture Problem 6-66
6.3.8.1.1 Industrial Hydraulic-Fracture Models (Oil and Gas Applications) 6-69
6.3.8.1.2 Hydraulic-Fracture Dike Propagation Models 6-70

CONTENTS (Continued)

Page

6.3.8.2 Effect of Expanding Magma on Dike Extension to the Surface 6-70
6.3.8.3 Electric Power Research Institute Analysis of Dike Propagation 6-71
6.3.9 Summary 6-72
6.4 ANALYSIS OF EFFUSIVE MAGMA FLOW INTO DRIFTS 6-73
6.4.1 Approximations and Simplifications 6-74
6.4.2 Magma Flow within the Dike 6-74
6.4.3 Description of Input 6-75
6.4.4 Initial and Boundary Conditions 6-76
6.4.5 Results 6-78
6.4.5.1 Wide Aperture Case 6-78
6.4.5.2 Narrow Aperture Case 6-85
6.4.6 Fully Coupled Dike Drift Interaction 6-85
6.4.7 Alternative Analyses 6-91
6.4.7.1 Analytic Solution for Effusive Flow into Drifts 6-91
6.4.7.1.1 Idealizations and Simplifications 6-91
6.4.7.1.2 Mathematical Formulation 6-92
6.4.7.1.3 Description of Input 6-96
6.4.7.1.4 Initial and Boundary Conditions 6-96
6.4.7.1.5 Results 6-96
6.4.7.2 Alternative Analysis of Pyroclastic Flow 6-97
6.4.7.2.1 Alternative Analysis for Pyroclastic Flow Into the Drift 6-97
6.4.7.2.2 Discussion of Alternative Analysis of Pyroclastic Flow into a Drift 6-101
6.4.7.3 EPRI Analysis of Magma-Drift Interactions 6-103
6.4.8 Magma Interactions with Waste Packages and Waste Forms 6-104
6.4.8.1 Degradation of Waste Packages 6-104
6.4.8.2 Movement of Waste Packages by Magma 6-106
6.4.8.3 Effect on Waste Forms 6-107
6.4.8.4 EPRI Analysis of Magma-Waste Interaction 6-109
6.4.8.5 Conclusion 6-111
6.4.9 Summary 6-111
6.5 ANALYSIS OF SECONDARY DIKE PROPAGATION 6-112
6.5.1 Secondary Dike Propagation for Effusive Flow 6-112
6.5.1.1 Description of Inputs 6-112
6.5.1.1.1 Inputs for Crack Opening Analysis 6-112
6.5.1.1.2 Inputs for Magma Cooling Rates Analysis 6-114
6.5.1.2 Opening of Pre-Existing Crack 6-114
6.5.1.3 Potential Location Of An Eventual Secondary Dike 6-129
6.5.1.3.1 Stress-Related Effects 6-129
6.5.1.3.2 Fracture Criteria 6-132
6.5.1.3.3 Results of Stress Calculations 6-132
6.5.1.4 Magma Cooling Rates 6-142
6.5.1.4.1 “Solidification” Temperatures 6-143

CONTENTS (Continued)

Page

6.5.1.4.2 Thermal Stoppage of New Dike 6-145
6.5.1.5 Synthesis: Likelihood of the Dog-Leg Scenario for Effusive Flow 6-145
6.5.2 Secondary Dike Propagation for Two-Phase Flow 6-147
6.5.2.1 Pyroclastic Flow 6-147
6.5.2.2 Analogue Hydrovolcanic Occurrence 6-148
6.5.2.3 Analysis of Hydrovolcanic Injection from the Drift into an Existing Crack 6-148
6.5.3 Alternative Analysis of Pyroclastic Flow: the "Woods et al." Scenario 6-155
6.5.3.1 Discussion of Alternative Analysis 6-155
6.5.3.2 Discussion of Woods et al. Model for Pyroclastic Flow from Drift to Surface 6-156
6.5.4 Conclusion 6-157
6.6 GAS FLOW BETWEEN DRIFTS 6-158
6.6.1 Description 6-160
6.6.2 Numerical Formulation and Code 6-160
6.6.3 Description of Inputs 6-161
6.6.3.1 Numerical Mesh 6-161
6.6.3.2 Initial Pore and Infiltrating Water and Gas Chemistry 6-163
6.6.3.3 Initial Mineralogy 6-164
6.6.3.4 Initial Volcanic Gas Chemistry 6-165
6.6.3.5 Hydrological and Thermal Properties 6-165
6.6.3.6 Aqueous and Gaseous Species Diffusion Coefficients 6-165
6.6.4 Initial and Boundary Conditions 6-166
6.6.4.1 Hydrological and Thermal 6-166
6.6.4.2 Chemical 6-167
6.6.5 Simulation Results 6-167
6.6.5.1 Simulation 1 6-167
6.6.5.2 Simulation 2 6-170
6.6.5.3 Gas Transport through a Backfilled Connecting Drift (at 300°C) 6-178
6.6.6 Summary of Gas Flow Analyses 6-183
6.7 EFFECTS ON NEIGHBORING DRIFTS OF MAGMA COOLING AND SOLIDIFICATION 6-183
6.7.1 Magma Cooling and Solidification 6-183
6.7.1.1 Problem Definition 6-184
6.7.1.2 Results of Model Simulations 6-185
6.7.2 Alternative Models 6-187
6.7.2.1 Sensitivity to Latent Heat Effects 6-187
6.7.2.2 Sensitivity to Saturation 6-187
6.7.2.3 Analytical Solution to Heat Flow 6-189
6.8 REACTION OF SEEPAGE WATER WITH BASALT AFTER REVERSION TO NORMAL IN-DRIFT ENVIRONMENTAL CONDITIONS 6-189
6.8.1 EQ6 Basalt/Water Interaction 6-191
6.8.2 Sensitivity Cases 6-195

CONTENTS (Continued)

Page

6.8.3 Results of EQ6 Simulations of Crown Seepage Water Reaction With Cooled Basalt 6-196
6.8.4 Discussion of uncertainties 6-198
6.8.4.1 Uncertainty in the Geochemical Modeling Using EQ6 6-198
6.8.5 Alternative Models for Water/Basalt Interactions 6-200
6.8.6 Summary 6-201

7. VALIDATION 7-1
7.1 IMPORTANCE LEVELS FOR MODEL VALIDATION 7-1
7.2 CONFIDENCE BUILDING DURING DEVELOPMENT 7-3
7.2.1 Dike Intrusion Submodel 7-4
7.2.2 Post-Intrusion 7-5
7.2.2.1 Drift-Scale Gas Flow 7-5
7.2.2.2 Magma Cooling 7-6
7.2.2.3 Basalt/Seepage Water Interaction 7-6
7.3 POST-DEVELOPMENT CONFIDENCE BUILDING 7-7
7.3.1 Dike Intrusion Submodel 7-7
7.3.1.1 Dike Propagation Model Component 7-7
7.3.1.1.1 Parícutin Volcano Natural Analog 7-7
7.3.1.1.2 Independent Technical Review of Dike Propagation Model 7-14
7.3.1.1.3 Uncertainty 7-15
7.3.2 Post-Intrusion Submodel 7-18
7.3.2.1 Drift-Scale Gas Flow Between Drifts Model Component 7-18
7.3.2.1.1 Corroboration with Laboratory Analog 7-18
7.3.2.1.2 Validation by Publication in Peer-Reviewed Journals 7-22
7.3.2.1.3 Uncertainty 7-23
7.3.2.1.4 Alternative Models 7-23
7.3.2.2 Magma Cooling and Solidification Model Component 7-24
7.3.2.2.1 Comparison with Alternative Mathematical Model 7-24
7.3.2.2.2 Comparison with Field Observations and Associated Mathematical Model 7-26
7.3.2.2.3 Uncertainty 7-26
7.3.2.3 Basalt/Water Seepage Model 7-26
7.3.2.3.1 Comparison and Corroboration with Field Analog Data 7-27
7.3.2.3.2 Comparison and Corroboration with Laboratory Analog Data 7-27
7.3.2.3.3 Uncertainty 7-28

8. CONCLUSIONS 8-1
8.1 SUMMARY OF MODELING ACTIVITIES 8-1
8.1.1 Dike Propagation 8-1
8.1.2 Magma Flow in Drifts 8-2

CONTENTS (Continued)

Page

8.1.3 Post-Intrusion Effects 8-4
8.2 MODEL OUTPUT 8-4
8.2.1 Developed Output Listed by Data Tracking Number 8-4
8.2.2 Migration of Magmatic Gases 8-4
8.2.3 Thermal Effects 8-5
8.2.4 Seepage Water Chemistry 8-6
8.3 OUTPUT UNCERTAINTY 8-9
8.3.1 Gas Flow Calculation 8-9
8.3.2 Heat Flow Calculation 8-9
8.3.3 EQ6 Calculations 8-9
8.4 RESTRICTIONS 8-9

9. INPUTS AND REFERENCES 9-1
9.1 DOCUMENTS CITED 9-1
9.2 CODES, STANDARDS, REGULATIONS, AND PROCEDURES 9-15
9.3 SOFTWARE 9-15
9.4 SOURCE DATA, LISTED BY DATA TRACKING NUMBER 9-16
9.5 DEVELOPED DATA, LISTED BY DATA TRACKING NUMBER 9-17

APPENDIX A – NUREG-1804 ACCEPTANCE CRITERIA ASSOCIATED WITH IGNEOUS ACTIVITY A-1
APPENDIX B – EQ6 MINERAL DISSOLUTION RATES B-1
APPENDIX C – VERIFICATION OF HEAT CONDUCTION MODEL SIMULATION CALCULATIONS C-1
APPENDIX D – ALTERNATIVE ANALYTICAL SOLUTION TO HEAT FLOW D-1
APPENDIX E – INFORMATION REGARDING INPUT/OUTPUT FILES AND SPREADSHEET FILES E-1
APPENDIX F – INDEPENDENT TECHNICAL REVIEW OF DIKE PROPAGATION SUBMODEL F-1
APPENDIX G – QUALIFICATION OF EXTERNAL SOURCES G-1

FIGURES

Page

1-1. Schematic Representation of the Stages of Interaction Between a Volcanic Dike and Repository Drifts 1-3

6-1. Topography at Yucca Mountain Nuclear Waste Repository Site 6-5
6-2. Contours of Vertical Normal Stress and Stress Tensors Due to Topography at Yucca Mountain Nuclear Waste Repository Site: Cross-Section Through N232000 6-6
6-4. Variation of Initial In situ Stresses With Depth at Yucca Mountain Nuclear Waste Repository Along the Vertical Scanline at E171000, N235000 6-7
6-5. Predicted Variation of Stresses With Depth at Yucca Mountain Nuclear Waste Repository Along the Vertical Scanline at E171000, N235000 After 500 Years of Heating 6-9
6-6. Predicted Variation of Stresses With Depth at Yucca Mountain Nuclear Waste Repository Along the Vertical Scanline at E171000, N235000 After 1000 Years of Heating 6-9
6-7. Predicted Variation of Stresses With Depth at Yucca Mountain Nuclear Waste Repository Along the Vertical Scanline at E171000, N235000 After 2000 Years of Heating 6-10
6-8. Plane-Strain, Fluid-Driven Vertical Fracture with a Lag Zone at the Tip 6-19
6-9. Relation between Far-Field Fluid Velocity and Far-Field Dike Opening from Equation 6-68 6-33
6-10. Dimensionless Solution for Dike Tip and Fluid Front as Functions of Time 6-35
6-11. Dike Tip and Fluid Front as Functions of Time: $\mathcal{D}$= 2.67, $\kappa\rho_r$= 2400 kg/m^3, μ = 10 Pa·s 6-36
6-12. Dike Tip and Fluid Front as Functions of Time: $\mathcal{D}$= 2.67, $\kappa\rho_r$= 1200 kg/m^3, μ = 10 Pa·s 6-37
6-13. Dike Tip and Fluid Front as Functions of Time: $\mathcal{D}$= 6.02, $\kappa\rho_r$= 2400 kg/m^3, μ = 10 Pa·s 6-37
6-14. Dike Tip and Fluid Front as Functions of Time: $\mathcal{D}$= 6.02, $\kappa\rho_r$= 1200 kg/m^3, μ = 10 Pa·s 6-38
6-15. Dike Tip and Fluid Front as Functions of Time: $\mathcal{D}$= 20.28, $\kappa\rho_r$= 2400 kg/m^3, μ = 10 Pa·s 6-38
6-16. Dike Tip and Fluid Front as Functions of Time: $\mathcal{D}$= 20.28, $\kappa\rho_r$= 1200 kg/m^3, μ = 10 Pa·s 6-39
6-17. Dike Tip and Fluid Front as Functions of Time: $\mathcal{D}$= 20.28, $\kappa\rho_r$= 2400 kg/m^3, μ = 40 Pa·s 6-39
6-18. Dike Tip and Fluid Front as Functions of Time: $\mathcal{D}$= 20.28, $\kappa\rho_r$= 1200 kg/m^3, μ = 410 Pa·s or μ = 40 Pa·s 6-40
6-19. Net Pressure Profile as a Function of Depth: $\mathcal{D}$= 2.67, $\kappa\rho_r$= 1200 kg/m3, μ = 10 Pa·s, v_∞= 1 m/s, w_∞= 0.16 6-42
6-20. Pressure History at Points Similar to Repository Depth for $\mathcal{D}$= 2.67, $\kappa\rho_r$= 1200 kg/m^3, μ = 10 Pa·s 6-43

FIGURES (Continued)

Page

6-21. Net Pressure Profile as a Function of Depth: $\mathcal{D}$ = 20.28, $\kappa\rho_r$ = 2400 kg/m3, μ = 10 Pa·s, v_∞ = 1 m/s, w_∞ = 0.32 m 6-43
6-22. Pressure History at Points Similar to Repository Depth for $\mathcal{D}$ = 20.28, $\kappa\rho_r$ = 2400 kg/m^3, μ = 10 Pa·s 6-44
6-23. Dimensionless Solution for Dike Tip and Fluid Front as Functions of Time: Effect of $\mathcal{S}$ for $\mathcal{D}$ = 2.67 6-45
6-24. Dike Tip and Fluid Front as Functions of Time: $\mathcal{D}$ = 2.67, $\mathcal{S}$ = -0.25, $\kappa\rho_r$ = 2400 kg/m^3, μ = 10 Pa·s 6-46
6-25. Dike Tip and Fluid Front as Functions of Time: $\mathcal{D}$ = 2.67, $\mathcal{S}$ = -0.25, $\kappa\rho_r$ = 1200 kg/m3, μ = 10 Pa·s 6-46
6-26. Dimensionless Solution for Dike Tip and Fluid Front as Functions of Time: Effect of $\mathcal{S}$ for $\mathcal{D}$ = 20.28 6-47
6-27. Dike Tip and Fluid Front as Functions of time: $\mathcal{D}$ = 20.28, $\mathcal{S}$ = -0.2, $\kappa\rho_r$ = 2400 6-47
6-28. Dike Tip and Fluid Front as Functions of time: $\mathcal{D}$ = 20.28, $\mathcal{S}$ = -0.2, $\kappa\rho_r$ = 1200 kg/m^3, μ = 10 Pa·s 6-48
6-29. Large-Scale UDEC Model 2000-m Deep by 4000-m Wide, in Two Blocks 6-50
6-30. UDEC Model 2000-m Deep by 4000-m Wide, in Two Blocks With Voronoi Polygons in the 500-m Deep by 1000-m Wide Rectangle Near the Surface 6-51
6-31. UDEC Model With Voronoi Polygons Near The Surface — Detail Near Ground Surface; Block of Polygons is 500-m Deep by 1000-m Wide 6-52
6-32. Contours of Temperature Increase (ºC) 1000 Years After Waste Emplacement 6-54
6-33. Contours of Horizontal Stress (Pa) 1000 Years After Waste Emplacement 6-55
6-34. Vertical Profile of Horizontal Stress 1000 Years After Waste Emplacement 6-56
6-35. Position of Magma Front as a Function of Time–Large Scale Model 6-57
6-36. Pressure (Pa, in blue) and Aperture (m, in black) Along the Dike Propagating in the Middle of the Repository 1000 Years After Waste Emplacement–1000 S After Start of Simulation (see Figure 6-35) 6-58
6-36a. Pressure (Pa) and Aperture (m) Along the Dike Propagating in the Middle of the Repository 1000 Years After Waste Emplacement–2500 s After Start of Simulation (see Figure 6-35) 6-59
6-36b. Dike Path Propagating in the Middle of the Repository 1000 Years After Waste Emplacement: Temperature Increase Contours (ºC), Dike Opening (m), and Magma Pressure (Pa) 6-62
6-36c. Dike Path Propagating 500 m Offset From the Middle of the Repository 1000 Years After Waste Emplacement: Temperature Increase Contours (ºC), Dike Opening (m), and Magma Pressure (Pa) 6-63
6-36d. Pressure (Pa) and Stress Tensors Colored By Magnitude Of Major Principal Stress (Pa) Along The Dike Propagating In The Middle Of The Repository 1000 Years After Waste Emplacement Assuming Coefficient Of Thermal Expansion to be 5×10^{-5} 6-64
6-36e. Position of the Magma Front as a Function of Time—Small Scale Model 6-65
6-36f. Pressure Histories in Magma as a Function of Time at the Repository Horizon—Small Scale Model 6-66

FIGURES (Continued)

Page

6-36g. Approximate Magma and Crack Propagation for an Expanding, but Still Effusive, Magma 6-71
6-37. Geometry of the Dike Model 6-77
6-38. Contours of Horizontal Stress (Pa) Perpendicular to the Drift and Displacement Vectors (m) After 1642 Seconds of Simulation: Wide Aperture Case 6-79
6-39. Rate of Magma Flow (m^3/s) From the Dike into the Drift as a Function of Time (s): Wide Aperture Case 6-80
6-40. Contours of Saturation of Dike With Magma 602 Seconds After Start of Simulation: Wide Aperture Case. The Position Of The Magma Front Corresponds To Saturation 0.5 6-81
6-41. Contours of Saturation of Dike With Magma 798 Seconds After Start of Simulation: Wide Aperture Case 6-82
6-42. Contours of Saturation of Dike With Magma 1642 Seconds After Start of Simulation: Wide Aperture Case 6-83
6-43. Contours of Magma Pressure (Pa) Inside the Dike 1642 Seconds After Start of Simulation: Wide Aperture Case 6-84
6-44. Rate of Magma Flow (m^3/s) From the Dike as a Function of Time (s): Narrow-Aperture Case 6-86
6-45. Contours of Saturation of Dike With Magma 1943 Seconds After Start of Simulation: Narrow-Aperture Case. 6-87
6-46. Contours of Magma Pressure (Pa) Inside the Dike 1943 Seconds After Start of Simulation: Narrow-Aperture Case 6-88
6-47. History of the Rate of Magma Inflow From the Dike as a Function of Time: Wide-Aperture Case 6-90
6-48. History of the Rate of Magma Inflow from the Dike as a Function of Time: Narrow-Aperture Case 6-90
6-49. Schematic Representing Flow of Magma From Dike Into Drift 6-93
6-50. Discharge Rate for Effusive Magma Flowing Into Drifts as a Function of Time 6-98
6-51. Length of Drift Filled by Effusive Magma Flowing Into Drifts as a Function of Time 6-99
6-52. Height of Magma in Dike Above Invert for Effusive Magma Flowing Into Drifts as a Function of Time 6-100
6-53. Displacement Vector Field (m) and Hydraulic Aperture (m) Along the Vertical Fracture: Case 101 6-118
6-54. Stress Tensor Field (Pa) and Pore Pressure (Pa) Along the Joint: Case 101 6-119
6-55. Histories of Joint Hydraulic Aperture (m) at Seven Locations Along the Joint: Case 101 6-120
6-56. Location (Relative to the Drift Periphery) of the Magma Front Inside a Joint as a Function of Time: Case 101 6-121
6-57. Displacement Vector Field (m) and Hydraulic Aperture (m) Along the Vertical Fracture: Case 103 6-122
6-58. Stress Tensor Field (Pa) and Pore Pressure (Pa) Along the Joint: Case 103 6-123
6-59. Histories of Joint Hydraulic Aperture (m) at Seven Locations Along the Joint: Case 103 6-124

FIGURES (Continued)

Page

6-60. Location (Relative to the Drift Periphery) of the Magma Front Inside a Joint as a Function of Time: Case 103 6-125
6-61 Magma Front Average Velocity Over The Whole Simulation, for each Case 6-126
6-62. Time needed for the Joint to Reach Several Thickness Increases at a 3.67 m Distance From the Drift Periphery (Except For Cases 105, 108, 109, for Which Distance is 3.08 m) 6-126
6-63. Dike-Induced Stress Changes as a Function of Horizontal Distance when the Tip is at a 411-m Depth 6-135
6-64. Dike-Induced Stress Changes as a Function of Horizontal Distance when the Tip is at a 300-m Depth 6-135
6-65. Dike-Induced Stress Changes as a Function of Horizontal Distance when the Tip is at a 150-m Depth 6-136
6-66. Dike-Induced Stress Changes as a Function of Horizontal Distance when the Tip is at a 16-m Depth 6-136
6-67. Total Stresses Acting on the Repository when the Crack Tip is at a 411-m Depth 6-137
6-68. Total Stresses Acting on the Repository when the Crack Tip is at a 300-m Depth 6-138
6-69. Total Stresses Acting on the Repository when the Crack Tip is at a 150-m Depth 6-138
6-70. Total Stresses Acting on the Repository when the Crack Tip is at a 16-m Depth 6-139
6-71. Stresses around the Drift Wall at 10 m from the Dike 6-140
6-72. Stresses around the Drift Wall at 40 m from the Dike 6-140
6-73. Stresses around the Drift Wall at 640 m from the Dike 6-141
6-74. Minimum Principal Stress at the Drift Wall versus Distance from the Dike, When the Tip is at Repository Elevation 6-141
6-75. Apparent Viscosity of Alkali Basalt Magmas During Crystallization 6-144
6-76. Time to Chill a Dike from Liquidus Temperature to the Temperature at Which the Apparent Viscosity is 1000 Pa·s, the Assumed Effective “Solidus” Temperature 6-146
6-77. Joint aperture (in meters, but note factor of 0.01 in vertical scale) at seven distances from the drift wall along an initial 1-mm crack 6-150
6-78. Location of the Magma Fluid Front (Relative to Edge of Drift) as a Function of Time for Four Simulations with Varying Scales 6-151
6-79. Speed of Fluid Front as a Function of Time for Four simulations of a Hydrovolcanic Dike with Varying Scales 6-152
6-80. Pressure histories used to drive simulations of hydrovolcanic dike injection 6-153
6-81. Height of Fluid Front (above drift) vs. Time For Simulated hydrovolcanic Injections 6-154
6-82. Plan View Schematic of Dike-Drift Intersection and Zones 1 and 2 6-161
6-83. Numerical Mesh Used in Volcanic Gas Transport Simulations 6-162
6-84. Enlargement of THC Seepage Model Numerical Mesh Showing In-Drift Discretization 6-163
6-85. Temperature Profiles Extending From the Center of the Intruded Drift Toward the Zone 2 Drift (Simulation 1) 6-168
6-86 Contoured gas compositions (CO_2, SO_2, HCl, and HF) in fractures after 7.5 months (Simulation 1) 6-169

FIGURES (Continued)

Page

6-87. Contoured pH values in Fractures and Matrix After 1 and 7.5 Months (Simulation 1) 6-170
6-88. Temperature Profiles Extending From the Center of the Intruded Drift Toward the Zone 2 Drift (Simulation 2) 6-171
6-89. Contoured gas compositions (CO_2, SO_2, HCl, and HF) in fractures after 6 months (Simulation 2) 6-172
6-90. Contoured gas compositions (CO_2, SO_2, HCl, and HF) in fractures after One year (Simulation 2) 6-173
6-91. Contoured gas compositions (CO_2 and SO_2) in fractures after 5, 20, and 100 years (Simulation 2) 6-174
6-92. Contoured gas compositions (CO_2 and SO_2) in fractures for an enlarged region of the grid after 200 years for CO_2 and 500 years for SO_2 (Simulation 2) 6-175
6-93. Contoured pH Values In Fractures and Matrix at Six months, 1, 5, 20, and 100 years (Simulation 2) 6-176
6-94. Contoured pH values in fractures and matrix for an enlarged region of the grid after 500 years (Simulation 2) 6-178
6-95. Gas-Phase CO_2 Concentrations After (a) 10 Days, (b) 20 Days, (c) 30 Days, and (d) 40 Days 6-180
6-96. Gas-Phase SO_2 Concentrations After (a) 10 Days, (b) 20 Days, (c) 30 Days, and (d) 40 Days 6-181
6-97. Distribution of pH After (a) 10 Days, (b) 20 Days, (c) 30 Days, and (d) 40 Days 6-182
6-98. Heat Conduction from Magma Flow for Dry Tptpll 6-185
6-99. Heat Conduction from Magma Flow for Wet Tptpll 6-186
6-100. Latent Heat Effect at Centerline 6-188
6-101. Latent Heat effect at Drift Wall 6-188

7-1. Dimensionless Front Velocity (Yellow) for D = 6.02 7-12
7-2. Self-Similar Dike Problem for K = 0: Dimensionless Opening (Ω) Versus Dimensionless Distance from the Crack Tip (ξ) 7-16
7-3. Self-Similar Dike Problem for K = 0: Dimensionless Pressure (Π) Versus Dimensionless Distance from the Crack Tip (ξ) 7-17
7-4. Schematic Illustration of the Evaporation/Condensation Experiment Conducted by Pulvirenti 7-19
7-5. Change in pH of the Condensate Versus Concentration Factor for the TOUGHREACT Model Simulations as Compared to the pH Measurement 7-22
7-6. Heat Conduction from Magma Flow for Dry Tptpll 7-24
7-7. Plot of Calculated Whole-Time Temperature Profiles for Various Cooling Times Assuming a Cylindrical Drift Geometry and Showing the Approximate Effect of Latent Heat 7-25

INTENTIONALLY LEFT BLANK

TABLES

Page

3-1. Computer Software 3-1

4-1. Input Parameters Used in Dike/Drift Interaction Conceptual Model 4-1
4-2. Summary of Input Parameters and Data for Thermal Calculations 4-4
4-3. Summary of Primary Thermal Conductivity Statistics 4-4
4-4. Summary of Input Parameters and Data for Seepage Chemistry 4-5
4-5. Mean Composition of Lathrop Wells basalt and Associated Uncertainties (1σ) 4-7
4-6. Mineral Densities 4-7
4-7. Dissolution Rates of Aluminosilicate Minerals 4-8
4-8. Dissolution Rates of Olivine and Pyroxene Minerals 4-9
4-9. Dissolution Rates of Hydroxylapatite, Magnetite, and Ilmenite 4-10
4-10. Water Composition Used in EQ3 4-10
4-11. Parameter and Values Changes for Abstraction Cases for Basalt/Water Interaction 4-11
4-12. Water Composition and Redox Conditions Used in the EQ3 for Sensitivity Cases 4-12

6-1. Included Features, Events, and Processes for This Model Report 6-3
6-2. Inputs to Dike Propagation from Depth Model 6-30
6-3. Independent and Derived Parameters for Base Case Simulations 6-34
6-4. Independent and Derived Parameters for Non-Zero Cavity Tip Pressure Simulations 6-45
6-5. Model Parameters 6-49
6-6. Inputs to Dike-Drift Interaction Analysis 6-76
6-7. Cases Evaluated for Effusive Magma Flow Into Drift 6-97
6-8. Input Parameters for Crack Opening Rates Analysis: Initial Stress 6-112
6-9. Input Parameters for Crack Opening Rates Analysis: Rock Mass 6-113
6-10. Input Parameters for Crack Opening Rates Analysis: Magma 6-113
6-11. Input Parameters for Thermal Calculations 6-114
6-12. Summary of Analyzed Cases of Magma Injection Into Joints 6-115
6-13. Distances from Drift Periphery to Recording Points for Cases 101 Through 104, and 106, 107, and 110 Through 120 6-116
6-14. Distances from Drift Periphery to Recording Points for Cases 105, 108, and 109 6-117
6-15. Input Parameters for Analysis of Hydrovolcanic Injections into an Existing Rock 6-149
6-16. Initial Pore-Water and Gas Compositions[1] 6-163
6-17. Summary of Lithostratigraphic Units of the Repository Horizon Considered in Thermal Calculation 6-184
6-18. Normative Mineral Composition of Basalt 6-190
6-19. Surface Area and Moles of Mineral Reactants 6-192
6-20. Dissolution Rates of Basaltic Minerals 6-192
6-21. Water Composition and Flow Rate Used in the EQ3/6 Input Files of Water/Basalt Interaction 6-193
6-22. Surface Area and Moles of Mineral Reactants with Different Pore Fraction and Saturation 6-194
6-23. Elements Added as “Trace” to Water 6-195

TABLES (Continued)

Page

6-24. Water Composition Used in the EQ3/6 Input Files of Water/Basalt Interaction for Sensitivity Cases 6-196
6-25. Temporal Maximum and Minimum Values for pH and Ionic Strength 6-199

7-1. Validation Levels for Submodels of the Dike/Drift Interaction Model 7-2
7-2. Confidence-Building and Post-Model Development Validation Activities 7-2
7-3. Earthquakes (M_S > 4.0) With Epicenters in the Parícutin Area During January and February 1943; after Yokoyama and de la Cruz (1990 [DIRS 108740]) 7-8
7-4. Summary of Parameters for the Dike that Fed Parícutin 7-10
7-5. Dike Intrusion/Eruption Parameters at Parícutin Scaled from Calculations Applied to Yucca Mountain 7-13
7-6. Initial Chemical Composition of the Synthetic Concentrated Pore Water Used in the Experiment 7-20
7-7. Summary of EQ3/6 and TOUGHREACT Simulation Results 7-21
7-8. Comparison of Cooling Model Results from Section 6.7 [Model 1] and from Alternate Model [Model 2] 7-25

8-1. Outputs for the Dike/Drift Interaction Model Report 8-5
8-2. Lookup Tables for Temperature of Waste Forms 8-6
8-3. Look-Up Table of Temporal Maximum and Minimum Values for pH and Ionic Strength for Use in TSPA-LA 8-8
8-4. Valid Range of pH and Ionic Strength Reported in This Model Report 8-10

ACRONYMS AND ABBREVIATIONS

1-D	1-dimensional
2-D	2-dimensional
3-D	3-dimensional
DST	Drift Scale Test
FEPs	features, events, and processes
GPa	gigapascal (10^9 pascals)
j/(g·K)	joules divided by grams times Kelvin
kg	kilogram
kJ	kilojoule (10^3 joules)
LEFM	linear-elastic fracture mechanics
m	meter
MPa	megapascal (10^6 pascals)
NRC	U.S. Nuclear Regulatory Commission
Pa·s	Pascal-second
ppmv	parts per million volume
s	second
THC	thermal-hydrological-chemical
TSPA	Total System Performance Assessment
TSPA-LA	Total System Performance Assessment-License Application
TWP	Technical Work Plan
W/(m·K)	Watts divided by meters times Kelvin
wt%	percent by weight

INTENTIONALLY LEFT BLANK

1. PURPOSE

1.1 SCOPE OF WORK

This report presents and documents the model components and analyses that represent potential processes associated with propagation of a magma-filled crack (dike) migrating upward toward the surface, intersection of the dike with repository drifts, flow of magma in the drifts, and post-magma emplacement effects on repository performance. The processes that describe upward migration of a dike and magma flow down the drift are referred to as the dike intrusion submodel. The post-magma emplacement processes are referred to as the post-intrusion submodel. Collectively, these submodels are referred to as a conceptual model for dike/drift interaction. The model components and analyses of the dike/drift interaction conceptual model provide the technical basis for assessing the potential impacts of an igneous intrusion on repository performance, including those features, events, and processes (FEPs) related to dike/drift interaction (Section 6.1). Specifically, these processes are represented by the following model components and analyses:

- Analysis of Natural and Induced Stresses (Stress Analysis)–An evaluation of regional, local, and thermally-induced stresses that may influence crack propagation (Section 6.2).

- Dike Propagation Model–A numerical model representing a dike tip propagating toward the surface and the properties of magma ascending within the crack considering the influence of rock properties, natural and induced stresses, and presence of a repository (Section 6.3).

- Analysis of Magma Flow in Drifts (Magma Flow Analysis)–An analysis of the behavior of magma as it intersects the repository drifts and flows down the drifts (Section 6.4). It establishes the boundary conditions for assessing the potential for a secondary dike propagation from within the repository or the performance of the engineered barriers. This analysis also considers the effects on the structural integrity of waste packages and drip shields following contact with magma.

- Analysis of Secondary Dike Propagation (Secondary Dike or Dog-Leg Analysis)–An evaluation of the potential for a secondary dike (dog-leg) to propagate to the surface from within the repository after magma initially fills repository drifts (Section 6.5). This analysis addresses potential secondary dike propagation under effusive and pyroclastic conditions. It also addresses the very unlikely scenario proposed by Woods et al (2002 [DIRS 163662]).

- Drift Scale Gas Flow Model–This model uses the previously validated gas flow model (BSC 2004 [DIRS 169856], Section 7) to address the post-intrusion migration of magmatic gas species, both reactive and non-reactive, from the magma filled drift to adjacent drifts through the pillar (Section 6.6). The purpose of the analysis is to evaluate the timing and reactivity of gas species during migration from the magma filled drift.

- Basalt Cooling and Solidification Model (Basalt Cooling Model) –This model addresses the dissipation of heat via conductive cooling from the magma-filled drifts toward adjacent drifts through the pillars (Section 6.7).

- Reaction of Seepage Water With Basalt Under Normal In-Drift Conditions Model (Basalt/Water Seepage Model)–This numerical model evaluates the potential chemical evolution of seepage water after magma emplacement as it begins to re-equilibrate with the minerals in basalt. This model provides a range of estimated ionic strengths and pH values, in discrete time steps and under variable concentrations of CO_2 (p_{CO_2}). This model also briefly considers the nature of potential changes in waste forms following contact with magma.

The sequence and description of the processes listed above represent the general evolution of the processes that would occur if an igneous event were to occur at a repository at Yucca Mountain. Figure 1-1 is a schematic representation of the stages related to an igneous event. The first two stages, "initial encounter" and "magma intrusion," are discussed in the dike propagation model and magma flow analysis. The "eruption" stage addresses the potential for magma to move to the surface and into the atmosphere. This movement to the surface is discussed in the analysis of magma flow in this report, and the eruption into the atmosphere is addressed in the model report *Atmospheric Dispersal and Deposition of Tephra from a Potential Volcanic Eruption at Yucca Mountain, Nevada* (BSC 2004 [DIRS 170026]). The "post-emplacement" stage is captured in the discussions of the gas flow model, magma cooling analysis, and water seepage model. This last stage includes transport of volcanic gases and heat through the rock and through backfilled access drifts separating individual drifts.

The overall concept represented in this model report is that of a dike propagating to the surface and intersecting the repository. If the rising magma encounters the repository drifts, it flows into and down the intersected repository drifts, filling them. This overall concept also takes into consideration the very unlikely scenario of pressurized magma filling the drift then breaking out to the surface along a separate pathway. This scenario is referred to as a "dog-leg" event (magma rises along the dike, flows down the intersected drifts, and then rises to the surface along a secondary dike). The characteristics and properties of magma that are used as input to the analyses and models in this model report are identified and described in the analysis report *Characterize Eruptive Processes at Yucca Mountain, Nevada,* (BSC 2004 [DIRS 169980]). The consequences of the dike intersecting the repository drifts and magma flow into the drifts are addressed in the *Number of Waste Packages Hit by Igneous Intrusion* analysis report (BSC 2004 [DIRS 170001]).

The models and analyses presented in this report support the total system performance assessment (TSPA) igneous intrusion-groundwater transport model case, and the results presented in this model report support the report *Features, Events, and Processes: Disruptive Events* (BSC 2004 [DIRS 170017]) by providing a quantitative description of the FEPs that may result in dike/drift interactions. This report also provides a technical basis for addressing the Nuclear Regulatory Commission's (NRC's) related Key Technical Issues and information needs, and the acceptance criteria of the NRC's *Yucca Mountain Review Plan, Final Report* (NRC 2003 [DIRS 163274]; see Appendix A of this report).

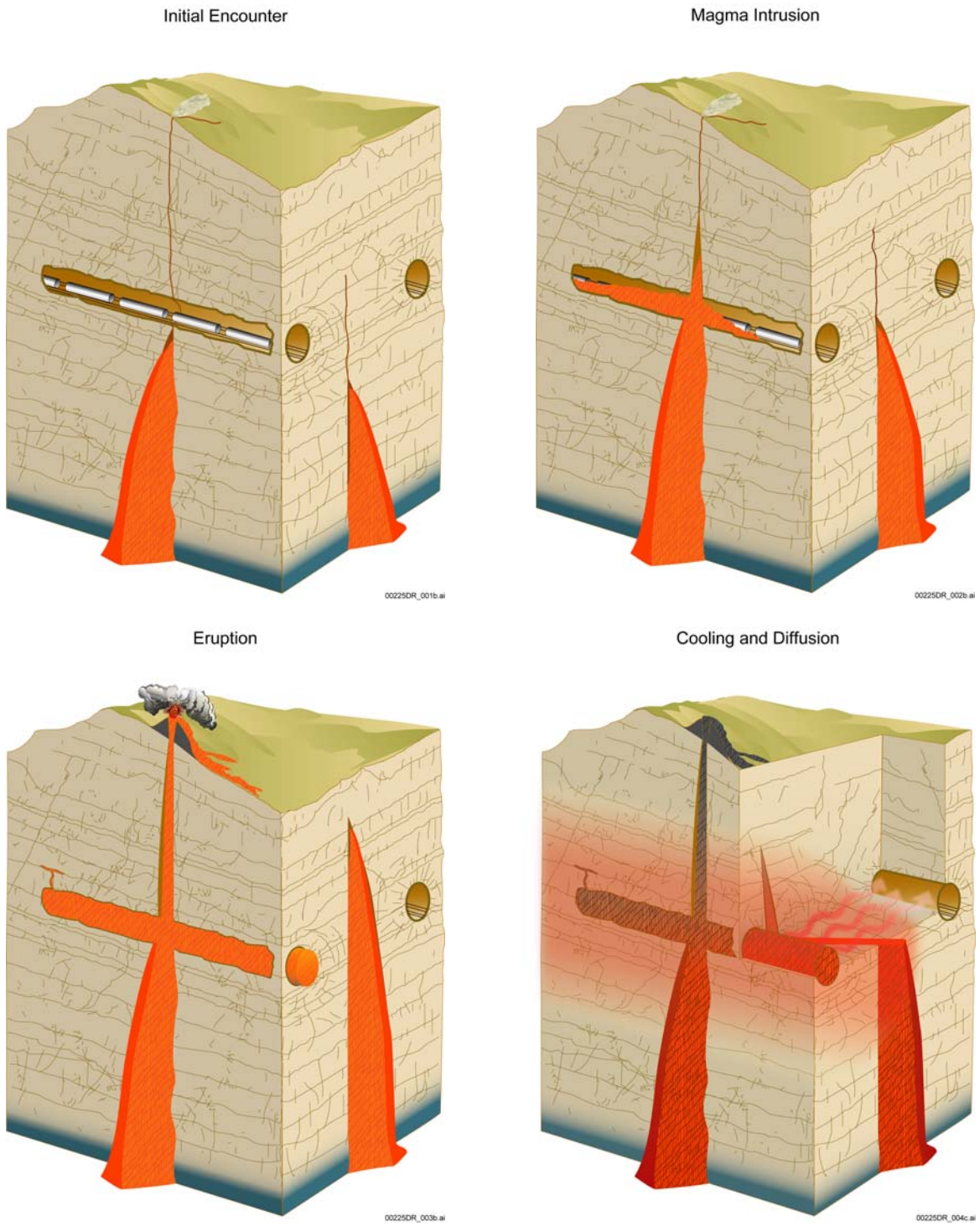

NOTE: For information purposes only.

Figure 1-1. Schematic Representation of the Stages of Interaction Between a Volcanic Dike and Repository Drifts

1.2 DIKE/DRIFT CONCEPTUAL MODEL

1.2.1 Dike Intrusion Submodel

The objective of the dike propagation modeling is to develop a representation of, and input conditions for, assessing the impacts of magma and gas flow within a repository at Yucca Mountain, and to assess the interaction of the magma with the repository drifts, waste packages, and other engineered features. Of particular importance are:

- The manner in which the dike intersects the repository
- The pressure (and pressure history) of the magma and volatiles
- The width of the dike (and thus the amount of magma available to flow into the drifts) as a function of time
- The effect of magma loss into the repository on the aforementioned items.

The dike propagation model component calculates the:

- Pressure conditions and dike parameters that would exist at the point of intersection with the repository for use as initial conditions for the magma flow analysis (Section 6.3.8)
- Effects of in situ and thermally-induced stress fields on the dike (i.e., potential halting or deflection of the dike away from the repository, and increased magma pressures in the dike).

Stress analysis (Section 6.3.7.3) shows that dike deflection, due to the shielding effect of increased horizontal stresses at the repository level, is unlikely, and that the increase in magma pressure is only a fraction of the extra stress.

The model provides support for determining boundary conditions related to dike propagation, including “leak-off” of magma into a drift. The model accommodates changing conditions to which the dike might react along a pathway, including the undisturbed area below the repository, the altered area around the repository, and conditions that would occur as the dike continues upward, after it has passed through the repository.

The magma flow analyses address the interaction of magma with the repository drifts and the flow down the drifts. The analyses describe the conceptual basis and the magmatic products that could occur in drifts, and calculate the conditions that could occur if magma were to enter an emplacement drift. The analyses address:

- The potential for the initiation of new fractures, or the reopening of existing joints around the drift, as a result of pressurized magma within the drift (Section 6.5.1.2)
- Change in stresses adjacent to the repository due to the presence of the dike (Section 6.5.1.3)

- Properties of a possible "dog-leg" dike initiating along a drift at some distance from the original dike/drift intersection (Section 6.5.1.4, 6.5.1.5).

1.2.2 Eruption Stage

This model report addresses the processes related to the propagation of a dike to the surface and the upward movement of magma. The eruption process is addressed in model report *Atmospheric Dispersal and Deposition of Tephra from a Potential Volcanic Eruption at Yucca Mountain, Nevada* (BSC 2004 [DIRS 170026]).

1.2.3 Post-Intrusion Submodel

The gas-flow model addresses the potential migration of volcanic gases through the surrounding tuff to an adjacent drift from a drift that has been filled with basaltic magma. This approach provides the basis for evaluating the potential for corrosion of waste packages by magmatic gases containing gases such as SO_2 and CO_2, as well as chlorine and fluorine species. FEP 1.2.04.04.0A regarding this issue is addressed in Section 6.6, as shown in Table 6-1.

The thermal impacts of a dike intersecting a drift are considered in the conductive cooling model component. One-dimensional radial conductive cooling calculations at variable wall rock temperatures, aqueous wallrock saturations, as well as with and without latent heat of crystallization effects, are considered. This thermal model component supports the analysis report *Number of Waste Packages Hit by Igneous Intrusion* (BSC 2004 [DIRS 170001]) by quantifying the thermal effect of a dike on nearby drifts that have not been intruded. FEP 1.2.04.04.0A regarding this issue is addressed in Section 6.6, as shown in Table 6-1.

The seepage water model component addresses the impacts on seepage water chemistry after a drift-filling magmatic event. As a basalt-filled drift cools, it leads to the formation of shrinkage joints. These fractures represent permeable pathways for water to re-infiltrate drifts. Thus, water flowing into basalt from the surrounding tuff will undergo water-rock reactions, modifying the composition of the water. This model provides a range of pH and ionic strength values to TSPA based on a range of p_{CO_2} values, reaction times, and mineral surface areas for basalt-filled drifts.

A range of potential interactions between magma, waste canisters/assemblies, cladding, and the waste forms is also considered within this report. This report supports the conservative assumption that waste packages and drip shields are immediately and totally compromised in the event of an intrusion.

1.3 BACKGROUND

This version (REV 01) of the *Dike/Drift Interactions* model report enhances the technical basis for its technical outputs for use in other analysis and model reports. It has been revised

consistent with the *Technical Work Plan for Igneous Activity Analysis for Disruptive Events* (TWP) (BSC 2004 [DIRS 171403]) for this activity. The following model reports are direct and indirect users of the output from this model report:

- *Features, Events, and Processes in UZ Flow and Transport* - Direct
- *Features, Events, and Processes: Disruptive Events* - Direct
- *Total System Performance Assessment (TSPA) Model/Analysis for the License Application* - Direct
- *Waste-Form Features, Events, and Processes* - Direct
- *Characterize Framework for Igneous Activity at Yucca Mountain, Nevada* - Indirect
- *Screening Analysis for Criticality Features, Events, and Processes for License Application* - Indirect
- *Characterize Eruptive Processes at Yucca Mountain, Nevada* - Indirect
- *Abstraction of Drift Seepage* - Indirect
- *Number of Waste Packages Hit by Igneous Intrusion* - Indirect

The following model reports are direct and indirect sources to this model report:

- *Drift Degradation Analysis* - Direct
- *Drift-Scale THC Seepage Model* - Direct
- *Thermal Conductivity of the Potential Repository Horizon* - Direct
- *Ventilation Model and Analysis Report* - Direct
- *Characterize Eruptive Processes at Yucca Mountain, Nevada* - Direct
- *Abstraction of Drift Seepage* -Direct
- *Drift-Scale Coupled Processes (DST and TH Seepage) Models* - Direct
- *Engineered Barrier System: Physical and Chemical Environment Model* - Direct
- *Heat Capacity Analysis Report* - Direct.
- *CSNF Waste Form Degradation: Summary Abstraction* - Indirect
- *Dissolved Concentration Limits of Radioactive Elements* - Indirect

- *Geologic Framework Model (GFM2000)* - Indirect
- *Multiscale Thermohydrologic Model* - Indirect
- *Waste Form and In-Drift Colloids-Associated Radionuclide Concentrations: Abstraction and Summary* - Indirect
- *Correction for Analysis of Hydrologic Properties Data* - Indirect
- *Drift Degradation Analysis* - Indirect

1.3.1 Previous Reports

This report represents a major revision to information included in *Dike Propagation Near Drifts* (CRWMS M&O 2000 [DIRS 151552]). It significantly expands the numerical analytical support for the conceptual model of dike/drift interaction. Revision 01 of this report incorporates analyses and results from Revision 01 of *Igneous Impacts on Waste Packages and Waste Forms* (BSC 2004 [DIRS 168960]). This is augmented by new corroborative material to enhance confidence in the results, which are unchanged.

1.3.2 Conceptual Model for Igneous Processes

The analysis report *Characterize Framework for Igneous Activity at Yucca Mountain, Nevada* (BSC 2004 [DIRS 169989]) provides a comprehensive discussion of the conceptual model for igneous activity at Yucca Mountain. The processes presented in this model report are captured in the discussion of the igneous activity conceptual model.

An igneous event begins with ascent from a mantle source of magma as a dike (magma-filled crack), which has a lower density than the surrounding rock. During magma ascent and decompression, which may be interrupted by temporary storage at intermediate levels, volatile gases such as H_2O and CO_2 exsolve, increasing the volume of the magma. The resulting volume expansion drives the basaltic magma farther through the upper few kilometers of crust. Because volatiles are concentrated near the crack tip of the ascending magma, the start of volcanism is typically characterized by pyroclastic eruptions (volcanic explosions and aerial expulsion of clastic rock from a volcanic vent) of gas-rich magma. Based on analog studies, the concentration of volatile species in basalts of the Yucca Mountain region is likely to range from 1 to 4 wt%. This range is higher than in most alkali (sodium/potassium-rich) basalt magmas, possibly because the volatile species originated in small percentages of partial melt of a hydrous lithospheric mantle source. The incompatible, element-enriched (i.e., enriched in elements that more readily separate from mafic igneous melts) nature of these alkali basalts relative to other alkali basalts in the western United States is consistent with these values (BSC 2004 [DIRS 169980]).

Basaltic magma is transported from a region of melting in the earth's mantle to the earth's surface through dikes. In the Yucca Mountain region, dikes are typically 1 to 2 m in width (BSC 2004 [DIRS 169980]) and have an average length of 4 km (BSC 2004 [DIRS 169980]). The longest expected dike length in the Yucca Mountain region is about 10 km. Based on the

regional stress field of the upper crust, dikes are expected to have an orientation that centers on N30°E, although other orientations are possible and are observed within the region (Section 6.3).

Although an ascending dike could be influenced by topographic and/or thermal-mechanical induced stress, the conceptual model described here indicates that the dike propagates through the repository; this is justified in Section 6.2. As the dike approaches the level of the drifts, the crack tip advances ahead of the magma front. When the magma within the dike reaches the level of the repository, magma will be available to flow into drifts. The flow regimes for basaltic magma can be homogeneous with small bubbles moving with the melt, bubbly flow with bubbles rising faster than the melt, or slug flow with bubble sizes approaching the width of the dike. Which flow regime is operative will be a function of many variables including but not limited to moisture content, other gases present, pressure, melt viscosity and surface tension. For example, as the magma first encounters a drift, it may do so under slug flow; as time progresses and the magma front continues up the dike, flow entering the drift may become bubbly. For any of these flow regimes, the dike tip will precede the magma by several seconds to a few hours. Because the entry of magma from the dike into the drift is not necessarily instantaneous with intersection, it is unlikely that dike intersection will result in an abrupt explosion into the drift. At the analog Parícutin volcano, the initial crack broke the surface several hours before the first manifestation of weak pyroclastic eruptions began.

The most likely scenario following dike intersection of repository drifts is that the dike continues to follow the path established by the dike tip and erupts to the surface without being influenced by the presence of the repository. An alternative scenario is that the lateral diversion of magma into drifts results with sufficient pressurization of drifts to propagate a dike to the surface at a location some distance from the site of the initial dike intersection. This alternative scenario could potentially lead to more waste entrained during an eruption compared to the case of conduits developed only above the site of initial dike intersection. The amount of waste potentially entrained in this scenario would depend on the length of drifts that transport magma to the site of the down-drift dike. As shown in Section 6.5, this alternative scenario is highly unlikely.

The rate and degree to which an intersected drift fills with magma depends on variables such as magma rise rate, magma viscosity, and the nature (effusive or pyroclastic) of the flow into the drifts. Magma rise rates between 1 and 15 m/s are investigated, while viscosities range between 10 and 40 Pa·s as presented in *Characterize Eruptive Processes At Yucca Mountain, Nevada* (BSC 2004 [DIRS 169980]).

The potential ascent of dikes and the formation of conduits at Yucca Mountain have been analyzed relative to the configuration of the repository, which consists of approximately 100 waste-emplacement drifts of 5.5-m diameter, spaced 81-m apart, and encompassing a total area of approximately 5 km^2. The number of waste-emplacement drifts intersected would depend on the orientation of a dike system intersecting the repository, the number of dikes in a dike swarm, and the lengths of the dikes lying within the repository footprint.

1.4 LIMITATIONS OF MODELS AND ANALYSES

This section addresses the limitations of the model components and analyses that support the overall dike/drift interaction conceptual model.

1.4.1 Analysis of Natural and Thermal Stresses

The analysis of natural and thermal stresses considers that all material is linear elastic, except that two cohesionless coulomb slip interfaces are used to represent the Ghost Dance and Solitario Canyon faults. Anelastic effects, which are likely to exist in the area, are not considered. This has a very limited impact because the gravitational stresses are statically determined and, therefore, are correctly computed, and because the analyses of horizontal stresses are calibrated using field measurements.

1.4.2 Dike Propagation Model

The ultimate limit of the dike propagation model is that dike propagation at Yucca Mountain has not been observed. Therefore it is necessary to infer behavior from observations of dike intrusion at other sites or from analysis. Dike propagation at other sites has been used to reduce the uncertainty of results in two ways. First, the analysis report *Characterize Eruptive Processes at Yucca Mountain, Nevada* (BSC 2004 [DIRS 169980], Section 6.3, pages 6-5 to 6-34) considered dike propagation as determined by field observation of Plio-Pleistocene volcanic centers in the Yucca Mountain region and in western North America. This analysis has been used to bound the inputs of the present dike propagation model. Second, field observations and post-eruption laboratory studies and analyses of the 1943 eruption of a new volcano in Mexico, which was observed from the first minutes of a crack opening in a cornfield, provide a unique insight into the processes that accompany dike intrusion and eruption at the surface. Taking into account the differences in geologic setting and magma characteristics between Paricutín and the postulated Yucca Mountain event, these insights have been applied to validate the results of the dike propagation model (Section 7.3.1.3).

A principal limitation of the dike propagation model is that it addresses the growth of a dike due to upward movement of an incompressible magma, whereas magma is expected to have varying degrees of compressibility (BSC 2004 [DIRS 169980], pp. 33 to 38). The effect of compressibility was addressed in the *Final Report of the Igneous Consequences Peer Review Panel* (Detournay et al. 2003 [DIRS 169660], pp. 44 to 45), which concluded that the two significant differences resulting from compressibility are "…the substantial increase in the flow velocity at the magma front and the amount by which this exceeds the velocity of the magma front. Both effects increase the gas flux into the cavity relative to the flux out." They conclude that at "…cavity pressures below the dike normal stress (lower by an amount that exceeds the dike excess pressure, so perhaps a few MPa), the tip becomes unstable." Hence, the effect of compressibility would be to increase the tendency for the dike tip to accelerate as it approaches the ground surface. This will increase the likelihood that the crack tip will break through the surface before any magma reaches repository depth.

The uncertainty effect of magma compressibility is approximated in Section 6.3.8.2. That section applies an analysis using results for incompressible magmas of progressively lower

densities at progressively decreasing depths to simulate some aspects of the behavior that would be expected for compressible magma that expanded and accelerated in a continuous manner as it approached the surface and the confining pressure dropped.

Another limitation of the dike propagation model is that viscous behavior of magma flowing in the dike is simplified. The flow of basaltic magma can be homogeneous with small bubbles moving with the melt, bubbly flow with bubbles rising faster than the melt, or slug flow with bubble sizes approaching the width of the dike. Which flow regime is operative will be a function of many variables including properties of the magma itself such as moisture content, other gases present, pressure, melt viscosity and surface tension and properties related to the dike such as its width and the speed of the rising magma. Any of these types of flow may occur in a dike when it approaches the surface. The approach taken in the dike propagation model is to use mathematical expressions that are based on Newtonian viscosity, with the value of the viscosity selected to be appropriate for the magma and flow regime expected. In some instances, results are presented for multiple viscosity values when it is desirable to highlight the effects of uncertainty in viscosity.

A number of other limitations are embedded in the model, including that the host rock behaves elastically and linearly and is a homogeneous, isotropic material and that the dike is a single fracture and the free surface is horizontal. The effect of these limitations is discussed in Section 6.3.2, and shown to be insignificant.

1.4.3 Analysis of Magma Flow

The limitations of the analysis of magma flow into drifts are, for the most part, the same as the ones for magma propagation from depth. An important analysis limitation is that it treats the magma as a single incompressible phase (Section 1.4.2). The processes and effects associated with expansion of bubbly or pyroclastic flow into a drift were not modeled. Therefore, the interaction between compressible phase (pyroclastic) magma and the drifts, and between the pyroclastic phase magma and repository components, has not been evaluated. However, the analysis of single-phase flow demonstrates that the drifts fill with magma within minutes and that all the waste packages within the intersected drifts will be engulfed in the magma (Section 6.4.5). Under these conditions the performance of the waste packages and their contents is compromised (Section 6.4.8); therefore, the analysis of single-phase flow bounds the impacts to the waste package and waste form.

The analysis used to quantify the interaction of magma intrusion with waste packages in Section 6.4.8 is limited in its use of a constant viscosity, whereas the viscosity of silicate liquids increases rapidly with falling temperatures. This will result in overestimating the rate of magma intrusion into waste packages. An uncertainty exists with the alteration of waste forms, both glass and spent fuel, by interaction with magma. Little or no direct information on waste-form-magma interactions is available. This uncertainty in possible phase changes results in a range of secondary oxide and silicate phases, as discussed in Section 6.4.8.

The analysis of the movement of waste packages by magma front pressure is limited by lack of a well-defined relationship between magma density and magma viscosity for highly extended (50 to 75 percent vesicles) and fragmented (>75 percent vapor by volume) pyroclastic phase

magma (Section 6.4.8.2). This results in an increased level of uncertainty in the possible movement of waste packages. Under these extreme conditions and with velocities on the order of tens of meters per second, waste packages could possibly move (Section 6.4.8.2) within the drifts; however, analyses show that the conditions necessary to move waste packages as suggested in the Woods et al. (2002 [DIRS 163662]) scenario are not credible (Section 6.5.4).

1.4.4 Secondary Dike Analysis

A limitation of the secondary dike analyses is similar to those of the magma flow analyses. These analyses treat the magma flowing through a secondary crack as though it were a single incompressible phase, whereas sustained two-phase, pyroclastic type flow is likely to occur during an igneous event. Nevertheless, the uncertainty in the consequences of a secondary dike propagating to the surface and distributing radioactive waste on the surface of the earth, is captured within the distribution of the number of waste packages hit in a volcanic eruption through the repository (BSC 2004 [DIRS 170001] Section 8).

1.4.5 Drift Scale Gas Flow Analysis

For the purposes of this analysis, the chief limitations are the:

- Degree to which the dual permeability capability of TOUGHREACT (LBNL 2002 [DIRS 161256]) represents the true permeability structure of the mountain

- The initial drift temperature is set to 500°C, which is much lower than the initial magma temperature (about 1,100°C); the effect of this limitation is minimal (Section 6.6).

- Degree to which kinetic rate laws and data, reactive surface areas, and thermodynamic data (Section 6.6) capture the overall rate of geochemical reactions. For gas transport, though, several years of data from the Drift-Scale Test validate the transport of CO_2 in the repository host rock, under elevated temperature conditions, and at a similar time scale to the cooling of a dike.

- Degree to which initial mineralogy, gas chemistry, and pore water chemistry are representative of Yucca Mountain. Solubilities of the volcanic gases are little affected by the range in initial water and rock chemistry, since the condensation zone that impedes transport in the fracture system is created by steam generated by boiling of matrix pore water.

1.4.6 Basalt Cooling and Solidification Model

Cooling calculations are limited by parameter uncertainty representing the thermal diffusivity of basalt and host rock, as well as changes in this parameter as a function of temperature. Cooling calculations are also limited by the manner in which they represent and implement the latent heat of crystallization. However, validation studies documented in Section 7.3.2 indicate that these limitations are of little consequence to model predictions.

1.4.7 Basalt/Water Seepage Model

Calculations of the change in seepage chemistry due to interactions of pore water with basalt in magma-filled drifts are also uncertain. For example, mineral dissolution reaction rates depend, in part, on knowledge of the surface area of minerals available for reaction, a parameter that is unknown and perhaps unknowable in this application. Yet, comparison with natural analog waters (waters sampled and analyzed from basalt aquifers) indicates that model output reported here is conservative because the range of predicted water compositions is more aggressive than that of analog waters.

2. QUALITY ASSURANCE

Development of this model report and the supporting activities have been determined to be subject to the Yucca Mountain Project's Quality Assurance program (BSC 2004 [DIRS 171403]). Approved quality assurance procedures identified in the TWP (BSC 2004 [DIRS 171403], Section 4) have been used to conduct and document the activities described in this model report. The TWP also identifies the methods that have been used to control the electronic management of data (BSC 2004 [DIRS 171403], Section 8.4). Unqualified data will be qualified within this report in accordance with AP-SIII.10Q and AP-SIII.2Q, *Qualification of Unqualified Data*, as appropriate. See Appendix G for further documentation.

The model report discusses phenomena associated with a potential volcanic intrusion into the drift complex of the repository. This model report examines potential alterations to engineered barriers that are classified in the *Q-List* (BSC 2004 [DIRS 168361]) as "Safety Category" because they are important to waste isolation, as defined in AP-2.22Q, *Classification Analyses and Maintenance of the Q-List*. The report contributes to the analysis and modeling data used to support performance assessment. The conclusions do not directly impact engineered features important to safety, as defined in AP-2.22Q.

INTENTIONALLY LEFT BLANK

3. USE OF SOFTWARE

3.1 SOFTWARE TRACKED BY CONFIGURATION MANAGEMENT

The computer codes used directly in this modeling activity are summarized in Table 3-1. All software except exempt software (Section 3.2) was fully qualified. All software was obtained from configuration management and is appropriate for the application. Qualified codes were used only within the range of validation, and have no limitations on their output within their intended use.

Table 3-1. Computer Software

Software Title and Version (V)	Software Tracking Number	Code Usage and Limitations	Computer, Type, Platform
NPHF2D V1.0 (BSC 2002 DIRS 163665])	10904-1.0-00	Dike Propagation Model; performs numerical modeling supporting analysis of magmatic dike propagation and analysis of the dike/drift interaction where magma enters a drift, modified and requalified for this task. This code was developed specifically for fracture propagation to the surface; no other code can evaluate the number of physical phenomena required.	PC; Windows; LAN
TOUGHREACT V3.0 (LBNL 2002 [DIRS 161256])	10396-3.0-00	Drift-Scale Gas Flow Model simulations; couples multiphase fluid flow, heat flow, aqueous and gaseous species transport, and kinetic and equilibrium mineral-water-gas reactions	DEC-Alpha with Unix OSF1 V5.1 and OSF1 V5.0, Sun Solaris 5.5.1, Linux Redhat 7.2
FLAC3D V2.1 (BSC 2002 [DIRS 161947])	10502-2.1-00	This is commercially available software that is used for a very broad range of geomechanical problems including hydraulic, mechanical, and thermal coupling. It is the preferred code to analyze regional stresses, accounting for topography; and opening of pre-existing fractures by magma.	PC Windows 2000/NT 4.0
FLAC3D V2.14 (BSC 2004 [DIRS 172323])	10502-2.14-00	This is commercially available software that is used for a very broad range of geomechanical problems including hydraulic, mechanical, and thermal coupling. It is the preferred code to analyze regional stresses, accounting for topography; and opening of pre-existing fractures by magma.	PC Windows 2000
EQ3/6 V7.2b (CRWMS-M&O 1999 [DIRS 153964])	LLNL: UCRL-MA-110662	Aqueous solubility and speciation code. This code was used because it was qualified for use on the Project for the purpose intended. EQ3/6 includes the component EQ3NR that is discussed in Sections 4 and 6 of this document.	Dell Optiplex GX300 Windows 95
EQ3/6 V8.0 (BSC 2003 [DIRS 162228])	10813-8.0-00	Software used to simulate acid gas generation and fugacity.	PC w/Windows 95/98/2000/NT 4.0
EQ6 V7.2bLV (CRWMS-M&O 1999 [DIRS 127275])	10075-7.2bLV-00	Reaction path code for the calculation of water chemistry produced by reaction of seepage water with basalt. This code was used because it was qualified for use on the Project for the purpose intended. This code is part of the EQ3/6 software package.	Dell Optiplex GX300 Windows 95

Table 3-1. Computer Software (Continued)

Software Title and Version (V)	Software Tracking Number	Code Usage and Limitations	Computer, Type, Platform
ASPRIN (BSC 2001 [DIRS 155712])	10487-1.0-00	Post-processing of EQ6 output. This code was used because it was qualified for use on the Project for the purpose intended.	Dell Optiplex GX300 Windows 95
UDEC V3.1 (BSC 2002 [DIRS 161949])	10173-3.1-00	Analyzes opening of pre-existing fractures by magma. This is the only code available for hydromechanic behavior of fracture media.	PC WINDOWS 2000/NT 4.0
UDEC V3.14 (BSC 2004 [DIRS 172322])	10173-3.14-00	Analyzes opening of pre-existing fractures by magma. This is the only code available for hydromechanic behavior of fracture media.	PC Windows 2000

Source: Output data calculation.

3.2 EXEMPT SOFTWARE

Standard, built-in functions of Microsoft Excel 2000 for the Dell Inspiron 8000 and Dell Optiplex computers or Microsoft Excel 97 for the Compaq V900 computer were used to calculate some parameters. Excel is used to support calculations in Sections 6.2, 6.3, 6.4, 6.5, 6.6, 6.8, and 7.3. Also, Mathematica V4.2.0.0 is used for the 3-D magma flow calculation in Section 6.4. This software is exempt from the software validation requirements contained in LP-SI.11Q, *Software Management*. The formulas, inputs and outputs of those formulas, and additional information required for an independent technically qualified person to verify the results of analyses using exempt software are provided in Section 6 and the data tracking numbers (DTNs) listed in Table 8-1.

3.3 USE OF UNQUALIFIED SOFTWARE

Two unqualified software codes were used to develop preliminary output from this model report: FLAC3D V2.1 (BSC 2002 [DIRS 161947]) and UDEC V3.1 (BSC 2002 [DIRS 161949]). Although these codes are listed on the configuration management report, they were used outside their validation range. These software codes have subsequently been qualified for the intended use and limitations as UDEC V3.14 (BSC 2004 [DIRS 172322]) and FLAC3D V2.14 (BSC 2004 [DIRS 172323]), as discussed in Table 3.1.

All of the analyses that produced the preliminary output were rerun using the qualified software versions listed in Table 3.1. Comparisons of the output data were made and the results were found to be identical. The comparisons were made using the following methods. The evaluation identified 2 files that had minor differences (less than 1 percent) in the resulting output. The apparent reason for the differences was determined to be the result of interruptions during the running of the code in the preliminary runs. Per the requirements of AP-SIII.10Q, the DTNs containing the preliminary output have been superseded with the output from the qualified software.

4. INPUTS

4.1 DATA, PARAMETERS, AND OTHER MODEL INPUTS

This subsection identifies all input parameters and other forms of model inputs that are used in the analyses detailed in this report.

Input information used in this model report comes from several sources, which are summarized in Table 4-1. The data are fully appropriate for the discussion of dike/drift interactions in this model report. The qualification status of the input sources is provided in DIRS and documented in the Technical Data Management System (TDMS) for DTNs. The status of the input information quality may be confirmed by review of the DIRS database. The data from external sources have been justified per the requirements of AP-SIII.10Q, and are considered to be qualified for intended use. These justifications are documented in Appendix G.

4.1.1 Data and Parameters

The input parameters for this model report are listed in Table 4-1. Input parameters from DTN: LB0302DSCPTHCS.001 [DIRS 164744] for the gas flow model are found in the model report *Drift-Scale THC Seepage Models* (BSC 2004 [DIRS 169856]). Inputs for the thermo-mechanical analysis in Sections 6.2.4 and 6.3.7.3 can be found in *Drift Degradation Analysis* (BSC 2004 [DIRS 166107]).

In many cases where a single value is given for a parameter, the value has been selected as a single value that is within the range of values in the cited document. Where the results of the input are not sensitive to the exact value of the input parameter, values may have been rounded while staying in the appropriate range. Uncertainties of the parameters are addressed in Section 6 (as noted in Column 3 of Table 4-1).

Table 4-1. Input Parameters Used in Dike/Drift Interaction Conceptual Model

Model or Analysis Parameter	Source	Section or Table where Discussed
Atomic weights of elements	Parrington et al. 1996 [DIRS 103896]	Table 4-4, 4.1.1.4.2
Stress concentrations around circular drift.	Jaeger and Cook 1979 [DIRS 106219], Section 10.4, pp. 249-254	6.2.3
Density of minerals	Roberts et al. 1990 [DIRS 107105]	Table 4-4, Table 4-6
Bulk density of host rock	DTN: SNL02030193001.027 [DIRS 108410]	6.3.5, Table 6-2; 6.3.7.3, Table 6-5, Table 6-6,
Dissolution of anorthite and enstatite	Brady and Walther 1989 [DIRS 110748]	Table 4-4, Table 4-7, Table 4-8
Poiseuille law formulation for case of flow between parallel plates	Bird, Stewart, and Lightfoot (1960 [DIRS 103524])	Section 6.4.2
Fluoride concentrations from basaltic aquifers	Hearn et al. 1985 [DIRS 166893 Hem 1985 [DIRS 115670] White et al. 1980 [DIRS 163752]	6.8.3
Equation for gaseous diffusion coefficient	Lasaga 1998 [DIRS 117091], p. 322	6.6.3.6

Table 4-1. Input Parameters Used in Dike/Drift Interaction Conceptual Model (Continued)

Model or Analysis Parameter	Source	Section or Table where Discussed
Molecular diameter for CO_2	Lide, D.R., ed. 1993 [DIRS 123032]	6.6.3.6
Dissolution of Magnetite and Ilmenite	White et al. 1994 [DIRS 131014]	Table 4-4, Table 4-9
Horizontal stress vs. depth	DTN: SNF37100195002.001 [DIRS 131356]	6.2.2
Ratio of horizontal stress vs. vertical stress	DTN: SNF37100195002.001 [DIRS 131356]	Table 6-2; 6.3.7.1, Table 6-5, Table 6-8, Table 6-15
Expression of mean system performance in terms of component variables.	Hahn, G.J. and Shapiro, S.S. 1967 [DIRS 146529]	Appendix C, Eq. C-14
Relationship for variance when higher order moments not used.	Hahn, G.J. and Shapiro, S.S. 1967 [DIRS 146529]	Appendix C, Eq. C-15
J-13 well water	DTN: MO0006J13WTRCM.000 [DIRS 151029]	Table 4-4, Table 4-12, 6.8.4.1
Equation for one-dimensional unsteady heat conduction	Chapman 1974 [DIRS 152938], p. 137	4.1.1.1, Appendix C1
Dissolution of albite	Chou and Wollast 1985 [DIRS 160182]	Table 4-4, Table 4-7
Thermodynamic data for aqueous species: equilibrium constants and molecular weights	DTN: MO0302SPATHDYN.000 [DIRS: 161756]	4.1.1.4.1
Equation for finite difference expression approximations to first and second order derivatives for the radial heat conduction	Carnahan et al. 1990 [DIRS 163096], p. 462	4.1.1.1, Appendix C, Eq. C-2
Dissolution of diopside	Brantley and Chen 1995 [DIRS 163275]	Table 4-4, Table 4-8, Figure B-6, Table B-3
Dissolution of nepheline	Tole et al. 1986 [DIRS 163289]	Table 4-4, Table 4-7, Table B-1
Dissolution of olivine	Wogelius and Walther 1991 [DIRS 163290]	Table 4-4, Table 4-8, Table B-2
Gravitational constant	Incropera and De Witt 2002 [DIRS 163337]	Table 6-2, Table 6-6
Density and specific heat of water	Incropera and De Witt 2002, p. 294, Table A-6 [DIRS 163337]	Table 4-2, Appendix C, Eq. C-10
Rock heat capacity	DTN: SN0307T0510902.003 [DIRS 164196]	Table 4-2, Table 4-3, Table C-1
Thermodynamic data, Kinetic data, Diffusion coefficient data	DTN: LB0302DSCPTHCS.001 [DIRS 164744]	4.1.1, 6.6
Magma properties for pyroclastic flow	Heiken et al. P. 4346, Figure 10 [DIRS 165566]	Table 6-15, 6.5.2.3
Flux rate	DTN: LB0310AMRU0120.001 [DIRS 166409]	Table 4-4, Table 4-11, Table 6-21, 6.8.1
Bin 8 seepage water	DTN: MO0310SPAEBSCB.003 [DIRS 166411]	Table 4-4, 4.1.1.2.4, Table 4-10, 6.8.1, 6.8.4.1
Bin 11 seepage water	DTN: MO0310SPAEBSCB.003 [DIRS 166411]	Table 4-4, Table 4-12, 6.8.4.1
Dissolution of Hydroxylapatite	Valsami-Jones et al. 1998 [DIRS 166412]	Table 4-4, Table 4-9

Table 4-1. Input Parameters Used in Dike/Drift Interaction Conceptual Model (Continued)

Model or Analysis Parameter	Source	Section or Table where Discussed
Drift diameter	BSC 2004 [DIRS 168489]	Table 6-6, 6.7.1.2
Drift spacing	BSC 2004 [DIRS 168489]	Table 6-6, 6.7.1.2
Overburden depth	BSC 2004, Section 7.7.5.2 [DIRS 166107]	6.5.2.1, Table 6-8, Table 6-15
Young's modulus of host rock	Detournay et al. 2003, Table 1-2 [DIRS 169660]	Table 6-2; Table 6-5, Table 6-6, Table 6-9, Table 6-15
Poisson's ratio of host rock	Detournay et al. 2003, Table 1-2 [DIRS 169660]	Table 6-2, Table 6-9
Fracture toughness of host rock	Detournay et al. 2003, Table 1-2 [DIRS 169660]	Table 6-2
Bulk density of magma	Detournay et al. 2003, Figure 2-1e [DIRS 169660]	Table 6-2, Table 6-5, Table 6-6, Table 6-10
Bulk viscosity of magma	Detournay et al. 2003, Figure 2-1e [DIRS 169660]	Table 6-2, Table 6-5, Table 6-6, Table 6-10
Magma rise velocity	Detournay et al. 2003, p. 56 [DIRS 169660]	Table 6-6
Magma thermal diffusivity	Detournay et al. 2003, Table 1-2 [DIRS 169660]	Table 6-11, Table D-1
Effective solidification temperature (Ts)	Detournay et al. 2003, Table 2E [DIRS 169660]	6.5.1.4.1; Table 6-11
Specific heat of magma	Detournay et al. 2003, Table 1-2 [DIRS 169660]	Table 6-11
Latent heat of magma	Detournay et al. 2003, Table 1-2 [DIRS 169660]	Table 6-11, Table D-1
Solid fraction vs. temperature	Detournay et al. 2003 [DIRS 169660], Table 2E	6.5.1.4, 6.5.1.4.1
Thermal conductivities, porosity, and density of rock units	BSC 2004 [DIRS 169854], Table 7-10	Table 4-2, Table 4-11 Table C-1
Equation for grain density of solids	BSC 2004 [DIRS 169854], p. 41, Equation 6-4	4.1.1.1, Appendix C, Eq. C-11
Pore fractions	BSC 2004 [DIRS 169854]	Tables 4-4, 4-5, 4-11
Temperature	BSC 2004 [DIRS 169856], Table 6.2-1	Table 6-16
pH	BSC 2004 [DIRS 169856], Table 6.2-1	Table 6-16
Pore-water composition	BSC 2004 [DIRS 169856], Table 6.2-1	Table 6-16
Gas composition	BSC 2004 [DIRS 169856], Table 6.2-1	Table 6-16
Numerical mesh	BSC 2004 [DIRS 169856] Figure 6.5-1 and Figure 6.5-2	6.6.3.1, Figures 6-83, 6-84
Host rock mineralogy	BSC 2004 [DIRS 169856]	6.6.3.3
Saturation	BSC 2004 [DIRS 169856]	Tables 4-4, 4-5, 4-11
Infiltration rate	BSC 2004 [DIRS 169565]	6.6.4.1
Mean and Standard Deviation values for uncertainty analysis (Delta Method)	BSC 2004 [DIRS 169862]	Table 4-2, Table C-3
Equation for volumetric heat capacity	BSC 2004 [DIRS 169862]	4.1.1.1, Appendix C1, Eq. C-8
Thermal properties of unsaturated zone model layers	DTN: LB0402THRMLPRP.001 [DIRS 168481]	6.6.3.5
Equation of state of water	Babcock & Wilcox 1963 [DIRS 170614]	6.5.2.3
Thermal stress	DTN: MO0407SPAMTSHR.000 [DIRS 170679]	6.2.4, Figures 6-5, 6-6, 6-7

Table 4-1. Input Parameters Used in Dike/Drift Interaction Conceptual Model (Continued)

Model or Analysis Parameter	Source	Section or Table where Discussed
Intrusion temperature	DTN: LA0407DK831811.001 [DIRS 170768]	4.1.1.1, 6.4.8.1, Table 6-11, Appendix C
Crystal-free viscosity	DTN: LA0407DK831811.001 [DIRS 170768]	Table 6-11
Gas composition	DTN: LA0407DK831811.001 [DIRS 170768], Table 7	6.6.3.4
Basaltic composition in oxides	DTN: LA0407DK831811.001 [DIRS 170768], Table 6	Table 4-4, 4.1.1.2.2, 6.8.4.1, Table 4-5

4.1.1.1 Inputs to Thermal Calculations

A summary of input data and parameters used in the cooling model and related analyses for cooling calculations is presented in Table 4-2.

Table 4-2. Summary of Input Parameters and Data for Thermal Calculations

Model Component	Input	Reference Document
Intrusive heat flow	Thermal conductivities, porosity and density of rock units (Values in Table 4-3 of this report)	BSC 2004 [DIRS 169854], Table 7-10
	Mean and Standard Deviation values for uncertainty analysis (Delta Method)	BSC 2004 [DIRS 169862]
	Heat capacity	DTN: SN0307T0510902.003 [DIRS 164196]
	Density & specific heat of water	Incropera and DeWitt 2002, p. 924, Table A.6 [DIRS 163337]

The primary thermal conductivity statistics used for thermal calculations are contained in Table 4-3.

Table 4-3. Summary of Primary Thermal Conductivity Statistics

Stratigraphic Unit	[a]Bulk Dry Rock Mass Thermal Conductivity, k_{rm} W/(m·K)	[a]Bulk Wet Rock Mass Thermal Conductivity, k_{rm} W/(m·K)	[a]Matrix Porosity ϕ_m	[b]Lithophysal Porosity, ϕ_l	[a]Dry Bulk Density, ρ_{bd} (kg/m^3)	[b]Heat Capacity of Solids, C_p J/(g·K)
Tptpul	1.18	1.77	0.17	0.12	1830	0.93
Tptpmn	1.42	2.07	0.13	0.03	2150	0.93
Tptpll	1.28	1.89	0.15	0.09	1980	0.93
Tptpln	1.49	2.13	0.11	0.03	2210	0.93

Sources: [a] BSC 2004 [DIRS 169854], Table 7-10.
[b] DTN: SN0307T0510902.003 [DIRS 164196].

NOTE: Porosity is the ratio of void volume to total rock volume, and has units of m^3 void/m^3 rock.

Heat flow equations and maximum magmatic temperatures were taken from the following sources:

- Equation for one-dimensional unsteady heat conduction in a rod model, subject to constant heat content (Chapman 1974 [DIRS 152938], p. 137)
- Equation for finite difference expression approximations to first and second order derivatives for the radial heat conduction (Carnahan et al. 1990 [DIRS 163096], p. 462)
- Equation for volumetric heat capacity (BSC 2004 [DIRS 169862])
- Equation for grain density of solids (BSC 2004 [DIRS 169854], p. 41, Equation 6-4)
- Liquidus temperature of intruding magma = 1046 to 1169°C (DTN: LA0407DK831811.001 [DIRS 170768]).

The sources for the conductivity, porosity, dry bulk density and heat capacity are listed in Table 4-2, and the temperature of the intruding magma are appropriate input for this report because they come from project work conducted specifically for the purpose of gathering this type of information, and were completed under the same quality program. The use of the equations in *Heat Transfer* (Chapman 1974 [DIRS 152938]) and *Applied Numerical Methods* (Carnahan et al. 1990 [DIRS 163096]) for the heat conduction model are appropriate because they are well-accepted heat transfer handbooks. For simplicity, the model for one-dimensional flow is an idealized concept of heat transfer, but it is conservative because it predicts the maximum radial heat flow by neglecting axial flow. The equations for volumetric heat capacity and grain density are appropriate input for this report because they come from project documents completed under the same quality program.

4.1.1.2 Inputs Into Seepage Chemistry Calculations

A summary of input data and parameters used in the model of seepage water interaction with basalt model and related analyses is presented in Table 4-4. Additional details of all input data are given below.

Table 4-4. Summary of Input Parameters and Data for Seepage Chemistry

Use of Parameter	Parameter	Reference
Reaction of seepage water with cooled basalt in EQ6	Dissolution of nepheline	Tole et al. 1986 [DIRS 163289]
	Dissolution of albite	Chou and Wollast 1985 [DIRS 160182]
	Dissolution of anorthite and enstatite	Brady and Walther 1989 [DIRS 110748]
	Dissolution of olivine	Wogelius and Walther 1991 [DIRS 163290]
	Dissolution of diopside	Brantley and Chen 1995 [DIRS 163275]
	Dissolution of Hydroxylapatite	Valsami-Jones et al. 1998 [DIRS 166412]

Table 4-4. Summary of Input Parameters and Data for Seepage Chemistry (Continued)

Use of Parameter	Parameter	Reference
Reaction of seepage water with cooled basalt in EQ6 (Continued)	Dissolution of Magnetite and Ilmenite	White et al. 1994 [DIRS 131014]
	Basaltic composition in oxides	DTN: LA0407DK831811.001 [DIRS 170768]
	Density of minerals	Roberts et al. 1990 [DIRS 107105]
	Atomic weights of elements	Parrington et al. 1996 [DIRS 103896]
	Pore fractions	BSC 2004 [DIRS 169854]
	Flux rate	DTN: LB0310AMRU0120.001 [DIRS 166409]
	Saturation	BSC 2004 [DIRS 169856]
EQ3 input water compositions	Bin 8 seepage water	DTN: MO0310SPAEBSCB.003 [DIRS 166411]
	Bin 11 seepage water	DTN: MO0310SPAEBSCB.003 [DIRS 166411]
	J-13 well water	DTN: MO0006J13WTRCM.000 [DIRS 151029]

4.1.1.2.1 Inputs for EQ6 Simulation of Water/Basalt Reaction Hydrochemistry

For EQ3/6 calculations, the incoming water composition is run through EQ3NR. The output composition from EQ3NR then becomes part of the EQ6 input file. In addition to the incoming water composition provided through EQ3NR, EQ6 also requires surface area, moles, and reaction rate (in this case, TST rates) of reactants (minerals) as inputs. These inputs were calculated through spreadsheet analysis and are presented in Section 6.8.1. Direct inputs that feed those spreadsheet analyses are presented in this section.

4.1.1.2.2 Composition of Intruded Basalt Material

The base case chemical composition of basalt and included 1 sigma uncertainties in Table 4-5 serve as the basis for the calculations of basalt/water interaction. This composition was derived in DTN: LA0407DK831811.001 [DIRS 170768] through analysis of 45 samples taken from the Lathrop Wells Cone. The Lathrop Wells Cone is the youngest volcanic center in the Yucca Mountain region, and, therefore, is considered an adequate analog for the composition of a possible igneous intrusion into Yucca Mountain. The densities of normalized minerals (mineral species calculated in *basalt-separated.xls* in Appendix E, Disc 1) are included in Table 4-6, and come from a handbook data source and are considered appropriate for use in the model. The normalized mineralogy used for EQ6 calculations are located in Section 6.8.1. The methodology used for the normative calculation for the conversion of major element composition to a suite of idealized endmember minerals is from McBirney (1993 [DIRS 163334]) and is discussed in Section 6.8. The saturation values chosen are those for the maximum and minimum saturation found in BSC 2004 ([DIRS 169856] Table 6.4-1). Saturation values are discussed further in Section 4.1.1.2.4. A high pore saturation allows maximum exposure of water with the basalt.

Effects of pore fraction on water chemistry were investigated in the EQ6 calculation (as indicated in Section 6.8), and were part of the abstracted values in Table 6-25.

Table 4-5. Mean Composition of Lathrop Wells basalt and Associated Uncertainties (1σ)

Basalt Composition[a]			
Oxide	**Mean Wt%**	**Oxide**	**Mean Wt%**
SiO_2	48.5±0.58	K_2O	1.84±0.04
Al_2O_3	16.74±0.22	TiO_2	1.93±0.06
Fe_2O_3	1.74±0.03	P_2O_5	1.22±0.03
MgO	5.83±0.11	MnO	0.17±0.00
CaO	8.6±0.22	FeO	8.9±0.17
Na_2O	3.53±0.09	**Total**	99
Pore fraction = 0.17 [b]			
Saturation = 0.12 [c]			

Sources: [a] DTN: LA0407DK831811.001 [DIRS 170768], Table 6.
[b] BSC 2004 [DIRS 169854], Table 7-10.
[c] BSC 2004 [DIRS 169856], Table 6.4-1.

Table 4-6. Mineral Densities

Mineral	Density (g/cm^3)	Mineral	Density (g/cm^3)
Anorthite	2.74-2.76 (p. 32)	Fayalite	4.32 (p. 268)
Albite	2.60-2.63 (p. 12)	Forsterite	3.275 (p. 291-292)
Nepheline	2.55-2.665 (p. 603)	Hedenbergite	3.50-3.56 (p. 353)
Sanidine	2.56-2.62 (p. 754)	Enstatite	3.209-3.431 (p. 250)
Magnetite	5.175 (p. 515)	Hydroxylapatite	3.08 (p. 389)
Ilmenite	4.72 (p. 394)		

Source: Roberts et al. 1990 [DIRS 107105].
NOTE: All density values are for measured density.

The minerals indicated in Table 4-6 were derived from the normative mineralogy resulting from the major element composition presented in Table 4-5.

4.1.1.2.3 Dissolution Rates of Basalt Minerals

The dissolution rates of minerals come from various peer-reviewed literature sources and are presented in Tables 4-7, 4-8, and 4-9. These values are used in Microsoft Excel spreadsheets (see Appendix E) to calculate EQ6 dissolution rates for minerals. All of the values for mineral dissolution were obtained through experiments specifically designed to determine the dissolution rates of the minerals in question, which is the intended use of the data in this report. Data are reported over a wide range of pH, often from 2 to 12, such that they encompass the full range of geochemical conditions expected in the repository, and where data are lacking across the full range of pH, reasonable extrapolations were performed. Also, all references come from top-tier peer-reviewed sources such as: Chemical Geology, Geochimica et Cosmochimica Acta, The American Journal of Science, and The Mineralogical Society of America Reviews in Mineralogy series (AP-SIII-10Q, Section 5.2.1k, "reliability of data source") and provide data from

experiments developed and carried out specifically to determine dissolution rates of minerals (AP-SIII-10Q, Section 5.2.1k, "extent to which the data demonstrates the properties of interest"). Therefore, the data are clearly in compliance with the requirements of AP-SIII-10Q, and are considered appropriate and qualified for use in this model.

Table 4-7. Dissolution Rates of Aluminosilicate Minerals

Albite[a]		Anorthite[b]		Nepheline[c]	
pH	Log DR (moles/cm^2·s)	pH	Log DR (moles/cm^2·s)	pH	DR (moles/m^2·s)
1.2	-14.25	3	-13.3	3	4.03E-07
2.1	-14.60	3	-13.9	5	4.00E-09
2.5	-14.86	3.1	-13.0	7	2.07E-09
2.95	-15.26	3.25	-13.5	11	1.28E-08
3.05	-15.18	3.5	-14.3	—	—
3.5	-15.44	4	-15.0	—	—
4.1	-15.50	4.5	-15.2	—	—
5.1	-15.82	5	-15.5	—	—
5.4	-15.78	5.5	-15.5	—	—
5.5	-15.68	5.5	-15.6	—	—
5.6	-15.82	6	-15.7	—	—
5.6	-15.92	6	-15.0	—	—
7.8	-15.86	6	-14.8	—	—
8	-15.70	6.5	-15.7	—	—
9.45	-15.30	7	-15.7	—	—
9.55	-15.22	7.25	-15.6	—	—
10	-15.18	9.5	-14.8	—	—
10	-15.04	10	-14.7	—	—
10.7	-15.00	12	-14.2	—	—
11.2	-14.60	—	—	—	—
11.6	-14.64	—	—	—	—
12.3	-14.40	—	—	—	—

Sources: [a] Chou and Wollast 1985, [DIRS 160182] Figure 5.
[b] Brady and Walther 1989, [DIRS 110748] Figure 4.
[c] Tole et al. 1986, [DIRS 163289] Table 2 (based on release of sodium).

NOTES: Due to lack of dissolution rates of sanidine, the rates for albite are used as a surrogate.

Units are those reported by the source document. Note that nepheline units are different from others (1 mole/m^2·s = 10^{-4} mole/cm^2·s).

DR = dissolution rate

Table 4-8. Dissolution Rates of Olivine and Pyroxene Minerals

Olivine[a]		Diopside[b]		Enstatite[c]	
pH	Log DR (moles/cm^2·s)	pH	Log DR (moles/cm^2·s)	pH	Log DR (moles/cm^2·s)
4.1	-13.07	2.4	-12.30	1	-12.30
5.7	-13.78	3	-12.60	2	-13.00
12	-14.36	4	-13.30	4	-14.30
10.4	-14.74	4.5	-13.90	6	-15.15
7.4	-13.80	5	-14.10	8.4	-15.20
9.9	-14.46	5.6	-14.50	9.4	-14.95
9.9	-14.58	6	-14.80	10.1	-14.40
9.9	-14.38	6	-14.90	12.2	-13.60
3.7	-12.27	7.6	-15.00	—	—
10.8	-15.27	9.4	-15.20	—	—
3	-12.79	12.1	-15.20	—	—
5	-12.73	1	-13.50	—	—
5.7	-14.34	1.5	-12.10	—	—
2	-11.99	2	-12.20	—	—
9.1	-14.54	1	-12.20	—	—
3.7	-12.31	—	—	—	—
2.5	-12.21	—	—	—	—
4.4	-12.52	—	—	—	—
3.1	-12.34	—	—	—	—
4	-12.42	—	—	—	—
3	-12.29	—	—	—	—
3.5	-12.30	—	—	—	—
3.1	-11.88	—	—	—	—
5.3	-12.77	—	—	—	—
10.8	-14.27	—	—	—	—

Sources: [a] Wogelius and Walther (1991 [DIRS 163290], Table 2 (based on release of Mg).
[b] Brantley and Chen (1995 [DIRS 163275], Table 1) (Data are from rate studies by Schott and Knauss which can be found in Brantley and Chen (1995), which is a compilation of dissolution data from different sources).
[c] Brady and Walther (1989 [DIRS 110748], Figure 5.

NOTES: Due to lack of dissolution rates of hedenbergite, the rates for diopside are used as a surrogate

Olivine rates used for both forsterite and fayalite.

DR = dissolution rate

Table 4-9. Dissolution Rates of Hydroxylapatite, Magnetite, and Ilmenite

Hydroxylapatite[a]		Magnetite[b]		Ilmenite[b]	
pH	DR (moles/m^2·min)	pH	DR (moles/cm^2·s)	pH	DR (moles/cm^2·s)
2.2	1.40E-07	1.01-1.02	1.31E-13	1.15-1.21	1.23E-13
2.8	6.00E-08	1.00-1.01	1.61E-13	3.01-3.02	2.51E-14
2.9	4.00E-08	2.01-2.07	6.61E-14	3.02-3.03	1.09E-14
6.5	3.20E-09	2.95-3.10	2.51E-14	4.00-4.04	8.10E-15
6.7	2.70E-09	2.98-3.05	3.71E-14	5.01-5.03	3.40E-15
—	—	3.98-4.05	2.51E-14	6.01-6.05	5.00E-16
—	—	4.01-4.03	3.10E-14	—	—
—	—	4.94-4.95	1.21E-14	—	—
—	—	5.98-6.02	1.02E-14	—	—
—	—	6.67-7.03	5.70E-15	—	—

Sources: [a] Valsami-Jones et al. (1998 [DIRS 166412], Table 2 . Note that Valsami-Jones et al. 1998, use different units than the other data cited in this table.
[b] White et al. (1994 [DIRS 131014], Table 2 (magnetite values for ISH magnetite. This study included 3 different magnetite specimens [ISH, MAR, and TAH magnetite, defined in White et al. 1994] of which ISH magnetite was the purest form)

NOTES: Rates used for magnetite and ilmenite are from anoxic tests. Since the Fe and Ti released by these minerals are quickly taken up into minerals and are not important to the aqueous parameters of interest, these rates are considered adequate for use.

Rates of hydroxylapatite dissolution are from tests using synthetic specimens. The synthetic specimens were used rather than the natural samples because rates for the synthetic samples covered a range of 5.5 pH units (2.20-6.70) while the range for the natural samples covered only 1.25 pH units (3.95-5.20). Also, five synthetic samples were tested at various pH values, whereas there were only two data points for the natural samples. The synthetic samples were used since the data cover a larger range of possible conditions.

DR = dissolution rate

4.1.1.2.4 Composition and Flow Rate of Incoming Water

The composition of the water flowing through the basalt (Table 4-10) is taken as that resembling Bin 8 seepage water from DTN: MO0310SPAEBSCB.003 [DIRS 166411]. Since the EQ6 simulations of water/basalt interaction were carried out at 25°C, Bin 8 (at 40.18°C) was chosen as all other water types were for higher temperatures. Sensitivity of results to groundwater composition is investigated in Section 6.8.4.1.

Table 4-10. Water Composition Used in EQ3

EQ3NR Input Composition Values		
Element	Concentration	Units
Na^+	7.31E-03	moles/kg
SiO_2(aq)	1.79E-03	moles/kg
Ca^{++}	5.73E-04	moles/kg
K^+	2.76E-04	moles/kg
Mg^{++}	8.51E-05	moles/kg

Table 4-10. Water Composition Used in EQ3 (Continued)

EQ3NR Input Composition Values		
Element	**Concentration**	**Units**
H^+	7.94	pH
F^-	6.43E-04	moles/kg
Cl^-	5.61E-04	moles/kg
NO_3^-	3.97E-05	moles/kg
SO_4^{--}	3.55E-04	moles/kg
AlO_2	1.50E-09	moles/kg
$HFeO_2(aq)$	1.49E-12	moles/kg

DTN: MO0310SPAEBSCB.003 [DIRS 166411], Temperature = 40°C.

A total of six cases of basalt/water interaction were run for each CO_2 fugacity. These cases involved a base case in which the flux is 0.4 mm/year, all mineral surfaces are available for reaction, saturation of 0.12, basalt is fractured in meter sized blocks, and a pore fraction of 0.17. The other five cases involve changing base-case parameters as shown in Table 4-11.

Table 4-11. Parameter and Values Changes for Abstraction Cases for Basalt/Water Interaction

Parameter	Base Case Value	Changed Value
Flux (mm/year)[a]	0.4 mm/year	3.8 mm/year
		11.7 mm/year
Saturation[b]	0.12	1.0
Pore Fraction[c]	0.17	0.13
Surface Area and Moles of Mineral Reactions	Values in Table 6-4 of this report	0.1 times values in Table 6.4

Sources: [a] DTN: LB0310AMRU0120.001 [DIRS 166409], *flow_field_summary_tables.doc* .
[b] BSC 2004 [DIRS 169856], Table 6.4-1.
[c] BSC 2004 [DIRS 169854], Table 7-10.

Saturation values chosen are 0.12 (lowest saturation) and 1.0 (highest saturation). These two states bound the range of possible saturations. The base case flux rate of 0.4 mm/year represents the lower-bound climate scenario flux for the repository area, which is used in TSPA (BSC 2004 [DIRS 169856], Table 6.4-1). Percolation fluxes of 3.8 and 11.7 from the mean climate scenario were also used to incorporate differences in percolation flux into the abstraction. Higher values of percolation flux (25, 50, and 100 mm/year) were used solely for determining the flux where groundwater was unaffected by reaction with basalt and are not part of the abstraction (Section 6.8.1).

4.1.1.3 Sensitivity Cases

Two sensitivity cases examine the effect that different water compositions have on the composition of water resulting from interaction with basalt. The compositions of the two modeled water types are presented below in Table 4-12. EQ3NR output for input into EQ6 is listed in Table 6-21.

Table 4-12. Water Composition and Redox Conditions Used in the EQ3 for Sensitivity Cases

EQ3NR Input Composition Values				
	Bin 11 Seepage Water[a]		J-13 Well Water[b]	
Species	Concentration	Units	Concentration	Units
Na^+	4.80E-03	moles/kg	45.8	mg/L
SiO_2(aq)	1.19E-02	moles/kg	28.5*	mg/L
Ca^{++}	3.34E-04	moles/kg	13.0	mg/L
K^+	7.50E-04	moles/kg	5.04	mg/L
Mg^{++}	6.34E-06	moles/kg	2.01	mg/L
H^+	7.759	pH	7.41	pH
F^-	1.38E-03	moles/kg	2.18	mg/L
Cl^-	1.30E-03	moles/kg	7.14	mg/L
NO_3^-	1.26E-04	moles/kg	8.78	mg/L
SO_4^{--}	7.29E-04	moles/kg	18.4	mg/L
AlO_2	1.42E-09	moles/kg	—	—
$HFeO_2$(aq)	2.08E-12	moles/kg	—	—
Temperature	95.6	°C	25	°C

Sources: [a] DTN: MO0310SPAEBSCB.003 [DIRS 166411].
[b] DTN: MO0006J13WTRCM.000 [DIRS 151029].

NOTE: * Value is for Si instead of SiO2

4.1.1.4 General EQ6 Inputs That Apply to All EQ6 Cases in This Model

4.1.1.4.1 Thermodynamic Database

The thermodynamic database used for the EQ6 calculations was the *data0.slt* file used at 25ºC, which is the database (*data0.ymp.R2*, DTN: MO0302SPATHDYN.000 [DIRS 161756]), but with commercial spent nuclear fuel and Savannah River Laboratory Glass included as "Minerals" and 34 gas species deleted. The changes made to the database were not made specifically for this report, but for general use in EQ6 calculations of waste package corrosion. The reason for deleting 34 gas species is that the EQ6 constraints only accommodate a limited number of gas species to be read from the database and the deleted gas species are not required for these types of calculations. See Appendix E for information regarding the location of the database. The *data0.ymp.R2* database is used in this model, as it is the most comprehensive database available for modeling of aqueous systems.

4.1.1.4.2 Atomic Weights

Atomic weights (Parrington et al. 1996 [DIRS 103896]) are established fact..

4.2 CRITERIA

The general requirements to be satisfied by the TSPA are stated in 10 CFR 63.114 [DIRS 156605]. Technical requirements to be satisfied by the TSPA are identified in the Yucca Mountain *Projects Requirements Document* (Canori and Leitner 2003 [DIRS 166275]). The acceptance criteria that will be used by the NRC to determine whether the technical requirements have been met are identified in the *Yucca Mountain Review Plan, Final Report* (NRC 2003 [DIRS 163274]).

Appendix A provides descriptions of how information in this report addresses the acceptance criteria of the *Yucca Mountain Review Plan, Final Report* (NRC 2003 [DIRS 163274]).

4.3 CODES, STANDARDS, AND REGULATIONS

No standards, regulations, or code requirements other than those cited in Section 4.2 apply to this model.

INTENTIONALLY LEFT BLANK

5. ASSUMPTIONS

This section deals with conceptual assumptions used in the models covered by this report. Parameter assumptions, those dealing with the selection of a particular number or numbers as input values for the models, are discussed within the discussion of model inputs for each model component. Conceptual assumptions specific to each component of this report are also mentioned in the main text of Section 6 with references back to the discussion in this section; hence, only the subsection numbers for those discussions are identified here. Assumptions are grouped here according to the individual supporting models and analyses they affect.

5.1 DIKE PROPAGATION FROM DEPTH

Pressure in Dike Tip Cavity

Assumption: The analysis of dike propagation from depth assumes that the pressure of the vapor in the cavity above the magma in the growing dike is negligible except as specifically noted to the contrary.

Sources of assumed values: The values are assumed to be equal to atmospheric pressure, which is the ambient pore pressure in the unsaturated zone.

Rationale: The pressure will be substantially lower than either the horizontal far-field stress or the vapor pressure of the magma because the rock into which the dike is intruding has a very high gas permeability of 10^{-2} m^2/s (Detournay et al. 2003 [DIRS 169660]).

Confirmation status: Confirmation is not required because the extremely high permeability of the rocks surrounding the repository will prevent accumulation of high pressure vapors. Gas pressures in the tip cavity that equal or approach the horizontal far-field stress will cause dike-tip instability. This means that the fracture that develops ahead of the ascending magma front will propagate rapidly to the surface, providing additional pressure release and establishing a pathway for magma to reach the surface.

Use in the Model: This assumption is used in Section 6.3.

5.2 MAGMA FLOW INTO DRIFTS FOR EFFUSIVE FLOW

Assumption: The analysis of magma flow into drifts assumes that the drifts are unobstructed by rubble or rockfall.

Source of assumption: The drift dimensions used to model magma flow into drifts are based on the planned diameters and lengths of drifts (BSC 2004 [DIRS 168489]).

Rationale: Although near-field seismic events with annual frequencies one to two orders of magnitude greater than the igneous event may cause rockfall to partially or totally fill drifts for much of the postclosure period (BSC 2004 [DIRS 169183]), the extent and timing of such filling cannot be predicted precisely. Use of unobstructed dimensions will result in maximum exposure of waste packages and waste forms to magma, providing a conservative result. An alternative

analysis is presented that indicates the nature of the effect of relaxing this assumption is to retard magma flow into drifts.

Confirmation status: The designed configuration is the only configuration well-enough defined to permit modeling. No confirmation is needed, this is a conservative assumption.

Use in the Model: This assumption is used in Section 6.4.

5.3 DRIFT-SCALE GAS FLOW

The general assumptions of the Drift-Scale Gas Flow are documented in the model report *Drift-Scale THC Seepage Models* (BSC 2004 [DIRS 169856]). Specific assumptions for this analysis are presented below.

Boundary Condition for Volcanic Gas Composition and Temperature of the Basalt

Assumption: The volcanic gas composition and temperature of the basalt are fixed for a specified time.

Rationale: The approach taken for the set-up of the volcanic gas concentration boundary conditions is considered to be conservative, because the concentration is fixed to the magmatic gas composition for a period longer than the time over which the magma is degassing significant quantities of volatiles (above the solidus temperature of approximately 900°C, whereas the actual volcanic gas amount would be limited by the volume of magma emplaced and its volatile content.

Confirmation Status: Confirmation is not needed, use of boundary conditions is conservative

Use in the Model: This assumption is used in Section 6.6.

5.4 COOLING OF BASALT-FILLED DRIFTS

This section identifies relevant assumptions, along with their respective rationales, that are essential for process modeling and assessing the thermal impacts of igneous intrusion on drifts.

5.4.1 Permeability of Metamorphic Aureole and Cooled Basalt

Assumption: The permeability of any contact metamorphic aureole surrounding the intruded drifts is assumed to be as great as that of the bulk host rock. The basalt will undoubtedly fracture during cooling, but will fracture to such an extent that the resulting secondary permeability will not provide an additional impediment to seepage.

Rationale: Natural analogs indicate that a number of different processes could lower permeabilities in the host rock immediately in contact with an intrusion (Lichtner et al. 1999 [DIRS 121006], pages 8 and 9, and Frankel, 1967 [DIRS 168717]). However, the extent or uniformity of any changes to the host rock caused by the intrusion is not known. Therefore, it is assumed that hydraulic properties of the aureole are the same as those of the host rock.

In the case of intruded basalt, the rock would fracture during magma cooling and degassing, providing paths for water flow. Maximum fracturing (or minimum fracture spacing) would occur at the dike/drift margins where cooling rates are greatest, resulting in relatively higher permeability at the margins than in the center of the flow. However, the amount of fracturing that would occur and the resulting permeability variation is unknown. The assumption is simply made that the fracturing is sufficiently intense, such that the basalt provides no barrier to flow. This is accomplished by setting the permeability of fractured basalt to that of the host rock.

Confirmation Status: This assumption is conservative because it does not restrict water flow through the basalt-filled drifts. Since the assumption is not used to limit flow of water through the basalt, confirmation is not required.

Use in the Model: This assumption is used in Section 6.8.

5.4.2 Fracturing of Basalt and Block Size

Assumption: It is assumed that basalt will fragment into meter-sized blocks.

Rationale: Joints in basaltic rocks can be from centimeter to meter scale. As an example, in numerous thin flows of the Hawaiian volcanoes, which cool quickly, most blocks are 0.5 meters across or smaller. However, in thicker flows where the magma has slowly cooled, blocks may be much larger. In several areas where flows remained thick due to confinement in valleys, blocks 3 m or more in diameter were noted (MacDonald, 1967 [DIRS 168719]). Hearn et al. (1985 [DIRS 166893], Page 8) report blocks approximately 1 m in diameter in the slowly cooled interior portion of flows from the Columbia Plateau, whereas the quickly cooled margins show much smaller columns.

Jointing is not solely restricted to surface basaltic flows. Many intrusive bodies also show well-developed joints. Dikes 1-m thick are known to be broken into irregular columns (MacDonald 1967 [DIRS 168719]). Joints develop progressively as the magma cools and, as shown above, size and shape are related to rate of cooling (larger flows whose interiors cool much more slowly than thin flows have larger joint blocks). The margins of the potential dike intrusion will likely cool quickly due to a chilling effect caused by the cooler drift walls. However, the interior of the magma (as shown in Section 6.7) cools relatively slowly, taking several months to solidify. Therefore, the fractures/joints that form in the basalt are expected to be large (meter scale), and 1-m size blocks were chosen for the base case scenario. Larger block sizes would effectively cause a decrease in the available reactive surface area in contact with water percolating through the basalt. One case in the abstraction looks at the effects of decreased surface area on the water chemistry. Therefore, the effect caused by even larger blocks has also been taken into account in the abstraction.

Confirmation Status: Use of one meter sized blocks represents the expected scale of jointed basalts in a repository setting. Therefore, no further confirmation needed.

Use in the Model: This assumption is used in Section 6.8.

5.4.3 Thermal Properties of the Magma

Assumption: It is assumed that thermal conductivity and thermal diffusivity of the magma are the same as the welded tuff, and that latent-heat effects related to magmatic crystallization have a minimal impact on the model.

Rationale: The properties of the magma that could intrude into the emplacement drift(s) are difficult to predict precisely. The assumption that the thermal properties (thermal conductivity and diffusivity) of the in-drift magma are the same as the drift wall rocks is reasonable. Latent heat effects are reasonably easy to simulate in cooling models, however the model is relatively insensitive to this as well. The sensitivity of these parameters to variation was examined in the validation section (Section 7.3.2.2).

Confirmation Status: Section 7.3.2.2 shows that the results are not sensitive to these parameters. Therefore, no further confirmation is needed.

Use in the Model: This assumption is used in Section 6.8.

6. MODELS AND ANALYSES

The objective of the modeling discussed in this report is to provide a description of the mechanical, thermal and chemical environment encountered by waste packages should an igneous intrusive event disrupt the repository. The dike/drift interaction conceptual model describes processes that would occur if an intrusion were to intercept the repository. The conceptual model consists of two submodels made up of several model components and analyses:

Dike Intrusion Submodel

- Natural and thermal stresses – analysis
- Dike propagation from depth – model
- Magma flow into the drifts at dike/drift intersections – analysis
- Magma flow to the surface–either via a secondary dike or directly via the continuation of the dike to the surface – analysis.

Post Intrusion Submodel

- Transport to neighboring drifts of magmatic gases after magma emplacement – model
- Heating of neighboring drifts from the cooling of emplaced magma – model
- Seepage water alteration by reaction with intruded basalt in drifts – model.

The organization of this section of the report is as follows.

The FEPs included in the model are described in Section 6.1.

The stresses active in the vicinity of the repository are an essential parameter of dike propagation. Therefore Section 6.2 analyses, for use in the later sections, the stresses in the region of the repository, both naturally occurring and those introduced from the engineered tunnels and subsequent heating from radioactive decay of waste.

To assess the interaction of the dike with an emplacement drift, one needs to define the physical conditions of its propagation until it effectively reaches the repository elevation. Section 6.3 discusses the propagation of the dike from depth and obtains the range of physical conditions relevant for later analyses.

Section 6.4 analyzes the flow of the magma into the drift and its interaction with the waste packages and their contents. One can then understand what happens while the magma is filling the drift and after the drift has been filled. Does the magma front continue up the original dike at the same speed? Does magma stall while the drift is filling? What pressures can be expected in the magma while the drift is filling, and after the drift is filled? What will be the impact of the magma flow on the waste packages and waste forms? Answers to these questions will support realistic scenarios for the transport of waste to the surface, and avoid unrealistic ones.

Section 6.5 contains simple analyses that evaluate features and processes associated with an igneous intrusion into the repository (1.2.04.03.0A). Woods et al. (2002 [DIRS 163662]) described a drift filling and a secondary dike opening to the surface at some distance from the original dike, with the magma flow being diverted through the drift and carrying the entire drift contents to the surface. This is commonly called the "Dog-Leg" scenario. Secondary dike propagation is analyzed, for the case of effusive and hydrovolcanic magma flows. The results of these analyses are then used to discuss the precise scenario described by Woods et al. (2002 [DIRS 163662]).

Post-emplacement effects are discussed in Sections 6.6, through 6.8. Section 6.6 looks at the flow of corrosive magmatic gases between drifts filled with magma and those outside the zone of magmatic emplacement. Section 6.7 addresses the issue of heat flow between magma-filled drifts and adjacent drifts. Section 6.8 investigates the effects of solidified basalt on the physical-chemical, environment, and seepage water composition.

Although this report considers a wide range of phenomena associated with dike propagation and magmatic interaction with drifts, the range of possible interactions with waste packages, cladding, and drip shields encompasses an unusually broad range of uncertainty. As a result, it is not possible at this time to predict the behavior of these elements in the event of an igneous intrusion. Thus, it is recommended that a conservative position be adopted in which waste canister/assembly, cladding, and drip shields contacted by magma provide no added protection to waste forms.

6.1 FEATURES, EVENTS, AND PROCESSES ADDRESSED BY THE DIKE/DRIFT INTERACTION MODEL

Development of a comprehensive list of FEPs potentially relevant to postclosure performance of the Yucca Mountain repository is an ongoing, iterative process based on site-specific information, design, and regulations. Table 6-1 provides a list of igneous-related FEPs (DTN: MO0407SEPFEPLA.000 [DIRS 170760]) that are included in the TSPA-License Application (TSPA-LA) through the use of the results of the calculations described in this document. A new FEP has been added to the FEP list (FEP 1.2.04.04.0B Chemical effects of magma and magmatic volatiles) and is discussed in this report. The rationale for inclusion or exclusion of igneous-related disruptive events FEPs is discussed in *Features, Events, and Processes: Disruptive Events* (BSC 2004 [DIRS 170017]). The analyses presented in the remaining parts of Section 6 support the technical bases for some of the exclusion arguments.

For the igneous intrusive scenario, the TSPA-LA postulates that a hypothetical dike propagates upward during an unlikely intrusive event, intersects the repository, provides a source for magma to enter the repository drifts, subjecting waste packages and waste forms to very high temperatures and exposing them to corrosive gases and that following intrusion, the chemistry of seepage waters may be altered by the presence of solidified basalt. For the igneous eruptive scenario, the TSPA postulates that, following or as an adjunct to an intrusive event, magma and ash, potentially with entrained waste, are released to the surface via an eruptive conduit. The FEPs listed in Table 6-1 are part of the conceptual basis for such scenarios. This report provides supporting analyses to help constrain the potential consequences of the listed FEPs.

Table 6-1. Included Features, Events, and Processes for This Model Report

TSPA-LA FEP Number, Name and Description	Section Where Disposition is Described
1.2.04.03.0A Igneous intrusion into repository	Section 6.3 contains the overall model description, assumptions and simplifications. Section 6.3.3 contains the mathematical description of the base case model for dike propagation from depth, including the potential for formation of a sill. Section 6.4 contains an analysis of the flow of magma into drifts. Section 6.5 contains an analysis of secondary dike (or sill) propagation from magma-filled drifts.
1.2.04.04.0A Igneous intrusion interacts with EBS components	Section 6.4 contains an analysis of the flow of magma into drifts and of the effects magma on waste packages and waste forms. Section 6.6 contains a description of a model of post-emplacement migration of volcanic gases out of a filled drift, which can be used to determine effects on adjacent drifts. Section 6.7 contains a description of a model of cooling of magma in a drift, which can be used to determine effects on adjacent drifts. Section 6.8 contains a description of a model of reaction of seepage water with cooled basalt and the resulting water chemistry, which can be used to determine solution of waste. Outputs related to igneous interaction with EBS components are found in Sections 8.2.2, 8.2.3, and 8.2.4.
1.2.04.04.0B Chemical effects of magma and magmatic volatiles	Section 6.4 contains an analysis of the flow of magma into drifts and of the effects magma on waste packages and waste forms. Section 6.6 contains a description of a model of post-emplacement migration of volcanic gases out of a filled drift, which can be used to determine effects on adjacent drifts. Section 6.8 contains a description of a model reaction of seepage water with cooled basalt and the resulting water chemistry for use in TSPA-LA.

Source: DTN: MO0407SEPFEPLA.000 [DIRS 170760].

6.2 ANALYSIS OF NATURAL AND INDUCED STRESSES AT THE REPOSITORY

The stresses active in the vicinity of the repository are an essential parameter of dike propagation. The purpose of the simple analyses below is to assess the stress field that needs to be taken into account for the dike propagation computations. Vertical stresses are essentially governed by gravity and the topography in the neighborhood. Horizontal stresses in the absence of the repository have been measured. However, thermal loading due to the waste may have a profound effect on the horizontal stresses. Also, at a much smaller scale, the presence of a drift changes the stresses around the excavation.

This section is organized as follows:

- Section 6.2.1 discusses inputs used in the analysis
- Section 6.2.2 discusses the effect of topography
- Section 6.2.3 discusses the effect of excavation
- Section 6.2.4 assesses the effect of thermal loading.

The computations described below use FLAC3D V2.1 software (BSC 2002 [DIRS 161947]) qualified for this use.

6.2.1 Inputs for Topographic and Thermal Effects

A large-scale, 3-D analysis was used for calculation of in situ (topography induced) and thermally-induced stresses. Inputs for this model were:

- Regional topography
- Layout of the repository
- Ratios of horizontal principal stresses to the vertical stress
- Orientations of the horizontal principal stresses
- Stratigraphy in the vicinity of the repository
- Elastic properties (Young's modulus and Poisson's ratio) and density of each geological unit
- Thermal properties for each geological unit (conductivity, specific heat, and coefficient of thermal expansion)
- Position and mechanical properties (friction angle) of two faults in vicinity of the repository
- Heat released by the waste as a function of time and amount of heat removed by ventilation.

All of the inputs and their sources are described in *Drift Degradation Analysis* (BSC 2004 [DIRS 166107]).

6.2.2 Stress Due to Natural Topography

Large-scale, 3-D, thermo-mechanical analysis of regional stresses accounting for topography at the Yucca Mountain site was conducted using the FLAC3D V2.1 code (BSC 2002 [DIRS 161947]). Detailed description of this analysis is found in the *Drift Degradation Analysis* (BSC 2004 [DIRS 166107], Appendix C). The topography of the site and its representation in the model are shown in Figure 6-1. Contours of the vertical stress and orientations of the principal stresses are shown in Figure 6-2 (larger scale in the vertical plane at N232000).

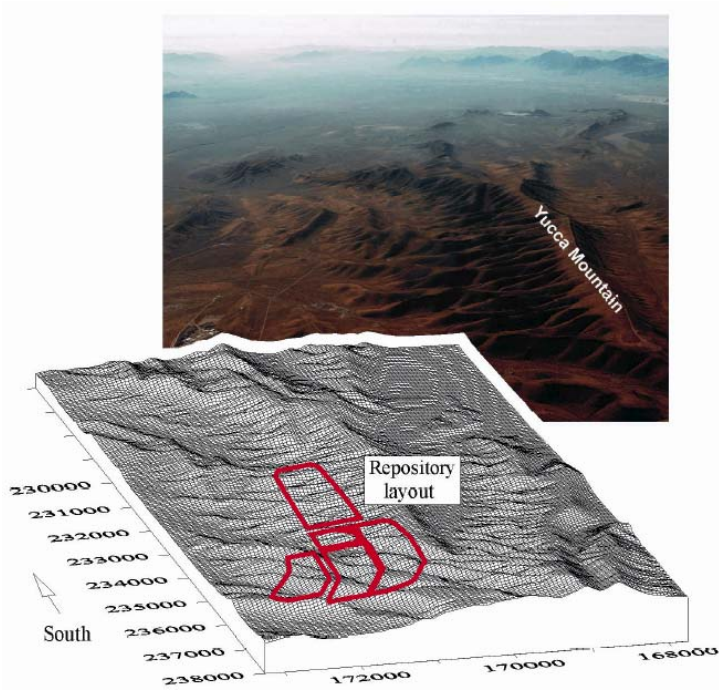

Source: BSC 2004 [DIRS 166107], Figure C-1a.

Figure 6-1. Topography at Yucca Mountain Nuclear Waste Repository Site

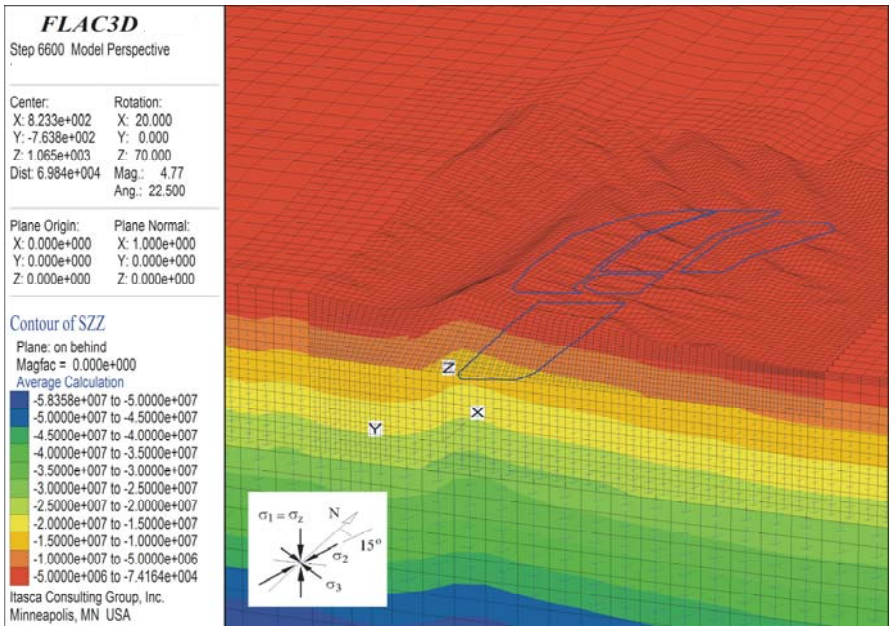

Source DTN: MO0408MWDDDMIO.002 [DIRS 171483].

NOTE: Negative stresses are compressive. Stress scale in Pa.

Figure 6-2. Contours of Vertical Normal Stress and Stress Tensors Due to Topography at Yucca Mountain Nuclear Waste Repository Site: Cross-Section Through N232000

NOTE: Figure 6-3 is deleted.

The in situ stress state at Yucca Mountain (before heating) is such that the vertical stress is the maximum principal compressive stress, whereas two other principal stresses of smaller magnitude are in the horizontal plane. The vertical in situ stress is gravitational (a function of topography and stratigraphy). The two orthogonal horizontal stresses are adjusted in the model (being statically undetermined) to match measurements of horizontal stresses (DTN: SNF37100195002.001 [DIRS 131356]); this provides the remaining constraint controlling how gravity, topography, stratigraphy, and two modeled faults interact to generate the horizontal stresses. The in situ stress profiles (normal stress components in the directions of the global coordinate axes) from the analysis, along the vertical scanline at (N171000, E235000), are shown in Figure 6-4. (The horizontal normal stresses in the directions of the global coordinate axes are almost coincident with the horizontal principal stresses.)

The repository is designed to be under the mountain—that is, the region of expected increased stresses. Heterogeneity of in situ stresses and rotation of the major principal stress from the vertical direction due to topography could affect the dike path and potentially divert it from the repository. It can be seen from the upward deflection of contours of vertical stress in Figure 6-2 that the topography above the repository will increase the vertical stress by less than 2 MPa, and that the vertical stress will remain the major principal stress. Note that the impact on horizontal stresses is significantly smaller. Since a dike tends to propagate towards the major principal stress, and since the vertical stress will remain major, based on current understanding of stress state, the topography at the Yucca Mountain will not cause deflection of the dike. Also, because horizontal stresses will be little affected, the impact on propagation will be minimal.

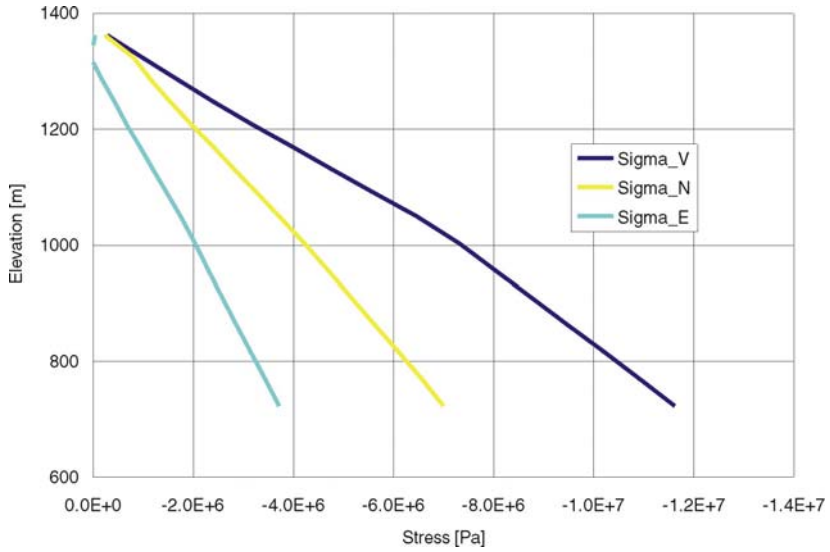

Source: DTN: MO0408MWDDDMIO.002 [DIRS 171483].

NOTES: Sigma_V is the vertical stress; Sigma_N and Sigma_E are the two normal horizontal stresses in directions of the global coordinate axes. These normal stresses are almost coincident with principal stresses.

Repository elevation is approximately 1070 m.

Figure 6-4. Variation of Initial In situ Stresses With Depth at Yucca Mountain Nuclear Waste Repository Along the Vertical Scanline at E171000, N235000

6.2.3 Stresses Due to Excavation of the Drift

The stress concentrations around a circular drift extending in the *z*-direction that are induced by the far-field stresses are well known and, at the tunnel wall, are given by (Jaeger and Cook 1979 [DIRS 106219], Section 10.4, pp. 249-254):

$$\sigma_\theta = (\sigma_x + \sigma_y) - 2(\sigma_x - \sigma_y)\cos(2\theta) - 4\tau_{xy}\sin(2\theta) \quad \text{(Eq. 6-1)}$$

$$\sigma_{zz} = \sigma_z - 2\nu(\sigma_x - \sigma_y)\cos(2\theta) - 4\nu\tau_{xy}\sin(2\theta) \quad \text{(Eq. 6-2)}$$

$$\tau_{\theta z} = 2(-\tau_{xz}\sin\theta + \tau_{yz}\cos\theta) \quad \text{(Eq. 6-3)}$$

$$\tau_{r\theta} = \tau_{rz} = 0 \quad \text{(Eq. 6-4)}$$

where:

θ = the angle about the drift axis as measured from the horizontal *x*-axis towards the vertical *y*-axis
σ_x, σ_y, σ_z = the far-field normal components of stress
τ_{xy} τ_{yz}, and τ_{zx} = the far-field shear stresses
σ_{zz} = the axial component of stress
σ_θ = the hoop stress
$\tau_{r\theta}$ and τ_{rz} = radial shear stress factors, which are zero at the tunnel wall (until pressurized by magma, which is considered later).

All of these stresses are at the drift wall, where the stress concentration is highest. Stress changes from the drift excavation are of limited spatial extent and decay quickly into the pillars separating drifts as a function of distance from the drift wall. The stress becomes almost equal to unperturbed, far-field stress state at a distance of three drift radii from the drift wall. Repository stresses will have an insignificant effect on dike propagation. Note that the scale effect mentioned here is valid because the analyses consider a kilometer(s)-long dike propagating towards the surface. Later analyses addressing the secondary dike, or "dog leg," scenario in Section 6.5, consider propagation from the drift of a diverted dike with a length in the same range as the drift. In this case, excavation-induced stresses will need to be taken into account.

6.2.4 Thermal Stresses Induced by Radioactive Decay of Waste

On average, the vertical stresses (statically determined) would not change as a result of heating. If heating increases the magnitude of the horizontal principal stresses such that both become larger than the vertical principal stress, the repository could be shielded from potential volcanic intrusion for a period of time (while the conditions of such stress "inversion" exist).

The temperature and stress changes due to heat generated by the emplaced waste were simulated through the entire regulatory period of 10,000 years. Detailed description of this analysis is found in *Drift Degradation Analysis* (BSC 2004 [DIRS 166107], Appendix C). The maximum increase in horizontal stress due to heating occurs between 500 and 1000 years after waste emplacement. Figures 6-5, 6-6, and 6-7 show the stress profiles after 500, 1000, and 2000 years, respectively, along the vertical scanline at N171000, E235000. The average elevation of the repository is 1073m, as calculated from *D&E / PA/C IED Subsurface Facilities* (BSC 2004 [DIRS 164519], Table 2). Between 500 and 1000 years of heating, the vertical stress becomes the least-compressive stress over a vertical range of approximately 200 m and, at most, 3 MPa smaller than the smaller horizontal principal stress (Figures 6-5 and 6-6). For times later than 1,000 years the stress difference and the spatial extent of the region with stress inversion decrease. After 2,000 years (Figure 6-7) of heating, normal stress in east-west direction is only 1 MPa larger than the vertical stress.

Figures 6-5, 6-6, and 6-7 show that the stress change due to heating extends to a depth of about 200 m below the repository. Realistic potential for dike deflection may exist for a limited time during the regulatory period (between 500 and 2,000 years after waste emplacement). Also, because the change in horizontal stresses is sizeable, the propagation parameters (specifically, magma pressure) may be affected. Although the base case model does not address this, Section 6.3.7.3 evaluates the effect of these increased stresses on dike propagation.

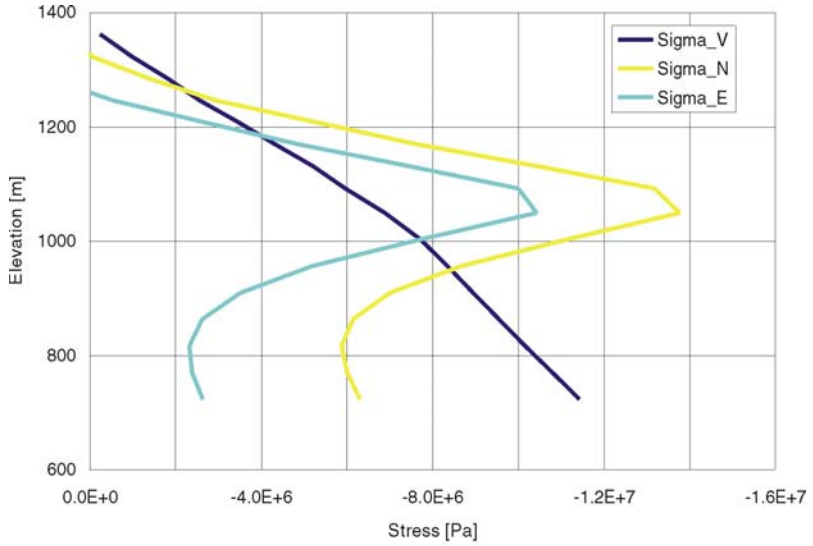

Source: DTN: MO0407SPAMTSHR.000 [DIRS 170679].

NOTES: Sigma_V is the vertical stress; Sigma_N and Sigma_E are the two normal horizontal stresses in directions of the global coordinate axes. These normal stresses are almost coincident with principal stresses.

Figure 6-5. Predicted Variation of Stresses With Depth at Yucca Mountain Nuclear Waste Repository Along the Vertical Scanline at E171000, N235000 After 500 Years of Heating

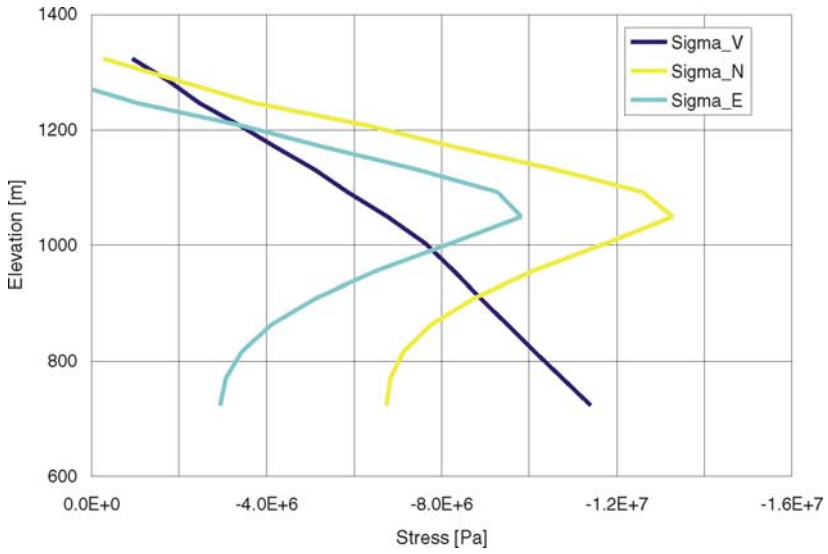

Source: DTN: MO0407SPAMTSHR.000 [DIRS 170679].

NOTES: Sigma_V is the vertical stress; Sigma_N and Sigma_E are the two normal horizontal stresses in directions of the global coordinate axes. These normal stresses are almost coincident with principal stresses.

Figure 6-6. Predicted Variation of Stresses With Depth at Yucca Mountain Nuclear Waste Repository Along the Vertical Scanline at E171000, N235000 After 1000 Years of Heating

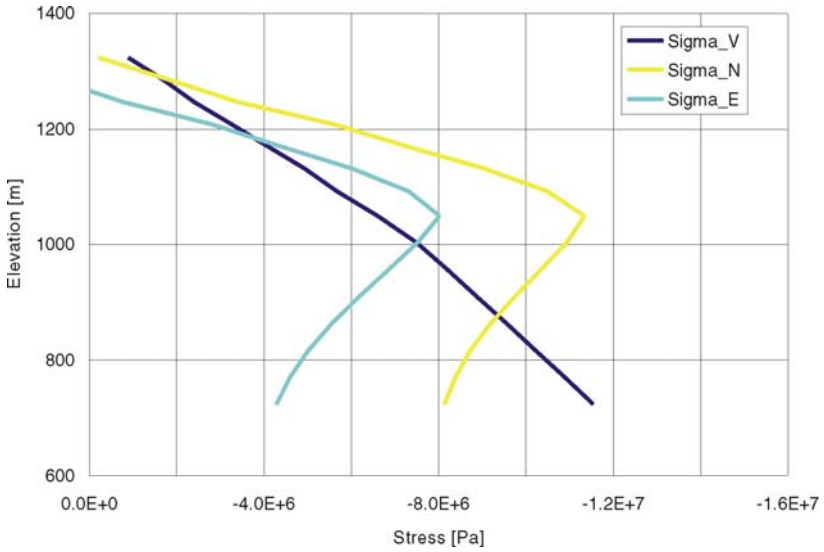

Source: DTN: MO0407SPAMTSHR.000 [DIRS 170679].

NOTES: Sigma_V is the vertical stress; Sigma_N and Sigma_E are the two normal horizontal stresses in directions of the global coordinate axes. These normal stresses are almost coincident with principal stresses.

Figure 6-7. Predicted Variation of Stresses With Depth at Yucca Mountain Nuclear Waste Repository Along the Vertical Scanline at E171000, N235000 After 2000 Years of Heating

6.2.5 Summary

Based on the results of the analyses presented above, the following results are carried forward to the dike propagation model presented in Section 6.3:

- Horizontal stresses at repository level are between 0.3 and 0.6 times the vertical stress;
- Differential topography-induced stresses are considered negligible;
- Excavation-induced stresses are considered negligible for the dike propagation from depth (they may not be negligible for dike breakout at drift scale);
- Thermally induced stresses during the first two millennia may be significant as addressed in Section 6.3.7.3.

6.3 DIKE PROPAGATION FROM DEPTH MODEL

In order to assess the interaction of the dike with a repository drift, one needs to define the physical conditions of its propagation as the dike approaches the repository elevation. Knowing these conditions (i.e. dike width, magma front velocity, magma pressure in the absence of a drift, lag between crack tip and magma) will then enable analysis of the flow of the magma into the drift and its effect on further dike propagation (i.e. propagation from repository elevation to the surface). The purpose of this section is to obtain the range of physical conditions relevant for later analyses.

The model is described in Section 6.3.1, while the assumptions and simplifications involved are listed in Section 6.3.2. The mathematical expression of the model, the uncertainties involved, and the relevant model inputs are detailed in Sections 6.3.3, 6.3.4, and 6.3.5 respectively. After setting out the boundary and initial conditions (Section 6.3.6), model results are detailed in Section 6.3.7. Alternative models are discussed in Section 6.3.8. Finally, a summary on dike propagation from depth (Section 6.3.9) spells out the inputs to be used in Section 6.4.

6.3.1 Model Description

6.3.1.1 Background

An igneous dike is a fracture that propagates upward from some deep source toward the surface, a pressurized fracture that is fed by a high-pressure source of magma deep in the earth. The high pressure of the magma in the dike pushes aside the surrounding rock, often creating widths of several meters or more. Nevertheless, the restricted width of the dike induces frictional losses in the viscous magma that result in a pressure drop along the propagation direction of the dike. Thus, the overall dike propagation problem is an interaction that results in a balance between the high pressure that opens the dike and the appropriate width restriction that keeps the pressure at the required level through viscous losses.

This process is essentially the hydraulic fracturing problem (with some complications and some simplifications) and can only be modeled in any realistic sense by using a fully coupled hydro-mechanical type model.

The basic components of a hydraulic fracture model include:

- The elastic deformation of the country rock due to the internal pressure of the fluid on the crack walls
- The viscous losses of the moving magma within the fracture
- Fluid losses into the surrounding medium
- A crack propagation criterion that accounts for the resistance of the rock to fracture.

The conceptual model for dike propagation is one that broadens a hydraulic fracture model for applications near a free surface. In general, hydraulic fracture models consider the propagation in an infinite medium, and effects near a free surface are not accounted for. Near-surface effects, like unstable growth and an altered width distribution, can be evaluated in the dike propagation model.

Inelastic processes associated with the crack tip are typically incorporated in hydraulic fracture models by way of fracture toughness, a measure of the energy required to open new crack surfaces. However, large-scale fractures, such as those produced by ascending magma, are not believed to have a strong dependence on fracture toughness.

In general, a dike propagating from a source at depth would be expected to start out with a radial front that expands outward from the source. Therefore, at least near the surface (in the vicinity

of the repository), a two-dimensional approximation of dike propagation is a reasonable approach for calculating dike parameters.

6.3.1.2 Implementation

The elastic deformation associated with dike propagation, can be modeled using either analytic or numerical approaches. A numerical approach has much more flexibility and, therefore, is used in this application. In particular, the boundary element approach—specifically the displacement discontinuity method—is used here because of its simplicity and flexibility for crack problems (Crouch and Starfield 1983 [DIRS 139600]).

This method is based on the analytic solution to the problem of a finite line crack whose opposing sides have been displaced relative to one another in an infinite elastic solid. A crack is divided into N segments, each of which has a constant displacement over its segment, but every segment may have a different displacement from other segments. Because the analytic solution for a single element is known, the numerical solution is found by summing the effects of all N elements; however, in this application discontinuities in displacement between the elements are not known and must be calculated. If the pressure is known everywhere in the crack, then values of the elemental displacement discontinuities that are necessary to produce the pressure can be calculated by solving a system of equations. In this way, the general deformation of the crack can be determined as accurately as desired by increasing the number of elements.

The rock material that is deforming is considered to be a linear-elastic material characterized by Young's modulus, E, and Poisson's ratio, ν. This approach is clearly appropriate for small, fluid-filled fractures but may be questioned for large-scale dikes where many faults, joints, and bedding discontinuities may be intersected and respond anelastically. No methods are available for a nonlinear analysis.

The primary model approaches for magma flow are Newtonian viscosity and laminar flow in the lubrication approximation of the Navier-Stokes equation (Batchelor 1967 [DIRS 103289]). Many of the calculations used in this model are for magmas less dense than 1300 kg/m^3, which consist of more than 50 percent by volume gas. Such low densities are needed to maintain buoyancy at drift level, where the ratio (κ) of horizontal to vertical stress drops to approximately 0.5. The viscosity of such a mixture is uncertain, so a viscosity range of 10 to 40 Pa·s, equivalent to the pure silicate liquid is used.

The laminar approximation is valid for the flow rates, dike widths, and magma viscosities that are anticipated. The dimensionless parameter, Reynolds Number, denoted $\mathrm{Re} = \rho_f v w/\mu$, signals a transition from laminar to turbulent flow of the fluid at $\mathrm{Re} \approx 2200$. A typical set of magma/dike parameters are: a magma density (ρ_f) of 1140 kg/m^3, a dike width (w) of 1.5 m, a magma/dike velocity (v) of 10 m/sec, and a magma viscosity (μ) of 10 Pa·s, the Reynolds number is 1710, implying laminar flow. The Reynolds number may exceed the threshold for the transition from laminar to turbulent flow in some cases, because of a wide dike fracture, high fluid density, or high velocity. No attempt is made to consider any transition effects because this would be largely speculative.

The viscous pressure drop along the propagation direction of the dike is calculated for laminar flow of a Newtonian fluid through parallel plates (Poiseuille flow) in the lubrication approximation. The Poiseuille flow approximation is valid because the dike width and magma velocity are very slowly varying functions of depth.

Standard hydraulic fracture models consider the leak-off of fracture-driving fluid into the surrounding rock formations. However, in the dike propagation case, the rock formations encountered by the dike will be impermeable to the viscous magma. Thus, no generalized leak-off is included in this model. However, leak-off of volatiles is still anticipated, which will reduce the pressure in the tip-cavity zone.

A crack propagation criterion is used in some hydraulic fracture models to include the effect of rock resistance to fracture, but it is also ignored in many models because the effects are negligible for large-scale fractures. In the dike propagation model, fracture toughness effects are included and can be evaluated. However, the scale of a dike is so large that it is not likely that the details of stress intensity calculations are strictly applicable. For example, the stresses are extremely large (on the order of several MPa) around the fracture tip and extend for many tens of meters. Damage, such as brittle fracture, likely occurs throughout this region, negating any rigorous use of Linear Elastic Fracture Mechanics (LEFM). In this model, the fracture toughness can be used as a convenient parameter for assessing possible scale-dependent, anelastic behavior that may provide additional resistance to fracture growth.

As the propagating dike approaches the level of the drifts, the crack tip separates from the magma front because of the inability of the high-viscosity fluid to reach the very narrow tip. This separation results in a vapor-filled cavity above the magma, which is the first part of the propagating dike that encounters the drift. Cavity formation is followed some time later by magma. To evaluate tip-cavity effects, a range of values is used to assess reasonable values of a tip pressure that might develop. In conjunction with other aspects of the model, the tip pressure controls the length of the tip-cavity region.

Most hydrofractures produced for petroleum applications occur at depths where the effect of the free surface can be ignored. That is not the case at Yucca Mountain, where the repository would be a few hundred meters beneath the surface. The importance of the free surface should be evident from the relatively small ratio of the depth to the crack tip relative to the vertical extent of the dike.

Therefore, the dike propagation model in this report also includes the effect of a free surface in the deformation calculations. In this case, the solution for a displacement dislocation in a half space (Hills et al. 1996 [DIRS 163626]) is used. This formulation allows for the correct deformation in the proximity of a free surface.

The mathematical basis for this conceptual model of dike propagation is described in Section 6.3.3. The model, yielding the results presented in Section 6.3.7.1 and 6.3.7.2, is implemented numerically with the Non-Planar Hydraulic Fracture 2D code (NPHF2D), described by Zhang et al. 2002 [DIRS 164368].

The dike propagation model calculates the growth history of a dike propagating toward the surface in the vicinity of the repository. No attempt is made to model the topography of the site, as a complex surface topography formulation is beyond the capabilities of any current model. However, aspects of topographical features can be accounted for through the incorporation of a horizontal in situ stress distribution that reflects the stresses around the repository. Also, thermo-mechanical and fluid-mechanical simulations, using UDEC V3.14 (BSC 2004 [DIRS 172322]) and the same conceptual model for dike propagation, account for the horizontal stresses induced by thermal loading. UDEC V3.14 is qualified for this use.

As the magma rises in the dike, the flow is concentrated toward the center of the dike, with the magma at the very edge of the dike not moving upward at all. The shearing between the center of the dike and the walls will result in elongation of any vapor bubbles in that part of the magma and thus, lowering the effective viscosity, so there may be a tendency for slug flow in the center of the dike.

There are two possibilities for the state of the magma in the center as it moves upward into the cavity. One possibility is, as magma rises in the dike and approaches the cavity, it releases gas in a steady way. Stasiuk et al. (1996 [DIRS 164459]) describe a silicic volcanic conduit exposed in southwestern New Mexico that shows clear evidence of this process. The other possibility is the liquid and vapor phases of the magma are so closely coupled that the release of gas is more catastrophic. The conceptual model adopted for the present report employs the former style because the

- Low viscosity of the basaltic melt will facilitate bubbles rising in the dike to release their gas at the fluid front
- Gas permeabilities of the repository host tuff are very high (on the order of 10^{-12} m^2/s, Detournay et al. 2003 [DIRS 169660]), which will permit much of the gas to leak out into the formation well ahead of the magma.

This is supported by findings of Detournay et al (2003 [DIRS 169660], Section 3.3.3.3) and by processes described in *Characterize Eruptive Processes at Yucca Mountain, Nevada* (BSC 2004 [DIRS 169980], Section 6.3.3).

6.3.2 Assumptions and Simplifications

To make this a tractable problem several simplifying assumptions have been incorporated in the model. These are summarized here:

1. Dike propagation can be treated in two dimensions: Although the problem of a dike propagating away from a deep magma source clearly is a three-dimensional problem, the behavior as the dike approaches the surface is considerably more constrained. Because the leading edge of the propagating crack is (ideally) an arc that is tangent to the surface when it erupts and its underground strike length may be much greater than its final surface expression, the flow of magma can safely be considered to be purely vertical. Also, the strike length of the dike is still large enough that out of plane effects do not impact the mechanical solution when the tip is nearing the surface; i.e.,

strike length is larger than the characteristic length of the problem, as mentioned later (Section 6.3.7.1). Thus, although the early time modeling of the dike may not be accurate using a two-dimensional model, the late time behavior (which is the behavior of interest) should be appropriately modeled using a two-dimensional approach that specifically takes account of the presence of the free surface.

2. Magma is incompressible: The analysis of dike propagation assumes that the magma is incompressible, whereas real magma is a mixture of liquid and gas (with or without solids) that can be highly compressible (BSC 2004 [DIRS 169980]). This is the standard assumption for hydrofracture analysis. The numerical model used is adapted from codes developed for oil field hydrofracture applications, which use water as the driving fluid. For these applications, incompressibility is a good assumption. Using the assumption of magma incompressibility in the magma flow model is not expected to have a major effect. Results from several incompressible magmas of successively lower densities are combined to approximate the effect of magma expansion on dike propagation.

3. Host rock behaves elastically: Elastic behavior is a reasonable assumption for small-scale pressurized fractures in the Earth but may be questionable for a dike-scale event. A dike would cross many joints, faults, bedding planes, and other discontinuities in the rock and would generate earthquakes as slippage occurs in response to the changes in stress generated by the inflated, propagating dike. However, such inelastic effects will generally serve to increase the width of the dike and decrease the pressure. These are competing effects at the repository level, with the pressure being the primary boundary condition for subsequent calculations of magma and gas flow, but the width of the dike provides a constraint on how much magma may be lost into the drift. As mentioned in assumption 10 below, "fracture toughness" is used to investigate the effect of any mechanism that resists fracture growth and thus increases the pressure.

4. Host rock behaves linearly: Most rocks have nonlinear behavior, with lower moduli (a) at low stress and (b) in the ground in the presence of joints and bedding planes. However, linear-elastic behavior would produce the greatest possible pressure and is, thus, a conservative assumption.

5. Host rock is a homogeneous, isotropic material: Rocks are typically transversely isotropic due to bedding and are jointed and faulted. In addition, there are many stratigraphic units with different values of Young's modulus and Poisson's ratio. In general, the rock properties of the strata below the repository are not known, and characteristics of joints and faults deep in the Earth are not known. However, although it is true that the deformation at any one point is a cumulative effect of the deformation everywhere in the dike, the influence of any point on another point decreases with distance. Thus, in lieu of a capability to incorporate multiple layers (which the numerical model does not possess) and in the absence of detailed information on other rock properties, the dike behavior near the repository is best modeled by using the rock properties at the repository. This approach is not

necessarily a conservative assumption but, rather, is the only assumption that can be made to obtain tractable models and sufficiently complete input parameters.

6. Dike is a single fracture: Although many hydraulic fractures and dikes are known to exhibit multiple fracture strands and *en echelon* behavior, the overall dike behavior is still reasonably modeled with a single fracture. The more complex behavior observed in the field is due to complexities of the formation that are not known or otherwise available for modeling endeavors.

7. Magma is a Newtonian fluid: A Newtonian fluid is one that obeys Stokes' law of friction, for which the relationship between stress and rate of strain is linear. This formulation considerably simplifies calculations of fluid resistance and is known to apply to many common fluid systems. Although a more complex fluid rheology might be used (e.g., with yield stress and power-law behavior), it is more appropriate to remain within the analytically more tractable Newtonian framework and vary the viscosity to account for possible differences. The limitations associated with this assumption of Newtonian viscosity for modeling basaltic magma are discussed below in Section 6.3.4.

8. Magma flow is laminar: Laminar flow will occur for Reynolds numbers less than 2,200. However, Reynolds numbers do approach and even exceed 2,200 for some combinations of dike propagation calculated. These few cases will be identified as the results are discussed.

9. Lubrication approximation: The lubrication approximation is appropriate (and exact) for slow, steady motion of viscous fluids for which the viscous forces are considerably greater than the inertial forces, thus allowing the inertial forces to be neglected. These flows are also called *creeping motion*. Creeping motion can be considered as solutions of the full Navier-Stokes equations for cases with small Reynolds number (i.e. laminar flow). The lubrication approximation is appropriate because flow in a long two-dimensional fracture is a "parallel flow," which is identical to the one-dimensional lubrication equation with the exception of an additional time derivative of the velocity and the dropping of one spatial derivative. Because hydraulic fractures—and deep dikes—are slowly varying with time and position, the time derivative is negligible, and the spatial derivative drops out as well. Consequently, the steady "parallel flow" approximation is the same as the one-dimensional lubrication equation:

(**NOTE**: Equation 6-5 has been deleted.)

$$q \equiv vw = -\frac{w^3}{\mu'}\left(\frac{\partial p_f}{\partial z}\right), \qquad \text{(Eq. 6-6)}$$

where q is the flux per unit length, v is the fluid velocity, w is the crack width, μ' is 12μ (μ being the dynamic viscosity), p_f is the fluid pressure, and z is the coordinate along the direction of crack propagation. In support of this reduction, the "lubrication approximation" has been used for 40 years in hydraulic fracturing (with even larger Reynolds numbers) with good success and no apparent discrepancies. Thus, this approximation is reasonable and appropriate for propagation from depth but may be less so very near the surface if magma begins accelerating.

10. Stress intensity factor governs tip behavior: LEFM is a discipline that has been well studied and is widely applicable to small-scale fractures in the laboratory, mines, concrete, and other typical engineering applications. In LEFM, the shape of the crack near its tip is governed by the relation

$$w(z) = \frac{K'}{E'}(z-h)^{\frac{1}{2}}, \qquad \text{(Eq. 6-7)}$$

where $w(z)$ is here an explicit function of vertical position z, h is the vertical coordinate of the crack tip, and E' and K' are given by

$$K' = 4\left(\frac{2}{\pi}\right)^{1/2} K_{Ic} \quad \text{and} \quad E' = \frac{E}{1-\nu^2}, \qquad \text{(Eq. 6-8)}$$

with K_{Ic} being the host rock fracture toughness and E and v being Young's modulus and Poisson's ratio, respectively, also for the host rock.

However, in hydraulic fracturing, the fracture toughness of the rock is generally negligible, and the applicability of LEFM has been questioned for large-scale fractures propagating under internal pressure. The dike propagation problem is concerned with an even larger-scale feature and undoubtedly involves anelastic behavior in the surrounding rock. Thus, LEFM may not be strictly appropriate for this application. However, the LEFM formulation allows the fracture toughness to be used as a parameter that is indicative of the resistance of the rock to fracture, whatever the actual mechanism may be. Treated as a parameter, fracture toughness can be used to investigate the effect of any mechanism that resists fracture growth and thus increases the pressure.

11. Horizontal free surface: The surface topography at Yucca Mountain is relatively severe, but the dike propagation model treats it as a horizontal surface. Analysis of in situ stresses in Section 6.2.2 demonstrates that topography has negligible effect on the dike path and propagation parameters.

6.3.3 Mathematical Description

Consider a liquid-filled vertical fracture propagating in a semi-infinite impermeable elastic medium that is impermeable to the liquid (see Figure 6-8). The fracture is driven by the liquid (an incompressible Newtonian fluid), which is injected at the base of the fracture at a constant volumetric rate. The ascent of a two-dimensional dike in Earth's crust can be represented by a vertical hydraulic fracture model if several simplifications are introduced to make the problem tractable:

- Plane strain conditions apply
- The magma is injected at infinity
- The dike propagates continuously in mobile equilibrium
- Lubrication theory and linear elastic fracture mechanics are applicable.

The material constants needed to represent deformation of the rock are Young's modulus, E, Poisson's ratio, ν, fracture toughness, K_{Ic}, and density, ρ_r, while the relevant constants for the fluid are the dynamic viscosity, μ, and the density, ρ_f.

The horizontal stress field, σ_o, is taken to vary with depth z according to $\sigma_0 = \sigma_c + \kappa\rho_r g z$, where σ_c is a constant stress, g is the acceleration of gravity, and κ is a number that is typically in the range $0.3 \leq \kappa \leq 1$. Finally, the boundary conditions at infinity correspond to a constant injection flow rate, q_∞.

The goal is to determine the fracture aperture, $w(z,t)$, the fluid pressure, $p_f(z,t)$ and the flow rate, $q(z,t)$, as functions of depth z and time t, as well as determine the dependence of the solution on the problem parameters. Note that q is taken positive when directed upward, in the opposite direction to the z-axis.

Of particular interest is mapping the dependence of the solution on the injection rate, q_∞, and on the three material parameters, μ', E', K' defined previously. While E' is the so-called plane strain modulus, μ' and K' are introduced simply to keep equations uncluttered by numerical factors. For convenience, μ', E', and K' will be referred to as viscosity, elastic modulus, and toughness, respectively. The system of equations governing w, p_f, and q are summarized in the next section.

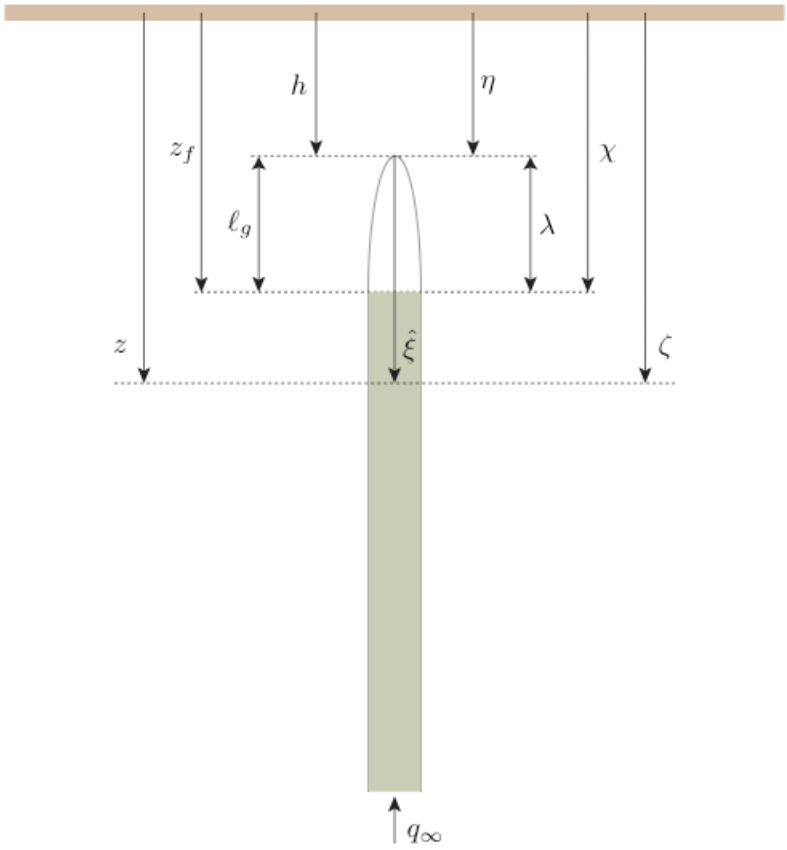

NOTES: The Roman symbols on the left side of the figure have dimensions of length.
The Greek symbols on the right are dimensionless scaled parameters as discussed in Section 6.4.3.2.

Figure 6-8. Plane-Strain, Fluid-Driven Vertical Fracture with a Lag Zone at the Tip

6.3.3.1 Governing Equations

Elasticity Equation–The elastic relation between the fluid pressure, $p_f(z,t)$, and the fracture aperture, $w(z,t)$, is expressed by a singular integral equation (Hills et al. 1996 [DIRS 163626])

$$p_f(z,t) - \sigma_o(z) = E' \int_{h(t)}^{\infty} M(z,s) \frac{\partial w(s,t)}{\partial s} \mathrm{d}s \qquad \text{(Eq. 6-9)}$$

where $M(z,s)$ is an elastic kernel that accounts for the presence of a free surface

$$M(z,s) = M_\infty(z,s) - \frac{1}{4\pi\,(z+s)} - \frac{2s}{4\pi\,(z+s)^2} + \frac{4s^2}{4\pi\,(z+s)^3} \qquad \text{(Eq. 6-10)}$$

with $M_\infty(z, s)$ denoting the Cauchy singular kernel for the infinite plane

$$M_\infty(z, s) = \frac{1}{4\pi\,(z - s)} \qquad \text{(Eq. 6-11)}$$

Hereafter $p_f - \sigma_o$ is referred to as the net pressure p.

Lubrication–The equation governing the flow of viscous fluid in the fluid-filled zone is the non-linear Reynolds differential equation from the lubrication theory

$$\frac{\partial w}{\partial t} = \frac{1}{\mu'}\frac{\partial}{\partial z}\left[w^3\left(\frac{\partial p_f}{\partial z} - \rho_f g\right)\right] \qquad \text{(Eq. 6-12)}$$

This equation is obtained by combining Poiseuille law (Equation 6-6) with the local continuity equation for an incompressible fluid:

$$\frac{\partial w}{\partial t} + \frac{\partial q}{\partial z} = 0 \qquad \text{(Eq. 6-13)}$$

For Poiseuille flow, $\partial w/\partial t$ is much less than the characteristic velocity of the problem, which is calculated below.

Boundary and Initial Conditions–The propagation criterion (Equation 6-7) imposes the asymptotic form of w at the tip.

$$w \simeq \frac{K'}{E'}(z - h)^{1/2}, \quad z \to h \qquad \text{(Eq. 6-14)}$$

This criterion obviously implies that $w = 0$ at $z = h$.

At the fluid front, $z = z_f(t)$, the fluid pressure is the pressure p_{fo} in the lag zone and the velocity of the front corresponds to the average fluid velocity at the front. Hence, recalling that $q = vw$,

$$p_f = p_{fo}, \quad \frac{\mathrm{d}z_f}{\mathrm{d}t} = \frac{w^2}{\mu'}\left(\frac{\partial p_f}{\partial z} - \rho_f g\right) \quad \text{at } z = z_f(t) \qquad \text{(Eq. 6-15)}$$

where the position of the fluid front, z_f, is given by

$$z_f = h + \ell_g \qquad \text{(Eq. 6-16)}$$

with ℓ_g being the length of the tip cavity.

The condition at infinity corresponds to a constant injection rate, q_∞:

$$q = q_\infty \quad \text{at } z = \infty \qquad \text{(Eq. 6-17)}$$

It can actually be shown that this condition corresponds to a constant mean velocity, v_∞.

The set consisting of the elasticity equation (Equation 6-9), Poiseuille law (Equation 6-6), fluid continuity (Equation 6-13), the propagation criterion (Equation 6-14), the conditions at the fluid front (Equation 6-15) and the flux at infinity (Equation 6-17) forms a complete system for determining $w(z,t)$, $p_f(z,t)$, $h(t)$ and $\ell_g(t)$, starting from known values of these quantities at an initial time, t_o. The issue of the initial conditions will be discussed below.

6.3.3.2 Scaling and Dimensionless Formulation

Scaling of this problem hinges on introducing the following characteristic quantities: length, ℓ_*; time, t_*; width, w_*; pressure, p_*; and flow rate, q_*. The values for these characteristic quantities will be determined in the following discussion. Using these quantities, the dimensionless depth, ζ, and time, τ, is defined as

$$\zeta = z/\ell_* \quad \text{and} \quad \tau = t/t_* \; ; \tag{Eq. 6-18}$$

the dimensionless fracture opening, $\Omega(\zeta, \tau)$, net pressure, $\Pi(\zeta, \tau)$, and flow rate, $\Psi(\zeta, \tau)$, as

$$\Omega = w/w_*, \; \Pi = p/p_*, \; \Psi = q/q_* \; ; \tag{Eq. 6-19}$$

as well as the depth of the fracture tip, $\eta(\tau)$, the length of the tip cavity, $\lambda(\tau)$, and the position of the fluid front, $\chi(\tau)$:

$$\eta = h/\ell_*, \; \lambda = \ell_g/\ell_*, \; \chi = z_f/\ell_* \; . \tag{Eq. 6-20}$$

From Figure 6-8, it can be seen that $\chi = \eta + \lambda$.

Using Equation 6-18 through Equation 6-20, the system of equations governing $\Omega(\zeta, \tau)$, $\Pi(\zeta, \tau)$, $\Psi(\zeta, \tau)$, $\eta(\tau)$, and $\chi(\tau)$ becomes

- Elasticity equation

$$\Pi = \mathcal{G}_e \int_\eta^\infty M(\zeta, s) \frac{\partial \Omega}{\partial s} \mathrm{d}s; \tag{Eq. 6-21}$$

- Poiseuille law

$$\mathcal{G}_m \Psi = -\Omega^3 \left(\frac{\partial \Pi}{\partial \zeta} + \mathcal{G}_\gamma \right); \tag{Eq. 6-22}$$

- Fluid continuity

$$\mathcal{G}_w \frac{\partial \Omega}{\partial \tau} - \frac{\partial \Psi}{\partial \zeta} = 0; \tag{Eq. 6-23}$$

- Fracture propagation criterion

$$\Omega = \mathcal{G}_k \, (\zeta - \eta)^{1/2} \text{ as } \zeta \to \eta; \tag{Eq. 6-24}$$

- Boundary condition in the tip cavity

$$\Pi = - \left(\mathcal{G}_s + \mathcal{G}_d \zeta \right), \; \eta < \zeta \leq \chi; \tag{Eq. 6-25}$$

- Boundary condition at the fluid front

$$\mathcal{G}_m \mathcal{G}_w \dot{\chi} = \Omega^3 \left(\frac{\partial \Pi}{\partial \zeta} + \mathcal{G}_\gamma \right); \tag{Eq. 6-26}$$

- Boundary condition at infinity

$$\Psi = \mathcal{G}_q \text{ as } \zeta \to \infty; \tag{Eq. 6-27}$$

where the eight dimensionless groups $\mathcal{G}_e, \mathcal{G}_m, \mathcal{G}_\gamma, \mathcal{G}_w, \mathcal{G}_q, \mathcal{G}_k, \mathcal{G}_s, \mathcal{G}_d$ are defined as follows:

$$\mathcal{G}_e = \frac{E' w_*}{p_* l_*}, \; \mathcal{G}_m = \frac{\mu' q_* l_*}{w_*^3 p_*}, \; \mathcal{G}_\gamma = \frac{\delta' l_*}{p_*}, \; \mathcal{G}_w = \frac{w_* l_*}{t_* q_*}, \; \mathcal{G}_q = \frac{q_\infty}{q_*} \tag{Eq. 6-28}$$

$$\mathcal{G}_k = \frac{K' \ell_*^{1/2}}{E' w_*}, \; \mathcal{G}_s = \frac{\sigma_c - p_{fo}}{p_*}, \; \mathcal{G}_d = \frac{\kappa \rho_r g \ell_*}{p_*} \tag{Eq. 6-29}$$

The particular scaling used in this problem, and hence the definitions of five characteristic quantities, ℓ_*, t_*, w_*, p_*, and q_*, is selected by imposing that the five dimensionless groups in 6-28 are all equal to one,

$$\mathcal{G}_e = \mathcal{G}_m = \mathcal{G}_\gamma = \mathcal{G}_w = \mathcal{G}_q = 1 \tag{Eq. 6-30}$$

which sets the values of five characteristic quantities to

$$\ell_* = \left(\frac{\mu' E'^3 q_\infty}{\delta'^4} \right)^{1/6}, \; w_* = \left(\frac{\mu' q_\infty}{\delta'} \right)^{1/3}, \; p_* = \left(\mu' E'^3 \delta'^2 q_\infty \right)^{1/6} \tag{Eq. 6-31}$$

$$t_* = \left(\frac{\mu' E'}{\delta'^2 q_\infty} \right)^{1/2}, \; q_* = q_\infty \tag{Eq. 6-32}$$

with $\delta' = \left(\kappa \rho_r - \rho_f \right) g$. Finally, the three remaining dimensionless groups are renamed to

$$\mathcal{G}_k \equiv \mathcal{K}, \; \mathcal{G}_s \equiv \mathcal{S}, \; \mathcal{G}_d \equiv \mathcal{D} \tag{Eq. 6-33}$$

where $\mathcal{K}$ is a scaled toughness, $\mathcal{S}$ a scaled reference stress, and $\mathcal{D}$ a scaled relative host rock density:

$$\mathcal{K} = K' \left(\frac{1}{\mu' E'^3 q_\infty} \right)^{1/4}, \quad \mathcal{S} = \frac{\sigma_c - p_{fo}}{\left(\mu' E'^3 \delta'^2 q_\infty \right)^{1/6}}, \quad \mathcal{D} = \frac{\kappa \rho_r}{\kappa \rho_r - \rho_f} \qquad \text{(Eq. 6-34)}$$

This scaling is an extension of that used by Lister (1990 [DIRS 126877]), to solve the self-similar propagation of a dike, for the time-dependent case. Note that this scaling collapses if $\delta' = 0$. In that case, an appropriate scaling would correspond to

$$\mathcal{G}_e = \mathcal{G}_m = \mathcal{G}_d = \mathcal{G}_w = \mathcal{G}_q = 1, \text{ when } \mathcal{G}_\gamma = 0 \qquad \text{(Eq. 6-35)}$$

from which new expressions for ℓ_*, t_*, w_*, p_*, and q_* can be derived

$$l_* = \left(\frac{\mu' E'^3 q_\infty}{g^4 \kappa^4 {\rho_r}^4} \right)^{\frac{1}{6}}, \quad w_* = \left(\frac{\mu' q_\infty}{g \kappa \rho_r} \right)^{\frac{1}{3}}, \quad p_* = \left(\mu' E'^3 q_\infty g^2 \kappa^2 {\rho_r}^2 \right)^{\frac{1}{6}} \qquad \text{(Eq. 6-36)}$$

$$t_* = \left(\frac{\mu' E'}{q_\infty g^2 \kappa^2 {\rho_r}^2} \right), \quad q_* = q_\infty \qquad \text{(Eq. 6-37)}$$

In summary, the set of scaled governing equations can be written as

$$\Pi(z,t) = \int_{\eta(t)}^{\infty} ds \; M(\zeta, s) \frac{\partial \Omega(s,t)}{\partial s}, \quad \Psi = -\Omega^3 \left(\frac{\partial \Pi}{\partial \zeta} + 1 \right), \quad \frac{\partial \Omega}{\partial \tau} - \frac{\partial \Psi}{\partial \zeta} = 0 \qquad \text{(Eq. 6-38)}$$

with the propagation criterion and the conditions in the lag zone, at the fluid front and at infinity given by

$$\Omega = \mathcal{K} (\zeta - \eta)^{1/2}, \quad \zeta \to \eta \qquad \text{(Eq. 6-39)}$$

$$\Pi = -(\mathcal{S} + \mathcal{D}\zeta), \quad \eta < \zeta \leq \chi \qquad \text{(Eq. 6-40)}$$

$$\dot{\chi} = \Omega^2 \left(\frac{\partial \Pi}{\partial \zeta} + 1 \right), \quad \zeta = \chi \qquad \text{(Eq. 6-41)}$$

$$\Psi = 1, \quad \zeta \to \infty \qquad \text{(Eq. 6-42)}$$

The system of equations (Equation 6-38 through Equation 6-42) is closed in the sense that it can be used to determine the solution $\mathcal{F}(\zeta, \tau; \mathcal{K}, \mathcal{S}, \mathcal{D})$ where $\mathcal{F} = \{\Omega, \Pi, \Psi, \eta, \chi\}$, given a suitable set of initial conditions.

The dependence of the solution on time arises through the boundary conditions in the tip cavity (which is changing with the depth η) and through the elastic kernel, which accounts for the distance to the free surface. The dependence on time, τ, can then be replaced by a dependence on the depth η, once the solution has been determined for $\eta = \eta(\tau)$. Thus, the solution can be

expressed as $\bar{\mathcal{F}}(\zeta, \eta; \mathcal{K}, \mathcal{S}, \mathcal{D})$ with $\bar{\mathcal{F}} = \{\bar{\Omega}, \bar{\Pi}, \bar{\Psi}, \bar{\lambda}\}$. The overbar denotes that the field quantities depend on η instead of the time as the dependent variable.

6.3.3.3 Simplifications in the Case of the Dike Problem

It has been noted by various authors that rock toughness in the case of dike propagation through the Earth's crust often is not relevant, as $\mathcal{K} \ll 1$ (Spence and Turcotte 1985 [DIRS 127068]; Lister and Kerr 1991 [DIRS 126889]; Rubin 1995 [DIRS 164118]). Also, the case $\mathcal{S} = 0$ is an appropriate case. In other words, the particular solution $\mathcal{K} = \mathcal{S} = 0$ is very relevant. This solution is denoted by $\mathcal{F}_o(\zeta, \tau; \mathcal{D})$ or by $\bar{\mathcal{F}}_o(\hat{\xi}, \eta; \mathcal{D})$; it only depends on parameter $\mathcal{D}$. Because $\mathcal{K} = 0$, aperture Ω behaves at the dike tip according to Rice (1968 [DIRS 164405])

$$\Omega \sim (\zeta - \eta)^{3/2}, \quad \zeta \to \eta \tag{Eq. 6-43}$$

where the coefficient of proportionality is unknown *a priori*, as it is part of the solution. For this case, the condition of zero toughness is best imposed by

$$\int_{\eta}^{\infty} \frac{\Pi(s)}{s^{1/2}}\, \mathrm{d}s = 0 \tag{Eq. 6-44}$$

which uses the integral representation of the stress intensity factor. Note that the particular asymptotic behavior (Equation 6-43) is based on λ being not very small. (The term in $(\zeta - \eta)^{3/2}$ actually corresponds to the next term of the fracture opening expansion when $\mathcal{K} > 0$, according to linear elastic fracture mechanics.) When $\lambda \ll 1$, the behavior (Equation 6-43) takes place over a region so small that it is not visible in this scaling. Under these conditions, an intermediate asymptote develops

$$\Omega \sim (\zeta - \eta)^{2/3}, \quad \zeta \to \eta \tag{Eq. 6-45}$$

(See Section 6.4.3.5 for a discussion of cases characterized by small tip cavities.)

It can be readily shown (as recognized by Lister (1990 [DIRS 126877]) for the self-similar case) that the solution behaves at infinity as

$$\Omega = 1, \ \Pi = \frac{1}{4\pi\zeta}, \ \zeta \to \infty \tag{Eq. 6-46}$$

The first of these equations implies that $w_\infty = w_*$.

The average scaled fluid velocity, Υ, is also found to be

$$\Upsilon \equiv \Psi/\Omega = 1, \ \zeta \to \infty \tag{Eq. 6-47}$$

In dimensional terms, the average fluid velocity at infinity, v_∞, is given as

$$v_\infty \equiv \frac{q_\infty}{w_\infty} = \frac{q_\infty}{w_*} = \left(\frac{\delta' q_\infty^2}{\mu'}\right)^{1/3} \quad \text{(Eq. 6-48)}$$

Actually, it is convenient to formulate the boundary conditions at infinity in terms of v_∞, rather thanq_∞; hence, the characteristic quantities can be formulated as follows

$$\ell_* = \left(\frac{\mu' E'^2 v_\infty}{\delta'^3}\right)^{1/4},\ w_* = \left(\frac{\mu' v_\infty}{\delta'}\right)^{1/2},\ p_* = \left(\mu' E'^2 \delta' v_\infty\right)^{1/4} \quad \text{(Eq. 6-49)}$$

$$t_* = \frac{\ell_*}{v_\infty},\ q_* = v_\infty w_*$$

and the dimensionless groups become

$$\mathcal{K} = K' \left(\frac{\delta'}{\mu'^3 E'^6 v_\infty^3}\right)^{1/8},\ \mathcal{S} = \frac{\sigma_c - p_{f0}}{\left(\mu' E'^2 \delta' v_\infty\right)^{1/4}} \quad \text{(Eq. 6-50)}$$

with $\mathcal{D}$ remaining unchanged.

As is discussed in Section 6.3.6, boundary conditions for dike propagation are not given as a rate of magma influx at infinity, q_∞, but in terms of a dike opening at infinity, w_∞, and the dike velocity at infinity, v_∞. Therefore, it is more convenient to express scaling quantities and dimensionless groups in terms of the dike opening and the dike velocity at infinity (i.e., at large distance from the dike tip). Using Equation 6-48 and the second line of Equation 6-49 with $w_* = w_\infty$, the scaling quantities can be written:

$$l_* = \left(\frac{E' w_\infty^3}{\mu' v_\infty}\right)^{1/2},\ w_* = w_\infty,\ p_* = \left(\frac{\mu' E' v_\infty}{w_\infty}\right)^{1/2} \quad \text{(Eq. 6-51)}$$

$$t_* = \left(\frac{E'^2 w_\infty^3}{\mu'^2 v_\infty^3}\right),\quad q_* = w_\infty v_\infty \quad \text{(Eq. 6-52)}$$

and the dimensionless groups become

$$\mathcal{K} = K' \left(\frac{1}{\mu' E'^3 v_\infty w_\infty}\right)^{1/4},\ \mathcal{S} = \frac{\sigma_c - p_{f_0}}{\left(\mu' E' v_\infty / w_\infty\right)^{1/2}},\ \mathcal{D} = \frac{\kappa \rho_r g {w_\infty}^2}{\mu' v_\infty} \quad \text{(Eq. 6-53)}$$

6.3.3.4 Self-Similar Problem of a Deep Dike

Formulation of the deep dike problem solved by Lister (1990 [DIRS 126877]) can be deduced from the more general equations derived in the previous subsections of this section. First, the equations are reformulated in terms of the moving coordinate $\hat{\xi} = \zeta - \eta$. The solution is now

of the form $\hat{\mathcal{F}}(\hat{\xi}, \tau; \mathcal{K}, \mathcal{S}, \mathcal{D})$ where $\hat{\mathcal{F}} = \{\hat{\Omega}, \hat{\Pi}, \hat{\Psi}, \eta, \lambda\}$. The spatial and time derivative transform as

$$\frac{\partial}{\partial \zeta} = \frac{\partial}{\partial \hat{\xi}}, \quad \left.\frac{\partial}{\partial \tau}\right|_{\zeta} = \left.\frac{D}{D\tau}\right|_{\hat{\xi}} - \dot{\eta}\frac{\partial}{\partial \hat{\xi}} \tag{Eq. 6-54}$$

In summary, the set of governing equations can be written as

$$\hat{\Pi} = \int_0^{\infty} \hat{M}(\hat{\xi}, \hat{s}; \eta)\, \frac{\partial \hat{\Omega}}{\partial \hat{s}} \mathrm{d}\hat{s}, \quad \hat{\Psi} = \hat{\Omega}^3 \left(\frac{\partial \hat{\Pi}}{\partial \hat{\xi}} + 1\right), \quad \frac{D\hat{\Omega}}{D\tau} - \dot{\eta}\frac{\partial \hat{\Omega}}{\partial \hat{\xi}} - \frac{\partial \hat{\Psi}}{\partial \hat{\xi}} = 0 \tag{Eq. 6-55}$$

where the elastic kernel $\hat{M}(\hat{\xi}, s; \eta)$ is now given by

$$\hat{M}(\hat{\xi}, \hat{s}; \eta) = \hat{M}_{\infty}(\hat{\xi}, \hat{s}) - \frac{1}{4\pi\left(\hat{\xi} + \hat{s} + 2\eta\right)} - \frac{2(\hat{s} + \eta)}{4\pi\left(\hat{\xi} + \hat{s} + 2\eta\right)^2} + \frac{(4\hat{s} + \eta)^2}{4\pi\left(\hat{\xi} + \hat{s} + 2\eta\right)^3} \tag{Eq. 6-56}$$

with $M_{\infty}(z, s)$ denoting the Cauchy singular kernel for the infinite plane

$$M_{\infty}(z, s) = \frac{1}{4\pi\left(\hat{\xi} - \hat{s}\right)} \tag{Eq. 6-57}$$

The propagation criterion and the conditions in the lag zone, at the fluid front and at infinity are given by

$$\hat{\Omega} = \mathcal{K}\hat{\xi}^{1/2}, \ \hat{\xi} \to 0 \tag{Eq. 6-58}$$

$$\hat{\Pi} = -\left[\mathcal{S} + \mathcal{D}\left(\hat{\xi} + \eta\right)\right], \ 0 < \hat{\xi} \leq \lambda \tag{Eq. 6-59}$$

$$\dot{\eta} + \dot{\lambda} = -\Omega^2 \left(\frac{\partial \Pi}{\partial \zeta} + 1\right), \ \zeta = \chi \tag{Eq. 6-60}$$

$$\hat{\Psi} = 1, \ \zeta \to \infty \tag{Eq. 6-61}$$

The equations of the problem solved by Lister (1990 [DIRS 126877]) can be deduced from the general system (Equation 6-55 through Equation 6-61) if the dike is deep enough that the effect of the free surface is negligible and the solution is self-similar. It can be easily shown that self-similarity implies that the average magma velocity is constant along the dike and equal to the velocity of ascent of the dike. This approach implies, therefore, that

$$\hat{M} = \hat{M}_{\infty}, \quad \frac{D\hat{\Omega}}{D\tau} = 0, \quad \dot{\lambda} = 0, \quad \dot{\eta} = -1 \tag{Eq. 6-62}$$

The solution is now of the form $\hat{\mathcal{F}}_{ss}(\hat{\xi}; \mathcal{K}, \mathcal{S}, \mathcal{D}, \eta)$, where $\hat{\mathcal{F}}_{ss} = \{\hat{\Omega}, \hat{\Pi}, \hat{\Psi}, \lambda\}$ and is governed by

$$\hat{\Pi} = \int_0^{\infty} \hat{M}_{\infty}(\hat{\xi}, \hat{s}) \frac{\mathrm{d}\hat{\Omega}}{\mathrm{d}\hat{s}} \mathrm{d}\hat{s}, \quad \hat{\Omega}^2 \left(\frac{\mathrm{d}\hat{\Pi}}{\mathrm{d}\hat{\xi}} + 1 \right) = 1 \qquad \text{(Eq. 6-63)}$$

and

$$\hat{\Omega} = \mathcal{K}\hat{\xi}^{1/2}, \ \hat{\xi} \to 0; \ \hat{\Pi} = -\left[\mathcal{S} + \mathcal{D}\left(\hat{\xi} + \eta \right) \right], \ 0 < \hat{\xi} \leq \lambda; \ \hat{\Omega} = 1, \ \zeta \to \infty \qquad \text{(Eq. 6-64)}$$

Note, however, that a strictly self-similar solution does not exist, as depth η enters into the problem formulation via the boundary condition in the lag zone. Thus, within the approximation of self-similarity, the evolution problem is actually seen as a sequence of self-similar solutions.

Numerical solution of the system of equations (Equation 6-63 to Equation 6-64) is given by Lister (1990 [DIRS 126877])[†]. This solution actually could be used as a suitable initial condition for the general problem—i.e.,

$$\mathcal{F}(\zeta - \eta_o, 0; \mathcal{K}, \mathcal{S}, \mathcal{D}, \eta) = \mathcal{F}_{ss}(\hat{\xi}; \mathcal{K}, \mathcal{S}, \mathcal{D}, \eta_o) \qquad \text{(Eq. 6-65)}$$

where $\eta_o \gg 1$. However, in practical terms, $\eta_o \simeq 2$, as the free-surface effect is negligible at those depths.

6.3.4 Model Uncertainties and Limitations

Uncertainties–Given that the dike propagation problem is relatively complex, any attempt at numerical modeling will have many embedded uncertainties. The approach taken in the base-case modeling is a two-dimensional model of a three-dimensional process. Because the large scale of a dike is very favorable for creating two-dimensional processes in the center of the dike, the effect of three-dimensional processes is not considered in this report.

Similar uncertainties exist with regard to fluid and rock properties. The modeling requires that the fluid be incompressible and the properties constant so that minimal differentiation (particularly vertically) within the magma is allowed except in the separate tip cavity. Clearly, there is also a large range of possible magma properties (viscosity and density) that could be employed, but evaluation of a range of conditions results in a bounding of the problem.

The boundary element approach also requires a constant material-property set for the host rock, so that no variation, either between layers or laterally, can be accommodated. Rather, a uniform, average condition is used in the calculation. This approach results in a model that does not account for stratigraphy. The effect of topography can be accounted for with respect to its effect on stress—which should be the dominating feature of topography—but other plausible effects

[†] Lister uses $\hat{x}$, $\hat{h}$ and $\hat{p}$ to denote the characteristic quantities used to scale distance, dike width, and net pressure, respectively. These quantities are related to those defined here according to $\hat{x} = \ell_*/2$, $\hat{h} = w_*/2$, $\hat{p} = p_*/2$.

(e.g., a modified free surface, rotation of the stress field, etc.) are so small that they need not be considered.

The dike propagation model is very flexible with respect to the far-field stress and either a density-defined stress field or an applied side load can be used. However, in the present model, the applied far-field stress affects only the condition of dike propagation. The stress gradient, which controls the magma pressure gradient, is defined by rock mass density and coefficient of lateral stress only. Consequently, magma buoyancy is independent of the applied far-field stress (e.g., repository-induced thermal stresses). Also, exact values for the stresses are based on only three stress measurements in the vicinity of Yucca Mountain (Stock et al. 1985 [DIRS 101027]) and on calculations of the stress field that might develop with heating of the repository (see Section 6.2.4).

For a large-scale dike, analysis of the important mechanisms suggests that the fracture criterion is immaterial for dike propagation. However, the application of LEFM principles to a problem of this scale has been questioned, and some other criterion could potentially be more appropriate. The LEFM approach was employed here, but elevated values of fracture toughness were considered to assess possible effects. Coupled with the fracture criterion is the pressure in the fluid-tip cavity. This pressure is controlled by the dike-fracture criterion, the permeability of the host rock, the pore pressure of the host rock, the exsolution of vapor from the magma, and the overall dike parameters. At this time, there is no method to calculate the tip-cavity pressure, so a range of values from atmospheric to considerably higher levels is employed.

Self-similar (far-field) conditions of dike ascent are defined by the dike aperture and magma velocity. The magma source is taken to be at a depth that is effectively equivalent to an infinite depth. The model allows only an injection-rate boundary condition at the source. It requires positive buoyancy of the magma to keep it moving vertically upward; otherwise, the magma will stagnate or form a sill. Ranges of magma density and the gradient of far-field stress were considered in the analysis.

Once the dike reaches the free surface, the calculations terminate. As a result, it is not possible to calculate any evolution of the conditions after intersection. Some speculations are offered about the continued development of the dike, but these are extrapolations of prior conditions.

Uncertainties in the future state, parameters, and processes are primarily those associated with the range of possible dike source conditions and magma properties. In situ stresses are not likely to change significantly except due to heating, which has already been accounted for using the thermo-mechanical response of the repository. Rock properties far from the repository drift will not change over this time frame, which is minute compared to usual geologic changes. The potential for changes in the rock properties adjacent to drifts has been addressed in *Drift Degradation Analysis* (BSC 2004 [DIRS 166107]). Thus, changes in magma outflow and viscosity are the most-likely variable properties. Because a range of these parameters is considered, it is expected that most future uncertainties have already been accounted for.

Limitations–The limitations of the dike propagation model are related to the simplifications discussed in Section 6.3.2. A limitation of the model is that the rock mass, which in reality is a heterogeneous, layered medium, is represented as homogeneous and isotropic. Another model limitation is that the actual ground surface topography cannot be represented. Instead, the ground surface is taken in the model to be planar. This is justified in Section 6.3.2.

A major limitation of the model is that it does not account for bulk density changes (compressibility) due to vesiculation of the magma, which is likely to occur as the magma rises above a depth of approximately 5 km (depending on the water content (BSC 2004 [DIRS 169980], Figure 6-3, p. 6-30; Detournay et al. 2003 [DIRS 169660], Figure 2.1c) and could lead to density changes of a factor of two or more in the upper 2000 m. To account for this, an approximation is developed in Section 6.3.8.2 to address the effect of magma compressibility.

An associated limitation of the model is that the rheology of the magma will be affected by the bubbles that form at less than 5 km depth (as described in the previous paragraph). At and below the magma front, the vapor fraction will be significant. The flow regimes for basaltic magma can be:

- Homogeneous with small, low Reynolds number bubbles moving with the melt
- Bubbly flow with bubbles rising faster than the melt
- Slug flow with bubble sizes approaching the width of the dike (Vergniolle and Jaupart 1986 [DIRS 115585]).

Which flow regime is operative will be a function of many variables including, but not limited to, moisture content, other gases present, pressure, melt viscosity and surface tension. For example, as the magma first encounters a drift, it may do so under slug flow; as time progresses and the magma front continues up the dike, flow entering the drift may become bubbly. The viscosity of bubbly flow is very complicated and in certain cases will be non-Newtonian. This could include either shear thinning or shear thickening depending on the variables listed above (Detournay et al. 2003 [DIRS 169660], Appendix 2, page 1, Figure 2B). Therefore, it is not possible to determine the effect of this uncertainty.

6.3.5 Model Inputs

The input data for the Dike Propagation Model consist of formation (rock) properties, magma properties, boundary stresses, and dike parameters (Table 6-2). Those parameters derived from sources external to this document (direct input) are also listed in Table 4-1. Other values are included in Table 6-2 where data values have been selected from a range of data presented in the source cited, or are for illustrative purposes. The basis for selection of such values is discussed below. There are uncertainties in these parameters because of the scale of the calculations (several kilometers) and the possible changes in properties over such distances. Section 6.3.8.2 addresses the effects of expanding magma related to magma properties.

Table 6-2. Inputs to Dike Propagation from Depth Model

Parameter	Value
Young's Modulus of Host Rock (E) (Detournay et al. [DIRS 169660], Table 1-2	15 GPa
Poisson's Ratio of Host Rock (ν) (Detournay et al. 2003 [DIRS 169660], Table 1-2)	0.21
Density of Host Rock (ρ_r) (DTN: SNL02030193001.027 [DIRS 108410])	2400 kg/m^3
Toughness of Host Rock (K_{Ic}) (Detournay et al. 2003 [DIRS 169660], Table 1-2)	0.3 MPa-m$^{1/2}$
Ratio of Minimum Principal Stress to Vertical Stress of Host Rock (κ) (coefficient of horizontal stress)	0.5, 1.0
Magma Density (ρ_f) Detournay et al. 2003 [DIRS 169660], Figure 2-1e)	751–2282 kg/m^3
Magma Viscosity (μ) Detournay et al. 2003 [DIRS 169660], Figure 2-1e)	10–40 Pa·s
Pressure in Dike Tip (p_{f0})	0.0–0.49 MPa
Far-Field Magma Velocity (v_∞)	1-15 m/s
Gravitational Acceleration (g) (Incropera and DeWitt 2002 [DIRS 163337])	9.81 m/s^2

The formation properties (those of the repository host rock) include Young's modulus, Poisson's ratio, and density, which have been measured and are available as qualified data. A fourth parameter, fracture toughness, has not been specifically measured for the repository. This lack is not a problem because fracture toughness is irrelevant at this scale because the rocks are already highly fractured prior to arrival of the crack tip and dike, and ascent of the dike is, therefore, accommodated by slip along these pre-existing fracture surfaces (Rubin 1995 [DIRS 164118], p. 321; Rubin and Gillard 1998 [DIRS 169786], pp. 10017 and 10026; Rubin et al. 1998 [DIRS 169787], p. 10011). In the analysis reported here, fracture toughness is treated as a parameter that is always small but may span a few orders of magnitude to account for non-ideal processes that may be associated with dike propagation.

Considering the scale (kilometers) of the analyzed problem, and that the main objective of the analysis is to describe phenomena associated with dike propagation in the vicinity of the repository, elastic properties (Young's modulus of 15 GPa and Poisson's ratio of 0.21) were selected to be representative of TSw1 and TSw2 thermal-mechanical units (Detournay et al. 2003 [DIRS 169660], Table 1-2). The input value for density of rock mass (2400 kg/m^3) was selected as representative of saturated density of Tptpln unit (DTN: SNL02030193001.027 [DIRS 108410]). Because the results can be rescaled for other formation property values, the exact values used in the inputs do not seriously constrain the applicability of the results.

The input magma properties are density and viscosity. Magma density varies depending on composition of magma but is also a function of depth (i.e., pressure). A range of magma densities between 751 and 2282 kg/m^3 was considered in the analysis. This range is derived from Detournay et al. (2003 [DIRS 169660], Figure 2-1e). Magma viscosity is a complicated function of composition (both silicate and volatile), temperature, and pressure. Many of the calculations used in this model are for magmas less dense than 1300 kg/m^3, which consist of

more than 50 percent by volume gas. The viscosity of such a mixture is uncertain, so a viscosity range of 10 Pa·s to 40 Pa·s, equivalent to the pure silicate liquid is used. The range of viscosities used in the analysis is derived from Detournay et al. (2003 [DIRS 169660], Figure 2-1e). Most of the results in this report are for a viscosity of 10 Pa·s, representing a fluid magma that would quickly fill the drifts and, therefore, a more conservative condition from the perspective of dike/drift interaction. Some supplementary results for 40 Pa·s were also calculated.

The data range used for pressure in the dike tip is defined based on scaling calculations discussed further in Section 6.3.7.2. Results are derived from far-field magma velocity of 1, 5, 10, and 15 m/s to illustrate the effect of this variable.

Another input parameter is the far-field magma flux, q_∞. The far-field dike width is calculated from q_∞, the formation properties, and the magma properties.

The boundary stresses include the overburden stress, which is obtained by integrating the density of the overlying rock, and the distribution of the minimum principal horizontal in situ stress (against which the dike must open). The NPHF2D code uses the relation $\kappa = \nu/(1-\nu)$ from linear elastic theory. In order to obtain values of minimum principal horizontal stress consistent with stress measurements at Yucca Mountain for in situ conditions and consistent with the host rock density of 2400 kg/m^3 and Poisson's ratio of 0.21 in Table 6-2, the input value of rock density to the code was set artificially to the value of 9022 kg/m^3; the magnitude of this input number has no other effect on the calculation because inertial forces are neglected. The height of the overburden varies between 250 and 400 m (BSC 2004 [DIRS 170029]). Approximate depth to the repository horizon (300m) was used as an input for the analysis.

In situ stress measurements (DTN: SNF37100195002.001 [DIRS 131356]) show that the ratio of the minor horizontal principal stress to the vertical stress is 0.361 and the ratio of the major horizontal principal stress to the vertical stress is 0.617. The ratio of the horizontal stress normal to the dike to the vertical stress (called the coefficient of horizontal stress) was set, as a model constraint, to be 0.5 or 1.0 to demonstrate the effect of this variable on the solution.

6.3.6 Boundary and Initial Conditions

The initial and boundary conditions required for analysis of fluid-driven fractures, in addition to the in situ stress state, are the initial depth of the fracture tip and the flow rate at the starting point of the fracture. The magma injection rate at the source depth may be cast in terms of the far-field magma velocity and the far-field dike width. However, on average, according to field observations (Rubin 1995 [DIRS 164118]), the dike openings are in a range between 0.1 m and 10 m. The range of far-field magma velocity for dike widths of .5 m, 1.5 m, and 4.5 m, calculated according to *Characterize Eruptive Processes at Yucca Mountain, Nevada* (BSC (2004 [DIRS 169980], Table 6-3), is 1 m/s, 5 m/s, and 12 m/s, respectively, if the buoyancy is 50 kg/m^3.

It was shown in Section 6.3.3.3 and in (Lister 1990 [DIRS 126865]) that for the case of a semi-infinite dike, the dike opening and magma velocity at large distances from the dike tip are:

$$w_\infty = \left(\frac{\mu' q_\infty}{\delta'}\right)^{1/3} \quad \text{(Eq. 6-66)}$$

$$v_\infty = \left(\frac{\delta' q_\infty^2}{\mu'}\right)^{1/3} \quad \text{(Eq. 6-67)}$$

Combining relations Equation 6-66 and Equation 6-67, the following expression is obtained:

$$v_\infty = \frac{\delta'}{\mu'} w_\infty^2 \quad \text{(Eq. 6-68)}$$

Equation 6-68 is plotted in Figure 6-9 for different values of ratio $\delta'/\mu' \equiv (\kappa\rho_r - \rho_f)\, g/12\mu$. Using the plot in Figure 6-9, it is possible to select the far-field dike opening, w_∞, and far-field dike ascent velocity*, v_∞, as function of controlling parameters, $\kappa\rho_r - \rho_f$ and μ. The range of velocities, v_∞, used in this simulation is taken to be from 1.0 to 15.0 m/s, covering the range calculated above. The range of values for the far field dike widths, w_∞, used was from 0.12 to 3.5 m. These parameters give a range of far-field injection rates, q_∞, from 0.12 to 53 m^2/s.

The boundary conditions associated with the medium include the horizontal principal minimum in situ stress and overburden stress acting within the formation.

6.3.7 Model Results

In this model, the problem of dike propagation is calculated in dimensional form using the relations in Section 6.3.3.1; the results are then reformulated in dimensionless form as is described in Section 6.3.3.2. The host rock density and magma density are combined into a dimensionless group called relative density, $\mathcal{D}$. Confining stress, pressure in the crack tip, magma viscosity, and density, Young's modulus, Poisson's ratio, and density of the host rock, gravitational acceleration and the magma supply rate, are combined to form a dimensionless group called reference stress, $\mathcal{S}$. A third dimensionless group, called toughness, $\mathcal{K}$, is formed from the fracture toughness of the host rock, the elastic properties of the host rock, the magma viscosity and the magma supply rate. Conditions of dike assent are calculated from the values of these dimensionless groups, not directly from the dimensional parameters listed here as input.

* At sufficient depth, the dike propagates as self-similar (Lister 1990 [DIRS 126877]). One of consequences of self-similarity is that the dike tip velocity, magma front velocity and magma velocity are the same.

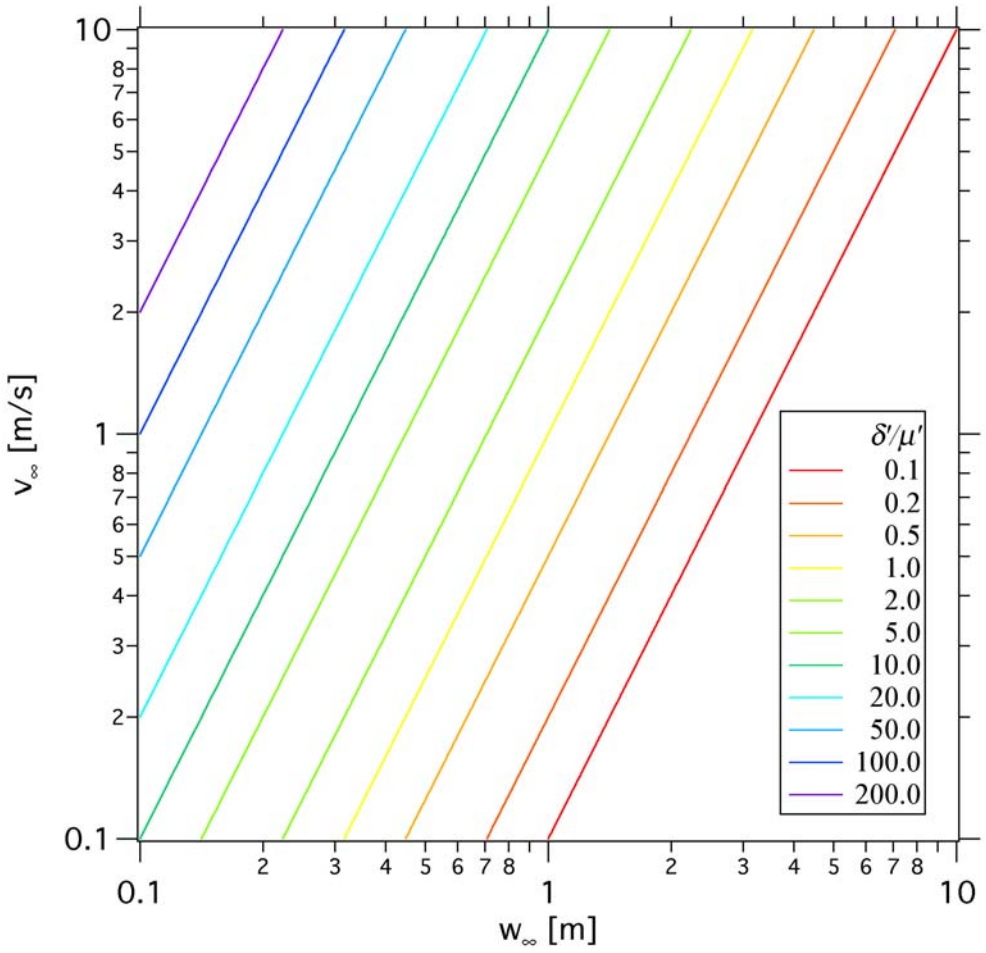

Figure 6-9. Relation between Far-Field Fluid Velocity and Far-Field Dike Opening from Equation 6-68

Results using a range of relative densities, $\mathcal{D}$, set to 2.67, 6.02, and 20.28 and reference stresses, $\mathcal{S}$, between –0.25 and 0.0 are given in this model report. A single value of toughness, $\mathcal{K}$, equal to 3.7 x 10^{-3} (corresponding to a host rock fracture toughness of 0.3 MPa-$m^{1/2}$) was used for all calculations that are discussed in detail, although one calculation with a toughness of 0.37 was done to demonstrate that the results are insensitive to values of this parameter.

The dimensionless fracture toughness for the range of mechanical parameters representative of the Yucca Mountain site has $\mathcal{K} \ll 1$. Consequently, if there is no leak-off into the repository, the problem solution is a function of two parameters only: $\mathcal{S}$ and $\mathcal{D}$.

The problem is solved first for the base case, in Section 6.3.7.1, with conditions of atmospheric pressure inside the tip cavity, $p_{fo} = 0$, and constant, far-field horizontal stress equal to zero, $\sigma_c = 0$. Under these conditions $\mathcal{S} = 0$. The base case corresponds to the in situ conditions, unaffected by the repository (i.e., there is no increase in the horizontal stresses due to heating or leak-off into the repository drifts). Also, by considering the diffusivity of the gas in the rock formations (on the order of 10^{-12} m^2/s, Detournay et al. 2003 [DIRS 169660]), the assumption of atmospheric gas pressure inside the tip cavity appears to be realistic. However, the problem was also analyzed for $\mathcal{S} < 0$, to investigate the effects of gas pressure inside the tip cavity in

Section 6.3.7.2. Increased horizontal stresses, $\delta > 0$, due to repository heating are addressed separately in Section 6.3.7.3 using a different numerical approach.

6.3.7.1 Base Case

Dimensionless results for the three values of: $\mathcal{D}$ 2.67, 6.02 and 20.28, are shown in Figure 6-10. From these three dimensionless solutions, dimensional solutions are derived for various combinations of parameters: two effective rock mass densities $\kappa\rho_r$ (i.e., rock density multiplied by the horizontal stress coefficient), four magma velocities v_∞, and two magma viscosities μ. Derived parameters for each value of $\mathcal{D}$ and for a number of parameter combinations are shown in Table 6-3. The selected range of $\mathcal{D}$ covers the expected range of variation of $\kappa\rho_r - \rho_f$. The curves shown in Figure 6-10 confirm that the solution is independent of $\mathcal{D}$ until the tip cavity develops (Zhang et al. 2002 [DIRS 164368]). As can be expected intuitively, the tip cavity forms earlier for smaller values of $\mathcal{D}$. For large values of $\mathcal{D}$, (i.e., $\mathcal{D} \sim O$ (10)), the tip cavity forms "close" to the ground surface.

Table 6-3. Independent and Derived Parameters for Base Case Simulations

Independent Parameters					Derived Parameters			
$\mathcal{D}$	v_∞ (m/s)	μ (Pa·s)	κ	$\kappa\rho_r$ (kg/m^3)	ρ_f (kg/m^3)	$\kappa\rho_r - \rho_f$ (kg/m^3)	w_∞ (m)	q_∞ (m^2/s)
2.67	15	10	1.0	2400	1501	899	0.452	6.78
2.67	10	10	1.0	2400	1501	899	0.369	3.69
2.67	5	10	1.0	2400	1501	899	0.261	1.30
2.67	1	10	1.0	2400	1501	899	0.117	0.12
6.02	15	10	1.0	2400	2001	399	0.678	10.18
6.02	10	10	1.0	2400	2001	399	0.554	5.54
6.02	5	10	1.0	2400	2001	399	0.392	1.96
6.02	1	10	1.0	2400	2001	399	0.175	0.18
20.28	15	10	1.0	2400	2282	118	1.245	18.68
20.28	10	10	1.0	2400	2282	118	1.017	10.17
20.28	5	10	1.0	2400	2282	118	0.719	3.59
20.28	1	10	1.0	2400	2282	118	0.322	0.32
20.28	15	40	1.0	2400	2282	118	2.490	37.35
20.28	10	40	1.0	2400	2282	118	2.033	20.33
20.28	5	40	1.0	2400	2282	118	1.438	7.19
20.28	1	40	1.0	2400	2282	118	0.643	0.64
2.67	15	10	0.5	1200	751	449	0.639	9.58

Table 6-3. Independent and Derived Parameters for Base Case Simulations (Continued)

Independent Parameters					Derived Parameters			
$\mathcal{D}$	v_∞ (m/s)	μ (Pa s)	κ	$\kappa\rho_r$ (kg/m^3)	ρ_f (kg/m^3)	$\kappa\rho_r - \rho_f$ (kg/m^3)	w_∞ (m)	q_∞ (m^2/s)
2.67	10	10	0.5	1200	751	449	0.522	5.22
2.67	5	10	0.5	1200	751	449	0.369	1.84
2.67	1	10	0.5	1200	751	449	0.165	0.16
6.02	15	10	0.5	1200	1001	199	0.959	14.39
6.02	10	10	0.5	1200	1001	199	0.783	7.83
6.02	5	10	0.5	1200	1001	199	0.554	2.77
6.02	1	10	0.5	1200	1001	199	0.248	0.25
20.28	15	10	0.5	1200	1141	59	1.761	26.41
20.28	10	10	0.5	1200	1141	59	1.438	14.38
20.28	5	10	0.5	1200	1141	59	1.017	5.08
20.28	1	10	0.5	1200	1141	59	0.455	0.45
20.28	15	40	0.5	1200	1141	59	3.522	52.83
20.28	10	40	0.5	1200	1141	59	2.876	28.76
20.28	5	40	0.5	1200	1141	59	2.033	10.17
20.28	1	40	0.5	1200	1141	59	0.909	0.91

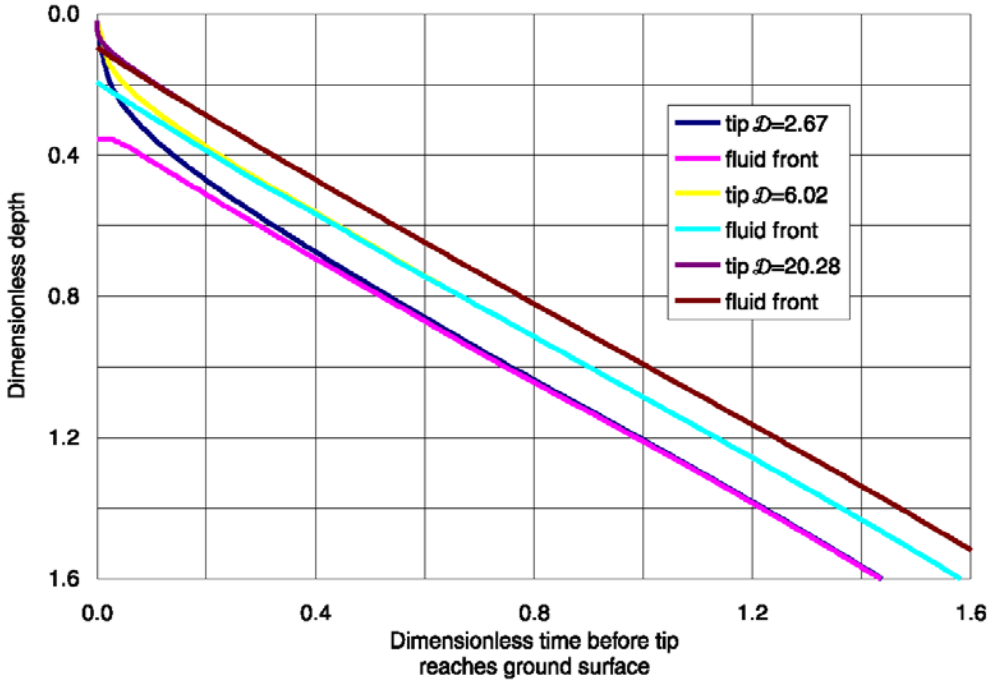

Output DTN: MO0408EG831811.004.

Source: Output data calculation plots.

Figure 6-10. Dimensionless Solution for Dike Tip and Fluid Front as Functions of Time

The dimensionless results from Figure 6-10 are rescaled using the relations from Section 6.3.3.2 to provide the results in dimensional form, assuming different values of v_∞. The positions of the dike tip and the fluid front as functions of time are shown in Figures 6-11 through 6-18.

For each value of $\mathcal{D}$, results are presented for two values for $\kappa\rho_r$: 2400 kg/m^3 and 1200 kg/m^3. The value of $\kappa\rho_r$ equal to 2400 kg/m^3 represents the case of a hydrostatic in situ stress state, in which the horizontal stress at the repository level (i.e., 300-m below the ground surface) would be 7.2 MPa. Measurements (DTN: SNF37100195002.001 [DIRS 131356]) at the site and knowledge of the regional stress state indicate that horizontal stress at the repository level is in the range of 3.5 MPa (i.e., κ is close to 0.5 for ρ_r = 2400 g/m^3). Therefore, $\kappa\rho_r$ equal to 1200 kg/m^3 seems to be a better representation of the in situ stress state at Yucca Mountain.

The results are shown for four velocities, v_∞= 1 m/s, 5 m/s, 10 m/s and 15 m/s. Corresponding dike openings, w_∞ were calculated from the condition that $\mathcal{D}$ remains invariant (see Equation 6-53).

Most of the results were generated for magma viscosity equal to 10 Pa·s, with some results for a viscosity of 40 Pa·s, (see Figures 6-17 and 6-18) resulting in wider dike apertures.

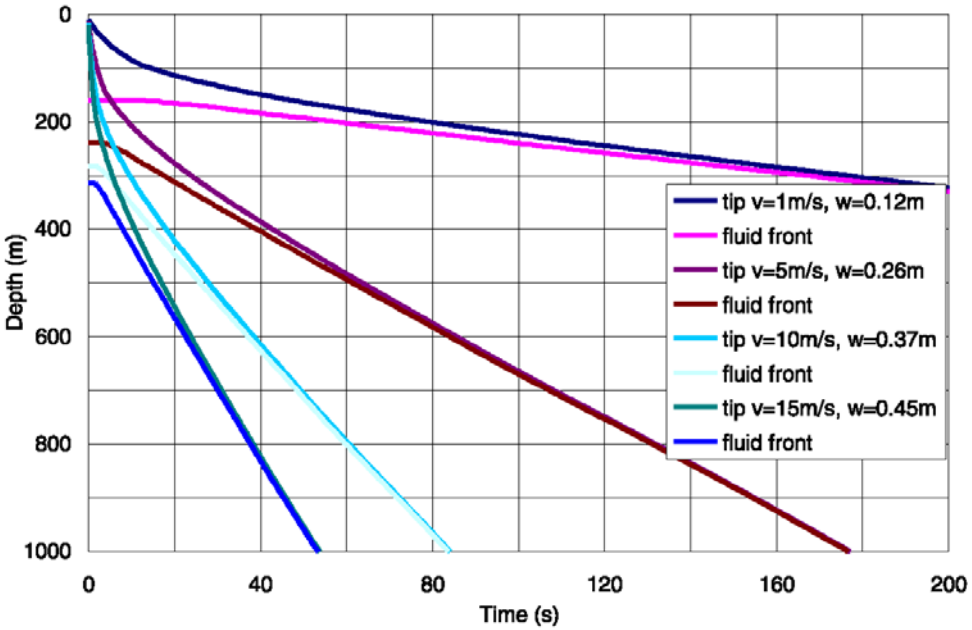

Output DTN: MO0408EG831811.004.

Source: Output data calculation plots.

Figure 6-11. Dike Tip and Fluid Front as Functions of Time: $\mathcal{D}$= 2.67, $\kappa\rho_r$= 2400 kg/m^3, μ = 10 Pa·s

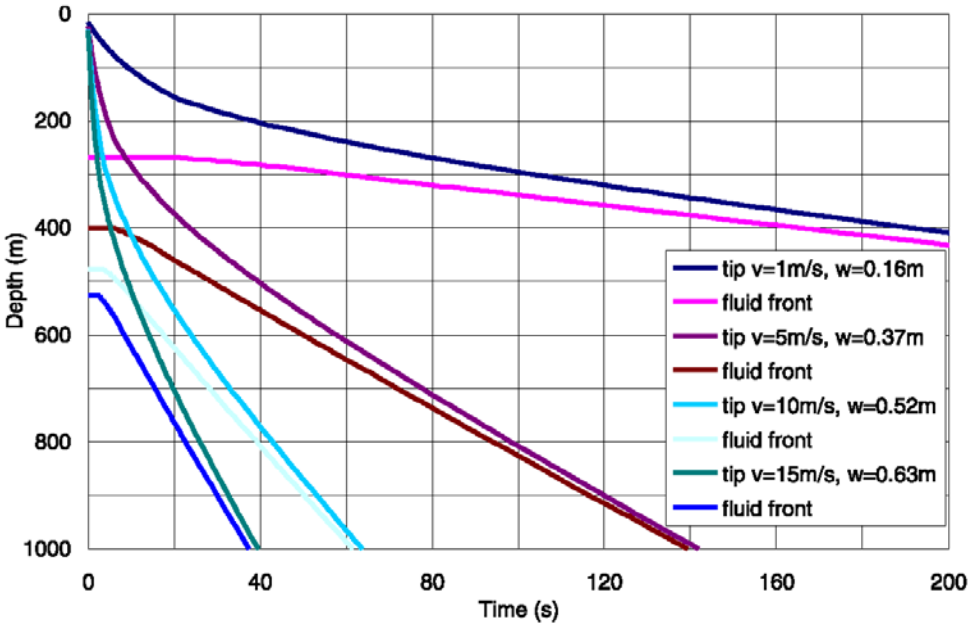

Output DTN: MO0408EG831811.004.

Source: Output data calculation plots.

Figure 6-12. Dike Tip and Fluid Front as Functions of Time: $\mathcal{D}$= 2.67, $\kappa\rho_r$= 1200 kg/m^3, μ = 10 Pa·s

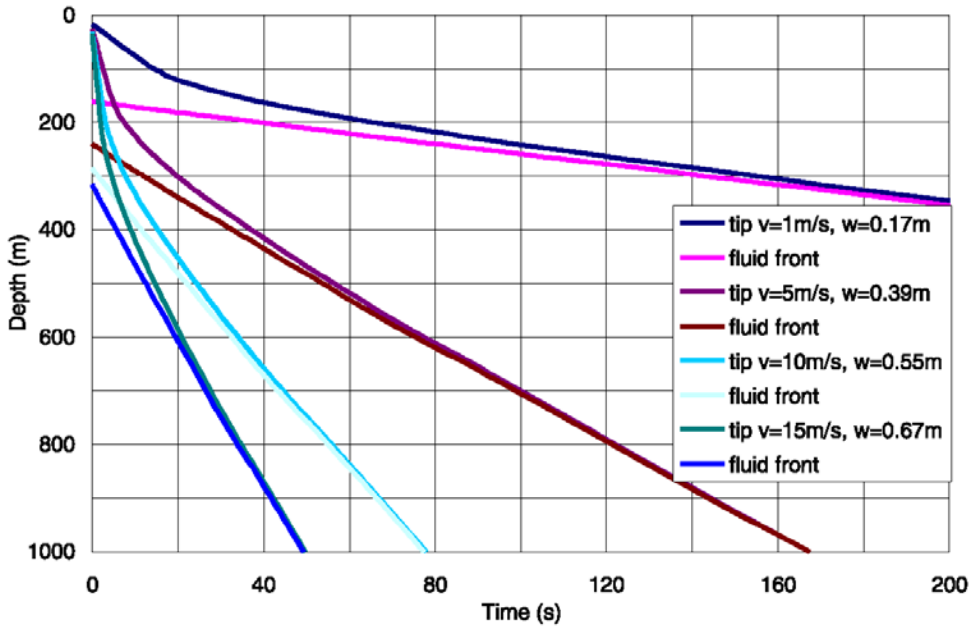

Output DTN: MO0408EG831811.004.

Source: Output data calculation plots.

Figure 6-13. Dike Tip and Fluid Front as Functions of Time: $\mathcal{D}$= 6.02, $\kappa\rho_r$= 2400 kg/m^3, μ = 10 Pa·s

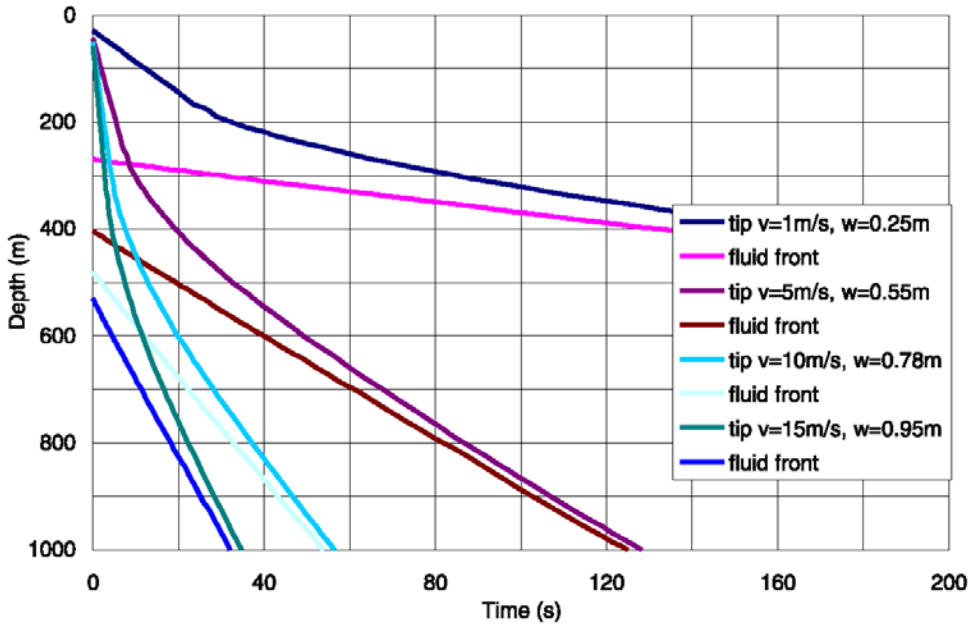

Output DTN: MO0408EG831811.004.

Source: Output data calculation plots.

Figure 6-14. Dike Tip and Fluid Front as Functions of Time: $\mathcal{D}$= 6.02, $\kappa\rho_f$= 1200 kg/m^3, μ = 10 Pa·s

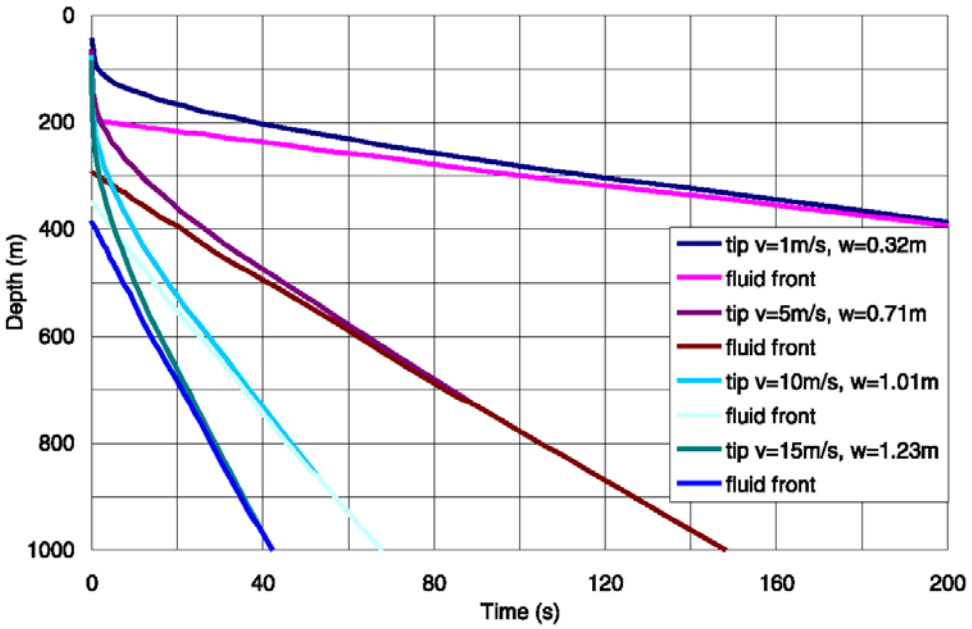

Output DTN: MO0408EG831811.004.

Source: Output data calculation plots.

Figure 6-15. Dike Tip and Fluid Front as Functions of Time: $\mathcal{D}$= 20.28, $\kappa\rho_f$= 2400 kg/m^3, μ = 10 Pa·s

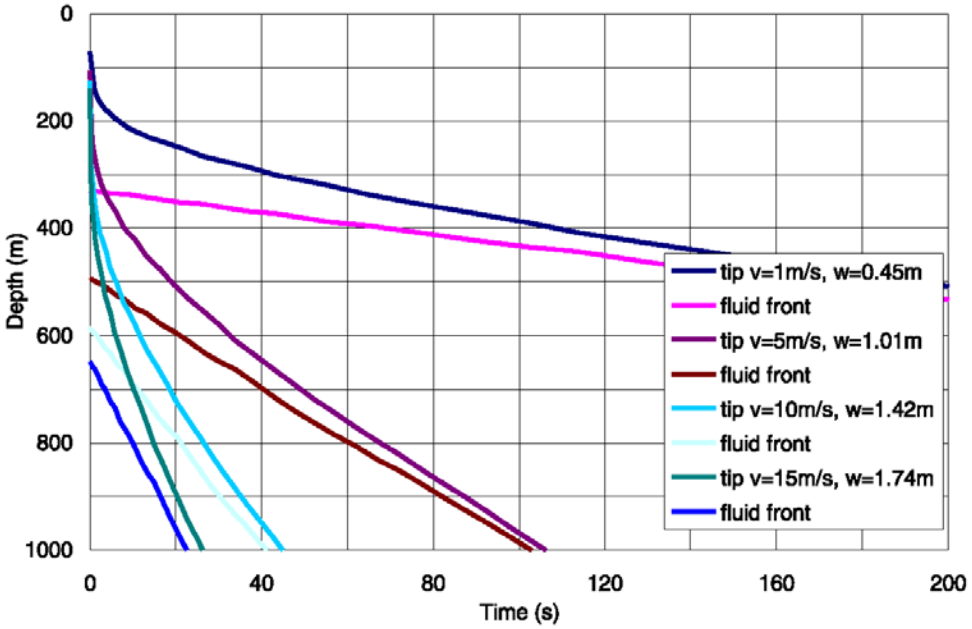

Output DTN: MO0408EG831811.004.

Source: Output data calculation plots.

Figure 6-16. Dike Tip and Fluid Front as Functions of Time: $\mathcal{D}$= 20.28, $\kappa\rho_r$= 1200 kg/m^3, μ = 10 Pa·s

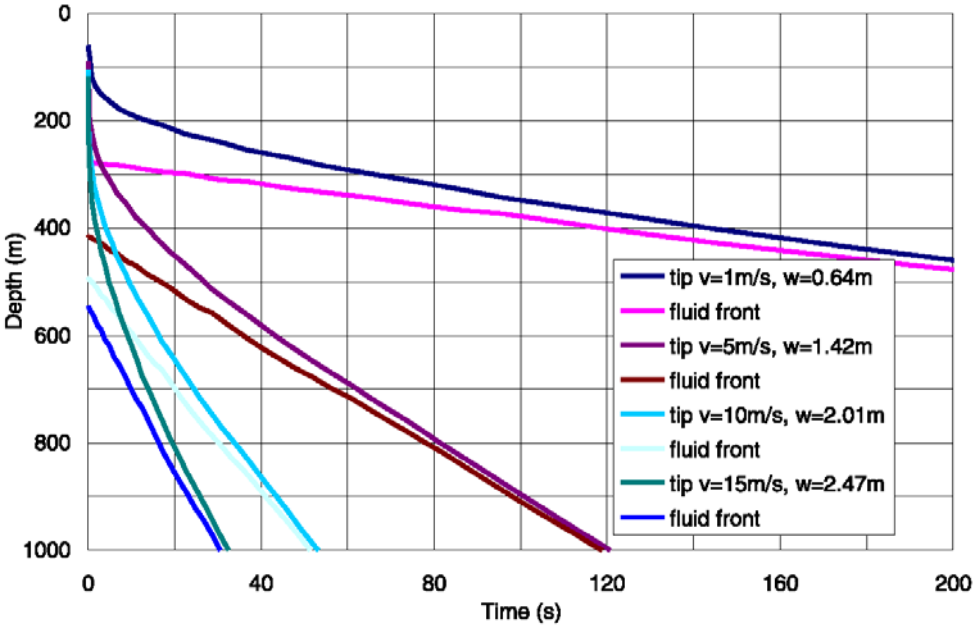

Output DTN: MO0408EG831811.004.

Source: Output data calculation plots.

NOTE: Flow parameters for v=10 m/s, 15 m/s indicate non-laminar flow.

Figure 6-17. Dike Tip and Fluid Front as Functions of Time: $\mathcal{D}$= 20.28, $\kappa\rho_r$= 2400 kg/m^3, μ = 40 Pa·s

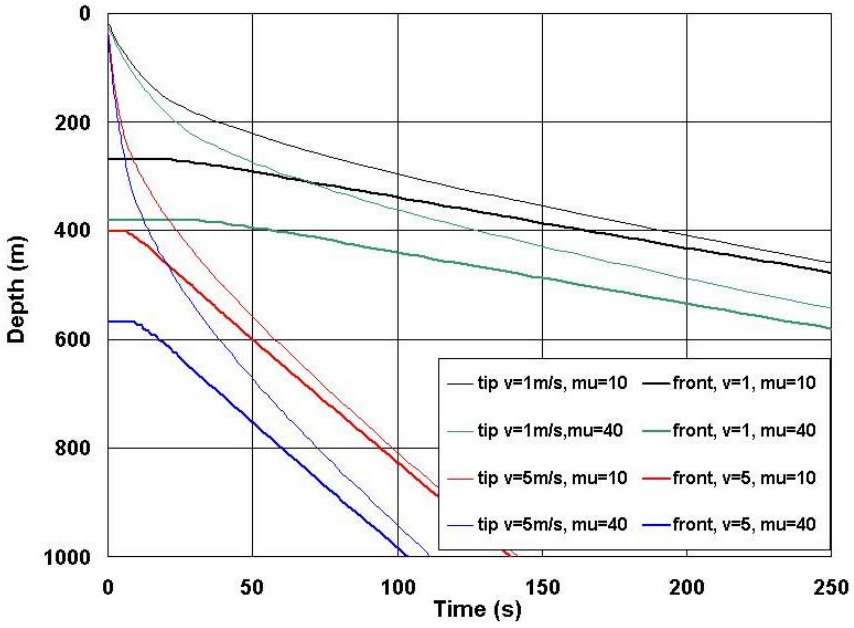

Output DTN: MO0408EG831811.003.

Source: Output data calculation plots.

Figure 6-18. Dike Tip and Fluid Front as Functions of Time: $\mathcal{D}$= 20.28, $\kappa\rho_r$= 1200 kg/m^3, μ = 410 Pa·s or μ = 40 Pa·s

In all cases considered, the tip cavity forms before the dike tip reaches the repository level (nominally 300 m). The cavity size at the repository level varies from case to case. Because the length scale decreases as δ' increases (Equation 6-49), the solutions for $\kappa = 1.0$ (i.e. $\kappa\rho_r = 2400$ kg/m^3) yield shorter cavity lengths than solutions for the more relevant, $\kappa = 0.5$ (i.e. $\kappa\rho_r = 1200$ kg/m^3). Similarly, the dike opening, w_∞, for a given velocity, v_∞, is smaller for $\kappa = 1.0$ than $\kappa = 0.5$. Note that some of the widths obtained are small (lower than 0.2m) and could result in freezing of the magma. However, these values are retained to show the relative effect of the parameters. Results for $\kappa = 0.5$ indicate (see Figures 6-12, 6-14, and 6-16) that the magma does not reach the repository level (i.e., a 300-m depth) before the dike tip reaches the ground surface, except for the lowest velocity cases considered (i.e., $v_\infty = 1$ m/s with $\mathcal{D} = 2.67$ where $w_\infty = 0.16$ m (Figure 6-12), and $\mathcal{D} = 6.02$ where $w_\infty = 0.25$ m (Figure 6-14)–note that these two cases are at the lower end of realistic dike widths). In these two cases, the length of the tip cavity is between 100 m and 200 m when the magma is at the repository horizon. In the case of $\mathcal{D} = 20.28$, illustrated in Figure 6-16, the tip cavity is longer than 300 m when the dike tip reaches the ground surface. As expected from Equation 6-49, an increase in magma viscosity, μ results in an increase in the tip cavity length, as illustrated in Figures 6-17 and 6-18 (for $\mu = 40$ Pa·s), compared to results in Figures 6-15 and 6-16 (for $\mu = 10$ Pa·s).

As expected from Equation 6-51, an increase in magma viscosity, μ, results in an increase in the tip cavity length. This is evident from Figure 6-18 where results for different viscosities are plotted for $\mathcal{D}$ =20.3. Increasing the viscosity from 10 Pa·s to 40 Pa·s for a fixed far-field

velocity of 1 m/s, doubles the cavity length at depth. As the crack tip approaches the surface, the effect is not quite so large, but the cavity length at breakout is still approximately 40 percent greater for the higher viscosity. For the lower velocity, this increase is enough that the magma does not reach the nominal 300-m repository level before breakout.

One objective of the dike propagation analysis is to estimate the magma pressure history at the repository level as the dike passes through the repository. However, the NPHF2D (BSC 2002 [DIRS 163665]) simulation stops when the dike tip reaches the ground surface. Consequently, the model does not provide the pressure history at repository depth in those cases where the magma does not reach the repository level by the time the tip reaches the ground surface. In other cases, when the magma is at the repository level before the dike ruptures the ground surface, the history is usually provided for only a short period.

To account for the strike dimension of the dike, the proper solution of this problem requires a three-dimensional model of fluid flow in the pre-existing fracture (there being then no need for simulation of fracture propagation). For present purposes, a pragmatic approach was adopted. The pressure profile in the magma behind the front remains invariant until magma is close to the ground surface. The only change in the net pressure profile is a variation of the minimum, which is controlled by the net pressure inside the cavity, and is equal to the horizontal far-field stress. The net pressure profiles for $\mathcal{D}$ equal to 2.67 and 20.28, at different times (the earliest being when the magma reaches a repository depth of 300 m), are shown in Figures 6-19 and 6-21, respectively. Clearly, in the case of $\mathcal{D}$ = 20.28 (Figure 6-21), all four pressure profiles (at four different times) have the same shape. All curves could have been obtained by horizontally translating the curve for t = 4086s and truncating those portions below the line corresponding to the horizontal far-field stress. The same argument can be applied to pressure profiles at t = 1339s and t = 1367s for $\mathcal{D}$ = 2.67 shown in Figure 6-19. However, the pressure profile at t = 1392s does not follow the same trend. The reason is, in the case of $\mathcal{D}$ = 2.67, that there is an effect on the magma front velocity when the dike tip approaches the ground surface (see Figure 6-10): the magma front stalls. The low lateral confinement and a large decrease in elastic stiffness as the dike tip approaches the ground surface, accommodate the influx of additional magma without forward movement of the magma front.

The pressure and time histories at the repository level can be approximated by convecting the pressure profile at the repository horizon using the known fluid front velocity. Pressure histories constructed using such an approach for $\mathcal{D}$ equal to 2.67 and 20.28, for different velocities (1 m/s, 5 m/s, 10 m/s and 15 m/s), are shown as curves in Figures 6-20 and 6-22. (Only the curve for 1 m/s velocity is a pressure history at the depth of 300 m. Other curves are at different depths, which correspond to the same dimensionless depth as a 300-m depth for a 1 m/s curve). The calculated pressure histories (labeled "sink data") at the repository depth for the case in which v_∞ = 1 m/s are shown as discrete points in Figures 6-20 and 6-22. The agreement between pressure histories derived from pressure profiles and fluid velocities, and the actual pressure—time history at the sink is very good.

It appears from the pressure history plots in Figures 6-20 and 6-22 that the two major factors controlling the evolution of magma pressure at a given depth are the far-field horizontal stress and magma front velocity. From these computations, the maximum magma pressure is at most

1 MPa larger than the horizontal far-field stress at the given depth[1]. Therefore, the maximum magma pressure at a 300-m depth is approximately:

- 4.5 MPa in the case of $\kappa\rho_r$ = 1200 kg/m^3 (horizontal far-field stress 3.6 MPa)
- 8.0 MPa in the case of $\kappa\rho_r$ = 2400 kg/m^3 (horizontal far-field stress is 7.6 MPa).

Clearly, a larger magma front velocity results in a larger rate of pressure change at a given depth. The length of the tip cavity provides a measure of the distance over which the magma pressure behind the front changes from zero to the maximum value. Consequently, as the tip cavity becomes shorter, the pressure gradient becomes larger, and the rate of pressure change at a given depth increases.

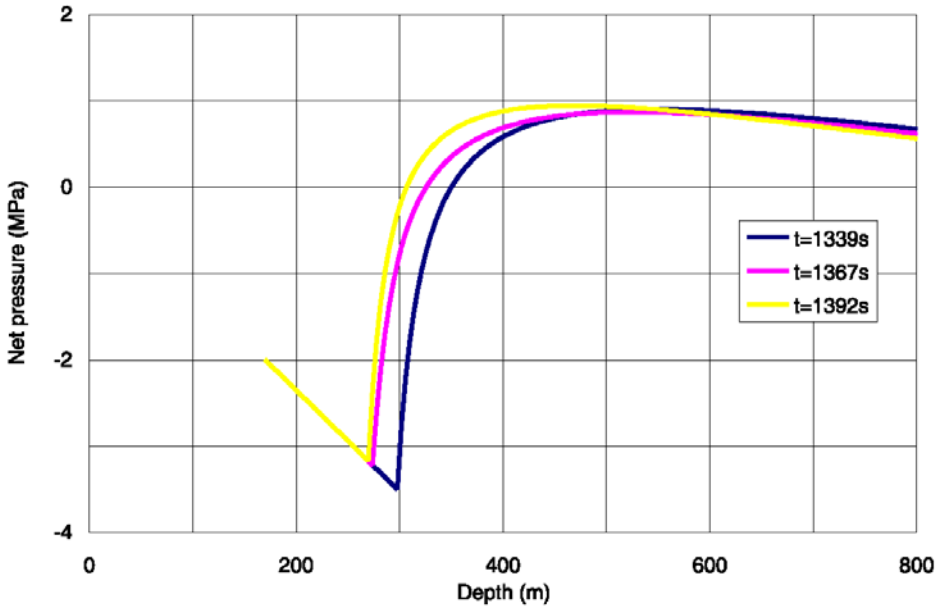

Output DTN: MO0408EG831811.004.

Source: Output data calculation plots.

Figure 6-19. Net Pressure Profile as a Function of Depth: $\mathcal{D}$= 2.67, $\kappa\rho_r$= 1200 kg/m3, μ = 10 Pa·s, v_∞= 1 m/s, w_∞= 0.16

[1] This is lower than the "few MPa" suggested by Dr. Rubin in his independent technical review of an early version of this report (Section 7.3.1.1.2 and Appendix F). This is result of the specific magma and far-field dike properties and the elastic properties used in this analysis.

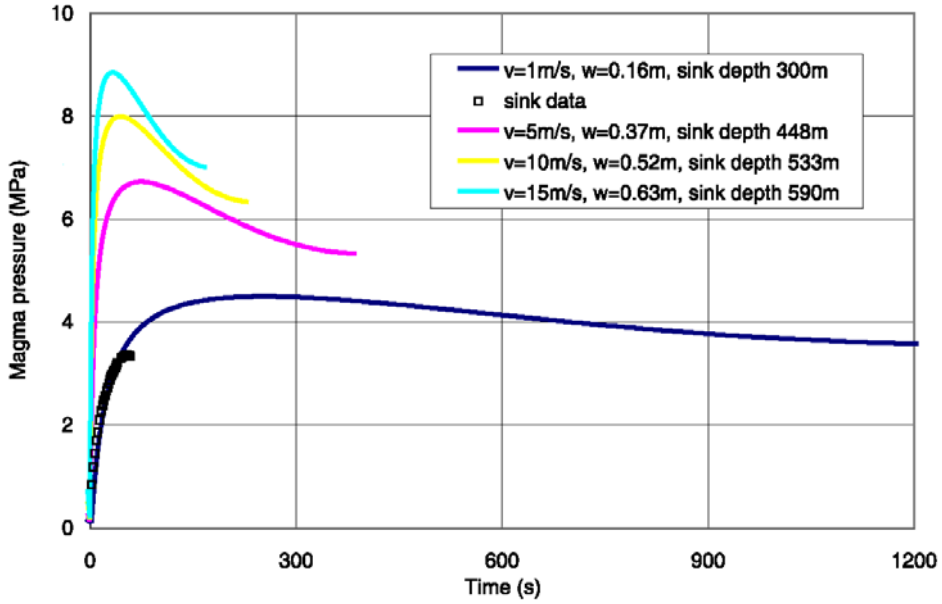

Output DTN: MO0408EG831811.004.

Source: Output data calculation plots.

Figure 6-20. Pressure History at Points Similar to Repository Depth for $\mathcal{D}$= 2.67, $\kappa\rho_r$= 1200 kg/m^3, μ = 10 Pa·s

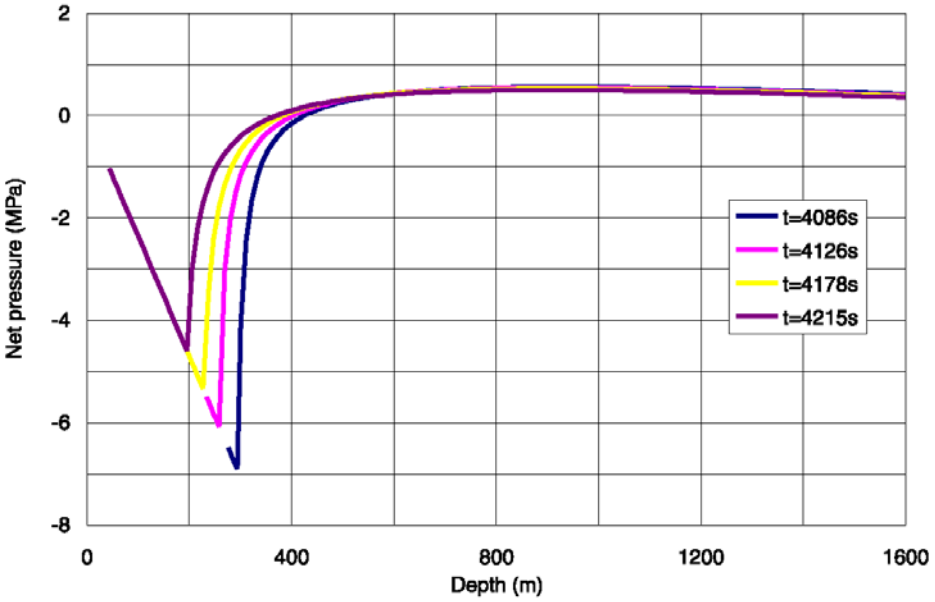

Output DTN: MO0408EG831811.004.

Source: Output data calculation plots.

Figure 6-21. Net Pressure Profile as a Function of Depth: $\mathcal{D}$ = 20.28, $\kappa\rho_r$ = 2400 kg/m3, μ = 10 Pa·s, v_∞ = 1 m/s, w_∞ = 0.32 m

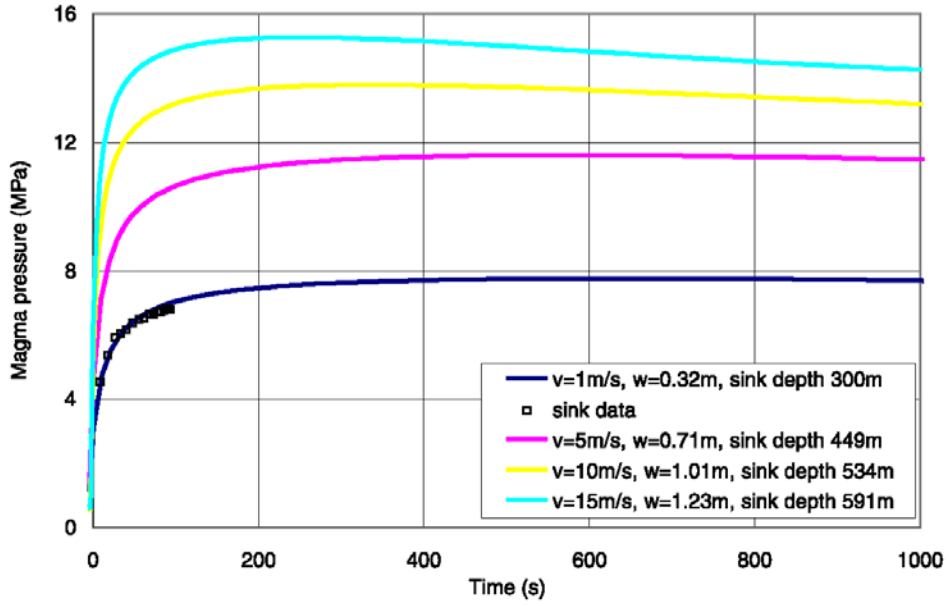

Output DTN: MO0408EG831811.004.

Source: Output data calculation plots.

NOTE: Flow parameters for v=10 m/s, 15 m/s indicate non-laminar flow.

Figure 6-22. Pressure History at Points Similar to Repository Depth for $\mathcal{D}$ = 20.28, $\kappa\rho_r$ = 2400 kg/m^3, μ = 10 Pa·s

6.3.7.2 Effect of Pressure Inside the Tip Cavity

Magmas contain volatile components, mainly H_2O and CO_2. At high pressures, the gases are completely dissolved in the magma. The magma pressure falls as the magma approaches the ground surface, exsolution takes place, and gases form bubbles inside the melt. The volumetric percentage of the bubbles increases as the magma pressure decreases. Near the tip cavity, the gases in the magma can move (due to the pressure gradient) and be released into the cavity. As pressure builds inside the cavity, the gases leak-off into the surrounding rock formations. The model discussed in this report does not simulate any of these processes. However, a simplified analysis (Detournay et al. 2003 [DIRS 169660]), based on consideration of the gas diffusivity in tuff at Yucca Mountain, shows that the cavity gas pressure will be insignificantly larger than the gas pressure in the surrounding formation (i.e., atmospheric pressure). Because this is a simplified analysis, the effect of gas pressure inside the tip cavity on the conditions of dike propagation was investigated. Table 6-4 shows the independent and derived parameters developed as inputs to evaluate the effect of gas pressure inside the tip cavity.

The results of the numerical model are illustrated in Figures 6-23 through 6-28. The dimensionless results are in Figures 6-23 and 6-26; the dimensional results are shown in Figures 6-24, 6-25 and 6-27, 6-28. Two cases were considered: $\mathcal{D}$ = 2.67, $\mathcal{S}$ = -0.25 and $\mathcal{D}$ = 20.28, $\mathcal{S}$ = -0.20. The former corresponds to 1.00 MPa, and the latter to 0.48 MPa cavity gas pressure in the case of $\kappa\rho_r$ = 2400 kg/m^3, μ = 10 Pa·s and v_∞= 1 m/s. The most realistic values are obtained with $\kappa\rho_r$ = 1200 kg/m^3, and yield pressures of 0.49 MPa to 0.20 MPa.

Table 6-4. Independent and Derived Parameters for Non-Zero Cavity Tip Pressure Simulations

Independent Parameters					Derived Parameters				
$\mathcal{D}$	$\mathcal{S}$	v_∞ (m/s)	κ	$\kappa\rho_r$ (kg/ m^3)	ρ_f (kg/ m^3)	$\kappa\rho_r - \rho_f$ (kg/ m^3)	w_∞ (m)	q_∞ (m^2/s)	σ_c-p_{f0} (MPa)
2.67	-0.25	15	1.0	2400	1501	899	0.452	6.78	**-1.98**
2.67	-0.25	10	1.0	2400	1501	899	0.369	3.69	-1.79
2.67	-0.25	5	1.0	2400	1501	899	0.261	1.30	-1.50
2.67	-0.25	1	1.0	2400	1501	899	0.117	0.12	-1.00
20.28	-0.20	15	1.0	2400	2282	118	1.245	18.68	-0.95
20.28	-0.20	10	1.0	2400	2282	118	1.017	10.17	-0.86
20.28	-0.20	5	1.0	2400	2282	118	0.719	3.59	-0.72
20.28	-0.20	1	1.0	2400	2282	118	0.322	0.32	-0.48
2.67	-0.25	15	0.5	1200	751	449	0.639	9.58	-1.66
2.67	-0.25	10	0.5	1200	751	449	0.522	5.22	-1.50
2.67	-0.25	5	0.5	1200	751	449	0.369	1.84	-1.26
2.67	-0.25	1	0.5	1200	751	449	0.165	0.16	-0.84
20.28	-0.20	15	0.5	1200	1141	59	1.761	26.41	-0.80
20.28	-0.20	10	0.5	1200	1141	59	1.438	14.38	-0.72
20.28	-0.20	5	0.5	1200	1141	59	1.017	5.08	-0.61
20.28	-0.20	1	0.5	1200	1141	59	0.455	0.45	-0.41

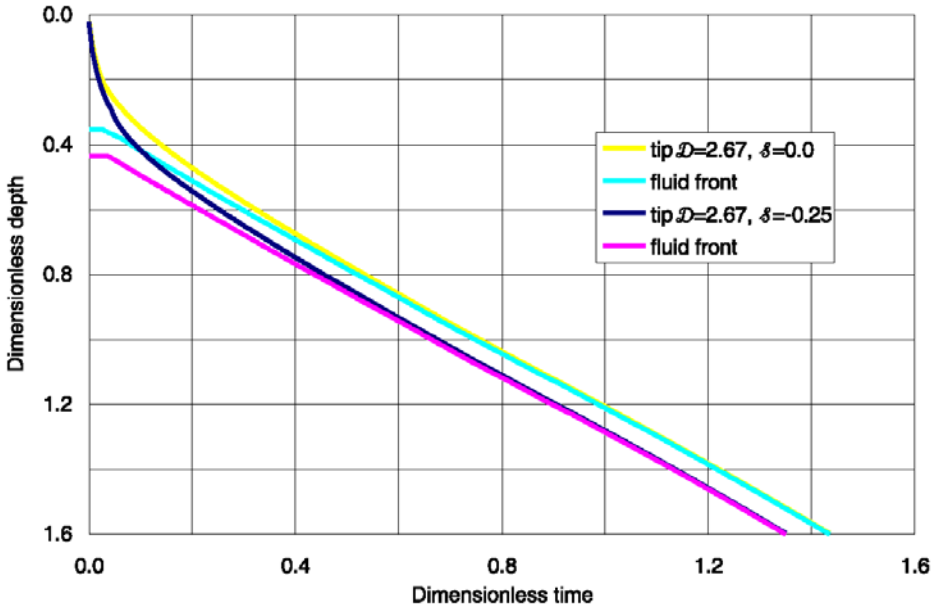

Output DTN: MO0408EG831811.004.

Source: Output data calculation plots.

Figure 6-23. Dimensionless Solution for Dike Tip and Fluid Front as Functions of Time: Effect of $\mathcal{S}$ for $\mathcal{D}$ = 2.67

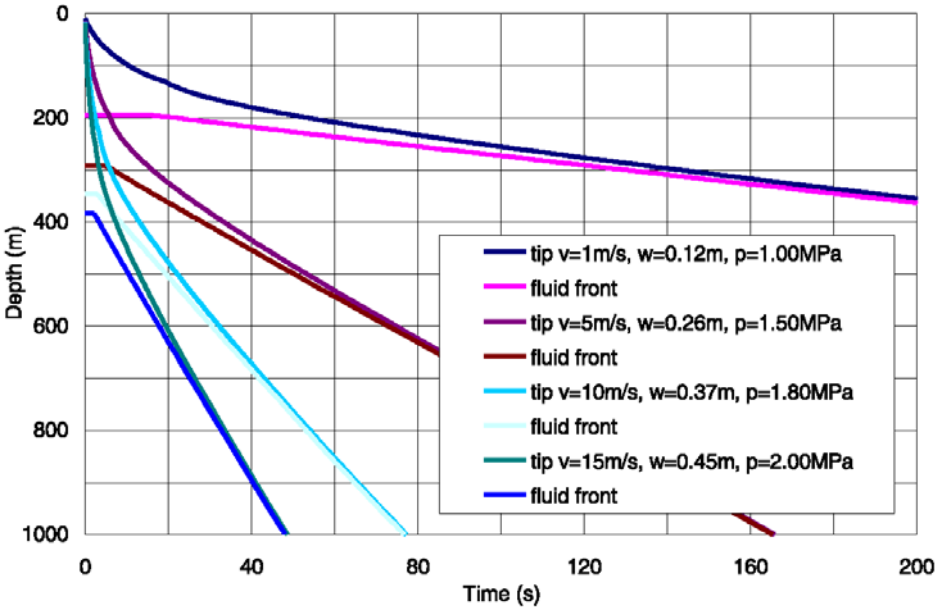

Output DTN: MO0408EG831811.004.

Source: Output data calculation plots.

Figure 6-24. Dike Tip and Fluid Front as Functions of Time: $\mathcal{D}$ = 2.67, $\mathcal{S}$ = -0.25, $\kappa\rho_r$ = 2400 kg/m^3, μ = 10 Pa·s

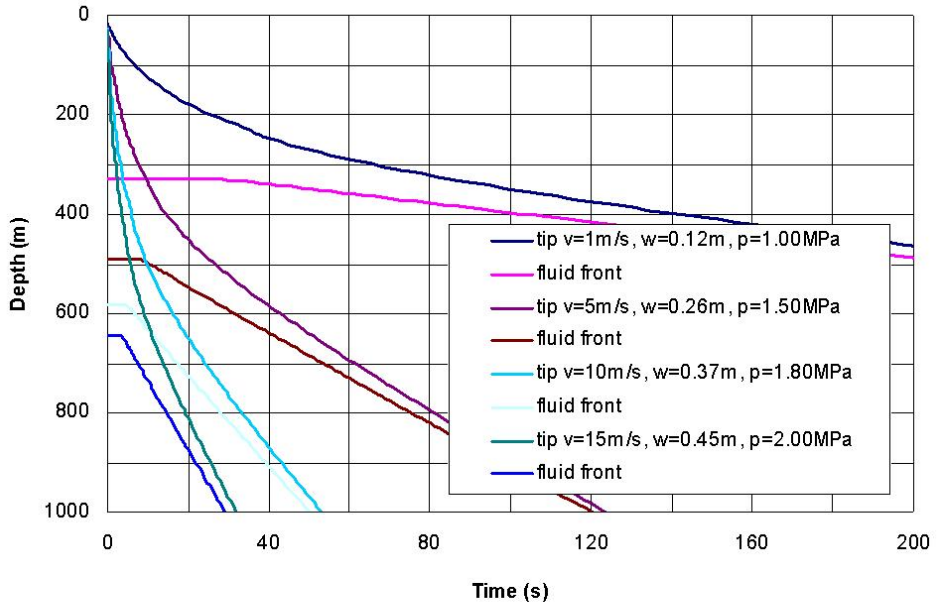

Output DTN: MO0408EG831811.004.

Source: Output data calculation plots.

Figure 6-25. Dike Tip and Fluid Front as Functions of Time: $\mathcal{D}$ = 2.67, $\mathcal{S}$ = -0.25, $\kappa\rho_r$ = 1200 kg/m3, μ = 10 Pa·s

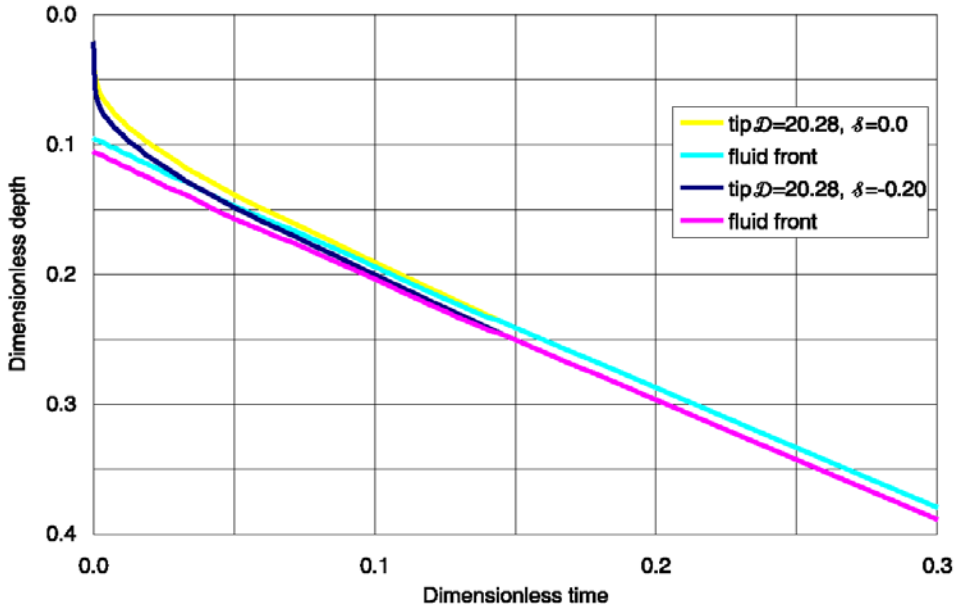

Output DTN: MO0408EG831811.004.

Source: Output data calculation plots.

Figure 6-26. Dimensionless Solution for Dike Tip and Fluid Front as Functions of Time: Effect of $\mathcal{S}$ for $\mathcal{D}$ = 20.28

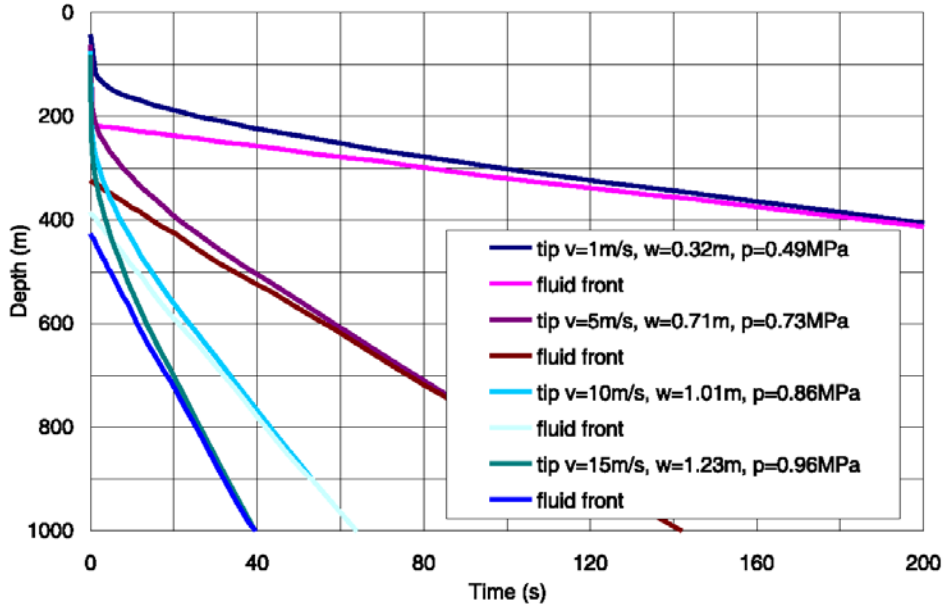

Output DTN: MO0408EG831811.004.

Source: Output data calculation plots.

NOTE: Flow parameters for v=10 m/s, 15 m/s indicate non-laminar flow.

Figure 6-27. Dike Tip and Fluid Front as Functions of time: $\mathcal{D}$ = 20.28, $\mathcal{S}$ = -0.2, $\kappa\rho_r$ = 2400

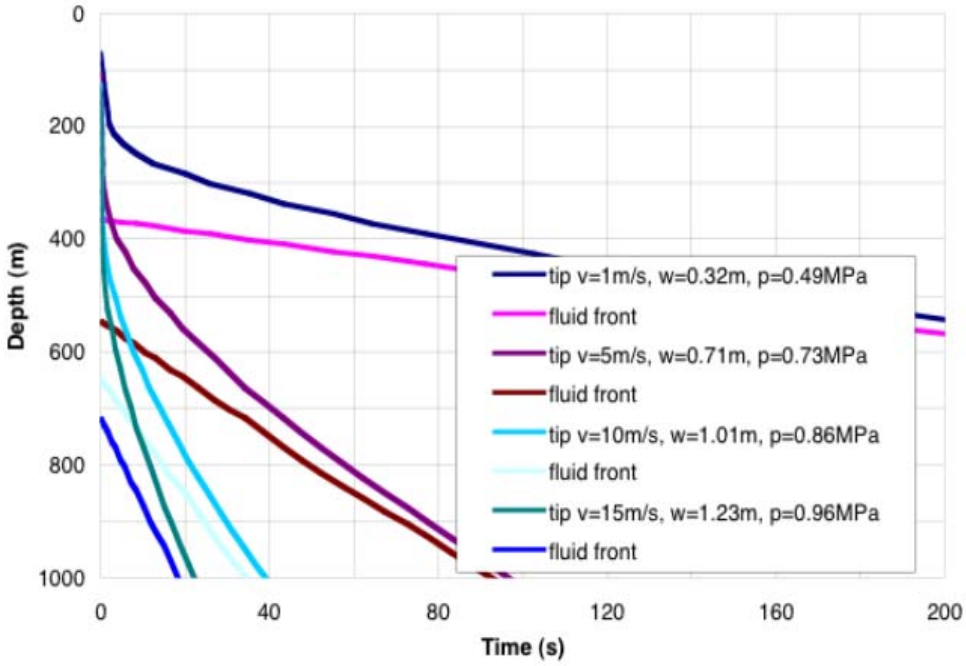

Output DTN: MO0408EG831811.004.

Source: Output data calculation plots.

Figure 6-28. Dike Tip and Fluid Front as Functions of time: $\mathcal{D}$ = 20.28, $\mathcal{S}$ = -0.2, $\kappa\rho_r$ = 1200 kg/m^3, μ = 10 Pa·s

The cavity gas pressure does not significantly affect the velocity of the magma front. The velocity of the dike tip is affected, particularly when the tip gets close to the ground surface (i.e., when the cavity pressure becomes a significant proportion of the horizontal far-field stress). Thus, the cavity pressure increases the cavity length. Because the cavity is longer, the magma will be deeper when the crack tip reaches the surface. For example, comparing Figure 6-25 with Figure 6-12, it is seen that even the small added pressure in the cavity causes the crack tip to reach the surface before the magma reaches the repository.

Neglecting the cavity gas pressure is a conservative assumption with respect to analysis of the magma flow inside the repository drifts, because it will overpredict the rate of magma pressure change.

6.3.7.3 Effect of Thermally Induced Increased Horizontal Stress

The analysis of thermally induced stresses in a large-scale model (Section 6.2.4) shows that the least compressive horizontal stress increases to a maximum of approximately 10 MPa at the repository level. This maximum stress occurs in a limited volume of the rock mass and over a limited time span. On one hand, this increase in horizontal stress could "pinch" the dike tip and force it to turn in the direction of the maximum compressive principal stress (which is, between 500 years and 2000 years after waste emplacement, horizontal approximately 80-m below and above the repository), thus forming a sill. On the other hand, if the dike proceeds vertically through the highly stressed repository, the magma pressure in the dike may be much larger than the pressure computed for non-thermally increased stresses.

In this section these effects are investigated numerically, using the distinct element code UDEC V3.14 (BSC 2004 [DIRS 172322]). This code solves the same equations as NPHF2D, except for the fracture criterion (Equation 6-15). In these simulations, the magma intrudes into pre-existing cracks, the location of which is determined by the geometric mesh used.

A set of properties (see Table 6-5) representative of the conditions studied in the previous sections were used:

Table 6-5. Model Parameters

Rock Young's Modulus[a] (GPa)	Rock Density[b] (kg/m^3)	Horizontal Stress Ratio, κ[c]	Magma Density[a] (kg/m^3)	Magma Viscosity[a] (Pa·s)	Magma Bulk Modulus* (MPa)	Magma Injection Rate* (m^2/s)
15	2400	0.5	1000	10	50	0.45

Sources: [a] Detournay et al. 2003 [DIRS 169660], Table 1-2, Figure 2-1e.
[b] DTN: SNL02030193001.027 [DIRS 108410].
[c] DTN: SNF37100195002.001 [DIRS 131356].

NOTE: *Specified value.

These parameters correspond to a value of the dimensionless parameter D = 6, a width at infinity w_∞ = 0.30 m, and a fluid velocity at infinity v_∞ = 1.5 m/s. The velocity used is, therefore, in the lower end of the range used for the base case (Table 6-3). The magma density used is a round value (Section 6.3.7.1); density is not a controlling factor in secondary dike propagation, hence a single value is used to demonstrate the effects of other variables on the process. A value for bulk modulus of the magma, which is required by the code employed, is specified but has no effect on the results as long as it is much greater than any pressure in the magma.

The analyses were carried out in two sets. Although the external sizes of both types of simulations are the same (4000 m wide and 2000 m high), the objective of the large-scale ones is dike propagation over the entire height of the model, while the small-scale simulations deal with dike propagation from a depth of 500 m. The geometry of the large-scale simulations is shown in Figure 6-29. There is only one joint—i.e., the dike path is predetermined, but not the solution of the problem. The geometry of the small-scale simulations is shown in Figures 6-30 and 6-31. It includes a rectangular box (1000 m wide and 500 m high) cut into a large number of polygonal blocks, which are discretized internally to become fully deformable. These "Voronoi polygons"

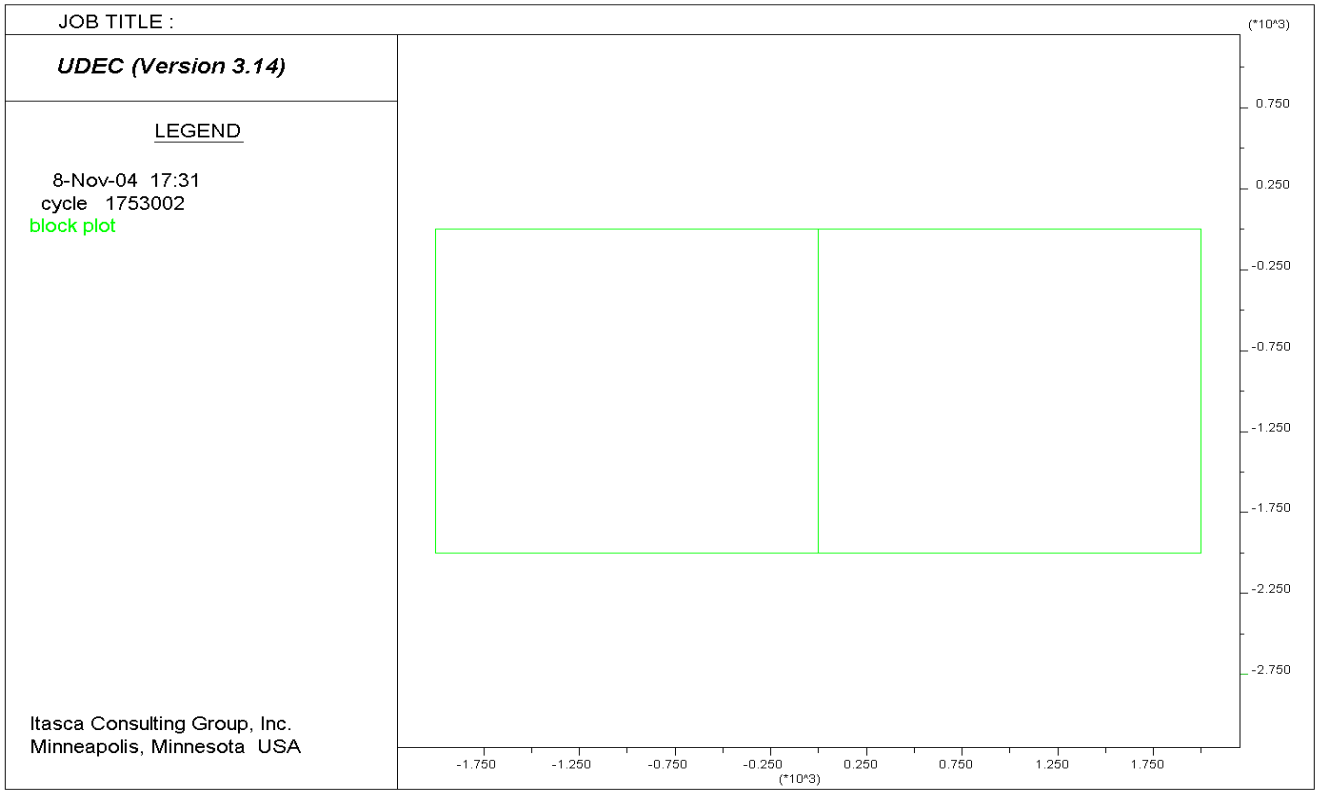

Output DTN: MO0408EG831811.000.

Figure 6-29. Large-Scale UDEC Model 2000-m Deep by 4000-m Wide, in Two Blocks

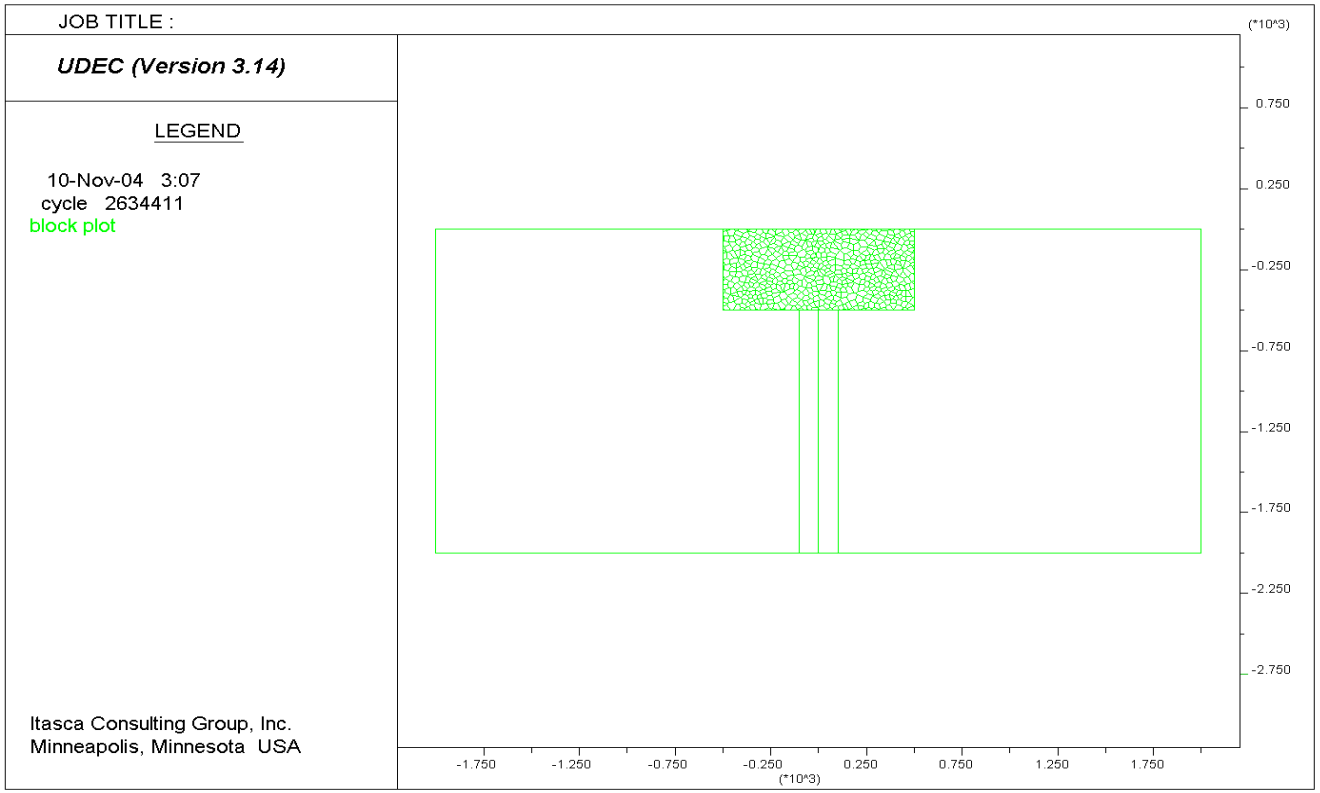

Output DTN: MO0408EG831811.000.

Figure 6-30. UDEC Model 2000-m Deep by 4000-m Wide, in Two Blocks With Voronoi Polygons in the 500-m Deep by 1000-m Wide Rectangle Near the Surface

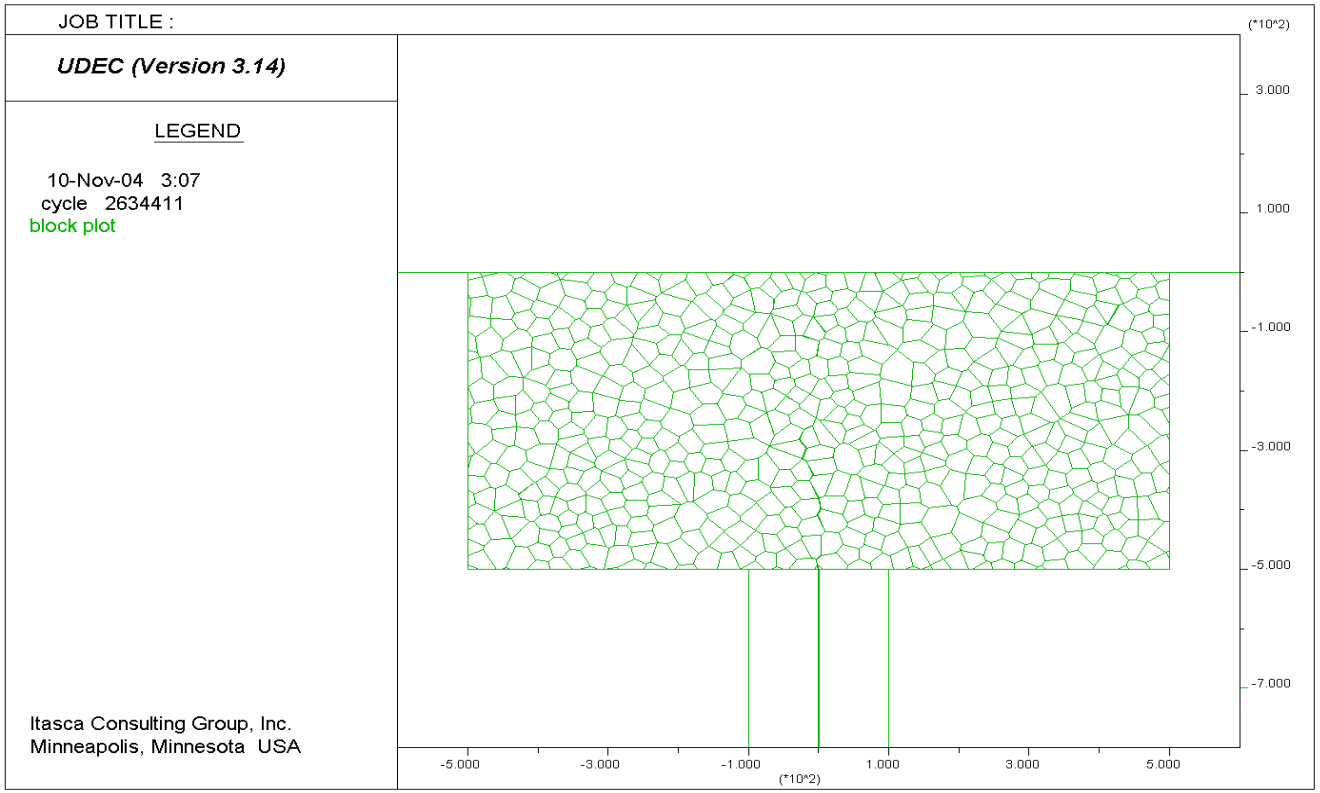

OUTPUT DTN: MO0408EG831811.000.

Figure 6-31. UDEC Model With Voronoi Polygons Near The Surface — Detail Near Ground Surface; Block of Polygons is 500-m Deep by 1000-m Wide

(Itasca 2002 [DIRS 160331]) have an average size of 30 m. The polygonal block boundaries define the crack or joint locations. Note that Voronoi polygons do not create any preferential orientation: the behavior of an assemblage of such polygons is isotropic by construction. The joints between blocks form a network with no preferential direction that can accommodate a number of possible dike paths. If the block size is sufficiently small, the dike path on the scale of the model is therefore defined by the conditions that control the direction of dike propagation (e.g., stress state ahead of the dike tip). To demonstrate that the results are not dependent on a particular model geometry, each small-scale simulation was solved for two different statistical realizations of the Voronoi block geometry. Also, the validity of the computation was checked by comparing the width of the dike computed in the simulation and the analytical value of w_∞ as given above, before applying the thermal load.

Both large-scale and small-scale simulations were applied to an in situ initial stress state and a stress state 1,000 years after waste emplacement (the maximum temperature of the rock mass, on the scale of the repository, will be reached approximately 1,000 years after waste emplacement). The in situ stress state is characterized by the gravitational vertical normal stress and the horizontal normal stress, which is taken as 50 percent of the vertical stress. The "1000 years" stress state is computed by performing a coupled thermo-mechanical simulation, using the temperature field in the east-west vertical cross section through the middle of the repository, as calculated in the mountain-scale thermo-mechanical model (BSC 2004 [DIRS 166107], Appendix C). This field is imported in UDEC V3.14 (BSC 2004 [DIRS 172322]). The contours of increase in temperature, as imported, are shown in Figure 6-32. The contours of the corresponding horizontal stress increase, calculated for a coefficient of linear thermal expansion of 10^{-5} K^{-1}, are shown in Figure 6-33. (The largest stress increase is expected in the horizontal direction.) The vertical profile of the horizontal stress along the joint (shown in Figure 6-34) shows a higher effect than the average of the horizontal stress profiles in Section 6.2.4. This is expected because of the 2-D nature of these new simulations. Still, the model size and the boundary conditions used in the thermo-mechanical calculation in UDEC are satisfactory.

In all mechanical simulations, the lower horizontal boundary of the simulation has "rollers" (i.e., it is free to move laterally, and restrained in the normal direction); the top horizontal boundary represents the ground surface and is stress free (the ground surface is flat in these analyses). The vertical boundaries have "rollers" during the thermo-mechanical calculation.

The magma ascent simulations are fully coupled fluid-mechanical computations, starting either from the in situ stress state (initial case), or from the stress state computed as described above (1000 years case). In these computations, constant stress vertical boundaries replace the previous "rollers" with corresponding reactions (in equilibrium with the stress state inside the model).

For magma ascent computations, the magma flow boundary conditions are the injection rate at the bottom, and a constant zero pressure at the top. In the large-scale simulations the volumetric fraction of magma in the joint is initially zero. Consequently, the initial magma pressure is also zero. The magma pressure and volumetric fraction of magma in the dike in the large-scale simulations, at the time when the magma front reaches the depth of 500 m below the ground surface, are used as the initial state in the small-scale flow simulations. A small-scale simulation is first equilibrated for the initial magma pressure distribution imported from the large-scale one.

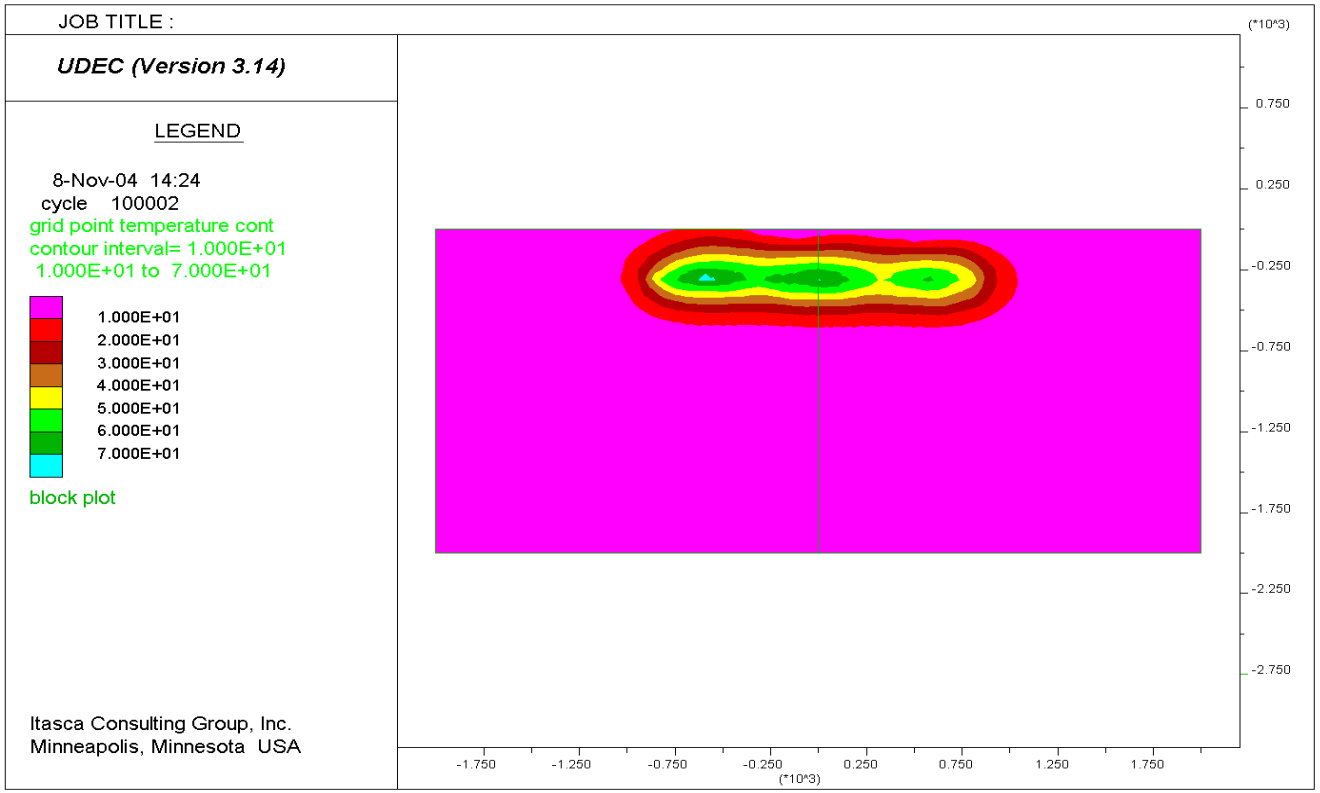

Output DTN: MO0408EG831811.000.

Figure 6-32. Contours of Temperature Increase (ºC) 1000 Years After Waste Emplacement

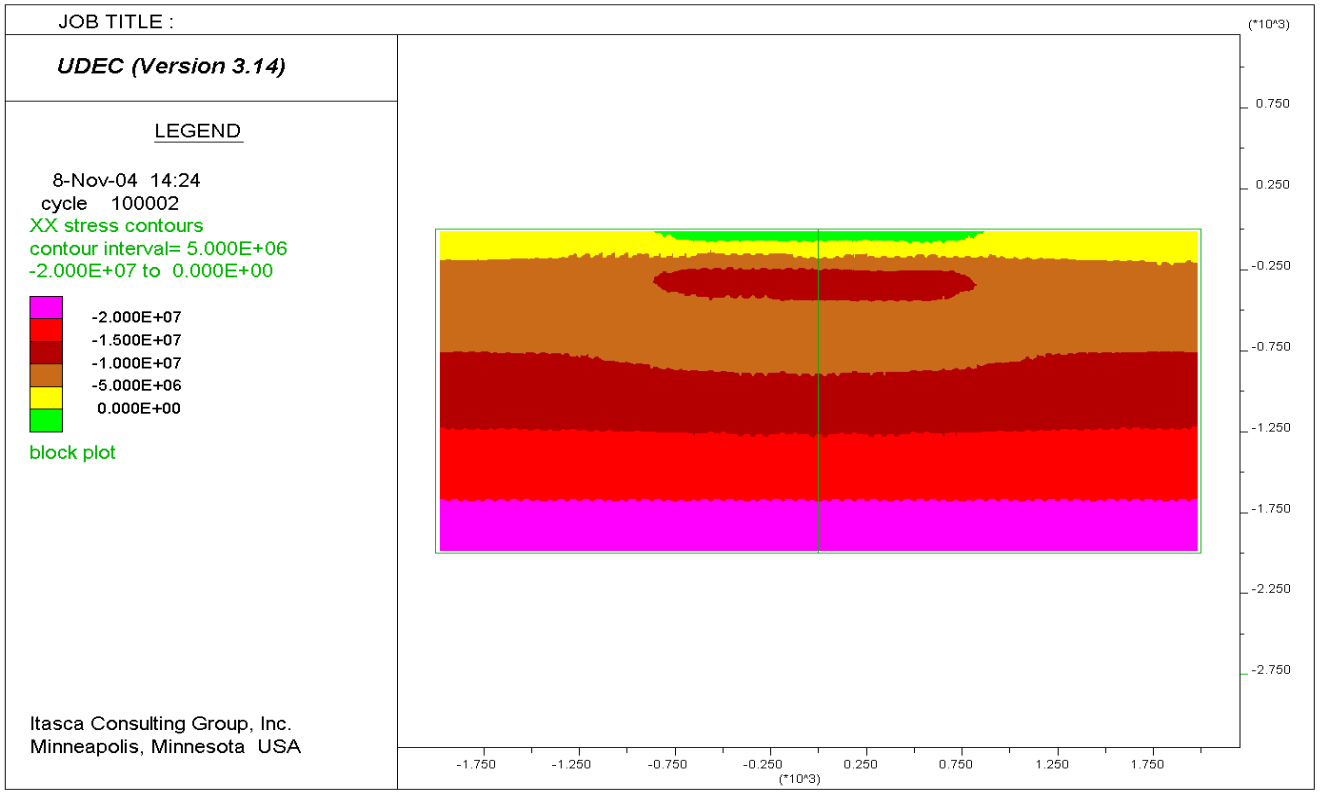

Output DTN: MO0408EG831811.000.

Figure 6-33. Contours of Horizontal Stress (Pa) 1000 Years After Waste Emplacement

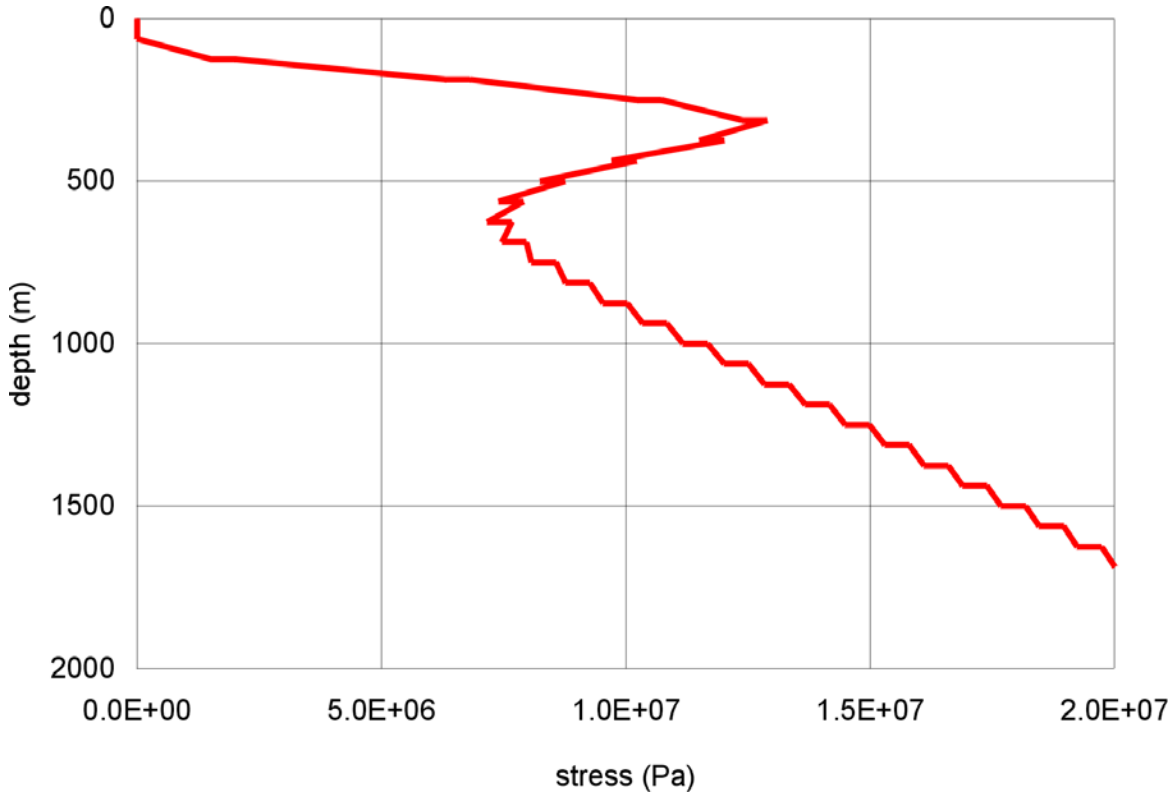

Output DTN: MO0408EG831811.000.

NOTE: Horizontal "steps" are a result of projection of two values from 3-dimensional model onto a single line; stresses used as input to the 2-dimensional calculation were averaged so no steps occurred.

Figure 6-34. Vertical Profile of Horizontal Stress 1000 Years After Waste Emplacement

The mesh size (discretization of Voronoi polygons) is on the order of 10m.

The objective of the large-scale simulations is to provide the initial conditions for the small-scale model, but also to investigate the effect of the stress field on the velocity of dike propagation. A summary of the stress field effect obtained is shown in Figure 6-35 as a plot of the position of the magma front as a function of time. In addition to the aforementioned cases (in situ stress state and the nominal case for state 1,000 years after waste emplacement), two additional cases are included:

- Thermally induced stresses 1,000 years after waste emplacement, for a dike propagating 500-m to one side of the center of the repository. This was done to illustrate the variability in dike propagation that might result from varying dike trajectories.

- Much higher confining stresses similar to thermally induced stresses 1,000 years after waste emplacement but with a coefficient of linear thermal expansion five times greater than the coefficient of TSw2 geological units at Yucca Mountain in which the repository will be located. This was done to demonstrate that the model will result in sill formation, as would be expected in the presence of extremely high confining stresses.

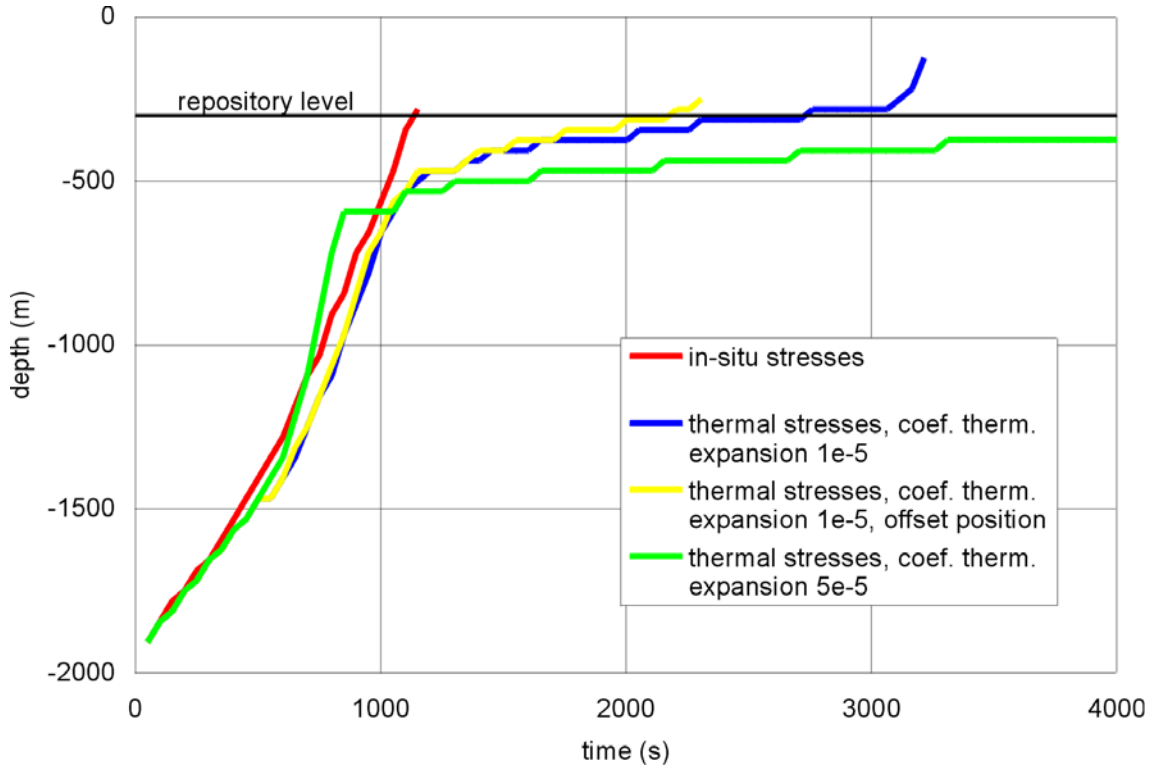

Output DTN: MO0408EG831811.000.

Figure 6-35. Position of Magma Front as a Function of Time–Large Scale Model

The results indicate that thermally induced stresses 1,000 years after waste emplacement significantly affect dike propagation. When the dike approaches the region of increased horizontal stresses approximately 200 m below the repository, the dike tip, and the magma front slow down. In the nominal case, the magma front velocity, after increasing from 0.7 m/s to more than 1 m/s when reaching a depth of 800m, slows to approximately 0.1 m/s upon reaching the repository level. The magma front advances from 500 m depth to 300 m depth (the repository horizon) in approximately 2000 s. The slow-down is less pronounced if the dike is propagating closer to the edges of the repository, because the thermally induced horizontal stresses are smaller at the edges than in the middle of the repository. An increased coefficient of thermal expansion logically results in even more slowdown. Once the dike passes through the region of increased horizontal stresses, the tip and magma front suddenly accelerate due to the very large horizontal stress gradient (see Figure 6-34) above the repository.

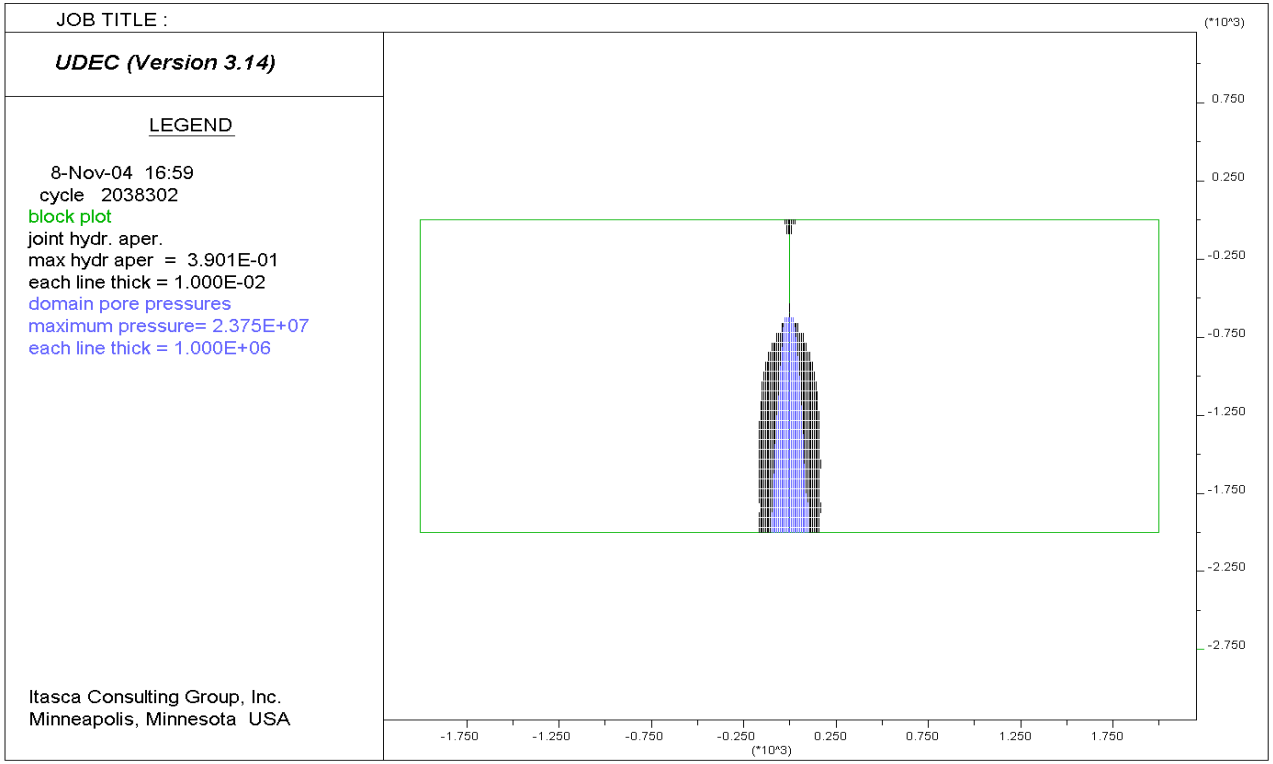

Output DTN: MO0408EG831811.000.

NOTE: Green outline is 2000-m deep by 4000-m wide; maximum aperture is 0.39 m, maximum pressure is 23.7 MPa.

Figure 6-36. Pressure (Pa, in blue) and Aperture (m, in black) Along the Dike Propagating in the Middle of the Repository 1000 Years After Waste Emplacement–1000 S After Start of Simulation (see Figure 6-35)

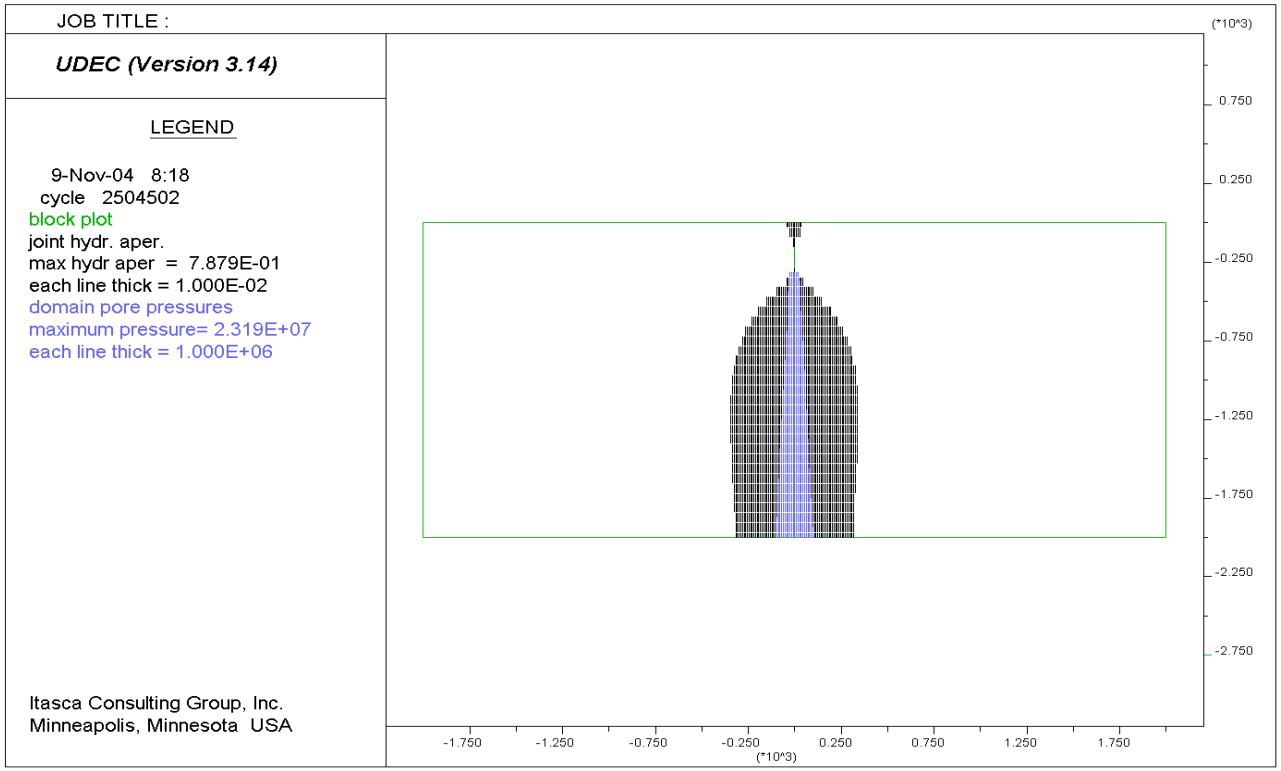

Output DTN: MO0408EG831811.000.

NOTE: Green outline is 2000-m deep by 4000-m wide; maximum aperture is 0.79 m, maximum pressure is 23.2 MPa.

Figure 6-36a. Pressure (Pa) and Aperture (m) Along the Dike Propagating in the Middle of the Repository 1000 Years After Waste Emplacement–2500 s After Start of Simulation (see Figure 6-35)

Two states of the flow model for the single-joint case 1000 years after waste emplacement are shown in Figures 6-36 and 6-36a (note that any asymmetry in these figures is an artifact from the plotting). The result shown in Figure 6-36 is at an early time and is not yet affected by either the thermal stresses or the free surface. The cavity between the dike tip (the location can be determined from the profile of dike opening) and the magma front (the location can be determined from the profile of magma pressure) is between 50 m and 100 m in length. That cavity almost completely disappears in the later result when the dike propagation has stalled (shown in Figure 6-36a). The magma pressure increases at relatively short distances from the tip, but remains unchanged elsewhere as it is controlled by far-field horizontal stress boundary conditions. However, the dike opening significantly increases and the dike propagation is retarded by the large confining stress.

Thermally induced stresses 1000 years after waste emplacement (Figure 6-6) create a stress field a few hundred meters below and above the repository in which the horizontal principal stress is the most compressive (more compressive than the vertical principal stress). The crack tip extends in the direction of the most compressive principal stress in the region ahead of the crack tip.

In the large-scale simulations, the dike is constrained by the computational model to propagate along the predefined joint vertically upward. The possibility of sill formation is investigated with the small-scale simulations. Note that the stress field ahead of the tip is a combination of the pre-existing state and the effect of the crack and the pressure inside the crack on that stress field. Therefore, the crack path does not always coincide with the trajectories of the most compressive principal stress existing before the crack propagates: because of the change of stress due to the presence of the dike itself, the tip will deviate more gradually than the in-situ principal stresses. The sharpness of the deviation will depend on the magnitude of the stress difference. Also, in the simulations, the sharpness of the deviation obviously depends on the size of the Voronoi polygons. Initially, all joints have the same properties. In the nominal case, as well as in the case with a dike position offset 500 m to the left and right of the center of the repository toward the edges, the dike propagation is essentially vertical (shown in Figures 6-36b and 6-36c). This is an indication that the thermal stresses are not expected to cause dike deflection and sill formation under conditions likely to occur at Yucca Mountain. However, dike deflection cannot be ruled out entirely, because the size of the Voronoi polygons may prevent the simulation from producing a sharp enough deflection. Note that the analysis did not consider the effect of a horizontal discontinuity that could arrest vertical dike propagation and provide a preferred horizontal path for magma flow, resulting in more favorable conditions for sill formation.

If the model fails to produce a sill under such conditions, the conclusion that sill formation will not occur under expected thermal stress conditions would not be credible. Therefore, a final simulation was performed to demonstrate that the model correctly simulates formation of a sill under the repository if confining stresses are extremely high. To obtain such a case, the coefficient of linear thermal expansion was increased to 5×10^{-5} K^{-1} (this coefficient is on the order of 10^{-5} for all geological units at Yucca Mountain (BSC 2004 [DIRS 166107])). The results for this extreme case are shown in Figure 6-36d. The calculated maximum horizontal stresses are approximately 50 MPa. Propagation of the dike in the original vertical direction is slowed down, as indicated in Figure 6-35. However, because the dike is free to "choose" the path in the model, the state after approximately 5000 s (shown in Figure 6-36d) shows a sill

beginning to form at the boundary of the box discretized into Voronoi blocks as indicated by the horizontal extension of the high-pressure region (black). Because sill formation in this case starts exactly at the lower edge of the box with Voronoi blocks, the position where dike deflection begins is a model artifact and is an upper limit to the location where sill formation would be expected if the box extended farther down. If the model was continued to longer time under the same driving condition, it is expected that the sill would propagate horizontally until reaching the edge of the repository, where it would revert to a vertical dike form of intrusion.

The positions of the magma front as functions of time (Figure 6-36e) extracted from the small-scale simulations, show the same trend as observed from the large-scale model. Note that the zero time in Figure 6-36e is offset from that in Figure 6-35 by about 1000 s. The dike propagating in the middle of the repository will be pinched by the thermal stresses 1000 years after waste emplacement and the magma front will slow down to approximately 0.1 m/s. The effect closer to the edges of the repository will be less.

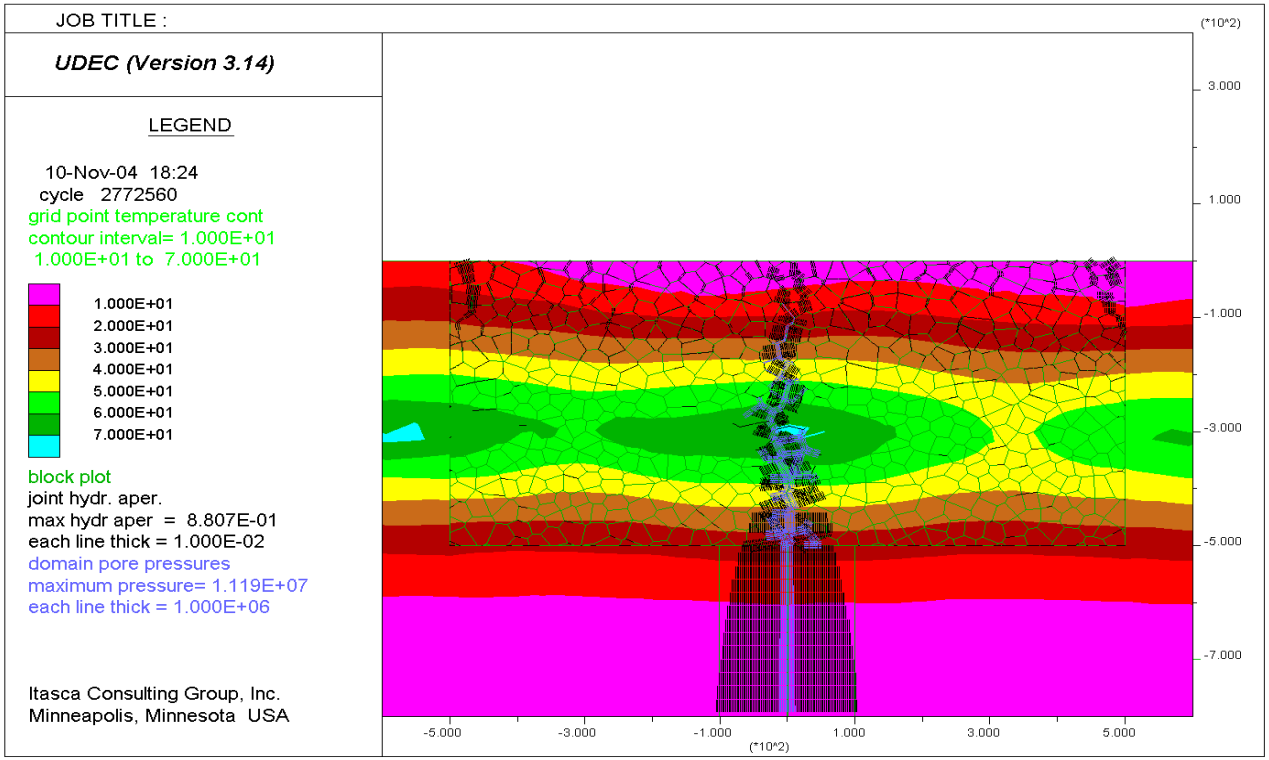

Output DTN: MO0408EG831811.000.

NOTE: Thickness of the black line proportional to dike opening, maximum aperture is 0.75 m; thickness of the blue line proportional to magma pressure, maximum pressure is 10.7 MPa. Green region filled with polygons is 500-m deep by 1000-m wide.

Figure 6-36b. Dike Path Propagating in the Middle of the Repository 1000 Years After Waste Emplacement: Temperature Increase Contours (ºC), Dike Opening (m), and Magma Pressure (Pa)

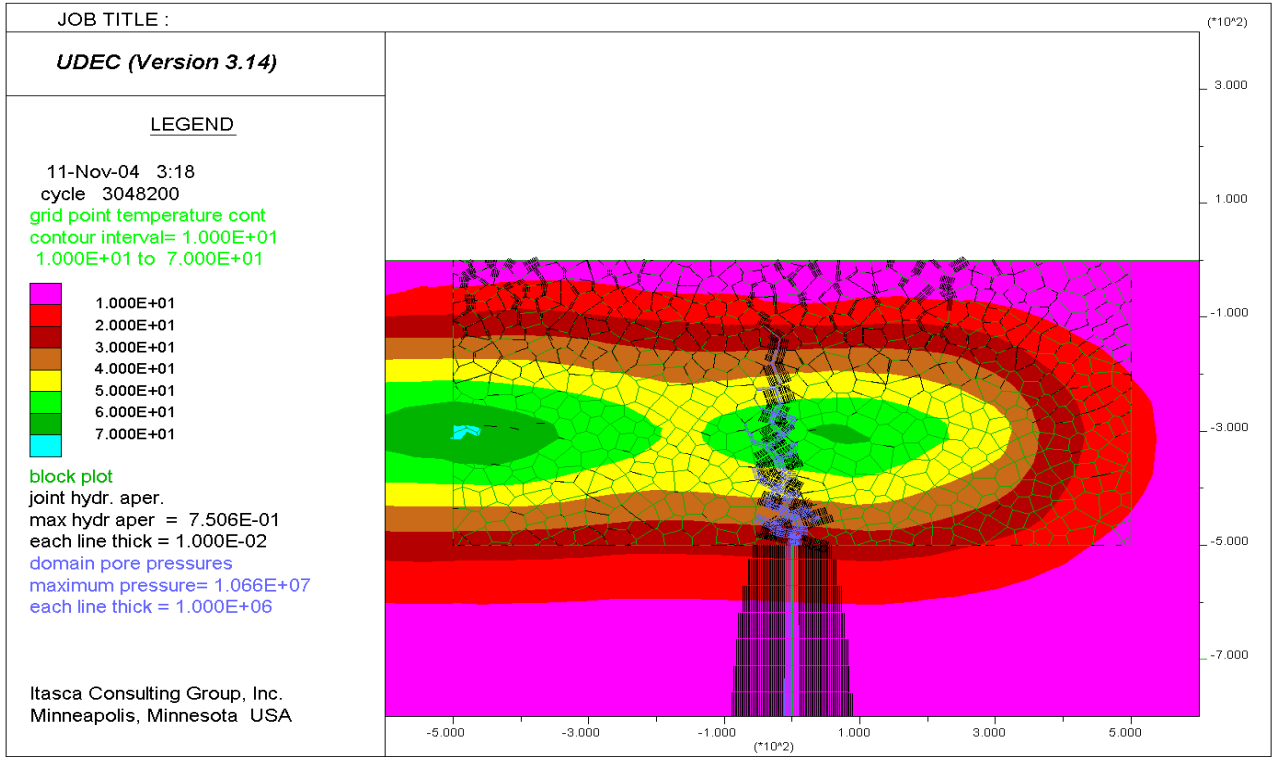

Output DTN: MO0408EG831811.000.

NOTE: Thickness of the black line proportional to dike opening, thickness of the blue line proportional to magma pressure.

Figure 6-36c. Dike Path Propagating 500 m Offset From the Middle of the Repository 1000 Years After Waste Emplacement: Temperature Increase Contours (ºC), Dike Opening (m), and Magma Pressure (Pa)

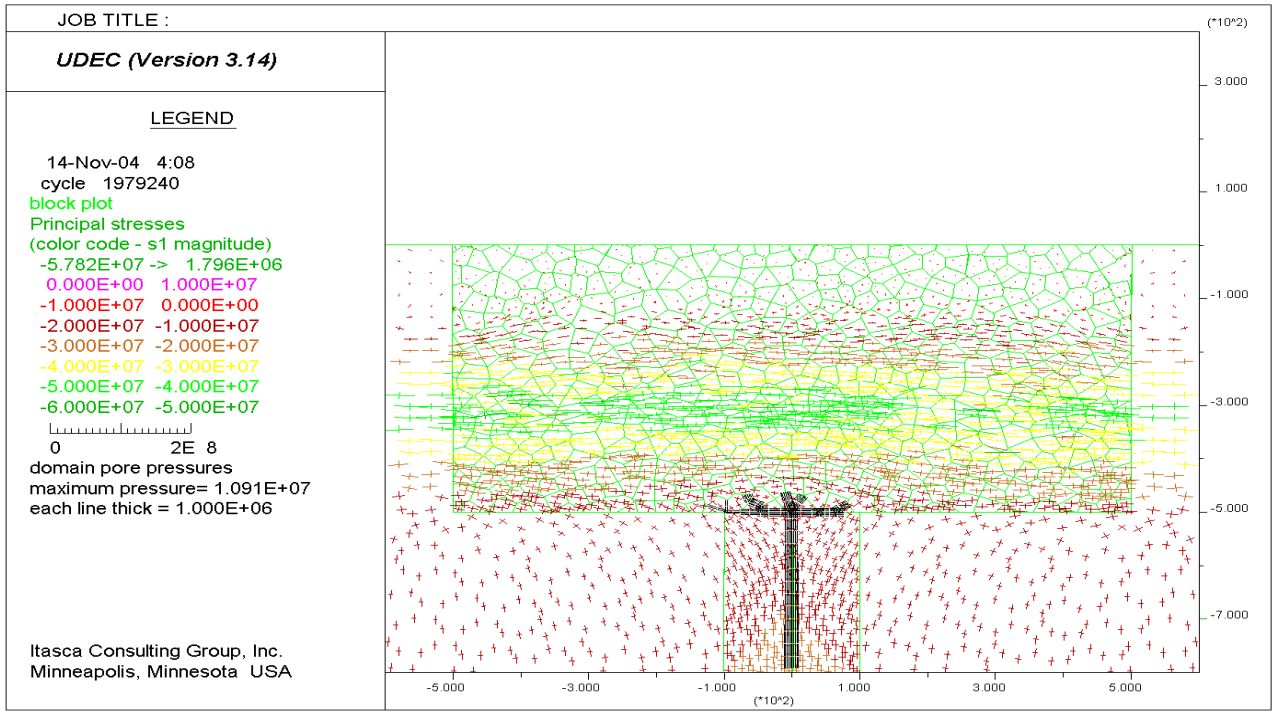

Output DTN: MO0408EG831811.000.

NOTE: Thickness of the black line proportional to magma pressure.

Figure 6-36d. Pressure (Pa) and Stress Tensors Colored By Magnitude Of Major Principal Stress (Pa) Along The Dike Propagating In The Middle Of The Repository 1000 Years After Waste Emplacement Assuming Coefficient Of Thermal Expansion to be 5×10^{-5}

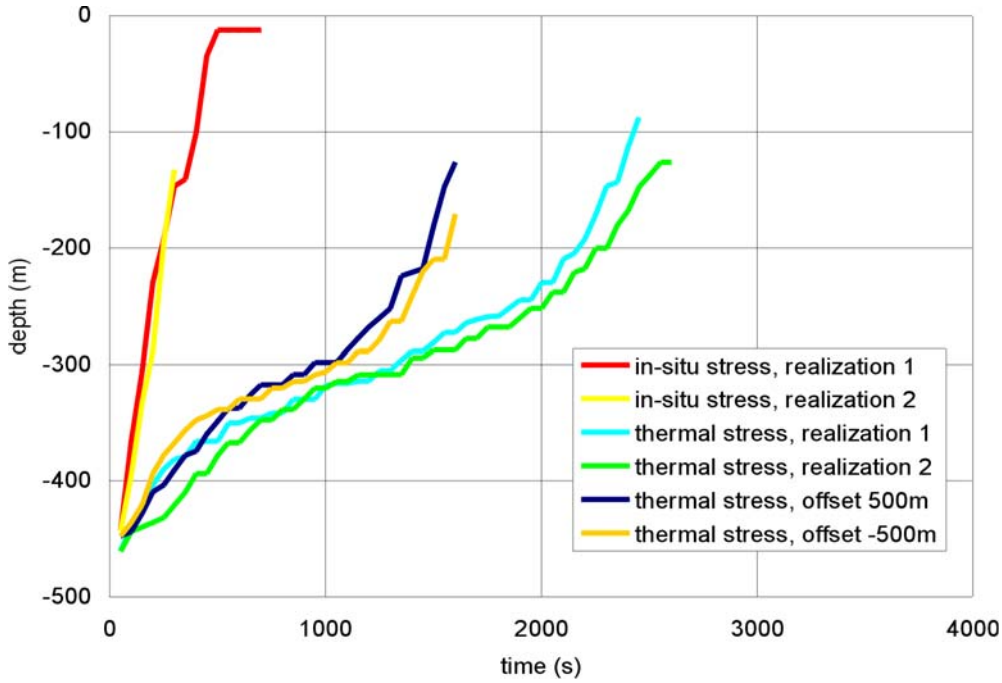

Output DTN: MO0408EG831811.000.

Figure 6-36e. Position of the Magma Front as a Function of Time—Small Scale Model

The pressure histories extracted from the simulations at the repository level—i.e., approximately 300 m below the ground surface, are shown in Figure 6-36f. The pressure history for the in situ stress state follows the trend observed in the simulations from Section 6.3.7.1. The difference between the maximum magma pressure and the horizontal far-field stress is close to 1 MPa. With thermally induced stresses, the maximum magma pressure is 6 MPa, much less than the peak horizontal stress of approximately 13 MPa.

The analysis of the effect of thermally induced stress increases on dike propagation has shown the following:

- The magma velocity decreases for the stress state expected 1,000 years after waste emplacement, at approximately 200-m below the repository level, from more than 1 m/s (for the analyzed case) to approximately 0.1 m/s.
- After passing the repository level, the dike tip, and magma front accelerate again.
- Slow-down is slightly greater if the dike propagates in the middle of the repository rather than at the edge of the repository.
- For the expected maximum stress increase 1000 years after waste emplacement, and for a homogeneous and isotropic rock mass (as represented by the isotropic Voronoi polygons), no dike deflection was produced in the model. However, the possibility of a deflection cannot be ruled out entirely because of possible effects of details of Voronoi block orientations and size.

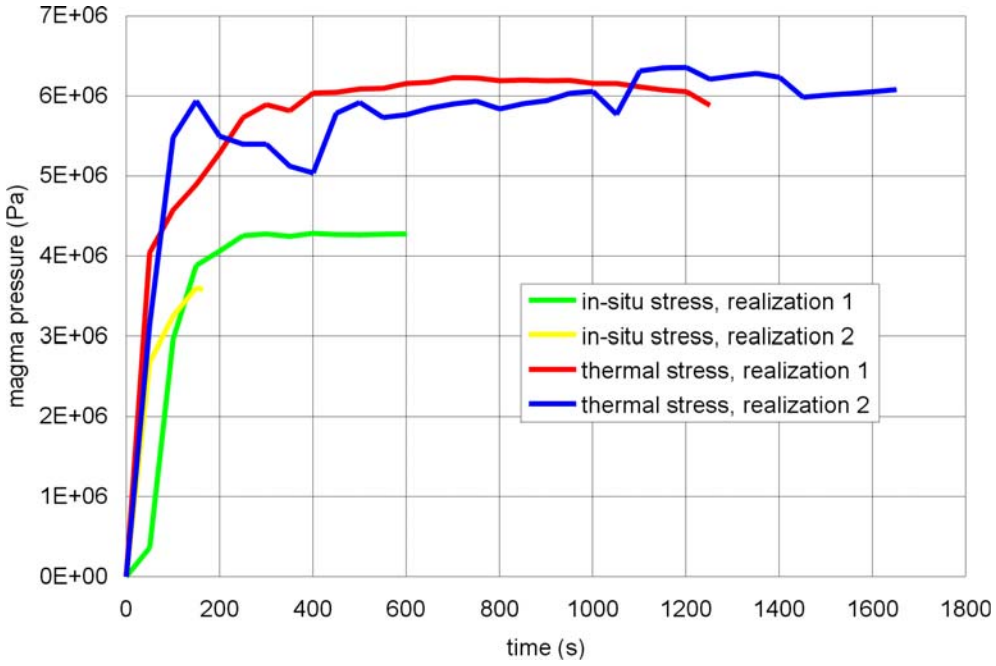

Output DTN: MO0408EG831811.000.

Figure 6-36f. Pressure Histories in Magma as a Function of Time at the Repository Horizon—Small Scale Model

The magma pressure at the repository level for the stress state 1000 years after waste emplacement and after the dike breaks through the region of increased horizontal stresses, is expected to be in the range of 6 MPa, which is much less than the maximum thermally induced stress increase. This maximum magma pressure limitation agrees well with the calculations showing the difficulty of sill formation.

6.3.8 Alternative Models for Dike Propagation

There are a number of analytic and commercial oil and gas hydraulic-fracture models available (including those used in geothermal hot-dry-rock and waste-injection applications), and there are hydraulic-fracture models adapted to the igneous dike problem. Each of these applications is discussed and considered.

6.3.8.1 Analytic Solutions of the Hydraulic-Fracture Problem

Although analytic solutions may not be sufficiently versatile to solve complex problems with free surfaces and loss into repositories, they are quite adequate for solving fracture propagation problems in general homogeneous media and are thus useful for comparisons and parameter estimation. The first hydraulic-fracture models were developed using a combination of two landmark papers on the topic. These included a paper on "Widths of Hydraulic Fractures" by Perkins and Kern (1961 [DIRS 163644]) and another on "Optimum Fluid Characteristics for Fracture Extension" by Howard and Fast with an appendix by Carter (Howard and Fast 1958 [DIRS 163628], Appendix) that was the basis for constructing a joint model.

Perkins and Kern considered two-dimensional fractures in both Cartesian and radial geometries with laminar and turbulent flow for both Newtonian and pseudo-plastic rheologies. In the Cartesian geometry, the dimensions of the dike are a width (w) in the direction of crack opening, a length (L) in the direction of crack propagation, and a height (H) orthogonal to the other two. This situation can be analyzed as a two-dimensional problem as long as L is very large compared to w. Perkins and Kern took the two previously developed width equations for fractures inflated by constant pressure (Sneddon 1946 [DIRS 163648]):

$$w = \frac{2\left(1-\nu^2\right)\left(p-\sigma\right)L}{E}, \text{ for Cartesian geometry} \qquad \text{(Eq. 6-69)}$$

and:

$$w = \frac{8\left(1-\nu^2\right)\left(p-\sigma\right)R}{\pi E}, \text{ for radial geometry} \qquad \text{(Eq. 6-70)}$$

where:

p = pressure of fluid in dike
σ = stress component normal to the dike
R = radius of the dike
E = Young's modulus of the confining rock
ν = Poisson's ratio of the confining rock

and added two pressure-drop equations of the form:

$$\frac{dp}{dx} = \frac{32Q\mu}{\pi Hw^3} \qquad \text{(Eq. 6-71)}$$

where:

x = the spatial coordinate in the L-direction
Q = the volume flux of the driving fluid
μ = the dynamic viscosity of the driving fluid

for linear flow through an elliptic cross-section, and

$$p = p_w - \frac{6Q\mu \ln\left[r/r_w\right]}{2\pi w^3} \qquad \text{(Eq. 6-72)}$$

where:

p = the pressure at radius r
p_w = the driving pressure
r_w = the radius of the source flux, Q, where the dike width is w

for radial flow through a constant-aperture fracture. In addition, Perkins and Kern added a mass-conservation formulation and solved for widths and pressures, obtaining equations of the form:

$$w_{\max} = 3\left[\frac{2\left(1-\nu^2\right)Q\mu L}{E}\right]^{\frac{1}{4}} \text{ for the Cartesian case} \qquad \text{(Eq. 6-73)}$$

and:

$$w_{\max} = 3\left[\frac{\left(1-\nu^2\right)Q\mu R}{\pi^2 E}\right]^{\frac{1}{4}} \text{ for radial conditions} \qquad \text{(Eq. 6-74)}$$

where $w_{\max}$ is the maximum fracture width.

Using volumetric considerations (e.g., volume = rate x time), the length of the fracture could be found as:

$$L = 0.6\left[\frac{EQ^3}{2\left(1-\nu^2\right)\mu H^4}\right]^{\frac{1}{5}} t^{\frac{4}{5}} \text{ for the Cartesian case} \qquad \text{(Eq. 6-75)}$$

and

$$R = \left[\frac{EQ^3}{16\pi^2\left(1-\nu^2\right)\mu}\right]^{\frac{1}{9}} t^{\frac{4}{9}} \text{ for radial conditions.} \qquad \text{(Eq. 6-76)}$$

where t is time.

The contribution by Howard and Fast (1958 [DIRS 163628]) to the hydraulic-fracturing problem was the incorporation of leak-off into the reservoir in the form of a square-root-of-time approximation. Although leak-off into the surrounding rocks is not necessary for dike propagation, an appendix in their paper written by R.D. Carter (Howard and Fast 1958 [DIRS 163628], Appendix) provided a more accurate coupling of width, pressure, and leak-off equations. Carter's equation, as it is known, expresses the area (height × length) of a fracture as a function of the width, leak-off, flow rate, and time. Coupled with equations from Perkins and Kern's (1961 [DIRS 163644]), and Equations 6-75 and 6-76 from this report, this solution allowed for analytic calculations of fracture growth in a much more exact form than the Perkins and Kern solution. Nevertheless, the Perkins and Kern solution is very useful in estimating

fracture parameters for most situations and can be used as a check on any model that predicts the length, width, and pressure of a fracture that has a constrained height. In this case, height is the major dimension *not* aligned with fluid flow; length is the major dimension aligned with fluid flow. This type of fracture has an elliptic crack profile (e.g., in the minor dimension).

Nordgren (1972 [DIRS 163641]) applied the Carter-type solution for fractures in the Cartesian case and obtained:

$$w_{\max} \approx 2.5\left[\frac{2\left(1-\nu^2\right)Q^2\mu}{EH}\right]^{\frac{1}{5}} t^{\frac{1}{5}} \qquad \text{(Eq. 6-77)}$$

and:

$$L = 0.68\left[\frac{EQ^3}{2\left(1-\nu^2\right)\mu H^4}\right]^{\frac{1}{5}} t^{\frac{4}{5}} \qquad \text{(Eq. 6-78)}$$

which is a relatively small change over the Perkins and Kern solution.

Geertsma and de Klerk (1969 [DIRS 163624]) provided analytic solutions for two-dimensional fractures that had a constant-width profile (e.g., the fracture extends to infinity or exhibits full slip at some boundary). For such a case, the width is given by:

$$w_{\max} \approx 2.27\left[\frac{2\left(1-\nu^2\right)Q\mu L^2}{E}\right]^{\frac{1}{4}} \text{ for the Cartesian case} \qquad \text{(Eq. 6-79)}$$

and:

$$w_{\max} \approx 2\left[\frac{2\left(1-\nu^2\right)Q\mu R}{E}\right]^{\frac{1}{4}} \text{ for radial conditions.} \qquad \text{(Eq. 6-80)}$$

Because the dike propagation modeling being performed here is applying the two-dimensional approximation used by Geertsma and de Klerk (1969 [DIRS 163624]), these equations are most appropriate for direct comparison with the model results.

Although such analytic conceptual models are useful for parameter estimation, they are not appropriate for the dike propagation problem in the vicinity of the free surface and with a sink point at some single location. Thus, these models cannot be used to provide the detail needed for understanding magma flow into a shallow repository due to an intersecting dike.

6.3.8.1.1 Industrial Hydraulic-Fracture Models (Oil and Gas Applications)

Industrial hydraulic-fracture models are based on the same concepts as the analytic solutions given above, but numerical solutions allow considerable flexibility, particularly with respect to

height evolution and length factors. Some of the major available industrial packages are FracPro, Stimtech, MFrac, and TerraFrac, each available from a software provider.

Because these are proprietary industrial models, no exact accounting for their equations, algorithms, and applications can be made, but general principles associated with these models are documented in the literature and elsewhere. The most significant differences between the analytic solutions and the industrial models are the ability to handle variable height growth (into other layers having different stresses and other properties), compressible fluids (e.g., for foam-fracturing fluids), and proppant transport (e.g., for carrying sand to keep the fracture open after the treatment ends and the pressure drops). Many other factors can also be accounted for, such as different types of leak-off behavior, different fracture-tip propagation conditions, three-dimensional coupling effects, and others.

An overview of these types of models, a comparison of their results, and references on the equations/algorithms can be found in Warpinski et al. (1993 [DIRS 163649]; 1994 [DIRS 163657]). In general, these review papers show that these models can result in widely different fracture geometries (and pressures) for the same input parameters, largely because of many unknown factors in the algorithms. In addition, these models are primarily appropriate for fracturing far away from the free surface in layered media (where fractures are relatively confined between horizontal strata). These limitations clearly make the industrial models unsuitable for the present application, and no further use is made of these models.

6.3.8.1.2 Hydraulic-Fracture Dike Propagation Models

There are a number of models of dike propagation using hydraulic-fracture models, but with the addition of the effects of buoyancy (buoyancy is normally ignored in most hydraulic-fracture models). Buoyancy has been found to be important for its effect on upward growth of the dike and for the effect of magma density on the width profile of the dike. Examples of these models are those due to Spence and Turcotte (1985 [DIRS 127068]; 1990 [DIRS 127086]), Lister (1990 [DIRS 126865]; 1995 [DIRS 163635]), Lister and Kerr (1991 [DIRS 126889]), and Turcotte et al. (1987 [DIRS 134364]) among others. These models have quite adequately shown how the buoyancy effects are a critical element of dike propagation.

However, none of these models has a free surface that can model the changing behavior of the dike as the surface is approached. No other use is made of these models except as validation comparisons.

6.3.8.2 Effect of Expanding Magma on Dike Extension to the Surface

It is important to understand what occurs between the time when the magma reaches the drifts and the time the fracture reaches the surface; once the fracture reaches the surface, it will be very unlikely that the magma in the drift can be pressurized sufficiently to open a new path to the surface. An approximation is developed to describe the effect of expanding magma as it moves upward by combining results for different magma densities from the calculations of Section 6.3.7.1. This analysis illustrates the type of changes that could be expected for an expanding magma. It does not take into account any interaction with a drift.

Figure 6-36g shows the result if the magma density was 1140 kg/m^3 with a far-field velocity of 1-m/s below 750 m and the magma expanded to 1000 kg/m^3 at 750 m and to 750-kg/m^3 above 500 m, with the far-field velocity increasing so that the product of density times velocity times dike width is constant (conserving mass flux). Expansion of rising magma will be accompanied by acceleration of the magma, which, in turn, will augment the acceleration of the crack tip as the tip approaches the surface. In the approximation illustrated, the magma-front velocity is approximately 2.3 m/s between 400-m depth and 340-m depth. The crack tip arrives at the surface three minutes earlier than it would have had no expansion of the magma occurred as it rose toward the surface. Selection of the depths (750 m and 500 m) for expansion in this approximation is arbitrary. Clearly, if magma began expanding at a deeper horizon, the surface arrival would be even earlier than the three minutes seen in Figure 6-36g.

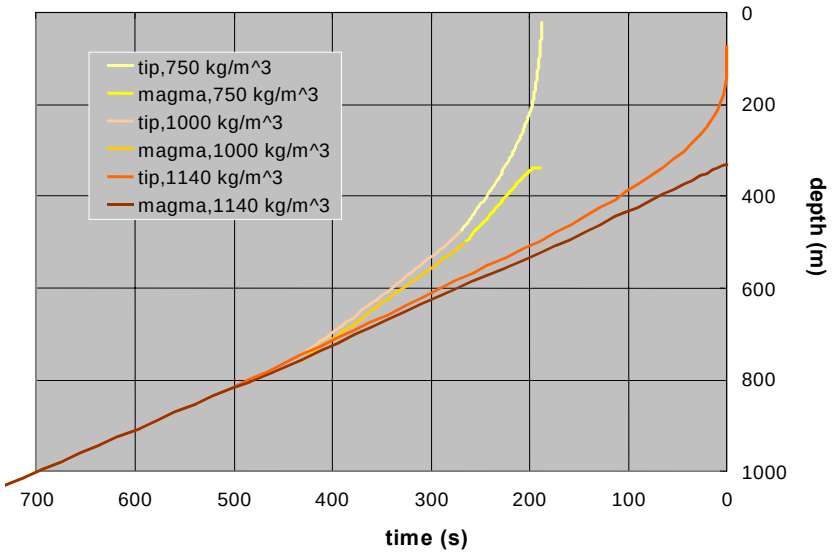

Output DTN: MO0408EG831811.002.

NOTE: The brown and orange (for tip) curves show the dike propagation for a dike (D = 20.3) with a magma density 1140 kg/m^3, a far-field velocity 1.00 m/s, and a far-field dike width of 0.45 m. The light orange and tan (for tip) lines between 750 m and 500 m are results for a dike (D = 6.02) with magma density 1.00 Mg/m^3, a far-field velocity 1.64 m/s, and a far-field dike width of 0.31 m and shifted earlier by 142 s to align with the results for D = 20.3 at 750 m. The yellow and light yellow (for tip) lines above 500 m are results for a dike (D = 2.67) with magma density 0.75 Mg/m^3, a far-field velocity 2.60 m/s, and a far-field dike width of 0.26 m shifted by 260 s.

Figure 6-36g. Approximate Magma and Crack Propagation for an Expanding, but Still Effusive, Magma

6.3.8.3 Electric Power Research Institute Analysis of Dike Propagation

The Electric Power Research Institute (EPRI) published an analysis of potential igneous processes at Yucca Mountain (EPRI 2004 [DIRS 171915]). Their analysis of dike propagation from depth coincides closely with the analysis of this section, with one major exception. Noting that the least compressive stress during the first 2000 years after closure will reach 10 MPa, with

the horizontal components exceeding the vertical, they concluded that "the potential for an extrusive release in the first 2000 years is zero" (EPRI 2004 [DIRS 171915], Section 3.3). Regarding intrusion of the repository, they state:

> Radiogenic heating, and associated modifications of the stress field, are at a maximum soon after repository closure. It is reasonable to assume that, under these conditions, in which the vertical principal stress is double the horizontal, that the probability of a dike intrusion into the repository is zero. At 2000 years after closure and thereafter, the probability of dike intrusion through the repository is set at the PVHA [probabilistic volcanic hazard analysis] value of 1.6×10^{-8}/year. It is assumed that the modification of the stress field is related to the heat generation of the repository, which gradually decreases over this 2000-year period.
>
> From the "reasonable expectation" case, therefore, the probability of dike intrusion into the repository for the expected case is considered to increase linearly between 0 at time zero (i.e., time of repository closure) and 1.6×10^{-8}/year at 2000 years. This approach is considered to be a reasonable intermediate approach between the bounding approach used in past analyses (i.e., in which the deflection effect is conservatively ignored), and assuming a zero probability for the first 2000 years. It is, therefore, considered to be neither overly conservative nor overly optimistic.

The analysis in Section 6.3.7.3 of this report finds that, because of the finite extent of the increased confining stresses during the first 2000 years after repository closure, dike propagation will not be stopped by the thermal stress field; it will merely be slowed down until the dike at depth widens enough to push the crack tip through the repository.

6.3.9 Summary

Dike ascent was analyzed for a variety of conditions. The effects of horizontal stress gradient, far-field dike velocity and opening, pressure inside the tip cavity, and additional horizontal confinement were considered. Although the dimensional results were provided for different values of v_∞ (up to 15 m/s) and $\kappa\rho_r$ (up to 2400 kg/m^3), the primary focus was on v_∞ = 1 m/s and 10 m/s, and on $\kappa\rho_r$ = 1200 kg/m^3.

The maximum magma pressure in the dike, in the absence of a drift, at the repository elevation, was computed to be about 1 MPa above in situ stress conditions (i.e., 4.5 MPa for a horizontal far-field stress of 3.5 MPa). Thermally-induced horizontal stresses only increase the magma pressure by a fraction of the increase of horizontal stresses: while horizontal stresses reach 13 MPa (i.e., an increase close to 10 MPa), the magma pressure reaches only 6 MPa, a 1.5 MPa increase only over magma pressures computed using non-thermal horizontal stresses. When uncertainty in the far-field width of the dike is taken into account, it is concluded that maximum magma pressures at the repository will be at most a few MPa greater (see Section 7.3.1.1.2 and Appendix F) than the in situ confining stress. With this reservation, both the thermal and non-thermal periods are covered.

The tip of the crack speeds up when approaching the surface, therefore lengthening the cavity, behind the dike tip, which is free of magma. In all cases, the cavity has grown to a significant length when the magma reaches the repository elevation. In fact, for the most realistic cases mentioned above, the dike tip has reached or is about to reach the surface when the magma reaches the repository.

The velocity of the ascending magma stays fairly constant when approaching the repository level, except in the lower buoyancy cases (Figure 6-10) for which the magma does slow down. The width of the dike at the repository level is essentially the same as w_∞, since the magma flow rate is constant and the magma velocity does not vary much. An increase of up to 20 percent in width was calculated, but that increase is not significant compared to the range of parameters analyzed. The magma front velocity and dike width are not considered to be significantly different from the values at infinity.

6.4 ANALYSIS OF EFFUSIVE MAGMA FLOW INTO DRIFTS

The purpose of this section is to analyze the flow of the magma into the drifts and its effect on further dike propagation (i.e., propagation from repository elevation to the surface), using the conditions in the dike as computed in Section 6.3. This will lend insight into the process of magma filling the drifts

- Does the magma front continue up the original dike at the same speed?
- Does magma stall while the drift is filling?
- What pressures can be expected in the magma while the drift is filling, and after the drift has filled?
- What are the effects of magmatic temperatures on waste packages and waste forms?

Answers to these questions allow the development of realistic scenarios for assessing the impacts to waste packages, and to eliminate those scenarios that are unrealistic.

The assumptions and simplifications involved in this analysis are discussed in Section 6.4.1. The mathematical formulation of the flow problem is detailed in Section 6.4.2. Note that this formulation uses the well-established Poiseuille formula (Bird et al. 1960 [DIRS 103524]) for flow in a parallel plate. No new mathematical development or modeling is attempted in this section. The inputs to the analysis and the initial/boundary conditions are given in Sections 6.4.3 and 6.4.4, respectively. Results are presented in Section 6.4.5. Corroboration with a more complete model is presented in Section 6.4.6. An alternative analytical formulation is presented in Section 6.4.7. Section 6.4.8 indicates how waste packages and waste forms are likely to be affected by the invading magma, while Section 6.4.9 summarizes the findings of the analysis.

The analyses described in Section 6.4.1 through 6.4.6 are carried out using FLAC3D V2.14 (BSC 2004 [DIRS 172323]). This code is qualified, and is used here within its range of intended use.

6.4.1 Approximations and Simplifications

Several approximations that were already detailed and justified in Section 6.3.2 are also used in this analysis:

- The host rock behaves elastically
- The elastic response of the host rock is linear
- The host rock is homogeneous and isotropic material
- The dike is a single fracture
- The free surface is horizontal
- The lubrication approximation is valid (i.e., that the flow is laminar, the viscosity is Newtonian, and that inertial forces are not important).

In addition to the ones mentioned above, a few simplifications are different from the ones in Section 6.3.

The fracture toughness is taken to be negligible (i.e., the propagation of the dike is not affected by the energy needed to break the rock at the crack tip). Therefore, the dike propagation can be simulated using a pre-existing crack along the vertical path of the dike. Section 6.3.2 discusses the supposition that fracture toughness is negligible for dike propagation.

The magma entering the drift from the dike is considered to be partially degassed so that it does not explosively decompress. This approximation is used in the analysis of flow within the dike as shown in Section 6.4.2. It is consistent with observations (at Hawaii and at Parícutin in Mexico) of magma behavior prior to magma reaching the surface.

The analysis treats the pressure as atmospheric at the intersection between the dike and the drift; therefore, the flow in the drift is not explicitly represented. In reality, some pressure buildup will take place. In this regard, the analysis in Section 6.4.2 effectively provides an upper bound for the amount of magma flowing into the drift, which can be considered as conservative from the perspective of estimating the magma inflow rate into the drift (overestimated) and the time required for magma to fill the drifts (underestimated). Note that a complementary analysis using a fully coupled dike flow/drift flow formulation will be presented in Section 6.4.6.

The analysis treats the magma entering the drift as free of obstructions, such as waste packages, backfill, or rubble. These features, if considered, may impact the thermal and mechanical characteristics of the magma as it flows into the drift.

6.4.2 Magma Flow within the Dike

FLAC3D V2.14 (2004 [DIRS 172323]) is fully capable of simulating coupled fluid-mechanical problems. For the specific analysis of dike propagation, magma flow is confined to one vertical

layer of zones only; there is no flow in the rest of the model. The fluid flow model implemented in the numerical code uses Darcy's law as a transport law:

$$Q_i = \sum_{j=1}^{3} k_{ij} \frac{\partial (p - \rho_f z g)}{\partial x_j} \quad \text{(Eq. 6-81)}$$

where Q_i is the specific discharge or volumetric flow rate per unit area, k_{ij} is the permeability tensor, p is magma pressure, ρ_f is magma density, z is elevation relative to a reference plane, g is the gravitational constant, and the summation convention is applied to repeated indices. However, the magma flow rate per dike width is considered to follow the cubic law, which is a special form of the Poiseuille law (Bird et al. 1960 [DIRS 103524]) for the case of flow between parallel plates:

$$Q_i = -\frac{a^3}{12\mu} (p - \rho_f z g)_i \quad \text{(Eq. 6-82)}$$

where a is the dike aperture and μ is magma viscosity. To correctly simulate magma flow inside the dike, the permeability tensor of the zones that represent the dike is calculated during the simulation according to the following relation:

$$k_{ij} = \delta_{ij} \frac{a^3}{12 \mu d} \quad \text{(Eq. 6-83)}$$

where d is the thickness of the layer of zones that represent the dike, and δ_{ij} is the Kronecker symbol.

The dike thickness is not explicitly represented in the model because it is zero initially, and even later, when the dike opens due to magma injection, it is much smaller than any characteristic length of the model. Instead, an arbitrary small value, d, is selected to be the thickness of zones that represent the dike. With the correction of permeability shown in Equation 6-83, the arbitrary number has no effect on the model solution. The dike aperture, a, is calculated during the simulation as a function of model deformation.

6.4.3 Description of Input

Inputs used in the analysis are shown in Table 6-6. Those parameters derived from sources external to this document (direct input) are also listed in Table 4-1. Magma density for this analysis uses a restricted subset of the values used previously in Table 6-2. A restricted subset was selected to minimize computation time while still providing a demonstration of the effect of key variables where the effect may not be readily discernible from the underlying equations. For example, fluxes in the dike vary as the third power of the dike width; therefore, two values were selected to show a typical range. A single value for magma viscosity was selected from the viscosities in Table 4-1 because the linear dependence of flow rate on viscosity can be extended readily to other viscosities. The bulk density of the host rock is the same as that used in Section 6.3.5. The value of magma compressibility is set to 50 MPa as a number required by the code but chosen such that it does not affect the results. Acceleration of gravity has been rounded

up to 10 m/s^2 from the value of 9.8 m/s^2 given in Incropera and DeWitt (2002 [DIRS 163337]). Calculational products developed in previous sections are used here.

Table 6-6. Inputs to Dike-Drift Interaction Analysis

Parameter	Value
Drift Diameter (BSC 2004 [DIRS 168489])	5.5 m
Half of Drift Spacing (BSC 2004 [DIRS 168489])	40.5 m
Young's Modulus of Host Rock (Detournay et al 2003 [DIRS 169660], Table 1-2)	15 GPa
Bulk Density of Host Rock (DTN SNL02030193001.027 [DIRS 108410])	2400 kg/m^3
Bulk Viscosity of Magma (μ) (Detournay et al 2003 [DIRS 169660], Figure 2-1e)	10 Pa·s
Magma Compressibility	50 MPa
Magma Rise Velocity (Detournay et al 2003 [DIRS 169660], p. 56)	1 m/s
Gravitational Acceleration (g) (Incropera and DeWitt, 2002 [DIRS 163337])	10 m/s^2

Two combinations of model parameters with different magma densities and, therefore, two different dike widths, were simulated. These two cases correspond to two of the dike propagation cases studied in Section 6.3 (see Table 6.3). Both cases correspond to a magma-front velocity far from the ground surface of 1 m/s. The dike width far from the ground surface can be calculated from the input values (Section 6.3.3.3). Consequently, the first case, or "wide aperture case," corresponds to a dike aperture (far from the ground surface) of 0.45 m; Case 2, or "narrow aperture case," corresponds to a dike aperture (far from the ground surface) of 0.25 m. Note that far-field velocity and the far-field dike width are used as approximations for the velocity of magma and the width of the dike when magma reaches the drift elevation, as discussed in Section 6.3.7. Besides the inputs from Section 6.3 already associated with these two cases, this analysis requires the drift diameter, drift spacing, and magma compressibility.

6.4.4 Initial and Boundary Conditions

The geometry used for the numerical simulations of dike propagation is shown in Figure 6-37. The model represents the portion of the dike between the vertical plane along the drift and the vertical symmetry plane halfway between the drifts. Symmetry conditions are used on those two planes in both the mechanical and the flow simulations.

The model extends 900 m below the repository level and 600 m on each side perpendicular to the dike. A stress boundary condition is applied on the model vertical boundaries parallel with the dike. The bottom model boundary is restrained in the vertical direction. The top model boundary corresponding to the ground surface is free.

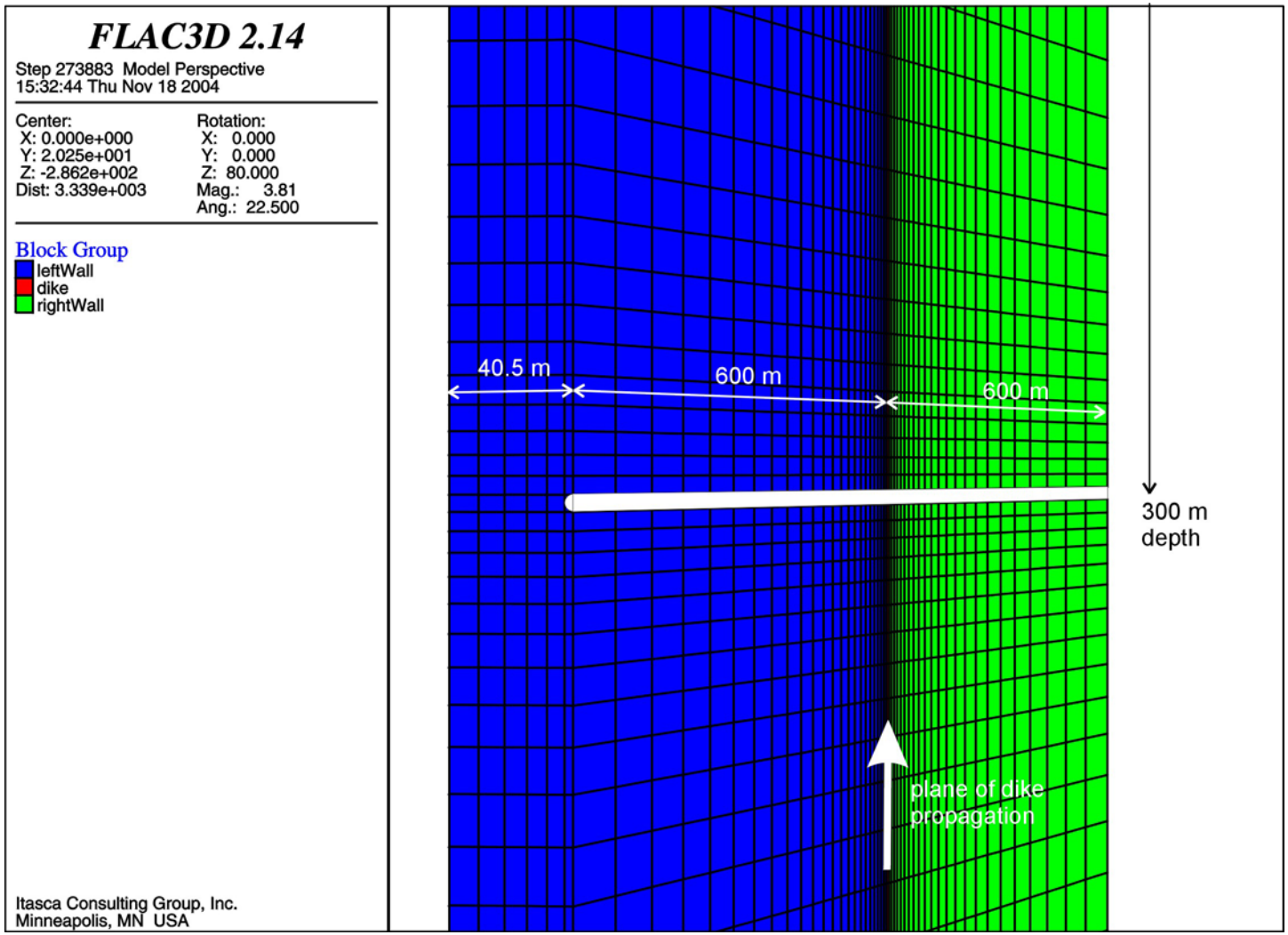

Output DTN: MO0408EG831811.001.

Source: Output Calculation Data Plot.

Figure 6-37. Geometry of the Dike Model

The magma is injected into the dike at the bottom of the model. The vertical in situ stress in the rock mass is gravitational. In the same manner as used in Section 6.3, the stress state in the horizontal plane is taken to be isotropic, with magnitude of the horizontal principal stress equal to half of the vertical stress magnitude.

One vertical layer of zones represents the dike, with magma flow into this layer simulated as explained in Section 6.4.2.

6.4.5 Results

The results for the wide aperture case are given in Section 6.4.5.1 and the results for the narrow aperture case are given in Section 6.4.5.2

6.4.5.1 Wide Aperture Case

The results for the wide aperture case are illustrated in Figures 6-38 through Figure 6-43.

Figure 6-38 shows the contours of the horizontal stress perpendicular to the dike and the displacement vectors at the end of the simulation, at which time the crack tip is between 125-m and 100-m deep. The plot illustrates that, far from the dike tip and the magma front (i.e., at the bottom of the model), the magma pressure and pressure gradient are determined by the in situ conditions in the rock mass. The maximum displacement results in the dike aperture of 0.47 m, which is close to the far field dike aperture of 0.45 m. This result indicates that the artificial bottom boundary is sufficiently far from the repository level.

The magma flow rate out of the dike as a function of time (Figure 6-39) shows a progressive increase of the magma loss after the magma has reached the level of the drift at time 540 s after the start of simulation. After another 1100 s, the flow rate out of the model is 18.1 m^3/s. This is already very close to steady state in which the complete magma flow rate inside the dike ($Q = 1.0$ m/s x 0.45 m x 40.5 m = 18.23 m^3/s) would be diverted into the drift. Integration of the flux out of the dike shows that a 500-m long drift is filled 15 minutes (900 s) after the magma has reached the repository level.

Positions of the magma front at three different states during the simulation (all states are after the magma front has reached the repository level) can be determined from contour plots of saturation shown in Figures 6-40 through Figure 6-42 (the magma front coincides with the contour line of 50 percent saturation). Figure 6-42 corresponds to the end of the simulation, at a time slightly larger than the time needed to fill the drift. Therefore, Figure 6-42 shows a slight overestimate of the level reached by the magma when the drift is full. It seems that, in this case, the magma front moves to a maximum of approximately 80-m above the repository level before the drift is filled with magma.

Contours of the magma pressure and the flow vectors for the same point in time are shown in Figure 6-43. Although the flow vectors are obviously diverted toward the drift, it is clear that the entire flow is not diverted into the drift in agreement with Figures 6-40 through 6-42.

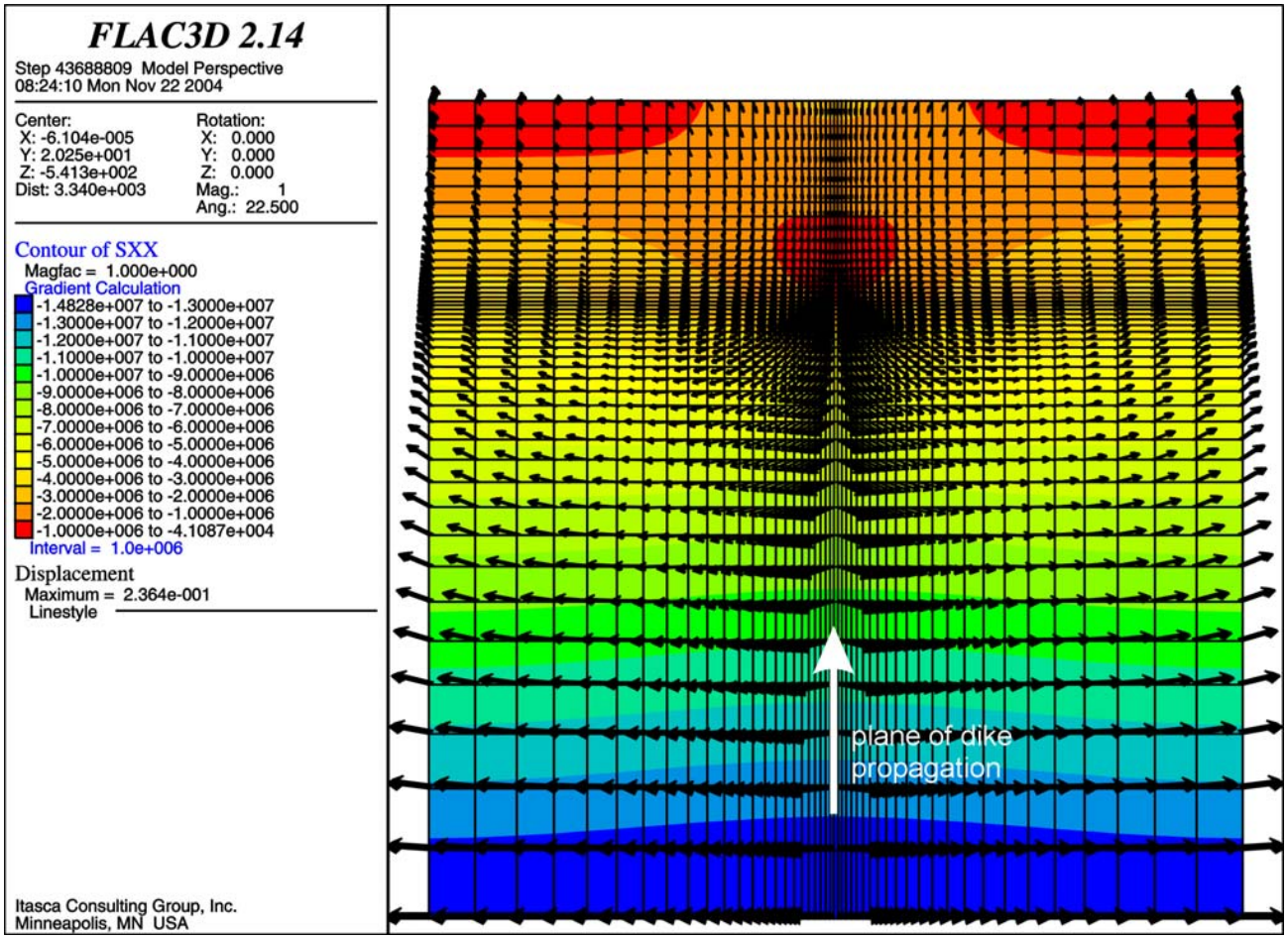

Output DTN: MO0408EG831811.001.

Source: Output Calculation Data Plots.

Figure 6-38. Contours of Horizontal Stress (Pa) Perpendicular to the Drift and Displacement Vectors (m) After 1642 Seconds of Simulation: Wide Aperture Case

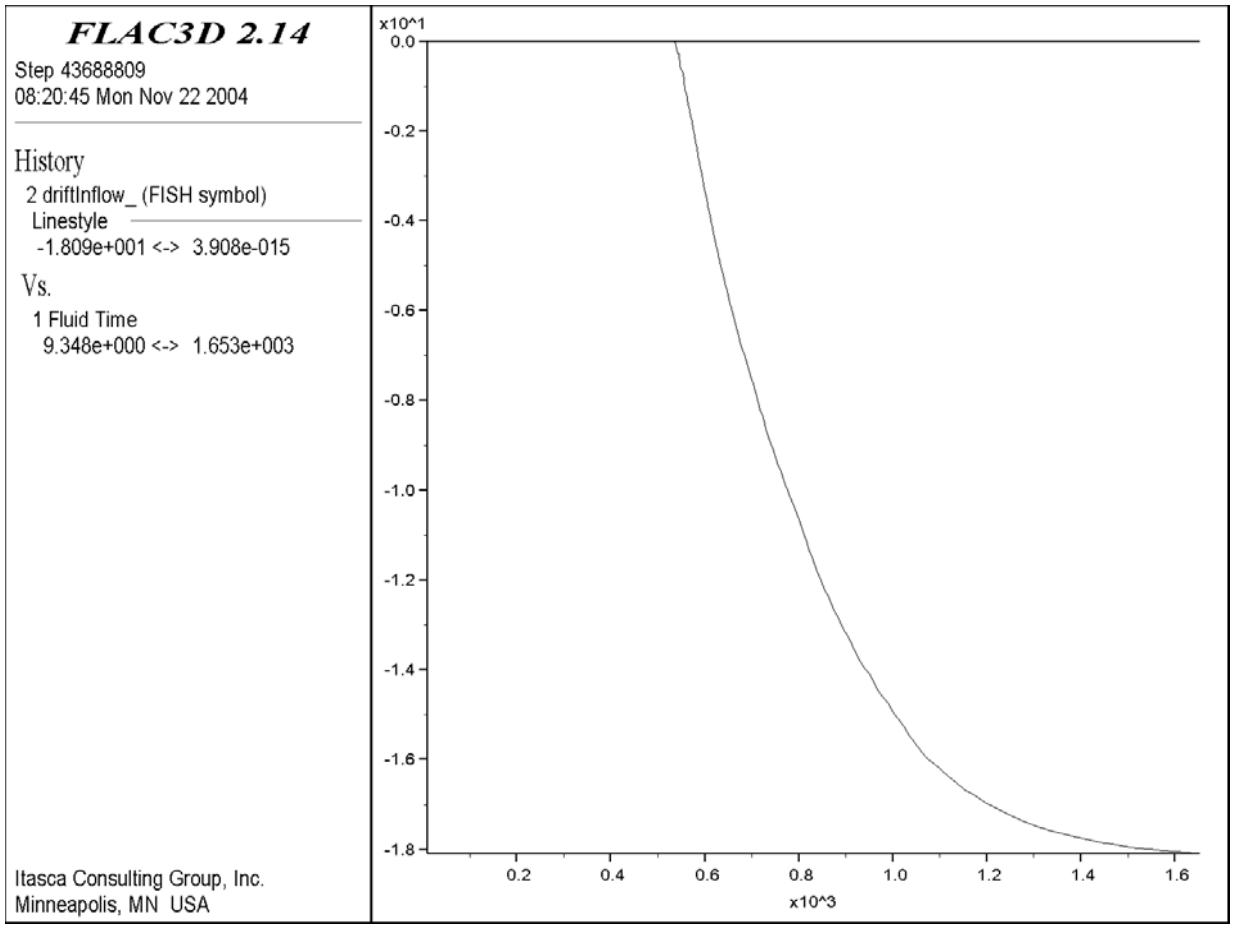

Output DTN: MO0408EG831811.001.

Source: Output Calculation Data Plot.

NOTE: Negative flow rates indicate flow from dike into drift. Vertical axis is magma flow rate (X10); horizontal axis is time (X103).

Figure 6-39. Rate of Magma Flow (m^3/s) From the Dike into the Drift as a Function of Time (s): Wide Aperture Case

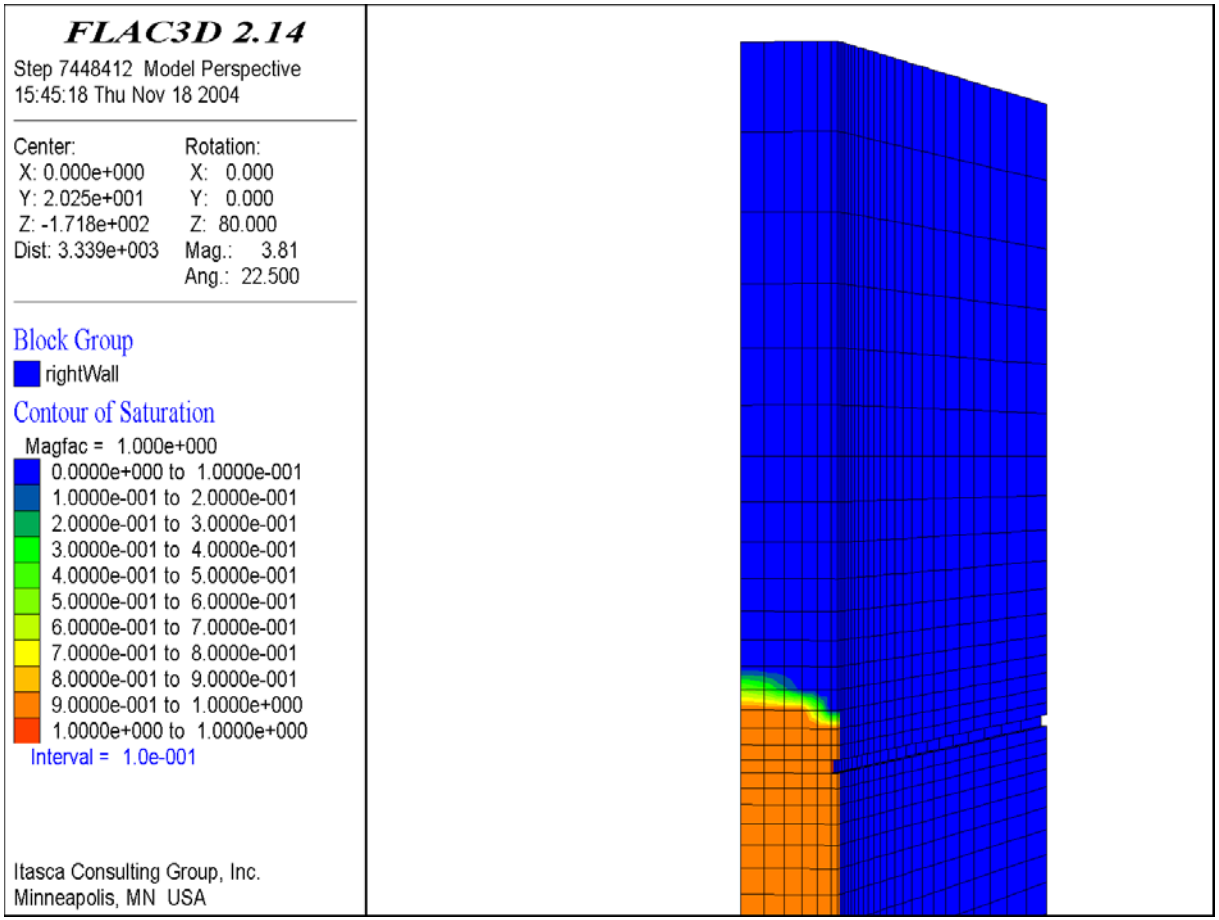

Output DTN: MO0408EG831811.001.

Source: Calculation Data Plots.

NOTES: The left wall of the dike is hidden.
Drift shown by notch along the right edge and indentation in the blue zone.
The scale is given by the drift depth (300 m)

Figure 6-40. Contours of Saturation of Dike With Magma 602 Seconds After Start of Simulation: Wide Aperture Case. The Position Of The Magma Front Corresponds To Saturation 0.5

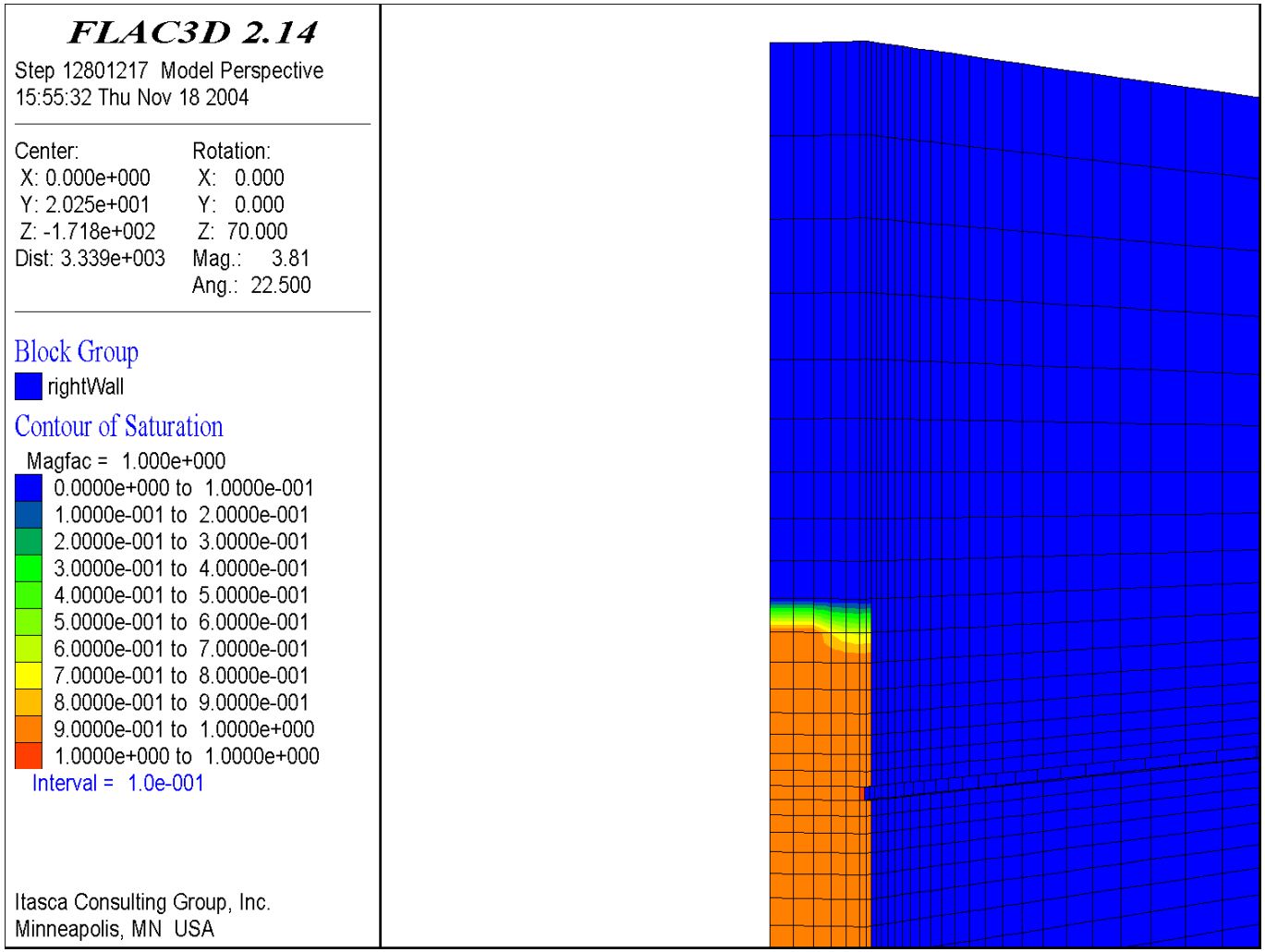

Output DTN: MO0408EG831811.001.

Source: Calculation Data Plots.

NOTES: The left wall of the dike is hidden. The scale is given by the drift depth (300 m). Drift shown by notch along the right edge and indentation in the blue zone. The position of the magma front corresponds to saturation 0.5.

Figure 6-41. Contours of Saturation of Dike With Magma 798 Seconds After Start of Simulation: Wide Aperture Case

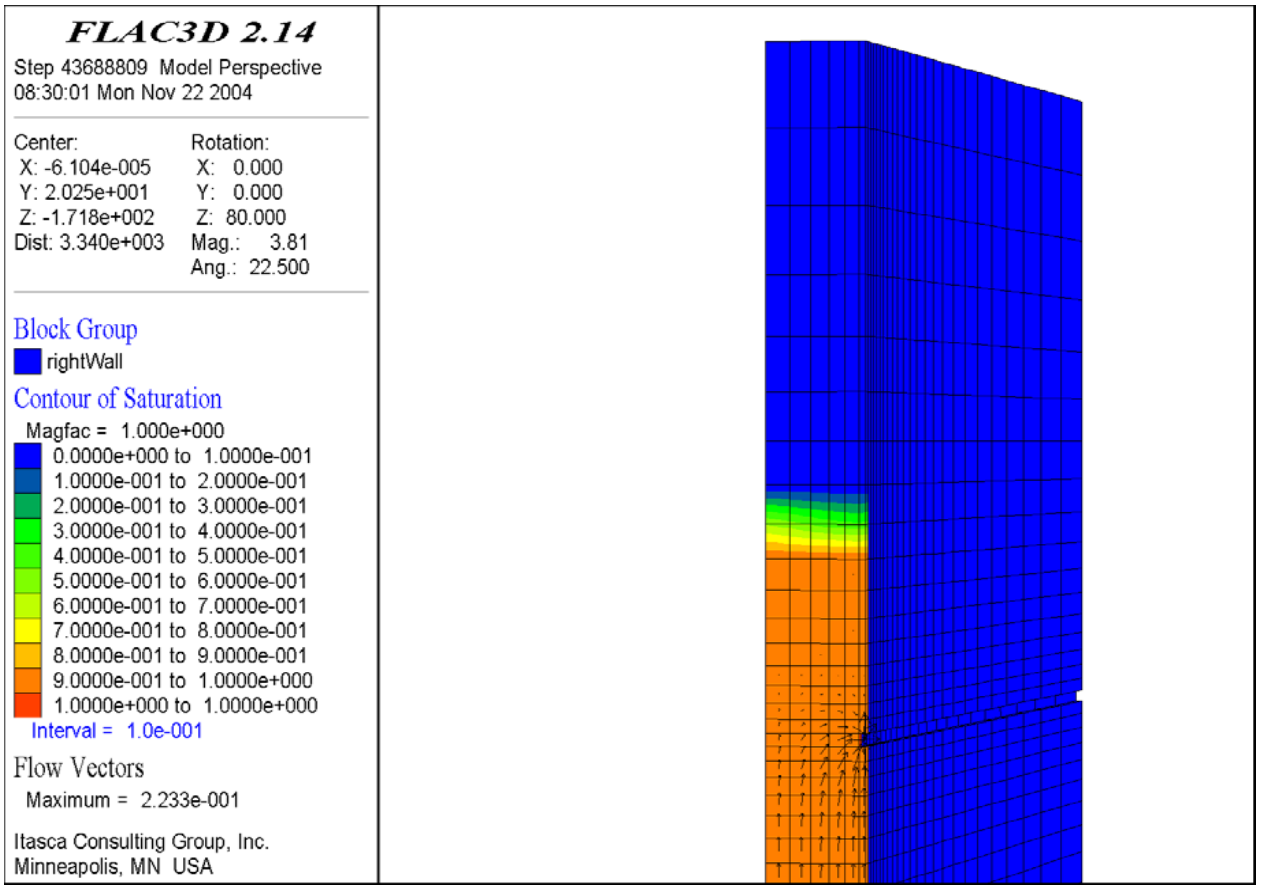

Output DTN: MO0408EG831811.001.

Source: Calculation Data Plots.

NOTES: The left wall of the dike is hidden.
Drift shown by notch along the right edge and indentation in the blue zone.
The scale is given by the drift depth (300 m).
The position of the magma front corresponds to saturation 0.5.

Figure 6-42. Contours of Saturation of Dike With Magma 1642 Seconds After Start of Simulation: Wide Aperture Case

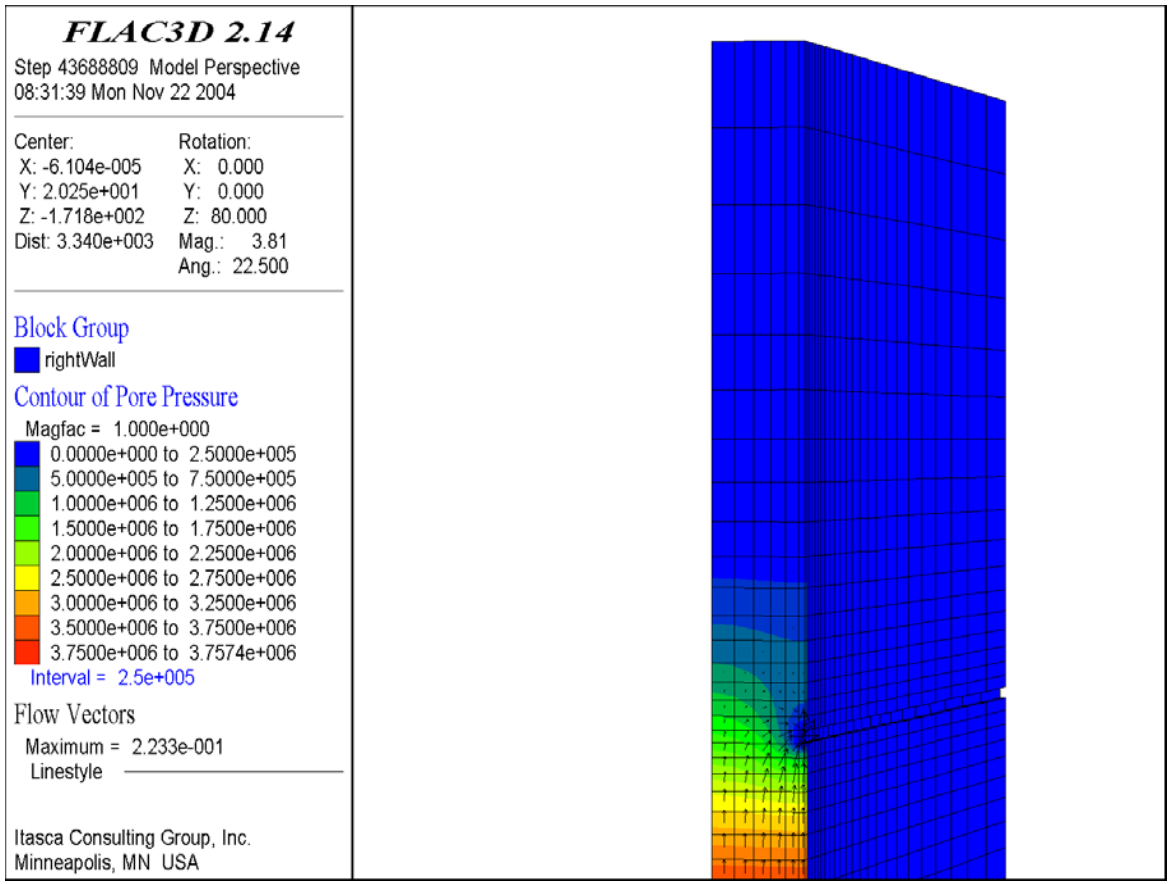

Output DTN: MO0408EG831811.001.

Source: Calculation Data Plots.

NOTES: The left wall of the dike is hidden.
The scale is given by the drift depth (300 m).
Drift shown by notch along the right edge and indentation in the blue zone.

Figure 6-43. Contours of Magma Pressure (Pa) Inside the Dike 1642 Seconds After Start of Simulation: Wide Aperture Case

6.4.5.2 Narrow Aperture Case

For the narrow aperture case, the results are illustrated in Figures 6-44 to 6-46. From Figure 6-44, it appears that the magma reaches the drift 740 s after the start of the simulation. It then takes another 1200 s after magma starts to flow into the drifts for the narrow aperture case to approach steady state (at the end of the simulation, the flow rate is 9.9 m^3/s compared to a full diversion steady state rate of Q = 1.0 m/s x 0.25 m x 40.5 m = 10.13 m^3/s). Integration of the flux out of the dike shows that a 500-m long drift is filled 25 minutes (1500 s) after the magma has reached the repository level, and 2240 s after the start of the simulation. Therefore, in this case, steady state is achieved and the magma front stalls before the drift is completely filled. The maximum elevation the magma front can reach is approximately 120-m above the repository level (saturation contours shown in Figure 6-45), which is more than in the wide aperture case. Contours of the magma pressure and the flow vectors for the narrow aperture case are shown in Figure 6-46.

In both cases analyzed, the magma does not reach the ground surface before the drifts are filled with the magma. Therefore, it is necessary to investigate conditions of magma injection into pre existing joints inside the drifts to assess potential for a secondary dike or "dog leg" scenario (see Section 6.5).

6.4.6 Fully Coupled Dike Drift Interaction

The numerical analysis in this section differs from the previous analyses by explicitly accounting for the coupling between flow in the dike and flow in the drift. This analysis is used simply to ensure that the condition of atmospheric pressure in the drift mentioned in Section 6.4.1 is appropriately justified.

The same two cases (wide and narrow aperture) are used to investigate the effect of coupling. These simulations are identical to the previous ones, except the magma pressure at the intersection between the dike and the drift, instead of being fixed at atmospheric, is calculated using the solution for fluid flow in a circular pipe.

Detournay et al. (2003 [DIRS 169660], Appendix 3.5, p. 62) give the equation for the volume flow rate through a circular pipe, Q_{pipe}, as

$$Q_{pipe} = \frac{\pi a^4}{8 \mu L} P \qquad \text{(Eq. 6-84)}$$

P is the pressure drop along the filled section of pipe
Q_{pipe} is the inflow rate into the drift,
L is the drift length filled with magma,
μ is the magma viscosity, and
a is the drift radius.

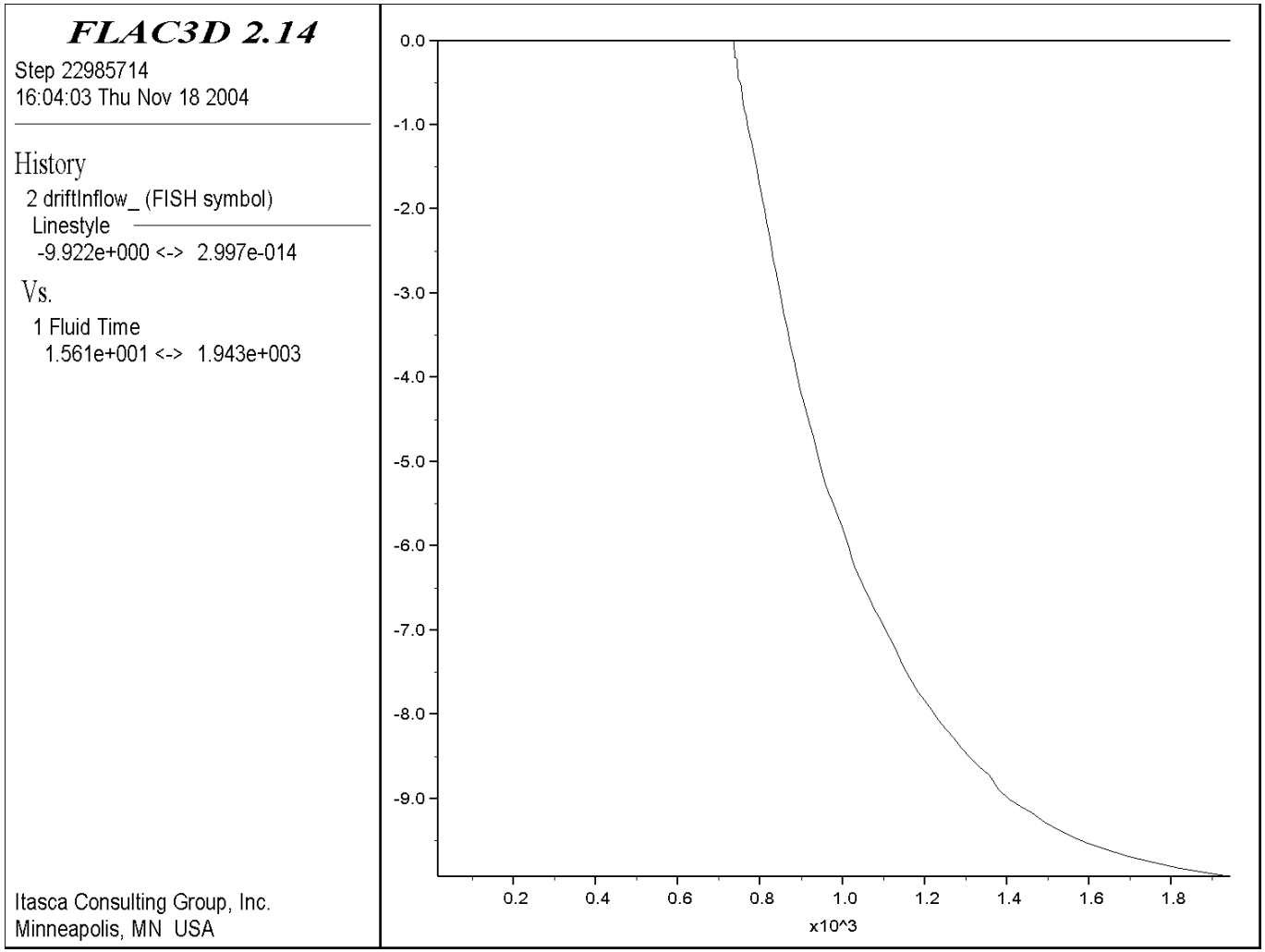

Output DTN: MO0408EG831811.001.

Source: Output Calculation Data Plot.

NOTE: Negative flow rates indicate flow from dike into drift. Vertical axis is magma flow rate (X10); horizontal axis is time (X103).

Figure 6-44. Rate of Magma Flow (m^3/s) From the Dike as a Function of Time (s): Narrow-Aperture Case

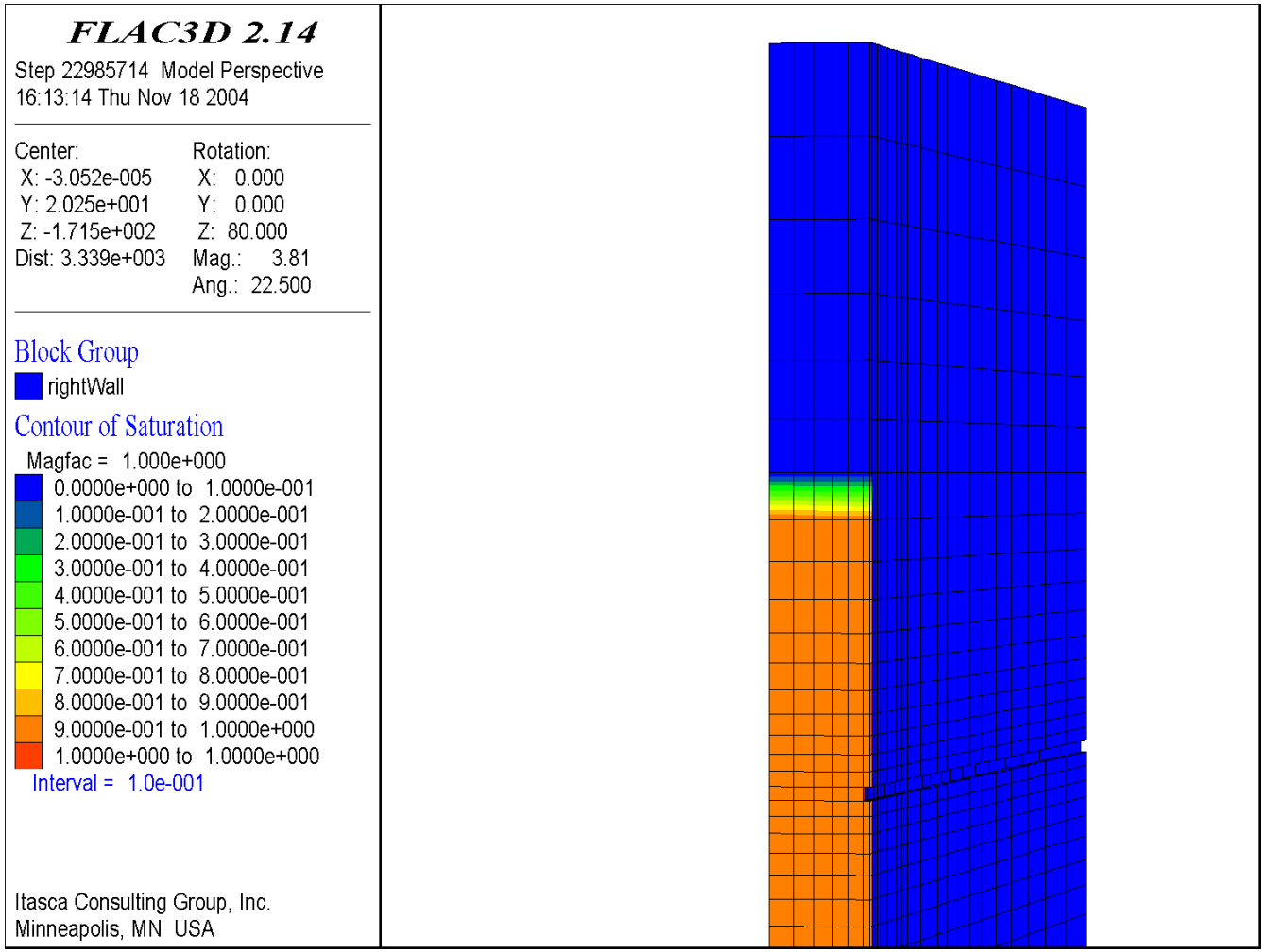

Output DTN: MO0408EG831811.001.

Source: Output Calculation Data Plots

NOTES: The left wall of the dike is hidden. The scale is given by the drift depth (300 m). The position of the magma front corresponds to saturation 0.5.

Figure 6-45. Contours of Saturation of Dike With Magma 1943 Seconds After Start of Simulation: Narrow-Aperture Case.

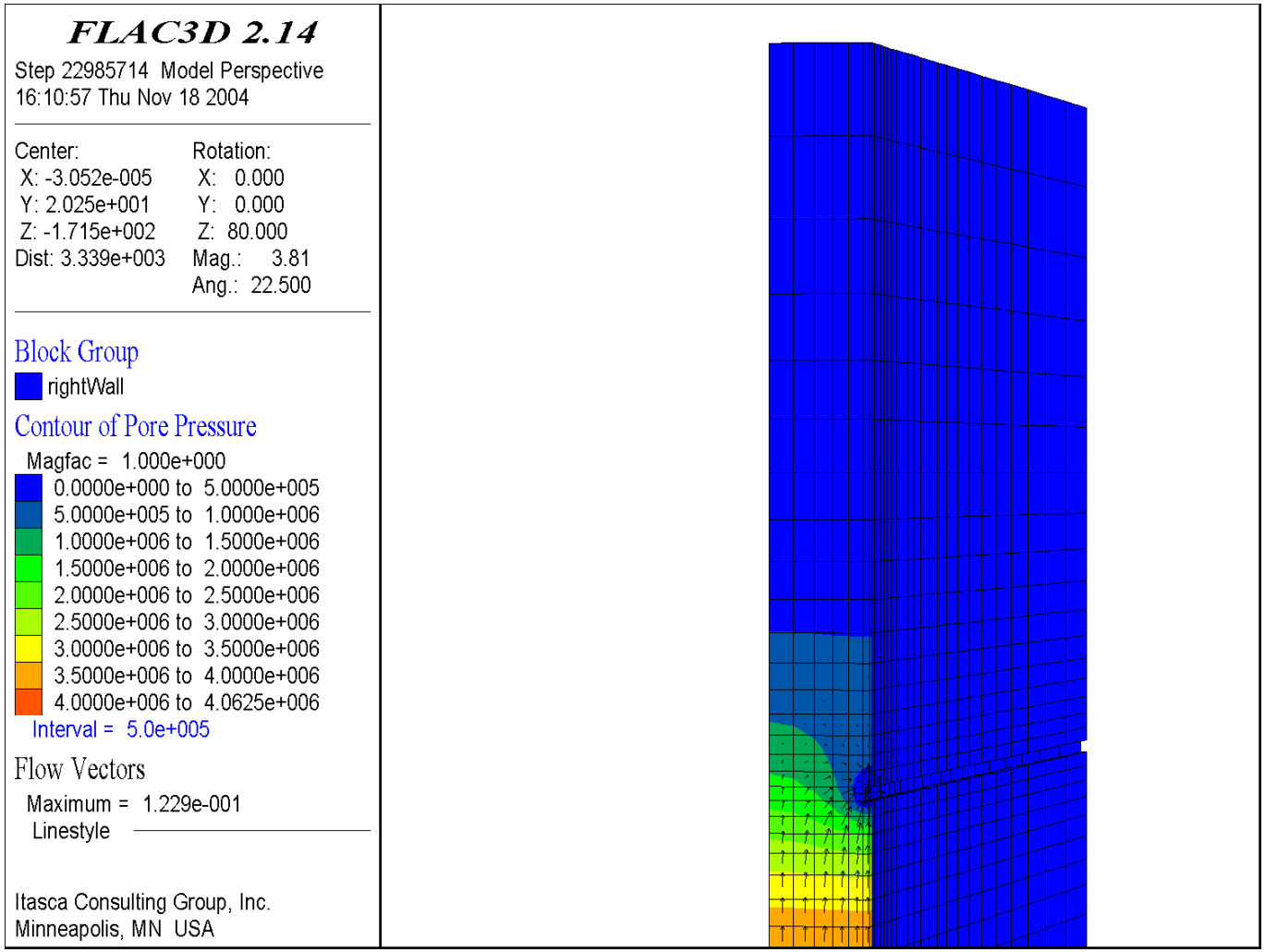

Output DTN: MO0408EG831811.001.

Source: Output Calculation Data Plots.

NOTES: The left wall of the dike is hidden. The scale is given by the drift depth (300 m).

Figure 6-46. Contours of Magma Pressure (Pa) Inside the Dike 1943 Seconds After Start of Simulation: Narrow-Aperture Case

Simplifying the expression for the inflow rate and adapting the equation yields:

$$P(t) = \frac{8\mu L(t)}{\pi a^4} q(t) \qquad \text{(Eq. 6-85)}$$

where:

q is the new notation for the inflow rate into the drift.

The drift length filled with magma can be calculated by integrating the inflow rate:

$$L(t) = \frac{\int_0^t q(\tau) d\tau}{\pi a^2} \qquad \text{(Eq. 6-86)}$$

The order of magnitude of magma pressure was estimated at the intersection by applying the above formulae for the following case:

- 300 m of the drifts are filled with magma
- The entire magma flow from the dike is diverted into the drift (Q = 1.0 m x 0.45 m x 40.5 m = 18.23 m^3/s)
- There are no obstacles to flow inside the drifts (i.e., $a = 2.75$ m).

The resulting pressure drop in the drift is 2.4 kPa. From the perspective of magma pressures inside the dike (which are on the order of MPa), the calculated pressure at the intersection is practically zero. Therefore, the original approximation seems to be appropriate.

To investigate the extreme case of pressure increase caused by such obstacles to flow as waste packages, drip shields, and eventual rockfall from partial drift degradation, the numerical simulation of the dike/drift interaction was conducted with the drift diameter ($2a$) of only 1.5 m in the calculation of pressure. Simulations were carried out for both wide- and narrow-aperture dike cases.

Figures 6-47 and 6-48 show the inflow rates into the drift as calculated in the original models (zero pressure at intersection) and in the coupled models with a restricted diameter, for the wide and narrow aperture case respectively. The effect of coupling is very small, particularly at early times when the pressure at the intersection is small. Later, the effect increases, but remains insignificant. The effect is slightly greater for the wide-aperture case.

For the considered parameters, the above analysis demonstrates that coupling between the magma flow in the dike and the drift is one-way only. Even for an extreme case of resistance to flow inside the drifts, the pressure at the intersection between the dike and the drift does not increase sufficiently to affect the flow inside the dike. In other words, the analyses in Sections 6.4.5 and 6.4.6 are equivalent for all practical purposes.

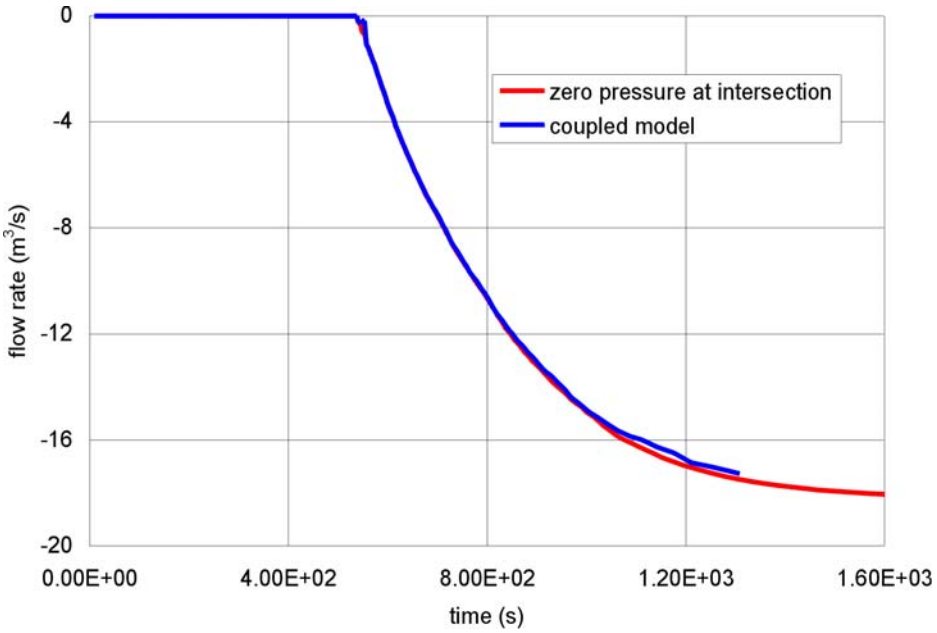

NOTE: Flow rates are positive when entering the model.

Output DTN: MO0408EG831811.001

Figure 6-47. History of the Rate of Magma Inflow From the Dike as a Function of Time: Wide-Aperture Case

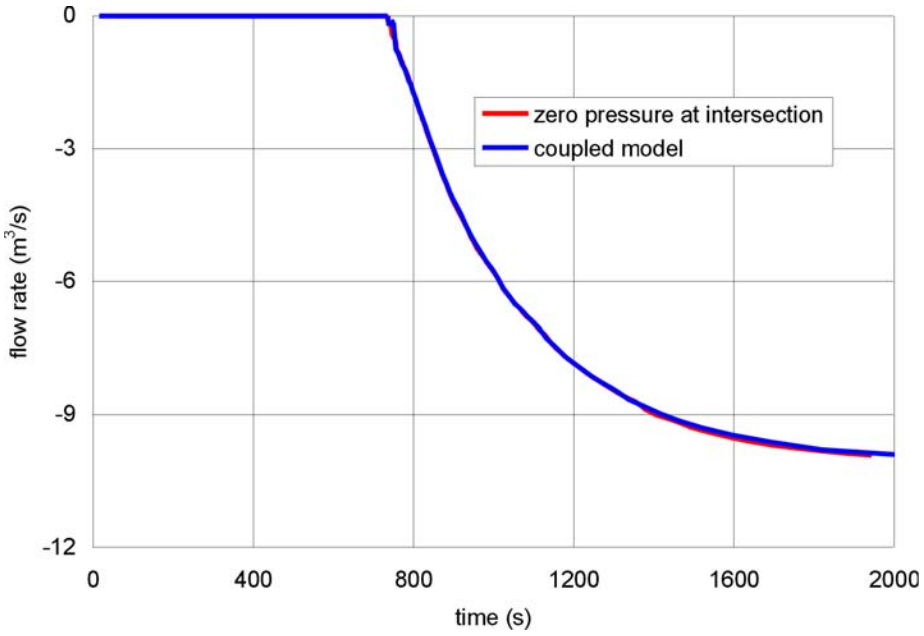

Output DTN: MO0408EG831811.001.

NOTE: Flow rates are positive when entering the model.

Figure 6-48. History of the Rate of Magma Inflow from the Dike as a Function of Time: Narrow-Aperture Case

6.4.7 Alternative Analyses

This section discusses three alternative analyses for magma flow into a drift. The first analysis is developed and discussed in Section 6.4.7.1. The first alternative (Section 6.4.7.1) uses well-established formulae for flow through a weir, for pipe flow, and for flow through an orifice, as well as an equation derived by Detournay et al. (2003 [DIRS 169660]). An alternative model postulating compressible, single-phase flow (Woods et al. 2002 [DIRS 163662]) is discussed in Section 6.4.7.2. Pyroclastic and hydrovolcanic flow into a drift are also addressed in Section 6.4.7.2. Section 6.4.7.3 provides a discussion of the analysis of magma flow into a drift presented in an independent report (EPRI 2004 [DIRS 171915]).

6.4.7.1 Analytic Solution for Effusive Flow into Drifts

In this analysis, magma rises in the dike (starting at the level of the bottom of the drifts at $t=0$) driven by a velocity as deduced in Section 6.3. At any time, the volume of magma rising above the base of the drifts can either flow into the drift or continue up the dike. The amount going into the drift is taken to be the minimum of that calculated by the three equations described in Section 6.4.7.2.

Initially, the magma flows into the drift (radius a) as it would flow through a weir of circular cross section until the height of the magma reaches the top of the drift. After the magma height (H) exceeds that of the drift, the problem is analogous to a fluid draining out of a tank through an orifice. Because the dike is fairly thin (on the order of 1 m with about 80 m between drifts) and the magma has a viscosity substantially larger than water (on the order of 10–40 Pa·s), for $H>>2a$ the orifice equation is modified to include the effect of viscous drag in the dike following the method of Detournay et al. (2003 [DIRS 169660], Appendix 3.5).

When the drift becomes sufficiently filled that viscous drag in the drift may control loss from the dike, the magma flow into the drift is calculated from the pipe-flow equation balanced by viscous drag in the dike.

6.4.7.1.1 Idealizations and Simplifications

The weir equation will give an overestimate of the flow into the drift because it considers that material flowing into the drift does not build up just inside the drift to decrease the head driving flow over the weir. Any frictional losses at the weir interface are also ignored. Similar comments apply to the orifice equation. Further, these equations ignore the effect of viscosity in the dike itself. As shown in the analysis of Sections 6.4.1 to 6.4.6, the magma surface in the dike is not at a uniform height, as is the case in this analysis.

The definition chosen for L (the length of the drift filled with magma) leads to inaccuracy in the discharge Q that is difficult to predict simply. This approximation is equivalent to taking the magma front in the drift to be vertical, which it certainly will not be. Early in the flow history, the fact that viscous drag on the walls only occurs along the bottom of the flow will probably result in greater discharge. Later, as the length, L, becomes long compared to the slope times the drift diameter, this approximation will become closer to reality.

The idealization of the drift cross-section as being perfectly circular ignores the drift invert, which is on the order of 4 percent of the cross-sectional area of the entire drift. The result will be a slight decrease in the hydraulic radius of the drift and in the volume of the drift and a change of the real weir cross-section that will be considerable at the earliest times of the flow. The decrease in the hydraulic radius will result in slightly lower discharge rate from the dike into the drift. The decrease in the volume of the drift will lead to a shorter time to fill the drift at a fixed discharge rate. These two effects have an opposite sign but do not exactly cancel each other.

The analysis idealizes the blockage of the drift to be only obstruction by waste packages, packed end-to-end. This approach ignores the effects of rails, pallets, and drip shields, and the effects of gaps between waste packages on the flow. The presence of rails, pallets, and drip shields will reduce the total volume to be filled by the magma and will increase the viscous drag forces. The gaps between waste packages will result in a larger volume to be filled and a longer time to fill the drift with magma. The net result of these compensating errors will be little change in the time required for magma to fill the drift.

6.4.7.1.2 Mathematical Formulation

The governing equations are those for flow of a liquid over a weir (weir equation, $H<<2a$), out of a tank through a circular orifice well below the top of the liquid in the tank (orifice equation, $2a<<H$), radially toward a point of discharge between two parallel plates (plate-drain equation), and through a pipe (pipe equation). The first two equations (Henderson 1966 [DIRS 164124]) are used separately. A simultaneous solution to the pipe equation and the plate-drain equations is used for $H<<2a$. Geometric configuration and nomenclature are illustrated in Figure 6-49.

The weir equation for a weir of arbitrary shape is

$$Q(H) = \sqrt{2g} \int_0^H dh \sqrt{h}\, w(h) \qquad \text{(Eq. 6-87)}$$

where $Q(H)$ is the discharge rate through the weir of the fluid at height, H, above the bottom of the weir, $w(h)$ is the width of the weir at depth (h) below the magma height, and g is the gravitational acceleration.

For a weir or orifice of circular cross-section with radius a and $0 \le H \le 2a$, $w(h)$ is given by

$$\begin{aligned} w(h) &= 2\sqrt{a^2 - (a - H + h)^2} \\ &= 2\sqrt{(H - h)(2a - H + h)} \end{aligned} \qquad \text{(Eq. 6-88)}$$

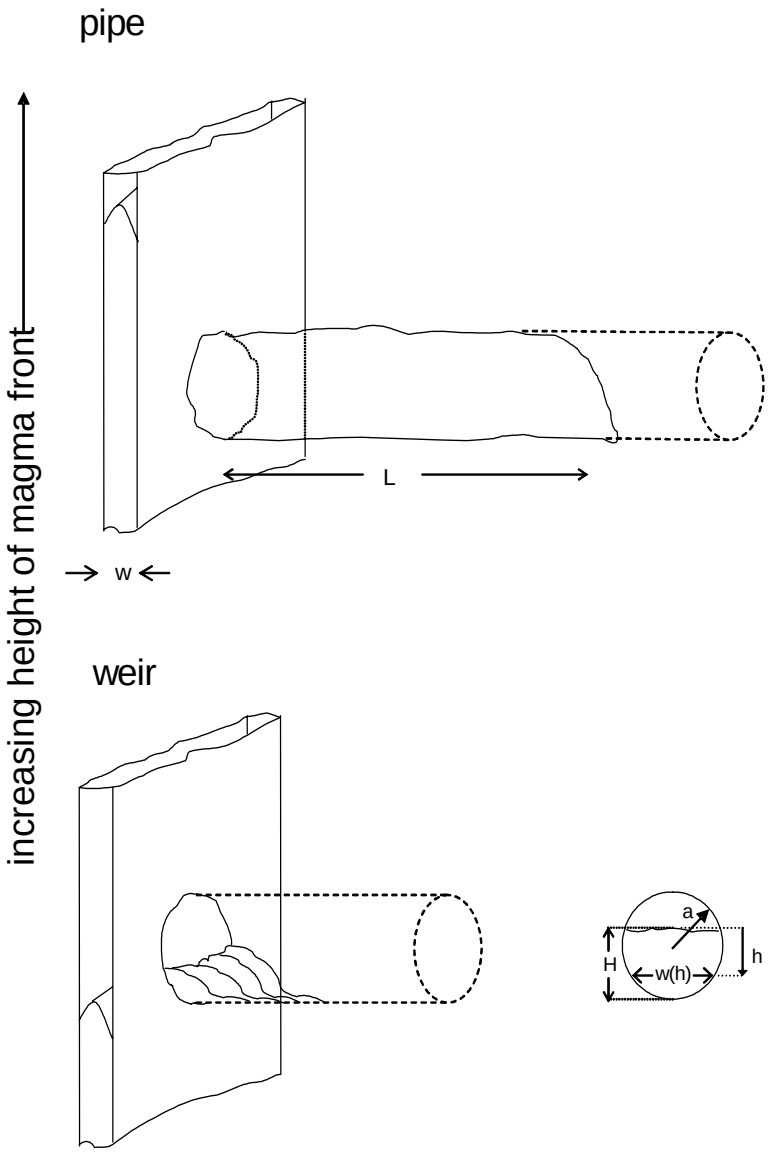

NOTES: For information purposes only.

The figure represents flow of magma for two distinct situations. In the lower drawing, the magma has not risen to the top of the drift, and a weir equation (Equation 6-89) is used. In the upper drawing, viscous drag in either the dike or the drift limits flow and Equation 6-92 or 6-98 is appropriate.

Figure 6-49. Schematic Representing Flow of Magma From Dike Into Drift

The flow rate equation becomes

$$\begin{aligned} Q(H) &= \sqrt{2g}\int_0^H dh\, 2\sqrt{h}\sqrt{(H-h)(2a-H+h)} \\ &= 2\sqrt{2gH^5}\int_0^1 dx\,\sqrt{x\left((2a/H)-x\right)(1-x)} \\ &= 4H^2\sqrt{ga}\int_0^1 dx\,\sqrt{x\left(1-(H/2a)x\right)(1-x)} \\ &= \frac{\pi}{2}H^2\sqrt{ag}\;{}_2F_1\left(-\frac{1}{2},\frac{3}{2};3;\frac{H}{2a}\right) \end{aligned} \qquad \text{(Eq. 6-89)}$$

$$= \frac{\pi}{2}H^2\sqrt{ag}\left(1+\frac{(-1/2)(3/2)}{1!3}\frac{H}{2a}+\frac{(-1/2)(-1/2+1)(3/2)(3/2+1)}{2!(3)(3+1)}\left(\frac{H}{2a}\right)^2+\cdots\right)$$

where the symbolic substitution has been made in the integral, $x = (H- h)/H$, and ${}_2F_1(a,b;c;z)$ is the hypergeometric function (Abramowitz and Stegun (1972 [DIRS 156927], Section 15.3). For $H = 2a$, the flow rate reduces to

$$Q(H) = (64/15)a^2\sqrt{ag} \qquad \text{(Eq. 6-90)}$$

For $H > 2a$, the flow rate is given by

$$Q(H) = (64/15)a^2\sqrt{ag} \qquad \text{(Eq. 6-91)}$$

where $w(h)$ is given by Equation 6-88. This yields a result similar to Equation 6-89

$$\begin{aligned} Q(H) &= \sqrt{2g}\int_{H-2a}^H dh\; 2\sqrt{h}\sqrt{(H-h)(2a-(H-h))} \\ &= 2\sqrt{2g}(2a)^{5/2}\int_0^1 dx\,\sqrt{x\left((H/2a)-x\right)(1-x)} \\ &= 8a^2\sqrt{2gH}\int_0^1 dx\,\sqrt{x\left(1-(2a/H)x\right)(1-x)} \\ &= \pi a^2\sqrt{2gH}\;{}_2F_1\left(-\frac{1}{2},\frac{3}{2};3;\frac{2a}{H}\right) \end{aligned} \qquad \text{(Eq. 6-92)}$$

The symbolic substitution, $x = (H-h)/2a$, has been made in the integral. This reduces to the orifice equation for flow from a half-space through a circular hole of radius a for $H>>2a$, as expected:

$$Q = \pi a^2\sqrt{2gH} \qquad \text{(Eq. 6-93)}$$

The equation for flow out of a dike into a pipe is derived following the method of Detournay et al. (2003 [DIRS 169660], Appendix 3.5, p. 62), which gives the volume flow rate from a dike through a circular hole q_{out} as

$$q_{out} = \frac{2\pi a w^3}{12\mu} \frac{d/2a}{\log(d/2a)} \frac{\rho g H - P}{d/2} \quad \text{(Eq. 6-94)}$$

and the flow rate down the drift, q_{pipe}, as

$$q_{pipe} = \frac{\pi a^4}{8\mu L} P \quad \text{(Eq. 6-95)}$$

where w is the width of the dike, μ is the magma viscosity, d is the spacing between drifts, ρ is the magma density, H is the height of magma above the drift, P is the pressure at the dike/drift interface, and L is the length of drift that is filled with magma.

Several things should be noted regarding differences between (Equations 6-94 and 6-95) and Equations (3) and (4) of Detournay et al. (2003 [DIRS 169660]). First, the variable, w, in Detournay et al. (2003 [DIRS 169660]), is the half-width of the dike, whereas the w in this document is the full-width of the dike. Thus, when comparing the above equations with Detournay et al. (2003 [DIRS 169660]), each occurrence of w in Detournay et al. must be changed to $w/2$ when compared to the equations in this document. Further, both Equations (2) and (3) are a factor of 2 too small in Detournay et al. (2003 [DIRS 169660]). Finally, the factor of 5.3 in Detournay et al (2003 [DIRS 169660]), Eq. (3), is the factor of $(d/2a)/\log(d/2a)$ in Equation 6-94. The expression in Equation 6-94 is explicitly used because the variable, a, is corrected as in Detournay et al. (2003 [DIRS 169660]), Eq. (4) for the presence of waste packages in the drift.

Equating q_{out} and q_{pipe} and solving for P yields the flow rate under the dual constraint of flow in the dike and flow in the drift (pipe-flow equation). After rearranging, placing this result in Equation 6-95 yields the equation for flow from the dike to the drift:

$$q_{pipe} = \frac{\pi a w^3}{3\mu d} \frac{d/2a}{\log(d/2a)} \rho g H \left[1 + \frac{8}{3} \frac{d/2a}{\log(d/2a)} \frac{a w^3 L}{d a^4} \right]^{-1} \quad \text{(Eq. 6-96)}$$

Defining a "scaling volume," V^*, as

$$V^* = \frac{a w^3}{3d} \frac{d/2a}{\log(d/2a)}, \quad \text{(Eq. 6-97)}$$

this equation simplifies to

$$. q_{pipe} = V^* \frac{\pi \rho g H}{\mu} \left(1 + 8 \frac{V^* L}{a^4} \right)^{-1} \quad \text{(Eq. 6-98)}$$

The time development of flow into the drift is solution to one of two differential equations described in the Mathematica Notebook contained in the output DTN: LA0408DA831811.001, where the flow into the drift is taken to be Equation 6-89 for $H \leq 2a$ and the minimum of Equations 6-92 and 6-98 for $H > 2a$.

6.4.7.1.3 Description of Input

The variables in Equations 6-89, 6-92 and 6-98 are the acceleration of gravity g, drift radius a (half the drift diameter), the filled drift length L, the distance between drifts d, the magma density ρ, and the magma viscosity μ. Most of the inputs are equivalent to the inputs described in Section 6.4.3 and are found in Table 4-1 and shown in Table 6-6. The calculations were done for a dike width calculated internally from the magma viscosity, the magma supply rate and the scaled relative density (which was taken from Table 6-3 to be 20.28 with $\kappa\rho_r = 1200$ kg/m^3). The parameters are equivalent to those used in Section 6.4.5.1 (Wide Aperture Case). The height of magma over the weir, H, in Equations 6-89 and 6-92 is internally generated in the analysis. For Equation 6-98, the filled drift length, L, is calculated internally as the cumulative discharge from prior flow divided by the cross-sectional area of the drift. In order to demonstrate the effects of deviations of magma viscosity and magma supply rate, calculations of magma flow have been done with two values of viscosity and two magma rise velocities, using values from Table 6-3 in Section 6.3.7.1. Sources for these parameters are found in Table 4-1.

6.4.7.1.4 Initial and Boundary Conditions

The initial condition consists of magma beneath the end of the drift at the height of the invert. The magma is moving upward at the chosen magma far field velocity. The drift is a horizontal tube, the diameter of which is four times the hydraulic radius; the drift is initially empty (except for the decreased hydraulic radius in obstructed cases).

All surfaces except the magma-free surface, if any, are rigid, and the equations are based on a no-slip boundary.

6.4.7.1.5 Results

Eight cases have been evaluated for the expected flow of magma into drifts. The eight cases cover variations in magma far field velocity, magma bulk viscosity, and whether the drifts are empty or filled with waste packages. These cases are listed in Table 6-7. Note that the second case in this table corresponds to the wide aperture case in Section 6.4.5.

Table 6-7. Cases Evaluated for Effusive Magma Flow Into Drift

Magma Viscosity (Pa·s)	Waste Package Radius (m)	Magma Rise velocity (m/s)
40	0	1
10	0	1
40	1	1
10	1	1
40	0	10
10	0	10
40	1	10
10	1	10

The results are presented in Figures 6-50 through 6-52, showing, respectively, the discharge rate out of the dike as a function of time, the length of drift filled as a function of time, and the height that magma rises above the drift invert.

Looking at Figure 6-50, this analysis predicts that for the case ($v = 1$ m/s, $\mu = 10$ Pa·s, empty drift), which corresponds to the wide aperture case in Section 6.4.5, that steady state is reached in about 8 s. Figure 6-52 shows that the magma will not rise more than 3 m above the drift. This is to be compared with the results from the previous analysis: steady state not achieved before the drift is filled, 900 s after magma reaches the drift, and a magma rise of about 80 m. The alternative analytical analysis is biased toward large flows because it only considers viscous drag in the dike after the pipe-flow condition occurs. It is presumed that better agreement between the models would be obtained if viscous forces in the dike were coupled to the wier equations (see Equations 6-89 and 6-92 in this report).

6.4.7.2 Alternative Analysis of Pyroclastic Flow

Pyroclastic flow from a dike into a drift is a complex problem beyond the current state of the art. A paper by Woods et al. (2002 [DIRS 163662]) provided a valuable first step. Their analysis is first summarized in Section 6.4.7.2.1. This is followed by a discussion in Section 6.4.7.2.2 that leads to the conclusion that assumptions associated with this alternative model are too unrealistic for evaluation of the expected consequences associated with an unlikely intrusive event.

6.4.7.2.1 Alternative Analysis for Pyroclastic Flow Into the Drift

Woods et al (2002 [DIRS 163662]) assume that the magma consists of liquid and vapor fractions that are fully coupled, meaning that they are constrained to move at exactly the same velocities and that they are at the same pressures and temperature. They also assume that the vapor is always at equilibrium with the liquid—that is, that vapor exsolves (or dissolves) from the liquid instantaneously in response to pressure changes. They then solve the hydrodynamic equations in a quasi-one-dimensional form in which the flow in both the dike and the drift is treated as being in the same direction, but the cross-section of the flow varies along the flow direction, as does the amplitude of the gravity vector.

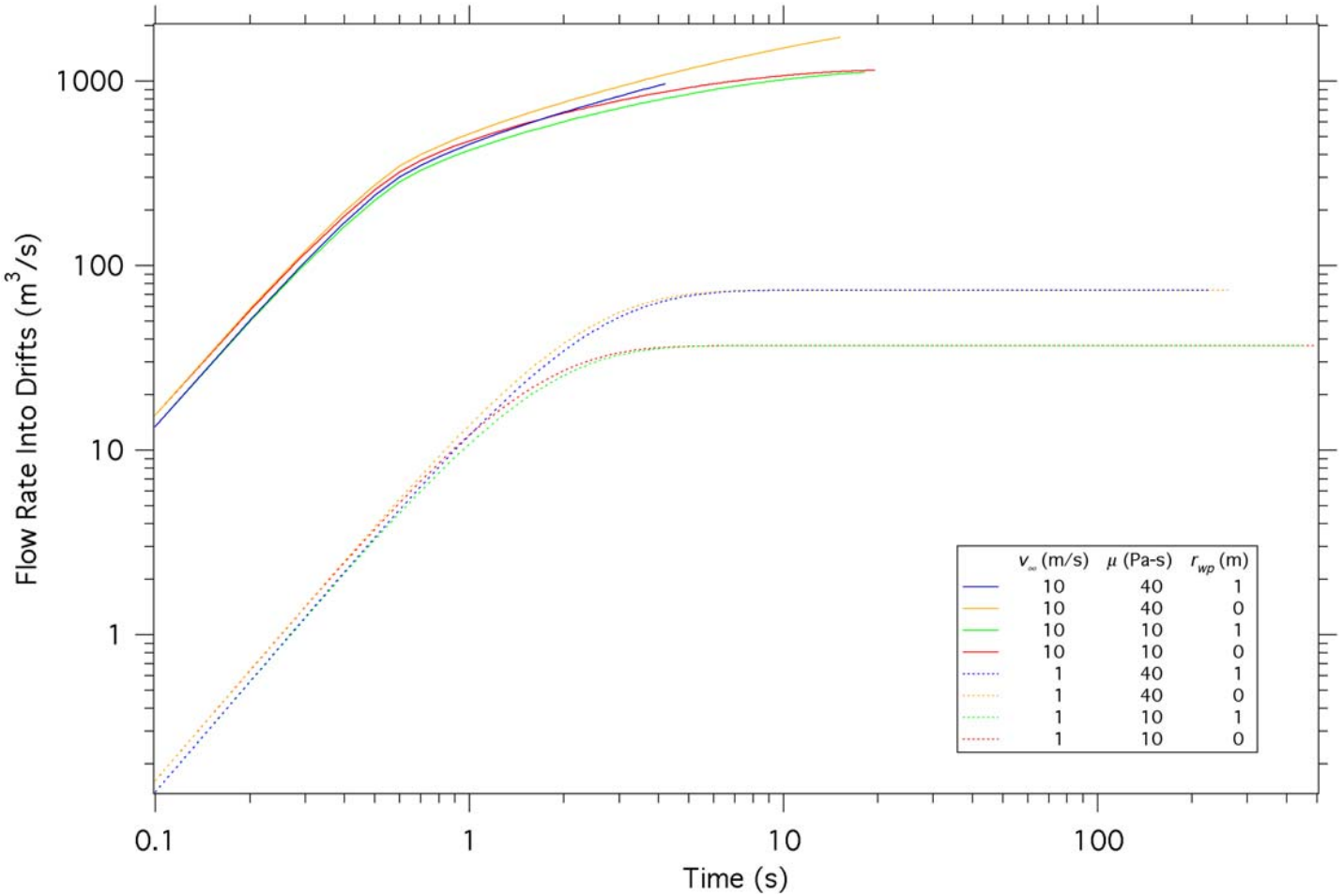

Output DTN: LA0408DA831811.001.

Source: Output Data Plots.

Figure 6-50. Discharge Rate for Effusive Magma Flowing Into Drifts as a Function of Time

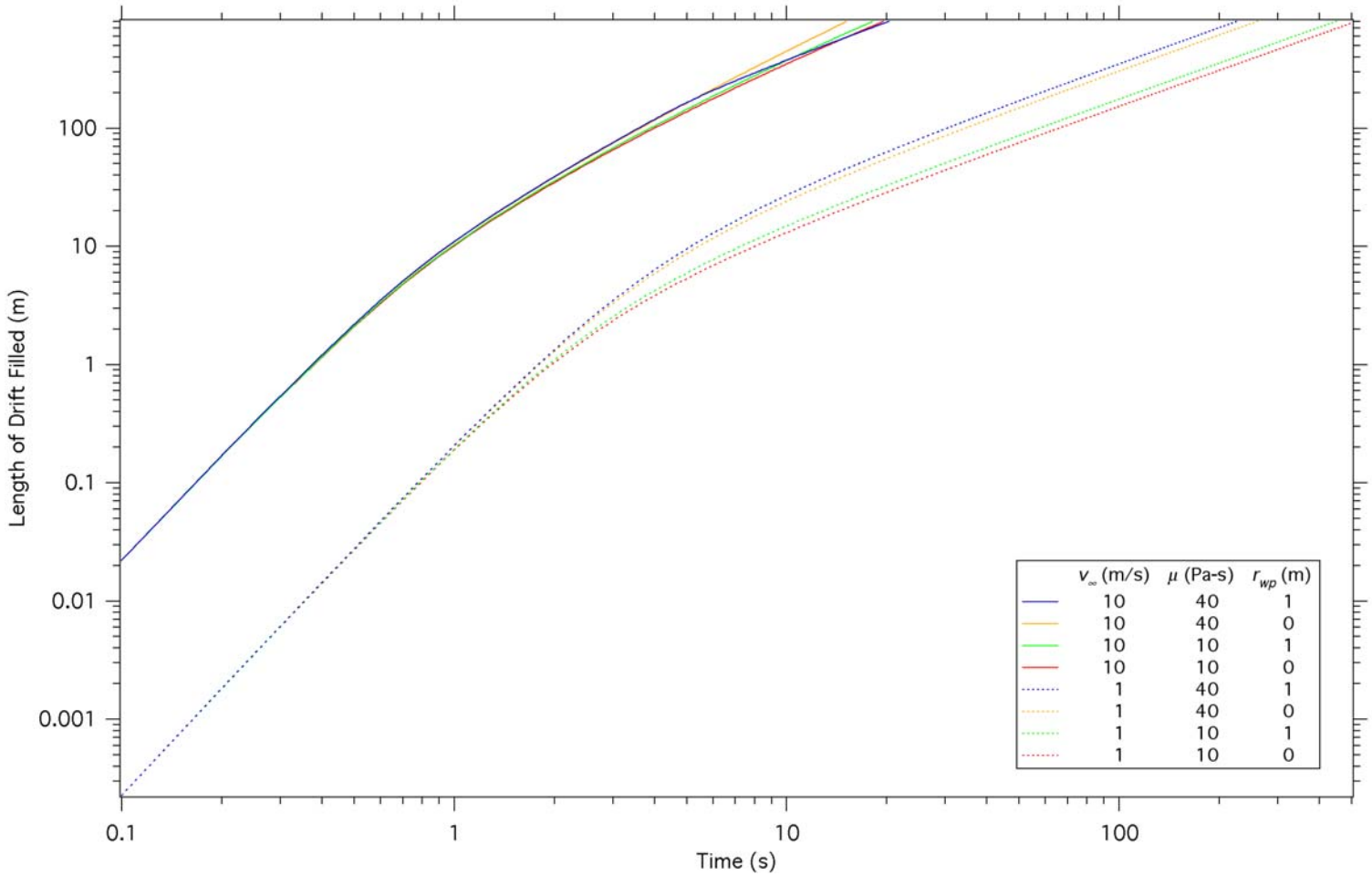

Output DTN: LA0408DA831811.001.

Source: Output Data Plots.

Figure 6-51. Length of Drift Filled by Effusive Magma Flowing Into Drifts as a Function of Time

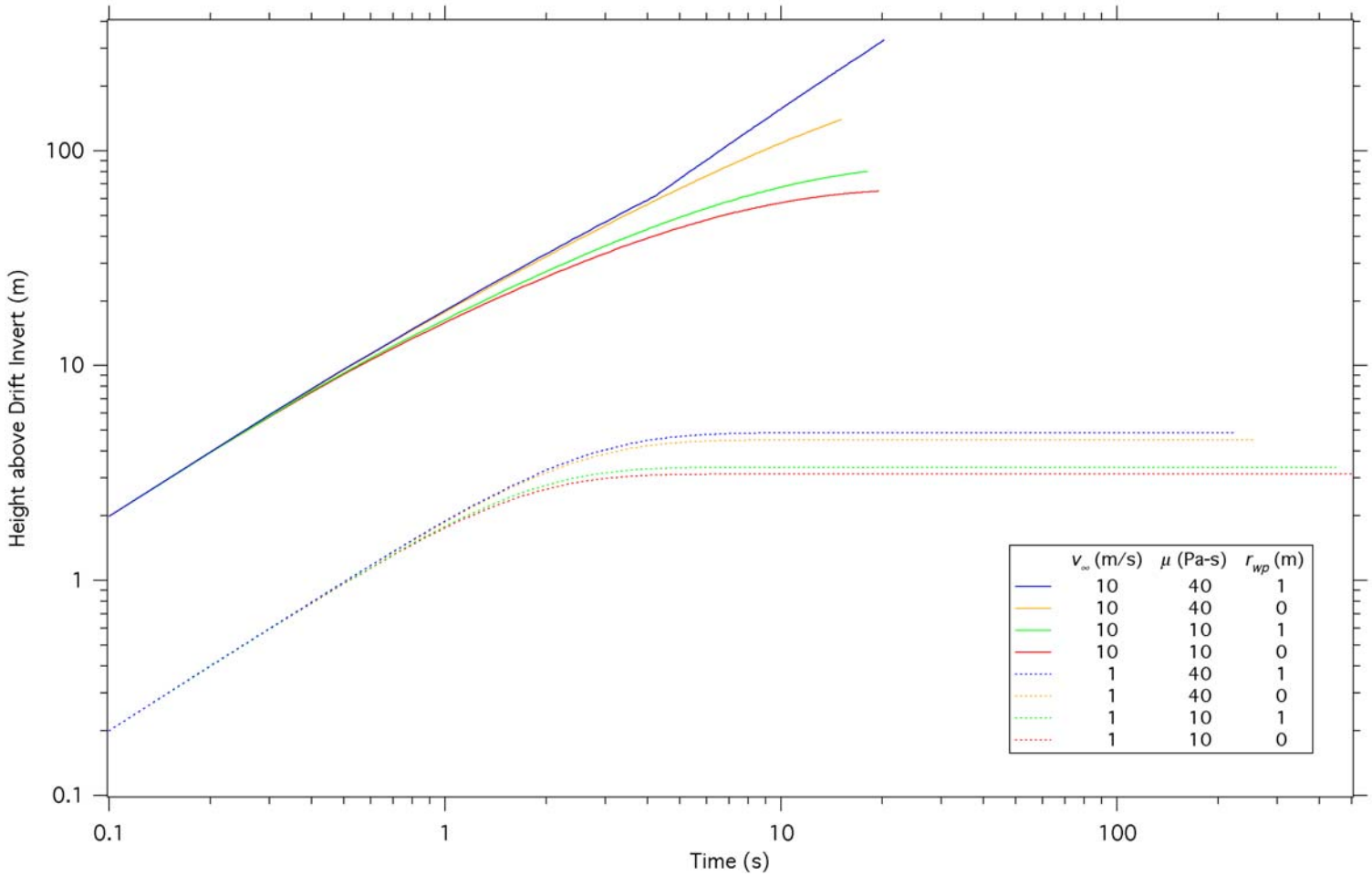

Output DTN: LA0408DA831811.001.

Source: Output Data Plots.

Figure 6-52. Height of Magma in Dike Above Invert for Effusive Magma Flowing Into Drifts as a Function of Time

The cross-sectional area in the vicinity of the dike-drift intersection is modified to provide some constriction to represent the change in direction of the flow and the restricted area where the two separate volumes intersect. The equations used do not solve for any motions transverse to the direction of flow, and as such, the model is *not* 2-D. The boundaries of the drift and dike are treated as impermeable and rigid. The initial condition is that magma at high pressure fills the dike portion of the model and air at atmospheric pressure fills the remainder of the computational volume. This condition results in a model that is mathematically quite tractable.

The Woods et al. (2002 [DIRS 163662], pp. 19-2 to 19-3) model results in a wall of magma accelerating into the drift at speeds reaching

> …tens to hundreds of meters per second, with the density decreasing as the pressure falls. Air is displaced and compressed ahead of the magma-volatile mixture and, as a result, a shock forms in the air and moves down the drift at speeds of several hundred meters per second. …on reaching the end of the drift, the shock is reflected and its amplitude increases by an order of magnitude. The shock then propagates back upstream, moving into the magma-volatile mixture and back towards the dike at speeds of 20–30 m/s. As the shock moves through the magma-volatile mixture, the mixture is recompressed. A region of higher pressure, of order several MPa, and hence higher density, develops between the end of the drift and the shock… The calculations suggest that, if the dike intersects the drift 200–300 m from the end of a closed drift, then the pressure within this drift will build up to about the initial level in the dike in a time of order 10 s.

6.4.7.2.2 Discussion of Alternative Analysis of Pyroclastic Flow into a Drift

The Igneous Consequences Peer Review Panel considered the Woods et al. (2002 [DIRS 163662]) analysis not to be credible (Detournay et al (2003 [DIRS 169660], Section 3.3.2.1, pp. 50-51).

In developing their model, Woods et al. (2002 [DIRS 163662]) made many approximations and assumptions in order to reach a result. Some of these affect the credibility of that result. By reducing the dimensionality from the fully 3-D nature of the real case, that model reduced the problem to one that is mathematically tractable enough that numerous specific scenarios can be addressed. However, as described by Detournay et al. (2003 [DIRS 169660], Section 3.3.2.1, pp. 50-51), the initial and boundary conditions in the Woods et al. (2002 [DIRS 163662]) model are unrealistic. In particular, the initial condition is not physically realizable; the combination of a discontinuity in pressure between the magma and the air in the drift with the stationary state of those two materials is unstable and is a state that cannot be reached by any combination of events. This leads to results that are not achievable in nature. As described in Section 6.3.8.2, magma does not fill the propagating crack completely, nor does the crack reach its full width immediately after opening. Rather, there will be a vapor-filled tip, which is expected to be on the order of tens to hundreds of meters long. Near the tip, this crack will be only millimeters wide. Even if the magma were to fill the crack nearly to the tip, the cross-sectional area of the intersection would be only a fraction of a square meter in this early phase, rather than the ~5.5 m^2 assumed by the Woods et al. (2002 [DIRS 163662]) model. This cross-section would

gradually increase as the crack propagated beyond the repository, a process that could take seconds to minutes.

Although the evolution of the cross-section is difficult to predict in detail, its rate of growth can be estimated from results of Section 6.3.7.1. If the velocity of the tip is twice that of the magma front near the surface, and the tip cavity is 100-m long, the area growth rate will be on the order of: (drift diameter)•(dike width at drift – dike width at tip)/[(cavity length)/(velocity of tip)] = (5.5 m)•(1 m – 0 m)/[(100 m)/(2 m/s)] = 0.11 m^2/s. To convert this value to a time derivative of the volume flow rate, one multiplies by the velocity of the magma, yielding 0.22 m^3/s^2. Even this rate is too large based on the analysis of Section 6.4.5, where Figure 6-39 indicates initial derivatives of 0.055 m^3/s^2 for a dike width of 0.45 m, and Figure 6-44 indicates a derivative of 0.028 m^3/s^2 for the narrow aperture case.

With such an opening rate, almost 50 s would elapse before the full drift cross-section of 5.5 m^2 is exposed. However, this estimate is also inappropriate because the magma will not extend into the narrow parts of the tip cavity. This result is better understood as the rate at which the connection opens between the atmosphere in the drifts and the volcanic vapors in the tip cavity. Nevertheless, the area of magma exposed to the drift cannot increase more rapidly than the magma's upward velocity multiplied by the diameter of the drift. For effusive magma, this rate would be approximately 5 m^2/s; for a pyroclastic flow rising at 100 m/s, this rate might be as high as 500 m^2/s. The former rate is unlikely to produce any shock waves in the drift; loading at the latter rate may require further investigation.

The model of Woods et al. (2002 [DIRS 163662]) assumes that the entire flow of the dike between two drifts (80.5 m for a dike intersecting perpendicular to a drift, greater for smaller angles) is diverted into the drift. Our analysis, illustrated in Figures 6-20, 6-22, 6-43, and 6-46 through 6-48, clearly shows that magma would continue to flow into the crack in the pillars between and above drifts while some of it is diverted into the drift. Thus, the amount of magma driving the flow in their model is much too large.

The assumption of rigid, impermeable boundaries in the Woods et al. (2002 [DIRS 163662]) model adds to the severity of the consequences of magma interaction with drifts. Air pressurized by the shock they describe would seep into the walls of the drift, reducing the pressure behind the shock and decreasing its amplitude as it propagated. An even larger effect is to be expected at the blocked end of the drift, where the shock will encounter backfill. The backfill is quite compressible and will not reflect an incident shock wave nearly as efficiently as the rigid wall assumed in the calculation. In addition, the edge of the backfill will not be a vertical wall, as required by the 1-D numerical model of Woods et al. (2002 [DIRS 163662]), but will lie at the angle of repose. The net result of these real-world situations will be to greatly reduce the amplitude of, or even eliminate, any shock that might develop.

Woods et al. (2002 [DIRS 163662]) have developed a model that ignores phase separation between the silicate liquid and the volatiles. Although the assumption of complete coupling may provide an adequate estimate of steady flow in such a mixture, it is precisely the response to dynamic events such as shocks and rapid decompression that is not well treated with this assumption. In situations with such high accelerations, the differences in density between the vapor and the silicate magma become important, and the phases will move at different speeds.

Only later, as viscous forces have had a chance to act, will the velocities approach each other. If these effects were included in the model, the result would be to reduce the sharpness of both compression and decompression waves and to increase dissipation of kinetic energy. Shock waves would be considerably dampened, if not eliminated altogether, when propagating through such mixtures, around backfill, and through drifts filled with rock rubble.

Woods et al. (2002 [DIRS 163662], p. 19-2) state that "the drift is assumed to be empty, and since the drift cross-sectional area is much larger than that of a 1.8-m diameter canister, $A(x)$ is taken to be the total drift cross-sectional area." Although it is true that the ratio of area of the drift (~23.8 m^2) to that of a canister (~2.5 m^2) is large, a more important comparison would be that of hydraulic radii, $R_h = A/P$, where A is the cross-sectional area and P is the perimeter (both exterior and interior) of the flow. The ratio of hydraulic radii is about 0.67, whereas the ratio of open areas is about 0.89. The smaller value will result in more drag and loss of energy in the flows than in the Woods et al. (2002 [DIRS 163662]) model. Furthermore, as mentioned in Section 5.2, rockfall caused by earlier seismic activity (for much of the post-closure period (BSC 2004 [DIRS 169183])) may partially or totally fill drifts, although the extent and timing of such filling cannot be predicted precisely.

In summary, the Woods et al. (2002 [DIRS 163662]) model of magma expansion into a drift overestimates the violence of the encounter. Realistic boundary conditions including compressible walls and backfill, permeable country rock and backfill, phase separation in the magma-volatile mixture, partial blockage of the drift by waste packages and other engineering features, backfill and rockfall, and the axial spacing of the packages would combine to greatly reduce the amplitude of any shock wave that might form in the initial encounter. More importantly, use of realistic initial conditions would preclude the formation of a shock wave for all but the most rapid magma ascent rates.

6.4.7.3 EPRI Analysis of Magma-Drift Interactions

The EPRI published an analysis of potential igneous processes at Yucca Mountain (EPRI 2004 [DIRS 171915]). Their analysis of magma-drift interaction provides a description of thermal effects in magma flowing in the drift. They note that surface temperatures of lava flows in Hawaii are as low as 450°C because "radiative cooling allows the surface temperature to drop several hundred degrees within minutes" (EPRI 2004 [DIRS 171915], Section 4.1.2, p. 4-4). They conclude, "These observations and analyses, predominantly reflecting conditions on the surface, are expected to be conservative compared to conditions in a drift. Flow into a drift is characterized by a higher surface area to volume ratio of the surroundings, which allows higher rates of heat loss than would be experienced at the ground surface. Consequently, in-drift heat losses from magma into waste packages and the surrounding rock would be higher than heat losses into the ground at the surface. Therefore, the same mass of magma would cool more quickly in a drift than on the surface" (EPRI 2004 [DIRS 171915], Section 4.1.2, p. 4-5). As the report notes, radiative cooling is a major contributor to the rapid cooling of lava surfaces. However, radiative cooling will be inhibited in an underground environment where the surrounding solid surface (the back of the drift) will heat up quickly. In addition, convective cooling due to movement of air will be less efficient in a 5.5-m diameter drift than in the open atmosphere.

6.4.8 Magma Interactions with Waste Packages and Waste Forms

Basaltic magma that may come in contact with waste package materials undoubtedly has the ability to modify their physical and chemical properties, but it is very difficult to predict, with confidence, the resulting effects. However, all such effects are expected to be deleterious to the integrity of waste packages and waste forms.

The physical and chemical environment of waste package and waste form materials in contact with active magma will include temperatures in excess of 1100ºC cooling to below 700ºC over about 50 to 100 days (Figure 6-99), abundant steam and other potentially corrosive or reactive volatiles including SO_2 and HCl, and, possibly, HF (BSC 2004 [DIRS 169980], Table 6-3). In addition, the magma will be flowing at least during the initial emplacement phase of the magmatic activity.

6.4.8.1 Degradation of Waste Packages

Analyses completed and presented in Sections 6.7 support the premise that the igneous intrusion would impact the integrity of the drip shields, waste packages, and cladding in the dike intersected emplacement drifts ineffective, i.e., the waste package and associated components would no longer provide protection. The temperature of the intruding magma may approach 1200ºC (BSC 2004 [DIRS 169980], Table 6-4). Although the melting temperatures of Alloy C-22 (1357ºC) and 316NG Stainless Steel (1375ºC) (CRWMS M&O 1999, Section 5.1 [DIRS 121300]) are above the magma temperature, the metals would likely lose their tensile strength and deform plastically at magmatic temperatures. Corrosion would also be enhanced.

Findings of a literature review on the performance of material similar to alloy 22 waste package and drip shield materials in magmatic environments (Gordon 2003 [DIRS 163357], Section 5), suggest that the structural integrity of these materials would be compromised. For example, Types 310 and 446 stainless steels, exposed to Hawaiian basaltic lava at 1300°C and 2 psi (15 kPa) for 100 hours, underwent extensive reaction, while alloy 718 suffered a loss of structural integrity. During the course of magma cooling, waste packages and canisters or assemblies may be subject to corrosion, the degree of which may vary depending on their composition, magma contact temperature, and in situ geochemical environment. Magma temperatures, pressures, and geochemical environment in the drift, influenced by the magma composition and volume of exsolving volatile gases, such as H_2O, H_2, CO_2, CO, SO_2, S_2, HCl, HF, and H_2S may have a significant impact on corrosion rates. Literature review findings related to oxidation, sulfidation and corrosion behavior and rates of Alloy 22 waste package materials, drip shield titanium alloy, and similar alloys in magmatic environments shed light on the potential degree of corrosion (Gordon 2003 [DIRS 163357], Section 2).

One study of binary and ternary alloys containing various amounts of molybdenum and chromium and exposed to basaltic magma at 1150°C for periods of 24 and 96 hours shows that the formation of secondary phases and oxidation or sulfidation of metals is extremely dependent on metal composition (Ehrlich and Douglass 1982 [DIRS 101097] and Douglass 1983 [DIRS 166999]). For a nickel alloy with 20 percent Cr and 10 percent Mo, a maximum corrosion (oxidation) rate of about 7 mm/year was obtained as estimated from metallography reported by Ehrlich and Douglass (1982 [DIRS 101097]). Another finding, from a qualitative

study of various alloys in contact with Hawaiian basalt lava, indicates that Types 310 and 446 stainless steel reacted extensively with the degassed lava while Udimet 700 and Alloy 718 suffered a loss of structural integrity (Gordon 2003 [DIRS 163357], Section 5). Findings from another study, conducted at 727°C for 96 hours, indicate that under a reducing atmosphere of 1.5 percent H_2S and 98.5 percent H_2, the corrosion is significantly higher than in an oxidizing-sulfidizing environment with 59 percent Ar, 3 percent O_2, 36.5 percent H_2, and 1.5 percent H_2S (Gordon 2003 [DIRS 163357], Section 2). All of these corroborative findings suggest that metals embedded in the cooling basalt magma would be subjected to various degrees of corrosion.

Analyses of pressure that would develop within waste packages as the result of gas expansion at high temperatures have been conducted (CRWMS M&O 1999 [DIRS 121300]). The results indicate that as the internal temperatures near the magmatic temperature, the resulting stresses on the packages would approach the tensile strength of the package materials, but that package would not fail. However, if a package were corroded or otherwise weakened it would have a lower tensile strength that could be exceeded by the internal pressure. This would provide a possible mechanism for package breaching.

Based on the information provided on the performance of waste package materials under high temperatures and high internal pressures the following interpretations are made regarding the expected performance of waste packages engulfed in magma at initial temperatures approaching 1200°C. At this temperature, the waste packages and their internals will quickly heat to near magma temperatures. This will produce high pressures within the waste packages. The non-corroded waste packages will not rupture from the internal pressures; however, the heat and external load of the magma will cause the waste packages to loose strength and deform plastically, collapsing onto their internal components. Some form of breaching may occur and the cladding is likely to fail.

Cracks are expected to be very narrow and tight due to constraints of surrounding magma. It is expected that the width of any crack opening on the outer surface may be on the order of several millimeters; however, the range may be from 0.1 mm to 10-mm wide, extending a meter or more. The cracks are considered to penetrate the 70-mm thick shells (20 mm alloy 22 and 50 mm stainless steel). Analyses of magma flow through such cracks is complicated by heat exchange between the host material and the magma and the sensitivity of magma viscosity to temperature (Section 6.4.5). In the absence of a complete analysis with temperature dependent viscosity and heat flow, and expected crack opening dimensions, rough estimates of the quantity of magma that can penetrate a waste package have been developed to bound the problem.

When magma contacts a waste package it will first cool and then re-heat as heat flows into the waste package from the surrounding magma. As a result, a single temperature is not appropriate for estimating the viscosity of the magma. At 1025°C, the magma viscosity, from Equation 6-110, is 890 Pa·s for magma with a liquidus temperature of 1106°C; at 975°C, it is 24,000 Pa·s. Using Equation 6-6, with dP = 1 MPa (50 m of head due to magma rising above the drift in a dike) and dz = 70 mm, a 1-m long crack 1-mm wide would allow 15 kg of magma to enter a waste package during 1000 s at 1050°C; at 975°C, less than 0.15 kg would penetrate. For a crack 3-mm wide, these values would increase by a factor of 27.

Even if magma were to penetrate a waste package, the magma outside of the waste package is expected to stagnate once the drift has filled (on the order of 1000 s) so that there are not likely to be driving forces that would result in flow through a waste package. Magma is likely to fill the drifts before the waste packages heat up to a point of failure. In view of these results, it is safe to conclude that, in the absence of major cracking of waste packages, significant amounts of magma will not flow into or through waste packages, and that the waste forms will remain in place.

6.4.8.2 Movement of Waste Packages by Magma

The possibility that magma movement can carry waste packages to the surface, either through drifts or along a drift into an erupting conduit, has been analyzed.

Movement through drifts to the surface as suggested by Woods et al (2002 [DIRS 163662]) is precluded by the planned use of backfill in access drifts. Although the backfill will not completely fill the drift, a gap of 0.5 to 1.0 m is expected at the crown, the backfill will still block movement of an intact waste package, however deformed it may become.

The velocity of magma required to move a waste package can be estimated from the density and dimensions of the waste packages and the density of the magma. The range of waste package density is from 2940 kg/m^3 to 4280 kg/m^3 (BSC 2004 [DIRS 170001]). If the magma is completely degassed, its density (ρ_m) will be 2663 kg/m^3 (BSC 2004 [DIRS 169980], Table 6-4). Although the dimensions of the waste packages vary, an approximate calculation of buoyant, viscous, and dynamic forces indicates that movement of waste packages in magma will not be facilitated. A 5-m long waste package with a diameter of 1.5 m (volume = V_{WP} = 8.9 m^3) with a bulk density (ρ_{WP}) of 2940 kg/m^3 will be subject to a net downward buoyant force of 24 kN [=($\rho_{WP} - \rho_m$) * g * V_{WP}]; for a density of 4280 kg/m^3, the force will be 140 kN. For lower magma densities, these forces will be correspondingly larger. Viscous forces on the waste package can be estimated from the magma viscosity (μ), the area of the package (A_{WP}) subject to drag, and the distance normal to that surface (dr) across which the velocity increases (dv_m) to the free-field velocity ($F_{visc} = A_{WP}\mu(dv_m/dr)$). A waste package 5-m long and 1.5-m in diameter has a cylindrical surface of 24 m^2; if the velocity increases to a free-field value of 1 m/s over 1 m radially from the package, the viscous drag will amount to only 2.4 kN for a magma viscosity of 100 Pa·s. The dynamic pressure ($P_{dyn} = \rho_m v_m^2$) of moving magma with density ρ_m impacting on the end of a waste package at 1 m/s would be similar to the viscous drag on the cylindrical surface. Even the combined force almost certainly would be too small to mobilize a package subject to a downward load of 24 to 140 kN.

Both the viscous forces and the dynamic pressure increase with magma velocity, and a magma velocity of 1 m/s is considered to be the speed of rising magma below the exsolution depth, which is on the order of a kilometer (BSC 2004 [DIRS 169980]). Any increase in magma velocity will be accompanied by expansion of the magma. In the simplest model of magma expansion in a dike or conduit of fixed area, mass flux is conserved so that an increase in velocity from 1 m/s to 5 m/s, for example, would coincide with a drop in density by the same factor. Thus, a velocity of 5 m/s would be associated with a magma density of only about 500 kg/m^3. Such a medium moving at 5 m/s would exert a dynamic force on the end of a waste package of 22 kN; but it is difficult to envision a scenario in which the end of a package could be

impacted by magma to move the package toward a dike or conduit. Viscous drag also depends on the velocity of the magma, but it is not possible to predict accurately what the viscosity of magma with a density of 500 kg/m^3 would be. Such a magma would be fragmented (BSC 2004 [DIRS 169980]), meaning that the continuous phase would be vapor rather than silicate liquid. The viscosity of the fragmented magma would probably be very low relative to the pure liquid. Counteracting the effect of increased velocity will be an increase in downward gravitational force due to lower buoyancy in the less dense magma. Unsupported gravitational forces on packages in magma of 500 kg/m^3 will be between 211 kN and 330 kN. Hence, it can be concluded that viscous drag will not be able to move intact waste packages in drifts as the magma expands. Magma of density 500 kg/m^3 would have to move faster than 15 to 20 m/s in order to lift waste packages in a conduit.

6.4.8.3 Effect on Waste Forms

Very little work has been conducted relevant to the ability of direct contact with magma to modify the physical and chemical properties of waste forms, making it impossible to predict their behavior in the event the entry of basaltic magma into repository drifts. As a result, a limited discussion regarding the kinds of expected behaviors is presented below.

The spent commercial fuel rods are composed of UO_2, a ceramic with a high melting temperature, ranging from approximately 2600°C (Todreas and Kazimi 1990 [DIRS 107735], p. 307 for light water reactor fuels) to 2800°C (Lide 2002 [DIRS 160832], p. 4-92 for UO_2).

Therefore, commercial spent nuclear fuel exposed to magma will not melt directly at magmatic temperatures [up to ~1169°C] (BSC 2004 [DIRS 169980], Table 7-1). However, when waste canisters/assemblies and fuel claddings are damaged, the fuel pellets/rods may be assimilated into cooling basalt magma. Under this scenario, three types of processes may alter spent fuel rods: chemical interaction between the waste forms and the metal of waste canisters/assemblies and cladding, chemical interaction between waste forms and the magma, and physical changes to the waste form.

Chemical interactions may also occur between cladding and spent fuel. Hofmann and Kerwin-Peck (1984 [DIRS 164038]) conducted experiments between UO_2 and Zircaloy-4 under isothermal and transient temperatures of 1000 to 1700°C and at 1 to 80 bars for a duration of 1-150 minutes. They showed that under reducing conditions, oxygen from UO_2 is transported to the Zircaloy via the gas phase, and as a result, uranium metal is formed. Uranium then diffuses to react with zirconium to form a layer of U-Zr alloy at about 800°C – 1150°C. Subsequently, several other solid solution layers of interactive U-Zr and Zr-oxides are formed at lower temperatures. However, there is considerable uncertainty relative to the work of Hofmann and Kerwin-Peck (1984 [DIRS 164038]) and the range of oxygen fugacities that will obtain during an intrusive scenario.

The presence of magmatic gases can also affect Zircaloy cladding in a relatively short time, the gases contact the cladding at temperatures near 1,100°C. Kinetic corrosion rate calculations suggest that Zircaloy cladding can be significantly damaged by corrosion in a matter of days in the presence of water vapor at temperatures between 250°C to 360°C (Hillner et al. 1998 [DIRS 100455]). Also, Fe-Zr and Ni-Zr liquid eutectics begin to form at about 940°C and would

likely lead to failure of the fuel cladding if the temperature were to increase above about 940°C (Haskin et al. 2002 [DIRS 171570], Figure 3.1-4).

In addition, radionuclides in the waste could be incorporated into crystallizing silicate mineral phases, or form higher oxide phases. The thermodynamic stability of secondary phases likely to form in cooling basalt is poorly known and it is difficult to predict which phases, if any, might form. Fission products (cesium, technetium, etc.) may also be incorporated into new mineral phases, with the size and charge of fission-product ions exerting primary control as to the resulting minerals that might contain them. Some fission products (e.g., cesium and strontium) may also be volatilized by the high temperatures. Thus, there is great uncertainty as to which phases and minerals are likely to accommodate the suite of radionuclides in spent-fuel and glass waste forms.

As temperatures decrease after initial emplacement and under oxidizing conditions, uranium oxide is expected to fragment, which increases the surface area of the waste (BSC 2004 [DIRS 169987], Section 6.2.2). This fragmentation will greatly increase its surface area, making it more susceptible to transport under nominal conditions. Oxidation of UO_2 fuel in the presence of water-rich volatiles exsolving from cooling basalt magma may also occur (Einziger et al. 1991 [DIRS 166177]).

A significant fraction of waste packages within the repository will contain radionuclides in a glass matrix. If glass waste is contained within waste packages, glass would be expected to re-melt and re-solidify as the drift cooled. The slow cooling would be expected to result in a smaller amount of cracking relative to cooling at higher rates and, therefore, a lower release rate (although no credit is taken for this phenomenon). The extent of devitrification will depend on the composition of the glass, temperature, and cooling rate. Borosilicate high-level radioactive waste glasses are currently formulated to avoid formation of phases, such as nepheline ($NaAlSiO_4$), because they lead to a composition change in the glass. Likewise, glass additives are controlled to avoid both the formation of soluble inclusion phases, such as lithium metasilicate (Li_2SiO_3), and glass/glass phase separation.

Less certain, however, are possible interactions between exposed and partially degraded glass waste and basalt magma. Given the low melting temperature of glass waste and the large difference in composition between glass waste and basalt magma, some reaction between them is inevitable. One might speculate that the interaction might result in the rimming of olivine crystals with pyroxene, or the crystallization of pyroxene rather than olivine in regions of the cooling drift that are rich in glass. Much like spent fuel, however, there remains considerable uncertainty as to the exact nature of materials that may form via glass—magma interactions.

In summary, although the range of possible secondary mineral phases that may form cannot presently be constrained, they are nonetheless expected to comprise silicate and oxide minerals, rather than salts. As oxide and silicate minerals tend to have slow dissolution rates compared to salts, significantly enhanced dissolution rates of minerals due to reaction of waste with basalt magma within drifts is not anticipated.

6.4.8.4 EPRI Analysis of Magma-Waste Interaction

The Electric Power Research Institute recently published an analysis of potential igneous processes at Yucca Mountain (EPRI 2004 [DIRS 171915]). Their analysis of interaction between magma and waste packages (EPRI 2004 [DIRS 171915], Section 5) and waste forms (EPRI (2004 [DIRS 171915], Section 6) is extensive. The following paragraphs summarize their findings and provide commentary on their relation to this report.

A most dramatic analysis is presented wherein a 4-m diameter by 5-m long cylinder of magma moving vertically parallel to its axis at 100 m/s impacts a horizontal 21-PWR waste package at mid-length (EPRI 2004 [DIRS 171915], Section 5.2). The waste package is modeled in considerable 3-D detail including:

- The outer and inner shells
- Outer, middle, and inner top lids
- Spreader ring and spacer rings
- Top and bottom trunion rings
- Inner and outer bottom lids
- Inner vessel structural guides
- Fuel basket assembly
- Fuel tubes and fuel assemblies (EPRI 2004 [DIRS 171915], Section 5.2.2.1) with elastic-plastic models for four different materials (EPRI 2004 [DIRS 171915], Section 5.2.2.2).

The magma has a density of 2600 kg/m^3 with very small tensile and shear strength (EPRI 2004 [DIRS 171915], Section 5.2.2.3). The initial condition has an internal gas pressure of 150 kPa. After an initial transient lasting approximately 10 ms, the waste package moves upward at 35-40 m/s, with its lower side dented inward by a third to a half of a meter, the dent encompassing the entire length and the lower half of the circumference. This deformation is sufficient to cause very great damage to the structural guides, the fuel basket assembly, and the fuel assemblies (EPRI 2004 [DIRS 171915], Section 5.2.3). However, there was no tearing of the inner structural shell, and the integrity of both end closures and of the package as a whole was maintained during the 30 ms of the simulation. They also note that, "Under the extreme magma conditions assumed for the analysis, the waste package will likely sustain a secondary impact with the roof of the chamber at an impact velocity of about 120 fps (36.6 m/s). This is equivalent to a drop from 224 feet (68 m), which is seen as extremely conservative compared to conditions in the drift." The EPRI report concludes by noting that, "The force applied to the waste package in this analysis was far in excess of the expected range of force that might be experienced by an actual waste package inside the repository drift. Despite the large conservatism of the analysis, the waste package survived without loss of containment

capability.… EPRI's position is that the analyses reported in this section eliminate mechanical impact of magma on a waste package within the repository drift during a volcanic event as a credible failure mechanism for waste packages at Yucca Mountain," (EPRI 2004 [DIRS 171915], Section 5.2.4).

This analysis applies a conservatively large load to the waste package. If the magma velocity were as high as 100 m/s, it is unlikely that the density of magma averaged over the dike cross section would attain even half that value (Section 6.4.8.2).

EPRI also considered erosive effects of flowing magma. They state that, "Mechanical erosion of the waste package could occur if the hardness of the solid material entrained in the flowing magma exceeds that of Alloy 22. No suitable data were found to judge the possibility of waste package erosion by flowing magma," (EPRI 2004 [DIRS 171915], Section 5.3). Regarding erosion-corrosion they state, "At elevated temperatures, Alloy 22 is protected from corrosion by an oxide (or sulfide) scale. An estimate of the maximum rate of erosion-corrosion can be obtained by assuming that erosion of the surface prevents the formation of a stable scale. Short-term corrosion rates of Ni-based alloys in molten magma and glasses are of the order of 10's of μm/day over the temperature range 1000-1200ºC. The extent of erosion-corrosion of the waste package during the eruption would amount to a maximum of 0.4-2.0 mm. Therefore, waste package failure due to erosion-corrosion by flowing magma is highly unlikely," (EPRI 2004, Section 5.3).

The EPRI report analyses the effects of internal pressurization during the thermal transient due to intrusion (EPRI 2004, Section 5.4). Addressing "pinhole" rupture due to overpressurization, they calculate that internal pressures after magma has engulfed a waste package will be compressive until the magma has solidified, thereafter increasing to approximately 0.45 MPa and then slowly declining to just over 0.3 MPa in 200 days. As a result, the maximum hoop stresses will be 19 MPa, whereas the 0.2 percent offset strength of Alloy 22 under those conditions will be at least 50 MPa. They conclude, "It is unlikely that the waste package shell will plastically deform, let alone undergo ductile failure, during the thermal transient. This conclusion applies equally to the weld material as to the outer shell of the waste package" (EPRI 2004 [DIRS 171915], Section 5.4.1). Creep rupture of the shell is considered "unlikely because geometrical constraints [from the solidified magma surrounding the waste package] limit the amount of strain" (EPRI 2004 [DIRS 171915], Section 5.4.2). The differences between these findings and those of Section 6.4.8.1 are the result of the EPRI analysts employing different inputs than are used in this model report.

The EPRI report also addresses corrosion of waste packages by magma (EPRI 2004 [DIRS 171915], Section 5.5). They present results of new experiments with remelted Hawaiian basalt and Alloy 22 (EPRI 2004 [DIRS 171915], Section 5.5.1). Their results were similar to those applied in Section 6.4.8.1. The EPRI analysis uses a magma composition without corrosive gases such as H_2S, SO_2, or HCl to attack Alloy 22. The EPRI analysis also included a probabilistic calculation of waste package corrosion with a range of activation energies (0, 40, 100 kJ/mole) and a range of temperature ranges over which corrosion occurred. They found that the maximum corrosion depth was 5.26 mm and occurred when corrosion continued down to temperatures as low as 800ºC (EPRI 2004 [DIRS 171915], Section 5.5.2). The differences in

EPRI results compared to those of Section 6.4.8.1 can likely be attributed to the absence of reactive gases, sulfur species, and halides.

6.4.8.5 Conclusion

The heat and oxidizing environment of the intrusion are expected to cause extensive fragmentation of oxide wastes. Glassy wastes are not expected to be substantially changed by an intrusion. Little is known about chemical reactions that might occur between basalt and waste forms, so reactivities of chemically unaltered waste are used in assessing reactions with seepage water.

Because of the high temperatures at which basalt magma and waste forms will interact, it is unlikely that the immediately resulting reaction products will grossly enhance dissolution rates of waste material. However, this conclusion should be considered in the light of the enormous uncertainty that exists.

Before considering these conclusions, however, it is important to remember that limited time will be available for interaction between magma, waste forms, and waste package materials. As demonstrated in Section 6.7 and Appendix D of this report, temperatures at the centerline of the drift will have relaxed to below solidus temperatures in ~60 days, and reaction rates typically decline in an exponential fashion with decreasing temperature.

6.4.9 Summary

This analysis describes how rapidly magma will flow from a dike into an intersecting drift and how far above a drift magma can rise while also still flowing into the drift.

The rate of magma flow into drifts will be limited by the rate of magma supply, except probably when the supply is very large (v_∞ on the order to 10 m/s) and the magma viscosity is high (on the order of 40 Pa·s). The time needed to fill 500 m of drift will be on the order of 15 minutes for a magma velocity of 1 m/s. It obviously depends on the supply rate, and the results can be linearly scaled to other drift lengths.

The presence of the drift will have an impact on the rise of the magma inside the dike. In fact, the magma front may stop rising, and a steady state flow into the drift (total magma flow inside the dike diverted into the drift) may be reached before it is completely filled. However, the magma will rise several tens of meters above the drift before if fully invades it. Pressures in the drift will be minimal (a few kilopascals) while the magma is invading it.

Uncertainty exists in the magmatic effects on waste package integrity. Flow of magma into drifts is likely to result in plastic deformation of waste packages, but it is unlikely to result in movement of waste packages over large distances. Exposure of packages to the high temperatures and corrosive gases of the magmatic environment is expected to enhance corrosion. Commercial spent fuel is expected to become comminuted due to oxidation. Other chemical effects are difficult to predict. Glassy waste forms are not expected to be significantly altered by encounter with magma. On balance, it would be proper to adopt the conservative position that all waste packages and associated drip shields that come in contact with basalt magma immediately fail.

6.5 ANALYSIS OF SECONDARY DIKE PROPAGATION

This Section contains analyses intended to evaluate a portion of FEP 1.2.04.03.0A, Igneous intrusion into repository. Woods et al. (2002 [DIRS 163662]) described a drift filling and a secondary dike opening to the surface at some distance from the original dike, with the magma flow being diverted through the drift and carrying the entire drift contents to the surface. This is commonly called the "Dog-Leg" scenario. Two distinct situations are analyzed. Secondary dike propagation, for the case of effusive magma flow, in which the magma is similar to that considered in Section 6.4, is analyzed in Section 6.5.1. Section 6.5.2 then presents an analysis for the unlikely case of hydrovolcanic magma flow, in which a small volume of water is rapidly mixed with an effusive magma to generate a volume of high-pressure steam mixed with fragments of magma. This mixture has a lower density and much lower viscosity that the original effusive magma. The precise scenario described by Woods et al. is then analyzed in Section 6.5.3 in the light of results from the first two Sections. Section 6.5.4 then summarizes the analyses.

6.5.1 Secondary Dike Propagation for Effusive Flow

It appears, from the analysis of dike propagation from depth, that in most cases the dike tip will have already reached the surface by the time the magma arrives at the depth of the emplacement drifts and more viscous magma would accentuate this tendency (Section 6.3.7.1). In addition, the upward progress of the magma front inside the dike may be slowed above a drift (relative to upward progress on magma in the pillars between drifts during the time that magma is flowing into the drifts (Section 6.4.5). Both of these effects will reduce the likelihood that magma would find a path out of the repository other than along the original trajectory of the dike. However, the analysis in this section 6.5.1 addresses the unlikely potential for such a diversion.

6.5.1.1 Description of Inputs

6.5.1.1.1 Inputs for Crack Opening Analysis

The inputs for the crack opening analysis in Section 6.5.1.2 are in situ stress state, drift geometry (diameter of 5.5 m), elastic properties of rock mass, joint properties and magma properties. The sources are listed in Table 4-1. Input values are listed in Tables 6-8 through 6-10.

Table 6-8. Input Parameters for Crack Opening Rates Analysis: Initial Stress

Overburden (m)	Ratio of Stress ∥ Axis of Drift to Vertical Stress	Ratio of Stress ⊥ Axis of Drift to Vertical Stress
250,300	0.35,0.50	0.5

Source: BSC 2004 [DIRS 166107].

Table 6-9. Input Parameters for Crack Opening Rates Analysis: Rock Mass

Initial Crack Aperture (mm)[1]	Young's Modulus of Rock (GPa)[2]	Poisson's Ratio[2]	Joint Normal Stiffness (GPa/m)*	Joint Shear Stiffness (GPa/m)*
1,3	5,15	0.21	20	20

Sources: [1] Value postulated relative to corroborating information discussed in this section.
[2] Values are representative of the Topopah Spring lower lithophysal unit (Detournay et al. 2003 [DIRS 169660], Table 1-2).

NOTE: * Specified values.

Table 6-10. Input Parameters for Crack Opening Rates Analysis: Magma

	Magma Pressure in Drift (MPa)*	Bulk Modulus of Magma (MPa)*	Magma Density (kg/m^3)**	Magma Viscosity (Pa·s)**
Value	4,8,10	50,500	1000	10,100

Source: **Detournay et al. 2003 [DIRS 169660].

NOTE: *Specified values.

The sources of the inputs for overburden and ratios of horizontal stresses to vertical stress (referred to in Table 6-8 as coefficients along and perpendicular to the drift) are the same as the sources for the inputs discussed in Section 6.3.5. Also, the sources for the elastic properties of the rock mass and the magma properties are the same as the sources for the inputs discussed in Section 6.3.5.

Somewhat wider ranges for Young's modulus and magma viscosity were considered in the crack opening analysis. Young's modulus of 5 GPa is representative of poor quality rock mass at the repository level. The increased viscosity of 100 Pa·s addresses the effect of magma cooling on the viscosity.

A single value of 1000 kg/m^3 for the magma density was used throughout the analysis (Table 6-10). This has a negligible effect on the result because the accelerations are very low, so inertial effects are small. Furthermore, the difference in using magma with a higher density is small.

Three values of magma pressure are considered. Results from Section 6.3.7 and Figure 6-19, indicate that the likely value of magma pressure at repository depth under in situ stress conditions is 4 MPa while drifts would be filling with magma. After magma has finished filling drifts, it may continue to rise to the surface, increasing the pressure head. At the nominal repository depth of 300 m, the pressure at the base of a column of magma with the largest possible density of 2600 kg/m^3 would be 8 MPa; this exceeds the maximum pressure expected during drift filling in the first 2000 years after closure as seen in Section 6.3.7.3 and Figure 6-36f. The greatest depths of drifts are just over 400 m, at which depth the pressure head in the column of magma would be about 10 MPa.

The results of this analysis are not sensitive to the joint normal and shear stiffnesses. Those input parameters were selected to correspond to the lower bound of measured values (BSC 2004 [DIRS 166107], Table E-4). (Smaller joint stiffness results in larger calculation time step.) The

same argument was used in selection of the input for magma bulk modulus. The analysis showed that there is insignificant effect on the results when the magma bulk modulus was increased from 50 MPa to 500 MPa. The joint openings (initial crack aperture) of 1 mm and 3 mm were used for the analysis. Measurements (Olsson and Brown 1997 [DIRS 106453]) found that initial joint openings at Yucca Mountain are less than 1 mm. Because a wider initial opening will be easier to enlarge and will carry more flow than a narrower one, this result is conservative.

6.5.1.1.2 Inputs for Magma Cooling Rates Analysis

The inputs for the magma cooling rates analysis are the thermal diffusivity and specific heat of the magma (heat capacity), the latent heat of crystallization of the magma (heat of fusion), the intrusion temperature, and the viscosity of crystal-free magma. The solution presented here makes the approximation that thermal properties (specific heat and thermal diffusivity) of the magma and the host rock are the same. The magma effective solidification temperature (T_s) is also required and is derived in the analysis (Section 6.5.1.4). Table 4-1 gives input sources.

Calculations were done for the six different magma compositions (differing in water content) used in the analysis report *Characterize Eruptive Processes at Yucca Mountain, Nevada* (BSC 2004 [DIRS 169980]).

The thermal diffusivity and specific heat of the magma, and its latent heat are selected to be consistent with the values used by the final Igneous Consequences Peer Review Report (Detournay et al. 2003 [DIRS 169660]), which are consistent with Spera (2000 [DIRS 164109]). The intrusion temperature is taken as the liquidus temperature from DTN: LA0407DK381811.001 [DIRS 170768]. The crystal-free viscosity is from the same source. The values used are included in Table 6-11.

Table 6-11. Input Parameters for Thermal Calculations

Water (%)	[a]Approximate Latent Heat ($J\ kg^{-1}$)	[a]Approximate Specific Heat ($J\ kg^{-1}K^{-1}$)	[a]Approximate Diffusivity (m^2s^{-1})	[b]Intrusion Temperature (°C)	[b]Crystal-free Viscosity (Pa·s)	[a]T_s (°C)
0	3.50×10^5	1100	3.00×10^{-7}	1169	48	1135
0.5	3.50×10^5	1100	3.00×10^{-7}	1153	37	1108
1.0	3.50×10^5	1100	3.00×10^{-7}	1137	30	1083
2.0	3.50×10^5	1100	3.00×10^{-7}	1106	19	1034
3.0	3.50×10^5	1100	3.00×10^{-7}	1076	13	998
4.0	3.50×10^5	1100	3.00×10^{-7}	1046	9.1	964

Sources: [a] Detournay et al. 2003 [DIRS 169660].
[b] DTN: LA0407DK831811.001 [DIRS 170768].

6.5.1.2 Opening of Pre-Existing Crack

To assess the possibility of a secondary dike propagation (i.e., magma finding a new path to the ground surface by re-opening some of the existing joints inside the drifts), the conditions of magma injection into the joints intersecting the drift were investigated. Specific evaluations

were conducted to determine if the pressure in a filled drift could sustain the propagation of a magma up a joint to the surface, and how fast the magma would rise.

This section discusses results of simulations of magma injection into pre-existing joints inside the emplacement drifts. The simulations discussed here investigate sensitivity of the predictions to variation of the parameters, such as magma compressibility, magma viscosity, magma pressure, initial joint aperture, rock mass stiffness (Young's modulus), and initial stress state. Magma freezing inside the joints is not considered. It will be analyzed later (Section 6.5.1.4). This analysis does not deal with the transient magma pressures that may develop at the precise time the magma finishes filling the drift. However, because the velocity of the magma in the drift is not high (not more than a few m/s, see Section 6.4), such transients will be minimal. Note that a case of high transient pressures will be analyzed later (Section 6.5.2.1).

All analyses discussed in this section were done using two numerical codes: UDEC V3.14 (BSC 2004 [DIRS 172322]) and FLAC3D V2.14 (BSC 2004 [DIRS 172323]). Both codes are qualified, and are used here within their range of intended use. The simulations are fully coupled hydro-mechanical computations, but do not take temperature into account. Starting from null initial fluid pressures everywhere, a fluid (magma) pressure is applied inside the drift. This pressure causes the adjacent joint to open and starts the process of magma flow into the joint. Note that the pressure applied in the drift is kept constant in time.

All simulated cases of magma injection into pre-existing joints inside the emplacement drifts are summarized in Table 6-12. (The order in which the cases are listed in Table 6-12 does not indicate a relation between different cases, only the sequence in which they were simulated.)

Table 6-12. Summary of Analyzed Cases of Magma Injection Into Joints

Case	Crack Orientation with Respect to Drift*	Initial Crack Aperture (mm)	Magma Pressure in Drift (MPa)	Initial Stress			Bulk Modulus of Magma (MPa)	Young's Modulus of Rock (GPa)	Magma Viscosity (Pa·s)
				Over-burden (m)	Coeff. Along Drift	Coeff. Perp. to Drift			
101	vertical along	1	4	300		0.5	50	15	10
102	vertical along	1	8	300		0.5	50	15	10
103	vertical along	1	10	250		0.5	50	15	10
104	horizontal	1	8	300		0.5	50	15	10
105	vertical perp.	1	10	300	0.35	0.5	50	15	10
106	vertical along	1	4	300		0.5	50	5	10
107	vertical along	1	4	300		0.5	500	15	10
108	vertical perp.	1	8	300	0.35	0.5	50	15	10
109	vertical perp.	1	8	300	0.5	0.35	50	15	10
110	vertical along	1	8	250		0.5	50	15	10
111	vertical along	3	8	250		0.5	50	15	10
112	vertical along	3	8	250		0.5	50	5	10
113	vertical along	3	8	250		0.5	500	5	10
114	vertical along	3	8	250		0.5	500	15	10

Table 6-12. Summary of Analyzed Cases of Magma Injection Into Joints (Continued)

Case	Crack Orientation with Respect to Drift*	Initial Crack Aperture (mm)	Magma Pressure in Drift (MPa)	Initial Stress			Bulk Modulus of Magma (MPa)	Young's Modulus of Rock (GPa)	Magma Viscosity (Pa·s)
				Over-burden (m)	Coeff. Along Drift	Coeff. Perp. to Drift			
115	vertical along	1	8	250		0.5	50	5	10
116	vertical along	1	8	250		0.5	50	15	100
117	vertical along	1	10	250		0.5	50	15	100
118	vertical along	3	8	250		0.5	50	15	100
119	vertical along	3	8	250		0.5	50	5	100
120	vertical along	1	8	250		0.5	50	5	100

Output DTN: MO0408EG831811.002.

NOTES: *Crack Orientation: vertical along = a vertical crack along the drift; vertical perp. = a vertical crack perpendicular to the rift

During simulations, joint apertures and magma pressures in the joint are recorded at seven different locations away from the drift. Table 6-13 and Table 6-14 show the positions of these seven points relative to the drift periphery, for all cases studied.

Table 6-13. Distances from Drift Periphery to Recording Points for Cases 101 Through 104, and 106, 107, and 110 Through 120

Point	Distance (m)
1	0.46
2	0.92
3	1.83
4	3.67
5	7.79
6	16.04
7	32.14

Output DTN: MO0408EG831811.002.

NOTES: Distances are measured from the drift periphery to the points at which histories of aperture and pressures are recorded for the various cases.

Table 6-14. Distances from Drift Periphery to Recording Points for Cases 105, 108, and 109

Point	Distance (m)
1	0.00
2	1.40
3	3.08
4	5.08
5	10.34
6	22.71
7	43.79

Output DTN: MO0408EG831811.002.

NOTES Distances are measured from the drift periphery to the points at which histories of aperture and pressures are recorded for the various cases.

The results for Case 101 (representative conditions) and Case 103 (extremely conservative conditions) are shown in Figure 6-53 through Figure 6-60. The following plots are shown for each case:

- Displacement vector field and hydraulic aperture along the joint at the end of the simulation
- Stress tensor field (colored by the magnitude of the minor principal stress) and pore pressure along the joint at the end of simulation
- Evolution of joint aperture at seven locations, as indicated in Table 6-13
- Position (distance from the drift periphery) of the magma front inside the joint as a function of time.

The results for all runs are summarized in Figures 6-61 and 6-62; plots similar to Figures 6-53 through 6-59 can be found in DTN: MO0411EG831811.002 Figure 6-61 shows the average magma front velocity computed for each simulation. Note that such a velocity tends to decrease with time, so the velocity shown here is an overestimate of the magma velocity at later times. Figure 6-62 compares the various simulations in terms of thickness achieved by the magma intrusion. The figure shows (at a distance of 3.6 m from the drift periphery), for each case studied, the time needed between the start of the injection and:

- Start of the joint opening
- 1.5-mm thickening of the joint
- 3-mm thickening of the joint opening
- 10-mm thickening of the joint
- 25-mm thickening of the joint opening.

For Case 101, the magma travels only 15 m in one hour, as shown in Figure 6-56. However, only 300 s after the drifts are completely filled with magma, the main dike would reach ground surface (for a magma front velocity of 1m/s). At that time, the magma has traveled only 5 m away from the drift.

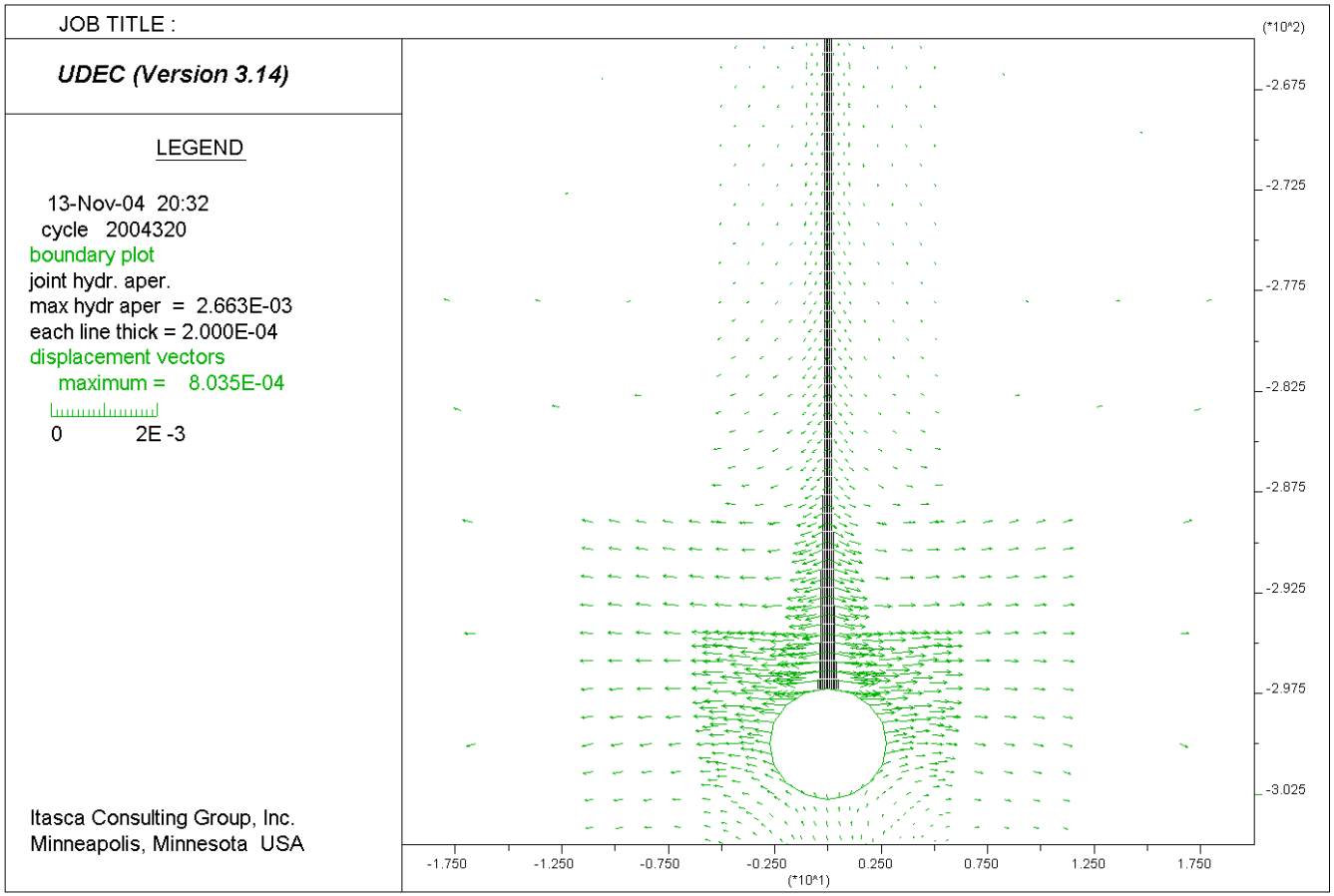

Output DTN: MO0408EG831811.002.

Source: Output Data Calculation Plot.

NOTES: Thickness of the black line is proportional to the hydraulic aperture of the joint. Deformation (green arrow) is due to pressure change inside the joint only. Scale in legend shows displacement vector lengths from 0 to 0.8 mm.

Figure 6-53. Displacement Vector Field (m) and Hydraulic Aperture (m) Along the Vertical Fracture: Case 101

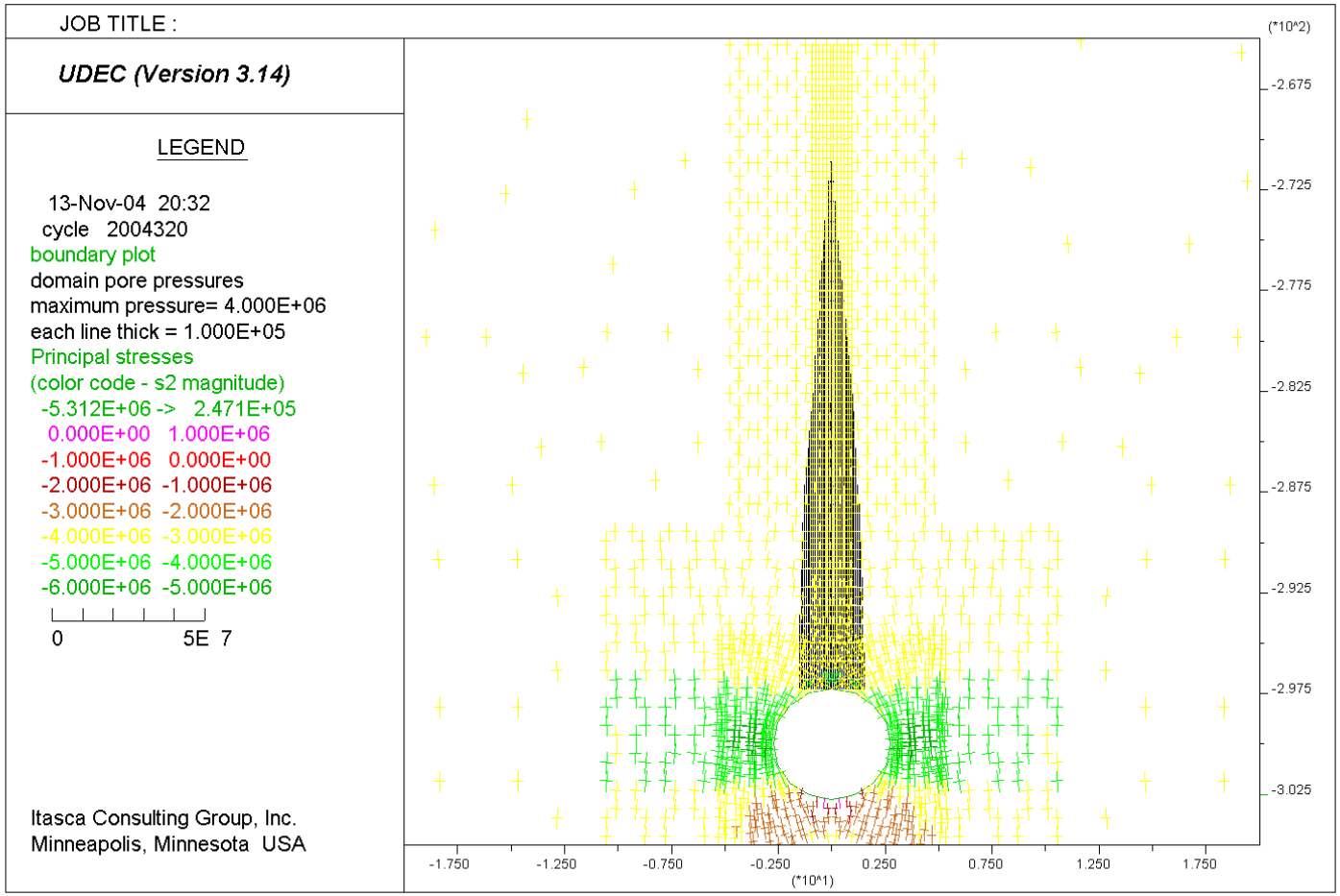

Output DTN: MO0408EG831811.002.

Source: Output Data Calculation Plot.

NOTES: Thickness of the black line is proportional to magma pressure in the joint; color of stress tensors indicates the magnitude of the minor principal stress.

Figure 6-54. Stress Tensor Field (Pa) and Pore Pressure (Pa) Along the Joint: Case 101

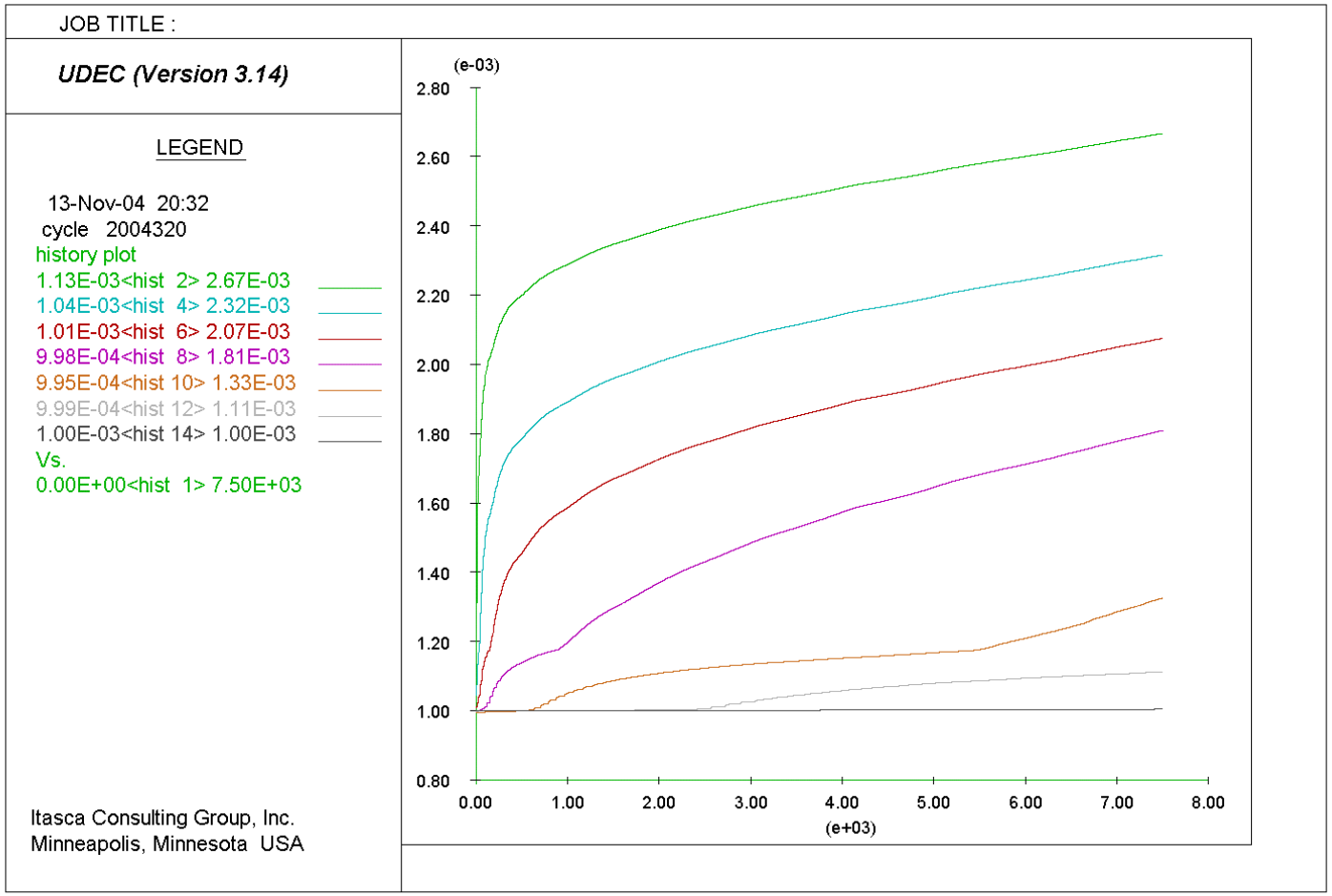

Output DTN: MO0408EG831811.002.

Source: Output Data Calculation Plots.

NOTES: Increasing history numbers correspond to points from Table 6-12, maintaining the same sequence. Time is in seconds.

Figure 6-55. Histories of Joint Hydraulic Aperture (m) at Seven Locations Along the Joint: Case 101

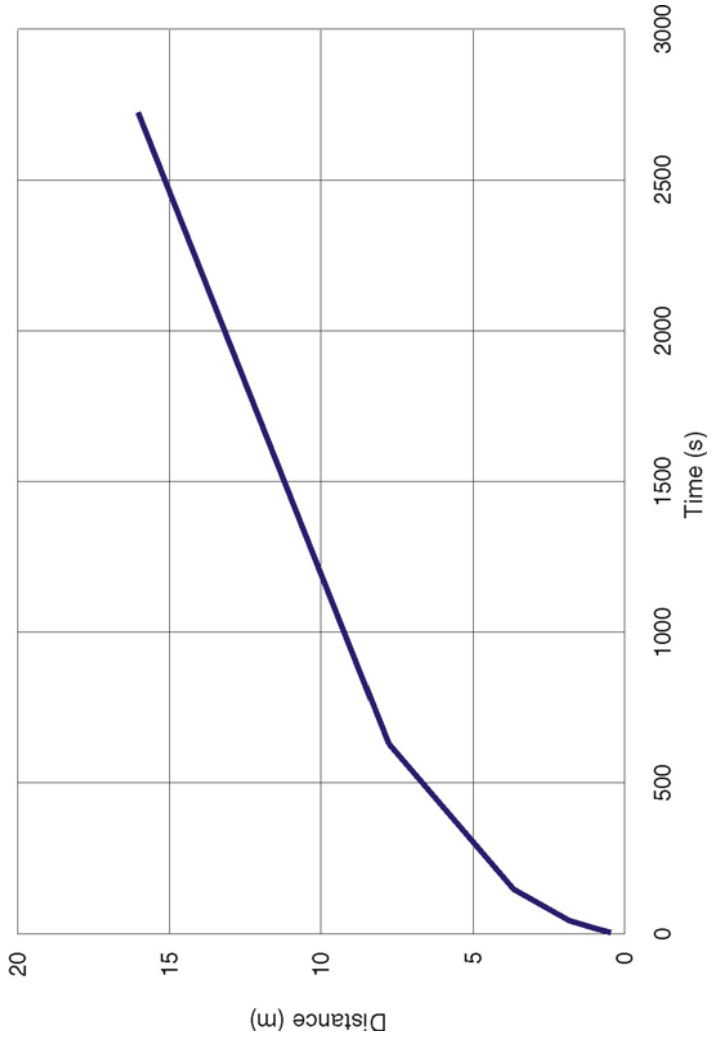

Output DTN: MO0408EG831811.002.
Source: Output Data Calculation Plot.

Figure 6-56. Location (Relative to the Drift Periphery) of the Magma Front Inside a Joint as a Function of Time: Case 101

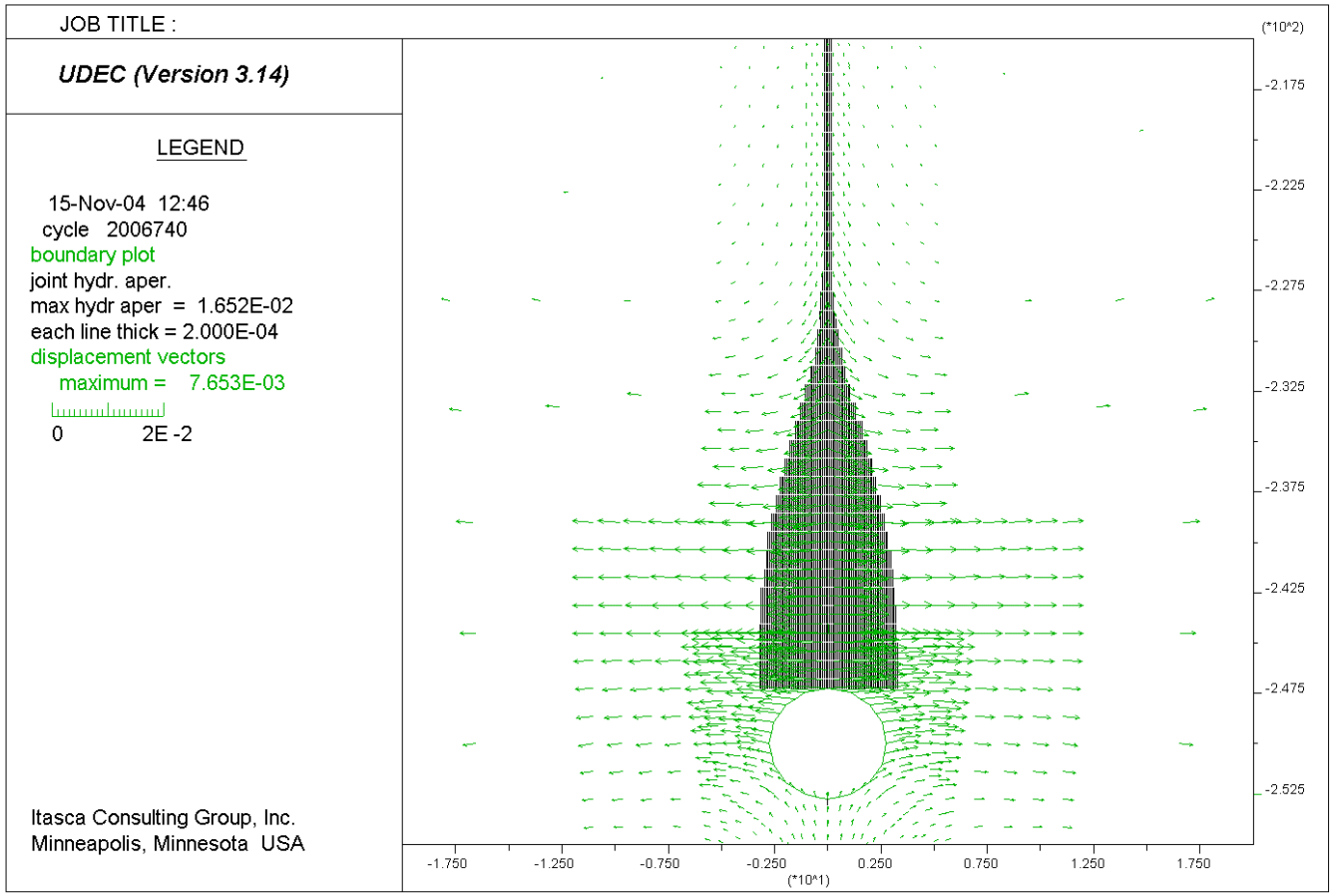

Output DTN: MO0408EG831811.002.

Source: Output Data Calculation Plot.

NOTES: Thickness of the black line is proportional to hydraulic aperture of the joint; deformation is due to pressure change inside the joint only.

Figure 6-57. Displacement Vector Field (m) and Hydraulic Aperture (m) Along the Vertical Fracture: Case 103

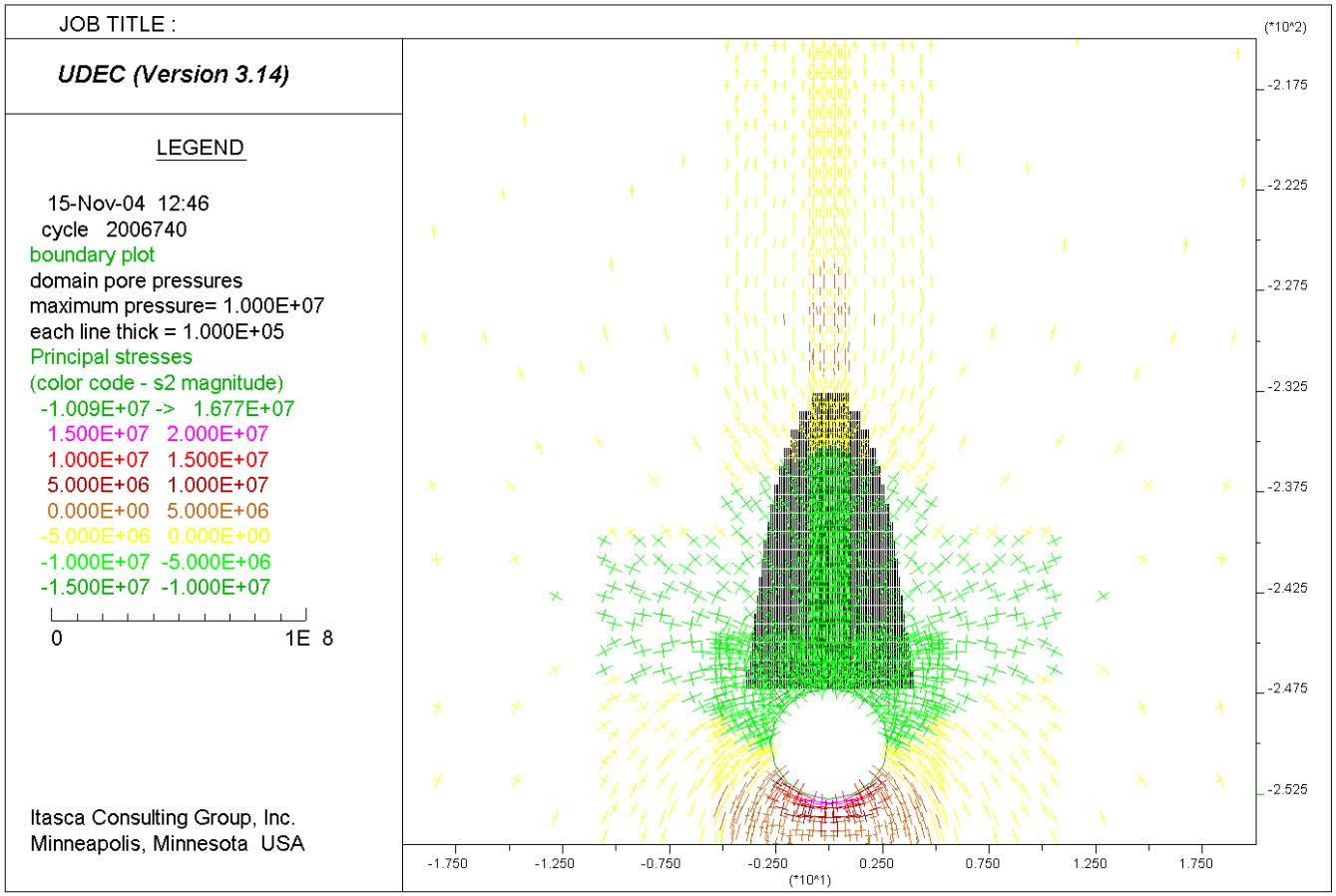

Output DTN: MO0408EG831811.002.

Source: Output Data Calculation Plot.

NOTES: Thickness of the black line is proportional to magma pressure in the joint; color of stress tensors indicates the magnitude of the minor principal stress.

Figure 6-58. Stress Tensor Field (Pa) and Pore Pressure (Pa) Along the Joint: Case 103

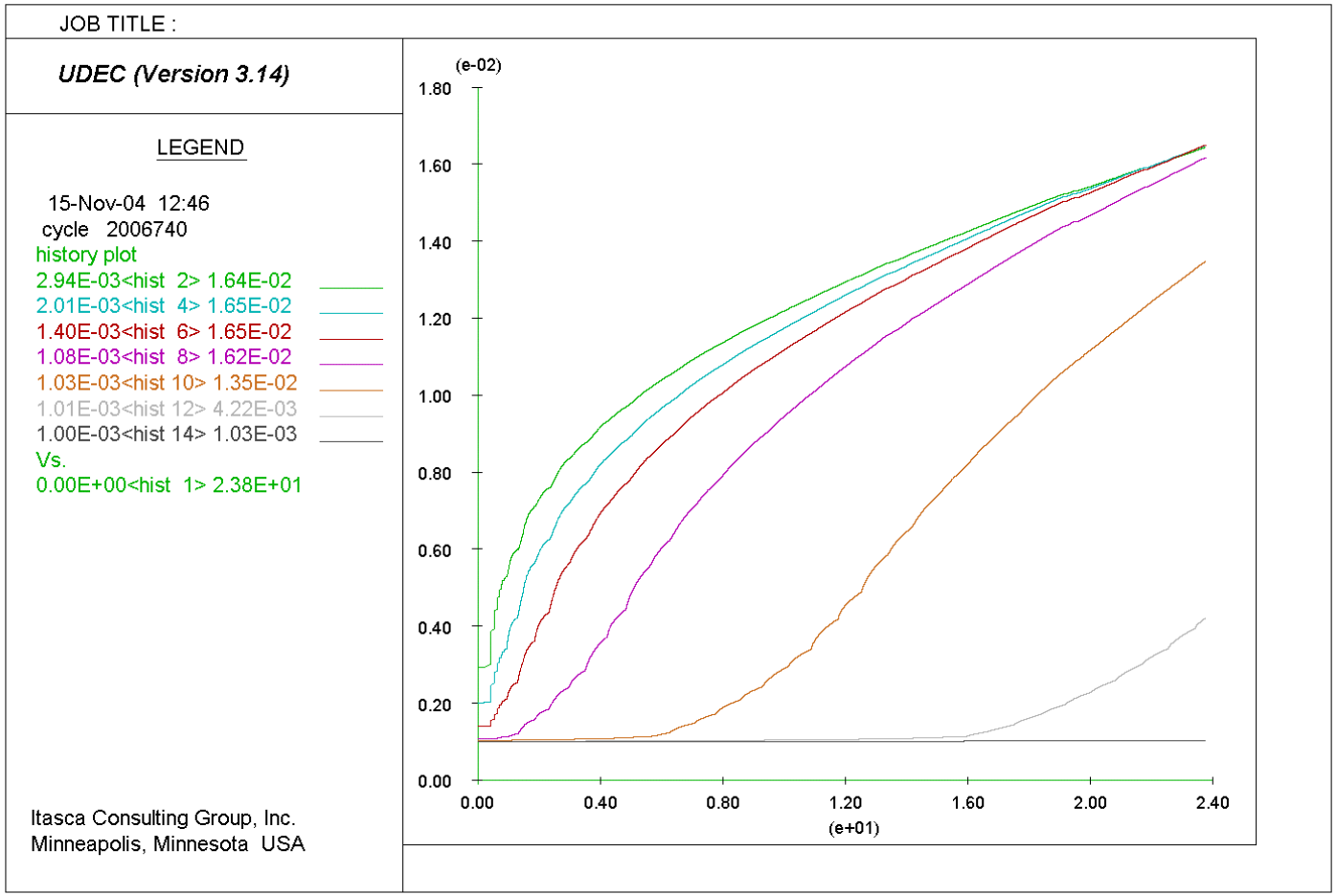

Output DTN: MO0408EG831811.002.

Source: Output Data Calculation Plots.

NOTES: Increasing history numbers correspond to points from Table 6-12, maintaining the same sequence. Time is in seconds.

Figure 6-59. Histories of Joint Hydraulic Aperture (m) at Seven Locations Along the Joint: Case 103

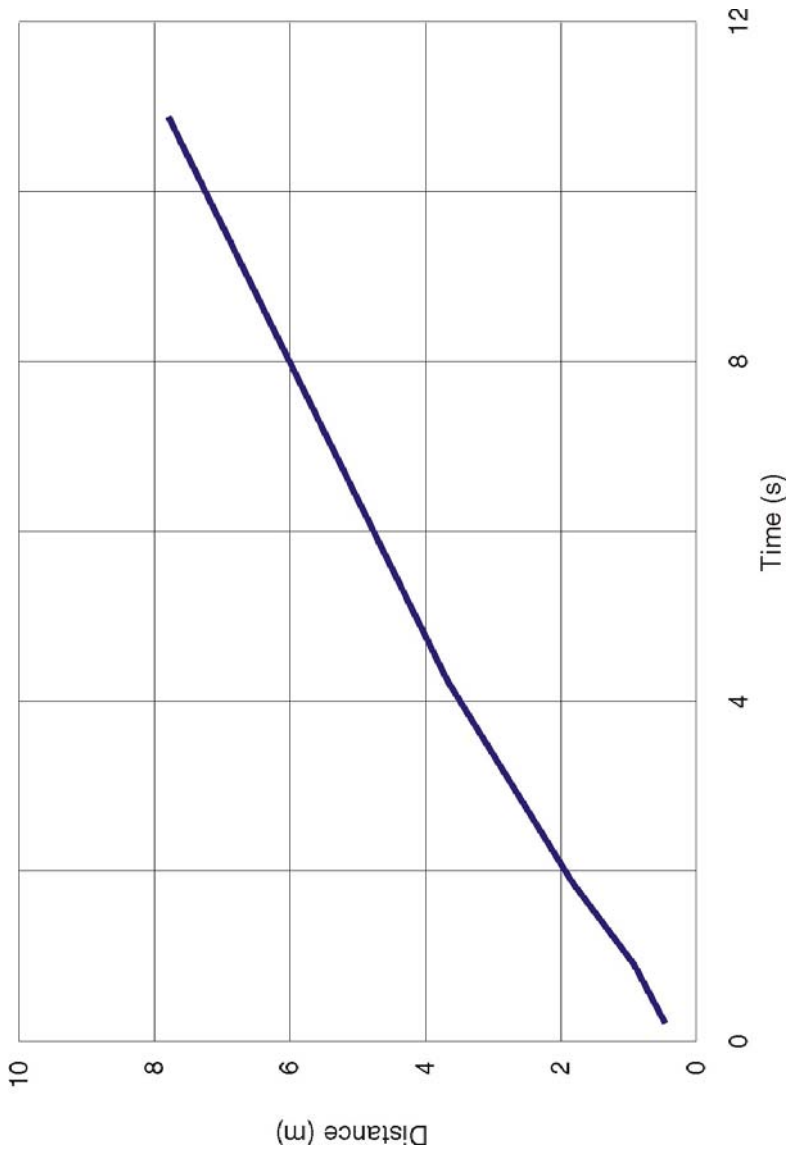

Output DTN: MO0408EG831811.002.

Source: Output Data Calculation Plot.

Figure 6-60. Location (Relative to the Drift Periphery) of the Magma Front Inside a Joint as a Function of Time: Case 103

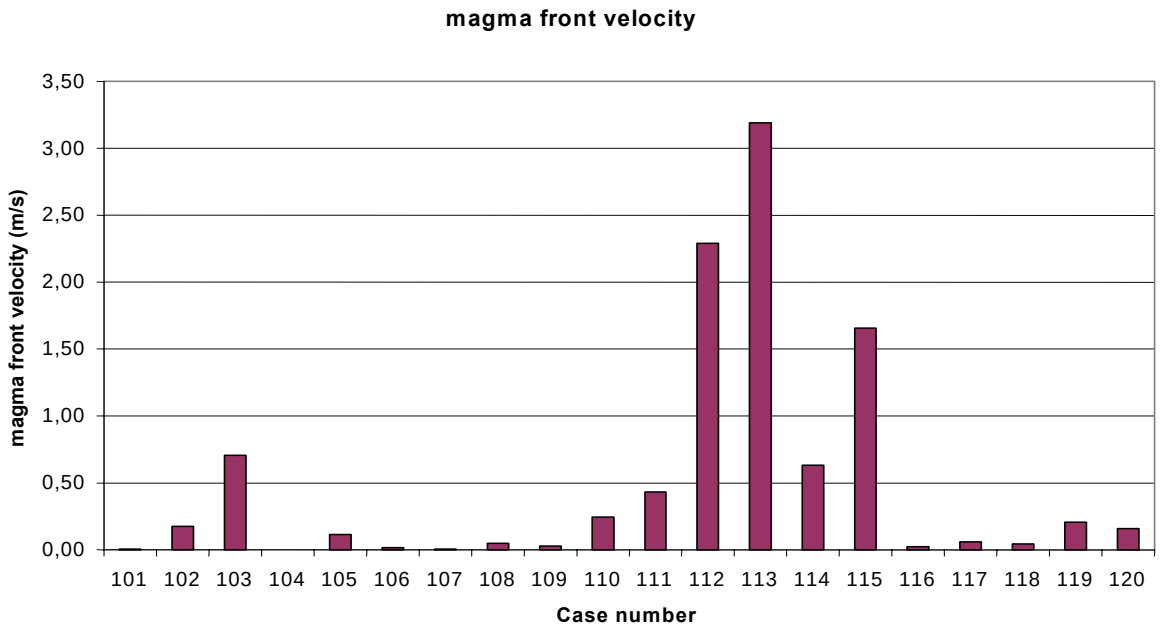

Output DTN: MO0408EG831811.002.

Figure 6-61 Magma Front Average Velocity Over The Whole Simulation, for each Case

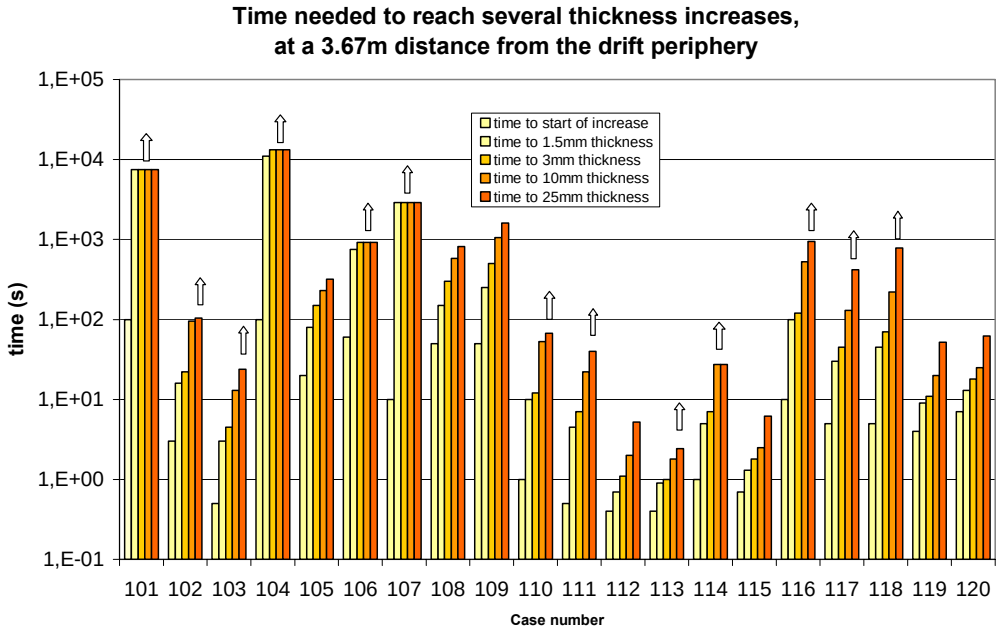

NOTE: Arrows above histogram bars mean that the time given is a minimum: the simulation was stopped before the corresponding thickness increase was reached.

Output DTN: MO0408EG831811.002.

Figure 6-62. Time needed for the Joint to Reach Several Thickness Increases at a 3.67 m Distance From the Drift Periphery (Except For Cases 105, 108, 109, for Which Distance is 3.08 m)

Case 103 represents extremely conservative conditions with a magma pressure inside the drift of 10 MPa, whereas stresses in the rock mass are due to in situ far-field conditions (no thermal effects). Plugging the main dike conduit at an elevation above the repository level could result in an increase in magma pressure without an increase in rock-mass stresses. However, it is not likely that magma pressure could reach 10 MPa because the main conduit would most likely re-open at lower pressures. Even for such extreme conditions, the mean velocity of the magma front inside a joint is approximately 0.7 m/s (with a trend to decrease as the pressure gradient decreases in response to the increasing length of the magma-filled portion of the joint). This is less than the expected velocity of the magma front inside the main dike.

As shown in Figure 6-61, the remaining base cases; i.e., 102, 104 and 105 yield low magma front velocities.

The results from Cases 106 through 120 investigate sensitivity of the predictions to variation of its parameters, such as magma compressibility, magma viscosity, magma pressure, initial joint aperture, rock mass stiffness (Young's modulus), and initial stress state.

Sensitivity of Case 101 to variation of Young's modulus of the rock mass is investigated in Case 106. Young's modulus of the rock mass in Case 106 is 5 GPa (poor quality lithophysal rock, between Categories 1 and 2), which compares to 15 GPa in Case 101 (good quality lithophysal rock, between Categories 4 and 5, and also representative of nonlithophysal rock mass). The results indicate that, in the case of more compliant rock mass, the increase in the joint aperture is faster (750 s needed to reach a 1.5 mm thickness increase, instead of more than 7500 s for Case 101, see Figure 6-62), but still relatively small. In this case, this indicates that the magma would freeze due to conductive heat loss into the surrounding rock mass.

To investigate the effect of magma compressibility, Case 107 was simulated using magma bulk modulus of 500 MPa (compared to 50 MPa in Case 101). The magma front velocities for Cases 101 and 107 are almost identical, at 0.01 m/s. Also, in this case as well as in Case 101, the joint thickness is not able to increase by 1.5 mm during the simulation time. Magma compressibility hardly affects the results in this case.

Cases 108 and 112, for a 3-D representation of a joint, perpendicular to the drift, compare with Case 105. Both new cases are for 8 MPa magma pressure (Case 105 is for 10 MPa). Case 109 represents the condition of a larger normal stress along the drift (perpendicular to the joint): 50 percent of the vertical stress compared to 35 percent of the vertical stress for Cases 105 and 108. Note that the simulations for these three cases indicated instability (due to the magma pressure being larger than the horizontal far-field stress perpendicular to the joint). However, there is a clear trend of the reduction in the rate of joint opening from Case 105 to 108 and from Case 108 to 109, as can be seen from Figure 6-62. The time needed for a 25 mm thickness increase varies from 320s (Case 105), to 820 s (Case 108) and 1600 s (Case 109).

The maximum vertical stress at the repository level is about 8 MPa. Under such conditions, the 10 MPa magma pressure considered in Case 103 is unrealistic. Case 110 investigates the effect of reduction in magma pressure from 10 MPa (considered in Case 103) to 8 MPa. The rate of fracture opening significantly reduces from Case 103 to Case 110. The time needed for a 25 mm

thickness increase varies from 24s (Case 103), to 67 s (Case 110). Also, the magma front velocity is significantly reduced, from 0.71 m/s to 0.25 m/S.

All of the analyses discussed so far had the initial joint aperture set at 1 mm. This input value is reasonable and even conservative considering measurements of joint apertures (Olsson and Brown 1997 [DIRS 106453]). However, to investigate the response of the initial joint aperture, Case 111 is simulated using the very conservative value of 3 mm for the initial joint aperture.

All parameters between Cases 110 and 111 are the same, except that the initial joint aperture in Case 110 is 1 mm and in Case 111 it is 3 mm. Magma front velocity increases from 0.25 m/s to 0.43 m/s. The 25 mm thickness increase is reached in 40 s (Case 111) instead of 67 s (Case 110).

Cases 112 and 115 investigate the effect of stiffness of the rock mass:

- Case 110 is for a Young's modulus of the rock mass of 15 GPa compared to Case 115 for a Young's modulus of 5 GPa (both cases are for a 1-mm joint aperture).

- Case 111 is for a Young's modulus of the rock mass of 15 GPa compared to Case 112 for a Young's modulus of 5 GPa (both cases are for a 3-mm joint aperture).

The effect of the stiffness of the rock mass is much more pronounced between Cases 111 and 112 and Cases 110 and 115 than between Cases 101 and 106.

This result was to be expected, since the magma pressure imposed in Cases 110, 111, 112, and 115 is twice as much as the one imposed in Cases 101 and 106. The effect of rock mass deformability is more significant in cases in which magma pressure causes complete joint opening (i.e., Cases 110, 111, 112, and 115) compared to cases (e.g., Cases 101 and 106) that consider injection of magma into a closed joint. It also appears that rock mass deformability has a more profound effect on the potential for the opening of a secondary dike inside the drift than the initial joint aperture.

It should be noted that joints with long trace lengths exist in good quality rock (i.e., nonlithophysal rock mass and better quality lithophysal rock mass). Such rock is characterized with a Young's modulus equal to or larger than 15 GPa. Poor quality rock mass at the repository level in Yucca Mountain (e.g., highly fractured lower lithophysal—Tptpll) is characterized by a large number of joints that are at small spacing with short trace lengths and not continuous. This kind of medium will not be susceptible to a mechanism of localized fracture propagation. Instead, it is more likely that magma will be injected into exposed lithophysae and into a number of non-continuous, mutually intersecting joints. Such a process will lead to quick magma freezing due to heat loss.

Cases 113 and 114 investigate the effect of an increase in magma bulk modulus from 50 MPa to 500 MPa relative to Cases 112 and 111. It appears from the results that such an increase in magma bulk modulus has a minor effect on the results.

All of the results presented to this point used magma viscosity of 10 Pa·s. As magma enters the drift and is being injected into the joints, it will cool off and, before freezing, magma viscosity will increase. Because a dimensional and scaling analysis was not carried out, simulations of Cases 116 through 120 were conducted to investigate the effect of an increase in magma viscosity from 10 Pa·s to 100 Pa·s. As expected, an increase in magma viscosity results in a proportional increase in time scale. For example, in Case 103 (viscosity 10 Pa·s) it takes 13 s to reach a 10-mm thickness increase; whereas, in Case 117 (viscosity 100 Pa·s) the thickness increase is reached after 130 s.

Even if the argument of magma freezing is not used, among all of the 20 analyzed cases, only in Cases 103 and 112 to 115 does a magma front inside the joint move faster than 0.5 m/s. That result implies that the magma front inside the original dike (which could also be 80 m or more above the repository level) will reach the ground surface much sooner than the magma injected into joints inside the drift.

6.5.1.3 Potential Location Of An Eventual Secondary Dike

By evaluating the altered stress field around the dike and the resultant stress concentrations, an assessment can be made of where along the drift a secondary dike would be most likely to develop.

6.5.1.3.1 Stress-Related Effects

Prior to the formation of the dike, the repository is characterized by some far-field principal stresses with known orientations and values. These stresses may change with time due to heating, but calculations of those changes are available using a thermo-mechanical model of the repository. The repository is also characterized by various material properties, but only Poisson's ratio is actually required for this analysis.

Effective In Situ Stresses–The effective in situ stresses are given by:

$$\sigma_1 = S_1 - \alpha P \qquad \text{(Eq. 6-99)}$$

$$\sigma_2 = S_2 - \alpha P$$

$$\sigma_v = S_v - \alpha P$$

where

S_1, S_2, and S_v are the principal in situ stresses
P = is the pore pressure
α = Biot's modulus.

All subsequent equations involving the principal far-field stresses will use the effective stress form. However, because the pore pressure at the repository level is zero, the effective stresses are equal to the total stresses, and Biot's modulus is not required.

Addition of Dike-Stress Perturbation–The presence of a pressurized dike results in additional stresses that must be superposed on the in situ stresses. However, because the dike is aligned normal to the minimum principal in situ stress and the dike calculation is 2-D, there are only perturbations to four of the stress components. The values of these stress perturbations come from the NPHF2D (BSC 2002 [DIRS 163665]) code calculations and are represented by:

σ_{dv}: the stress perturbation of the dike in the vertical direction
σ_{dh}: the stress perturbation of the dike in the horizontal plane
τ_{dhv}: the shear stress in the horizontal-vertical plane
$\sigma_{dp} = \nu(\sigma_{dv} + \sigma_{dh})$: the stress parallel to the dike (out of plane)

With the presence of the dike, the new stress field is characterized by:

$$\begin{aligned} \sigma_1' &= S_1 + \nu(\sigma_{dv} + \sigma_{dh}) \\ \sigma_2' &= S_2 + \sigma_{dh} \\ \sigma_v' &= S_v + \sigma_{dv} \\ \tau_{2v}' &= \tau_{dhv} \end{aligned} \qquad \text{(Eq. 6-100)}$$

Note that because of the existence of some shear in the minimum/vertical plane, the principal stresses would be rotated slightly by the presence of the dike.

Transformation of Principal and Dike Stresses into the Drift Plane–Due to geometric simplifications, the transformation of superposed principal and dike stresses is straightforward. The drifts are essentially horizontal so that the vertical stress is always normal to the tunnel. It is only necessary to rotate the horizontal stresses into a new plane aligned with the drift, which adds a shear stress, and appropriately distributes the shear from the dike. The rotation is taken through the angle φ from the maximum principal horizontal in situ stress to the axis of the drift.

These rotations yield stresses σ_x, σ_y, and σ_z and shear stresses τ_{xy}, τ_{yz}, and τ_{xz}, given by:

$$\begin{aligned} \sigma_x &= \sigma_1' \cos^2\varphi + \sigma_2' \sin^2\varphi \\ \sigma_y &= \sigma_1' \sin^2\varphi + \sigma_2' \cos^2\varphi \\ \sigma_z &= \sigma_v' \\ \tau_{xy} &= \frac{1}{2}(\sigma_1' - \sigma_2')\sin(2\varphi) \\ \tau_{yz} &= \tau_{2v}' \cos(\varphi) \\ \tau_{xz} &= \tau_{2v}' \sin(\varphi) \end{aligned} \qquad \text{(Eq. 6-101)}$$

In this rotated space, z is vertical, x is along the axis of the drift, and y is normal to the drift.

Drift Stress Concentration–The stress concentrations around the drift that are induced by the far-field stresses are well known and, at the tunnel wall, are given by:

$$\begin{aligned} \sigma_\theta &= (\sigma_x + \sigma_y) - 2(\sigma_x - \sigma_y)\cos(2\theta) - 4\tau_{xy}\sin(2\theta) \\ \sigma_{zz} &= \sigma_z - 2\nu(\sigma_x - \sigma_y)\cos(2\theta) - 4\nu\tau_{xy}\sin(2\theta) \\ \tau_{\theta z} &= 2(-\tau_{xz}\sin\theta + \tau_{yz}\cos\theta) \\ \tau_{r\theta} &= \tau_{rz} = 0 \end{aligned} \qquad \text{(Eq. 6-102)}$$

In these equations, θ is the angle around the drift as measured from the *x*-axis towards the *y*-axis, so σ_θ is the hoop stress. Also, σ_r (not in the equations above) is the radial stress, but it is zero at the tunnel wall (until pressurized by magma, which is considered later). All of these stresses are at the drift wall, where the stress concentration is highest.

Drift Pressurization–The pressurization of the drift, to a value P_w, induces a radial and a tangential component. These are given by:

$$\begin{aligned} \sigma_{pr} &= P_w \\ \sigma_{p\theta} &= -P_w \\ \sigma_{pz} &= \nu\left(\sigma_{pr} + \sigma_{p\theta}\right) = 0 \end{aligned} \qquad \text{(Eq. 6-103)}$$

because there is no leak-off of magma into the pore space to induce poroelastic stress variations. Thermoelastic stresses are not considered here, but the heating of the drift by magma would cause the drift to expand and increase the hoop stress, further reducing the potential for initiation of a fracture.

Principal Stresses–To examine if fracture initiation could occur, the principal stresses around the drift must be determined. The radial stress is always a principal stress because there are no shear components in the radial plane at the drift surface. In the *z*-θ plane, the principal stresses are given by:

$$\sigma_p, \sigma_q = \frac{1}{2}(\sigma_\theta + \sigma_z) \pm \frac{1}{2}\left[(\sigma_\theta - \sigma_z)^2 + 4\tau_{\theta z}^2\right]^{\frac{1}{2}} \qquad \text{(Eq. 6-104)}$$

and the angle of failure is given by:

$$\alpha = \tfrac{1}{2}\tan^{-1}\left(\frac{2\tau_{xy}}{\sigma_x - \sigma_y}\right) \qquad \text{(Eq. 6-105)}$$

6.5.1.3.2 Fracture Criteria

Assessment of Fracture Re-initiation–A new fracture can initiate from the drift only if the magma pressure is sufficient to increase either the hoop stress or the axial stress to overcome the smallest compressive stress that exists on the tunnel wall. Thus, the determination of the smallest principal stress at the tunnel wall solves this aspect of the problem. This determination can be done rigorously by superposing the pressurization stresses with the stress concentration around the tunnel. However, for the particular geometry of the repository (e.g., the drifts nearly aligned with the stress field), the effects of the shear stresses are minimal, and the stress field is almost aligned with the drift. Thus, the principal stresses are essentially in the hoop, radial, and axial directions, and direct comparisons with the pressure can be made by examining the tunnel stress concentrations.

Assessment of Fracture Propagation–An assessment of fracture propagation is direct. The pressure in the drift must be greater than the minimum principal stress at that location. If it is less, the pressure cannot open the fracture and propagate.

6.5.1.3.3 Results of Stress Calculations

An evaluation of the stress field (due to the presence of the pressurized dike) around the repository drifts was performed for a number of the cases run for the dike propagation analysis (Section 6.3). This evaluation includes the stress perturbation (due to the dike) as well as the stress concentration around the drift. These calculations allow for assessment of the conditions under which a potential secondary dike could initiate from the drift and/or propagate in the far field.

Calculations using the NPHF2D (BSC 2002 [DIRS 163665]) code require some manipulation of the dimensionless parameters in order to choose the location of the repository, the distance away from the dike, the location of the dike tip and magma front, the pressure, and other parameters. An example using one of the base-case calculations is given below to demonstrate the process.

The scaled parameters derived from the input parameters described in Table 4-1 for dike propagation, and developed in proceeding parts of Section 6 for this case, are given by:

Length	$l^* = (\mu' E'^3 q_\infty / \delta^4)^{1/6} = 945.01$ m
Pressure	$p^* = (\mu' E'^3 \delta^2 q_\infty)^{1/6} = 8488596$ Pa
Time	$t^* = (\mu' E' / \delta^2 q_\infty)^{1/2} = 43.309$ s

and the resultant dike far-field width and velocity are given by:

Width	$w_\infty^* = (\mu' q_\infty / \delta')^{1/3} = 0.5112$ m
Velocity	$v_\infty^* = (\delta' q_\infty^2 / \mu')^{1/3} = 19.5617$ m/s

Because the problem is formulated in terms of dimensionless parameters and only two of the dimensionless parameters are critical, a wide suite of calculations can be derived from each numerical run. In this particular case with zero cavity pressure and zero confining stress, only one dimensionless quantity needs to be considered, namely:

$$\mathbf{D} = \frac{\kappa\rho_r}{\kappa\rho_r - \rho_f} = \frac{g\kappa\rho_r}{\delta'} \qquad \text{(Eq. 6-106)}$$

Since the input conditions that will be matched are those of dike propagation rate and width at infinity (v_∞ and w_∞), and using the scaled-width equation to substitute for δ', then the dimensionless group can be reformulated as:

$$\mathbf{D} = \frac{g\kappa\rho_r w_\infty^2}{\mu' v_\infty} \qquad \text{(Eq. 6-107)}$$

As long as this dimensionless group is kept constant, this case can be used to extract numerous valid solutions.

To continue with this example, suppose that this is a case where:

- A lower horizontal stress is preferred (e.g., as determined by the relative density difference)
- The desired infinite velocity is 1.0 m/s, as expected for locations near the repository.

The dimensionless group is kept constant if the far-field width drops from 0.5112 to 0.1634. However, making these changes alters the scaling parameters. These must be recomputed from the new values of the parameters and it is sensible to do so using somewhat more simple relations. For this case, these are:

Length $l_* = (E' w_\infty^3 / \mu' v_\infty)^{1/2} = 755.3$ m
Pressure $p_* = (\mu' E' v_\infty / w_\infty)^{1/2} = 3394736$ Pa
Time $t_* = (w_\infty^3 E' / \mu' v_\infty^3)^{1/2} = 755.3$ s

Note that the scaled length and time are the same for this case only because $v_\infty = 1$ m/s.

Given the information above, the output data from each calculation can be rescaled for the appropriate desired case. To determine the position of the dike or the magma front or to find a position in space (e.g., the location of the repository or the position where a stress determination is required), it is necessary to take the output and rescale by:

new length = calculated length x (l_*/l*).

To determine the pressure or the stress at any position, it is necessary to rescale by:

new pressure = calculated pressure x (p_*/p*).

To determine the correct time, it is necessary to rescale by:

$$\text{new time} = \text{calculated time} \times (t_*/t^*) .$$

To determine the opening of the dike at any position, it is necessary to rescale by:

$$\text{new opening} = \text{calculated opening} \times (w_\infty/w_\infty^*) .$$

For this same example, the repository location is nominally at a 300 m depth, however, the mathematically correct scaled location is the inverse of the rescaling calculation, or a depth of 375.35 m. Similarly, offset distances normal to the fracture are scaled in the same manner. For desired offset values of 10, 20, 40, 80, 160, 320, and 640 m, the input values must be 12.51, 25.02, 50.05, 100.09, 200.19, 400.37, and 800.75 m, respectively. Note, however, that these values will not be the correct depth positions for different density or far-field velocity rescaling.

Applying this process to the case with D = 2.67, v_∞ = 1 m/s, μ = 10 Pa·s, and κ = 0.5 (Table 6-3), additional stress induced by the pressurized dike can be computed (as measured at the repository level and as a function of distance from the dike). Figures 6-63 through 6-66 show the induced horizontal, vertical, and shear stress as a function of distance at four different times when the dike tip is below the repository, at the repository, halfway between the repository and the surface, and as close to the surface as the calculations allow (i.e., the time when dike unstably propagates to the surface). Since this calculation is two-dimensional, the other horizontal stress would be calculated by multiplying Poisson's ratio times the sum of the vertical and horizontal calculated stresses.

In these cases, the effect of the dike on the stress field is somewhat different from that commonly observed with hydraulic fractures occurring at depth. Of particular interest are the large size of the tensile zone and the extension of the tensile region along the dike. In most hydraulic fractures, the tensile zone is narrow and the stress becomes compressive just behind the fracture tip. In this case, however, the large size of the dike, the large cavity region, and the pressure gradient dominated by the weight of the magma, serve to generate a large amount of curvature in a sizable area around the tip resulting in a large extension of the tensile zone. For example, Figures 6-63 and 6-64 show the horizontal stress decreasing as the dike tip approaches, but Figures 6-65 and 6-66 show that the stress around the dike remains tensile even when the fracture tip is near the surface (nearly 300 m above the repository).

The vertical stress also becomes tensile ahead of the crack tip, but it is slightly compressive a few hundred meters beyond the side of the dike. In addition, there is a stress reversal behind the tip that is probably due to the adjustment required to match the cavity pressure condition existing at the dike wall (or to match the magma pressure if the fluid front passed this location, as illustrated in Figure 6-66).

Finally, the stress decay length is on the order of several hundred meters. Beyond this point, the effect of the dike is minimal. Clearly, this decay length is a function of the dike tip position and other conditions.

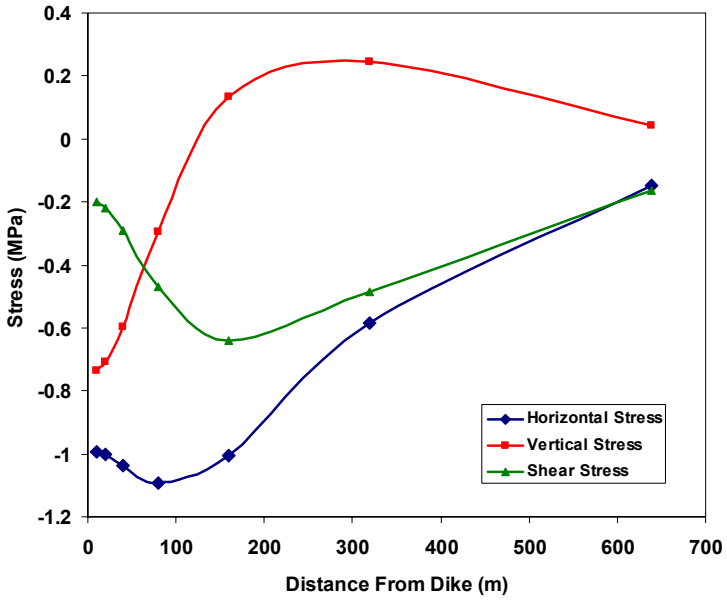

Output DTN: MO0408EG831811.002.

Source: Output Data Calculation Plots.

Figure 6-63. Dike-Induced Stress Changes as a Function of Horizontal Distance when the Tip is at a 411-m Depth

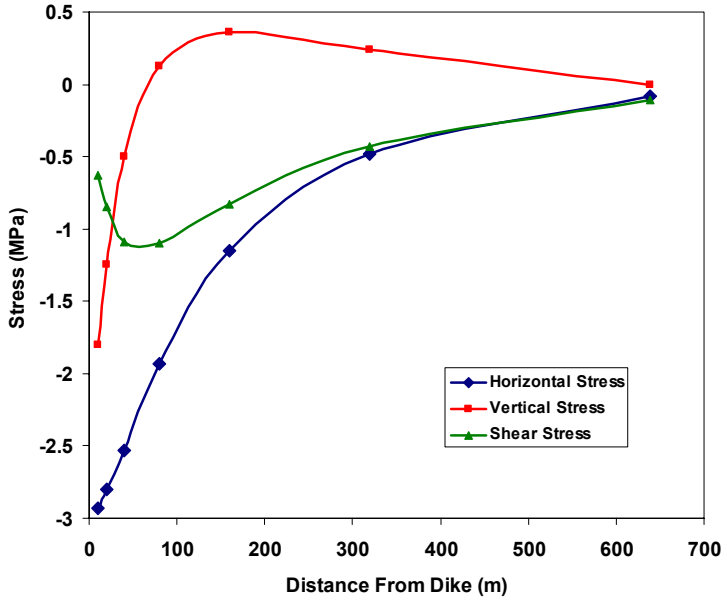

Output DTN: MO0408EG831811.002.

Source: OUTPUT DATA CALCULATION PLOTS.

Figure 6-64. Dike-Induced Stress Changes as a Function of Horizontal Distance when the Tip is at a 300-m Depth

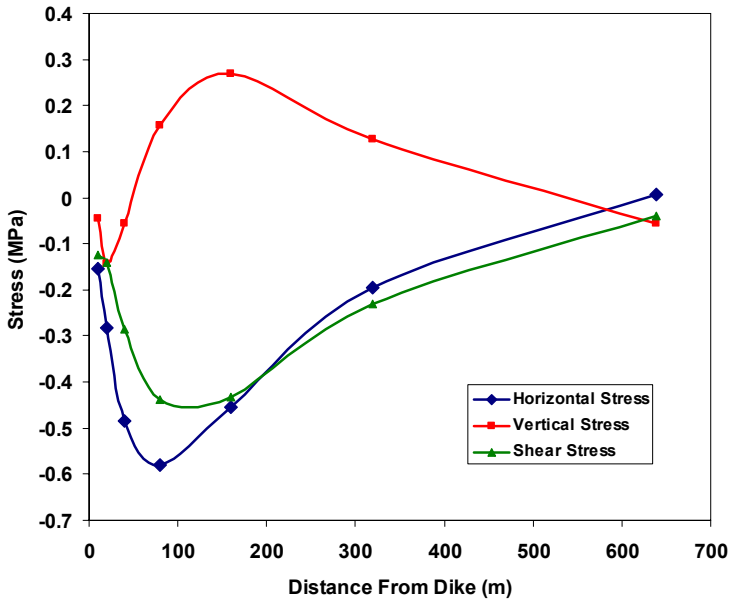

Output DTN: MO0408EG831811.002.

Source: Output Data Calculation Plots.

Figure 6-65. Dike-Induced Stress Changes as a Function of Horizontal Distance when the Tip is at a 150-m Depth

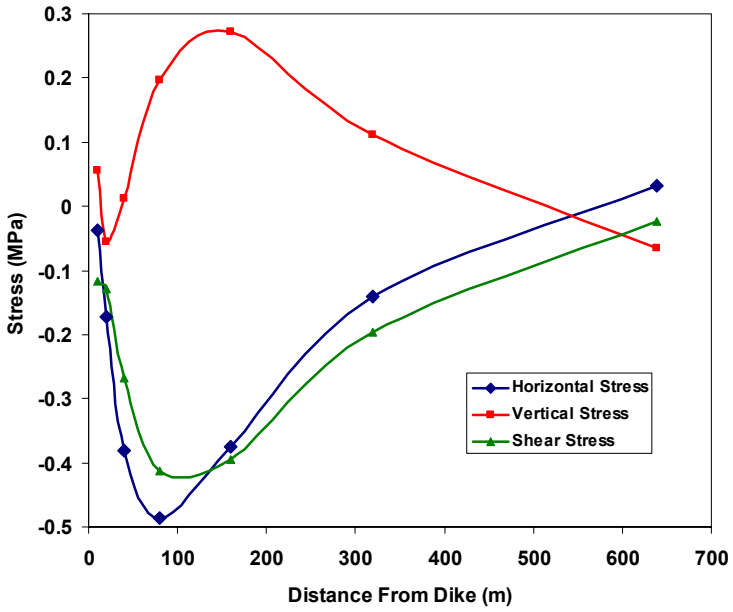

Output DTN: MO0408EG831811.002.

Source: Output Data Calculation Plots.

Figure 6-66. Dike-Induced Stress Changes as a Function of Horizontal Distance when the Tip is at a 16-m Depth

To assess the importance of these stress perturbations on the repository, it is necessary to superimpose them on the existing stress field, determine the resultant effect on the stress field and the stress concentrations around the repository drifts. Given that:

- The minimum horizontal stress is 3.6 MPa (e.g., this analysis was rescaled to a net rock density of 1200 kg/m, which would yield a scaled stress of 3.6 MPa)
- The maximum horizontal stress is somewhat greater (5.5 MPa)
- The overburden stress is about 7 MPa
- The orientation of the maximum horizontal stress is N55°E, and
- The drift orientation is approximately N70°E.

Then, the full stress field in the vicinity of the dike can be calculated.

Figure 6-67 shows the new stress field acting on the repository when the dike is 411 m below the surface.

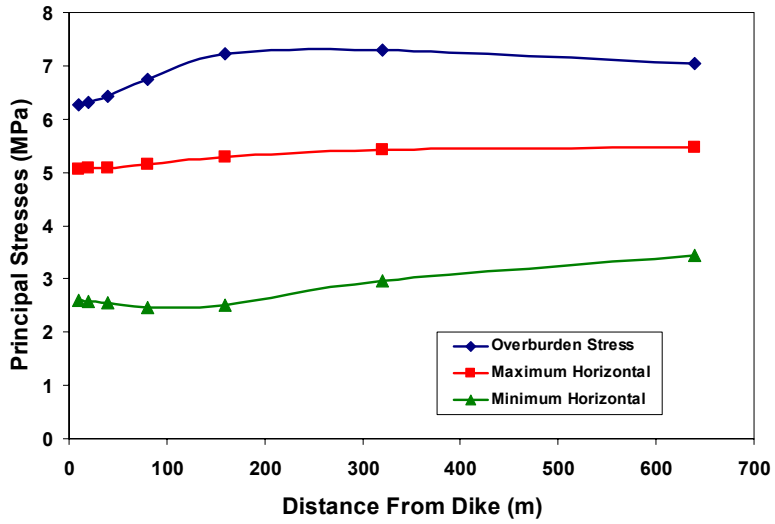

Output DTN: MO0408EG831811.002.

Source: Output Data Calculation Plots.

Figure 6-67. Total Stresses Acting on the Repository when the Crack Tip is at a 411-m Depth

Figures 6-68 to 6-70 show the same results for dike tip positions of 300, 150, and 16 m from the surface. As expected from the previous plots, the largest perturbation on the existing in situ stresses occurs when the dike tip is near the repository and extends for a few hundred meters along it.

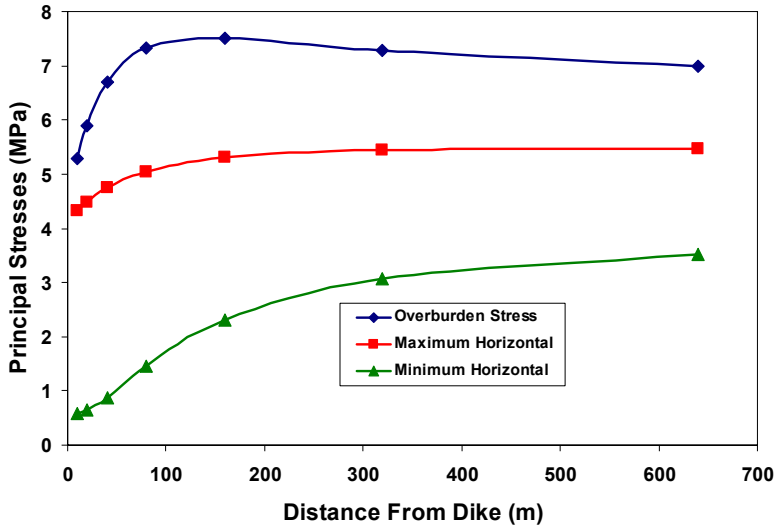

Output DTN: MO0408EG831811.002.

Source: Output Data Calculation Plots.

Figure 6-68. Total Stresses Acting on the Repository when the Crack Tip is at a 300-m Depth

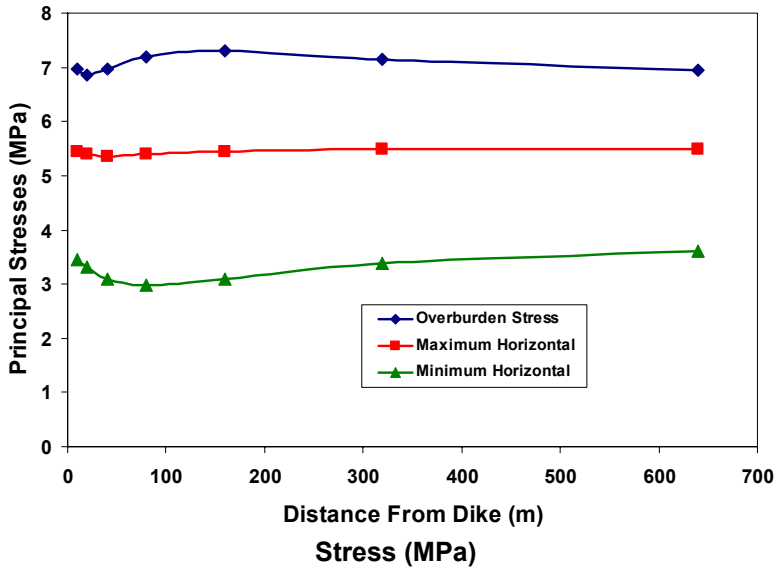

Output DTN: MO0408EG831811.002.

Source: Output Data Calculation Plots.

Figure 6-69. Total Stresses Acting on the Repository when the Crack Tip is at a 150-m Depth

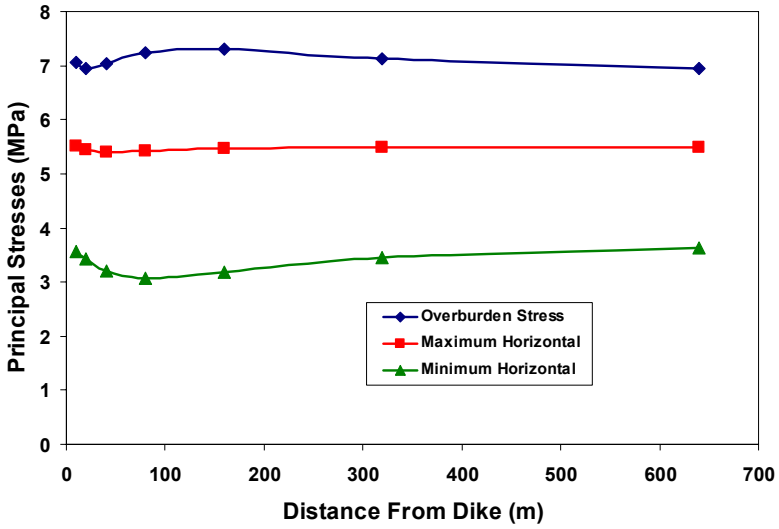

Output DTN: MO0408EG831811.002.

Source: Output Data Calculation Plots.

Figure 6-70. Total Stresses Acting on the Repository when the Crack Tip is at a 16-m Depth

Given the principal stresses acting on the tunnel, the stress concentrations around the tunnel are calculated as a function of angular position. The principal stresses along the tunnel are also calculated for several distances from the dike. Examples are shown in Figures 6-71 through 6-73 for positions along the drift at distances of 10, 40, and 640 m from the dike, when the tip is at repository elevation, 300 m from the surface. In general, the principal stresses are not very different from hoop and axial stresses because the repository is nearly aligned with the stress field, but stress re-orientation does become significant near the dike. The non-symmetric behavior of the stress field is due to shear stresses generated by the dike and by the misalignment of the repository with the stress field. Near the dike, hoop stresses are reduced and less stress will be required to initiate the fracture than is required to propagate it far from the dike.

Taking the minimum cyclic stress values from Figures 6-71 through 6-73, along with data from other positions in the curves, the plot of Figure 6-74 can be developed. This plot shows the minimum principal stress present when the tip is at repository elevation on the drift wall at any angular position as a function of distance. This stress is the minimum pressure required to start a secondary dike at that position. In this case, the most likely place for re-initiation of a new dike is close to the original dike. Nevertheless, at this time the magma is still a long distance from reaching the repository, so the consequences are minimal. By the time the magma reaches the repository, the stress perturbation is small (e.g., Figure 6-66) and the effect on the stress concentrations around the tunnel is minimal. Of course, if the dike is to propagate any significant distance, it must also exceed the minimum stresses shown in Figures 6-67 through 6-70.

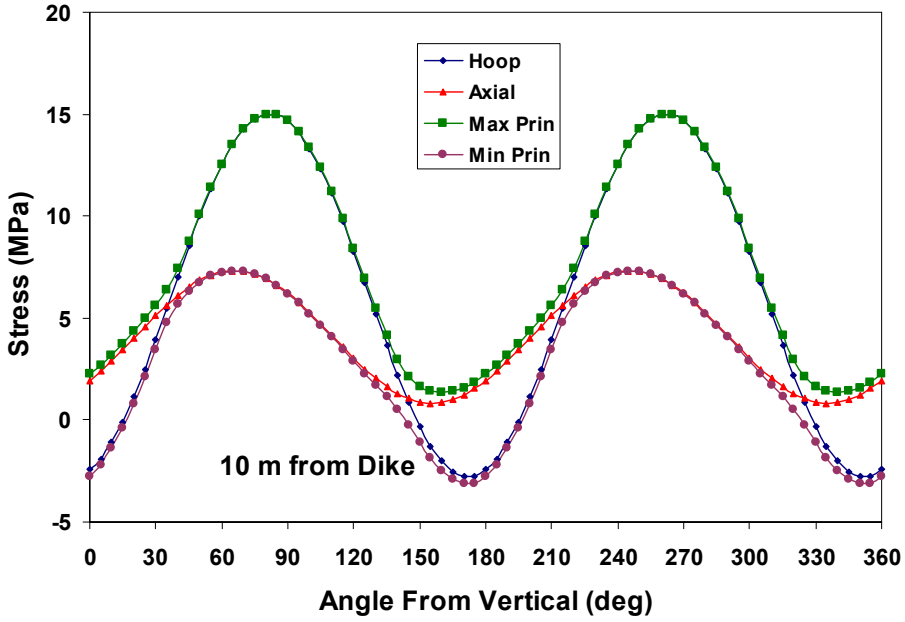

Output DTN: MO0408EG831811.002.

Source: Output Data Calculation Plots.

Figure 6-71. Stresses around the Drift Wall at 10 m from the Dike

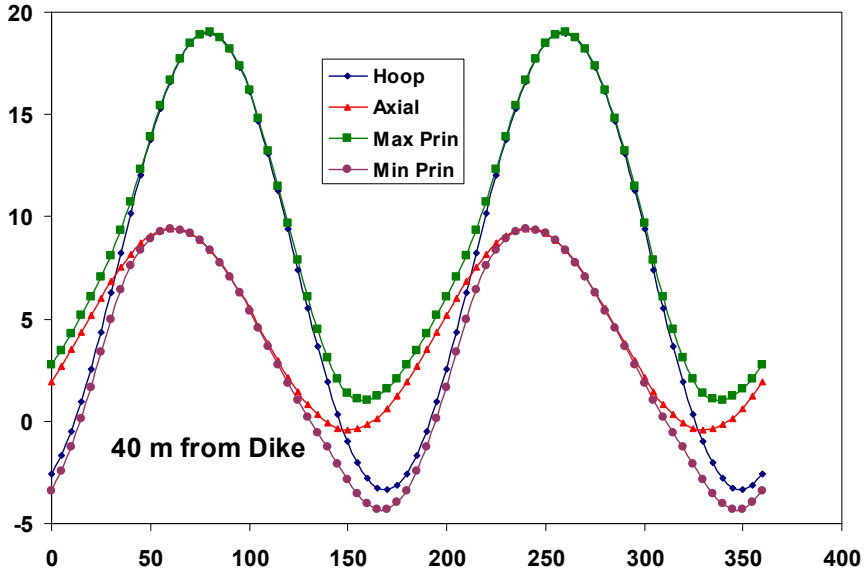

Output DTN: MO0408EG831811.002.

Source: Output Data Calculation Plots.

Figure 6-72. Stresses around the Drift Wall at 40 m from the Dike

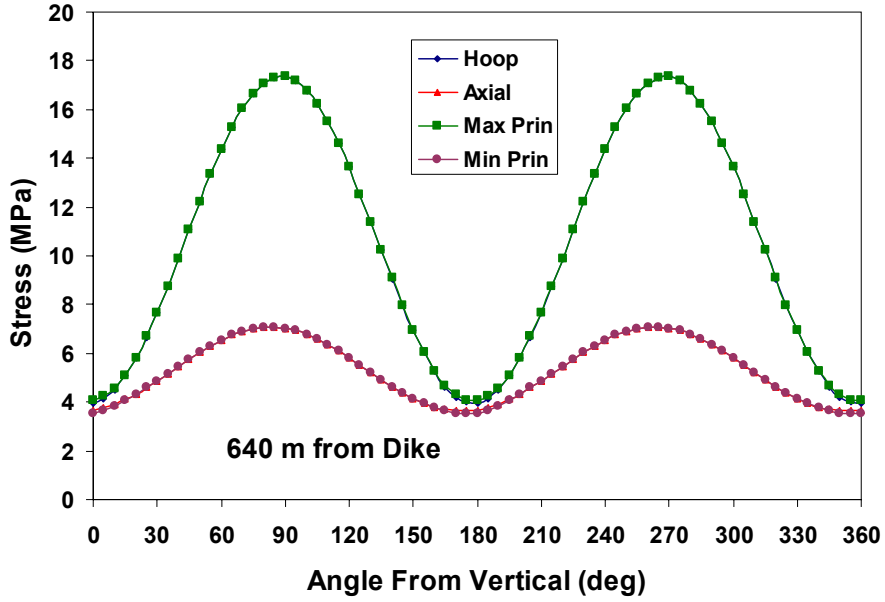

Output DTN: MO0408EG831811.002.

Source: Output Data Calculation Plots.

Figure 6-73. Stresses around the Drift Wall at 640 m from the Dike

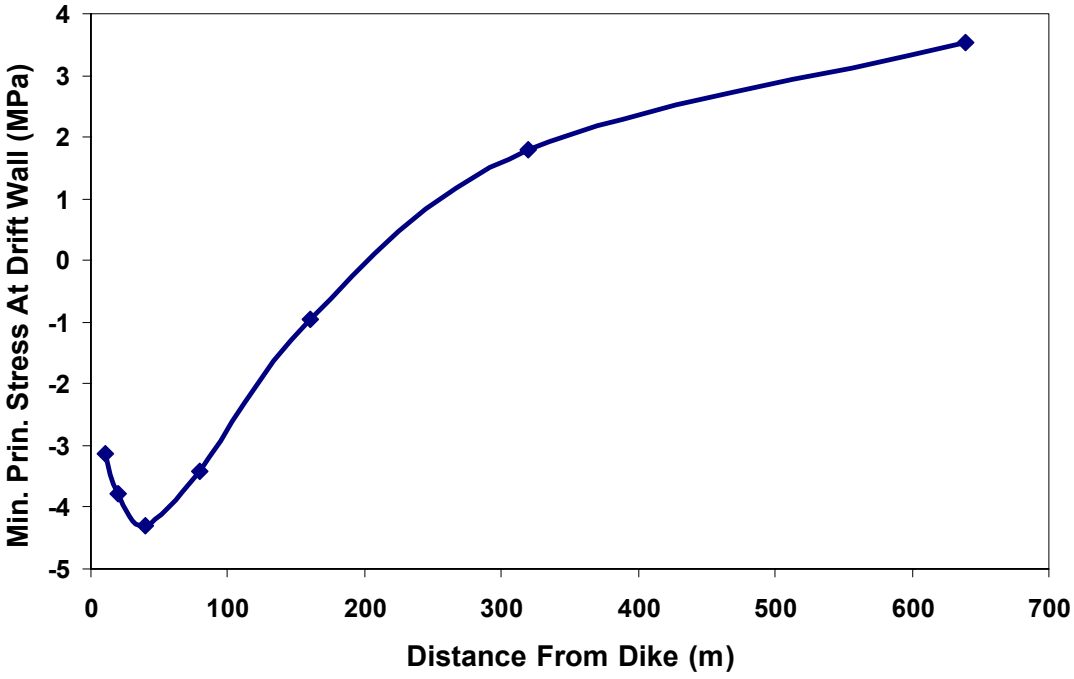

Output DTN: MO0408EG831811.002.

Source: Output Data Calculation Plot.

Figure 6-74. Minimum Principal Stress at the Drift Wall versus Distance from the Dike, When the Tip is at Repository Elevation

Figures 6-67 to 6-70 indicate that stress changes at repository depth due to the dike intrusion have a strong minimum as the crack tip passes but return to less than 1 MPa by the time the magma reaches repository depth. Although the dike-induced stress change causes a minimum in the least horizontal stress at approximately 75- to 100-m away from the dike along the drift (Figure 6-66), the magnitude of the difference (0.6 MPa) is not considered large enough to effect the location of any secondary dike that may form.

6.5.1.4 Magma Cooling Rates

In Section 6.5.1.1, the rate at which a potential new dike (or sill in Case 104) would open under a variety of conditions was discussed. This section presents an analysis of how fast such an opening dike would be chilled by the surrounding cold rock to the extent that magma could no longer feed the crack-tip region and force the crack to continue growing. The analysis follows that of *Final Report of the Igneous Consequences Peer Review Panel* (Detournay et al. [DIRS 169660], Appendix 3.4, p. 53). Following Carslaw and Jaeger (1959 [DIRS 100968], Chapter 11, Section 11.2), the thickness of the chilled margin δ of a sheet of magma in cold rock with no advection is:

$$\delta = 2\lambda_d \sqrt{\kappa t} \qquad \text{(Eq. 6-108)}$$

where:

t = time
κ = the thermal diffusivity

and where:

parameter λ_d is the solution to:

$$\frac{\sqrt{\pi}\Lambda}{k(T_m - T_r)} = \frac{e^{-\lambda_d^2}}{\lambda_d}\left[\frac{1}{1+erf(\lambda_d)} - \frac{T_m - T_s}{(T_m - T_r)erfc(\lambda_d)}\right] \qquad \text{(Eq. 6-109)}$$

where:

Λ = is the latent heat of fusion for the magma

k = is the thermal conductivity

T_m = is the initial magma temperature

T_s = is the temperature at which the magma viscosity becomes high enough to stop dike growth

T_r = the temperature of the surrounding rock

erf and *erfc* = the error function and the complementary error function, respectively

The simplifying approximation is made that all properties of the magma and the host rock are identical. The parameter λ_d is solved for by trial and error given values of the other parameters in the equations.

6.5.1.4.1 "Solidification" Temperatures

The determination of "solidification" temperatures, T_s, is described next.

To stop a newly forming dike by "thermal death," it is not necessary that the magma freeze, completely. As the fraction of crystals increases in the magma, the apparent viscosity of the mixture increases very dramatically. A complete treatment of this phenomenon is beyond the scope of this report. The apparent viscosity, $\mu_A(T)$, of a partially crystallized magma at temperature T below its liquidus temperature T_L is given by:

$$\eta_A(T) = \eta_o(T)\left(1 - \frac{(T_L - T)}{(T_L - T_{\phi_{mx}})}\right)^{-2.5} e^{0.04(T_L - T)} \qquad \text{(Eq. 6-110)}$$

where:

$\mu_0(T)$ = the viscosity of the pure liquid at T

ϕ_{mx} = the maximum crystal volume fraction that will allow flow

$T_{\phi_{mx}}$ = the temperature at which the volume fraction of solids is ϕ_{mx}

This equation is derived from Griffiths (2000 [DIRS 163625], Equation 2 by way of Equation 3) with these postulates:

- The initial temperature is the liquidus temperature, so the initial volume fraction of solids is 0.
- The volume fraction of crystals varies linearly with temperature.
- ϕ_f is equal to ϕ_{mx} with $T_f = T_{\phi_{mx}}$.

Estimates of ϕ_{mx} in the literature, summarized by Griffiths (2000 [DIRS 163625]), range from 0.4 to 0.6; the central value 0.5 has been used in this analysis. Temperatures at which the magma is 50% solidified are derived from figures for the appropriate water content in Detournay et al (2003 [DIRS 169660], Appendix, Table 2E). Temperatures from the figures were adjusted downward by the difference in liquidus temperature between that source and *Characterize Eruptive Processes* (BSC 2004 [DIRS 169980], Table 6-4, p. 6-23) in order to obtain consistent values for the analysis. For water contents not calculated by Detournay et al (2003 [DIRS 169660]), temperatures were interpolated or extrapolated from values at other water

contents. Viscosities of the pure liquid were calculated at the liquidus with the method of Shaw used in *Characterize Eruptive Processes at Yucca Mountain, Nevada* (BSC 2004 [DIRS 169980]). This will underestimate the effective viscosity because it

- Does not take into account the increase in viscosity of the pure liquid as it cools
- It does not take into account any increase in viscosity due to increasing silica content of the remaining liquid when crystals begin to form
- It does not consider the existence of a glass transition temperature, which will cause very large increases in the viscosity of the remaining liquid.

Using this relation, the apparent viscosity of partially crystallized alkali basalt magmas of several water contents as functions of temperature both above and below their liquidus temperatures, are shown in Figure 6-75. The effect of only 10 to 20 percent of crystals on the rheology of the partially crystallized magma is dramatic. This increase in percent crystals results in an increase in viscosity of 1.5 to 2 orders of magnitude, as roughly indicated by the highlighted region in Figure 6-75.

In light of the very rapid increase of apparent viscosity as temperatures drop, the temperature at which the apparent viscosity reaches 1000 Pa·s has been chosen as T_s in Table 6-11.

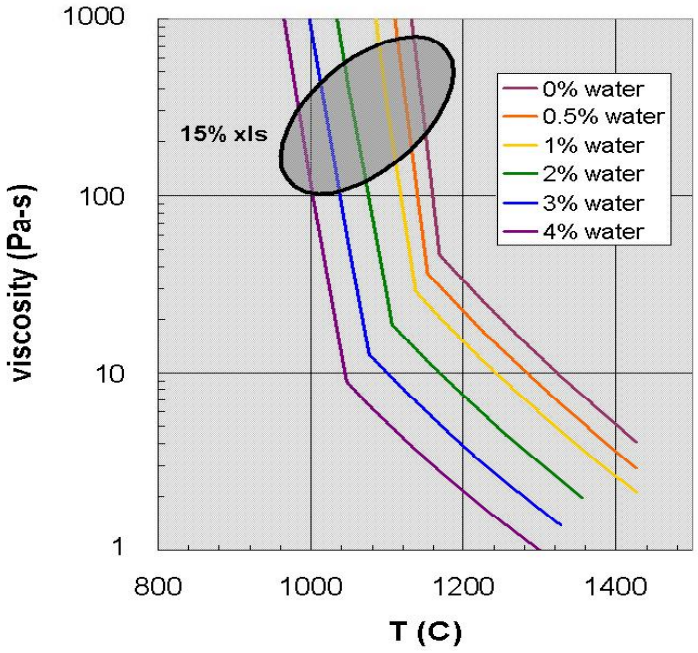

Output DTN: MO0408EG831811.002.

NOTE: Liquidus = a line drawn through the break in slope of each plotted curve.

Figure 6-75. Apparent Viscosity of Alkali Basalt Magmas During Crystallization

6.5.1.4.2 Thermal Stoppage of New Dike

From the input values shown in Table 6-11, the time needed for new dikes to solidify in cold country rock can be calculated. These times vary as the square of the thickness of the dike. The results are illustrated in Figure 6-76. The points indicated in the legend with the red square labeled "new dike" are plotted in filled dark blue symbols as follows:

- For the triangles bottom to top, respectively: the time for a new crack to reach the widths plotted for the most extreme conservative Case 103 of Section 6.5.1.2 when the crack has initiated parallel to the drift and propagated 3.67 m, 7.79 m, and 16.04 m. By the time a new dike has reached 16 m from the drift, the most favorable direction for it to continue opening will be normal to the drift axis.

- For the squares bottom to top, respectively: the time for a new crack to reach the widths plotted for Case 105 where the crack has initiated perpendicular to the drift axis and propagated to a range of 3.08 m, 5.08 m, and 43.8 m.

- For the circle: the highly unfavorable case of sill formation where the crack has reached a range of 3.67 m for Case 104.

Clearly, such cracks will not be able to grow to any appreciable width before they are halted by solidification.

6.5.1.5 Synthesis: Likelihood of the Dog-Leg Scenario for Effusive Flow

Figure 6-76 shows time and width points from calculations from Section 6.5.1.2 of the growth history for a new dike under the most favorable assumptions for growth of Case 103. The new dike, in that case, started out at 1-mm half-width and took 13 s to grow to a width of only 11 mm at a range of 3.67 m from the edge of the drift. At greater ranges the time to reach the same width is greater (20 s at 8 m from the drift, see Figure 6-59). Comparing this growth history for a constant viscosity magma with the results of the chill-zone growth rate, it is seen that the dike will never be able to propagate more than a few meters from the drift because the magma will chill rapidly, blocking off the flow of fluid to drive the crack growth. Note, however, that the effect of advection on the heat balance has been neglected in deriving this result.

In Section 6.3.7.1, it was shown that during an encounter with a drift, for the more realistic case of horizontal stresses equal to half the vertical stresses, the crack will intersect the drift before the magma to wit:

- For a relatively slow magma rise velocity of 1 m/s, the crack tip will lead the magma by about 40 s if the magma viscosity is 10 Pa·s (Figures 6-14 and 6-16). Therefore, before any magma can be diverted into the drifts, the crack will already be more than 50 m above the drift. For a more viscous magma (40 Pa·s), the tip has already broken out at the surface before the magma reaches the drift level (Figure 6-18).

- For a magma velocity of 5 m/s, the tip has already broken out at the surface before the magma reaches the drift level (Figure 6-14, for example).

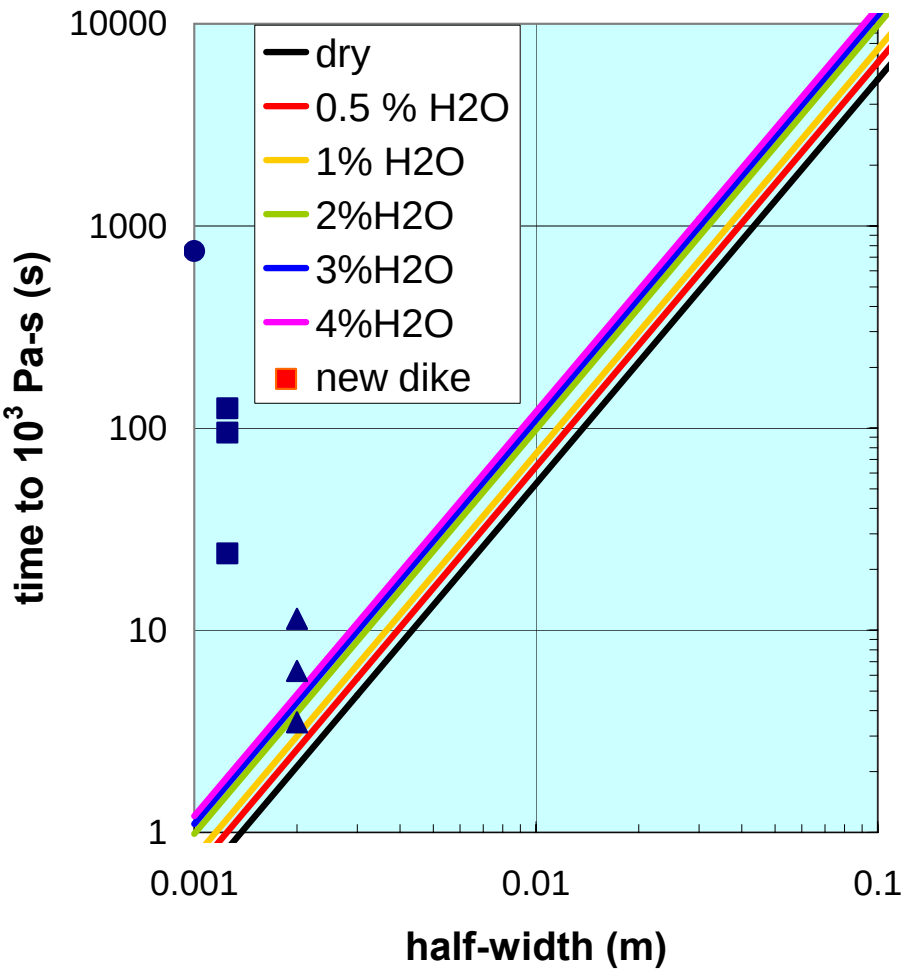

Output DTN: MO0408EG831811.002.

NOTES: Blue triangles represent times calculated from Equation 6-108 for Case 103 opening to 2-mm half-width.

Blue squares represent times for Case 105 opening to 2.5 mm; Blue circle represents time for Case 104.

Figure 6-76. Time to Chill a Dike from Liquidus Temperature to the Temperature at Which the Apparent Viscosity is 1000 Pa·s, the Assumed Effective "Solidus" Temperature

Results of Section 6.4.8 indicate that, as magma continues up the original dike path while also being diverted into the drifts, the vertical velocity will be lower directly above a drift than at the midpoint between two drifts. This result can be seen most clearly in Figure 6-40, which is a snapshot taken shortly after magma first encounters a drift. The effect persists at least as long as the simulation ran (Figure 6-42). It is also seen that pressures in the dike above the drift are almost an order of magnitude lower than between drifts (Figure 6-43).

Based on the results discussed in the preceding paragraphs, it is concluded that the most likely scenario for magma to erupt to the surface after intruding the drift complex is for it to continue along the trajectory of the original dike. The analysis report *Characterize Eruptive Processes at Yucca Mountain, Nevada* (BSC 2004 [DIRS 169980]) describes the basic processes by which the

sheet flow of a dike is transformed into the more concentrated flow of a conduit, and that is considered the most likely outcome of a dike intersecting the repository.

6.5.2 Secondary Dike Propagation for Two-Phase Flow

Two-phase flow occurs when the liquid and vapor phases of the magma move at different velocities but are still closely coupled. Such phenomena may occur in two ways.

First, as the magma rises into the advancing dike before it reaches the drift, the vapor will expand rapidly as the magma rises because of the very low cavity pressures, and the flow of magma will accelerate upward (the only direction in which it is unconstrained) until it reaches the drifts. When magma reaches the drifts, the expansion will then occur both into the drift and upward into the crack tip, which precedes the magma front. This would lead to an intrusive equivalent to pyroclastic behavior sometimes seen when volcanoes erupt. Pyroclastic deposits of this type are discussed in Section 6.5.2.1.

Second, magma sometimes encounters large amounts of water, either surface water or groundwater, that will trigger hydrovolcanic flow, and possibly the injection of hydrovolcanic material up an existing crack. A natural occurrence of this type of dike is discussed in Section 6.5.2.2, followed in Section 6.5.2.3 with an analysis of pressures and masses of water needed to drive such an event.

6.5.2.1 Pyroclastic Flow

The possibility of secondary dike propagation will depend on the nature of the magma flow into drifts. The observed record of basaltic volcanism in the Yucca Mountain region over the past 10 Ma indicates that volcanic centers have been constructed out of both effusive and pyroclastic deposits (BSC 2004 [DIRS 169980], Section 6.3.3). Therefore, pyroclastic filling of drifts must be considered to be as probable as effusive flow, which has been addressed above (Section 6.4).

Pyroclastic flow requires expansion of the volatile component of magma, tearing the magma into fragments and accelerating them. A summary description of the types of pyroclastic deposits that can be formed provides an interpretation of the corresponding depositional environments (Valentine et al. 2000 [DIRS 171641], pp. 194-196, Table 1). Deposits range from poorly sorted to vertical coarse-tail graded. Zones may be characterized by abundant flattened, fluidal splatter clasts; “rags and tatters” extending down flow from splatter clasts; or matrix material and quench margins within splatter clasts. These are indicative of deposition while hot with considerable syndepositional shear and dragging, folding or coalescence of clasts during lateral transport. Many of the formations were deposited on slopes that are less steep than the angle of repose, which is consistent with derivation from pyroclastic density currents rather than being the result of avalanching down a steep slope. Such deposits are part of a spectrum ranging from lava flows remobilized from hot, fluid clasts that have accumulated on the ground to widespread high-energy ignimbrites (Freundt 1998 [DIRS 171642]).

Of the many potential manifestations of pyroclastic flow into dikes, only remobilization of splatter clasts into a mass similar to an effusive “lava” flow and high-energy ignimbrite have the potential to generate pressures high enough to open pre-existing cracks at repository depth. The former is indistinguishable from the effusive secondary dike analysis of Section 6.5.1. For the

high-energy ignimbrite driving a secondary dike, the pressure would derive from the kinetic energy of the flow down the drift. Velocities in excess of 300 m/s would be needed with a flow density of 100 kg/m^3; this is not a likely flow environment (see Section 6.5.3 below) and, in any event would be unlikely to generate sustained pressures.

6.5.2.2 Analogue Hydrovolcanic Occurrence

A natural example of hydrovolcanic magma intrusion is found at Obsidian Dome, California, where fractures, filled with clastic intrusive material and extending away from a dike that feeds the dome, were observed and sampled by a scientific borehole (Heiken et al. 1988 [DIRS 165566]).

Boreholes were cored through the 51-m-diameter conduit of Obsidian Dome, the largest of the Inyo Domes, and through an unvented portion of the intrusion (dike) located 1 km to the south. Hydroclastic-bearing fractures were intersected in both boreholes:

- 7-cm to 40-cm-thick fractures in the welded basaltic scoria and quartz monzonite country rock are adjacent to the conduit at depths of 400 to 411 m and 492 to 533 m; they contain gray, clastic deposits, which show truncated cross bedding and convolute bedding.

- Adjacent to the dike, 1 to 8 cm thick massive fracture fillings occur at depths of 289 to 302 m (129 m east of the dike) and 366 to 384 m (95 to 87 m east of the dike).

The characteristics of these fractures and fracture-fillings were analyzed by Heiken et al. (1988 [DIRS 165566]) to derive the conditions under which they formed. They found that the intruded fluid (a mixture of supercritical water and other gases containing fragments of host rock and juvenile magma) had an estimated bulk density near that of water, a viscosity in the range 0.2-0.8 Pa·s, and a fluid overpressure (i.e., pressure in excess of the confining stress) of 5 to 9 MPa. These overpressures are consistent with either vapor exsolution from decompressed magma or rapid heating of groundwater by mixing with magma. However, the textural and chemical similarity of the hydrovolcanic clasts to phreatomagmatic tephra that appears late in the explosive eruption sequence, suggests that the latter hydrovolcanic mechanism caused the fracturing. Based on details of the structures observed in the injected material, flow speeds in the fracture were estimated to be 25-200 m/s.

Although the magma compositions involved were rhyolitic rather than basaltic, analysis of this mechanism may provide bounds for two-phase flow processes at Yucca Mountain.

6.5.2.3 Analysis of Hydrovolcanic Injection from the Drift into an Existing Crack

This section reports an analysis of single-phase flow conducted to approximate hydrovolcanic magma flow into a preexisting crack (assumed to be initially 1-mm thick as in Section 6.5.1) using magma properties representative of those derived by Heiken et al. (1988 [DIRS 165566]) to determine the feasibility of a similar phenomenon occurring at Yucca Mountain. The analysis used values listed in Table 6-15. Those parameters derived from sources external to this document (direct input) are also listed in Table 4-1. Other values are included in Table 6-15 where data values have been assumed. Young's modulus values for the hydrovolcanic magma

were selected in steps to cover the range shown in Table 4-1 for Young's modulus that would apply to hydrovolcanic magma. This is addressed further in the discussion on bulk modulus below.

Table 6-15. Input Parameters for Analysis of Hydrovolcanic Injections into an Existing Rock

	Source	Value
Overburden (m)	BSC 2004 [DIRS 166107]	300
Lateral Stress Coefficient	BSC 2004 [DIRS 166107]	0.5
Young's Modulus of Rock (GPa)	Detournay et al. [DIRS 169660]	15
Hydrovolcanic Magma Pressure (MPa)	Heiken et al. (1988 [DIRS 165566]	9 MPa over confining stress
Hydrovolcanic Magma Viscosity (Pa·s)	Heiken et al. (1988 [DIRS 165566]	0.5
Hydrovolcanic Magma Young's Modulus (MPa)	Selected Value	50, 20, 10, 5

The pressure selected corresponds to the upper limit estimated by Heiken et al. (1988 [DIRS 165566]), while the viscosity is the center of their range, as discussed in Section 6.5.2.1.

The analysis consisted of two groups of simulations using the distinct element code UDEC V3.14 (BSC 2004 [DIRS 172322]). Initial simulations were done with a constant pressure source (12.6 MPa or 9 MPa above the overburden stress) and fluid moduli of 50 MPa, 20 MPa, 10 MPa and 5 MPa. Results of these simulations include the crack width history at selected locations, the location of the fluid front in the opening crack, and the velocity of the fluid front. The simulations were carried out at three different scales. Figure 6-77 illustrates the progressive opening of the crack in terms of the crack opening (initially 1 mm) at several ranges from the edge of the drift for the finely zoned (small scale) simulation with a modulus of 50 MPa for the injected fluid. The maximum crack width is about 27 mm, which is the same as the maximum derived from the intermediate scale simulation. By 1.65 s the magma has almost reached 32-m, where the crack width has opened to about 8 mm. The maximum opening for the large-scale simulations is about 170 mm at about 110 m from the dike (not shown); the opening at the surface is about 100 mm. These simulations indicate that a hydrovolcanic dike would reach the surface in less than 20 seconds, and they show that the progress of the magma into the crack depends strongly on the modulus of the intruding fluid.

Figure 6-78 illustrates the position of the fluid front in the crack as a function of time for each of the calculations. At early times, the smaller scale simulations show the magma farther up the joint than do the larger scale results, probably due to better treatment of the flow near the source. However, as seen at later times in the flow, the magma in the large-scale results accelerates in response to the decreasing confinement as the surface is approached. The two large-scale simulations indicate that the hydrovolcanic dike will reach the surface in 6 to 10 seconds. Linear extrapolation of the intermediate scale simulations supports this conclusion, although the time to breakout would be about twice as long (18 s).

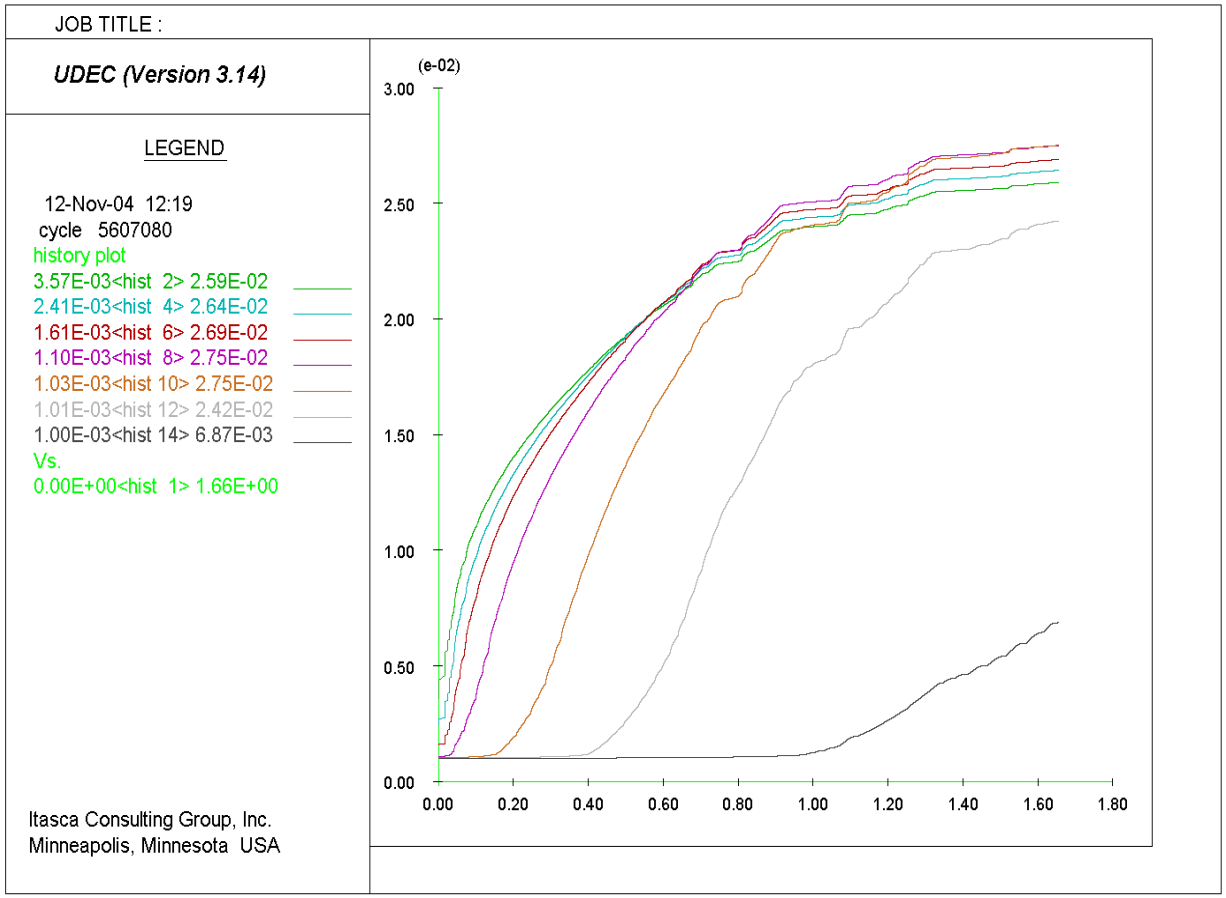

Output DTN: MO0408EG831811.002.

NOTE: Horizontal axis is time in seconds and vertical axis is crack opening in meters. History plots are for distances into the crack from the edge of the drift of 0.46 m, 0.92 m, 1.83 m, 3.67 m, 7.79 m, 16.04 m, and 32.14 m, as indicated in LEGEND from top to bottom, respectively.

Figure 6-77. Joint aperture (in meters, but note factor of 0.01 in vertical scale) at seven distances from the drift wall along an initial 1-mm crack

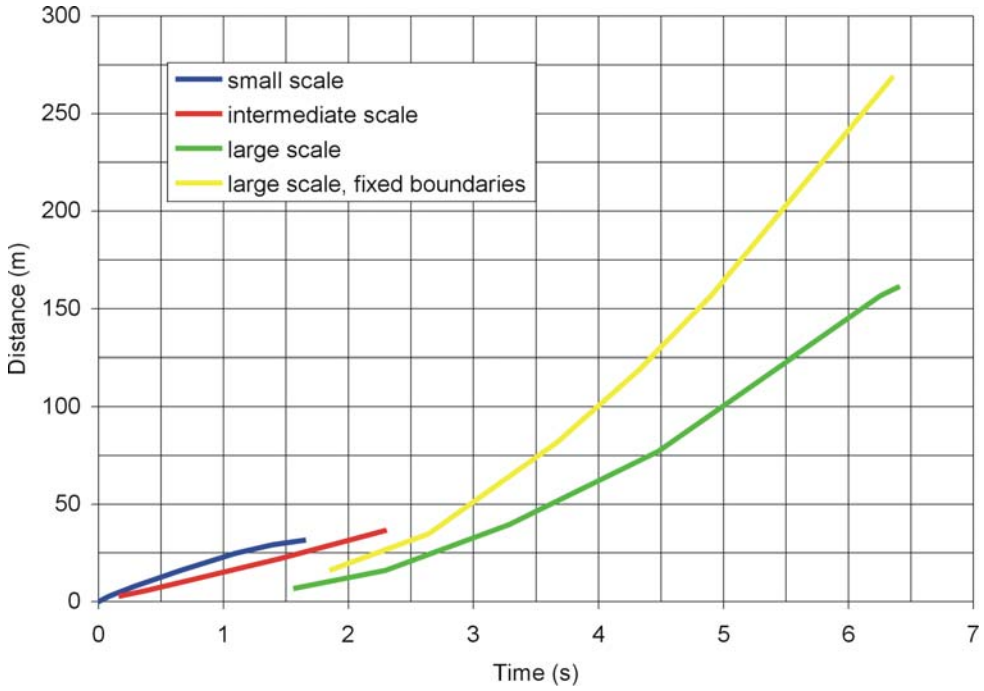

Output DTN: MO0408EG831811.002.

Figure 6-78. Location of the Magma Fluid Front (Relative to Edge of Drift) as a Function of Time for Four Simulations with Varying Scales

The simulations of "thermal death" in Section 6.5.1.4 have not been applied to analysis of a secondary dike initiated from the hydrovolcanic event because the physical state of the magma under hydrovolcanic conditions is not well enough understood to permit an estimate of its thermal conductivity. However, the addition of heat loss to the analysis of a hydrovolcanic event in the drift may limit either the propagation of a secondary fracture or the movement of magma in the secondary fracture.

Figure 6-79 shows the velocity of the fluid front for all four simulations. The velocities range from approximately 6 m/s to 77 m/s. The velocity of the fluid front will be close to the magma flow velocity because the analysis represents as a single phase, and the bulk modulus is at least four times the pressures. These results are consistent with the findings of Heiken et al. (1988 [DIRS 165566]), which were obtained with analytical forms, increasing confidence in the numerical approach.

The results illustrated in Figures 6-77 through 6-79 describe events that would occur if a source of low-viscosity fluid at a constant pressure of 12.6 MPa were exposed to pre-existing cracks. They demonstrate the range of results that can be expected given variations in mesh size and boundary conditions.

For a hydrovolcanic source of the type described above, given a crack width of 0.2 m, an average crack speed of 50 m/s, and a strike length of 10 m, the total volume flow rate would be 100 m^3/s, which would sum over 10 s to only 1000 m^3 or 1000 Mg at a bulk density near that of water.

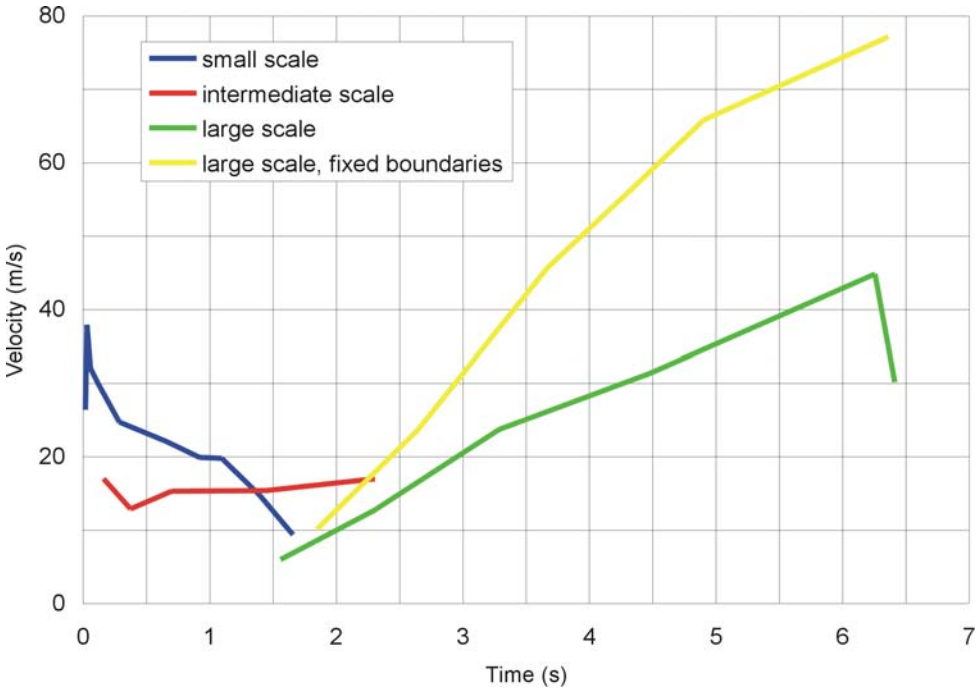

Output DTN: MO0408EG831811.002.

Figure 6-79. Speed of Fluid Front as a Function of Time for Four simulations of a Hydrovolcanic Dike with Varying Scales

This is not a very large mass of water for a perched water table, but is too large to be credible as water collected in the bottom of a drift.

An important issue not addressed by the above calculations is whether a pressure of 9 MPa above overburden can be maintained for the 6 to 18 seconds needed for the hydrovolcanic dike to reach the surface. For a non-hydrovolcanic source, where the pressure would derive from the kinetic energy of a flow down a drift, velocities in excess of 30 m/s would be needed with a flow density of 1000 kg/m3; this is not a likely flow environment (see Section 6.5.3 below) and, in any event would be unlikely to generate sustained pressures. This simple approximation indicates that insufficient pressures would accompany intrusion into drifts to sustain a hydrovolcanic dog-leg unless magma were to come in contact with a substantial source of underground water, which is not considered likely at Yucca Mountain.

To develop a portrayal of a hydrovolcanic breakout from an emplacement drift with a limited amount of water, an analysis was done in which a given mass of liquid water was postulated to mix rapidly with magma forming a hot, high pressure volume of gas within a drift. Note that such an event is in itself highly unlikely, because:

- This would need the actual presence of a ponded water, which is not expected given the geologic environment at the repository drifts
- The efficient conversion of thermal to mechanical energy requires thorough commingling of magma and water.

Most magma/water encounters do not result in hydrovolcanic activity.

The hydrovolcanic breakout was approximated as a sphere tangent within the 5.5-m diameter drift, with a pressure determined from the equation of state of water (extrapolated from Babcock & Wilcox 1963 [DIRS 170614]) contained in the spherical volume minus a volume of magma equal to 60 percent of the spherical volume and the temperature obtained by mixing the same masses of liquid water and magma. This sphere of hydrovolcanic material, consisting of about 100,000 kg of magma plus the 100-300 kg of water vapor, was then allowed to expand into the drift away from the intruding magma at a rate controlled by its sound speed. The resulting pressure histories for 100 kg, 150 kg, 200 kg and 300 kg of water mixed with magma (illustrated in Figure 6-80) were then used as source functions in a second set of calculations.

The bulk modulus of the fluid is expected to decrease with decreasing pressure; for an ideal gas the bulk modulus is equal to the pressure. For this second set of calculations, the modulus of the injected fluid was taken as a parameter with a range of values to illustrate the combined effects of a decaying pressure source and the changing modulus of the injected fluid using the variable-pressure sources of Figure 6-80. In addition, to account for the fact that loss of material injected into the crack would lower the source pressure further, calculations with 150 kg or more of water also tracked the amount injected and reduced the source pressure further. The peak masses of hydrovolcanic material injected into the opening crack for initial water masses of 150 kg, 200 kg, and 300 kg were about 5600 kg, 11000 kg and 14000 kg leading to pressure reductions of 5, 11, and 14 percent at 3, 1.3 and 0.7 seconds after the magma-mixing event, respectively. An additional calculation was done with both pressure and modulus equal to 12.6 MPa.

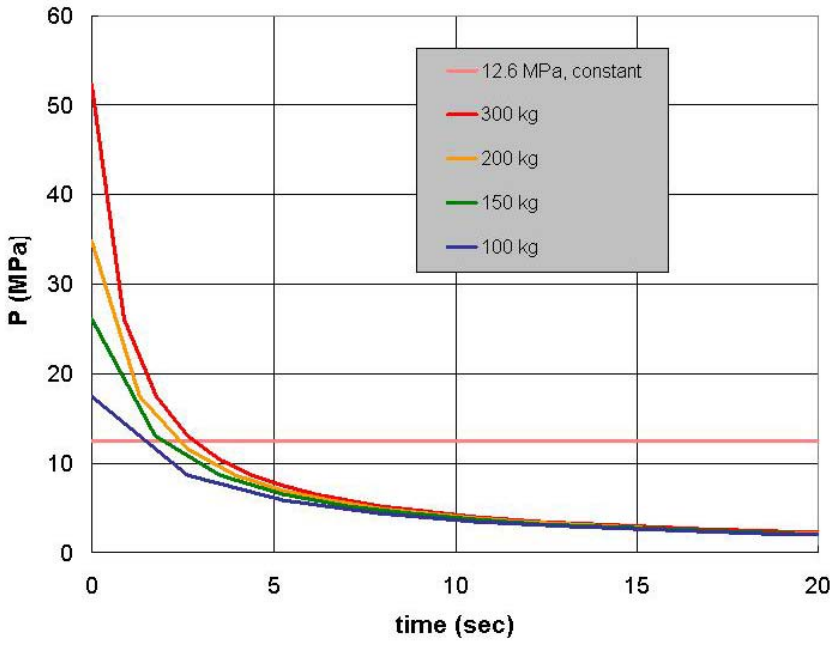

Output DTN: MO0408EG831811.001.

Figure 6-80. Pressure histories used to drive simulations of hydrovolcanic dike injection

Figure 6-81 illustrates the position of the magma height in the crack as a function of time for different water amounts and pressure. The dashed lines were derived after a rezoning of the calculation to permit running to later times without encountering round-off errors in these single precision calculations. The later-time results for greater water masses were also calculated with the same type of rezone. All but one of the calculations indicate that the hydrovolcanic dike is expected to reach the surface. A modulus of 5 MPa is used only for the 100 kg case because that is the only one for which the pressure drops below 5 MPa before the injected fluid reaches the surface. As higher proportions of water are incorporated into the source, the breakout occurs progressively earlier. Since all of the time varying pressure sources start out with higher pressures than the constant pressure source, the early progress of the latter is retarded. But the fixed pressure source soon overtakes the smaller time-dependent sources as their driving pressures fall well below 12.6 MPa.

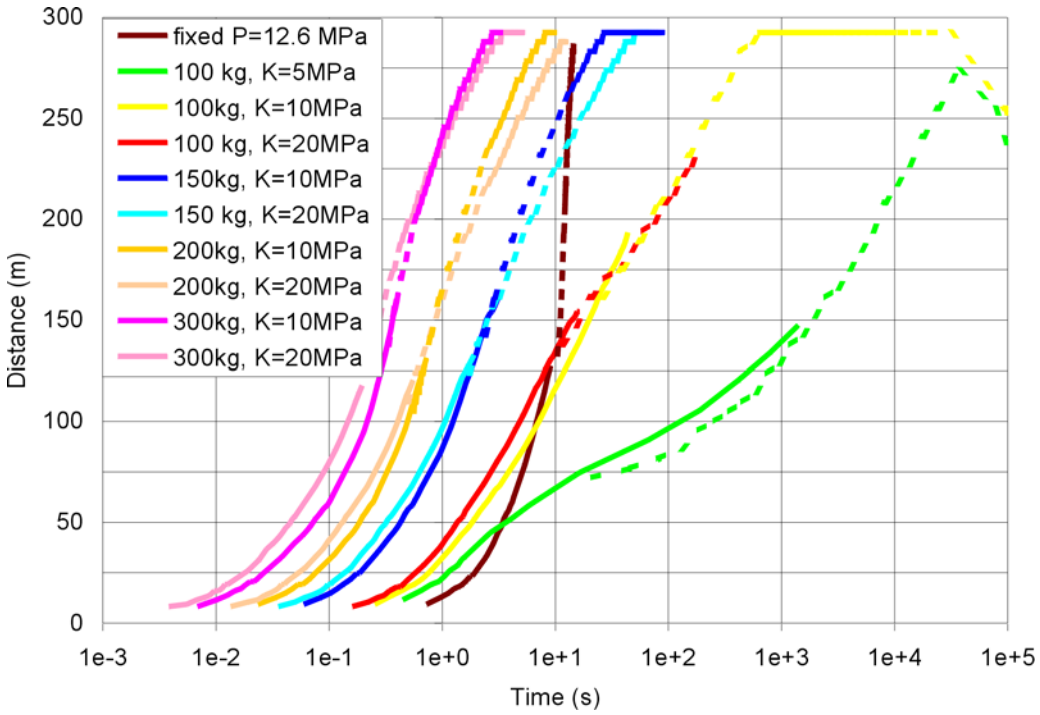

Output DTN: MO0408EG831811.002.

Figure 6-81. Height of Fluid Front (above drift) vs. Time For Simulated hydrovolcanic Injections

The results in Figure 6-81 fall into close clusters according to water mass except for the 100-kg water results with a 5 MPa modulus, which show considerable softening at later times (note that the time scale is logarithmic). For model assumptions (i.e., impermeable crack walls and no heat loss and viscosity change), once the magma is injected in an open fracture, some mass of injected magma will eventually reach the ground surface because of positive buoyancy:

$$\rho_m < \frac{1}{g}\frac{d\sigma_h}{dz} \qquad \text{(Eq. 6-111)}$$

Events involving more than 150 kg of water can be expected to result in venting, but the amount of material vented would never exceed the initial pyroclastic mass of 100,000 kg. Events involving much less than 100 kg (say 50 kg or lower) would be expected to lead to formation of pyroclastic dikes such as those studied by Heiken et al. (1988 [DIRS 165566]) at Obsidian Dome, but would not be expected to lead to any significant venting of primary magmatic material.

This result is consistent with the assessment of Crowe et al. (1986 [DIRS 101532], p. 59) that there are "two important categories of evidence for the possibility of hydrovolcanic activity at Yucca Mountain: (1) theoretical models of magma/water interaction show that hydrovolcanic explosions are possible at the Yucca Mountain setting, and (2) geologic evidence shows that explosions that could lead to exhumation of a repository at Yucca Mountain are unlikely." However, they are referring to magma-water interactions at the water table or at a perched water table, not to small amounts of hypothetical ponded water.

Based on the results of these few calculations, it does appear that a secondary hydrovolcanic dike could reach the surface if it is driven by a sufficient quantity of water. However, such cracks would be narrow, so much so that no entire waste package, no matter how deformed would be able to traverse it. Thus, the only possibility for waste form to escape by such a route would be if it were removed from its waste package; the analysis in Section 6.4.8.1 demonstrates that that is highly unlikely, if not impossible.

Because of the narrowness of the cracks involved in the hydrovolcanic vent as described, waste could only reach the surface if it is removed from a waste package and the analysis in Section 6.4.8.1 shows that no through-going flow is expected in waste packages. However, there is no mechanism for exposing the waste in this hypothetical case. Furthermore, accumulation of sufficient quantities of water to enable this scenario through seepage is highly unlikely, even assuming the upper-bound mean annual seepage rates for the glacial transition climate state (BSC 2004 [DIRS 169131], pp. 207-208, Tables 6.8-1 and 6.8-2). Drift orientation, invert water retention characteristics, and the highly permeable nature of the host rock will preclude accumulation of these relatively large quantities of water. Condensation water, as described in *In-Drift Natural Convection and Condensation* (BSC 2004 [DIRS 164327]) is also not expected to accumulate for the same reasons.

6.5.3 Alternative Analysis of Pyroclastic Flow: the "Woods et al." Scenario

The paper by Woods et al. (2002 [DIRS 163662]) that contained the alternative analysis of pyroclastic flow from a dike into a drift, discussed in Section 6.4.7.2, also presented a scenario by which magma might be diverted from the original trajectory onto an alternative path to the surface. This alternative "dog-leg" analysis is summarized briefly in Section 6.5.3.1 and discussed in Section 6.5.3.2.

6.5.3.1 Discussion of Alternative Analysis

Woods et al. (2002 [DIRS 163662]) described a concept in which, after a dike intersected a drift at Yucca Mountain, the drift was filled with magma and the magmatic system, including the drift, was repressurized; this repressurization generated a new opening some length down the

drift or caused a magma flow to the surface through access drifts. In their model, this new opening propagated to the surface and became the main opening of the system. Specifically, they state (p. 19-3):

> "The precise location of the preferred magma pathways from the drift to the surface will depend on many factors … we compare three different cases which might bound the range of possibilities … (Case 1) that the deep dike path continues to the surface without any major perturbation by the repository system, (Case 2) that the pathway to the surface is shifted to a new position, 500 m along a drift with an area of 20 m^2, and (Case 3) that the magma uses the main access drift to the repository for flow to the surface… Breakout from the access drift, which is likely to be closed at each end, may occur at a variety of locations (e.g., structural weaknesses, ventilation shafts)… in the case in which the flow is diverted along a drift, the flow pressure is elevated relative to lithostatic in the upper kilometer or so as the flow advances along the drift (case 2) and main drift (case 3) towards the surface. … If a conduit formed initially in response to flow down a 4-km-long access drift, these large flow pressures would be likely to cause significant widening of the conduit or the formation of additional conduits."

6.5.3.2 Discussion of Woods et al. Model for Pyroclastic Flow from Drift to Surface

The calculations of Woods et al. (2002 [DIRS 163662]), especially when viewed in conjunction with the high pressure accompanying the shock waves calculated in their model of magma flow into drifts (see Section 6.4.7.2.1), might lead one to conclude that a high probability for magma to flow through a drift to the surface exists. However, it must be emphasized that this alternative analysis does not make any evaluation of the relative likelihood of the three cases. The Igneous Consequences Peer Review Panel considered the analysis just summarized and found it to be unlikely (Detournay et al (2003 [DIRS 169660], Section 3.4.8, p. 58).

Woods et al. (2002 [DIRS 163662]) calculate steady state magma velocities where the flow is constrained to equal the sound speed in highly compressible magma at the point where it emerges from the surface. This assumption of "choked" flow results in high driving pressures at depth, and modest (10s of m/s) flow velocities through the drift. Their calculation does not address the approach to the final steady state from an initial transient solution. Nor does their approach address the possibility that the flow could separate into vapor and liquid fractions moving at different velocities.

The EPRI recently published an analysis of potential igneous processes at Yucca Mountain (EPRI 2004 [DIRS 171915]). Their analysis of magma-drift interaction included an extensive analysis of the dike/drift interaction model of Woods et al. (2002 [DIRS 163662]). This analysis indicated that the shock-wave aspects described by Woods et al. (2002 [DIRS 163662]) were exaggerated due to a misinterpretation of the results as a shock-tube problem instead of as a converging-diverging nozzle problem (EPRI 2004 [DIRS 171915], Section 4.2.3).

The Electric Power Research Institute's analysis of the same configuration used a 2-D, compressible fluid code and explicitly included the perpendicular intersection of the dike with the drift (EPRI 2004 [DIRS 171915], Section 4.3). This analysis evaluates the effect of the

boundary conditions of the Woods et al. (2002 [DIRS 163662]) analysis, but it still uses the unrealizable initial condition of a static, high-pressure magma in contact with static, low-pressure air. Electric Power Research Institute concluded (Section 4.4):

> "The 2-dimensional re-analysis of the Woods et al. (2002) model performed for EPRI demonstrates that at high-pressure gradients between the dike and the drift, the original dike would be expected to propagate to the surface. This is because the vertical flow creates a high-pressure (stress) region at the top of drift immediately above where the dike intersects the drift. These localized stresses far exceed what is necessary to open or create a fracture in the roof of the drift that will enable the dike to continue propagating upward. This strongly favors the original dike as the main pathway for magma to reach the surface."
>
> "Conclusions drawn by Woods et al. (2002) have been discredited both by ICPR (2003) and by model for EPRI reported herein. Magma-drift interactions are far less severe than those postulated by Woods et al. (2002). The only credible ascent mechanism for the dike is continued propagation along the original line of ascent."

In the above quotations, the ICPR (Igneous Consequences Peer Review Panel) refers to the Detournay et al. report (2003 [DIRS 169660]). The analysis described has two major aspects that counteract each other. First, because of the 2-D nature of the calculation, the "drift" described represents a void of infinite lateral extent; this leads to exaggeration of the effect of the localized stresses in the back of the drift above the dike. In fact, these stresses would only occur over 5.5 m out of 81 m (less than 7 percent) of the rock at the repository horizon. This is counteracted by neglect of the dike cavity preceding the magma; the analysis of Section 6.4.5 indicates that this cavity will cross the drift and an open crack will exist above the magma as it enters the drift. Despite these differences, this model report agrees with their conclusion.

The analysis of Woods et al. (2002 [DIRS 163662]) is purely dynamical and does not address the thermal aspects of magma flow to the surface. Thermal aspects were addressed by the Igneous Consequences Peer Review Panel (Detournay et al. 2003 [DIRS 169660]) for case 2, in which a new dike is initiated 500 m along a drift from the original point of intersection. The Panel concluded that it was unlikely that a new dike beginning from the repository could grow to any appreciable dimension before it cooled, so much as to become effectively solid. Section 6.5.1.4 contains an elaboration of that thermal analysis.

6.5.4 Conclusion

Based on the discussion in this section, the following conclusions are drawn:

- In the case of effusive flow, magma will continue along the trajectory of the original dike after intruding the drift complex. In the unlikely event that an existing joint at the drift periphery is invaded by magma, the flow will be interrupted by magma freezing long before it is able to reach the surface.

- In the very unlikely event that magma encounters an accumulation of water in the drift, and that the mixing of magma and water is thorough enough to warrant a hydrovolcanic explosion next to an existing joint, a limited amount of magma is likely to vent to the surface. However, the volume of magma involved would be small (about 100 m^3), and the new secondary dike would freeze as soon as the pressure from the explosion levels out.

- The Woods et al. (2002 [DIRS 163662]) model of magma expansion into a drift greatly overestimates the violence of the encounter, an assertion that is supported by findings of the Igneous Consequences Peer Review Panel (Detournay et al 2003 [DIRS 169660]) as well as the findings of this report. Use of realistic initial conditions would preclude the formation of a shock wave for all but the most rapid magma ascent rates, while realistic boundary conditions would greatly reduce of a shock wave, should any occur. Then thermal aspects of the propagation of a thin secondary dike were overlooked.

6.6 GAS FLOW BETWEEN DRIFTS

This section looks at the flow of magmatic gases between drifts filled with magma and those outside the zone of magmatic emplacement.

After discussing the general background for this problem, Sections 6.6.1 and 6.6.2 describe the simple conceptual model used and the numerical formulation. Inputs and initial boundary conditions are given in Sections 6.6.3 and 6.6.4, respectively. Section 6.6.5 is a detailed account of the results obtained, while Section 6.6.6 summarizes the modeling.

Analysis of gas flow between drifts, discussed below, constitutes a strong case that impacts to Zone 2 drifts from intrusions into Zone 1 drifts is expected to be inconsequential. It should be noted, however, that considerable acidity may be developed in host rock adjacent to cooling intrusions via the release of acid volatiles. A good example of this phenomenon may be the ~550 ka Ngatamariki dioritic pluton in New Zealand, which drove intense phyllitic [quartz-sericite-pyrite] (Arehart et al. 2002 [DIRS 170390]) alteration in overlying country rock.

Although it would be a mistake to consider a long-lived, pluton-driven hydrothermal system as an analog to magmatic gas flow and mineral alteration at Yucca Mountain, due to the effects of basaltic magma intruding a drift, modeling of the pore-fluid chemistry adjacent to a dioritic intrusion (i.e., Ngatamariki pluton) suggests that magmatic volatile release may lead to zones of low pH in regions adjacent to the intrusion (White and Christenson 2000 [DIRS 170388]). Thus, although there may be little to no effect on Zone 2 drifts, the high solubility of acid volatiles may lead to the formation of low pH fluids near the boiling point isotherm around Zone 1 drifts. Ultimately, these low pH fluids will be neutralized via hydrolysis reactions with feldspar and other minerals, depending upon reaction rates. Equation 6-112 clearly shows that hydrogen ions are consumed in hydrolysis reactions, leading to the eventual neutralization of acidity.

$$2NaAlSi_3O_8 \text{ (albite)} + 2H^+ + 9H_2O \rightarrow Al_2Si_2O_5(OH)_4 \text{ (kaolinite)} + 4H_4SiO_4 + 2Na^+ \quad \text{(Eq. 6-112)}$$

Thus, it is important to recognize that chemically aggressive fluids could exist near disrupted drifts for some period until sufficient time has passed that they may be neutralized by natural processes. This problem is considered below.

In the event of the intrusion of an igneous dike into the repository block, the volcanic gas that is exsolved from the magma as it depressurizes and crystallizes, and the latent and sensible heat of the magma have the potential for affecting waste packages in drifts not directly intersected by the dike. The migration of volcanic gas associated with a dike emplaced in a waste-emplacement drift into a neighboring drift is discussed in this section based on reaction-transport modeling that couples thermal, hydrological, and chemical processes for a multi-phase, multi-component, multi-mineralic system, and feedback of mineral precipitation/dissolution on porosity, permeability, and capillary pressure for a dual-permeability (fracture-matrix) system. Results are presented for the migration of volcanic gas out of a waste emplacement drift through the fractured tuff repository rock toward an adjacent waste emplacement drift and, alternatively, through a backfilled access drift.

Input data were incorporated from the calibrated thermal-hydrological property sets, the three-dimensional mineralogical model, the unsaturated zone flow and transport model, thermal test geochemical data (fracture and matrix mineralogy, aqueous geochemistry, and gas chemistry), thermodynamic data (minerals, gases, and aqueous species), kinetic data for mineral-water reactions, and transport (diffusion coefficient) data (DTN: LB0302DSCPTHCS.001 [DIRS 164744]). The models include a wide range of major and minor aqueous species and minerals (primary and potential secondary phases).

Many uncertainties exist in modeling coupled thermal-hydrological-chemical (THC) processes (model report *Drift-Scale THC Seepage Model* - BSC 2004 [DIRS 169856], Section 6.9), because of the large amount of input data needed and the complexity of natural systems. Therefore, a quantitative measure of model uncertainty based on the uncertainties of the data themselves is difficult. Model validation provides a better test of whether the system can be described sufficiently well for the intended purposes of the model.

Partial validation was accomplished through analyses of the Drift-Scale Test (DST), and experiments involving HCl gas + water vapor transport and dissolution into a condensed water phase. As summarized further in *Drift-Scale THC Seepage Model* (BSC 2004 [DIRS 169856], Section 7.1), the results of DST THC simulations captured the important changes in pH, aqueous species concentrations, gas-phase CO_2 concentrations, and mineral deposition at specific locations over time. This provides sufficient validation of the model's capability to predict trends of spatial and temporal variations in water and gas chemistry owing to thermal effects, gas transport and gas dissolution, around emplacement drifts, at temperatures of over 200ºC. The duration of the heating phase of the DST (approximately four years) and its subsequent slow cooling period are comparable to the time over which a dike, if emplaced, would cool and crystallize. However, temperatures in the DST are well below that of the initial magmatic temperature of approximately 1150ºC, which takes about one year to drop to around 200ºC. Therefore, the DST THC Model and data from the DST can be used to validate some, but not all aspects of volcanic gas transport model predictions. Further validation is described in Section 7.3.2.1.

One important aspect of the unsaturated zone at Yucca Mountain makes the model of gas transport and THC processes around an emplacement drift more tenable. Because the system is unsaturated and the ambient gas pressure just below one bar, the boiling front is always close to 100ºC, regardless of the temperature of the heat source. Therefore, water-rock reactions and gas phase dissolution into water are well within the range of validation of the TOUGHREACT (LBNL 2002 [DIRS 161256]) code and the drift-scale THC model representations. Therefore, the only region of concern is in the high-temperature region adjacent to the dike, where predominantly gas phase transport is the important process. Because this region is quite narrow (less than 3 m, based on Figure 6-88, and Figure D-5, Appendix D), any uncertainties in gas transport velocities would have a relatively minor effect on the transport times for gases to an adjacent drift more than 80 m away.

6.6.1 Description

The intersection of a basaltic dike with one or more drifts would result in a region directly affected by the magma (Zone 1) and a region (including nearby drifts) only potentially impacted (Zone 2 as depicted in Figure 6-82).

The pressure, volume, composition, and temperature history of volcanic gas potentially entering a repository drift depends on several factors, including the volume of magma emplaced in a drift, its rate of ascent, and its composition. Given these uncertainties, a simple conceptual model was employed to consider the effects of gas migration out of a drift into the surrounding fractured host tuff. The models consider a volcanic gas source inside the drift that allows gas species to migrate via advection and diffusion either through the fractured tuff around the drift, or alternatively, through a backfilled access drift. The rate of advance of the volcanic gas in the fracture network is examined to assess the potential effect on a neighboring drift. The actual emplacement of magma in a drift is not simulated, nor are the actual pressure-temperature conditions over time realistically evaluated. Simulations were performed that provide bounds on the potential rate of advance of the gas and examine the controls on the migration of soluble gas species.

The model of the geochemical system includes the major aqueous species, minerals, and gaseous components in the unsaturated zone. Additionally, minor species, such as F^-, are included for their relevance to waste package corrosion. Gaseous components include air, H_2O, CO_2, HCl, HF, and SO_2. Oxidation-reduction reactions were not treated; however, reactions involving sulfur oxidation would result in stronger retardation of SO_2.

6.6.2 Numerical Formulation and Code

Simulations were performed using TOUGHREACT (LBNL 2002 [DIRS 161256]) that couples multiphase fluid flow (water and air), heat flow, aqueous and gaseous species transport, and kinetic and equilibrium mineral-water-gas reactions. Gas species are transported via advection and diffusion. Gaseous species diffusion coefficients are calculated as a function of molecular weight, molecular diameter, temperature, and pressure, with effective diffusivities related to porosity, tortuosity, and water saturation. Inputs to the model simulations are described in the following section. Simulations used the EOS3 (Equation of State Module 3) option of TOUGHREACT (LBNL 2002 [DIRS 161256]). Drift-Scale THC seepage simulations presented

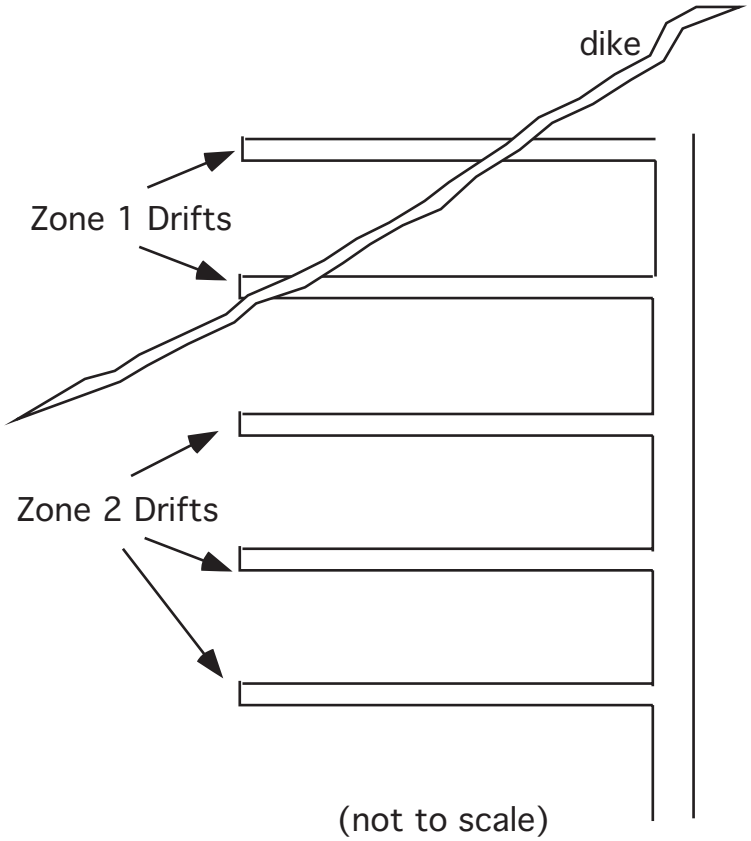

NOTE: For illustration purposes only.

Figure 6-82. Plan View Schematic of Dike-Drift Intersection and Zones 1 and 2

in *Drift-Scale THC Seepage Model* (BSC 2004 [DIRS 169856]), used both EOS3 and EOS4 options of TOUGHREACT, with EOS4 considering vapor-pressure lowering as a result of capillary pressure. The latter module cannot be used for the high-temperature simulations presented in this report; however, effects of vapor pressure lowering on drift-scale THC evolution was shown to be minor in *Drift-Scale Coupled Processes (DST and THC Seepage) Models* (BSC 2004 [DIRS 169856]).

6.6.3 Description of Inputs

6.6.3.1 Numerical Mesh

The numerical mesh was created by connecting two meshes from the THC Seepage Model for a repository drift emplaced in the Tptpll lithostratigraphic unit (BSC 2004 [DIRS 169856], Section 6.5.1). Modifications to the model as part of this report are presented here. In short, the model represents a cross-section of two repository drifts, which by symmetry have been cut in half. The mesh extends vertically from the ground surface to the water table and horizontally from the drift center of a Zone 1 drift to the center of the adjacent Zone 2 drift (81 m). The numerical mesh showing both drifts is shown in Figure 6-83.

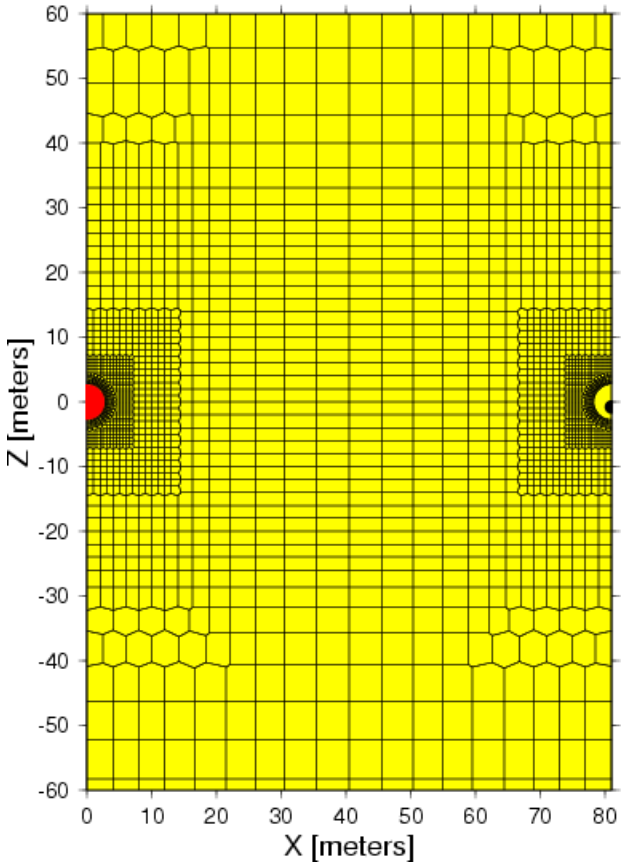

NOTE: Mesh extends vertically upward to the ground surface and down to the water table, outside the region shown. The red-shaded drift at left denotes the Zone 1 intruded drift.

Source: BSC 2004 [DIRS 169856], Figure 6.5-1.

Figure 6-83. Numerical Mesh Used in Volcanic Gas Transport Simulations

An enlargement of the numerical mesh showing the in-drift configuration of the Zone 2 drift is shown in Figure 6-84. The grid for the Zone 1 drift is identical, however the properties of the waste package, inner, and outer zones of the drift have been modified to account for the intrusion of basaltic magma and associated volcanic gas phase.

With this geometry, the potential effects of gas migrating from volcanic intrusion in a drift to an adjacent drift may be assessed.

A dual-permeability approach was adopted whereby coexisting fracture and rock-matrix continua in the rock are used to model the separate, yet interacting, effects of flow and transport in and between fractures and the rock matrix. The total mesh, including fracture and matrix, consists of 6402 grid blocks with each continuum assigned its own hydrological, geochemical, and mineralogical properties.

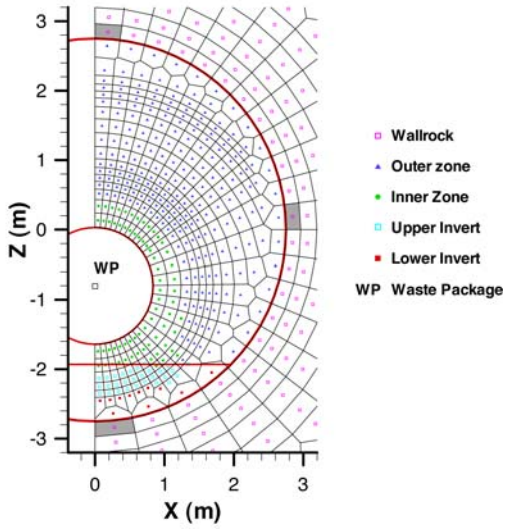

Source: BSC 2004 [DIRS 169856], Figure 6.5-2.

Figure 6-84. Enlargement of THC Seepage Model Numerical Mesh Showing In-Drift Discretization

6.6.3.2 Initial Pore and Infiltrating Water and Gas Chemistry

The geochemical model consists of the following primary aqueous species: H^+, Na^+, K^+, Ca^{2+}, Mg^{2+}, AlO_2^-, NO_3^{2-}, SO_4^{2-}, SO_2(aq), F^-, Cl^-, HCO_3^-, SiO_2(aq), and $HFeO_2$(aq). The initial pore-water chemistry (Table 6-16) was based on a sample that was ultracentrifuged from a core taken from the repository host rock (Tptpmn) in Alcove 5 near the Drift Scale Test. The initial CO_2 partial pressure in the Zone 2 drift was set to the ambient CO_2 partial pressure in the adjacent wallrock. Because oxidation-reduction reactions are not considered in the simulations presented in this report, SO_2(aq) and SO_4^{2-} are considered as separate non-interacting species.

Table 6-16. Initial Pore-Water and Gas Compositions[1]

Component or Variable	Units	Water Input Type	
		Fracture and Matrix	Boundary
Temperature	°C	25	17
pH (measured)	pH	8.31	—
pH (calc)[2]	pH	—	7.750
Na^+	mg/L	61.5	61.3
K^+	mg/L	8	8
Ca^{2+}	mg/L	101	101
Mg^{2+}	mg/L	17	17
SiO_2(aq)	mg/L	70.5	70.5
Cl^-	mg/L	117	117
SO_4^{2-}	mg/L	116	116
HCO_3^- (measured)	mg/L	—	—

Table 6-16. Initial Pore-Water and Gas Compositions[1] (Continued)

Component or Variable	Units	Water Input Type	
		Fracture and Matrix	Boundary
HCO_3^- (calc)[2]	mg/L	200	216
NO_3^-	mg/L	6.5	6.5
F^-	mg/L	0.86	0.86
Al^{3+} (calc)[2]	Molal	6.173×10^{-10}	9.775×10^{-11}
Fe^{3+} (calc)[2]	Molal	1.155×10^{-12}	5.162×10^{-13}
$\log(P_{CO_2})$[2]	Bars	-3.1	-2.5
CO_2 (approx)[3]	Ppmv	900	3100

Sources: [1] BSC 2004 [DIRS 169856], Table 6.2-1.
[2] Calculated (see Table 6.2-1 in BSC 2004 [DIRS 169856]).
[3] Converted to ppmv using total pressure equal to one bar.

ppmv = parts per million volume

NOTE: Sample ID: HD-PERM (Alcove 5) Lithostratigraphic unit: Tptpmn.

6.6.3.3 Initial Mineralogy

The initial mineralogy of the tuff matrix and fracture coatings is represented by the following assemblage (some as end members of an ideal solid-solution phase): α-cristobalite, opal, tridymite, quartz, K-feldspar, albite, anorthite, Ca-smectite, Na-smectite, Mg-smectite, illite, calcite, fluorite, rhyolitic glass, hematite, stellerite, clinoptilolite, mordenite, and heulandite. Several other potential secondary phases are considered (e.g., amorphous silica, kaolinite, sepiolite, gypsum) as well as various salt phases, such as halite and sylvite, which precipitate only under conditions of complete evaporation.

These input data consist of mineral volume fractions per total solid volume and their reactive surface areas. Reactive surface areas are used to characterize minerals either in the matrix of the rock (cm^2/g mineral), or those on the surface of fractures (m^2/m^3 of total medium, including pore space), respectively.

The rock matrix mineralogical data are for a stratigraphic column near the center of the repository showing relative mineral abundance with depth. These data are given in BSC 2004 [DIRS 169856] Appendix I (volume fractions) and Appendix II (reactive surface areas), respectively.

A complete description of the rationale for these phases/components, thermodynamic and kinetic data, derivation of various properties, and sources for all data can be found in BSC 2004 [DIRS 169856].

6.6.3.4 Initial Volcanic Gas Chemistry

The volcanic gas composition (in mole percent) was set to 14.28 percent CO_2, 9.45 percent SO_2, 0.87 percent HCl, and 0.17 percent HF (DTN: LA0407DK831811.001 [DIRS 170768], Table 7). The water content of the gas is fixed to that given by the pressure-temperature conditions for a vapor plus air mixture calculated by TOUGHREACT (LBNL 2002 [DIRS 161256]). The volcanic gas concentrations are mean values of several measured compositions from volcanoes having different magmatic compositions (tholeiitic and alkali basalts, hawaiite, and nephelinite).

6.6.3.5 Hydrological and Thermal Properties

Sources for hydrological and thermal properties are listed in Table 4-1. Specific values of hydrological and thermal properties for the repository hydrogeologic model units TSw33, TSw34, and TSw35 (Topopah Spring Tuff upper-lithophysal, middle-nonlithophysal, and lower-lithophysal units, respectively), are summarized in *Drift-Scale Coupled Processes (DST and THC Seepage) Models* (BSC 2004 [DIRS 169856], Table 6.4-1).

Modeling analyses utilized data from the "mean calibrated" hydrological property sets for the present-day climate. The data sets include properties that were calibrated, such as fracture and matrix permeabilities and van Genuchten parameters, and properties such as porosity, heat capacity, and thermal conductivity obtained from field measurements.

Thermal properties for the unsaturated zone model layers are taken from DTN: LB0402THRMLPRP.001 [DIRS 168481]. In most cases, especially for repository-level units, the new values are identical to or vary only slightly from the earlier dataset (LB0210THRMLPRP.001 [DIRS 160799]).

6.6.3.6 Aqueous and Gaseous Species Diffusion Coefficients

Diffusion coefficients of all aqueous species are set to the same value (the value for the chloride anion). This is justified because the tracer diffusion coefficients of aqueous species differ by at most about one order of magnitude, with many differing by less than a factor of 2 (Lasaga 1998 [DIRS 117091], p. 315). The strong effects of water-rock interaction, boiling condensation, and rapid fracture drainage at the time-scale of a dike emplacement, overwhelm any effects of aqueous species diffusion.

Diffusion coefficients for gases are calculated. Binary diffusion of water vapor and air is calculated simultaneously with the flow calculations in TOUGHREACT (LBNL 2002 [DIRS 161256]). Diffusion of HCl, HF, SO_2, and CO_2 in the gas phase is based on a model of tracer diffusion in an ideal gas as a function of temperature and pressure (Lasaga 1998 [DIRS 117091], p. 322), as follows:

$$D = \frac{RT}{3\sqrt{2}\pi P N_A d_m^2}\sqrt{\frac{8RT}{\pi M}} \qquad \text{(Eq. 6-113)}$$

where

D = diffusion coefficient (m^2/s)

R = gas constant (8.31451 m^2 kg s^{-2} mol^{-1} K^{-1})

T = temperature in Kelvin units

P = pressure (kg m^{-1} s^{-2})

N_A = Avogadro's number (6.0221367 x 10^{23} mol^{-1})

d_m = molecular diameter (m)

M = molecular weight (kg/mol)

Diffusion coefficients for HCl, HF, SO_2, and CO_2 were calculated using input values of d_m and M. Molecular weights come directly from the thermodynamic database, along with the equilibrium constants for mineral-water and water-gas reactions. The molecular diameter for CO_2 (3.23 x 10^{-10} m) was derived from Lide (1993 [DIRS 123032], pp. 14-19). Molecular diameters for SO_2, HCl, and HF approximated as the same value.

The use of this expression is entirely appropriate, because it is used as it was intended by Lasaga (1998 [DIRS 117091], p. 322).

6.6.4 Initial and Boundary Conditions

6.6.4.1 Hydrological and Thermal

The boundary conditions are derived from *Drift-Scale THC Seepage Model* (BSC 2004 [DIRS 169856]). A column location near the repository center was chosen to locate the inputs (BSC 2004 [DIRS 169856], Table 6.5-1). The infiltration rate was fixed to 6 mm/year for the present-day repository-wide average; the value was calculated as arithmetic average of the 31 repository locations considered in the *Multiscale Thermohydrologic Model* (BSC 2004 [DIRS 169565], Section 6.3.1). The calculated average was rounded to 6 mm/yr, for use in this model report. This value varies slightly from current estimates; its use in this model is justified in BSC (2004 [DIRS 169856], Section 4.1.1.2, Table 6.5-3). The remaining boundary conditions, pressure, temperature, and gas saturation, for the model are given in *Drift-Scale THC Seepage Model* (BSC 2004 [DIRS 169856], Table 6.5-2).

The initial temperature of the magmatic gas phase was assumed to be 500ºC because the thermodynamic data for aqueous and gaseous species used in the calculations are not verified above that temperature. Despite being well below the temperature of the volcanic gases as they are first exsolved from the magma, the temperature is high enough to show the effects of boiling of pore water in the rock surrounding the drifts. Thermal analyses discussed in Section 6.7 also indicate that temperatures at the drift wall drop below 773 K in two months. At greater ranges or longer times there will be little effect at all.

Two simulations were performed with slightly different thermal histories and in-drift thermal properties. In the first simulation, this temperature was fixed for the first 5 months; the time was approximated from Figure 6-98. The 500ºC temperature was assigned only to the volume

occupied previously by the waste package within the drift, and this volume was given the physical attributes of the surrounding drift gas. In the second simulation, the grid block corresponding to the waste package was given the following thermal properties: thermal conductivity (1.0 W/m K), heat capacity (1200 J/kg·K), and density of the magma (2800. kg/m^3), equal to the magma properties in DTN: LA0307EG831811.001 [DIRS 166942]. The hydrological properties were kept the same as the waste package (porosity = 0.0001, permeability = 0.). This simulation also included a slightly elevated initial total gas pressure of 1 bar, compared to the ambient value of around 0.88 bars. This also resulted in a higher volcanic gas flux out of the drift, compared to the first simulation.

For both simulations, a high effective thermal conductivity was used in the drift interior to approximate heat transfer by convection and radiation, based on models of waste package heat transfer, as used in the THC Seepage Model (BSC 2004 [DIRS 169856]). With this setup, heat transfer from the drift interior to the drift wall is rapid.

The 500ºC used for the drift temperature is much lower than actual initial magma temperature (about 1,100ºC). However, the wall rock temperature will be considerably lower, as shown in Section 6.7.1.2. The effect of increasing temperature is to boil more water, resulting in significant amounts of water condensation in fractures. The increased liquid saturation in the fractures results in dissolution of a greater mass of soluble gas species, and in retardation of gas-phase diffusion. Therefore, temperatures above 500ºC are expected to further slow diffusive and advective gas phase transport processes in drift walls.

6.6.4.2 Chemical

The initial ambient pore water and gas chemistry were set to be the same everywhere in the fractures and matrix, except for the gas composition at the ground surface (see Table 6-16, above). The volcanic gas composition was assigned to all in-drift grid blocks in the intruded drift.

6.6.5 Simulation Results

6.6.5.1 Simulation 1

This simulation had a fixed 500ºC in the drift center for five months. Grid blocks in the drift interior (except for the invert) were set to the thermal properties of air plus water vapor, with the volcanic gas composition assigned to all in-drift gas. After 5 months, the Zone 1 drift was allowed to cool naturally. Horizontal temperature profiles extending from the center of the intruded drift toward the Zone 2 drift are shown in Figure 6-85. After 5 months, the drift wall temperature reached approximately 416ºC, with a sharp decline to about 100ºC at 6m from the drift center. The nearly 1m-wide plateau in temperature at about 100ºC is a result of boiling and condensation. Due to a reduction in time steps related to rapid cooling, this simulation was only run to 7.5 months.

Gas compositions (CO_2, SO_2, HCl, and HF) are shown contoured in Figure 6-86 after 7.5 months with temperature contours overlain. High CO_2 and SO_2 gas-phase concentrations are evident outside the boiling zone, near the 50ºC isotherm. High HCl and HF gas phase concentrations are

limited to the above-boiling region very close to the drift, owing to their extremely high solubilities.

Effects of the migration and dissolution of HCl and HF (in particular) on water chemistry are best illustrated by the change in pH to more acidic values, as shown in Figure 6-87. The evolution in pH from one to 7.5 months follows the migration of the gas phase and the condensation front. Fracture and matrix pH values are similar at these times. However, the drop in pH is limited in the rock from about 8.3 to a minimum of slightly less than 6.0, owing to the presence of calcite in the fractures and hydrolysis reactions with feldspars, as discussed previously.

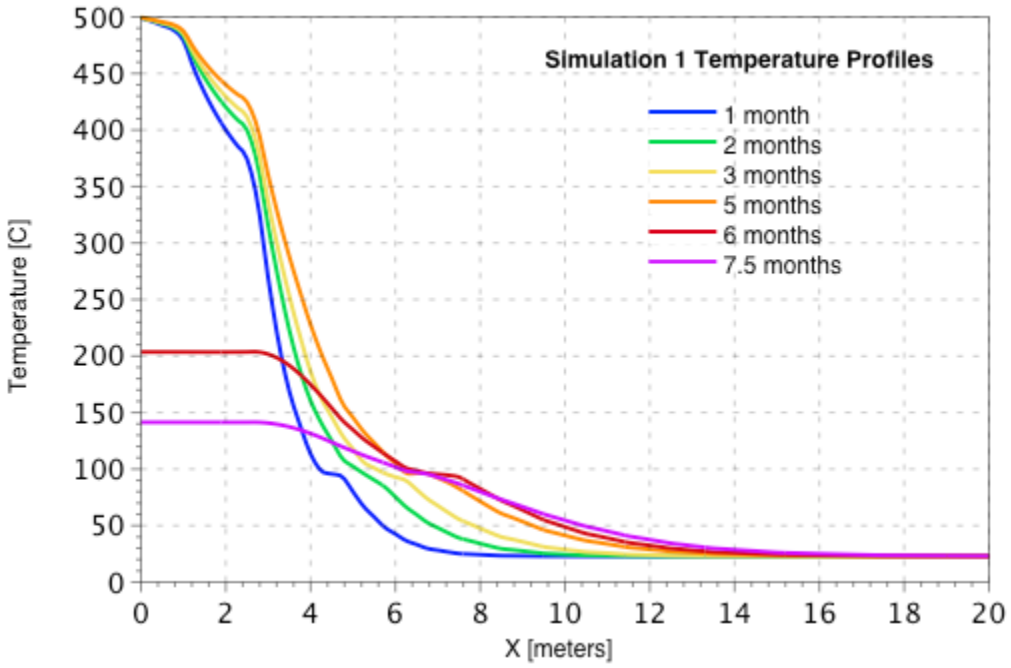

Output DTN: LB0408AMRT0020.001, LB0408AMRT0020.002.

NOTE: Breaks and slope represent edge of waste package at 1 m and edge of drift at 2.5 m; thermal plateau at 100°C.

Figure 6-85. Temperature Profiles Extending From the Center of the Intruded Drift Toward the Zone 2 Drift (Simulation 1)

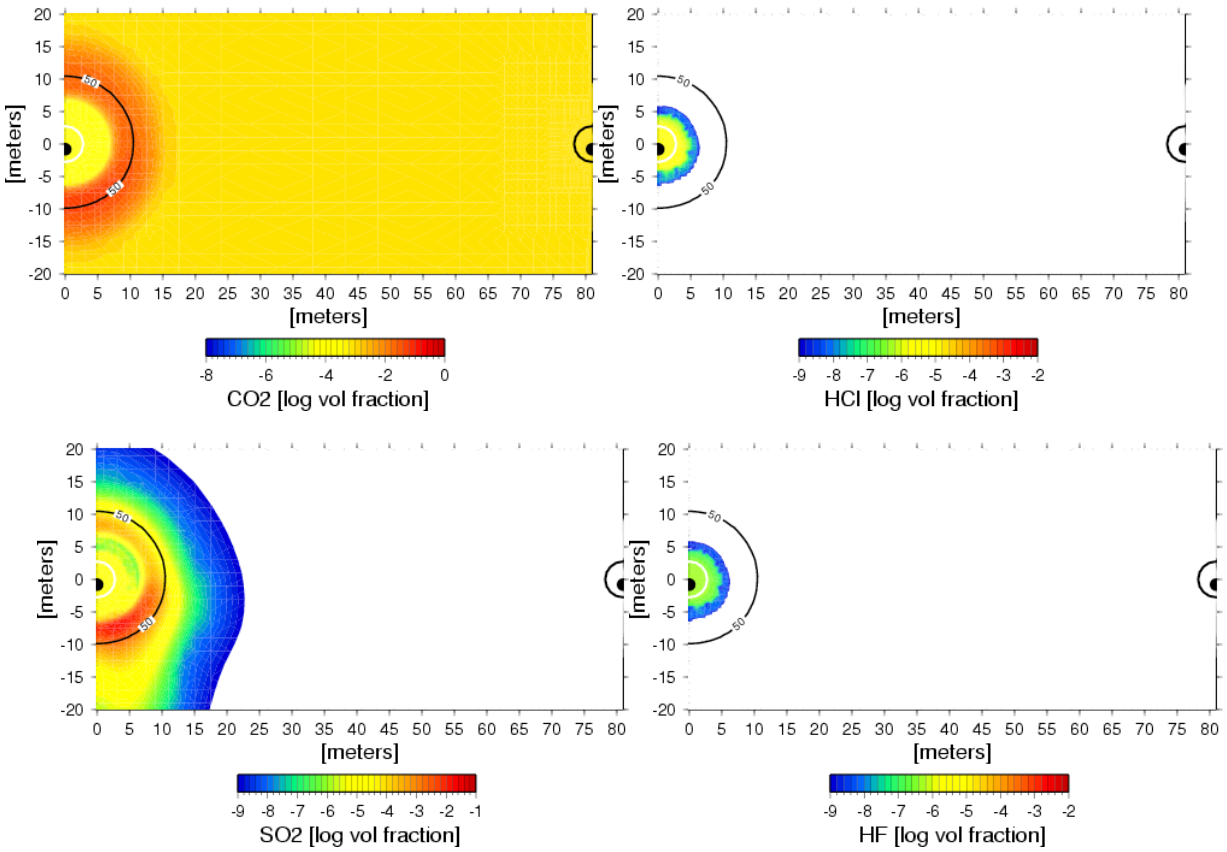

Output DTN: LB0408AMRT0020.001, LB0408AMRT0020.002.

NOTES: Temperature contours are overlain. Plots use a cut-off in gas concentration (10^{-9} for SO_2, HCl, and HF, and 10^{-9} for CO_2) in order to visualize the migration of the volcanic gas source and neglect contouring of negligibly low ambient concentrations that are subject to numerical inaccuracies.

Figure 6-86 Contoured gas compositions (CO_2, SO_2, HCl, and HF) in fractures after 7.5 months (Simulation 1)

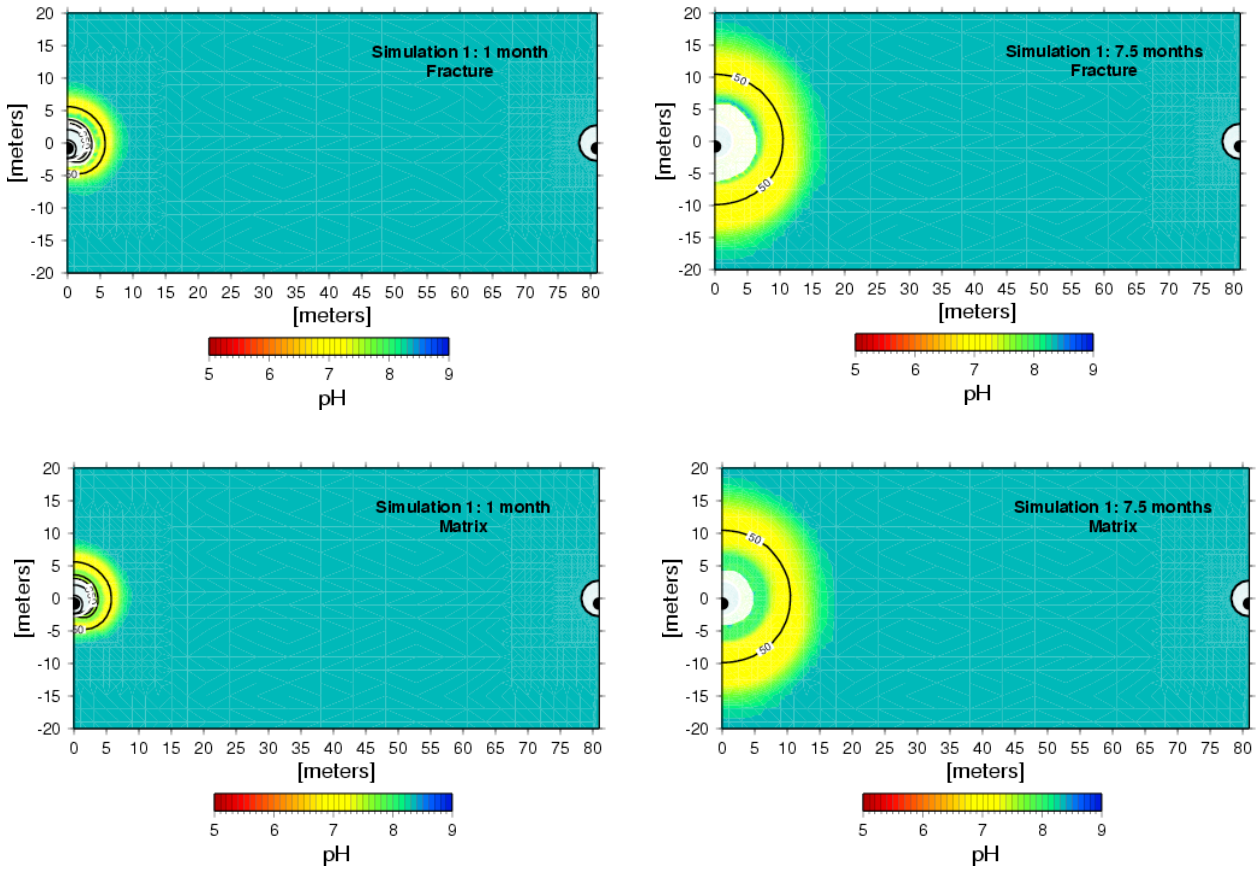

Output DTN: LB0408AMRT0020.001, LB0408AMRT0020.002.

NOTES: Areas that are essentially devoid of water due to evaporation as a result of boiling or being within a gas-filled drift are filled in white.

Temperature contours are overlain.

Figure 6-87. Contoured pH values in Fractures and Matrix After 1 and 7.5 Months (Simulation 1)

Consideration of the change in oxidation state of sulfur to form H_2S could potentially lead to more acidic waters than are modeled; however, it would also lead to greater immobilization of the volcanic gas as it is transported into the rock outside the drift. Other factors that would lead to more acidic condensates include a lowering of the water vapor pressure due to a reduction in water activity at high dissolved chloride concentrations. Again, this process would take place at above-boiling temperatures that are attained less than 10 meters from the drift wall.

6.6.5.2 Simulation 2

This simulation had a fixed 500ºC in the drift center for 6 months. The time was extended over the first simulation to allow for a slightly higher rock temperature, and a longer emanation of volcanic gas. Grid blocks in the drift interior (except for the waste package and invert) were set to the thermal properties of air plus water vapor, with the volcanic gas composition assigned to

in-drift gas compositions, initially. After six months, the Zone 1 drift was allowed to cool naturally, and the simulation continued to approximately 500 years.

Horizontal temperature profiles extending from the center of the intruded drift toward the Zone 2 drift are shown in Figure 6-88 to a period of 5 years. After six months, the drift wall temperature reached approximately 422ºC, with a sharp decline to about 100ºC just past 6.5m from the drift center. The plateau in temperature at about 100ºC (owing to boiling and condensation) is slightly wider than in the first simulation. After five years the maximum temperature dropped to a value less than 50ºC. At 20 meters from the drift center, the maximum temperature rise is only about 10ºC after five years.

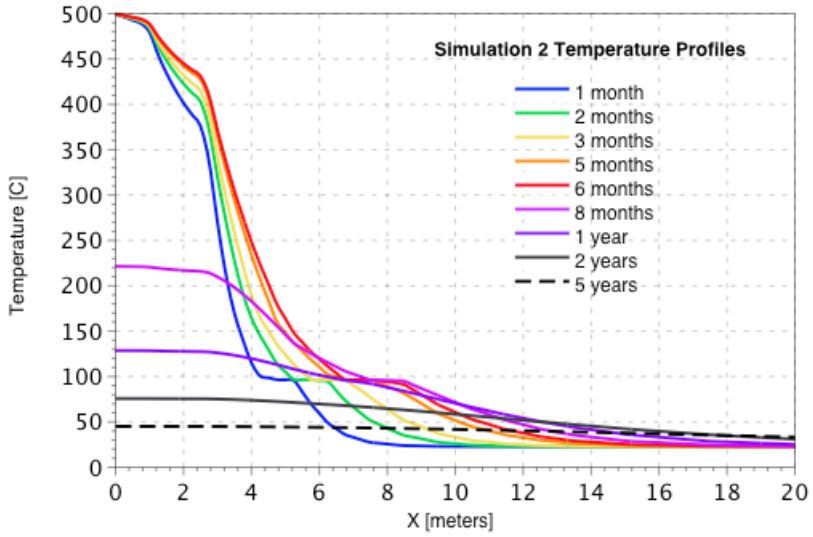

Output DTN: LB0408AMRT0020.001, LB0408AMRT0020.002.

Figure 6-88. Temperature Profiles Extending From the Center of the Intruded Drift Toward the Zone 2 Drift (Simulation 2)

Gas compositions (CO_2, SO_2, HCl, and HF) are shown contoured in Figures 6-89 to 6-92 from six months to 500 years. After six months (Figure 6-89) there are markedly high CO_2 and SO_2 concentrations well outside the drift, with localized high HCl and HF concentrations close to the drift. After one year, the regions of high CO_2 and SO_2 concentrations have continued to migrate slowly outward, with a small decline in their maximum concentrations. In contrast, gas phase HCl and HF concentrations have dropped dramatically to values below 10^{-9} as a result of cooling and dissolution into fracture condensate and matrix pore water. Over an extended period (500 years), CO_2 concentrations slowly decline toward the ambient value of approximately 10^{-3} (volume fraction) from the initial volcanic gas composition of approximately 0.14, with no noticeable effect on the adjacent Zone 2 drift. SO_2 concentrations decline much more slowly, as a result of its lower solubility and smaller diffusivity, with concentrations on the order of 1 ppmv, reaching the Zone 2 drift after 500 years (Figure 6-91). By 200 years, CO_2 concentrations are only slightly elevated above background values (Figure 6-91), and by

500 years the CO_2 concentrations have completely equilibrated with the surrounding gas compositions. Although gas-phase SO_2 concentrations are elevated relative to the background, this simulation assumes that there is no longer any waste-generated heat output from the Zone 2 drift (that would result in a less penetrable boiling /condensation zone) and that there is no air flow through the drift.

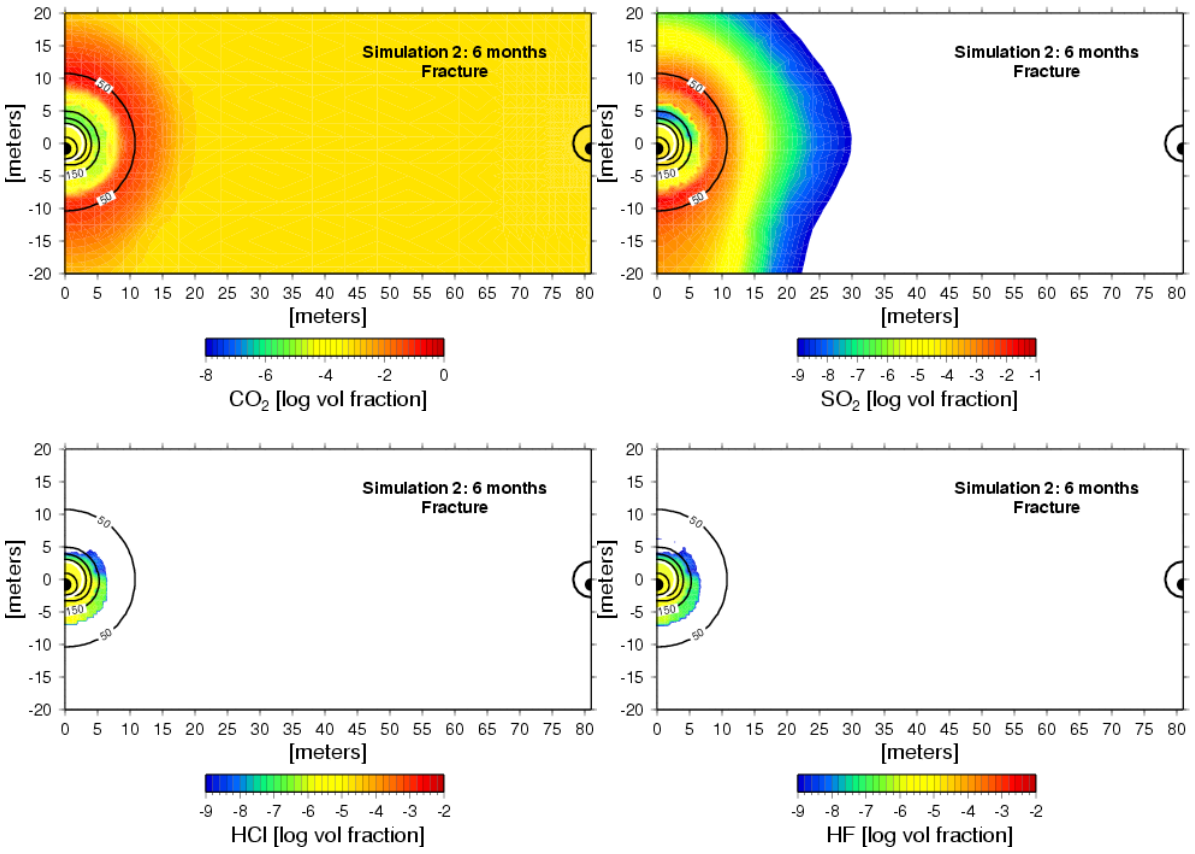

Output DTN: LB0408AMRT0020.001, LB0408AMRT0020.002.

NOTES: Temperature contours are overlain. Plots use a cut-off in gas concentration (10^{-9} for SO_2, HCl, and HF, and 10^{-8} for CO_2) to visualize the migration of the volcanic gas source and neglect contouring of negligibly low ambient concentrations that are subject to numerical inaccuracies.

Figure 6-89. Contoured gas compositions (CO_2, SO_2, HCl, and HF) in fractures after 6 months (Simulation 2)

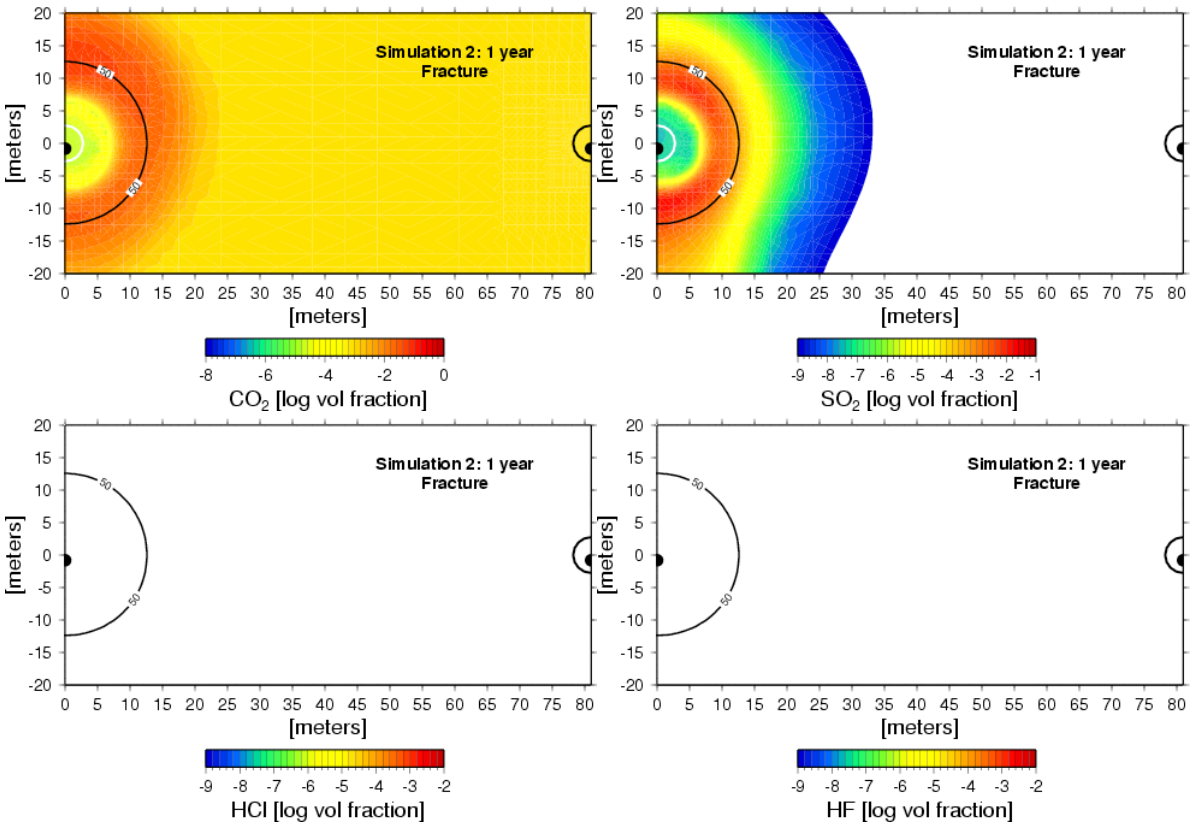

Output DTN: LB0408AMRT0020.001, LB0408AMRT0020.002.

NOTE: Plots use a cut-off in gas concentration (10^{-9} for SO_2, HCl, and HF, and 10^{-8} for CO_2) to visualize the migration of the volcanic gas source and neglect contouring of negligibly low ambient concentrations that are subject to numerical inaccuracies; temperature contours are overlain.

Figure 6-90. Contoured gas compositions (CO_2, SO_2, HCl, and HF) in fractures after One year (Simulation 2)

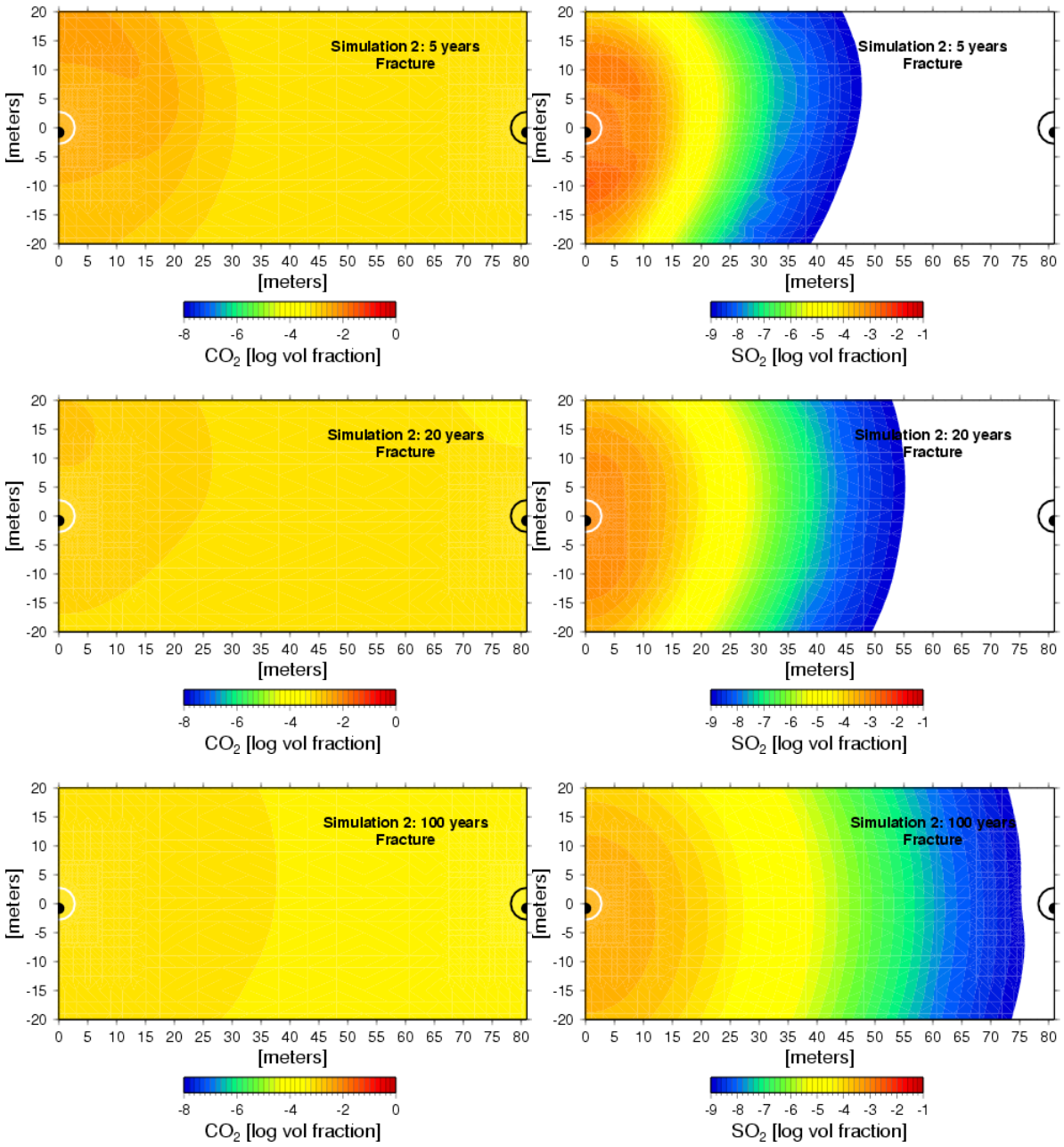

Output DTN: LB0408AMRT0020.001, LB0408AMRT0020.002.

NOTE: Plots use a cut-off in gas concentration (10-9 for SO2, HCl, and HF, and 10-8 for CO2) in order to visualize the migration of the volcanic gas source and neglect contouring of negligibly low ambient concentrations that are subject to numerical inaccuracies.

Figure 6-91. Contoured gas compositions (CO_2 and SO_2) in fractures after 5, 20, and 100 years (Simulation 2)

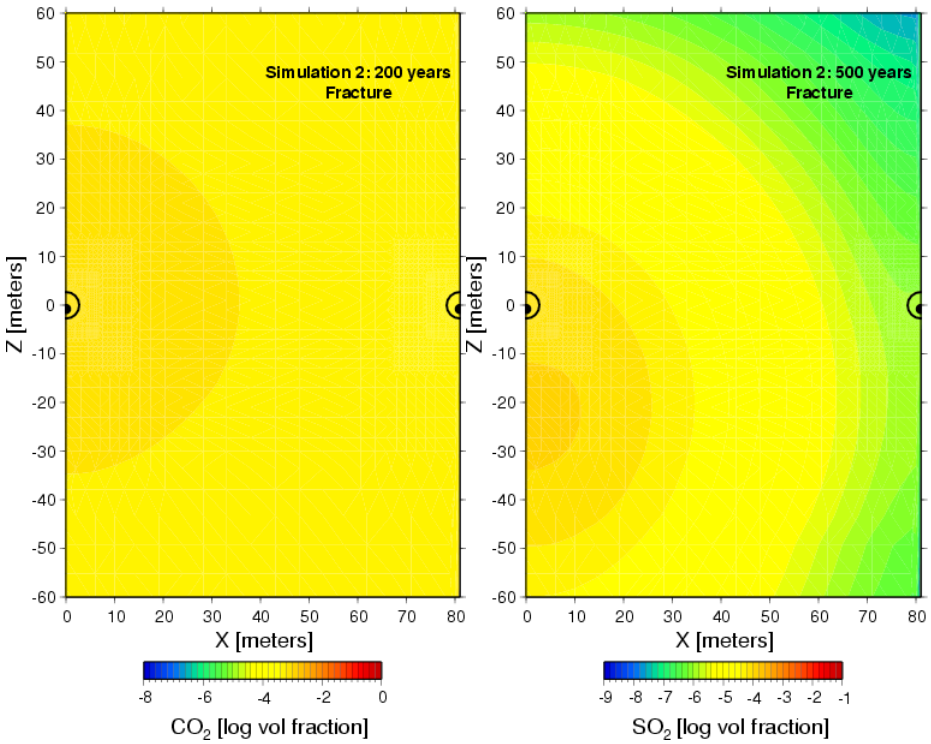

Output DTN: LB0408AMRT0020.001, LB0408AMRT0020.002.

NOTE: Plots use a cut-off in gas concentration (10^{-9} for SO_2, HCl, and HF, and 10^{-8} for CO_2) to visualize the migration of the volcanic gas source and neglect contouring of insignificantly low ambient concentrations that are subject to numerical inaccuracies.

Figure 6-92. Contoured gas compositions (CO_2 and SO_2) in fractures for an enlarged region of the grid after 200 years for CO_2 and 500 years for SO_2 (Simulation 2)

The different patterns in the CO_2 and SO_2 concentrations are a result of differences in their behavior and initial ambient concentrations. The CO_2 concentrations are elevated nearly symmetrically around the Zone 1 drift, because of the increase in CO_2 partial pressure at the very slightly elevated temperatures, which temperatures are symmetric around the drift. SO_2 concentrations in the gas phase reflect equilibration with the aqueous phase that became enriched in aqueous SO_2 during the initial partition of SO_2 into the matrix pore water. Continued water percolation has resulted in a migration of this water down below the drift.

The evolution in pH from 6 months to 100 years is shown in Figure 6-93. Initially, the lowest pH (around 5.6) occurs in the fracture water near the drift wall. These lowest pH values are found in the fractures because of the more rapid migration of gas into the fractures, and owing to their initially low water contents. The extent of dry-out is also larger for the fractures than for the matrix. As the system cools, and there is some condensation and very slow imbibition of water back into the matrix, the pH values become lower in the matrix relative to the fractures, a pattern which is still evident in the "shadow zone" below the Zone 1 drift after 500 years (Figure 6-94).

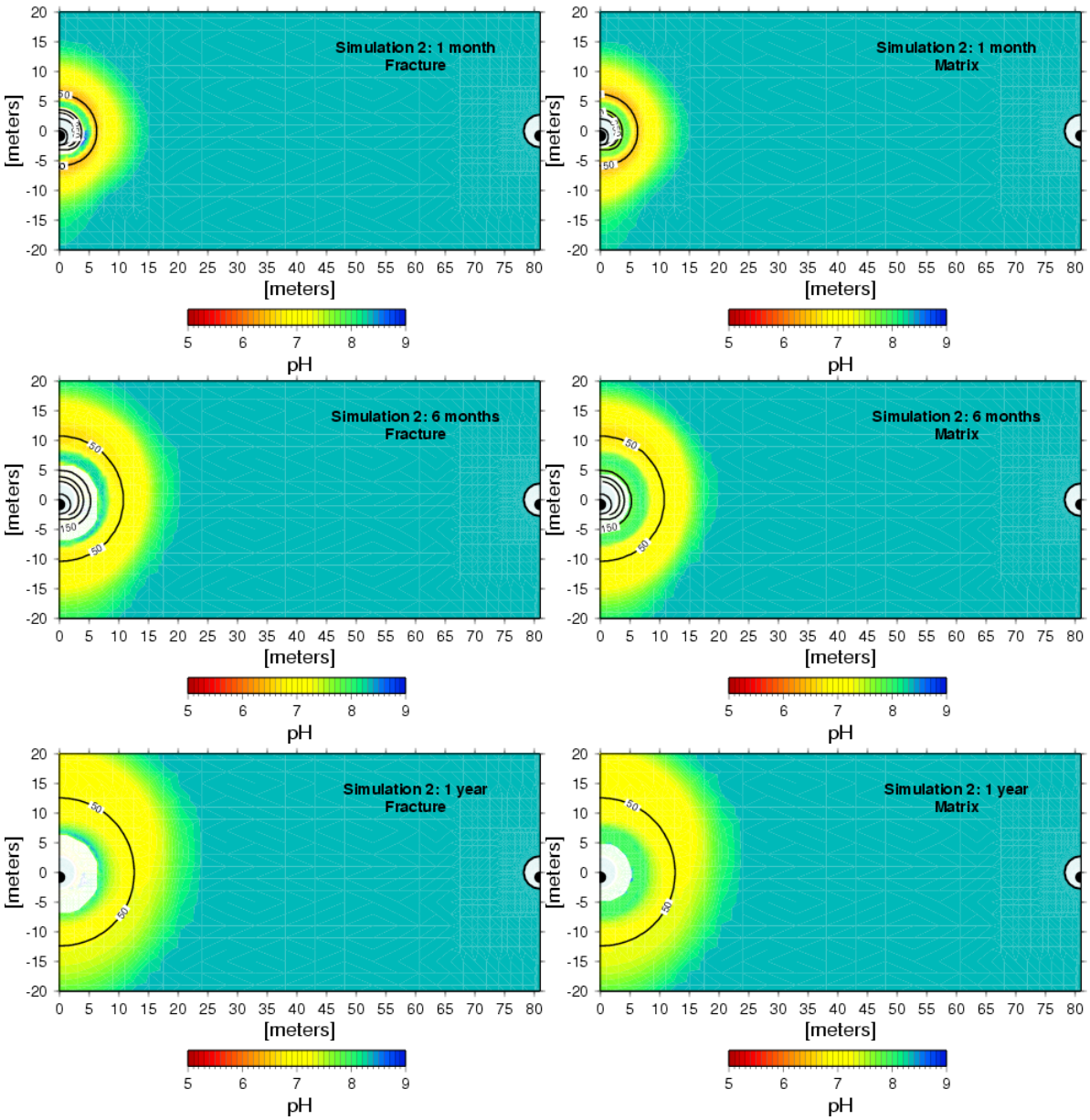

Output DTN: LB0408AMRT0020.001, LB0408AMRT0020.002.

NOTES: Temperature contours are overlain (where 50ºC or above).

Areas that are essentially devoid of water due to evaporation as a result of boiling or being within a gas-filled drift are filled in white.

Figure 6-93. Contoured pH Values In Fractures and Matrix at Six months, 1, 5, 20, and 100 years (Simulation 2)

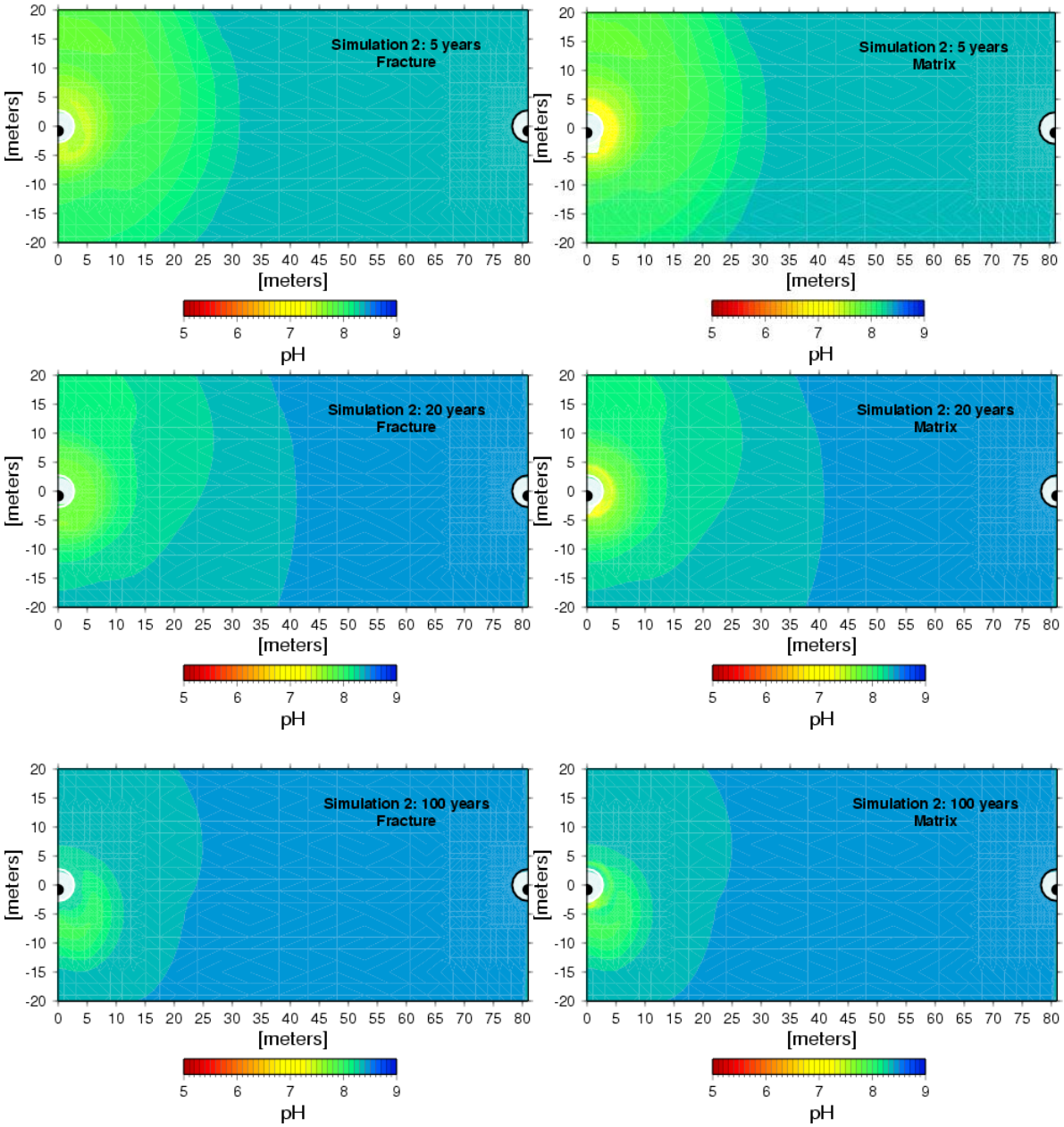

Output DTN: LB0408AMRT0020.001, LB0408AMRT0020.002

NOTE: Temperature contours are overlain (where 50ºC or above). Areas that are essentially devoid of water due to evaporation as a result of boiling or being within a gas-filled drift are filled in white.

Figure 6-93. Contoured pH Values In Fractures and Matrix at Six months, 1, 5, 20, and 100 years (Simulation 2) (Continued)

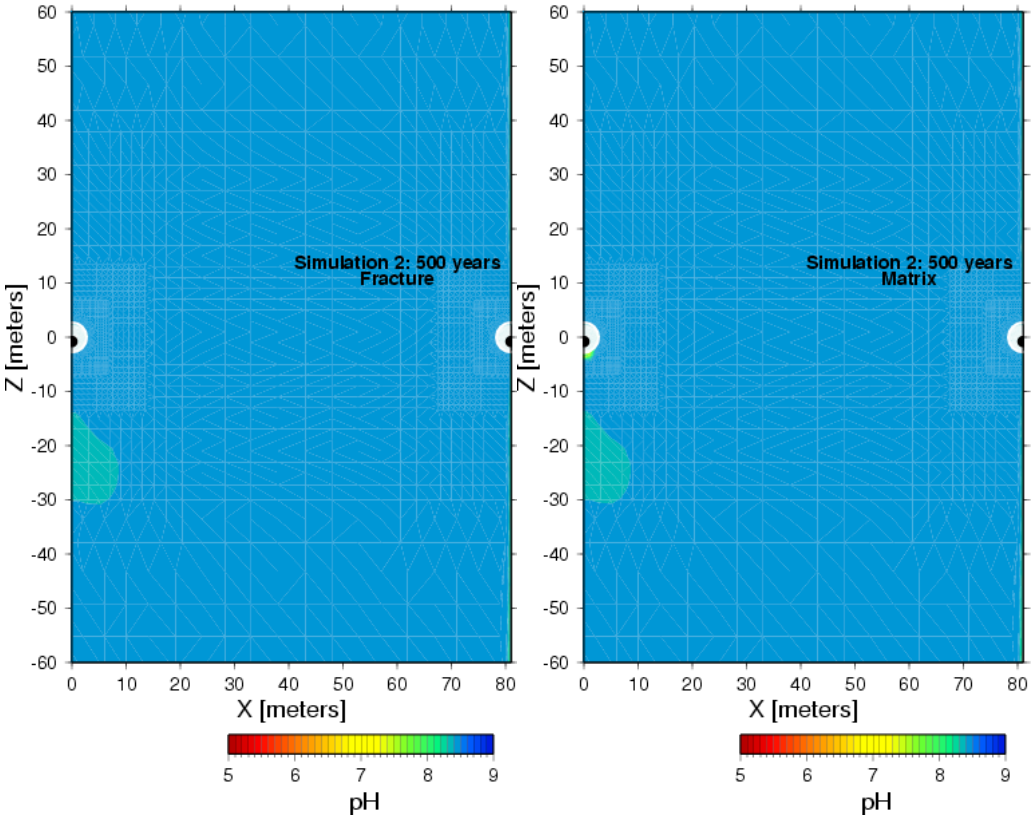

Output DTN: LB0408AMRT0020.001, LB0408AMRT0020.002.

NOTE: Areas that are essentially devoid of water due to evaporation as a result of boiling or being within a gas-filled drift are filled in white.

Figure 6-94. Contoured pH values in fractures and matrix for an enlarged region of the grid after 500 years (Simulation 2)

6.6.5.3 Gas Transport through a Backfilled Connecting Drift (at 300°C)

The purpose of this model simulation is to study the migration of volcanic gas through a backfilled connecting drift. This simulation was performed for Rev. 00 of this model report, using a single half-drift configuration; therefore, it addresses a blockage only on the order of 35 m. It considers a volcanic gas consisting of only water vapor, CO_2, and SO_2. The results of Section 6.6.5.1 show clearly that more reactive gases, such as HF and HC1, are much more strongly attenuated than are those two oxides. The volcanic gas temperature is fixed to 300°C. Although this is lower than the temperature employed in the flow-through pillar calculations of Sections 6.6.5.1 and 6.6.5.2, it remains well above the boiling point of pore water, so the same saturation front effects seen in those results are still simulated when conditions warrant. The pressure is at the ambient value of approximately 88 kPa. This model considers a horizontal region (about 5.5 m in width) filled with crushed tuff extending from the drift wall to the right boundary of the model. Thus, the model is applicable to a backfilled access drift that has been further blocked by seismically induced caving or rockfall, as was determined to be likely at later times (BSC 2004 [DIRS 166107]), or to any fully blocked section of a drift. The backfill material is given the same porosity as the invert (0.545; BSC 2004 [DIRS 169856], Table 4.1-6). The saturation of the crushed tuff is set initially to zero (BSC 2003 [DIRS 169856]). The

volcanic gas composition (in mole percent) was set to 14.3 percent CO_2 and 9.3 percent SO_2, with the water content fixed to that given by the pressure-temperature conditions for a vapor plus air mixture calculated by TOUGHREACT (LBNL 2002 [DIRS 161256]). The CO_2 and SO_2 percentages were derived from *Characterize Eruptive Processes at Yucca Mountain, Nevada* (BSC 2004 [DIRS 169980], Table 6-3).

Modeled distributions of CO_2 concentrations (log-volume fractions) are shown after 10 days, 20 days, 30 days, and 40 days in Figure 6-95. A high-CO_2-concentration region migrates rapidly along the horizontal region that is filled with crushed tuff. At 45 days, volcanic CO_2 reaches the distance of 30 m along the backfilled connecting drift.

Figure 6-96 shows modeled SO_2 concentrations (log-volume fractions) after 10 days, 20 days, 30 days, and 40 days. Comparison of contours in Figure 6-96 with contours in Figure 6-95 reveals the retardation of the highest levels of SO_2 relative to the highest levels of CO_2, while the front of the diffusion moves at similar rates for both species. Thus, the backfill will serve as an effective block to the most corrosive gases, retarding the reactive species as it slows and diffuses the general flow of gas.

Figure 6-97 shows the distribution of pH at 10 days, 20 days, 30 days, and 40 days. The black color in Figure 6-97 indicates pH below 6. Two low-pH regions extend horizontally along the edges of the backfilled tunnel from the drift toward to the right. These regions formed through diffusion of CO_2 into the rock, followed by dissolution in the ambient pore water and a lowering of the pH. Disturbances seen at about 2-8 m and 14-18 m are numerical artifacts caused by mesh irregularities.

Simulation results are shown only for 40 days because gas transport is much more rapid through this material, reaching the boundary 40.5 m away in less than 1.5 months. Temperatures are slightly depressed in this zone relative to that in the rock because of the low thermal conductivity of this mostly gas-filled porous material and the lack of a significant advective component out of the drift, which would result in higher temperatures and faster gas migration. Although in the actual system, vapor condensation and redox reactions would likely cause some retardation of the gas migration front, these reactions would likely not be a major factor because of the high porosity and low water saturation of the crushed tuff.

The backfill in the main drifts is not expected to completely fill the drift cross-section; rather there will be a gap on the order of a meter high at the top of the backfill. However, the magmatic gases modeled in the above analysis are expected to be contained using a sand-backfilled keyway described in *Magma Bulkhead Analysis* (BSC 2004 [DIRS 171070]), which is designed to ensure at least several meters of complete closure when magma presses against it. At higher applied pressures, the length of tightly closed drift is greater, reaching 18 m for 6 MPa magma pressure. Using that result in conjunction with the results illustrated in Figures 6-95 through 6-97, it is concluded that the backfilled keyway will act as an impediment to migration of the most corrosive gases. Although this backfill gas flow calculation did not include either HCl or HF, Figure 6-90 indicates both those gases will lag far behind SO_2 and CO_2; and Figure 6-96 shows that SO_2 is diluted by an order of magnitude (down from its initial concentration of 9.3 percent) at a range of 18 m after 40 days and the highest concentrations are confined to less than 10 m from the source.

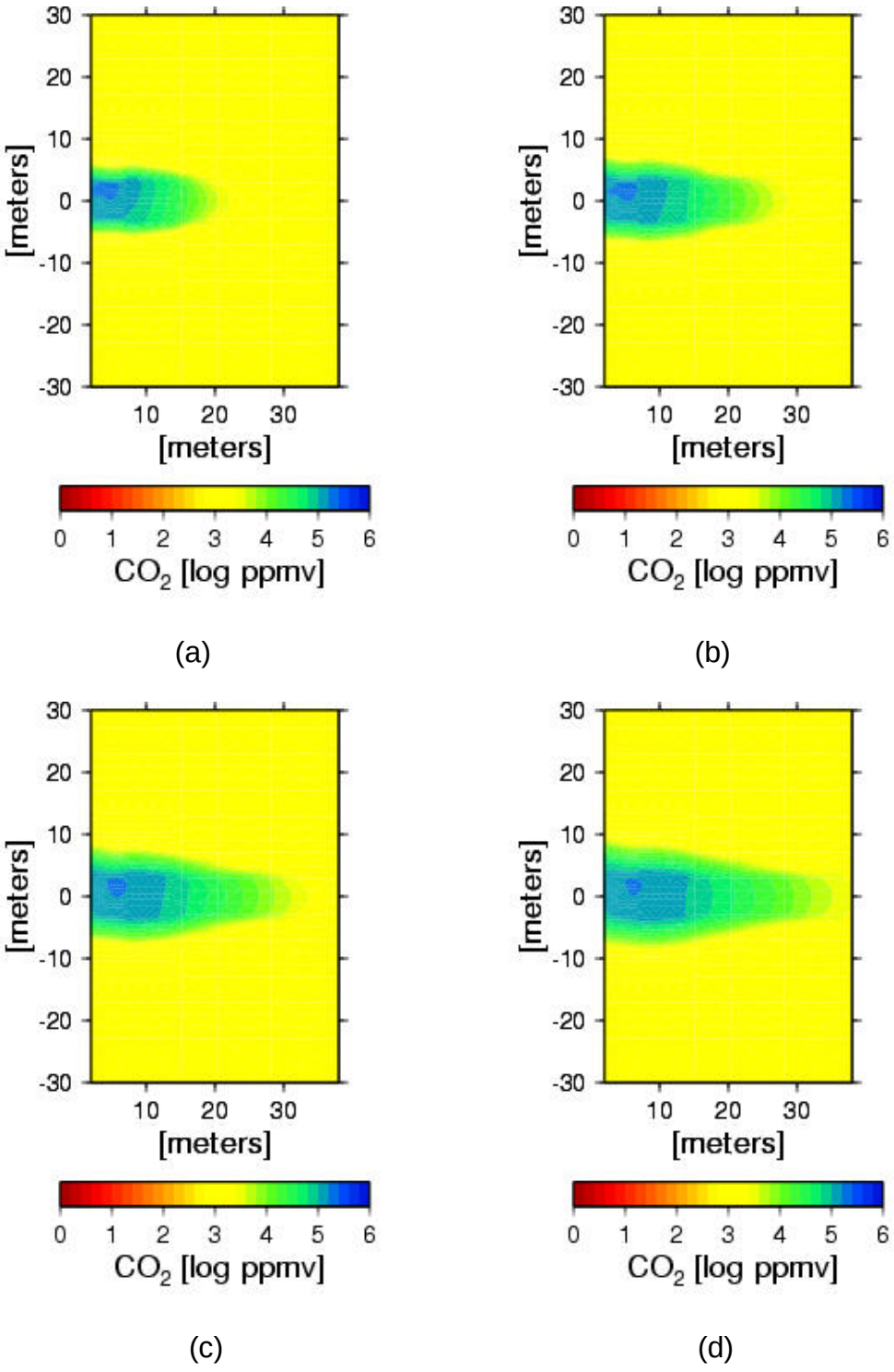

Output DTN: LB0306AMRT0020.001.

Source: Output Data Plots.

Figure 6-95. Gas-Phase CO_2 Concentrations After (a) 10 Days, (b) 20 Days, (c) 30 Days, and (d) 40 Days

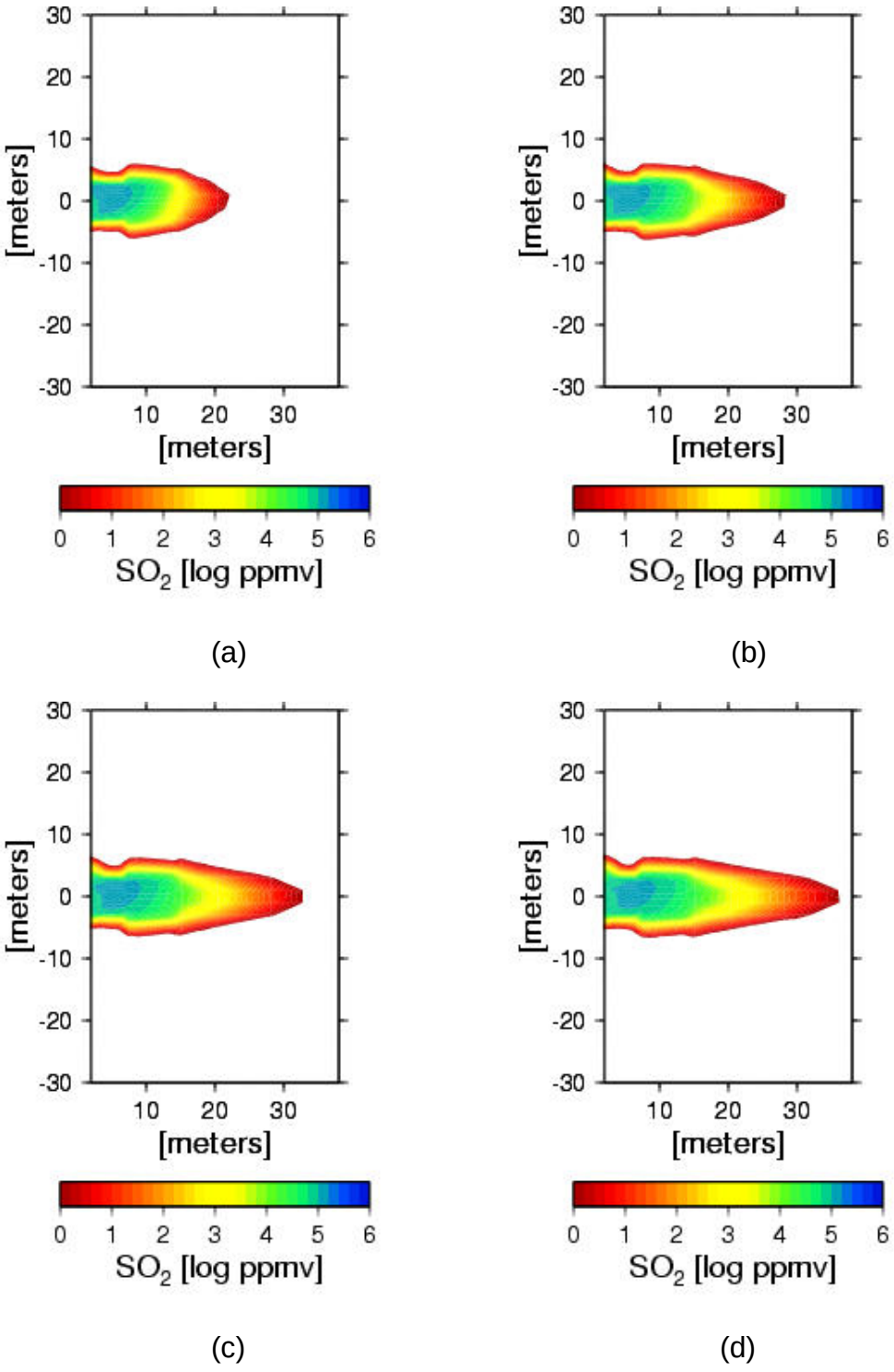

Output DTN: LB0306AMRT0020.001.

Source: Output Data Plots.

Figure 6-96. Gas-Phase SO_2 Concentrations After (a) 10 Days, (b) 20 Days, (c) 30 Days, and (d) 40 Days

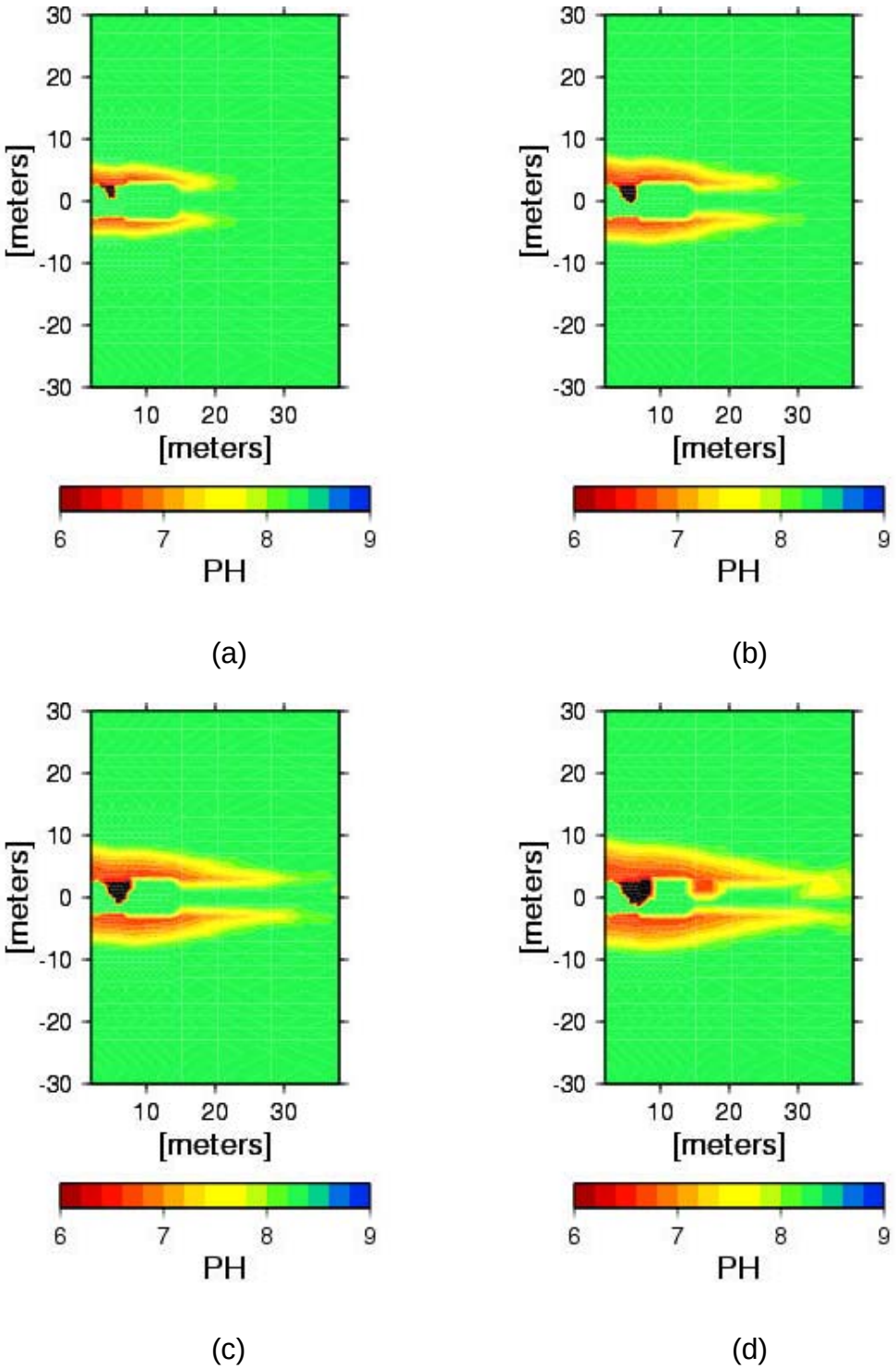

Output DTN: LB0306AMRT0020.001.

Source: Output Data Plots.

Figure 6-97. Distribution of pH After (a) 10 Days, (b) 20 Days, (c) 30 Days, and (d) 40 Days

6.6.6 Summary of Gas Flow Analyses

The calculations consider only a "cold repository" (i.e., after the end of the thermal phase) so that the analysis is not representative of intrusion during the first 2000 years after closure. However, because the effect of the boiling-condensation zone is to impede gas flow through the rock, and thermal-mechanical effects and mineral precipitation tend to reduce fracture permeability, the consideration of an initially cold repository is conservative with respect to gas transport.

The high solubility in water of HCl and HF (and their relatively low initial concentrations in the volcanic gas) and, to a lesser extent, SO_2 and CO_2, along with the development of a boiling zone around a drift where magma has been emplaced, limits the migration of these gases through the repository host rock. The model results, under near-ambient pressure conditions, indicate that CO_2, HCl, and HF gas species would not migrate to an adjacent drift through the rock over a 500-year period after a single injection into a drift. HCl and HF gases are essentially immobilized by dissolution into condensate and matrix pore water within the boiling zone and do not migrate in significant concentrations more than about 10 meters from the Zone 1 drift wall. A low concentration of SO_2 gas does reach an adjacent Zone 2 drift over a period of about 500 years with concentrations on the order of 1 ppmv in the drift. The migration of SO_2 in the gas phase to the other drift, in contrast to the other gas species, is a result of its lower solubility and secondarily to it smaller diffusivity.

In addition to the dissolution of SO_2 into the aqueous phase, oxidation-reduction reactions involving sulfur species that were not considered in the model would further retard gas migration in two ways. First, the mineral-water reactions would generate sulfide or sulfate phases. Second, sulfur reduction would likely result in acidic fluids, thus enhancing mineral alteration in fractures. The resulting formation of clay minerals in fractures would reduce the permeability, thereby retarding further migration of gas through the rock. Therefore, the model for SO_2 gas migration to an adjacent Zone 2 drift is considered to be conservative.

Volcanic gas migration may be relatively rapid through a connecting drift filled with coarse crushed tuff. In this case, an adjacent emplacement drift could be affected by migrating volcanic gas within a year or less without any strong advective flow due to large pressure differences, if the gas production is constant for some time (a month or longer). As the gas migrates through the connecting drifts and into a neighboring emplacement drift, the volcanic gas will be diluted by air, and as the gas source from the magma declines over time the extent of dilution by air will increase. The crushed tuff filling the connecting drifts would likely have some initial water content, and therefore retardation of the gas would likely be somewhat greater than the case modeled.

6.7 EFFECTS ON NEIGHBORING DRIFTS OF MAGMA COOLING AND SOLIDIFICATION

6.7.1 Magma Cooling and Solidification

The thermal history of a magma-filled drift after intrusion will impact the evolution of the integrity of the waste packages and the waste form and also will affect the movement of volatile

phases through the pore volume of the surrounding rock. Therefore, this section discusses the dispersal of the heat associated with the magma over the years following a hypothetical drift-filling magmatic event.

6.7.1.1 Problem Definition

Consider a drift 5.5 m in diameter and 637-m long created in tuff at a depth of 300 m below the surface, and where the ambient tuff temperature is ~30°C. The aspect ratio of such an excavation is >100. Thus, for the vast majority of the volume of the drifts, heating can be treated as a cylindrical 1-dimensional heat flow problem. If a drift were to be instantaneously and entirely filled with basaltic magma at a temperature of ~1150°C (BSC 2004 [DIRS 169980]), the tuff surrounding the drift would begin to heat up as the magma cooled, and the temperature profile through the drift and surrounding rock would evolve with time.

The temperature distribution for magma filling a Zone 1 emplacement drift can be estimated using an idealized model of one-dimensional unsteady heat conduction in a cylinder [i.e., drift], subject to constant heat content. This simplified model may be used to estimate the length of time it takes for the repository to cool back to any temperature of interest. The contribution of latent heat and heat transfer due to convection is neglected in the base case, although the effects of latent heat are considered to evaluate uncertainty, as well as in greater detail in Section 7. Any advection of gases in the surrounding host rock, as well as the release of volatiles from the cooling magma will enhance the cooling rate; thus, these purely convective calculations will tend to overestimate magmatic and host-rock cooling rates with respect to the mass flow of hot gases.

In this model, the temperature of the repository host rock is considered to be between 25°C and 200°C at the time of the intrusion. The thermal properties of the magma are considered to be the same as those for the densely welded tuff (see Section 4) for a first order analysis. Details for the heat conduction model are presented, along with pertinent equations, in Appendix C.

The simulations consider the four types of lithophysal and nonlithophysal units that comprise the repository horizon of the Topopah Spring Tuff, as summarized in Table 6-17.

Table 6-17. Summary of Lithostratigraphic Units of the Repository Horizon Considered in Thermal Calculation

Formation Symbol	Phenocryst Content Symbol	Lithophysal Content Symbol	Total Lithostratigraphic Symbol
Tpt= Topopah Spring Tuff	p=crystal poor	ul=upper lithophysal	Tptpul
		mn=middle non-lithophysal	Tptpmn
		ll=lower lithophysal	Tptpll
		lower non-lithophysal	Tptpln

To cover a broad range of potential conditions, the analysis assumes two different alternative thermal states for the tuff matrix where: a) the matrix is saturated with water, and b) the matrix is dry. Of course, these conditions are idealized, although they encompass the full range of possible states with respect to matrix water content.

6.7.1.2 Results of Model Simulations

The results of the analysis for different repository horizon rock units for a period of 100 years are presented in Figures 6-98 and 6-99 for wet and dry states of Tptpll. The results for the three other lithostratigraphic horizons are so similar to the Tptpll results that the differences cannot be distinguished graphically. Only the results for Tptpll are shown.

The calculations show that initial temperatures near the drift are high and attenuate rapidly into the surrounding tuff. Outside the drift, peak temperatures are always less than magmatic temperatures and are not reached until sufficient time has passed to accommodate conductive heating of the wall rock. For example, the peak temperature at a 10-m radius is less than boiling, and is attained only after one year for both conditions of saturation. Under endmember saturations, the temperature reaches near ambient conditions of ~30°C at drift center in ~30 years (Figures 6-98 and 6-99). The analysis also shows that the maximum temperature rise in an adjacent, unaffected drift [Zone 2] is small (less than 10°C), and the rock provides an effective thermal barrier to the impacts of heat transfer from magmatic intrusion.

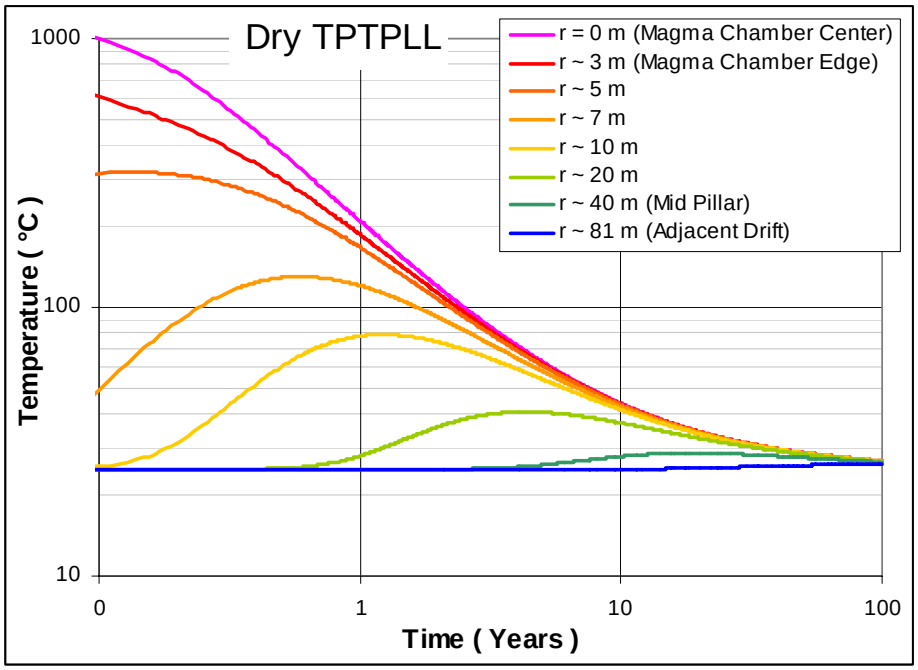

Output DTN: MO0408EG831811.008.

Figure 6-98. Heat Conduction from Magma Flow for Dry Tptpll

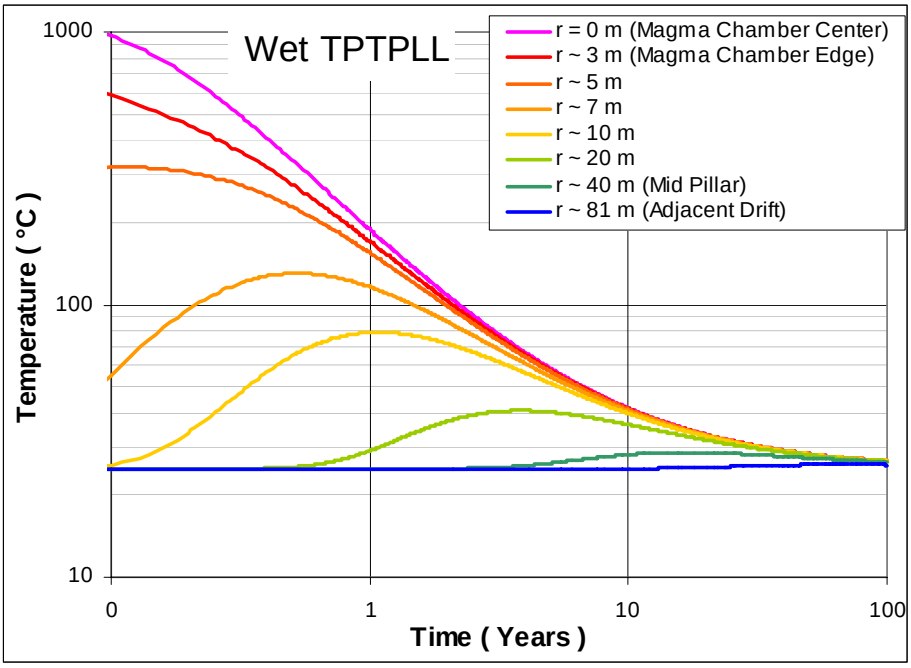

Output DTN: MO0408EG831811.008

Figure 6-99. Heat Conduction from Magma Flow for Wet Tptpll

This conclusion of minimal thermal impact on Zone 2 drifts is based on a conceptualization of the filling of a single drift with magma, when, in fact, a dike may intersect multiple drifts, raising the potential for the development of overlapping thermal aureoles. However, it can be easily shown that for a multiple drift intersection scenario, the volume of intersected drifts is about 6 percent of the volume of the *smallest* rectangular volume that can contain those drifts. For example, 10 drifts contain the following volume:

$$V = \pi r^2 L$$
$$V = \pi \cdot 2.75^2 \cdot L \qquad \text{(Eq. 6-114)}$$

V=volume of a single drift [m^3]=23.76L m^3

r=drift radius [m]=2.75 m (BSC 2004 [DIRS 168489])

L=drift length [m]

Thus, the volume of 10 drifts is 237.6 L m^3

The rectangular volume containing these drifts is:

$$V_1 = 81nLH$$
$$V_1 = 81 \cdot 10 \cdot L \cdot 5.5 = 4455.0 \cdot Lm^3 \qquad \text{(Eq. 6-115)}$$

V_n =rectangular volume containing n drifts

81=drift spacing [m] (BSC 2004 [DIRS 168489])

n=number of drifts=10

Thus: $\frac{V}{V_1} \cong 5.3\%$

The additive thermal impact of multiple drift intersections is therefore necessarily small as the surrounding rock mass presents an enormous volumetric heat sink. Therefore, the spatial and temporal heat conduction simulations and analyses suggest that the waste packages in Zone 2 emplacement drifts would not be affected by the heat conduction from magma intruded into multiple Zone 1 emplacement drifts.

6.7.2 Alternative Models

6.7.2.1 Sensitivity to Latent Heat Effects

The latent heat generated by crystallization of cooling magma can be significant, lengthening the time required to cool a drift/wallrock system to back to ambient conditions. Latent heat is liberated during crystallization of the magma; thus, its effects are most pronounced at early times while the magma is still above its solidus temperature.

A simple way to simulate latent heat is by increasing the initial temperature of the magma. In this section, cooling calculations are repeated by raising the initial magmatic temperature by 100°C to 1250°C to roughly account for the latent heat. The results are compared with the base case and presented in Figures 6-100 and 6-101. The figures show little change in the results. At the center of the drift, the temperature falls below 100°C at 2.5 years, or at 2.7 years if the effects of latent heat are included. At the drift wall, the temperature falls below 100°C at 2.5 years, or at 2.6 years if the effects of latent heat are approximated. As will be shown in Section 7.3.2.2, a more conservative conceptualization of latent heat effects [i.e., higher latent heat content] shows that cooling to 100°C is accomplished within 2 to 5 years. Considering the geologic timeframes of interest and inherent uncertainty in these calculations, these differences are negligible.

6.7.2.2 Sensitivity to Saturation

Ventilation Model and Analysis Report (BSC 2004 ([DIRS 169862], Section 8) shows that the change in temperature based on the saturation of the matrix is less than 5 percent, therefore the effects of enhanced vapor diffusion will be minimal. Convection in a saturated matrix is also a consideration, but is expected to be minimal based on the low porosity of the rock, the fact that the temperatures attenuate rapidly over time, and that the high temperatures are only sustained over short distances.

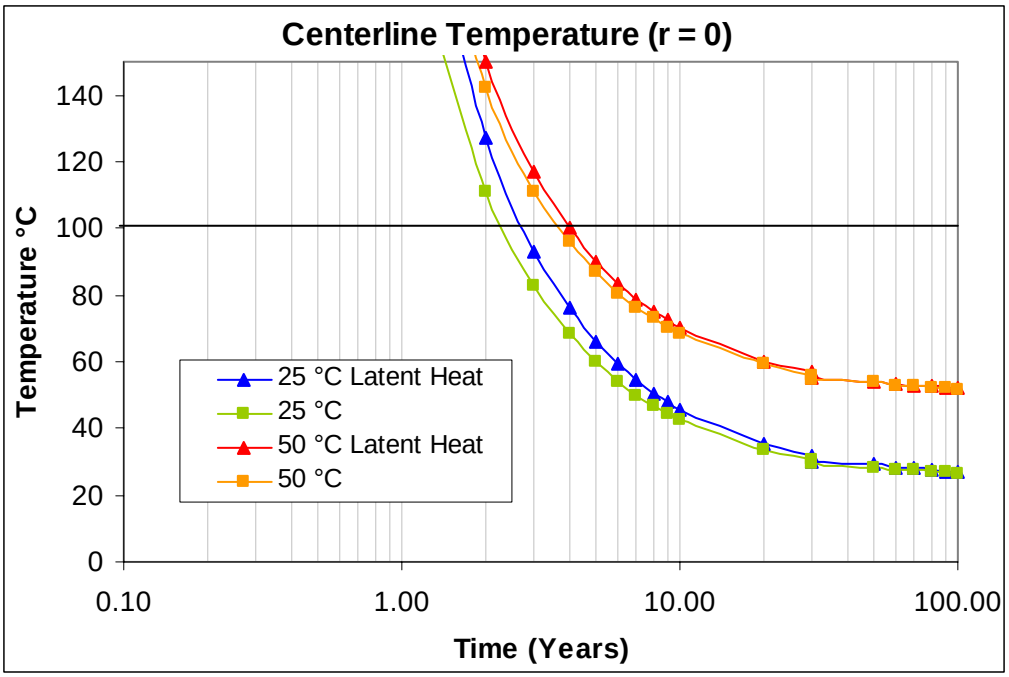

Output DTN: MO0408EG831811.008.

Figure 6-100. Latent Heat Effect at Centerline

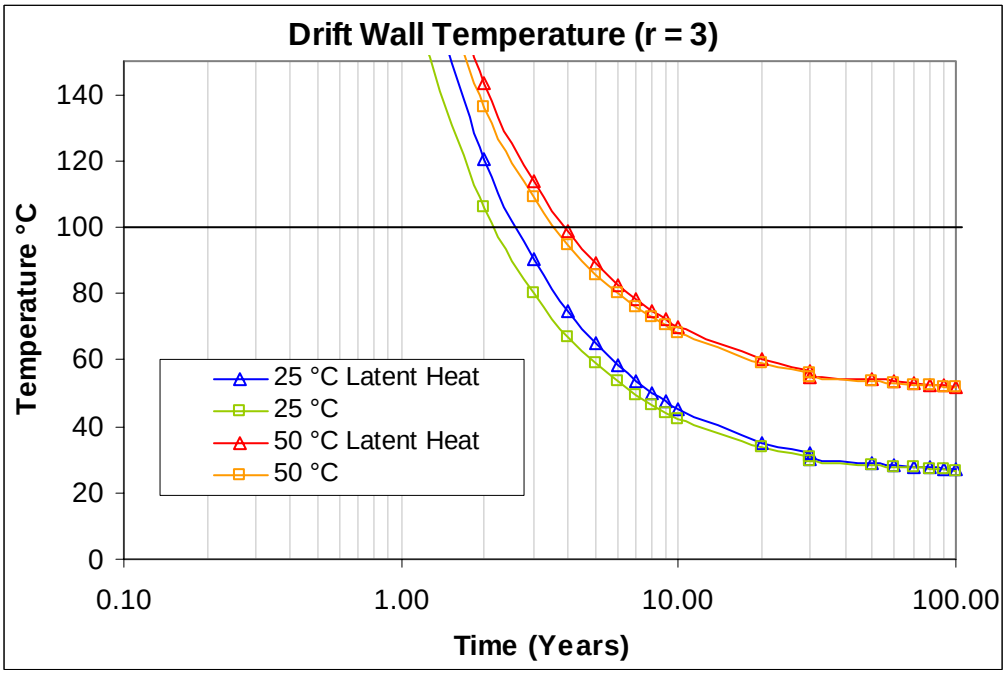

Output DTN: MO0408EG831811.008.

Figure 6-101. Latent Heat effect at Drift Wall

6.7.2.3 Analytical Solution to Heat Flow

An alternative model for heat conduction from Zone 1 to Zone 2 emplacement drifts involves the use of analytical solutions, whereas the base case model presented in Section 6.7.1 uses a finite difference approach. This analysis is presented in full detail in Appendix D.

6.8 REACTION OF SEEPAGE WATER WITH BASALT AFTER REVERSION TO NORMAL IN-DRIFT ENVIRONMENTAL CONDITIONS

After post-intrusive magma cooling to ambient conditions, the seepage water is expected to flow through any contact metamorphic aureole that may form and react with the basalt in the intruded emplacement drifts, resulting in a seepage water modified by interaction with the mineralogy of basalt. It is assumed in this model that the permeability of any contact metamorphic aureole is not significantly different from that of the unaltered tuff (Section 5.4.1). This modified seepage water chemistry is addressed in TSPA-LA in terms of its effect on waste forms. The geochemical interaction of seepage water with the basalt and the resulting hydrochemistry are simulated using EQ3/6 (CRWMS M&O 1999 [DIRS 153964]).

The following subsections describe calculated parameters used as inputs into EQ6 (CRWMS-M&O 1999 [DIRS 153964]) simulations. All data for EQ6 simulations taken directly from controlled sources can be found in Section 4.1.1.2. The results of the EQ6 simulations are located in Section 6.8.3. The effects of the presence of solid solution minerals within basalt are approximated in EQ3/6 (CRWMS M&O 1999 [DIRS 153964]) by the specification of relevant endmember minerals as reactant phases. The abstracted minerals used in the simulations reflect the normative mineralogy of basalt (Table 6-18) calculations from major element oxide data in *Characterize Eruptive Processes at Yucca Mountain, Nevada* (BSC 2004 [DIRS 169980], Table 6-2; pp. 6-19 and 6-20). The "normative calculation," which is a standard petrologic tool for converting major element composition (in oxides) to a suite of idealized endmember minerals (McBirney 1993 [DIRS 163334], Appendix A, pp. 459-462), uses endmember compositions to deal with solid solution minerals such as feldspar and pyroxene. Although this may lead to minor inaccuracies in solubilities and kinetic factors, it is expected to simulate the general geochemical behavior properly. A comparison of the normative mineralogy to the modal mineralogy of Lathrop Wells basalt follows:

- Vaniman et al. (1982 [DIRS 101031]) indicates that the groundmass is primarily plagioclase, pyroxene, and olivine with olivine phenocrysts (up to 3 percent). Perry and Straub (1996 [DIRS 106490]) indicate a groundmass composition of plagioclase, olivine, titanomagnetite, and clinopyroxene with olivine and plagioclase phenocrysts. Plagioclase phenocrysts are found primarily in chronostratigraphic unit I and largely absent from chronostratigraphic units II, III, and IV (See Perry and Straub 1996 [DIRS 106490] for definition of units).

- Olivine phenocrysts comprise three modal percent of the youngest basalt at Crater Flat Vaniman et al. (1982 [DIRS 101031]). The olivine in the normative calculation was divided between the two end members of forsterite (Mg-olivine) and fayalite (Fe-olivine) with forsterite composing between 76-79 percent of the olivine (Vaniman et al. 1982 [DIRS 101031]).

Table 6-18. Normative Mineral Composition of Basalt

EQ6 Minerals	EQ6 Mineral Formula	Mineral Molecular Weight	Wt%[a]
Forsterite	Mg_2SiO_4	140.69	2.363
Fayalite	Fe_2SiO_4	203.77	0.90977
Magnetite	Fe_3O_4	231.53	6.06248
Ilmenite	$FeTiO_3$	151.71	3.69225
Hydroxylapatite	$Ca_5(PO_4)_3(OH)$	502.31	2.8987
Sanidine	$KAlSi_3O_8$	278.33	10.9511
Anorthite	$CaAl_2(SiO_4)_2$	278.21	24.5643
Albite	$NaAlSi_3O_8$	262.22	25.6512
Nepheline	$NaAlSiO_4$	142.05	2.40048
Hedenbergite	$FeCaSi_2O_6$	248.09	9.25437
Enstatite	$MgSiO_3$	100.39	11.2524

Source: [a] Values above calculated in *basalt-separated.xls* (see Appendix E) from composition provided in Table 4-5 of this report.

- Plagioclase has a solid solution composition equivalent to andesine is indicated as the major plagioclase species in the Crater Flat area (Vaniman et al. 1982 [DIRS 101031]). As a mineral of intermediate composition in a solid solution series, it was represented in the normative analysis by the two end members, albite and anorthite. According to Vaniman et al. (1982 [DIRS 101031]), the end member anorthite represents 30-53 percent of the plagioclase.

- Pyroxenes are solid solution minerals and therefore present a similar problem to plagioclase. Basalts in the Crater Flat area include both clinopyoxene (augite) and orthopyroxene (hypersthene). Thus, end-member pyroxene compositions were substituted. Enstatite and hedenbergite were used for orthopyroxene and clinopyroxene, respectively.

- Nepheline is not present as a major mineral at Crater Flat (Vaniman et al. 1982 [DIRS 101031]). However, it is included in their normative analysis of the Lathrop Wells Cone at between 0 and 2.2 percent. It is conceivable that nepheline or some other feldspathoid, could be present as a minor groundmass phase, or that a small percentage of interstitial, alkali-rich glass exists.

- As a phenocryst phase, sanidine is not present nor is it expected to be present in basaltic rocks. However, it appears as a normative component in the composition of Lathrop Wells basalt. The true major K_2O-bearing phase is likely to consist of an alkali or ternary feldspar component in the groundmass, a small proportion of a residual glass differentiate [rhyolitic in composition], or both.

- Apatite is a common accessory phase in silicic igneous rocks. In basalt, however, it is most likely to be found as a microcrystalline phase in the groundmass, or as a component in residual interstitial silicic glass.

- Although some mafic silicate minerals common to basalts, especially clinopyroxenes, may contain measurable TiO_2, the presence of titanium cannot be explicitly accounted for in the idealized mineralogy of the EQ6 database. The presence of ~2.5 percent normative ilmenite in Lathrop Wells basalt (Vaniman et al. 1982 [DIRS 101031]) must be accounted for, however. The only practical choice for EQ3/6 (CRWMS M&O 1999 [DIRS 153964]) modeling is ilmenite, so this phase was included. In terms of modal phases in the rock, however, titanium is almost certainly present in Lathrop Wells basalt as a solid-solution constituent in pyroxene and especially magnetite.

- Magnetite was allotted the remaining iron in the normative analysis. This phase is abundant in the groundmass of Lathrop Wells basalt, and as mentioned above, may contain significant titanium.

6.8.1 EQ6 Basalt/Water Interaction

The approach to establishing a range of conservative values of ionic strengths and pH involved the use of the EQ3/6 geochemical modeling software (CRWMS M&O 1999 [DIRS 153964]). These values are conservative in the sense that the resulting ionic strengths are higher, and, therefore, chemically more aggressive, than analog compositions of waters from basalt aquifers (see Section 7.3.2.3). In summary, selected waters (Bin 8, 11 and J-13) were allowed to react with the mineralogy outlined above. Bin 8 water was used as a base case, whereas Bin 11 and J-13 waters were considered in sensitivity analyses. Multiple calculations were based upon varied seepage rates, fCO_2 values, matrix saturations, and mineral surface areas. Resulting water compositions, in terms of pH, ionic strength, and time step are summarized in Section 6.8.4.1.

For reactive transport, EQ6 (CRWMS-M&O 1999 [DIRS 153964]) requires the input of mineral surface areas and moles. These values, calculated in *basalt-separated.xls* (see Appendix E) are shown in Table 6-19. It should be noted that these values are based on having meter sized basalt blocks (see Section 5.4.2) in the fractured drifts and a saturation of 0.1 (saturation of 0.12 from Table 4-11 rounded to 0.1).

Table 6-19. Surface Area and Moles of Mineral Reactants

Mineral	Moles	Surface Area (cm^2)
Forsterite	2.531E+01	6.92E+01
Fayalite	6.728E+00	2.67E+01
Magnetite	3.946E+01	1.78E+02
Ilmenite	3.668E+01	1.08E+02
Hydroxylapatite	8.697E+00	8.49E+01
Sanidine	5.930E+01	3.21E+02
Anorthite	1.331E+02	7.20E+02
Albite	1.474E+02	7.51E+02
Nepheline	2.547E+01	7.03E+01
Hedenbergite	5.622E+01	2.71E+02
Enstatite	1.689E+02	3.30E+02

NOTE: Calculated in *basalt-separated.xls* (see Appendix E, Disk 1).

The dissolution rates of materials come from peer-reviewed literature sources and are presented in Tables 4-7, 4-8, and 4-9. The dissolution rates employed by EQ6 (CRWMS-M&O 1999 [DIRS 153964]) calculations use these values, which are summarized in Table 6-20 and Appendix B. The rates for the minerals in the EQ6 cases were cast in the transition state theory formalism (Wolery and Daveler 1992 [DIRS 100097], Section 3.3.3). A more in-depth discussion on the mineral dissolution rates can be found in Appendix B.

The composition of the water running through the basalt block (Table 6-21) is Bin 8 seepage water from DTN: MO0310SPAEBSCB.003 [DIRS 166411]. The flow rates below were derived from infiltration rates in DTN: LB0310AMRU0120.001 [DIRS 166409] and are calculated in *basalt-separated.xls* (see Appendix E).

Table 6-20. Dissolution Rates of Basaltic Minerals

Mineral	Acidic leg		Basic Leg	
	k_1	S1	k_2	S2
Anorthite	1.58E-11	0.91	2.0E-18	-0.3
Albite_low	7.94E-15	0.33	5.01E-19	-0.32
Nepheline	3.98E-08	1.0	7.94E-15	-0.2
Sanidine_high	Used same rate as albite			
Fayalite	7.94E-12	0.4	5.25E-15	0
Forsterite	7.94E-12	0.4	5.25E-15	0
Enstatite	1.58E-12	0.57	1.26E-19	-0.44
Hedenbergite	3.16E-11	0.7	6.31E-16	0

Table 6-20. Dissolution Rates of Basaltic Minerals (Continued)

Mineral	Acidic leg		Basic Leg	
	k_1	S1	k_2	S2
Hydroxylapatite	1.00E-12	0.35	1.17E-17	-0.35
Ilmenite	4.57E-13	0.462	1.55E-19	-0.462
Magnetite	2.09E-13	0.232	1.17E-16	-0.232

NOTES: Total Dissolution Rate = $k_1[H^+]^{S1} + k_2[H^+]^{S2}$ (moles/cm^2·s).
All values above were extrapolated in Microsoft Excel spreadsheets *Aluminosilicate rates.xls*, *pyroxene rates.xls*, *olivine rate.xls*, *oxides rate.xls*, and *apatite rate.xls* (see Appendix E) from rates in Tables 4-7, 4-8, and 4-9.

"S" represents the negative slope of the Log(rate) versus pH presented in this table (see Appendix E).

Table 6-21. Water Composition and Flow Rate Used in the EQ3/6 Input Files of Water/Basalt Interaction

EQ3NR Input Composition Values				EQ6 Input File Composition[c]		
Element	Basis Switch	Concentration[a]	Units	Element	Concentration	Units
redox		-0.7 [b]	log (fO_2/bar)	Na	7.31E-03	Moles/kg
Na^+		168.0	mg/L	Si	1.80E-03	Moles/kg
SiO_2(aq)		108.0	mg/L	Ca	5.74E-04	Moles/kg
Ca^{++}		23.0	mg/L	K	2.76E-04	Moles/kg
K^+		10.8	mg/L	Mg	8.52E-05	Moles/kg
Mg^{++}		2.07	mg/L	O	5.55E+01	Moles/kg
H^+		7.94	pH	F	6.42E-04	Moles/kg
F^-		12.2	mg/L	Cl	5.61E-04	Moles/kg
Cl^-		19.9	mg/L	N	3.97E-05	Moles/kg
NO_3^-	NH_3(aq)	2.46	mg/L	S	3.55E-04	Moles/kg
SO_4^{--}		34.1	mg/L	Al	1.50E-09	Moles/kg
Al		4.05E-05	mg/L	Fe	1.49E-12	Moles/kg
Fe^{++}		8.32E-08	mg/L			

Table 6-21. Water Composition and Flow Rate Used in the EQ3/6 Input Files of Water/Basalt Interaction (Continued)

EQ3NR Input Composition Values				EQ6 Input File Composition[c]		
Element	Basis Switch	Concentration[a]	Units	Element	Concentration	Units
pH and Carbon Concentrations[c]						
Log f_{CO_2} value (bar)	-2	-2.5	-3	-3.5	-4	
EQ6 Starting pH	7.65	8.13	8.60	9.01	9.38	
C (moles/kg)	7.09E-03	6.75E-03	6.29E-03	5.58E-03	4.73E-03	

Flow Rate			
Rate	Saturation	Porosity	EQ6 Rate[d]
0.4 mm/year*	0.1	0.17	1.73E-10 moles/s
	1.0	0.17	1.73E-11 moles/s
	0.1	0.13	2.26E-10 moles/s
3.8*	0.1	0.17	1.64E-09 moles/s
11.7*	0.1	0.17	5.05E-09 moles/s

Source: * LB0310AMRU0120.001 [DIRS 166409].

[a] Calculated in *conversions.xls* (see Appendix E) from values in Table 4-10.
[b] Equilibrium atmospheric levels of oxygen.
[c] These values are the output from EQ3NR for input into EQ6 input files. Charge balance was maintained for EQ3 calculations by varying hydrogen activities.
[d] Calculated in Microsoft Excel spreadsheet *basalt-separated.xls*.

By changing the saturation to 1.0 from 0.1 and the pore fraction from 0.17 to 0.13, the moles and surface areas of minerals input into EQ6 (CRWMS M&O 1999 [DIRS 153964]) also change slightly from the base case. These values are presented in Table 6-22.

Table 6-22. Surface Area and Moles of Mineral Reactants with Different Pore Fraction and Saturation

	Saturation of 1.0		Pore fraction of 0.13	
Mineral	Moles	Surface Area (cm^2)	Moles	Surface Area (cm^2)
Forsterite	2.531E+00	6.92E+00	3.470E+01	9.49E+01
Fayalite	6.728E-01	2.67E+00	9.223E+00	3.65E+01
Magnetite	3.946E+00	1.78E+01	5.409E+01	2.43E+02
Ilmenite	3.668E+00	1.08E+01	5.028E+01	1.48E+02
Hydroxylapatite	8.697E-01	8.49E+00	1.192E+01	1.16E+02
Sanidine	5.930E+00	3.21E+01	8.128E+01	4.40E+02
Anorthite	1.331E+01	7.20E+01	1.824E+02	9.86E+02
Albite	1.474E+01	7.51E+01	2.021E+02	1.03E+03
Nepheline	2.547E+00	7.03E+00	3.491E+01	9.64E+01
Hedenbergite	5.622E+00	2.71E+01	7.706E+01	3.72E+02
Enstatite	1.689E+01	3.30E+01	2.315E+02	4.52E+02

NOTE: Calculated in *basalt-separated.xls* (see Appendix E).

Another case involves decreasing the surface area in the case by a factor of 10. To find the flow rate at which the incoming water is unaffected by reaction with the basalt, three cases were run that increased the flow rate of the water from that listed in Section 6.8.4. These rates include fluxes of 25 mm/year (1.079E-08 moles/sec), 50 mm/year (2.158E-08 moles/sec), and 100 mm/year (4.315E-08 moles/sec).

For EQ3 and EQ6 runs, trace concentrations of elements are added to Bin 8 seepage water, Bin 11 seepage water and J-13 well water composition that are not in the original composition, but represent components in the basalt. This ensures numerical stability in EQ6 runs. The trace elements added are found in Table 6-23.

Table 6-23. Elements Added as "Trace" to Water

Ti[a]	P[a]	Mn[a]	Al[b]	Fe[b]

[a] Added to all three water types as trace.
[b] Added only to J-13 well water as trace.

During EQ6 simulations, upon reaction with basalt, mineral phases precipitate from solution into the fractures within the basalt. Several minerals are suppressed from forming in the EQ6 runs because, though thermodynamically favored, they are kinetically unlikely to form upon reaction of water with cooled basalt. The following minerals were suppressed (not allowed to form) in all EQ6 runs:

- Quartz
- Celadonite
- Tridymite
- Dolomite
- Phlogopite
- Dolomite-dis
- Annite
- Dolomite-ord
- Muscovite

The micas (muscovite, annite, celadonite, and phlogopite), quartz, and tridymite are high temperature (>500°C) minerals (Roberts et al. 1990 [DIRS 107105]) and are not expected to form. Celadonite can form at low temperatures, but this is due to either diagenesis of pre-existing material, very low-grade metamorphic processes, or concentration of the liquid environment through evaporation (Li et al. 1997 [DIRS 159034]; 1997 [DIRS 148201]). Dolomite is usually derived by secondary mineralization. Since it rarely occurs as a primary mineral, it was also suppressed (Klein and Hurlbut 1999 [DIRS 124293]).

6.8.2 Sensitivity Cases

Two different water types were used for the sensitivity analysis. The EQ6 input file compositions of Bin 11 seepage-water and J-13 well water (from EQ3NR output) are presented in Table 6-24.

Table 6-24. Water Composition Used in the EQ3/6 Input Files of Water/Basalt Interaction for Sensitivity Cases

EQ6 Input File Composition					
Bin 11 Seepage Water			J-13 Well Water		
Element	Concentration	Units	Element	Concentration	Units
pH	8.00	pH	pH	8.1	pH
Na	4.78E-03	Moles/kg	Na	1.99E-03	Moles/kg
Si	1.19E-02	Moles/kg	Si	1.02E-03	Moles/kg
Ca	3.34E-04	Moles/kg	Ca	3.24E-04	Moles/kg
K	7.49E-04	Moles/kg	K	1.29E-04	Moles/kg
Mg	6.34E-06	Moles/kg	Mg	8.27E-05	Moles/kg
O	5.55E+01	Moles/kg	O	5.55E+01	Moles/kg
C	5.62E-04	Moles/kg	C	2.07E-03	Moles/kg
F	1.38E-03	Moles/kg	F	1.15E-04	Moles/kg
Cl	1.30E-03	Moles/kg	Cl	2.01E-04	Moles/kg
N	1.26E-04	Moles/kg	N	1.42E-04	Moles/kg
S	7.30E-04	Moles/kg	S	1.92E-04	Moles/kg
Al	1.42E-09	Moles/kg	Al	1.00E-16	Moles/kg
Fe	2.08E-12	Moles/kg	Fe	1.00E-16	Moles/kg
P	1.00E-16	Moles/kg	P	1.00E-16	Moles/kg
Mn	1.00E-16	Moles/kg	Mn	1.00E-16	Moles/kg
Ti	1.00E-16	Moles/kg	Ti	1.00E-16	Moles/kg

NOTE: These values are the output from EQ3NR for input into EQ6 input files. Input values for EQ3NR are located in Table 4-12 of this document.

6.8.3 Results of EQ6 Simulations of Crown Seepage Water Reaction With Cooled Basalt

Due to the large amount of output generated through the EQ6 simulations of crown seepage water reaction with cooled basalt in an emplacement drift, information regarding the relevant computer files is located in Appendix E. The recommended abstraction of values (pH, ionic strength, and the fugacities of oxygen and carbon dioxide, fO_2 and fCO_2) for use in TSPA-LA is presented in Section 6.8.4.1, "Discussion of Uncertainties" in Table 6-25 in order to fully bracket the range of expected geochemical conditions. There is no basis for choosing preferred values of pH and ionic strength in Table 6-25 for any given fCO_2 or time increment. Therefore, it is recommended that TSPA sample uniformly between the minimum and maximum values in Table 6-25.

Fluoride content of the water in contact with basalt is listed as one of the outputs of this model in *Technical Work Plan for Waste Form Degradation Modeling, Testing, and Analyses in Support of LA* (BSC 2004 [DIRS 167796]). Many EQ6 simulations of basalt/water interactions show no change in fluoride content. In other words, the final fluoride content largely reflects the starting water composition. Therefore, no abstraction of this parameter was completed on the basis of EQ6 simulations.

It is possible to compare modeled fluoride concentrations to natural systems. Fluoride concentrations from basalt aquifers are usually quite low. Data for 32 waters from basalt aquifers (Hearn et al. 1985 [DIRS 166893]; White et al. 1980 [DIRS 163752]; and Hem 1985 [DIRS 115670]) have a mean F^- content of 0.8±0.8 (1σ) mg/L. The median value is 0.5 mg/L, reflective of the fact that the mean is skewed upward on the basis of a few analyses with F^- compositions in the range of a few mg/L.

All starting waters (Bin 8, 11, and J-13 waters) have F^- contents substantially higher than those typically found in natural basalt aquifers. Given the incomplete reaction of starting waters with basalt, and accompanying precipitation of fluoride-bearing phases, seepage waters may be considered to vary in fluoride content between 0.5 mg/L and the values represented by Bin 8, Bin 11, and J-13, although fluoride concentrations are currently not employed in TSPA abstractions.

In some instances, TSPA may need pH and ionic strength values for a range of parameters that are outside the range of values recommended in this report. Such parameters include flux rate and log fCO_2. In the case of flux, it was observed in EQ6 calculations (see Appendix E for information regarding the location of the file *rate comparison.xls*) that when a flux rate of 50 mm/year or greater was obtained, the output water composition was within 0.08 pH units and 1.15E-03 moles/kg of the original pH and ionic strength values (i.e., Time=0 values), respectively. For this reason, a flux rate of 50 mm/year is chosen for TSPA as the point where the pH and ionic strength of the water (equilibrated with atmospheric gas levels) percolating into the basalt block equals the pH and the ionic strength of the water leaving the basalt block. In other words, the flux rate is so high that little or no reaction occurs. For flux rates less than 50 mm/year, the values from Table 6-25 can be used. As shown in *Dissolved Concentration Limits of Radioactive Elements* (BSC 2004 [DIRS 169425]), the two most important parameters affecting the solubility of radioelements include pH and fCO_2. Since pH decreases with increasing flux rate, using the values for flux rate between 0.4 and 11.7 mm/year for all cases where the flux rate is below 50 mm/year is conservative since many radionuclides will be more soluble at the higher pH values shown in Table 6-25.

Convergence difficulties arise in EQ6 calculations carried out at high pH and low CO_2 levels. For this reason, the model includes log (fCO_2/bar) values only from -2 to -4. For TSPA calculations where the log (fCO_2/bar) is between -4 and -5, it is recommended that the values in Table 6-25 for log (fCO_2/bar) of -4 be used. Ionic strength is shown to be between 1.8E-02 to a minimum of 7.4E-03 moles/kg. Therefore, the pH and ionic strength for log (fCO_2/bar) between -4 and -5 should, realistically, not be much greater than those presented in Table 6-25. For high (fCO_2/bar) values used by TSPA (-1.7), log (fCO_2/bar) values at -2 should be used.

6.8.4 Discussion of uncertainties

6.8.4.1 Uncertainty in the Geochemical Modeling Using EQ6

Uncertainties in input values related to geochemical modeling using the EQ6 code for the base case include:

- Pore fraction
- Reactive surface area of materials
- Flow rate of water through the basalt
- Saturation
- Composition of oxides that make up the basalt
- CO_2 and O_2 fugacity
- Type of water flowing through the basalt (water types investigated are presented in Table 4-10 and Table 4-12).

In terms of absolute uncertainty, estimates of mineral surface area are clearly the most poorly constrained. Several of these parameters are included in cases that were used in the pH abstractions and are thus already incorporated into the model output. These parameters, as well as the range of values used, are:

- Pore Fraction: 0.13 through 0.17.
- Flux: 0.4 mm/year through 11.7 mm/year.
- Surface Area: all surfaces are available and 10 percent of all surfaces available.
- Saturation: 0.1 through 1.0.
- Log (fCO_2/bar): -2 through –4

The composition of oxides that make up the basalt was taken from DTN: LA0407DK831811.001 [DIRS 170768], Table 6, based on 45 samples collected from the Lathrop Wells Cone. Materials from the 0.08 Ma Lathrop Wells Cone (Heizler et al. 1999 [DIRS 107255]) represent the most recent eruptive event in the Yucca Mountain region. Therefore, it may better represent the composition of the hypothetical igneous intrusion than older volcanic centers in the area ranging in age from approximately 1.1 million to nearly 5 million years (CRWMS M&O 1996 [DIRS 100116]). The composition of the Lathrop Wells Cone along with corresponding uncertainty is presented in Table 4-5.

Because of the small deviations from the mean, any differences arising in water chemistry from basalt water interactions with a slightly different basalt composition would be very small due to the low dissolution rates of basaltic minerals. Therefore, no meaningful change to the water chemistry from that presented for reaction with mean basalt composition is expected. In fact, the modal mineralogy of basalt will largely control the water-rock reactions that determine solute

content. Since the mineralogical content of most basalts will be similar, the results are expected to be fairly insensitive to potential variations among different basalt compositions. The abstraction results (using the normative minerals) provided in Table 6-25 have been validated using natural analog studies on the chemical characteristics of basalt ground water. They are therefore considered valid and appropriate for use.

The base case water type reacted with the basalt was Bin 8 seepage water from DTN: MO0310SPAEBSCB.003 [DIRS 166411]. To determine the effects that other water types had on the pH, ionic strength, and fluoride content of water reacted with basalt, the base-case EQ6 run (see Section 6.8.3 for definition of this run) was rerun with Bin 11 seepage water from DTN: MO0310SPAEBSCB.003 [DIRS 166411], and with J-13 well water from DTN: MO0006J13WTRCM.000 [DIRS 151029]. These two water types represent seepage waters that are: 1) more concentrated, and 2) more dilute than the Bin 8 seepage water. The EQ6 output (spreadsheet *sensitivity.xls*, see Appendix E) shows that the values for ionic strength and pH for the three water types are very similar. Therefore, the type of water percolating through the basalt will not have a meaningful impact on the final reacted water chemistry.

The EQ6 cases for this report were run at atmospheric oxygen condition for the repository horizon (log (fCO_2/bar) = -0.7) and at log (fCO_2/bar) between -2 and -4. To use the solubility look-up table in *Dissolved Concentration Limits of Radioactive Elements* (BSC 2004 [DIRS 169425]), a constant value for these parameters must be used for any abstraction.

The water chemistry parameters required for use in TSPA are temporal values for pH, ionic strength, and fluoride content. As pointed out in Section 6.8.3, many EQ6 simulations of basalt/water interactions show no change in fluoride content. Therefore, the fluoride content of the aqueous fluid is dependent solely on the content that is already in the fluid as it contacts the basalt. The temporal variation of pH and ionic strength along with corresponding uncertainty in the form of maximum and minimum values are presented in Table 6-25.

Values were obtained by first calculating a time-weighted average for each case in the abstraction. The minimum and maximum of these time-weighted averages are then presented in Table 6-25. Time-weighted averages were used due to the large time steps used in TSPA calculations.

Table 6-25. Temporal Maximum and Minimum Values for pH and Ionic Strength

Log (fCO_2/bar) = -2				
	pH		**Ionic Strength (moles/kg)**	
Time Period*	**Maximum**	**Minimum**	**Maximum**	**Minimum**
$x \leq 25$ years	7.9	7.6	1.87E-02	9.64E-03
$25 > x \leq 250$ years	8.1	7.8	3.59E-02	1.23E-02
$250 > x \leq 2500$ years	8.1	7.8	4.00E-02	1.22E-02
$2500 > x \leq 20000$ years	8.1	7.7	3.58E-02	1.15E-02

Table 6-25. Temporal Maximum and Minimum Values for pH and Ionic Strength (Continued)

Log (fCO_2/bar) = -2.5				
	pH		Ionic Strength (moles/kg)	
Time Period*	**Maximum**	**Minimum**	**Maximum**	**Minimum**
x ≤ 25 years	8.4	8.1	2.09E-02	9.23E-03
25 > x ≤ 250 years	8.6	8.3	4.33E-02	1.31E-02
250 > x ≤ 2500 years	8.6	8.3	5.50E-02	1.29E-02
2500 > x ≤ 20000 years	8.6	8.2	4.22E-02	1.18E-02
Log (fCO_2/bar) = -3				
	pH		Ionic Strength (moles/kg)	
Time Period*	**Maximum**	**Minimum**	**Maximum**	**Minimum**
x ≤ 25 years	8.9	8.6	2.43E-02	9.14E-03
25 > x ≤ 250 years	9.0	8.8	6.85E-02	1.40E-02
250 > x ≤ 2500 years	9.1	8.8	8.85E-02	1.37E-02
2500 > x ≤ 20000 years	9.1	8.7	8.79E-02	1.19E-02
Log (fCO_2/bar) = -3.5				
	pH		Ionic Strength (moles/kg)	
Time Period*	**Maximum**	**Minimum**	**Maximum**	**Minimum**
x ≤ 25 years	9.4	9.0	3.00E-02	9.44E-03
25 > x ≤ 250 years	9.5	9.2	9.78E-02	1.67E-02
250 > x ≤ 2500 years	9.6	9.2	1.60E-01	1.62E-02
2500 > x ≤ 20000 years	9.5	9.1	9.65E-02	1.30E-02
Log (fCO_2/bar) = -4				
	pH		Ionic Strength (moles/kg)	
Time Period*	**Maximum**	**Minimum**	**Maximum**	**Minimum**
x ≤ 25 years	9.7	9.4	3.42E-02	1.02E-02
25 > x ≤ 250 years	9.9	9.6	1.17E-01	1.97E-02
250 > x ≤ 2500 years	9.9	9.6	1.86E-01	1.89E-02
2500 > x ≤ 20000 years	9.9	9.6	1.07E-01	1.43E-02

Source: Calculated in Spreadsheets abstraction-2.xls, abstraction-25.xls, abstraction-3.xls, abstraction-35.xls, and abstraction-4.xls (see Appendix E).

NOTE: * Time period represents time after re-establishment of seepage flow.

"x" = "time"

6.8.5 Alternative Models for Water/Basalt Interactions

Section 6.8.4 discusses uncertainties associated with reaction of minerals with water inside EQ6 calculations. These include:

- Pore fraction
- Reactive surface area of materials
- Flow rate of water through the basalt
- Saturation, composition of oxides that make up the basalt
- CO_2 and O_2 fugacity, and type of water flowing through the basalt.

Several of these parameters (pore fraction, flux, surface area, saturation, and CO2 and O2 fugacity are included in the model abstraction. Alternative model abstractions using different basalt and incoming water compositions could be obtained. However, as shown in Section 6.8.4, these parameters have little to no effect on the overall final chemistry of the abstracted pH and ionic strength values. Additionally, where large uncertainties in EQ6 inputs existed, conservative values were always used. Therefore, no alternative models are presented for reaction of basalt with seepage waters.

6.8.6 Summary

Chemical reactions between basalt intruded into a drift and water seeping through it will modify the composition of any seepage water that might encounter waste after an intrusive event. Both the pH and the ionic strength of the resulting water will depend on the activity of CO_2, with more CO_2 resulting in lower pH and generally lower ionic strength. For example, for p_{CO_2} = 1 kPa, the pH ranges from 7.6 to 8.1 with ionic strengths between 9.6×10^{-3} and 4.0×10^{-2} moles/kg, while for p_{CO_2} = 10 Pa, the pH ranges from 9.4 to 9.9, and ionic strengths are between 1.0×10^{-2} and 1.9×10^{-1} moles/kg (Table 6-25). Variation with time after beginning of seepage is less than 0.2 in pH and less than a factor of 6 in ionic strength. Because of the ready availability of Ca to waters equilibrating with basalt, fluoride concentrations are quite low, as they are in basaltic terrains in nature.

INTENTIONALLY LEFT BLANK

7. VALIDATION

AP SIII.10Q, *Models*, requires that models supporting TSPA model components be validated to the level of confidence required by the component's relative importance to the potential performance of the repository system. Validation, or confidence building, is a way of ensuring that the processes represented and simulated by the numerical models are consistent with observed behavior to give confidence in model results. AP-2.27Q, *Planning for Science Activities*, describes three levels of model importance and corresponding validation guidelines commensurate with each level. These levels of model importance are based on the TSPA system sensitivity analyses and conclusions presented in *Risk Information to Support Prioritization of Performance Assessment Models* (BSC 2003 [DIRS 168796]). Although not all models directly support the TSPA-LA model, some do provide input or a scientific basis for the component models that directly support the TSPA-LA model. The Dike Intrusion Submodel consists of one model component, Dike Propagation Model. It does not directly feed to the TSPA-LA model, but does address FEPS and the *Yucca Mountain Review Plan, Final Report* (NRC 2003 [DIRS 163274]). The activities necessary to build confidence and validate these models are described in *Technical Work Plan: Igneous Activity Assessment for Disruptive Events* (BSC 2004 [DIRS 171403]). The model components of the Post-Intrusion Submodel, Magma Cooling and Basalt/Water Seepage, provide direct output to the model components of the TSPA-LA model. The activities necessary to build confidence and validate these models are described in *Technical Work Plan for Waste Form Degradation Modeling, Testing, and Analyses in Support of LA* (BSC 2004 [DIRS 167796]). The model validation for these later models is presented in *Igneous Intrusion Impacts to Waste Packages and Waste Forms* (BSC 2004 [DIRS 168960]) and included in this section with some supplemental material.

7.1 IMPORTANCE LEVELS FOR MODEL VALIDATION

The *Technical Work Plan: Igneous Activity Assessment for Disruptive Events* (BSC 2004 [DIRS 171403]) and *Technical Work Plan for Waste Form Degradation Modeling, Testing and Analysis in support of LA* (BSC 2004 [DIRS 167796]) identify the levels of importance based on the effect model uncertainty could have on repository performance. They also identify the validation approaches for the models presented in this model report. The levels of importance identified in this model report are summarized in Table 7-1. The Dike Propagation Model provides direct input to the Waste Package/Drip Shield Degradation and the Number Waste Packages Impacted by Igneous Intrusion model components that support the TSPA-LA model. The magma-cooling component of the post-intrusion submodel provides direct input to the Waste Package/Drip Shield Degradation component model that supports the TSPA-LA model. The Basalt/Water Seepage component of the post-intrusion submodel provides direct input to the Waste Package/Drip Shield Degradation and the Seepage Temperature, Amount and Chemistry of Water in Waste Package model components that support the TSPA-LA model.

Table 7-1. Validation Levels for Submodels of the Dike/Drift Interaction Model

Submodel in this Report	TSPA Component Models	Level of Validation
Dike Intrusion Submodel Dike Propagation component	Waste Package/Drip Shield Degradation Number Waste Packages impacted by igneous intrusion	III
Post-intrusion Submodel Magma Cooling component	Waste Package/Drip Shield Degradation	III
Post-intrusion Submodel Basalt/ Water Seepage component	Waste Package / Drip Shield Degradation Temperature, Amount and Chemistry of Water in Waste Package	III

The approaches used for confidence building during model development and post-model development are summarized in Table 7-2. Model uncertainty, which may arise for several reasons, is naturally addressed both during model development and after model development. Sources contributing to model uncertainty include:

- Inaccuracy of numerical solutions
- Uncertainty of input due to lack of knowledge
- Uncertainty of input due to natural, frequently stochastic, variability of properties or configurations
- Inadequate state of knowledge or understanding of phenomena or processes

The effect of model uncertainty is discussed in Section 7.3 at the end of each post-development confidence building discussion.

Table 7-2. Confidence-Building and Post-Model Development Validation Activities

AP-SIII.10Q Validation Approaches	Location of Discussion in this Model Report
Confidence Building Activities Related to Model Development	
Ensure that validation of the mathematical model and its underlying conceptual model includes documentation of decisions or activities that are implemented to generate confidence in the model: Selection of input parameters and/or input data, and a discussion of how the selection process builds confidence in the model (5.3.2(b)(1)).	**Dike Intrusion Submodel:** development is consistent with the procedures and recommendations of the Igneous Consequences Peer Review Panel (Section 7.2). Input parameters were selected to be well within the applicability of the formulation of the model, and are conservative regarding the expected repository conditions. Parameter selection is discussed for the dike propagation model in Section 7.2.1
Ensure that validation of the mathematical model and its underlying conceptual model includes documentation of decisions or activities that are implemented to generate confidence in the model: Description of calibration activities, and/or initial boundary condition runs, and/or run convergences, and a discussion of how the activity or activities build confidence in the model (5.3.2(b)(2)).	**Dike Intrusion Submodel:** development is consistent with the findings of the Igneous Consequences Peer Review Panel (Section 7.2.1). Initial and boundary condition selection is addressed in Section 7.2 and Section 6.

Table 7-2. Confidence-Building and Post-Model Development Validation Activities (Continued)

AP-SIII.10Q Validation Approaches	Location of Discussion in this Model Report
Confidence Building Activities Related to Model Development	
Ensure that validation of the mathematical model and its underlying conceptual model includes documentation of decisions or activities that are implemented to generate confidence in the model: Discussion of the impacts of uncertainties to model results (5.3.2 (b)(3)).	**Dike Intrusion-Post Intrusion Submodels**: Parameter uncertainties are discussed in Section 7.3 and Section 6.
Ensure that validation of the mathematical model and its underlying conceptual model includes documentation of decisions or activities that are implemented to generate confidence in the model: Selection of input parameters and/or input data, and a discussion of how the selection process builds confidence in the model (5.3.2(b)(1)).	**Post-Intrusion Submodel** used data from qualified sources. Parameter selection is discussed in Section 7.2.2 and Section 6.6.
Post-Development Model Validation Activities	
Dike Intrusion Submodels	
Corroboration of model results with the results of auxiliary analyses (5.3.2(c)(6)).	Corroboration was performed using analytical solutions for a vertical self-similar dike. The results are documented in Section 7.3.1.1.3.
Corroboration of model results with data acquired from the laboratory, field experiments, analog studies, or other relevant observations not previously used to develop or calibrate the model (5.3.2(c)(1)).	Calculations were performed to compare model and analyses results for a dike interacting with a free surface, to those from the Parícutin analog. The results are documented in Section 7.3.1.1.1.
Conduct independent technical review, planned in the applicable TWP (5.3.2(c)(5)).	An independent technical review was performed for the Dike Propagation Model. The results are documented in Section 7.3.1.1.2.
Post Intrusion Submodels	
Corroboration of model results with results of experimental analog data (5.3.2(c)(1))	Corroboration was performed for gas flow for the species analyzed by comparing results with published laboratory experiment, documented in Section 7.3.2.1.1.
Corroboration of analytical methods by publication in peer-reviewed journals (5.3.2(c)(3)).	Corroboration of aspects of the gas-flow modeling approach and data was achieved by publication in peer-reviewed journals are documented in Section 7.3.2.1.2.
Corroboration of model results with the results of auxiliary analyses (5.3.2(c)(6)).	Corroboration was performed using analytical solutions for magma cooling. The results are documented in Section 7.3.2.2.1.
Corroboration of model results with data acquired in field experiments (5.3.2(c)(1)).	Corroboration with field data was performed for magma cooling for thermal evolution of a shallow cooling lava lake. The results are contained in Section 7.3.2.2.1.
Corroboration of model results with data acquired from the laboratory, field experiments, analog studies, or other relevant observations not previously used to develop or calibrate the model (5.3.2(c)(1)).	Corroboration with laboratory data and field studies was conducted for seepage water component. The results are contained in Section 7.3.2.3.

7.2 CONFIDENCE BUILDING DURING DEVELOPMENT

All input parameters are well within the applicability of the formulation of the numerical model, or are conservative regarding the expected conditions in the repository. Initial and boundary conditions are addressed in Section 6, as are parameter uncertainties.

7.2.1 Dike Intrusion Submodel

During development, the Dike Propagation Model and supporting analyses related to igneous consequence were presented to the Igneous Consequence Peer Review panel, a group of experts chosen for their expertise in fracture mechanics, dike propagation, magma properties, flow dynamics, and igneous processes. They used similar conceptual and numerical approaches to those reported in this model report. They employed some of the same software, and they obtained similar results. In response to the Peer Review findings, many of the models and analyses presented in this model report have been modified to be consistent with recommendations and technical information presented in their final report (Detournay et al. 2003 [DIRS 169660]). Specific applications of the findings of the Panel include:

- Many of the input parameter values used in Sections 6.3, 6.4, and 6.5 are drawn from their report (Table 4-1).

- Their discussion of the impact of the high gas permeability of the host rock (Detournay et al. 2003 [DIRS 169660], Section 3.4.3.2, p. 50) provides support for neglecting cavity pressure in models in Section 6.3.7.1.

- Their equations for the coupled flow from a dike into a drift (Detournay et al. 2003 [DIRS 169660], Appendix 3.5, p. 62) provides the basis for the coupled flow model in Section 6.4.6 and for the alternative analysis of effusive flow in Section 6.4.7.

- Their analysis of the Woods et al. (2002 [DIRS 163662]) paper pointed the way for much of the discussions in Sections 6.4.7.2 and 6.5.3.

- The analysis in Section 6.5.1.4 of magma cooling rates is based on a similar analysis of the Panel (Detournay et al. 2003 [DIRS 169660], Appendix 3.4, p. 53). The extension of this analysis to include changes in magma viscosity due to partial crystallization (Section 6.5.1.4.1) used their values for the extent of partial crystallization as a function of temperature (Detournay et al. 2003 [DIRS 169660], Appendix 2, Table 2E).

The Igneous Consequences Peer Review Panel found: (1) the scientific basis is adequate and reflects current scientific understanding; (2) that the models and analyses are accurate for their intended use; (3) that the models and analyses incorporate appropriate data. These findings provide confidence in the analyses and models of this report.

The Dike Propagation Model Component is, in the most general case, a function of three dimensionless numbers that reflect rock and magma density, reference stress, and fracture toughness (defined in Equation 6-8). The dimensionless toughness is a small number compared to unity under very general conditions of dike propagation. This implies that fracture toughness can be neglected when considering dike propagation; thus, it is not considered in this section.

The simulations of dike ascent were carried out for variation of relative density between 2.67 and 20.28, which is a range of almost one order of magnitude. Such variation of the relative rock density corresponds to the variation in the difference between normal far-field stress and magma density (buoyancy) between 600 Pa/m and 9000 Pa/m (with rock mass densities of 1,200 kg/m^3

and 2400 kg/m^3). This range includes, for example, the 3,000 Pa/m assumed by Rubin (1995 [DIRS 164118] in his analysis of propagation of magma-filled cracks. Dimensional results are generated for a number of far-field magma velocities and dike openings, which satisfy the scaling laws and are within the expected ranges for the opening, $0.1\text{ m} \le w_\infty \le 10\text{ m}$; and for the velocity, $0.1\text{ m/s} \le v_\infty \le 15\text{ m/s}$ (BSC 2004 [DIRS 169980]).

The dimensionless reference stress accounts for the effects of gas pressure inside the tip cavity and of changes in confining stress normal to the dike. Most of the simulations were carried out with a reference stress of zero (i.e., in situ stress conditions equal to gas pressure inside the tip cavity). The effect of the cavity gas pressure, which is unlikely to be much larger than the atmospheric pressure, is investigated by taking the cavity gas pressure to be as large as 2.1 MPa. This is very close to the pressure that would trigger dike-tip instability at the repository depth. The effect of thermal stresses in the first 2000 years after closure on dike propagation cannot be modeled with the same approach because the effect of heating is to induce horizontal confining stresses that are not linear with depth. Thermal stresses from calculations done for *Drift Degradation Analysis* (BSC 2004 [DIRS 166107]) were used as input to a complementary implementation to estimate the effect such stress variations would have on dike intrusion during this thermal period.

The model assumes homogeneous rock mass properties. Results presented in the report were generated for a Young's modulus of 15 GPa. This value is representative of the stiffness of the rock mass at Yucca Mountain on the scale of a potential dike. However, results for any other value of Young's modulus can be obtained readily by rescaling the existing results. Section 6.3.7.1 provides an example of such re-scaling.

7.2.2 Post-Intrusion

Confidence in the Post-Intrusion submodel, consisting of drift scale gas flow between drifts, magma cooling and solidification, and basalt/water seepage model components, was developed by the selection of input data, by calibration activities, by assessment of the impacts of uncertainties, by use of appropriate assumptions and simplifications, and by consistency with physical principles. These activities are discussed in the following subsections.

7.2.2.1 Drift-Scale Gas Flow

The model of drift-scale gas flow used data inputs from qualified sources. Specific aspects of model input and development related to the volcanic gas thermodynamic and transport properties, boundary conditions, and simulation parameters are given in Section 6 and are documented by Wang (2003 [DIRS 164068], pp. 1 to 32). The following is a summary of the data inputs and boundary conditions discussed in Section 6:

- The initial pore-water chemistry is based on a sample from a core taken from the repository host rock (Tptpmn) near the Drift Scale Test.
- The rock matrix mineralogical data are for a stratigraphic column near the center of the repository showing relative mineral abundance with depth.

- The volcanic gas concentrations are mean values of several measured compositions from volcanoes having magmatic compositions similar to the hypothesized intrusion.

- Diffusion coefficients of all aqueous species are set to the same value, which is justified based on the evaluation of variability in tracer diffusion coefficients of aqueous species.

- The boundary conditions are set according to those appropriate for the column location near the repository center.

- The pressure and temperature are set to be constant at the top and bottom boundaries.

- The infiltration rate is fixed to the present-day repository-wide average; which was calculated as arithmetic average of 31 locations within the repository.

- A high value of effective thermal conductivity is used in the drift interior to approximate heat transfer by convection and radiation, based on models of waste package heat transfer.

7.2.2.2 Magma Cooling

Input parameters were selected to be consistent with measured values for the appropriate stratigraphic units at the Yucca Mountain site as described in Section 6.7.1.1 and Appendix C. The sensitivity of the model to the saturation level of the host rock is as discussed in Section 6.7.2.2. The effect of including or excluding the latent heat of crystallization of the magma in the heat flow calculation is assessed in Section 7.2.2.1. Approximations and parameters used in development and application of the model such as approximating the configuration as two-dimensional and the thermal properties of the host rock formations are discussed in Section 4.1.1.1. Assumptions regarding the thermal properties of the magma are discussed in Section 5.4.3.

7.2.2.3 Basalt/Seepage Water Interaction

The selection of the mineral phases used for the basalt composition in EQ6 simulations, as documented in Section 6.8, is based on field observations at natural analogue sites and on standard petrologic methods such as normative minerals.

Discussion of the chemical system (temperature, water chemistry, initial pH, basalt composition, f_{CO_2}, etc) used in model runs is described in Sections 6.8 and 6.8.1. The pH and ionic strength span the range of intended use conditions for each of the factors that influence the pH and ionic strength of the modeled system (see Table 6-21 in Section 6.8.1). Run non-convergences were restricted to low CO_2 activity where waters are least aggressive to waste forms (Section 6.8.4).

The uncertainty associated with inputs to the model is discussed in Section 6.4.8.1, which addresses pore fraction, seepage flux, reactive surface area, degree of saturation and CO_2 activity.

Discussion of assumptions and their rationale are provided in Sections 5.4.1 and 5.4.2.

Sections 4.1.1.1, 4.1.1.2, 4.1.1.3, 4.1.1.4, and Section 6.8.1 discuss the choice of inputs for the heat and water reaction models. Most choices are consistent with physical principles. For example, charge balance is maintained in calculated solution compositions just as occurs in nature, by varying the activity of hydrogen. Where this was not possible due to model constraints, as is the case with low CO_2 fugacity, reasoning is provided and the uncertainty that it introduces is discussed.

7.3 POST-DEVELOPMENT CONFIDENCE BUILDING

7.3.1 Dike Intrusion Submodel

This submodel consists of one model component, Dike Propagation.

7.3.1.1 Dike Propagation Model Component

Post-development confidence building for the Dike Propagation Model component was accomplished by comparing model results with natural analog (Section 7.3.1.1.1) and by independent technical review (Section 7.3.1.1.2). Uncertainty is addressed in Section 7.3.1.1.3.

7.3.1.1.1 Parícutin Volcano Natural Analog

One of the best-documented historic de novo volcanic eruptions began near the west Mexican village of Parícutin on 20 February 1943. The eruption was preceded by earthquakes felt by the local population and the fissure (dike tip cavity) was observed immediately by farm workers in the field as it broke through the surface. The rate of magma production is also well documented from the very beginning of the eruption. The first lava erupted was a basaltic andesite with about 55 percent silica (Wilcox 1954 [DIRS 163659]). Although the propagation of the dike within the earth was not directly observed, the phenomena associated with the initial eruption of Parícutin are well documented. Thus, the Parícutin eruption provides a good analog for dike propagation.

The first seismic activity in the Parícutin vicinity was a magnitude 4.4 event recorded on January 7, 1943, in Mexico City, 320 km to the east (Yokoyama and de la Cruz-Reyna 1990 [DIRS 108740]), with four more quakes ($3.9 < M_S < 4.2$, M_S being surface wave magnitude) over the next month. Locally-felt earthquakes began about noon on 5 February according to Luhr and Simkin (1993 [DIRS 144310]), although Yokoyama and de la Cruz-Reyna (1990 [DIRS 108740]) report an early morning event at 0455h that day (times are reported in local time, which is GMT-0600). Thereafter, seismic events were frequent. Events of $M_S > 4.0$ are summarized in Table 7-3. The depth of the hypocenters is not well-constrained but, based on the direct-wave delays, Yokoyama and de la Cruz-Reyna (1990 [DIRS 108740]) concluded that most are probably in the range of 10 to 15 km deep.

Table 7-3. Earthquakes (M_S > 4.0) With Epicenters in the Parícutin Area During January and February 1943; after Yokoyama and de la Cruz (1990 [DIRS 108740])

Y&D Event #	Day	Hour	Minute	M_S
1	07 Jan	17	40	4.4
4	28 Jan	19	33	4.2
6	08 Feb	04	55	4.3
13	14 Feb	03	31	4.4
14	14 Feb	03	48	4.5
16	14 Feb	13	05	4.1
19	17 Feb	17	40	4.2
20	18 Feb	18	39	4.5

NOTE: Times are local time, GMT-0600.

Luhr and Simkin (1993 [DIRS 144310]) provide details from many sources on events immediately following the first surface manifestations at Parícutin. Presented here is an abbreviated outline; page references in that volume are shown as *{page#}*.

20 Feb 1943 *{54-65}*

1600: Half-meter deep fissure noticed (~5 cm wide and 30 m long).

A few minutes later, the ground swelled up to 2-2.5 m and "smoke" began rising from the fissure.

A few minutes more, hissing sounds and smoke and smell of sulfur.

The spring near the fissure had dried up (time not observed).

1800: A ~km-long fissure with activity concentrated in a central depression about 12-m wide and 20-m long, "smoke" and sulfurous vapors issued from pit, small rocks thrown 5-m high.

~2300-0000(21Feb): Volcano began to roar, incandescent stones hurled up with great force, column of "smoke" arose.

21 Feb 1943 *{66-68}*

8 AM: A 10-m high hill had formed and rocks were hurled out with great violence.

By 1 PM: A 30-m high cone.

By evening, explosions and bombs hurled to 500 m.

22 Feb 1943

0300: Heavy seismic activity, first lava flows, cone about 50-60 m high. *{68-69}*

That night: Ordonez reported that "lava was flowing from three vents aligned from east to west and located precisely in the center of the crater." *{65}*

25 Feb 1943 *{68-69}*

First lava flow ceases to be fed from vent.

26 Feb 1943 *{69-70}*

Volume of cone .0195 km^3, growing at .00333 km^3/day.

Volume of lava flow .007 km^3.

The time lag between the first opening at the surface and the arrival of substantial magma at the surface is well-constrained by these observations to be about 7-8 hours. The estimate given above of magma supply rate to Parícutin in the early days (0.0033 km^3/day or 39 m^3/s) agrees well with the total supply rate for all of the year 1943 estimated at 0.0026 km^3/day and the later history of an exponential drop in magma flux *{314}*. The values for time-lag and magma supply rate are the best-established metrics for the Parícutin eruption.

The composition of material erupted on 22 February was reported by Wilcox (1954 [DIRS 163659]) to be a basaltic andesite with the following major oxide weight percentages: SiO_2 55.04, Al_2O_3 18.82, Fe_2O_3 1.97, FeO 5.69, CaO 7.17, MgO 5.68, K_2O 0.85, Na_2O 3.88, TiO_2 0.94, H_2O 0.16 *{328}*. Eggler (1972 [DIRS 163623]) estimates, on the basis of the phenocryst compositions, that the actual water content of the source lava was higher, on the order of 2.2 weight percent *{362}*. Based on the compositions of glass inclusions, a "before eruption" water content of about 1.5 weight percent was estimated *{351-352}*.

There were no measurements of lava temperature at this early stage. The earliest available measurements were from May 1945, when optical pyrometer measurements of lava yielded a temperature of 1200 to 1250°C (1475 to 1525 K) *{318}*. Wilcox (1954 [DIRS 163659]) reports compositions for material from six months earlier and six months later. Silica by that time had increased to 55.6–56.4 percent and alumina had decreased to 17.7 percent *{328}*. The liquidus of such a magma would be slightly lower than for the original magma, but the 1946 material had slightly fewer phenocrysts than the earliest material, so it may be assumed that the temperature of the material being erupted in February 1943 was similar. The liquidus temperature for a magma with the composition given in the previous paragraph and calculated by the method used in *Characterize Eruptive Processes at Yucca Mountain, Nevada* (BSC 2004 [DIRS 169980]) is 1104°C (1377 K), much lower than the measurements. Given the primitive nature of the instrumentation available at the time, the calculated temperature seems likely to be more reliable. In addition, the early Parícutin magma had about 3.3 percent phenocrysts *{326}*; therefore, 1325 K (1052°C) represents the most appropriate estimate of magma temperature. This value is slightly lower than the estimate of Eggler (Luhr and Simkin 1993 [DIRS 144310]), but the oldest rock he worked with was not erupted until 1947, four years after the first eruption began *{360-363}*.

The viscosity of such a magma would be much higher than that expected for igneous activity at Yucca Mountain. As calculated by the method of Shaw (*Characterize Eruptive Processes at Yucca Mountain, Nevada* (BSC 2004 [DIRS 169980])), it would range from about 60 Pa·s at 1200°C to about 900 Pa·s at 1000°C. This is likely to be an underestimate because the effects of phenocrysts (a few percent), xenoliths, and bubbles are not considered. Krauskopf calculated the viscosity of lava at Parícutin based on flow speeds, flow depths, and slope values and found viscosities of 10^4 to 10^5 Pa·s *{320}*. This is likely to be an overestimate because the surface portions of the lava were not at the same temperature as the central portions. Hence, 10^3 Pa·s to 10^4 Pa·s is considered an appropriate range of viscosities for the Parícutin magma.

The eruption was centered in a small valley so the fracture extent of ~1 km should be considered a lower limit for the strike length of the feeder dike.

There is little information on the depth of the magma chamber that fed Parícutin. Eggler's experimental petrology studies indicated some pressure and water were needed to prevent pyroxene phenocrysts from forming, but did not establish any strong limits. His experiments that most closely replicated the real Parícutin phases were at pressures of about 550 MPa, equivalent to a depth of about 20 km. Experiments at the same water content but at 750 MPa (about 28 km) contained pyroxene, so the depth must have been less than about 25 km *{360-363}*.

Although the magma chamber feeding Parícutin may have been 20 km deep, it is unlikely that the final movement of the dike leading to the surface originated so deeply. Basaltic magma may be stored at depths in the range of 2 km to 4 km due to decreased tensile strength of near-surface rocks or neutral buoyancy (Ryan 1987 [DIRS 170320]). Physical model experiments by Mastin and Pollard (1988 [DIRS 169783)] and elastic analysis indicate that a zone of tension will exist directly above a propagating dike. This will be manifested by development of a graben where the dike will eventually emerge but the feature will have a depth on the order of the dike width and a width on the order of the depth to the magma. No such phenomena were observed at Parícutin, although the reported ground swell may be related to sudden release of such tension.

Given that both the beginning of seismic activity related directly to dike formation and the depth of origin of the dike feeding the new Parícutin volcano (whether from seismic data or from petrologic constraints) are uncertain, only a rough order of magnitude estimate of the velocity of magma moving up the dike can be developed. The range of possible values based on the seismic data and possible source depths covers 0.001 m/s to 0.1 m/s.

Based on the above discussion, Table 7-4 presents a summary of the observational constraints on the Parícutin eruptive process.

Table 7-4. Summary of Parameters for the Dike that Fed Parícutin

Feeder Dike Property	Value	Reliability
Magma flux (m^3/s)[a]	39	Well-constrained by geometric measurements
Time lag: crack to magma @ surface (h)[a]	7.5	Well-constrained, ±0.5 h
Magma viscosity (Pa·s)[a]	100-100,000	Estimates based on composition do not agree with values calculated from lava flow velocities
Water content (wt%)[a]	1.5-2.2	Well-constrained by measurement and petrology
Magma velocity in dike (m/s)	0.001-0.1	Little real observational constraint
Strike length (km)[a]	>~1	Approximate lower limit
Magma chamber depth (km)[a]	<25	Upper limit
Magma “holding” depth (km)[b]	2-4	Inferred at other sites (see text)
Origin time (days before 20Feb43)[c]	2-45	Little real observational constraint

[a] Luhr and Simkin 1993 [DIRS 144310].
[b] Ryan 1987 [DIRS 170320].
[c] Yokoyama and de la Cruz-Reyna 1990 [DIRS 108740].

Acceptance Criteria–The observed phenomena and features of the eruption at Parícutin include the times of seismicity, of first opening of the fissure at the surface, and of the beginning of magma eruption at the surface; the nature of the first emanations from the fissure and the chemical and physical properties of the magma; observations of ground displacements; and the rate of magma eruption over the first several days.

The magma volume flux rising in the dike is fixed at the observed rate of eruption, given assumptions about the length of the dike feeding Parícutin. The model output can be considered corroborated if the time between crack opening and magma arrival is within a few hours, given the observed or inferred properties of the magma and country rock. The sequence of emanations should agree with observations. The calculated magma density must be consistent with the density expected due to exsolution of volatiles at the depths of the "final" phase of intrusion (i.e., after earthquake #20 in Table 7-1) for a magma with an "original" concentration of 1.5 to 2.5 weight percent. Because psychological factors can affect eyewitness accounts of magnitude of ground motion, displacement amplitudes are not considered, but ground displacements from the model should be in the same direction as those observed.

Approach– The dike propagation results described in Section 6.3 were rescaled with values appropriate for Parícutin. To account for the stiffer basalts of the Trans Mexican Volcanic Field relative to the rhyolite tuffs of Yucca Mountain, Young's modulus was taken as 30 GPa with Poisson's ratio being 0.3 as estimated by Yokoyama and de la Cruz-Reyna (1990 [DIRS 108740]). To address uncertainties in other parameters, calculations were done for three country rock densities (ρ_{rock} = 2200, 2400, 2600 kg/m^3), two viscosities (μ = 10 kPa, 100 kPa), and three strike lengths (L = 1, 2, 4 km) for each of the three values of Δ used in Section 6.3. The magma density, calculated from ρ_{rock} and Δ as $\rho_{magma} = \rho_{rock} \times (1\text{-}1/\Delta)$, ranged from 1376 km/m^3 to 2472 kg/m^3. For each combination of ρ_{rock}, μ, L and Δ, the far-field width was calculated for a magma flux of 39 m^3/s with Equation 6-52 and Equation 6-53. The far-field magma velocity was then obtained from Equation 6-48. The scaling length and scaling time were derived from Equation 6-31. The lag time was calculated by multiplying by the scaled depth to the magma front at breakout and dividing by the dimensionless magma front velocity. For each case, three estimates of dimensionless velocity were used. Based on a plot of magma front velocity *vs.* depth, it was seen that the magma front velocity approached v_∞, but that the value fluctuated considerably, as the crack neared the surface (Figure 7-1 shows such a plot for Δ = 6.02; plots for Δ = 2.67 and 20.3 are very similar except that scatter as crack tip approaches the surface is lower for Δ = 20.3 and greater for Δ = 2.67). To reflect the uncertainty associated with the fluctuation, factors of 0.75 v_∞, 1.0 v_∞ and 1.25 v_∞ were used to calculate the time lag.

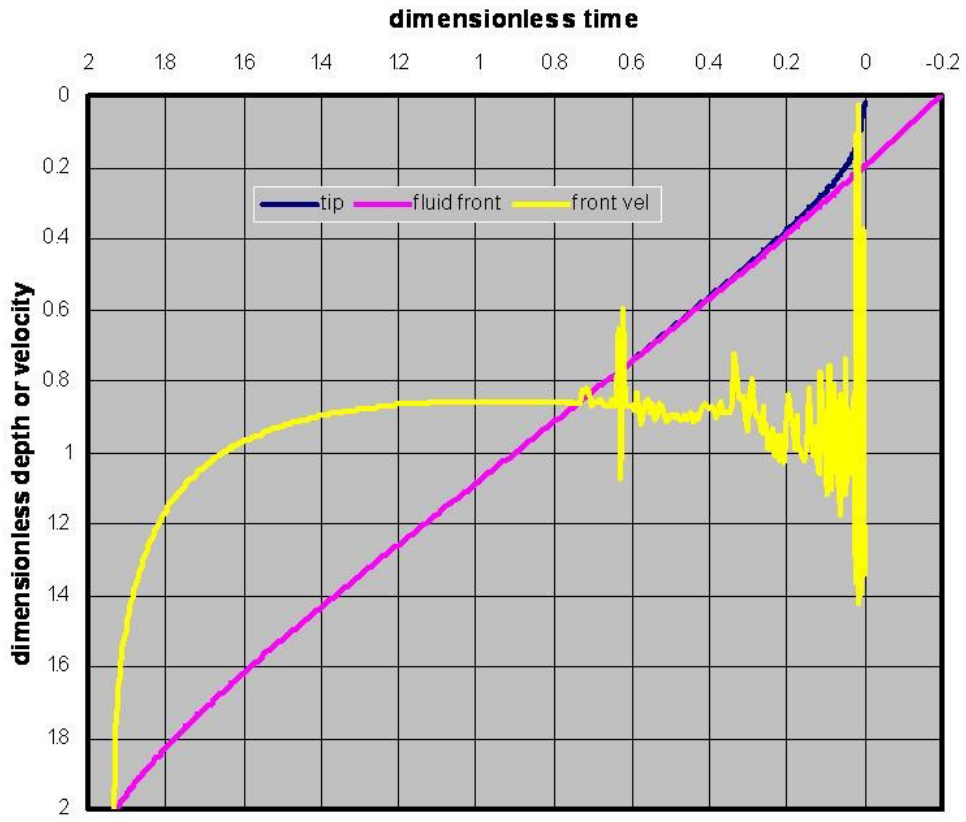

Output DTN: MO0408EG831811.000.

Figure 7-1. Dimensionless Front Velocity (Yellow) for Δ = 6.02

For each rock density and viscosity combination, one set of results was selected for which the time lag fell between 5 and 10 hours (7.5 hours being the observed lag); if more than one set of results met that criterion, only the set nearest to 7.5 hours was carried forward.

The depth of magma at the time of the last large (M_S > 4) earthquake, which occurred on the evening of 18 February (#20 in Table 7-4), was calculated as the magma front velocity divided by the time elapsed from the earthquake to the arrival of magma at the surface. This depth was then used with equations 6-1, 6-5a, and 6-8 of *Characterize Eruptive Processes at Yucca Mountain, Nevada* (BSC 2004 [DIRS169980], pp. 6-22 and 6-27) to calculate the density at that depth expected for magma with a vesicle-free density of 2600 kg/m^3 and a dissolved water content of 2.5 weight percent. This provided a value to compare with the magma density calculated from ρ_{rock} and Δ above.

Results–The results of these calculations are presented in Table 7-5. For the lower viscosity calculated, μ=10 kPa·s, there are cases from each value of Δ for which time between crack opening and magma arrival is within 7.5±2.5 hours. No acceptable solutions were found with μ=100 kPa·s, providing more support for the upper limit of 10 kPa deemed appropriate above for lavas at Parícutin. However, the only cases for which the magma density calculated from exsolution relations is within 20 percent of that derived from the scaling relations (highlighted in **boldface** in Table 7-5) have Δ = 20.3 or 6.02. One of those, with ρ_{rock} = 2600 kg.m^3 and

D = 20.3, has agreement between the densities within less than 1 percent, is highlighted in ***bold italics*** in Table 7-5.

Table 7-5. Dike Intrusion/Eruption Parameters at Parícutin Scaled from Calculations Applied to Yucca Mountain

Viscosity	Strike length	D	Magma density (scaled)	Crack-to-eruption	Far-field width	Far-field velocity	Magma front velocity	Depth to Q#20	Magma density (calc)
(kPa·s)	(km)	-	(kg/m^3)	(hours)	(m)	(mm/s)	(mm/s)	(km)	(kg/m^3)
ρ_{rock} = 2200 kg/m^3									
10	4.0	2.67	1376	7.1	0.5	19	19	3.5	2467
10	4.0	6.02	1835	8.8	0.7	14	14	2.7	2209
10	1.0	20.3	2092	8.6	1.6	24	24	4.5	2600*
ρ_{rock} = 2400 kg/m^3									
10	4.0	2.67	1501	7.1	0.5	19	19	3.6	2566
10	4.0	6.02	2001	8.8	0.7	15	15	2.8	2323
10	2.0	20.3	2282	8.2	1.3	15	19	3.7	2282
ρ_{rock} = 2600 kg/m^3									
10	4.0	2.67	1626	6.6	0.5	16	16	3.7	2600*
10	4.0	6.02	2168	8.1	0.7	15	15	2.8	2424
10	2.0	20.3	2472	9.5	1.2	20	20	3.0	2475

NOTE: Q#20 is seismic event number 20 from the list in Table 7-3.

* indicates that magma was below the depth for exsolution.

The sequence of emanations (several hours of gas and dust prior to actual magma) agrees with observations. The calculations indicate a length of the crack-tip cavity of about 540 m at the time of first breakout. Although not illustrated above, elastic analysis of deformation accompanying dike intrusion (Smith et al. 1996 [DIRS 101020]) indicates that the surface will be depressed in the immediate vicinity over the dike. When the dike breaks the surface, the ground would rebound upward as was observed. The observed magnitude may not agree with elastic analysis, but only the sign is included in the acceptance criteria.

Comparisons with field observations at Paricutin support the phenomenology described in the model. These results meet the acceptance criteria, and the model output has been corroborated by comparison with the analog volcanic activity. Specifically, the model may be considered valid for applications that include a free surface and an appreciable lag time between the first cracking at the surface and the arrival of the magma front. The existence of a crack-tip cavity of considerable height is also corroborated.

Uncertainty–The deviations from the field observations can be attributed to:

- Uncertainties associated with lay observers and the primitiveness of the instrumentation available at the time.
- Uncertainties in the material properties used in the rescaling of dimensionless results to the specific environment of the Paricutin eruption.

- The fact that the model was scaled from one of the existing simulations rather than being developed specifically for the volcanic activity at Parícutin.

7.3.1.1.2 Independent Technical Review of Dike Propagation Model

Consistent with the guidance in AP-SIII.10Q, Models, for post development model validation of mathematical models, an independent technical review was conducted to enhance confidence that the dike propagation model presented in this model report is adequate for its intended purpose. The independent review was conducted by Dr. Allan Rubin, Professor of structural geology for the Department of Geosciences at Princeton University, a former member of the Igneous Consequence Peer Review Panel. His full report can be found in Appendix (F).

Dr. Rubin was requested to consider the following five questions:

1. *Is the conceptual model reasonable and appropriate for its intended use?*

   Dr. Rubin finds the conceptual model here to be "reasonable and appropriate for its intended use." Although he mentions that some possibly rather severe simplifications (neglect of magma compressibility, magma freezing, inelastic deformation of the host rock, etc.) are made, he stresses that the goal "is not the faithful numerical reproduction of dike propagation (…), but to understand in a general sense what would happen if a dike intersected the repository." He mentions the objective stated in the opening section of the report that the "dog-leg" scenario be precluded and asserts that this claim is not justified in the document he reviewed. The "dog-leg" scenario is in fact dealt with in an analysis, not included in the model. This analysis, which was not reviewed by Dr. Rubin, is reported in detail in Section 6.5 of the report.

2. *Are the mathematical relationships appropriate and representative of the scientific understanding of fracture/dike propagation?*

   Dr. Rubin mentions that he agrees in general with the main model assumptions, however, he points out that a number of them could be more accurately justified.

   Section 6.3.2, which deals with assumptions and simplifications of the dike propagation model, has been extensively revised to meet Dr. Rubin's comments. The assumption of the 2-D elasticity/1-D flow model is now justified both for flow and geomechanical aspects of the model. The linear-elastic behavior assumption has been revised, and does not state that this is always conservative. The "fracture toughness" parameter is used to investigate the effect of any mechanism that resists fracture growth (Section 6.3.1.2). The laminar flow assumption is complemented by a qualitative discussion on the likely effect that turbulent flow would have on the solution (Section 6.3.2, Assumption 8). The assumption of a horizontal ground surface is now based only on computation results from the analysis in Section 6.2.

3. *Are the outputs of the model reasonable and representative?*

   Although he finds the outputs reasonable and representative, Dr. Rubin has concerns about the way the effect of thermal loading was represented (uniform load over the full

model height). This has been changed, and replaced by a computation where local thermal stresses are properly included (Section 6.3.7.3).

Otherwise, Dr. Rubin questions the robustness of the statement that "the maximum magma pressure is at most 1 MPa larger than the horizontal far-field stress at the given depth." In his view, this should be changed to "a few MPa", in order to account for the range of possible dike thicknesses. In the final conclusion of the Dike Propagation Model section of this report (Section 6.3.9), the text has been modified to coincide with this comment although this primarily reflects the findings of Section 6.3.7.3.

He states that one of the conclusions from computations of the effect of thermal stresses is not justified by what is presented: the dike (…) is not expected to turn and create a sill if rock mass properties are homogeneous and isotropic. The text has been revised to mention that dike deflection was not obtained for Yucca Mountain conditions (Section 6.3.7.3).

Overall, Dr Rubin states that the simplifications mentioned in 1) above do not alter significantly the estimate of the maximum excess pressure and the pressure-vs-depth profile, although he mentions the difficulty in evaluating whether the neglected processes might introduce any qualitatively new behavior.

4. *Are there alternative models or approaches that should be considered?*

   Dr. Rubin agrees that alternative models or approaches are adequately discussed.

5. *Are limitations of the model adequately described?*

   Dr. Rubin agrees limitations of the model are adequately described.

Dr. Rubin's review has been addressed in the current version of this report.

7.3.1.1.3 Uncertainty

Uncertainty in the Dike Propagation Model arises from diverse sources and has been addressed in various ways. One type of uncertainty is related to how closely the numerical solutions agree with analytical solutions when the latter are available. Results just below indicate that such uncertainty is small. Larger uncertainties arise from the natural variability of geologic phenomena and have been addressed both in application of the model and in post-development model validation.

Numerical Uncertainties–The magnitude associated with numerical uncertainties can be estimated by comparing code results with analytical solutions for similar problems. The problem of propagation of a vertical dike far from any free surface is solved using NPHF2D V1.0 (BSC 2002 [DIRS 163665]). For the case in which the lag does not exist, the solution depends on dimensionless fracture toughness only. A specific subset of that case, in which the toughness is vanishingly small ($K \sim 0$), is considered here. A self-similar condition is achieved when both the dimensionless dike length and the dimensionless distance from the ground surface are larger than 2.0. Dimensionless lengths are obtained by scaling lengths to the characteristic length

defined in Equation 6-31. To ensure a self-similar condition, the initial position of the fracture tip was selected to be at 4000-m depth (a dimensionless depth of 5.208). The dike was propagated for 2000 m (a dimensionless depth of 2.604), or half way to the ground surface. At that point, the model results were compared with the Lister (1990 [DIRS 126865]) analytical solution for a self-similar vertical dike. The dimensional model parameters used in the particular simulations were:

- Young's modulus: 15 GPa
- Poisson's ratio: 0.21
- Horizontal stress gradient: 6645 Pa/m
- Magma viscosity: 1 Pa·s
- Magma density: 400 kg/m^3
- Magma injection rate: 0.2 m^2/s.

Comparisons between the numerical and the analytical solutions of the dimensionless dike aperture and pressure versus scaled distance from the fracture tip are shown in Figures 7-2 and 7-3 (see Section 6.3.4 for a discussion of dimensionless, or scaled, dike properties).

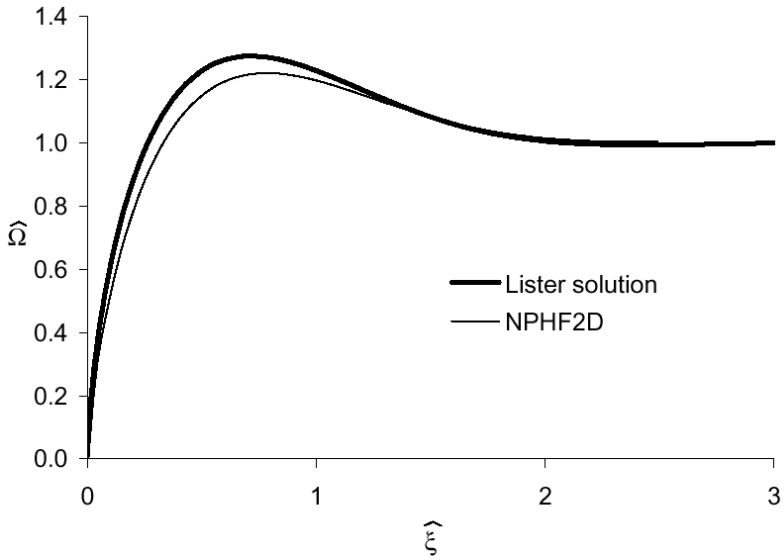

Source: Zhang et al. 2002 [DIRS 164368].

Figure 7-2. Self-Similar Dike Problem for K = 0: Dimensionless Opening (Ω) Versus Dimensionless Distance from the Crack Tip (ξ)

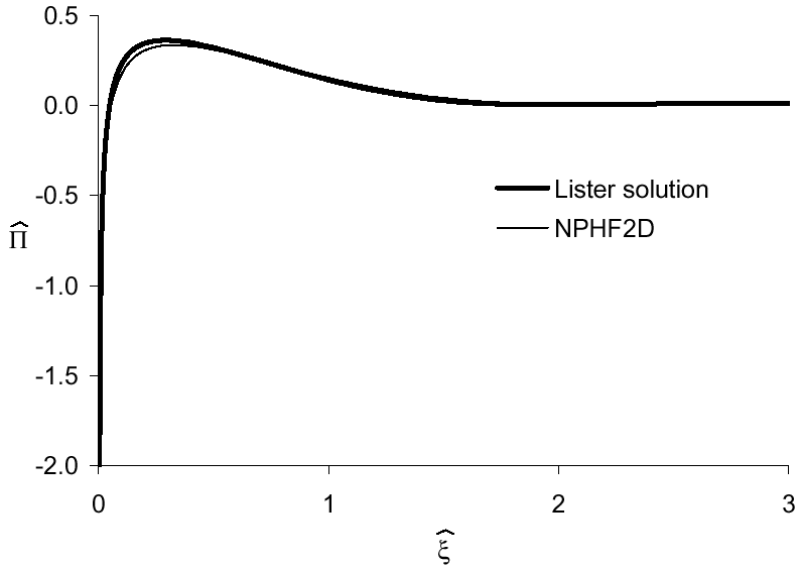

Source: Zhang et al. 2002 [DIRS 164368].

Figure 7-3. Self-Similar Dike Problem for K = 0: Dimensionless Pressure (Π) Versus Dimensionless Distance from the Crack Tip (ξ)

The agreement with the analytic solution is close. The solutions far below the tip are almost coincident. The dimensionless dike opening far from the tip should be 1; the dimensionless pressure far from the tip should be 0. According to the Lister (1990 [DIRS 126865]) analytical solution, the dimensionless fracture opening has a maximum of 1.274, at a dimensionless distance from the tip equal to 0.729. The NPHF2D V1.0 (BSC 2002 [DIRS 163665]) code yields a maximum opening of 1.218, which is a difference of 4.4 percent. The discrepancy is due to the finite fracture length and an effect of the free surface in the model, compared to the idealized conditions of a semi-infinite fracture in an infinite elastic medium assumed in the Lister (1990 [DIRS 126865]) solution.

Uncertainties associated with the fidelity of the numerical approximations used in the NPHF2D code are on the order of a few percent. Such uncertainties will not affect the applicability of the results of the dike propagation model.

Geological Uncertainties–Uncertainty is also associated with the extent to which a numerical model is a faithful representation of conditions "in the ground." Although the analysis of Section 6.3.7.3, addressing the effect of thermally-induced stresses and the possibility of sill formation, is a substantial improvement on the simpler analysis in Sections 6.3.7.1 and 6.3.7.2, the use of Voronoi polygons to represent the mechanical behavior of even poorly stratified rocks introduces its own uncertainty. In particular, the isotropic nature represented may not be as faithful as some other structure with a larger proportion of horizontal discontinuities. This may contribute to the apparent difficulty of sill formation found in the analysis.

Uncertainties of the Dike Propagation Model associated with the variability of real geologic media can be inferred from intermediate results in the Parícutin natural analogue calculations (Section 7.3.1.1.1). For example, for strike lengths that differ by a factor of 2, but keeping the magma supply rate and magma density constant, variations of about 25 percent in dike widths

and of about 60 to 65 percent in most other properties are found. Comparing results with different densities, it is seen that variations on the order of 50 percent in magma density will lead to similar variations in timing, but smaller variations (10 to 15 percent) in dike width and magma velocity. The effect of uncertain geologic properties has also been addressed in the application of the model. For instance, the model is applied to a range of country rock densities, magma velocities, and magma viscosities; these lead to corresponding variations in calculated magma density, dike width and magma flux (Table 6-3). Selection of inputs has leaned toward conservative outcomes, when consistent with the state of knowledge regarding geologic properties.

Clearly, natural geological variability will be the greatest source of uncertainty in the results of the dike propagation model. Uncertainties of a factor of 2 or larger in such results as the time needed for magma to flood a drift or the depth of magma when the crack tip reaches the surface may arise from this source. This uncertainty related to dike propagation, specifically the potential for formation of a "dog-leg," has no effect on the Post-Intrusion Model results.

7.3.2 Post-Intrusion Submodel

Post-development validations of the components of the Post-Intrusion Submodel were conducted. Validation of the Drift-Scale Gas Flow between Drift Model components is described in Section 7.3.2.1. The Magma Cooling and Solidification Model component is described in Section 7.3.2.2. The Basalt/Seepage Water Model component is considered in Section 7.3.2.2.

7.3.2.1 Drift-Scale Gas Flow Between Drifts Model Component

This section addresses the validation of the TOUGHREACT (LBNL 2002 [DIRS 161256]) simulations of vapor and acid gas transport, vapor condensation, and acid gas dissolution accompanying intrusion of magma into a drift (described in Section 6.6). Validation by comparison with laboratory analogue data is discussed in Section 7.3.2.1.1. Publication in peer-reviewed journals as validation is presented in Section 7.3.2.1.2. Uncertainty is discussed in Section 7.3.2.1.3, and alternative models are discussed in Section 7.3.2.1.4.

7.3.2.1.1 Corroboration with Laboratory Analog

This validation is based on an experiment involving gas transport under boiling conditions and dissolution into a condensing water phase. The validation criterion is that the model captures the pH of the condensed water measured in the experiment within one pH unit.

The Experiment – Pulvirenti et al. (2004 [DIRS 169631]) conducted a laboratory evaporation-condensation experiment on a synthetic concentrated Yucca Mountain unsaturated zone pore water with an initial concentration factor of 1243 (the ratio between the chemical concentrations of the synthetic concentrated solution and the concentrations in the unsaturated zone pore water). This experiment was focused on the potential for corrosion of the alloy22 (a Ni-Cr-Mo alloy) waste package material as a result of acid degassing of salts and subsequent formation of low pH condensates on the waste package and/or drip shield. They heated the synthetic concentrated solution in a 12L flask at 144°C producing vapor and acid gases. The vapor and acid gases

migrated out from the flask through a pipe connecting to a water-cooled condenser, where the vapor condensed. The acid gases simultaneously dissolved in the condensate, resulting in a very acid condensate with pH 1 or less (Pulvirenti et al. 2004 [DIRS 169631]). A schematic diagram of the experiment is shown in Figure 7-4.

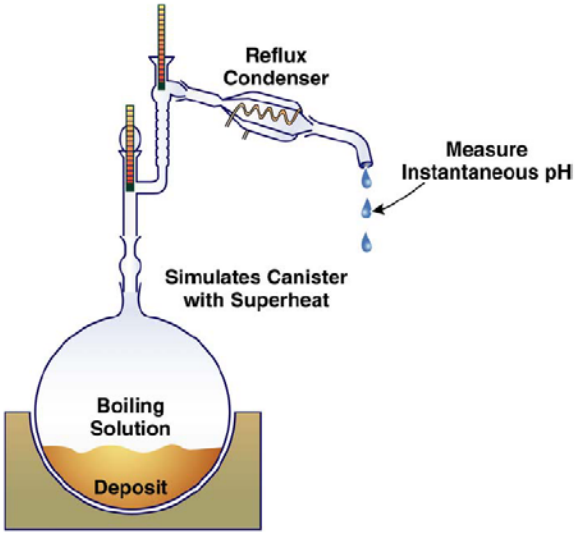

Source: LBL drawing.

Figure 7-4. Schematic Illustration of the Evaporation/Condensation Experiment Conducted by Pulvirenti

The synthetic concentrated pore water (12L) with concentration factor 1243 was prepared using a mixture of salts and distilled in a 12L round-bottom flask, using a heating mantle at 144°C, until 40-250 mL of liquid remained in the flask. The water-cooled condenser was attached at the top of the flask through a pipe. Condensates were collected at intervals for pH measurement. The pH of the condensed droplets fell to 1.0 or less when the majority of the solution in the flask was vaporized.

Model Inputs–The initial chemical composition of the synthetic concentrated pore water used in the validation calculation was determined according to the recipe used in the experiment (Pulvirenti et al. 2004 [DIRS 169631], Table 1), and listed in Table 7-6. The derivation of these values is provided in Appendix H. The pH of the solution is estimated according to the chemical equilibrium calculation to be 7.7825. The density of the solution was estimated as 1.06565 using the densities of the pure salt solutions from Lide (2002 [DIRS 160832], pp. D-204 and D-215).

Table 7-6. Initial Chemical Composition of the Synthetic Concentrated Pore Water Used in the Experiment

Components	Concentration (Moles/kg of Water)
Ca^{++}	0.402
K^{+}	6.97E-2
Mg^{++}	0.235
Na^{+}	0.279
Cl^{-}	1.505
F^{-}	2.92E-2
HCO_3^{-}	7.43E-4
NO_3^{-}	4.26E-2
$SO4^{--}$	2.23-E-2
SiO_2	9.21E-3
pH	7.783

Source: The derivation of these values is provided in Appendix H.

The initial temperature of the synthetic concentrated pore water was 144°C, as in the experiment of Pulvirenti et al. (2004 [DIRS 169631]).

Modeling Methodology and Software–In order to simulate the concentration processes taking place in this experiment, a multiphase flow and Pitzer-type reactive geochemical simulator is required because of the high ionic strength of the solution generated during the vaporization processes. The Pitzer model is not available in the current qualified version of TOUGHREACT code, TOUGHREACT V3.0 (LBNL 2002 [DIRS 161256]) that was used to conduct the 'volcanic gas' model. However, the 'volcanic gas' model is focused on acid gas transport, vapor condensation and acid gas dissolution rather than the acid gas generation. Therefore, this validation effort addresses the part of the experiment involving acid gas transport, vapor condensation, and acid gas dissolution. The acid gas generation and fugacity was simulated using EQ3/6, V8.0 (BSC 2003 [DIRS 162228]). The acid gas fugacity calculated using EQ3/6 was then used as the acid gas source for TOUGHREACT gas transport, condensation, and dissolution simulations.

Model Setup and Results–To model the acid gas source in TOUGHREACT simulations, the flask was represented as a fixed concentration and volume source, under conditions of elevated pressure and low permeability to maintain the constant high temperature of 144°C, and constant acid gas fugacity (calculated using EQ3/6) producing vapor at that temperature. The pipe connecting the flask and the condenser was represented using several thin blocks. The condenser is represented using a block assigned to room temperature (25°C) to condense the vapor produced in the flask and transport through the pipe. The end of the pipe is connected with atmosphere allowing the extra vapor to flow out.

In total, nine EQ3/6 simulations and nine TOUGHREACT simulations were performed corresponding to a range of concentration factors (Table 7-7) until the EQ3/6 simulation fail to converge due to extremely high ionic strength and low water activity. Three main acid gases are

considered in the TOUGHREACT simulations: HCl, HF, and CO_2. The simulation results are summarized in Table 7-7.

Table 7-7. Summary of EQ3/6 and TOUGHREACT Simulation Results

Concentration Factor	Acid gas fugacity (calculated using EQ3/6)			pH of condensate (TOUGHREACT V3.0)*
	HCl	HF	CO_2	
1x1243	6.08 E-11	1.02 E-08	1.12 E-04	4.278
5x1243	1.27 E-08	4.73 E-07	1.38 E-03	3.007
10x1243	8.65 E-07	1.16E-05	3.49 E-03	1.268
15x1243	8.37 E-06	1.56 E-04	5.11 E-03	0.504
20x1243	1.41 E-05	1.32 E-03	1.17 E-02	0.355
25x1243	3.20 E-05	1.02 E-02	5.11 E-02	0.144
30x1243	4.16E-05	6.23 E-02	2.28 E-01	0.128
35x1243	2.78059E-05	3.08669E-01	3.19623E-01	0.348
40x1243	1.07075E-05	1.32679E+00	7.07154E-03	0.665

Output DTN: LB0408AMRT0020.003.

NOTE: The condensed water without the acid gas dissolved had a measured pH of 6-7. The simulated pH using TOUGHREACT is 6.306.

The simulated pH of the condensate is plotted versus the concentration factor of the solution in the flask in Figure 7-5. The modeled pH of the condensate decreased as the solution was evaporated and dropped to less than 1 when the concentration factor was greater than 15,000. This low pH is consistent with the pH measured in the experiment (Pulvirenti et al. 2004 [DIRS 169631]), although the temporal evolution of the pH in the experiment was not presented by the latter authors. This match demonstrates that the simulation using TOUGHREACT V3.0 correctly reproduced acid gas transport, vapor condensation and acid gas dissolution, as used in Section 6.6 for the volcanic gas transport model. This validates the input thermodynamic data, transport model, and dissolution for acid gases under boiling conditions, similar to that present in the boiling region that would surround a drift filled with magma. However, low pH values were not observed in the model simulations involving the rock around the intruded drift because of the buffering of mineral-water reactions not present in the experiment.

The EQ3/6 and TOUGHREACT simulation results of this validation activity have been submitted in Output DTN: LB0408AMRT0020.003 and Output DTN: LB0408AMRT0020.004.

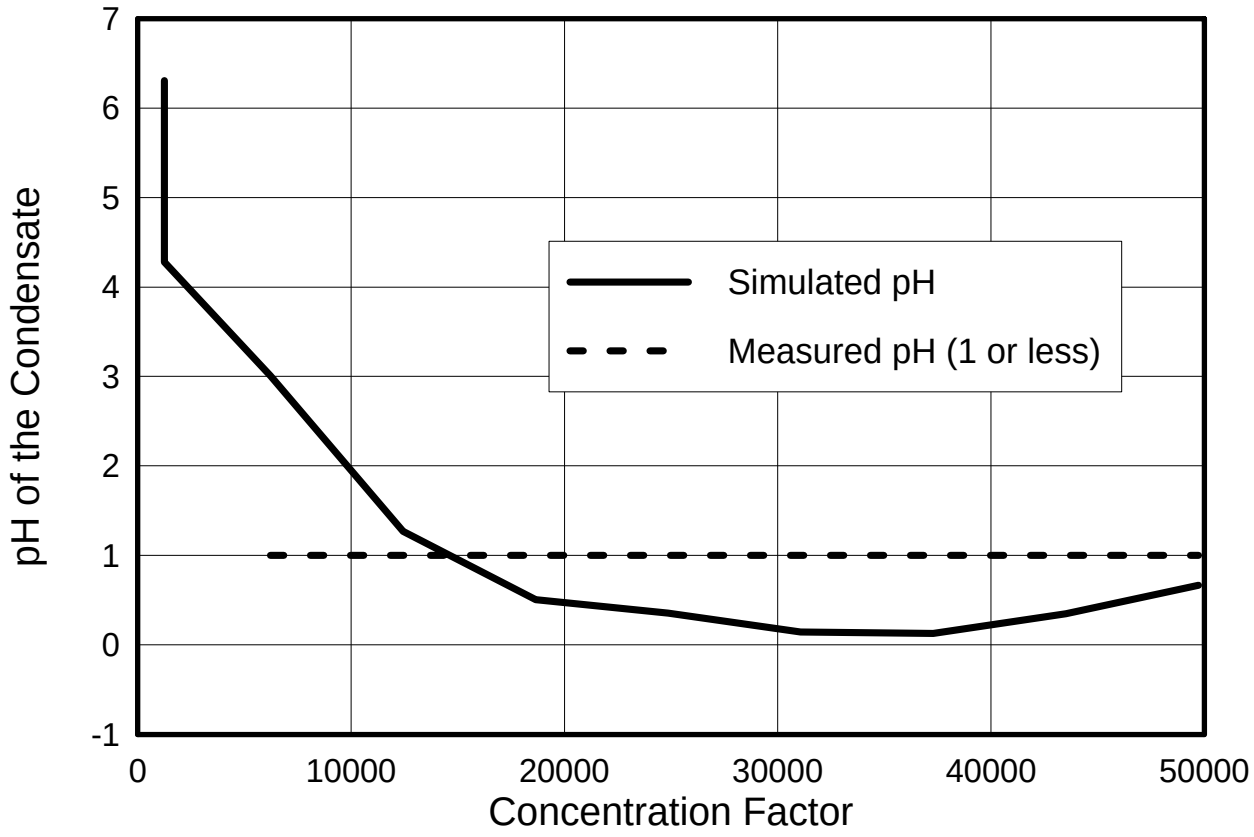

Output DTN: LB0408AMRT0020.003, LB0408AMRT0020.004.
Source: Measured pH: Pulvirenti et al. 2004 [DIRS 169631].

Figure 7-5. Change in pH of the Condensate Versus Concentration Factor for the TOUGHREACT Model Simulations as Compared to the pH Measurement

7.3.2.1.2 Validation by Publication in Peer-Reviewed Journals

Several aspects of the thermal-hydrological-chemical modeling approach and data have been published in the following peer-reviewed journals, thus validating their use in the gas flow analysis:

- "Experimental and Numerical Simulation of Dissolution and Precipitation: Implications for Fracture Sealing at Yucca Mountain, Nevada." *Journal of Contaminant Hydrology* (Dobson et al. 2003 [DIRS 165949]).

- "Simulation of Water-Rock Interaction in the Yellowstone Geothermal System using TOUGHREACT." *TOUGH Symposium 2003, Proceedings* (Dobson et al. 2003 [DIRS 168273]).

- "Fluid Flow and Reactive Transport Around Potential Nuclear Waste Emplacement Tunnels at Yucca Mountain, Nevada." *Journal of Contaminant Hydrology* (Spycher et al. 2003 [DIRS 162121]).

- "A Reactive-Transport Model for Calcite Precipitation and Evaluation of Infiltration Fluxes in Unsaturated Fractured Rock." *Journal of Contaminant Hydrology* (Xu et al. 2003 [DIRS 162124]).

7.3.2.1.3 Uncertainty

Uncertainties in the Drift -Scale Gas Flow Model are primarily related to the specifics of the magma intruding into a drift. These include the length of time that the drift has magma flowing through it, the gas pressure, and the composition of the gas. A prolonged flux of magma through the drift would lengthen the cooling period and would allow for a greater gas flux relative to a single injection. Several meters into the rock, the main effect would be a slightly greater extent of the boiling zone. However, simple cooling models discussed in this report predict that the extent of the 100 degree isotherm is less than 8 m from the drift wall. This isotherm is not likely to migrate more than a few meters further because the volume of rock heated is proportional to the square of the radius so that the outward advance of the boiling front slows over time given a constant heat input. The same geochemical reactions, involving dissolution of gases into water condensing in the rock and drainage through fractures would still take place, retarding gas transport in the rock.

Model-specific uncertainties are associated with thermodynamic data for the gas species at magmatic temperatures. However, such temperatures would be confined to the rock immediately adjacent to the drift and all gas would still have to pass through a boiling zone that surrounds the magma-filled drift. Migration of gases by diffusion and advection, followed by mineral-water-gas reactions, have been validated through the modeling of the laboratory experiment and through the measurements and modeling of CO_2 transport in the Drift Scale Test (BSC 2004 [DIRS 169856], Section 7.1). These tests and models validate the approach and data used for modeling the coupled thermal-hydrological-chemical processes that govern the transport of volcanic gases through the fractured tuff at temperatures predominantly below 200°C.

7.3.2.1.4 Alternative Models

As discussed in the last section, the possible scenarios for intrusion of magma into a drift could give rise to different initial and boundary conditions for models of gas transport into the surrounding tuff. There are several other alternative methodologies for treating gas flow, diffusion, water-rock interaction in the unsaturated zone. These other methodologies include discrete fracture models, in which flow through individual fractures is considered, instead of the dual-continuum approach. Such models, because of the great number of fractures in the rock, are not computationally feasible at the scale greater than a few meters. Therefore, the approach taken for the modeling of coupled thermal-hydrological-chemical processes in the unsaturated zone has been developed over several years with model improvements, incorporation of new data, and sensitivity studies with validation to laboratory experiments and the Drift Scale Test. Alternative geochemical models were also considered in the validation modeling performed for the Drift Scale Test in *Drift-Scale THC Seepage* Model (BSC 2004 [DIRS 169856])

(comparisons of gas phase CO_2 concentrations and pH of thermal waters collected from boreholes).

7.3.2.2 Magma Cooling and Solidification Model Component

The Magma Cooling and Solidification model component is corroborated by comparison with an alternative analytical solution (Section 7.3.2.2.1) and with field observations and an associated numerical analysis (Section 7.3.2.2.2). Uncertainty is addressed in Section 7.3.2.2.3.

7.3.2.2.1 Comparison with Alternative Mathematical Model

The approach outlined in Section 6.7 involved a finite difference methodology as summarized in Appendix C. The alternative approach, for which summary results are presented here, uses analytical solutions to the same equations as does the model solution, but uses a very different treatment of latent heat effects. A complete discussion of the method and results is presented in Appendix D.

Acceptance Criteria–Results of both calculations at selected times and places within the repository system following an intrusive event should differ by no more than 25 percent.

Results–Figures 7-6 and 7-7 are included below to facilitate comparisons between base case and validation thermal models. Figure 7-6 shows the thermal evolution of a magma-filled drift using the thermal conductivity of dry tuff with latent heat is not included, as discussed in Section 6.7.1.1.1. Figure 7-7 shows the estimated effects of latent heat, as determined by an alternate approach documented fully in Appendix D.

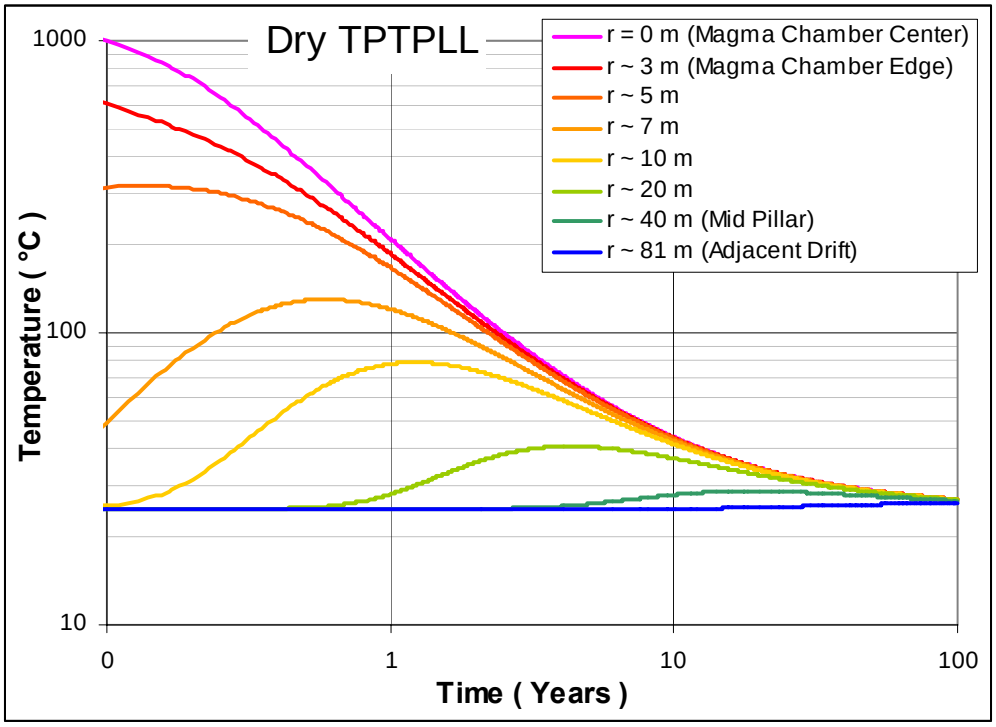

Source: Figure 6-98 in this report.

Figure 7-6. Heat Conduction from Magma Flow for Dry Tptpll

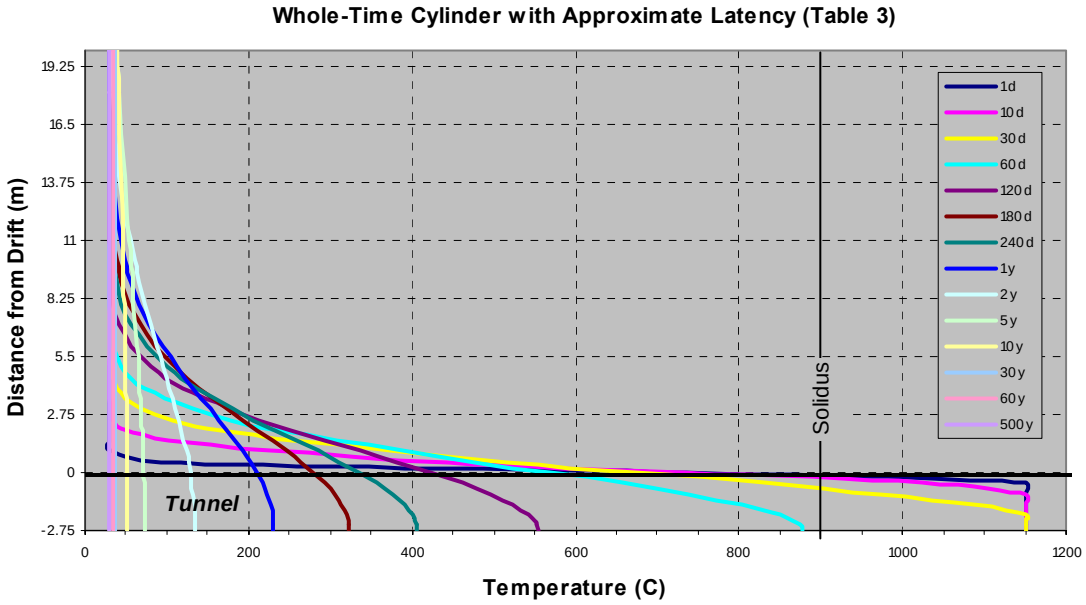

DTN: LA0307EG831811.001.

Figure 7-7. Plot of Calculated Whole-Time Temperature Profiles for Various Cooling Times Assuming a Cylindrical Drift Geometry and Showing the Approximate Effect of Latent Heat

Values listed below in Table 7-8 agree to within 20 percent or less relative to the models presented in Section 6.7. Note that, for short periods, finite difference models slightly under-predict temperatures, whereas they over-predict thermal effects for long times. Thus, models presented in Section 6.7 above are conservative for long times. The agreement between the models is considered to be excellent given the wide range of natural variation in input parameters, as well as the simplifications of natural processes that have been made.

Table 7-8. Comparison of Cooling Model Results from Section 6.7 [Model 1] and from Alternate Model [Model 2]

Location	Model 1[a] T°C	Model 2[b] T°C
After 1 year		
drift center	~200	~215
drift wall	~190	~205
20 m from drift center	~37	~40
After 10 years		
drift center	~55	~50
drift wall	~55	~50
20 m from drift center	~48	~40

[a] Base case model: finite difference, Tptpll, no latent heat, dry pore volume. See Figure 7-8.
[b] Validation model: analytical solution, approximate latent heat effects considered. See Figure 7-9 and Figure D-2, Appendix D.

7.3.2.2.2 Comparison with Field Observations and Associated Mathematical Model

Shaw et al. (1977 [DIRS 170321]) and Peck et al. (1977 [DIRS 170318]) monitored and modeled the thermal evolution of a shallow (~15-m deep) cooling lava lake (Alae Lava Lake, formed in August 1963 during an eruptive phase of the Kilauea volcano, Hawaii) and successfully modeled and measured its cooling over the period of several years. This work illustrates that models of conductive cooling can adequately reproduce the behavior of volcanic systems.

Acceptance Criteria–The acceptability of this analog is established by a close correspondence between predicted and observed temperature profiles in which the simplifying assumptions of a constant thermal conductivity for the magma/host rock system are similar to cooling calculations in Section 6.7.

Results–Shaw et al. (1977 [DIRS 170321]) and Peck et al. (1977 [DIRS 170318]) describe the evolution of a lava lake, initially extruded at 1160°C, as it cooled over a 4-year period to less than 100°C. The modeling was more complex than that presented in this report because it had to account for the dissipation of energy through the heating and vaporization of rainwater. Nonetheless, conductive cooling models were successful in closely reproducing the temporal thermal evolution of the lava lake. For example, the average deviation between observed and modeled profiles was 21°C. This is a remarkable correspondence given the additional complexity of the irregular shape of the bottom of the lava lake, the vaporization of rainwater, and the formation of cooling joints that accommodated the advective loss of hot gas from the cooling and solidifying magma body. This correspondence builds confidence in the use of constant conductivity cooling models of magma-filled drifts, which are conceptually much simpler than a cooling lava lake, to provide estimates of the thermal history of a drift filled with magma.

7.3.2.2.3 Uncertainty

Uncertainty in the Magma Cooling component of the Post-Intrusion Model was explicitly evaluated in Section 7.3.2.1.1. The results, particularly the explicit comparison made in Table 7-8, demonstrate that the model is fairly insensitive to natural parameter variations. The comparisons in Table 7-8 were made at critical locations such as the drift center, drift wall, as well as the pillar interior. Differences after 10 years would have no significant effect on repository function. Conservatism was added to the model by using an initial magma intrusive temperature of 1150°C which is near the maximum temperature of 1169°C presented in *Characterize Eruptive Processes at Yucca Mountain, Nevada* (BSC 2004 [DIRS 169980]). Additionally, the drift was considered to be entirely filled with magma effectually causing slower cool down than would occur in a partially filled emplacement drift.

7.3.2.3 Basalt/Water Seepage Model

The approach used for validating water chemistry equilibration with basalt at ambient conditions is through corroboration by comparison with both natural (Section 7.3.2.3.1) and laboratory (Section 7.3.2.3.2) analogs. Uncertainty is discussed in Section 7.3.2.3.3.

Acceptance Criteria–Analog data must show a range in output values similar to water chemistry modeled in Section 6.8, or if there is a significant lack of correspondence, the abstracted data for performance assessment calculations should lead to waters that are more chemically aggressive (i.e., higher ionic strength or higher pH).

7.3.2.3.1 Comparison and Corroboration with Field Analog Data

All basalts have a roughly similar mineralogy (pyroxene + calcic plagioclase + olivine + magnetite), so reactions consuming hydrogen ions will tend to buffer pH toward a similar range of values regardless of tectonic setting. For the reaction of seepage water with the cooled basalt body, EQ6 indicates that the pH of the water is highly dependent on the p_{CO_2} of the system, and likely to be between 7.6 and 9.9. Higher p_{CO_2} values show pH values between 7.6 and 8.6. Values of pH as high as 9.0 to 9.6 are obtained with a log p_{CO_2} of –3.5 (bars) and pH values between 9.4 and 9.9 can be obtained with a log p_{CO_2} of –4 (bars). These pH values largely overlap with those obtained from groundwater taken from basalts, especially units within the Columbia Plateau, Washington (Hearn et al. 1985 [DIRS 166893]; White et al. 1980 [DIRS 163752]; and Hem 1985 [DIRS 115670]). Values of pH in these natural analog waters are normally distributed (mean = 7.9±0.5; median = 7.9; n = 32), with a total range of 6.7 to 9.3.

Minimum ionic strength values calculated with EQ6 are between 9.14E-03 and 1.97E-02 moles/kg. The same suite of natural analog waters discussed above (Hearn et al. 1985 [DIRS 166893]; White et al. 1980 [DIRS 163752]; and Hem 1985 [DIRS 115670]) tends to be somewhat more dilute. Ionic strengths of these waters range from 2.15E-03 to 1.5E-02, with a mean value of 5.90E-03 ± 3.06E-03 moles/L. Even thermal waters from the Snake River Plain basaltic aquifer tend to have a lower solute load than EQ6 results. McLing et al. (2001 [DIRS 170322]) report several selected waters with a mean ionic strength of 1.03E-03 ± 5.60E-03 moles/L. Although the units of molality (moles/kg) from the EQ6 calculations differ from those of molarity (moles/L) reported for analog waters, at these dilute concentrations the two are essentially identical.

Natural waters interacting with basalt in natural systems tend to be somewhat basic, albeit less so than the output of EQ6 models, likely due to higher p_{CO_2} values in natural systems. Natural ionic strengths are similar to, but slightly below, those calculated. The model waters are more aggressive than the natural waters, thus validating the model.

7.3.2.3.2 Comparison and Corroboration with Laboratory Analog Data

Gislason and Eugster (1987 [DIRS 168716]) carried out laboratory studies on the reaction of meteoric waters with basalt. They show that at higher p_{CO_2} values, the pH of the system tends to be near neutral (between 7 and 8) whereas those for which p_{CO_2} was limited had much higher pH waters (between 9 and 10). At higher p_{CO_2} values, the buffering capacity of aqueous CO_2 dominates. However, when CO_2 is diminished, the buffering capacity is controlled by aqueous silica and other carbon species, allowing the pH to rise to values between 9 and 10 (Gislason and Eugster (1987 [DIRS 168716]).

At high pH, there will be a higher proportion of carbonate versus bicarbonate in the dissolved inorganic carbon fraction. Note, however, that this does not necessarily equate to a higher

dissolved inorganic carbon fraction in solution. For example, high pH will reduce calcite solubility, so it is reasonable to expect that total dissolved inorganic carbon could decrease. Inasmuch as the solubility of actinide species is related to carbonate availability (CRWMS M&O 2001 [DIRS 154629], Figure 1, p. 22), the dissolved inorganic carbon cannot be said to result in waters that are definitively either more or less aggressive.

In summary, analog data validate the use of water compositions abstracted from EQ6 calculations for the purpose of Total System Performance Assessment. Values of pH include an overall range that is broader and has a more alkaline upper limit than the range indicated by analogs. The range of ionic strengths calculated by the model lead to geochemically more aggressive waters. Thus, ionic strengths developed in this report are also conservative.

7.3.2.3.3 Uncertainty

Modeled compositions of water reported in Table 6-24 show a considerable range of pH and ionic strength. For each p_{CO_2} and time increment, pH varies over 0.2 to 0.4 log units, whereas ionic strength varies from a minimum of 32 percent to a maximum of 82 percent. However, as discussed above, the output of this model produces waters with a higher average ionic strength than waters from analog basalt aquifers. On the other hand, pH is often higher in the model output relative to natural waters due to the low p_{CO_2} values used in the model. The net effect is that these uncertainties largely cancel each other. On a conceptual level, the approach employed in EQ6 calculations embeds conservatism into the results. For example, since the nature and extent of fracturing of the solidifying basalt and its resulting permeability cannot be known, the basalt in the intersected drifts was assumed to have permeability at least as great as the drift wall rock (see Section 5.4.1). This assumption is conservative because it ensures that the cooled magma does not act as a barrier to the flow of seepage water from the rock above the drifts to the waste forms after reversion of the system to normal conditions. The degree to which the seepage water would, in fact, equilibrate with basalt during its movement through the basalt is unknown, although some degree of chemical interaction toward a state of equilibration is expected.

Convergence difficulties arise in EQ6 calculations carried out at high pH and low CO_2 levels. For this reason, the model includes p_{CO_2} values only from 10^{-2} to 10^{-4} bars. Natural analogues (Hearn et al. 1985 [DIRS 166893] and DOE 1982 [DIRS 166892]) show that the pH of water in contact with basalt (depending on the CO_2 levels) can be between 6.7 and 10.1 with the majority of data showing pH values of 8.5 to almost 10. Ionic strength is between 7.4E-03 and 1.8E-02 moles/kg. Therefore, the pH and ionic strength for p_{CO_2} between 10^{-4} and 10^{-5} bar should, realistically, not be much greater than those calculated here.

The ionic strength of water from different basalt units is discussed in Section 6.8. Calculated ionic strength was dependent on the available data on ionic species from basalt waters. EQ6 shows that as the pH increases, the ionic strength increases, the highest ionic strength values occurring at the highest pH (correlating with the lowest CO_2 values). At higher pH values, many more carbonate and silica species will be present in solution. These ions are not reported in the references cited for validation in Section 6.8. It is therefore reasonable that at higher pH values (lower CO_2), the ionic strength is higher than that represented in Section 6.8. Therefore, this model recommends using the upper bound of waste colloid stability presented *Waste Form and In-Drift Colloids-Associated Radionuclide Concentrations: Abstraction and Summary*

(BSC 2004 [DIRS 170025], Table 17) in cases where the maximum ionic strength exceeds 0.05 moles/kg. Since this value (0.05 moles/kg) represents the upper bound at which waste colloids are stable, it is conservative in that it allows colloids to exist. As indicated in Section 6.4.9, chemical interaction between waste forms and the magma and chemical interaction between the waste forms and the metal of waste canisters/assemblies and cladding in the presence of hot magma can occur. Since the extent of development of mineral phases is unknown but would tend to limit subsequent reactivity of the altered waste forms, the waste is considered conservatively chemically unchanged.

INTENTIONALLY LEFT BLANK

8. CONCLUSIONS

8.1 SUMMARY OF MODELING ACTIVITIES

Information concerning dike propagation, the fluid dynamics and thermal evolution of magma, the migration of magmatic gases through rock, and potential processes associated with the interaction between magma, waste package materials, and waste forms was assembled. This was done to develop a dike/drift interaction model that represents the interactions of a rising basaltic dike with a repository drift mined in silicic tuff, intrusion into that drift, and the post-emplacement effects. This model is summarized in Sections 8.1.1 through 8.1.3. A series of validation activities were completed to build confidence in the model. Limitations of the use of this model are discussed in Section 1.3. *Yucca Mountain Review Plan, Final Report* (NRC 2003 [DIRS 163274]) acceptance criteria have been addressed, as described in Section 4.2 and Appendix A of this report. Finally, results of this model are provided as outputs in Section 8.2, and the associated uncertainties are discussed in Section 8.3.

8.1.1 Dike Propagation

The following conclusions are drawn from modeling results presented in this report:

- The in situ state of stress at Yucca Mountain (before heating) is such that the vertical stress is the maximum principal compressive stress, whereas two other principal stresses of smaller magnitude are in the horizontal plane. Based on current understanding of the state of stress, the topography of Yucca Mountain will not cause deflection of the dike (Section 6.2.2).

- Stress changes caused by drift excavation will be of limited spatial extent and will have insignificant effect on dike propagation (Section 6.2.3).

- A dike propagating upward from depth will consist of a vapor-filled crack tip moving ahead of the magma. Properties of the propagating dike, including the length of the crack-tip cavity, the velocity of the magma, and the width of magma in the dike, depend on the density and viscosity of the magma and on the stiffness of the rock and the confining stresses normal to the dike plane. Properties of the magma and the environment can be reduced to two dimensionless parameters, one ($\mathcal{D}$) related to the density of the host rock and of the magma, and the other ($\mathcal{S}$) to the stress, the stiffness, and the viscosity. Large values of $\mathcal{D}$ are associated with denser magmas, and negative values of $\mathcal{S}$ are associated with excess gas pressure in the tip cavity (Section 6.3.3.3).

- As the dike propagates, the length of the crack tip increases due to the decrease in the confining stresses from the overburden. As the tip of the crack approaches the surface, it accelerates even more. For normal lateral confinement (κ = 0.5), appropriate after about 2000 years postclosure, magma with nominal (10 Pa·s) viscosity and a density of 750 kg/m^3 rising at 1 m/s would arrive at drift level less than 60 s before the crack tip breached the surface 300 m above. Denser magmas will arrive at drift level even closer to the time of breaching the surface. Magmas with a density of 1140 kg/m^3 will stall just below repository depth as the crack races to the surface. This occurs because the crack

widens rapidly enough to accommodate all of the new magma arriving from depth. After the crack has opened to its full extent, magma will resume its upward motion. Faster rising magma also opens the crack faster, so that such magmas would not reach repository level before the crack tip breached the surface. Larger lateral stresses (up to 12 MPa during the first 2,000 years postclosure) would retard crack-tip acceleration so that magmas rising as fast as 5 m/s would reach the repository level before the crack tip breached the surface (Figures 6-11 through 6-16).

- More viscous magma will result in wider dikes and longer tip-cavity lengths (Figures 6-17 and 6-18).

- Fluid pressure in the cavity is expected to be near atmospheric due to the high gas permeability of the host tuff. The model predicts that pressures in excess of atmospheric will increase the length of the tip cavity (Figure 6-23 vs. Figure 6-10), thereby increasing the likelihood that the crack tip will reach the surface before magma reaches the drift.

- The results indicate that thermally-induced stresses 1,000 years after waste emplacement significantly affect dike propagation. When the dike approaches the region of increased horizontal stresses approximately 200 m below the repository, the ascending dike tip and magma front will slow. The dike opening significantly increases while the progress of the crack tip nearly stalls; the magma front will slow to approximately 0.1 m/s. A dike at the center of the repository is slowed more than one near the edge because the temperature (and, hence, the thermally induced horizontal stresses) is greatest in the middle of the repository and decreases toward its margins. Once the dike passes through the region of increased horizontal stresses, the tip and magma front are free to accelerate under the very large vertical stress gradient (see Figure 6-34) above the repository. Below this region, the gap between the dike tip and the magma front is between 50 m and 100 m. The gap almost completely disappears as the dike penetrates the repository (shown in Figure 6-36a). The thermal stresses are not expected to cause dike deflection and sill formation (Section 6.3.7.3).

- The maximum magma pressure at repository depth is estimated to be about 4.5 MPa under in situ stress conditions. Magma pressure would increase to 6 MPa in the case of thermally-induced horizontal stresses up to 13 MPa (Section 6.3.9).

8.1.2 Magma Flow in Drifts

- The opening of pre-existing cracks due to pressure build-up in the drift was analyzed. Even for extremely conservative conditions of a wide initial opening of a pre-existing crack and large driving pressures, the velocity of a magma front inside a joint is approximately 0.5 m/s, which is less than the expected velocity of the magma front inside the main dike. The re-opening cracks would only be millimeters to centimeters wide so that magma would freeze due to conductive heat loss into the surrounding rock mass. Furthermore, because the highly fractured, lithophysal rock mass at the repository level in Yucca Mountain is characterized by a large number of closely spaced joints, it is more likely that magma will be injected into exposed lithophysae and into a number of

intersecting joints. Such a process leads to rapid magma freezing due to heat loss (Section 6.5.1.2).

- By the time magma reaches the repository level, the stress-induced perturbation is small (e.g., Figure 6-66), and its effect on the stress concentrations around the tunnel is minimal (Section 6.5.1.3).

- Even under the most favorable assumptions for growth, a subsidiary dike will never be able to propagate effusively more than a few meters from the drift because the magma will be halted by solidification (Section 6.5.1.5).

- The most likely scenario for magma to erupt to the surface after intruding the drift complex is for it to continue along the trajectory of the original dike (Section 6.5.1.6).

- Hydrovolcanic events arising from magma interaction with hypothetical ponded water in the drifts were analyzed. Events involving more than 150 kg of water can be expected to result in venting, but the amount of material vented would never exceed the initial pyroclastic mass of 100,000 kg. Events involving much less than 100 kg (e.g., 50 kg or lower) would be expected to lead to formation of pyroclastic dikes such as those studied by Heiken et al. (1988 [DIRS 165566]) at Obsidian Dome, but would not be expected to lead to any significant venting of primary magmatic material (Section 6.5.2.1).

- The Woods et al. (2002 [DIRS 163662]) model of magma expansion into a drift overestimates the violence of the encounter. Realistic boundary conditions including compressible walls and backfill, permeable country rock and backfill, phase separation in the magma-volatile mixture, partial blockage of the drift by waste canisters, backfill, and rockfall, and the axial spacing of the canisters would combine to greatly reduce the amplitude of any shock wave that might form in the initial encounter. More importantly, use of realistic initial conditions would preclude the formation of a shock wave for all but the most rapid magma ascent rates (Section 6.5.3.2).

- It is difficult to predict with certainty the effects of basaltic magma interacting with waste package materials. However, a survey of known effects suggests that they are all deleterious to waste package integrity, and often seriously so. Thus, this report is supportive of the position that all waste packages, cladding, and drip shields are immediately and completely compromised if and when they come in contact with magma (Section 6.4.8).

- Magmatic effects on waste form are difficult to predict, but are expected to include comminution of oxide fuel and volatilization of some fission daughter products. Because of the high temperatures at which basalt magma and waste forms will interact, the formation of oxide and silicate phases are the most likely hosts for radionuclides. The solubility of such phases has not been assessed. Chemical reactions between magmatic volatiles and waste forms are also possible, but have not been evaluated. Glass waste forms are not expected to be devitrified. However, these conclusions should be considered in light of the large uncertainty that exists (Section 6.4.8).

8.1.3 Post-Intrusion Effects

In this model, thermal and geochemical impacts from an igneous intrusion into one or more repository drifts are considered in terms of two damage zones. Zone 1, comprising all drifts intersected by the intrusion, and Zone 2, comprising all other parts of the repository. With respect to thermal effects, this model provides information regarding impacts on Zone 1, as well as nearby Zone 2 drifts. Regarding changes in the composition of seepage water, impacts affect only Zone 1 drifts.

- The high solubility in water of chlorine- and fluorine-bearing gases, SO_2 and to a lesser extent CO_2, along with the development of a boiling zone around a drift where magma has been emplaced, limits the migration of these gases through the repository host rock. Model results indicate that these gases are unlikely to migrate to an adjacent drift through the rock to any meaningful degree.

- The impacts of magmatic heat conduction on the waste packages in Zone 2 emplacement drifts were modeled. Temperatures were modeled by numerical simulations of non-steady state heat conduction with radial flow. The simulation modeling of heat conduction away from the intruded drifts demonstrates that the initial 1150°C temperature reduces to about 30°C at the center of the drift in about 30 years, and the maximum temperature rise expected in the Zone 2 emplacement drifts is less than 1°C. The drift-rock in Zone 2 provides an effective thermal insulation barrier to the impacts of high temperature of the intruded magma, and there would not be any impact of igneous heat on the waste packages in Zone 2 emplacement drifts. Table 8-2 provides lookup values for waste form temperatures for a range of post-intrusion times and wall rock temperatures.

- The chemistry of the incoming seepage is expected to be affected by basalt-water reactions within the drift. The effects of these reactions on a typical crown seepage water have been modeled and the results of the abstraction for feed to TSPA are outlined in Section 6.8.4.

8.2 MODEL OUTPUT

8.2.1 Developed Output Listed by Data Tracking Number

The outputs associated with the Dike/Drift Interaction model are listed in Table 8-1 by data tracking number.

8.2.2 Migration of Magmatic Gases

Under near-ambient pressure conditions, highly corrosive magmatic gases such as HCl, HF, and SO_2 would not migrate to an adjacent drift through the rock. Specific output values can be obtained from the source DTN: LB0306AMRT0020.001.

Table 8-1. Outputs for the Dike/Drift Interaction Model Report

Sub-Model/Component Output Description	Data Tracking Number
Estimates of Magma Flow from Dike into Drifts	LA0408DA831811.001
Post-Intrusion Model/Gas Flow Gas Migration	LB0306AMRT0020.001
Post-Intrusion Model/Gas Flow Gas Migration & Water Chemistry	LB0408AMRT0020.001 LB0408AMRT0020.002
Post-Intrusion Model/Gas Flow Validation	LB0408AMRT0020.003 LB0408AMRT0020.004
Post-Intrusion Model/Magma Cooling/Solidification Temperature of Waste Forms (Lookup)	MO0402SPAHWCIG.002
Post-Intrusion Model/Basalt-Seepage Water Interaction pH and Ionic Strength	MO0402SPAHWCIG.002
Dike Intrusion Model/Secondary Dike Formation Pressure Histories	MO0408EG831811.001
Dike Intrusion Model/Propagation, Expanding Magma and Crack Tip Positions	MO0408EG831811.002
Dike Propagation Model Results Using NPHF2D	MO0408EG831811.003
Dike Intrusion Model/Propagation, Ambient Stresses Dike & Magma Properties	MO0408EG831811.004
Post-Intrusion Model/Magma Cooling & Solidification Temperature	MO0408EG831811.008

8.2.3 Thermal Effects

The information in Section 6.4 supports the use of the TSPA assumption that waste packages in Zone 1 emplacement drifts no longer provide protection for the waste forms. The waste packages and other drift materials would be enclosed by the magma. The full detail of effects of magma intrusion on waste packages and cladding are not known. However, these results are conservative because, in this approach, no credit is taken for any residual waste-containment of remaining waste package or cladding material.

The impacts of magmatic heat conduction on the waste packages in Zone 2 emplacement drifts were modeled. Temperatures were modeled by numerical simulations of non-steady-state heat conduction with radial flow.

The simulation modeling of heat conduction away from the intruded drifts demonstrates that the initial 1150°C temperature reduces to about 30°C at the center of the drift in about 30 years, and the maximum temperature rise expected in the Zone 2 emplacement drifts is less than 1°C. The drift-rock in Zone 2 provides an effective thermal insulation barrier to the impacts of high temperature of the intruded magma, and there would not be any impact of igneous heat on the waste packages in Zone 2 emplacement drifts. Table 8-2 provides lookup values for waste form temperatures, which are the same as centerline temperatures (Section 6.7), for a range of post-intrusion times and wall rock temperatures.

Table 8-2. Lookup Tables for Temperature of Waste Forms

Time after Intrusion	For an Intrusion into a Repository at 25°C		For an Intrusion into a Repository at 50°C		For an Intrusion into a Repository at 100°C		For an Intrusion into a Repository at 150°C		For an Intrusion into a Repository at 200°C	
Years	$T_{r=0m}$	$T_{r=3m}$	$T_{r=0m}$	$T_{r=3m}$	$T_{r=0m}$	$T_{r=3m}$	$T_{r=0m}$	$T_{r=3m}$	$T_{r=0m}$	$T_{r=3m}$
0	1150	1150	1150	1150	1150	1150	1150	1150	1150	1150
0.1	977	592	1006	620	1012	644	1019	668	1026	692
0.2	702	462	749	494	768	524	786	553	804	583
0.3	530	382	577	416	603	449	629	483	655	516
0.4	422	326	467	360	498	396	529	432	560	468
0.5	351	284	394	318	428	356	462	394	497	431
0.6	301	252	341	286	378	325	415	364	452	403
0.7	264	226	303	260	341	300	380	341	418	381
0.8	236	206	273	239	313	281	353	322	392	363
0.9	213	189	249	222	290	264	331	306	372	349
1	195	175	230	208	272	251	314	293	356	336
2	111	106	142	136	187	182	233	228	279	274
3	82.8	80.4	111	109	158	156	206	203	253	251
4	68.4	67.0	96.0	94.5	144	142	192	190	240	238
5	59.7	58.9	86.8	85.8	135	134	183	183	232	231
6	54.0	53.4	80.7	80.0	129	129	178	177	227	226
7	49.8	49.4	76.3	75.8	125	125	174	173	223	222
8	46.7	46.4	73.0	72.6	122	122	171	171	220	220
9	44.3	44.0	70.5	70.2	120	119	169	168	218	217
10	42.4	42.2	68.4	68.2	118	117	167	167	216	216
20	33.7	33.6	59.2	59.2	109	109	158	158	208	208
30	30.8	30.8	56.1	56.1	106	106	156	156	205	205
30	29.3	29.3	54.6	54.6	104	104	154	154	204	204
50	28.5	28.5	53.7	53.7	104	104	153	153	203	203
60	27.9	27.9	53.1	53.1	103	103	153	153	203	203
70	27.5	27.5	52.6	52.6	103	103	152	152	202	202
80	27.2	27.2	52.3	52.3	102	102	152	152	202	202
90	26.9	26.9	52.0	52.0	102	102	152	152	202	202
100	26.7	26.7	51.8	51.8	102	102	152	152	202	202

Output DTN: MO0402SPAHWCIG.002.

Source: Calculated in various spreadsheets in (see Appendix E).

Values archived in output DTN: MO0402SPAHWCIG.002.

NOTE: $T_{r=0}$ is the centerline temperature and $T_{r=3}$ is the temperature at the edge of the dike.

8.2.4 Seepage Water Chemistry

Processes accompanying magma intrusion and cooling will clearly influence environmental conditions affecting radionuclide release from Zone 1. These processes include physical damage

and disruption of the drift walls, formation of a contact metamorphic aureole, and the filling of the drift with solid basalt. Based on consideration of the properties of natural analogs of contact metamorphic aureoles, and of the development of fractures in cooling basalt, it was assumed that seepage rate through the basalt-filled Zone 1 drifts would be the same as if no intrusion had occurred. *Abstraction of Drift Seepage* (BSC 2004 [DIRS 169131]) indicates that it is reasonable to use non-degraded drift water inflow as the estimated water flow after an igneous event. Additional conservatism can be added by using the seepage for a collapsed drift. For the aqueous chemistry of the in-drift environment, it is appropriate to use the non-degraded configuration.

The chemistry of the incoming seepage may be affected by basalt water reactions within the drift. The effects of these reactions on a typical crown seepage water have been modeled and the results of the abstraction for feed to TSPA are outlined in Section 6.8.

The values presented in Table 8-3 do not represent an absolute range, but the range of values for the parameters expressed in Section 6.8. If those ranges were slightly modified, it is expected that the pH and ionic strength values may change slightly. Therefore, it is recommended that TSPA sample uniformly between the minimum and maximum values in Table 8-3. These values are contained in output DTN: MO0402SPAHWCIG.002.

Fluoride content of the water in contact with basalt is listed as one of the outputs of this model in *Technical Work Plan for Waste Form Degradation Modeling, Testing, and Analyses in Support of LA* (BSC 2004 [DIRS 167796]). Many EQ6 simulations of basalt/water interactions show no change in fluoride content. Therefore, no abstraction of this parameter was completed on the basis of EQ6 simulations. Fluoride concentrations in basalt aquifers are quite low. Data for 32 waters from basalt aquifers (Hearn et al. 1985 [DIRS 166893]; White et al. 1980 [DIRS 163752]; and Hem 1985 [DIRS 115670]) have a mean F^- content of 0.8 ± 0.8 1σ mg/L. The median value is 0.5 mg/L, reflective of the fact that the mean is skewed on the basis of a few analyses with F^-compositions in the range of a few mg/L.

Starting waters (Bin 8, 11, and J-13 waters) all have F^- contents substantially higher than those found in natural basalt aquifers. Given the incomplete reaction of starting waters with basalt, and accompanying precipitation of fluoride-bearing phases, it is recommended that TSPA adopt fluoride concentrations that vary linearly between starting waters and 0.5 mg/L to represent varying degrees of basalt seepage water interaction.

In some instances, TSPA may need pH and ionic strength values for a range of parameters that are outside the range of validity of this model. These parameters include flux and Log fCO_2. In the case of flux, it was observed in EQ6 calculations (refer to Appendix E; see file *rate comparison.xls*) that after a flux rate of 50 mm/year was obtained, the output water composition was within 0.8 pH units and 1.15E-03 moles/kg of the original pH and ionic strength values (i.e., Time=0 values). For this reason, a flux rate of 50 mm/year is chosen for TSPA as the point were the pH and ionic strength of the water (equilibrated with atmospheric gas levels) flowing into the basalt block equals the pH and the ionic strength of the water leaving the basalt block.

Table 8-3. Look-Up Table of Temporal Maximum and Minimum Values for pH and Ionic Strength for Use in TSPA-LA

Log (fCO_2/bar) = -2				
	pH		**Ionic Strength (moles/kg)**	
Time Period*	**Maximum**	**Minimum**	**Maximum**	**Minimum**
x ≤ 25 years	7.9	7.6	1.87E-02	9.64E-03
25 > x ≤ 250 years	8.1	7.8	3.59E-02	1.23E-02
250 > x ≤ 2500 years	8.1	7.8	4.00E-02	1.22E-02
2500 > x ≤ 20000 years	8.1	7.7	3.58E-02	1.15E-02
Log (fCO_2/bar) = -2.5				
	pH		**Ionic Strength (moles/kg)**	
Time Period*	**Maximum**	**Minimum**	**Maximum**	**Minimum**
x ≤ 25 years	8.4	8.1	2.09E-02	9.23E-03
25 > x ≤ 250 years	8.6	8.3	4.33E-02	1.31E-02
250 > x ≤ 2500 years	8.6	8.3	5.00E-02	1.29E-02
2500 > x ≤ 20000 years	8.6	8.2	4.22E-02	1.18E-02
Log (fCO_2/bar) = -3				
	pH		Ionic Strength (moles/kg)	
Time Period*	**Maximum**	**Minimum**	**Maximum**	**Minimum**
x ≤ 25 years	8.9	8.6	2.43E-02	9.14E-03
25 > x ≤ 250 years	9.0	8.8	5.00E-02	1.40E-02
250 > x ≤ 2500 years	9.1	8.8	5.00E-02	1.37E-02
2500 > x ≤ 20000 years	9.1	8.7	5.00E-02	1.19E-02
Log (fCO_2/bar) = -3.5				
	pH		**Ionic Strength (moles/kg)**	
Time Period*	**Maximum**	**Minimum**	**Maximum**	**Minimum**
x ≤ 25 years	9.4	9.0	3.00E-02	9.44E-03
25 > x ≤ 250 years	9.5	9.2	5.00E-02	1.67E-02
250 > x ≤ 2500 years	9.6	9.2	5.00E-02	1.62E-02
2500 > x ≤ 20000 years	9.5	9.1	5.00E-02	1.30E-02
Log (fCO_2/bar) = -4				
	pH		**Ionic Strength (moles/kg)**	
Time Period*	**Maximum**	**Minimum**	**Maximum**	**Minimum**
x ≤ 25 years	9.7	9.4	3.42E-02	1.02E-02
25 > x ≤ 250 years	9.9	9.6	5.00E-02	1.97E-02
250 > x ≤ 2500 years	9.9	9.6	5.00E-02	1.89E-02
2500 > x ≤ 20000 years	9.9	9.6	5.00E-02	1.43E-02

Output DTN: MO0402SPAHWCIG.002.

NOTES: * Time period represents time after re-establishment of seepage flow.

Values archived in output DTN: MO0402SPAHWCIG.002.

The values from Table 8-3 can be used for flux rates less than 50 mm/year. As shown in *Dissolved Concentration Limits of Radioactive Elements* (BSC 2004 [DIRS 169425]), the two most important parameters affecting the solubility of radioelements include pH and fCO_2. Since pH decreases with increasing flux rate, using the values for flux between 0.4 and 11.7 mm/year for cases where the flux is below 50 mm/year is conservative because the radionuclides will be more soluble at the higher pH values shown in Table 8-3.

8.3 OUTPUT UNCERTAINTY

8.3.1 Gas Flow Calculation

Many uncertainties exist in modeling coupled THC processes (BSC 2004 [DIRS 169856], Section 6.9) because of the large amount of input data needed and the complexity of natural systems. Therefore, a quantitative measure of model uncertainty based on the uncertainties of the data themselves is difficult. The model is well validated to predict trends of spatial and temporal variations in water and gas chemistry owing to thermal effects, gas transport and gas dissolution around emplacement drifts, at temperatures below 200ºC. Therefore, the only region of concern is in the high-temperature region adjacent to the dike, where predominantly gas phase transport is the important process. Because this region is quite narrow, any uncertainties in gas transport velocities would have a relatively minor effect on the transport times for gases to an adjacent drift more than 80 m away.

8.3.2 Heat Flow Calculation

Uncertainties from various sources have been addressed in this model report (Appendices C and D and Section 6.7). These include thermal conductivity, grain density, specific heat capacity, matrix porosity, saturation, lithophysal porosity, and initial temperature. Of these, it was shown that only the initial temperature had any effect. The uncertainty in the temperature is ±3°C for the temperature output.

8.3.3 EQ6 Calculations

Uncertainties from various sources have been addressed in this report (Section 6.8). These include pore fraction, reactive surface area of materials, flow rate of water through the basalt, saturation, composition of oxides that make up the basalt, CO_2 and O_2 fugacity, and type of water flowing through the basalt. The uncertainty in the output for reaction of basalt and seepage waters is summarized in Table 8-3.

8.4 RESTRICTIONS

As discussed in Section 6.8, the pH and ionic strength values developed in this model report for reaction of seepage water and basalt are valid for certain parameter ranges. These are provided in Table 8-4.

Table 8-4. Valid Range of pH and Ionic Strength Reported in This Model Report

Parameter	Value or Range of Values Used
Pore fraction	0.13 through 0.17
Flow rate (flux)	0.4mm/year through 11.7 mm/year
Surface area	All surfaces are available and 10% of all surfaces available
Saturation	0.1 through 1.0
Log f_{CO2}	-2 through –4 bar
Log f_{O2}	-0.7 bar

9. INPUTS AND REFERENCES

9.1 DOCUMENTS CITED

Abramowitz, M. and Stegun, I.A., eds. 1972. *Handbook of Mathematical Functions with Formulas, Graphs, and Mathematical Tables.* New York, New York: Dover Publications. TIC: 240610. 156927

Altman, W.D.; Donnelly, J.P.; and Kennedy, J.E. 1988. *Peer Review for High-Level Nuclear Waste Repositories: Generic Technical Position.* NUREG-1297. Washington, D.C.: U.S. Nuclear Regulatory Commission. TIC: 200651. 103597

Altman, W.D.; Donnelly, J.P.; and Kennedy, J.E. 1988. *Qualification of Existing Data for High-Level Nuclear Waste Repositories: Generic Technical Position.* NUREG-1298. Washington, D.C.: U.S. Nuclear Regulatory Commission. TIC: 200652. 103750

Arehart, G.B.; Christenson, B.W.; Wood, C.P.; Foland, K.A.; and Browne, P.R.L. 2002. "Timing of Volcanic, Plutonic and Geothermal Activity at Ngatamariki, New Zealand." *Journal of Volcanology and Geothermal Research, 116,* ([3-4]), 201-214. [New York, New York]: Elsevier. TIC: 256231. 170390

Babcock & Wilcox. 1963. *Steam, its Generation and Use.* 37th Edition. New York, New York: Babcock & Wilcox. TIC: 256290. 170614

Batchelor, G.K. 1967. *An Introduction to Fluid Dynamics.* Page 594. New York, New York: Cambridge University Press. TIC: 241827. 103289

Bird, R.B.; Stewart, W.E.; and Lightfoot, E.N. 1960. *Transport Phenomena.* New York, New York: John Wiley & Sons. TIC: 208957. 103524

Brady, P.V. and Walther, J.V. 1989. "Controls on Silicate Dissolution Rates in Neutral and Basic pH Solutions at 25°C." *Geochimica et Cosmochimica Acta, 53,* 2823-2830. New York, New York: Pergamon Press. TIC: 235216. 110748

Brantley, S.L. and Chen, Y. 1995. "Chemical Weathering Rates of Pyroxenes and Amphiboles." Chapter 4 of *Chemical Weathering Rates of Silicate Minerals.* White, A.F. and Brantley, S.L., eds. Reviews in Mineralogy Volume 31. Washington, D.C.: Mineralogical Society of America. TIC: 222496. 163275

BSC (Bechtel SAIC Company) 2003. *Risk Information to Support Prioritization of Performance Assessment Models.* TDR-WIS-PA-000009 REV 01 ICN 01 [Errata 001]. Las Vegas, Nevada: Bechtel SAIC Company. ACC: MOL.20021017.0045; DOC.20031014.0003. 168796

BSC (Bechtel SAIC Company) 2004. *Abstraction of Drift Seepage.* MDL-NBS-HS-000019 REV 01. Las Vegas, Nevada: Bechtel SAIC Company. ACC: DOC.20041103.0003. 169131

BSC (Bechtel SAIC Company) 2004. *Atmospheric Dispersal and Deposition of Tephra from a Potential Volcanic Eruption at Yucca Mountain, Nevada.* MDL-MGR-GS-000002 REV 01. Las Vegas, Nevada: Bechtel SAIC Company. ACC: DOC.20041025.0003. 170026

BSC (Bechtel SAIC Company) 2004. *Characterize Eruptive Processes at Yucca Mountain, Nevada.* ANL-MGR-GS-000002 REV 02. Las Vegas, Nevada: Bechtel SAIC Company. ACC: DOC.20041004.0006. 169980

BSC (Bechtel SAIC Company) 2004. *Characterize Framework for Igneous Activity at Yucca Mountain, Nevada.* ANL-MGR-GS-000001 REV 02. Las Vegas, Nevada: Bechtel SAIC Company. ACC: DOC.20041015.0002. 169989

BSC (Bechtel SAIC Company) 2004. *CSNF Waste Form Degradation: Summary Abstraction.* ANL-EBS-MD-000015 REV 02. Las Vegas, Nevada: Bechtel SAIC Company. ACC: DOC.20040908.0001. 169987

BSC (Bechtel SAIC Company) 2004. *D&E / PA/C IED Emplacement Drift Configuration and Environment.* 800-IED-MGR0-00201-000-00B. Las Vegas, Nevada: Bechtel SAIC Company. ACC: ENG.20040326.0001. 168489

BSC (Bechtel SAIC Company) 2004. *D&E / PA/C IED Subsurface Facilities.* 800-IED-WIS0-00101-000-00A. Las Vegas, Nevada: Bechtel SAIC Company. ACC: ENG.20040309.0026. 164519

BSC (Bechtel SAIC Company) 2004. *Dissolved Concentration Limits of Radioactive Elements.* ANL-WIS-MD-000010 REV 03. Las Vegas, Nevada: Bechtel SAIC Company. ACC: DOC.20041109.0006. 169425

BSC (Bechtel SAIC Company) 2004. *Drift Degradation Analysis.* ANL-EBS-MD-000027 REV 03. Las Vegas, Nevada: Bechtel SAIC Company. ACC: DOC.20040915.0010. 166107

BSC (Bechtel SAIC Company) 2004. *Drift-Scale THC Seepage Model.* MDL-NBS-HS-000001 REV 03. Las Vegas, Nevada: Bechtel SAIC Company. ACC: DOC.20041111.0001. 169856

BSC (Bechtel SAIC Company) 2004. *Features, Events, and Processes: Disruptive Events.* ANL-WIS-MD-000005 REV 02. Las Vegas, Nevada: Bechtel SAIC Company. ACC: DOC.20041108.0002. 170017

BSC (Bechtel SAIC Company) 2004. *Geologic Framework Model (GFM2000).* MDL-NBS-GS-000002 REV 02. Las Vegas, Nevada: Bechtel SAIC Company. ACC: DOC.20040827.0008. 170029

BSC (Bechtel SAIC Company) 2004. *Igneous Intrusion Impacts on Waste Packages and Waste Forms.* MDL-EBS-GS-000002 REV 01. Las Vegas, Nevada: Bechtel SAIC Company. ACC: DOC.20040421.0002. 168960

BSC (Bechtel SAIC Company) 2004. *In-Drift Natural Convection and Condensation.* MDL-EBS-MD-000001 REV 00. Las Vegas, Nevada: Bechtel SAIC Company. ACC: DOC.20041025.0006. 164327

BSC (Bechtel SAIC Company) 2004. *Magma Bulkhead Analysis.* 800-K0C-SSP0-00100-000-00A. Las Vegas, Nevada: Bechtel SAIC Company. 171070

BSC (Bechtel SAIC Company) 2004. *Multiscale Thermohydrologic Model.* ANL-EBS-MD-000049 REV 02. Las Vegas, Nevada: Bechtel SAIC Company. ACC: DOC.20041014.0008. 169565

BSC (Bechtel SAIC Company) 2004. *Number of Waste Packages Hit by Igneous Intrusion.* ANL-MGR-GS-000003 REV 01. Las Vegas, Nevada: Bechtel SAIC Company. ACC: DOC.20041015.0001. 170001

BSC (Bechtel SAIC Company) 2004. *Q-List.* 000-30R-MGR0-00500-000-000 REV 00. Las Vegas, Nevada: Bechtel SAIC Company. ACC: ENG.20040721.0007. 168361

BSC (Bechtel SAIC Company) 2004. *Seismic Consequence Abstraction.* MDL-WIS-PA-000003 REV 01. Las Vegas, Nevada: Bechtel SAIC Company. ACC: DOC.20041025.0004. 169183

BSC (Bechtel SAIC Company) 2004. *Technical Work Plan for Igneous Activity Assessment for Disruptive Events.* TWP-WIS-MD-000007 REV 06. Las Vegas, Nevada: Bechtel SAIC Company. ACC: DOC.20040820.0001. 171403

BSC (Bechtel SAIC Company) 2004. *Technical Work Plan for Waste Form Degradation Modeling, Testing, and Analyses in Support of LA.* TWP-WIS-MD-000008 REV 02 ICN 04. Las Vegas, Nevada: Bechtel SAIC Company. ACC: DOC.20040218.0001. 167796

BSC (Bechtel SAIC Company) 2004. *Thermal Conductivity of the Potential Repository Horizon.* MDL-NBS-GS-000005 REV 01. Las Vegas, Nevada: Bechtel SAIC Company. ACC: DOC.20040928.0006. 169854

BSC (Bechtel SAIC Company) 2004. *Ventilation Model and Analysis Report.* ANL-EBS-MD-000030 REV 04. Las Vegas, Nevada: Bechtel SAIC Company. ACC: DOC.20041025.0002. 169862

BSC (Bechtel SAIC Company) 2004. *Waste Form and In-Drift Colloids-Associated Radionuclide Concentrations: Abstraction and Summary.* MDL-EBS-PA-000004 REV 01. Las Vegas, Nevada: Bechtel SAIC Company. ACC: DOC.20041028.0007. 170025

Canori, G.F. and Leitner, M.M. 2003. *Project Requirements Document.* TER-MGR-MD-000001 REV 02. Las Vegas, Nevada: Bechtel SAIC Company. ACC: DOC.20031222.0006. 166275

Carnahan, B.; Luther, H.A.; and Wilkes, J.O. 1990. *Applied Numerical Methods.* Malabar, Florida: Krieger Publishing. TIC: 224042. 163096

Carslaw, H.S. and Jaeger, J.C. 1959. *Conduction of Heat in Solids.* 2nd Edition. Oxford, Great Britain: Oxford University Press. TIC: 206085. 100968

Chapman, A.J. 1974. *Heat Transfer.* 3rd Edition. New York, New York: Macmillan Publishing. TIC: 245061. 152938

Chou, L. and Wollast, R. 1985. "Steady-State Kinetics and Dissolution Mechanisms of Albite." *American Journal of Science, 285,* 963-993. [New Haven, Connecticut: Yale University, Kline Geology Laboratory]. TIC: 223169. 160182

Crouch, S.L. and Starfield, A.M. 1983. *Boundary Element Methods in Solid Mechanics, with Applications in Rock Mechanics and Geological Engineering.* Boston, Massachusetts: Allen & Unwin. TIC: 4370. 139600

Crowe, B.M.; Wohletz, K.H.; Vaniman, D.T.; Gladney, E.; and Bower, N. 1986. *Status of Volcanic Hazard Studies for the Nevada Nuclear Waste Storage Investigations.* LA-9325-MS. Volume II. Los Alamos, New Mexico: Los Alamos National Laboratory. ACC: NNA.19890501.0157. 101532

CRWMS M&O 1996. *Probabilistic Volcanic Hazard Analysis for Yucca Mountain, Nevada.* BA0000000-01717-2200-00082 REV 0. Las Vegas, Nevada: CRWMS M&O. ACC: MOL.19971201.0221. 100116

CRWMS M&O 1999. *Waste Package Behavior in Magma.* CAL-EBS-ME-000002 REV 00. Las Vegas, Nevada: CRWMS M&O. ACC: MOL.19991022.0201. 121300

CRWMS M&O 2000. *Dike Propagation Near Drifts.* ANL-WIS-MD-000015 REV 00 ICN 1. Las Vegas, Nevada: CRWMS M&O. ACC: MOL.20001213.0061. 151552

CRWMS M&O 2001. *Pure Phase Solubility Limits - LANL.* ANL-EBS-MD-000017 REV 00 ICN 01. Las Vegas, Nevada: CRWMS M&O. ACC: MOL.20010126.0005. 154629

Delaney, P.T. 1987. "Heat Transfer During Emplacement and Cooling of Mafic Dykes." *Mafic Dyke Swarms, A Collection of Papers Based on the Proceedings of an International Conference held at Erindale College, University of Toronto, Ontario, Canada, June 4 to 7, 1985.* Halls, H.C. and Fahrig, W.F., eds. Special Paper 34. Pages 31-46. St. John's, Newfoundland, Canada: Geological Association of Canada. TIC: 225006. 102776

Detournay, E.; Mastin, L.G.; Pearson, J.R.A.; Rubin, A.M.; and Spera, F.J. 2003. *Final Report of the Igneous Consequences Peer Review Panel, with Appendices.* Las Vegas, Nevada: Bechtel SAIC Company. ACC: MOL.20031014.0097; MOL.20030730.0163. 169660

Dobson, P.F.; Kneafsey, T.J.; Sonnenthal, E.L.; Spycher, N.; and Apps, J.A. 2003. "Experimental and Numerical Simulation of Dissolution and Precipitation: Implications for Fracture Sealing at Yucca Mountain, Nevada." *Journal of Contaminant Hydrology, 62-63,* 459-476. New York, New York: Elsevier. TIC: 254205. 165949

Dobson, P.F.; Salah, S.; Spycher, N.; and Sonnenthal, E. 2003. "Simulation of Water-Rock Interaction in the Yellowstone Geothermal System Using TOUGHREACT." *TOUGH Symposium 2003, Proceedings, Revision 2.0, Berkeley, California, May 12-14, 2003.* Berkeley, California: Lawrence Berkeley National Laboratory. TIC: 255880. 168273

DOE (U.S. Department of Energy) 1982. *Site Characterization Report for the Basalt Waste Isolation Project.* DOE/RL 82-3. Three volumes. Washington, D.C.: U.S. Department of Energy. ACC: MOL.20040120.0079. 166892

Douglass, D.L. 1983. "The Corrosion of Ferritic Stainless Steels and High-Purity Fe–Cr Alloys in Basaltic Lava and Simulated Magmatic Gas." *Oxidation of Metals, 20,* (3/4), 161-183. New York, New York: Plenum Press. TIC: 238278. 166999

Eggler, D.H. 1972. "Water-Saturated and Undersaturated Melting Relations in a Parícutin Andesite and an Estimate of Water Content in the Natural Magma." *Contributions to Mineralogy and Petrology, 34,* 261–271. [Berlin, Germany]: Springer-Verlag. TIC: 254481. 163623

Ehrlich, S.A. and Douglass, D.L. 1982. *The Effect of Molybdenum Plus Chromium on the Corrosion of Iron-, Nickel, and Cobalt-Base Alloys in Basaltic Lava and Simulated Magmatic Gas at 1150°C.* SAND82-7055. Albuquerque, New Mexico: Sandia National Laboratories. ACC: MOL.19981028.0003. 101097

Einziger, R.E. 1991. "Effects of an Oxidizing Atmosphere in a Spent Fuel Packaging Facility." *Proceedings of the Topical Meeting on Nuclear Waste Packaging, FOCUS '91, September 29–October 2, 1991, Las Vegas, Nevada.* Pages 88-99. La Grange Park, Illinois: American Nuclear Society. TIC: 231173. 166177

EPRI (Electric Power Research Institute) 2004. *Potential Igneous Processes Relevant to the Yucca Mountain Repository: Extrusive-Release Scenario.* EPRI TR-1008169. Palo Alto, California: Electric Power Research Institute. TIC: 256654. 171915

Frankel, J.J. 1967. "Forms and Structures of Intrusive Basaltic Rocks." *Basalts, the Poldervaart Treatise on Rocks of Basaltic Composition.* Volume 1. Hess, H.H. and Poldervaart, A., eds. Pages 63-102. New York, New York: Interscience Publishers. TIC: 254505. 168717

Freundt, A. 1998. "The Formation of High-Grade Ignimbrites, 1: Experiments on High- and Low-Concentration Transport Systems Containing Sticky Particles." *Bulletin of Volcanology, 59,* (6), 414-435. New York, New York: Springer-Verlag. TIC: 256522. 171642

Gaffney, E.S. 2003. Magma and Gas Flow Analysis. Scientific Notebook SN-LANL-SCI-279-V1. ACC: MOL.20031009.0141. 163631

Geertsma, J. and de Klerk, F. 1969. "A Rapid Method of Predicting Width and Extent of Hydraulically Induced Fractures." *Journal of Petroleum Technology, [21],* ([12]), 1571–1581. [Dallas, Texas: American Institute of Mining and Metallurgical Engineers]. TIC: 254512. 163624

Gislason, S.R. and Eugster, H.P. 1987. "Meteoric Water-Basalt Interactions. I: A Laboratory Study." *Geochimica et Cosmochimica Acta, 51,* ([10]), 2827-2840. [New York, New York]: Pergamon. TIC: 235295. 168716

Gordon, B.M. 2003. *Literature Review of Waste Package and Drip Shield Materials' Corrosion Performance in Magmatic-Type Environments.* SIR-02-168, Rev. 0. San Jose, California: Structural Integrity Associates. ACC: MOL.20030414.0260. 163357

Griffiths, R.W. 2000. "The Dynamics of Lava Flows." *Annual Review of Fluid Mechanics, 32,* 477–518. [Palo Alto, California]: Annual Reviews. TIC: 254466. 163625

Hahn, G.J. and Shapiro, S.S. 1967. *Statistical Models in Engineering.* New York, New York: John Wiley & Sons. TIC: 247729. 146529

Haskin, F.E.; Camp, A.L.; Hodge, S.A.; and Powers, D.A. 2002. *Perspectives on Reactor Safety.* NUREG/CR-6042, Rev. 2. Washington, D.C.: U.S. Nuclear Regulatory Commission. ACC: MOL.20040910.0330. 171570

Hearn, P.P.; Steinkampf, W.C.; Bortleson, G.C.; and Drost, B.W. 1985. *Geochemical Controls on Dissolved Sodium in Basalt Aquifers of the Columbia Plateau, Washington.* Water-Resources Investigations Report 84-4304. Tacoma, Washington: U.S. Geological Survey. TIC: 230835. 166893

Heiken, G.; Wohletz, K.; and Eichelberger, J. 1988. "Fracture Fillings and Intrusive Pyroclasts, Inyo Domes, California." *Journal of Geophysical Research, 93,* (B5), 4335-4350. Washington, D.C.: American Geophysical Union. TIC: 252109. 165566

Heizler, M.T.; Perry, F.V.; Crowe, B.M.; Peters, L.; and Appelt, R. 1999. "The Age of Lathrop Wells Volcanic Center: An^{40} $Ar/^{39}Ar$ Dating Investigation." *Journal of Geophysical Research, 104,* (B1), 767-804. Washington, D.C.: American Geophysical Union. TIC: 243399. 107255

Hem, J.D. 1985. *Study and Interpretation of the Chemical Characteristics of Natural Water.* 3rd Edition. Geological Survey Water-Supply Paper 2254. Washington, D.C.: U.S. Government Printing Office. ACC: NNA.19940427.0181. 115670

Henderson, F.M. 1966. *Open Channel Flow.* Upper Saddle River, New Jersey: Prentice Hall. TIC: 254509. 164124

Hillner, E.; Franklin, D.G.; and Smee, J.D. 1998. *The Corrosion of Zircaloy-Clad Fuel Assemblies in a Geologic Repository Environment.* WAPD-T-3173. West Mifflin, Pennsylvania: Bettis Atomic Power Laboratory. TIC: 237127. 100455

Hills, D.A.; Kelly, P.A.; Dai, D.N.; and Korsunsky, A.M. 1996. *Solution of Crack Problems, The Distributed Dislocation Technique.* Solid Mechanics and its Applications Volume 44. Boston, Massachusetts: Kluwer Academic. TIC: 254533. 163626

Hofmann, P. and Kerwin-Peck, D. 1984. "UO_2/Zircaloy-4 Chemical Interactions from 1000 to 1700°C Under Isothermal and Transient Temperature Conditions." *Journal of Nuclear Materials, 124,* 80-105. [New York, New York]: North-Holland. TIC: 253983. 164038

Howard, G.C. and Fast, C.R. 1958. "Optimum Fluid Characteristics for Fracture Extension." *Drilling and Production Practice.* Pages 261-270. Washington, D.C.: American Petroleum Institute. TIC: 254514. 163628

Incropera, F.P. and DeWitt, D.P. 2002. *Fundamentals of Heat and Mass Transfer.* 5th Edition. [New York, New York]: John Wiley & Sons. TIC: 254280. 163337

Itasca Consulting Group. [2002]. *Itasca Software–Cutting Edge Tools for Computational Mechanics.* Minneapolis, Minnesota: Itasca Consulting Group. TIC: 252592. 160331

Jaeger, J.C. 1968. "Cooling and Solidification of Igneous Rocks." *Basalts, The Poldervaart Treatise on Rocks of Basaltic Composition.* Volume 2. Hess, H.H. and Poldervaart, A., eds. Pages 503–536. New York, New York: Interscience Publishers. TIC: 254505. 163630

Jaeger, J.C. and Cook, N.G.W. 1979. *Fundamentals of Rock Mechanics.* 3rd Edition. New York, New York: Chapman and Hall. TIC: 218325. 106219

Klein, C. and Hurlbut, C.S., Jr. 1999. *Manual of Mineralogy.* 21st Edition, Revised. New York, New York: John Wiley & Sons. TIC: 246258. 124293

Kotra, J.P.; Lee, M.P.; Eisenberg, N.A.; and DeWispelare, A.R. 1996. *Branch Technical Position on the Use of Expert Elicitation in the High-Level Radioactive Waste Program.* NUREG-1563. Washington, D.C.: U.S. Nuclear Regulatory Commission. TIC: 226832. 100909

Lasaga, A.C. 1998. *Kinetic Theory in the Earth Sciences.* Princeton, New Jersey: Princeton University Press. TIC: 246279. 117091

Li, G.; Peacor, D.R.; Coombs, D.S.; and Kawachi, Y. 1997. "Solid Solution in the Celadonite Family: The New Minerals Ferroceladonite, $K_2Fe^2{}_2+Fe^3{}_2+Si_8O_{20}(OH)_4$, and Ferroaluminoceladonite, $K_2Fe^2{}_2+Al_2Si_8O_{20}(OH)_4$." *American Mineralogist, 82,* (5-6), 503-511. Washington, D.C.: Mineralogical Society of America. TIC: 252472. 159034

Li, J.; Lowenstein, T.K.; and Blackburn, I.R. 1997. "Responses of Evaporite Mineralogy to Inflow Water Sources and Climate During the Past 100 k.y. in Death Valley, California." *Geological Society of America Bulletin, 109,* (10), 1361-1371. Boulder, Colorado: Geological Society of America. TIC: 247723. 148201

Lichtner, P.C.; Keating, G.; and Carey, B. 1999. *A Natural Analogue for Thermal-Hydrological-Chemical Coupled Processes at the Proposed Nuclear Waste Repository at Yucca Mountain, Nevada.* LA-13610-MS. Los Alamos, New Mexico: Los Alamos National Laboratory. TIC: 246032. 121006

Lide, D.R., ed. 1993. *CRC Handbook of Chemistry and Physics.* 74th Edition. Boca Raton, Florida: CRC Press. TIC: 209252. 123032

Lide, D.R., ed. 2002. *CRC Handbook of Chemistry and Physics.* 83rd Edition. Boca Raton, Florida: CRC Press. TIC: 253582. 160832

Lister, J.R. 1990. "Buoyancy-Driven Fluid Fracture: Similarity Solutions for the Horizontal and Vertical Propagation of Fluid-Filled Cracks." *Journal of Fluid Mechanics, 217,* 213-239. Cambridge, United Kingdom: Cambridge University Press. TIC: 225065. 126865

Lister, J.R. 1990. "Buoyancy-Driven Fluid Fracture: The Effects of Material Toughness and of Low-Viscosity Precursors." *Journal of Fluid Mechanics, 210,* 263-280. Cambridge, United Kingdom: Cambridge University Press. TIC: 246674. 126877

Lister, J.R. 1995. "Fluid-Mechanical Models of the Interaction Between Solidification and Flow in Dykes." *Physics and Chemistry of Dykes, Selected Papers Presented at the Third International Dyke Conference, Jerusalem, Israel, 4-8 September 1995.* Baer, G. and Heimann, A., eds. Pages 115-124. Brookfield, Vermont: A.A. Balkema. TIC: 254504. 163635

Lister, J.R. and Kerr, R.C. 1991. "Fluid-Mechanical Models of Crack Propagation and Their Application to Magma Transport in Dykes." *Journal of Geophysical Research, 96,* (B6), 10,049-10,077. Washington, D.C.: American Geophysical Union. TIC: 225066. 126889

Luhr, J.F. and Simkin, T., eds. 1993. *Paricutin, The Volcano Born in a Mexican Cornfield.* Phoenix, Arizona: Geoscience Press. TIC: 247017. 144310

MacDonald, G.A. 1967. "Forms and Structures of Extrusive Basaltic Rocks." *Basalts, the Poldervaart Treatise on Rocks of Basaltic Composition.* Volume 1. Hess, H.H. and Poldervaart, A., eds. Pages 1-62. New York, New York: Interscience Publishers. TIC: 254505. 168719

Mastin, L.G. and Pollard, D.D. 1988. "Surface Deformation and Shallow Dike Intrusion Processes at Inyo Craters, Long Valley, California." *Journal of Geophysical Research, 93,* (B11), 13,221-13,235. [Washington, D.C.]: American Geophysical Union. TIC: 256132. 169783

McBirney, A.R. 1993. *Igneous Petrology.* 2nd Edition. Boston, Massachusetts: Jones and Bartlett Publishers. TIC: 254279. 163334

McLing, T.L.; Smith, R.W.; and Johnson, T.M. 2001. "Chemical Characteristics of Thermal Water Beneath the Eastern Snake River Plain." *Eastern Snake River Plain.* Link, P.K. and Mink, L.L., eds. Special Paper 353. Pages 205-211. Boulder, Colorado: Geological Society of America. TIC: 256229. 170322

Nordgren, R.P. 1972. "Propagation of a Vertical Hydraulic Fracture." *Society of Petroleum Engineers Journal, 12,* (4), 306–314. Dallas, Texas: Society of Petroleum Engineers. TIC: 254486. 163641

NRC (U.S. Nuclear Regulatory Commission) 2003. *Yucca Mountain Review Plan, Final Report.* NUREG-1804, Rev. 2. Washington, D.C.: U.S. Nuclear Regulatory Commission, Office of Nuclear Material Safety and Safeguards. TIC: 254568. 163274

Olsson, W.A. and Brown, S.R. 1997. *Mechanical Properties of Fractures from Drillholes UE25-NRG-4, USW-NRG-6, USW-NRG-7, USW-SD-9 at Yucca Mountain, Nevada.* SAND95-1736. Albuquerque, New Mexico: Sandia National Laboratories. ACC: MOL.19970224.0064. 106453

Parrington, J.R.; Knox, H.D.; Breneman, S.L.; Baum, E.M.; and Feiner, F. 1996. *Nuclides and Isotopes, Chart of the Nuclides.* 15th Edition. San Jose, California: General Electric Company and KAPL, Inc. TIC: 233705. 103896

Peck, D.L.; Hamilton, M.S.; and Shaw, H.R. 1977. "Numerical Analysis of Lava Lake Cooling Models: Part II, Application to Alae Lava Lake, Hawaii." *American Journal of Science, 277,* (4), 415-437. New Haven, Connecticut: Yale University. On Order TBV-7004 170318

Perkins, T.K. and Kern, L.R. 1961. "Widths of Hydraulic Fractures." *Transactions of the Society of Petroleum Engineers of the American Institute of Mining, Metallurgical, and Petroleum Engineers, Inc., 222,* 937-949. Dallas, Texas: American Institute of Mining and Metallurgical Engineers. TIC: 254487. 163644

Perry, F.V. and Straub. K.T. 1996. *Geochemistry of the Lathrop Wells Volcanic Center.* LA-13113-MS. Los Alamos, New Mexico: Los Alamos National Laboratory. ACC: MOL.19961015.0079. 106490

Pulvirenti, A.L.; Needham, K.M.; Adel-Hadadi, M.A.; Barkatt, A.; Marks, C.R.; and Gorman, J.A. 2004. "Multi-Phase Corrosion of Engineered Barrier Materials." *Corrosion/2004, 59th Annual Conference & Exposition, March 28-April 1, 2004, New Orleans.* Paper No. 04694. Houston, Texas: NACE International. TIC: 255943. 169631

Rice, J.R. 1968. "Mathematical Analysis in the Mechanics of Fracture." Chapter 3 of *Fracture, An Advanced Treatise.* Volume II: Mathematical Fundamentals. Liebowitz, H., ed. New York, New York: Academic Press. TIC: 254573. 164405

Roberts, W.L.; Campbell, T.J.; and Rapp, G.R., Jr. 1990. *Encyclopedia of Minerals.* 2nd Edition. New York, New York: Van Nostrand Reinhold. TIC: 242976. 107105

Rubin, A.M. 1995. "Propagation of Magma-Filled Cracks." *Annual Review of Earth and Planetary Sciences, 23,* 287-336. [Palo Alto, California]: Annual Reviews. TIC: 254554. 164118

Rubin, A.M. and Gillard, D. 1998. "Dike-Induced Earthquakes: Theoretical Considerations." *Journal of Geophysical Research, 103,* (B5), 10,017-10,030. [Washington, D.C.]: American Geophysical Union. TIC: 256130. 169786

Rubin, A.M.; Gillard, D.; and Got, J-L. 1998. "A Reinterpretation of Seismicity Associated with the January 1983 Dike Intrusion at Kilauea Volcano, Hawaii." *Journal of Geophysical Research, 103,* (B5), 10,003-10,015. [Washington, D.C.]: American Geophysical Union. TIC: 256131. 169787

Ryan, M.P. 1987. "Neutral Buoyancy and the Mechanical Evolution of Magmatic Systems." *Magmatic Processes: Physicochemical Principles.* Mysen, B.O., ed. Pages 259-287. Dordrecht, The Netherlands: Kluwer. On Order TBV-7005 170320

Shaw, H.R.; Hamilton, M.S.; and Peck, D.L. 1977. "Numerical Analysis of Lava Lake Cooling Models: Part I, Description of the Method." *American Journal of Science, 277,* (4), 384-414. New Haven, Connecticut: Yale University. On Order TBV-7006 170321

Smith, R.P.; Jackson, S.M.; and Hackett, W.R. 1996. "Paleoseismology and Seismic Hazards Evaluations in Extensional Volcanic Terrains." *Journal of Geophysical Research, 101,* (B3), 6277-6292. Washington, D.C.: American Geophysical Union. TIC: 238265. 101020

Sneddon, I.N. [1946]. "The Distribution of Stress in the Neighbourhood of a Crack in an Elastic Solid." *[Proceedings of the Royal Society of London, Series A: Mathematical and Physical Sciences, 187],* 229–260. [London, England: Harrison and Son]. TIC: 254550. 163648

Spence, D.A. and Turcotte, D.L. 1985. "Magma-Driven Propagation of Cracks." *Journal of Geophysical Research, 90,* (B1), 575-580. Washington, D.C.: American Geophysical Union. TIC: 225148. 127068

Spence, D.A. and Turcotte, D.L. 1990. "Buoyancy-Driven Magma Fracture: A Mechanism for Ascent Through the Lithosphere and the Emplacement of Diamonds." *Journal of Geophysical Research, 95,* (B4), 5133-5139. Washington, D.C.: American Geophysical Union. TIC: 246860. 127086

Spera, F.J. 2000. "Physical Properties of Magma." *Encyclopedia of Volcanoes.* Sigurdsson, H., ed. Pages 171-190. San Diego, California: Academic Press. TIC: 254454. 164109

Spycher, N.F.; Sonnenthal, E.L.; and Apps, J.A. 2003. "Fluid Flow and Reactive Transport Around Potential Nuclear Waste Emplacement Tunnels at Yucca Mountain, Nevada." *Journal of Contaminant Hydrology, 62-63,* 653-673. New York, New York: Elsevier. TIC: 254205. 162121

Stasiuk, M.V.; Barclay, J.; Carroll, M.R.; Jaupart, C.; Ratté, J.C.; Sparks, R.S.J.; and Tait, S.R. 1996. "Degassing During Magma Ascent in the Mule Creek Vent (USA)." *Bulletin of Volcanology, 58,* ([2-3]), 117-130. [New York, New York]: Springer-Verlag. TIC: 254576. 164459

Stock, J.M.; Healy, J.H.; Hickman, S.H.; and Zoback, M.D. 1985. "Hydraulic Fracturing Stress Measurements at Yucca Mountain, Nevada, and Relationship to the Regional Stress Field." *Journal of Geophysical Research, 90,* (B10), 8691-8706. Washington, D.C.: American Geophysical Union. TIC: 219009. 101027

Todreas, N.E. and Kazimi, M.S. 1990. *Nuclear Systems I, Thermal Hydraulic Fundamentals.* New York, New York: Hemisphere Publishing. TIC: 226511. 107735

Tole, M.P.; Lasaga, A.C.; Pantano, C.; and White, W.B. 1986. "The Kinetics of Dissolution of Nepheline ($NaAlSiO_4$)." *Geochimica et Cosmochimica Acta, 50,* (3), 379-392. New York, New York: Pergamon Press. TIC: 253992. 163289

Turcotte, D.L. and Schubert, G. 1982. *Geodynamics, Applications of Continuum Physics to Geological Problems.* New York, New York: John Wiley & Sons. TIC: 235924. 139651

Turcotte, D.L.; Emerman, S.H.; and Spence, D.A. 1987. "Mechanics of Dyke Injection." *Mafic Dyke Swarms, A Collection of Papers Based on the Proceedings of an International Conference held at Erindale College, University of Toronto, Ontario, Canada, June 4-7, 1985.* Halls, H.C. and Fahrig, W.F., eds. Pages 25-29. St. John's, Newfoundland, Canada: Geological Association of Canada. TIC: 246897. 134364

Valentine, G.A.; Perry, F.V.; and WoldeGabriel, G. 2000. "Field Characteristics of Deposits from Spatter-Rich Pyroclastic Density Currents at Summer Coon Volcano, Colorado." *Journal of Volcanology and Geothermal Research, 104,* (1-4), 187-199. New York, New York: Elsevier. TIC: 256521. 171641

Valsami-Jones, E.; Ragnarsdottir, K.V.; Putnis, A.; Bosbach, D.; Kemp, A.J.; and Cressey, G. 1998. "The Dissolution of Apatite in the Presence of Aqueous Metal Cations at pH 2-7." *Chemical Geology, 151,* ([1-4]), 215-233. [New York, New York]: Elsevier. TIC: 255204. 166412

Vaniman, D.T.; Crowe, B.M.; and Gladney, E.S. 1982. "Petrology and Geochemistry of Hawaiite Lavas from Crater Flat, Nevada." *Contributions to Mineralogy and Petrology, 80,* 341-357. Berlin, Germany: Springer-Verlag. TIC: 201799. 101031

Vergniolle, S. and Jaupart, C. 1986. "Separated Two-Phase Flow and Basaltic Eruptions." *Journal of Geophysical Research, 91,* (B12), 12,842-12,860. Washington, D.C.: American Geophysical Union. TIC: 239308. 115585

Wang, J.S. 2003. "Scientific Notebook Referenced in Model Report, MDL-MGR-GS-000005 REV 00, Dike/Drift Interaction." Memorandum from J.S. Wang (BSC) to File, July 2, 2003, with attachment. ACC: MOL.20030707.0261. 164068

Warpinski, N.R.; Abou-Sayed, I.S.; Moschovidis, Z.; and Parker, C. 1993. *Hydraulic Fracture Model Comparison Study: Complete Results.* GRI-93/0109. Chicago, Illinois: Gas Research Institute. TIC: 254276. 163649

Warpinski, N.R.; Moschovidis, Z.A.; Parker, C.D.; and Abou-Sayed, I.S. 1994. "Comparison Study of Hydraulic Fracturing Models—Test Case: GRI Staged Field Experiment No. 3." *SPE Production & Facilities, 9,* (1), 7–16. Richardson, Texas: SPE Production & Facilities. TIC: 254277. 163657

Weast, R.C. and Astle, M.J., eds. 1981. *CRC Handbook of Chemistry and Physics.* 62nd Edition. Boca Raton, Florida: CRC Press. TIC: 240722. 100833

White, A.F.; Peterson, M.L.; and Hochells, M.F., Jr. 1994. "Electrochemistry and Dissolution Kinetics of Magnetite and Ilmenite." *Geochimica et Cosmochimica Acta, 58,* (8), 1859-1875. Oxford, United Kingdom: Elsevier. TIC: 246373. 131014

White, D.E.; Hem, J.D.; and Waring, G.A. 1980. "Chemical Composition of Subsurface Waters." Chapter F of *Data of Geochemistry.* 6th Edition. Geological Survey Professional Paper 440-F. Washington, D.C.: U.S. Government Printing Office. TIC: 249975. 163752

White, S.P. and Christenson, B.W. 2000. "Modelling the Alteration Halo of Diorite Intrusion." *Proceedings of the World Geothermal Congress 2000, Kyushu - Tohoku, Japan, May 28 - June 10, 2000.* Iglesias, E.; Blackwell, D.; Hunt, T.; Lund, J.; and Tamanyu, S., eds. Pages 3969-3974. [Aukland, New Zealand: International Geothermal Association]. TIC: 256232. 170388

Wilcox, R.E. 1954. "Petrology of the Paricutin Volcano." *Petrology of the Parícutin Volcano Mexico, Geologic Investigations in the Parícutin Area, Mexico.* Geological Survey Bulletin 965-C. Pages 281-353. Washington, D.C: U.S. Government Printing Office. TIC: 254485. 163659

Wogelius, R.A. and Walther, J.V. 1991. "Olivine Dissolution at 25°C: Effects of pH, CO_2, and Organic Acids." *Geochimica et Cosmochimica Acta, 55,* (4), 943-954. New York, New York: Pergamon Press. TIC: 236732. 163290

Wolery, T.J. and Daveler, S.A. 1992. *EQ6, A Computer Program for Reaction Path Modeling of Aqueous Geochemical Systems: Theoretical Manual, User's Guide, and Related Documentation (Version 7.0).* UCRL-MA-110662 PT IV. Livermore, California: Lawrence Livermore National Laboratory. ACC: MOL.19980701.0459. 100097

Woods, A.W.; Sparks, S.; Bokhove, O.; LeJeune, A-M.; Conner, C.B.; and Hill, B.E. 2002. "Modeling Magma-Drift Interaction at the Proposed High-Level Radioactive Waste Repository at Yucca Mountain, Nevada, USA." *Geophysical Research Letters, 29,* (13), 19-1 through 19-4. [Washington, D.C.]: American Geophysical Union. TIC: 254467. 163662

Xu, T.; Sonnenthal, E.; and Bodvarsson, G. 2003. "A Reaction-Transport Model for Calcite Precipitation and Evaluation of Infiltration Fluxes in Unsaturated Fractured Rock." *Journal of Contaminant Hydrology, 64,* ([1-2]), 113-127. New York, New York: Elsevier. TIC: 254008. 162124

Yokoyama, I. and de la Cruz-Reyna, S. 1990. "Precursory Earthquakes of the 1943 Eruption of Paricutin Volcano, Michoacan, Mexico." *Journal of Volcanology and Geothermal Research, 44,* 265-281. Amsterdam, The Netherlands: Elsevier. TIC: 234990. 108740

Zhang, X.; Jeffrey, R.; and Detournay, E. 2002. *NPHF2D, Non-Planar Hydraulic Fracture 2D User's Manual.* Minneapolis, Minnesota: University of Minnesota, Department of Civil Engineering. TIC: 253445. 164368

9.2 CODES, STANDARDS, REGULATIONS, AND PROCEDURES

10 CFR 63. Energy: Disposal of High-Level Radioactive Wastes in a Geologic Repository at Yucca Mountain, Nevada. Readily available. 156605

AP-2.22Q, Rev. 1 ICN 1, *Classification Analyses And Maintenance Of The Q-List*. Washington, D.C.: U.S. Department of Energy, Office of Civilian Radioactive Waste Management. ACC: DOC.20040714.0002.

AP-SIII.2Q, Rev. 1 ICN 2, *Qualification of Unqualified Data*. Washington, D.C.: U.S. Department of Energy, Office of Civilian Radioactive Waste Management. ACC: DOC.20040127.0008.

AP-SIII.10Q, Rev. 2 ICN 7, *Models*. Washington, D.C.: U.S. Department of Energy, Office of Civilian Radioactive Waste Management. ACC: DOC.20040920.0002.

LP-S1.11Q, Rev. 0 ICN 1, *Software Management*. Washington, D.C.: U.S. Department of Energy, Office of Civilian Radioactive Waste Management. ACC: DOC.20041005.0008.

9.3 SOFTWARE

BSC (Bechtel SAIC Company) 2001. *Software Code: ASPRIN.* V1.0. 10487-1.0-00. 155712

BSC (Bechtel SAIC Company) 2002. *Software Code: NPHF2D.* V 1.0. PC, Windows 2000. 10904-1.0-00. 163665

BSC (Bechtel SAIC Company) 2002. *Software Code: UDEC.* V3.1. PC WINDOWS 2000/NT 4.0. 10173-3.1-00. 161949

BSC (Bechtel SAIC Company) 2002. *Software Code: FLAC3D.* V2.1. PC WINDOWS 2000/NT 4.0. 10502-2.1-00. 161947

BSC (Bechtel SAIC Company) 2003. *Software Code: EQ3/6.* V8.0. PC w/ Windows 95/98/2000/NT 4.0. 10813-8.0-00. 162228

BSC (Bechtel SAIC Company) 2004. *Software Code: FLAC3D.* V2.14. PC, WINDOWS 2000. 10502-2.14-00. 172323

BSC (Bechtel SAIC Company) 2004. *Software Code: UDEC.* V3.14. PC, WINDOWS 2000. 10173-3.14-00. 172322

CRWMS M&O 1999. *Software Code: EQ3/6.* V7.2b. UCRL-MA-110662 (LSCR198). 153964

CRWMS M&O 1999. *Software Code: EQ6, Version 7.2bLV.* V7.2bLV. 10075-7.2bLV-00. 127275

LBNL (Lawrence Berkeley National Laboratory) 2002. *Software Code: TOUGHREACT.* V3.0. DEC ALPHA/OSF1 V5.1, DEC ALPHA/OSF1 V5.0, Sun UltraSparc/Sun OS 5.5.1, PC/Linux Redhat 7.2. 10396-3.0-00. 161256

9.4 SOURCE DATA, LISTED BY DATA TRACKING NUMBER

LA0307EG831811.001. Analytical Calculations of Heat Flow for YMP Drift Filled with Basaltic Magma. Submittal date: 07/24/2003. 166942

LA0407DK831811.001. Physical Parameters of Basaltic Magma and Eruption Phenomena. Submittal date: 07/15/2004. 170768

LB0207REVUZPRP.002. Matrix Properties for UZ Model Layers Developed from Field and Laboratory Data. Submittal date: 07/15/2002. 159672

LB0210THRMLPRP.001. Thermal Properties of UZ Model Layers: Data Summary. Submittal date: 10/25/2002. 160799

LB0302DSCPTHCS.001. Drift-Scale Coupled Processes (THC Seepage) Model: Simulations. Submittal date: 02/11/2003. 164744

LB0310AMRU0120.001. Supporting Calculations and Analysis for Seepage Abstraction and Summary of Abstraction Results. Submittal date: 10/23/2003. 166409

LB0402THRMLPRP.001. Thermal Properties of UZ Model Layers: Data Summary. Submittal date: 02/20/2004. 168481

SN0307T0510902.003. Updated Heat Capacity of Yucca Mountain Stratigraphic Units. Submittal date: 07/15/2003. 164196

SNF37100195002.001. Hydraulic Fracturing Stress Measurements in Test Hole: ESF-AOD-HDFR1, Thermal Test Facility, Exploratory Studies Facility at Yucca Mountain. Submittal date: 12/18/1996. 131356

SNL02030193001.027. Summary of Bulk Property Measurements Including Saturated Bulk Density for NRG-2, NRG-2A, NRG-2B, NRG-3, NRG-4, NRG-5, NRG-6, NRG-7/7A, SD-9, and SD12. Submittal date: 08/14/1996. 108410

9.5 DEVELOPED DATA, LISTED BY DATA TRACKING NUMBER

LA0408DA831811.001. Estimates Of Magma Flow From Dike Into Drifts. Submittal date: 08/26/2004.

LB0306AMRT0020.001. Volcanic Gas Transport Simulations. Submittal date: 06/12/2003.

LB0408AMRT0020.001. Post-Intrusion Model/Gas Flow Gas Migration & Water Chemistry. Submittal date: 8/25/2004.

LB0408AMRT0020.002. Post-Intrusion Model/Gas Flow Gas Migration & Water Chemistry. Submittal date: 8/25/2004.

LB0408AMRT0020.003. Post-Intrusion Model/Gas Flow Validation. Submittal date: 9/1/2004.

LB0408AMRT0020.004. Post-Intrusion Model/Gas Flow Validation. Submittal date: 9/1/2004.

MO0402SPAHWCIG.002. Heat And Water Chemistry Output From Igneous Intrusion. Submittal date: 02/23/2004.

MO0408EG831811.001. Pressure Histories Used To Drive Simulations Of Hydrovolcanic Dike Injection. Submittal date: 8/24/2004.

MO0408EG831811.002. Expanding Magma. Submittal date: 9/7/2004.

MO0408EG831811.003. Dike Propagation Model Results Using NPHF2D. Submittal date: 9/29/2004.

MO0408EG831811.004. Dike Propagation Model Results Using NPHF2D. Submittal date: 9/13/2004.

MO0408EG831811.008. Magma Cooling and Solidification. Submittal date: 9/13/2004.

INTENTIONALLY LEFT BLANK

APPENDICES FOR

DIKE/DRIFT INTERACTIONS

APPENDIX A NUREG-1804 ACCEPTANCE CRITERIA ASSOCIATED WITH IGNEOUS ACTIVITY A-1
A1. INTEGRATED SUBISSUES MECHANICAL DISRUPTION OF ENGINEERED BARRIERS A-1
A1.1 Acceptance Criterion 1: System Description and Model Integration Are Adequate A-1
A1.2 Acceptance Criterion 2: Data Are Sufficient for Model Justification A-4
A1.3 Acceptance Criterion 3: Data Uncertainty is Characterized and Propagated Through the Model Abstraction A-7
A1.4 Acceptance Criterion 4: Model Uncertainty is Characterized and Propagated Through the Model Abstraction A-10
A1.5 Acceptance Criterion 5: Model Abstraction Output is Supported by Objective Comparisons A-12
A2. VOLCANIC DISRUPTION OF WASTE PACKAGES A-14
A2.1 Acceptance Criterion 1: System Description and Model Integration are Adequate A-14
A3. AIRBORNE TRANSPORT OF RADIONUCLIDES A-15

APPENDIX B EQ6 MINERAL DISSOLUTION RATES B-1

APPENDIX C VERIFICATION OF HEAT CONDUCTION MODEL SIMULATION CALCULATIONS C-1
C1. HEAT FLOW MODEL C-1
C2. HEAT FLOW MODEL UNCERTAINTY ANALYSIS OF PEAK TEMPERATURE IN THE ROCK MASS AT A DISTANCE OF 10 M C-5

APPENDIX D ALTERNATIVE ANALYTICAL SOLUTION TO HEAT FLOW D-1
D1. DEFINITION OF THE PROBLEM D-1
D2. MATERIAL PROPERTY INPUTS D-7
D3. DERIVATION OF EQUATIONS D-8
D4. THERMAL PROPERTY CONTRASTS AND LATENT HEAT D-11
D5. WHOLE-TIME SOLUTIONS D-15
D6. CONCLUSIONS D-16

APPENDIX E INFORMATION REGARDING INPUT/OUTPUT FILES AND SPREADSHEET FILES E-1

APPENDIX F INDEPENDENT TECHNICAL REVIEW OF DIKE PROPAGATION SUBMODEL F-1

APPENDIX G QUALIFICATION OF EXTERNAL SOURCES G-1
G1. BRADY AND WALTHER 1989 ..... G-1
G2. BRANTLEY AND CHEN 1995 ..... G-2
G3. CHOU AND WOLLAST 1985 ..... G-3
G4. TOLE, LASAGA, PANTANO, AND WHITE 1986 ..... G-4

G5. VALSAMI-JONES, RAGNARSDOTTIR, PUTNIS, BOSBACH, KEMP, AND CRESSEY 1998 ..... G-4
G6. WHITE, PETERSON, AND HOCHELLS 1994 ..... G-5
G7. WOGELIUS AND WALTHER 1991 ..... G-6
G8. LASAGA 1998 ..... G-7
G9. WHITE, D.E.; HEM, J.D.; AND WARING, G.A. 1980; HEARN, P.P.; STEINKAMPF, W.C.; BORTLESON, G.C.; AND DROST, B.W. 1985; HEM, J.D. 1985 ..... G-7
G10. HEIKEN, G.; WOHLETZ, K.; AND EICHELBERGER, J. 1988 ..... G-9

APPENDIX H VALIDATION CALCULATIONS H-1
H1. INITIAL SOLUTION H-1
H1.1 Recipe H-1
H1.2 Concentration of aqueous species: H-1
H1.3 Solution density H-2
H1.4 Conversion of concentration unit from moles/L of solution into moles/kg of water H-2
H1.5 Estimate of pH of the solution H-3

FIGURES

Page

B-1. EQ6 Dissolution Rate of Albite (also used for Sanidine) B-1
B-2. EQ6 Dissolution Rate of Anorthite B-2
B-3. EQ6 Dissolution Rate of Nepheline B-2
B-4. EQ6 Dissolution Rate of Olivine (Used for Forsterite and Fayalite) B-3
B-5. EQ6 Dissolution Rate of Hydroxylapatite B-4
B-6. EQ6 Dissolution Rate of Diopside (Used for Hedenbergite) B-5
B-7. EQ6 Dissolution Rate of Enstatite B-6
B-8. EQ6 Dissolution Rate of Magnetite B-6
B-9. EQ6 Dissolution Rate of Ilmenite B-7
B-10. Comparison of Rates Used in EQ6 Calculations B-7

C-1. Peak Temperatures for Variations in Key Inputs C-7

D-1. Plot of Calculated Temperature Profiles for Various Cooling Times Comparing Results for a 1-D Slab-Like Geometry (upper plot) With Results for a 2D Cylindrical Drift Geometry (lower plot) D-2
D-2. Plot of Calculated Whole-Time Temperature Profiles for Various Cooling Times Assuming a Cylindrical Drift Geometry and Showing the Approximate Effect of Latent Heat D-3
D-3. Plot of Calculated Temperature Profiles for Various Cooling Times with Latency Modeled as Occurring at a Specific Temperature (Ts = Tm) D-3
D-4. Plot of Calculated Temperature Profiles for Various Cooling Times With Latent Heat, Calculated for T_s = 900°C and for the Cases With (lower panel) and Without (upper panel) Property Contrasts Between Magma and Tuff D-4
D-5. Plot of Calculated Temperature Profiles at 60 and 99 Days Comparing the Whole-Time Solutions with Early-Time Solutions D-5
D-6. Whole-Time Solution Combining the Results for Early-Time Latency (Turcotte and Schubert (1982 [DIRS 139651, pp. 168 to 170]) With Those Late-Time Results Calculated by the Modified Method of Delaney (1987 [DIRS 102776]) D-6

INTENTIONALLY LEFT BLANK

TABLES

Page

B-1. Additional Nepheline Dissolution Rates Shown on Figure B-3 ..... B-3
B-2. Additional Olivine Dissolution Rates Shown on Figure B-4 ..... B-4
B-3. Additional Diopside Dissolution Rates Shown on Figure B-6 ..... B-5

C-1. Summary of Primary Thermal Conductivity Statistics C-4
C-2. Summary of Volumetric Heat Capacity and Thermal Diffusivity Calculations C-5
C-3. Sensitivity of Uncertainty in Input Parameters (with Standard Deviation for Use in Delta Method) C-6

D-1. Thermal Properties of Magma and Tuff D-7

H-1. Recipe H-1
H-2. Solution Concentration in Moles/L and Moles/Kg of Water H-3

INTENTIONALLY LEFT BLANK

APPENDIX A

NUREG-1804 ACCEPTANCE CRITERIA ASSOCIATED WITH IGNEOUS ACTIVITY

APPENDIX A
NUREG-1804 ACCEPTANCE CRITERIA ASSOCIATED WITH IGNEOUS ACTIVITY

Information in this attachment identifies information in the Dike/Drift Interactions model report that addresses the *Yucca Mountain Review Plan, Final Report* acceptance criteria (NRC 2003 [DIRS 163274]) associated with the following integrated subissues:

- Mechanical disruption of engineered barriers (Section 2.2.1.3.2.3)
- Volcanic disruption of waste packages (Section 2.2.1.3.10.3)
- Airborne transport of radionuclides (Section 2.2.1.3.11.3).

This information is required by 10 CFR 63.114 (a) to (c) and (e) to (g) [DIRS 156605].

The following discussion identifies the relevant acceptance criteria associated with each of the integrated subissues and briefly summarizes the information in this report that addresses the acceptance criteria.

A1. INTEGRATED SUBISSUES MECHANICAL DISRUPTION OF ENGINEERED BARRIERS

A1.1 Acceptance Criterion 1: System Description and Model Integration Are Adequate

The objective for modeling dike/drift interactions is described in Section 6 of the model report and includes describing the mechanical, thermal, and chemical environment that would be applied to waste packages should a future volcanic event disrupt the proposed repository.

1. Total System Performance Assessment (TSPA) adequately incorporates important design features, physical phenomena, and couplings, and uses consistent and appropriate assumptions throughout the mechanical disruption of engineered barrier abstraction process.

   Three models and four analyses describe the processes that could occur if an igneous intrusion were to intersect the repository. The first model describes dike propagation from depth (Section 6.3.1), and Section 6.3.3 provides the mathematical description of the model. Assumptions related to the model are described in Section 6.3.2, and uncertainties associated with the model are described in Section 6.3.4. Alternative models of dike propagation are described in Section 6.3.8. Results from exercise of the base-case model are described in Section 6.3.7, and the inputs for the analysis of magma flow into drifts are provided in Section 6.3.6.

   The second model describes heating of neighboring drifts from cooling of the emplaced magma (Section 6.7). The conceptual model for magma cooling and solidification is described in Section 6.7.1, and the results are described in Section 6.7.1.2. Sensitivity to latent heat effects is described in Section 6.7.2.2, and sensitivity to saturation is described in Section 6.7.2.3.

The third model describes seepage water alteration by reaction with intruded basalt in drifts (Section 6.8). The EQ6 modeling of basalt-water interactions is described in Section 6.8.1, and the results are described in Section 6.8.3. Sensitivity cases are described in Section 6.8.2, and modeling uncertainties, including uncertainties associated with EQ6 are described in Section 6.8.4.1. Alternate models for water/basalt interactions are described in Section 6.8.5.

The analyses documented in this report are natural and thermal stresses (Section 6.2), magma flow into drifts at dike/drift intersections (Section 6.4). Alternative models for dike propagation are described in Section 6.3.8. The effects of expanding magma on dike extension to the surface are described in Section 6.3.8.2. Magma flow to the surface along a secondary pathway developed at some distance from the intersection is described in Section 6.5. Gas flow between drifts is described in Section 6.6.

For dike propagation, effects of pressure inside a tip cavity are described in Section 6.3.7.2, and effects of thermally-induced increases in horizontal stress are described in Section 6.3.7.3.

An analysis of fully coupled dike/drift interaction is presented in Section 6.4.6, and an analysis of magma-waste package and magma waste-form interactions in intersected drifts is presented in Section 6.4.8.

Section 6.3.7 provides the results of dike propagation modeling. Section 6.3.8 summarizes the alternative models for dike propagation, and Section 6.4.3 provides the inputs for the analysis of magma flow into drifts. Section 6.5 describes the analysis of secondary dike propagation, and Section 6.5.4 provides the conclusion about secondary dike propagation and the basis to discount the potential for development of the shock wave scenario proposed by Woods et al. 2002 [DIRS 163662]. Sections 6.6.5 and 6.7.1.2 provide the basis to discount the likelihood that waste packages in Zone 2 would be damaged by gas flow and/or thermal flow effects.

Assumptions used to model dike propagation from depth are described in Section 5.1 and implementing assumptions are described in Section 6.3.2. Assumptions related to the magma flow model are described in Section 5.2 and implementing assumptions are described in Section 6.4.7.1.1. Assumptions related to modeling drift scale gas flow are described in Sections 5.3. Results of gas flow modeling for two (2) simulations are described in Section 6.6.5. Assumptions related to the modeling of magma cooling and solidification are described in Section 5.4.

2. The description of geological and engineering aspects of design features, physical phenomena, and couplings that may affect mechanical disruption of engineered barriers, is adequate. For example, the description may include materials used in the construction of engineered barrier components, environmental effects (e.g., temperature, water chemistry, humidity, radiation, etc.) on these materials, and mechanical failure processes and concomitant failure criteria used to assess the performance capabilities of these materials. Conditions and assumptions in the

abstraction of mechanical disruption of engineered barriers are readily identified and consistent with the body of data presented in the description.

Parameters used in the modeling of dike/drift interactions are summarized in Table 4-1. Assumptions related to modeling of dike propagation are described in Sections 5.1 and 6.3.2. Assumptions related to the analysis of magma flow are described in Sections 5.2 and 6.4.7.1.1. Assumptions related to drift scale gas flow analysis are described in Section 5.3, and assumptions related to modeling of magma cooling and solidification are described in Section 5.4.

Results of the modeling of dike propagation through the repository horizon are described in Sections 6.3.7, 6.3.9, and 8.1.1. Results of analysis of magma flow, including flow in drifts and the effects on dike propagation to the surface, are described in Section 6.4.9 and Section 8.1.2. Results of the analysis of gas flow into drifts are provided in Section 6.6.5, and results for modeling of magma cooling and solidification, are described in Sections 6.7.1.2. The modeling of post-intrusion effects is summarized in Section 8.1.3.

3. The abstraction of mechanical disruption of engineered barriers uses assumptions, technical bases, data, and models that are appropriate and consistent with other related U.S. Department of Energy abstractions. For example, assumptions used for mechanical disruption of engineered barriers are consistent with the abstraction of degradation of engineered barriers (Section 2.2.1.3.1 of the Yucca Mountain Review Plan). The descriptions and technical bases provide transparent and traceable support for the abstraction of mechanical disruption of engineered barriers.

   Parameters used in the analysis of dike/drift interactions are summarized in Table 4-1. Modeling activities for dike propagation are summarized in Section 8.1.1; modeling activities for magma flow in drifts are summarized in Section 8.1.2, and modeling of post-intrusion effects are summarized in Section 8.1.3. Model outputs for migration of magmatic gases are summarized in Section 8.2.2. Model outputs for thermal effects are summarized in Section 8.2.3, and model outputs for seepage water chemistry are summarized in Section 8.2.4. Uncertainties associated with the outputs of the gas flow calculation are described in Section 8.3.1. Uncertainties associated with the outputs of heat flow calculation are described in Section 8.3.2, and uncertainties associated with the EQ6 calculations for seepage water chemistry are described in Section 8.3.3. Restrictions on the use of information from the modeling and analyses described in this report are summarized in Section 8.4.

4. Boundary and initial conditions used in the TSPA abstraction of mechanical disruption of engineered barriers are propagated throughout the abstraction approaches.

   Boundary and initial conditions used in the modeling of dike propagation are described in Section 6.3.6. Boundary and initial conditions used in the analysis of magma flow are described in Section 6.4.4, and initial and boundary conditions used in the analysis of gas flow between drifts are described in Section 6.6.4. Propagation of the boundary and initial conditions into the dike propagation model are described in

the mathematical description of the dike propagation model in Section 6.3.3, and the results are described in Section 6.3.7 similar description for the analysis of magma flow in drifts is provided in Section 6.4.4 and 6.4.7.4. Initial and boundary conditions for the analysis of gas flow between drifts are described in Section 6.6.4, and simulation results are described in Section 6.6.5. The problem definition for the modeling of effects of magma cooling is described in Section 6.7.1.2 and results are described in Section 6.7.1.1.1. Inputs for the modeling of the reaction of seepage water with basalt are described in Section 6.8, and results of the simulations are described in Section 6.8.3.

5. Sufficient data and technical bases to assess the degree to which features, events, and processes have been included in this abstraction are provided.

   FEPs that are specifically addressed by information in this model report are identified in Section 6.1 and described in more detail in Table 6-1. The table identifies sections of the report in which disposition of the FEP is described and includes a summary of the Total System Performance Assessment - License Application (TSPA-LA) disposition. Basically, the outputs of the dike/drift interactions model provide descriptions of physical and chemical conditions (Section 8.2) and the uncertainties associated with those outputs (Section 8.3) for application in the TSPA-LA in-drift submodels.

6. The conclusion, with respect to the impact of transient criticality on the integrity of the engineered barriers, is defensible.

   This model report does not address the impact of transient criticality on the integrity of the engineered barriers.

7. Guidance in NUREG-1297 (Altman et al. 1988 [DIRS 103597]) and NUREG-1298 (Altman et al. 1988 [DIRS 103750]) or other acceptable approaches, is followed.

   NUREG-1297 describes the generic technical position with respect to the use of peer reviews on high-level waste repository programs. The use of information from the *Final Report of the Igneous Consequences Peer Review Panel* (Detournay et al. 2003 [DIRS 169660]) is summarized in Section 7.1. NUREG-1298 describes the generic technical position with respect to qualification of existing data. External sources have provided unqualified data that have been used as direct input to this document. The inputs from these sources are qualified for intended use within the document using the criteria found in AP-SIII.9Q, *Scientific Analyses*. These criteria represent a subset of the methods and attributes required for qualification of data per AP-SIII.2Q, *Qualification of Unqualified Data.* These methods and attributes are based on those that are presented in NUREG-1298, which are meant to provide "the level of confidence in the data … commensurate with their intended use.

A1.2 Acceptance Criterion 2: Data Are Sufficient for Model Justification

1. Geological and engineering values used in the license application to evaluate mechanical disruption of engineered barriers, are adequately justified. Adequate

descriptions of how the data were used, and appropriately synthesized into the parameters, are provided.

Inputs for the modeling of dike propagation are described in Section 6.3.5, and the use of the information is described in Section 6.3.3. Model results are described in Section 6.3.7. Inputs for the analysis of effusive flow of magma into drifts are described in Section 6.4.3; the use of the information is described in Section 6.4.2, and results are provided in Section 6.4.5. Magma-waste package interactions are described in Section 6.4.8. Inputs for the analysis of secondary dike propagation are described in Section 6.5.1.1. The analysis examines the potential for development of secondary dikes under effusive flow conditions (Section 6.5.1) and for two-phase flow conditions Section 6.5.2). A synthesis describing the likelihood of the dog-leg scenario for effusive flow is presented in Section 6.5.1.5. Conclusions are presented in Section 6.5.4. Inputs for the analysis of gas flow between drifts are described in Section 6.6.3, and the use of the information is described in the numerical formulation in Section 6.6.2. Results are presented in Section 6.6.5. Inputs and the use of the information for the analysis of the effects of magma cooling and solidification on neighboring drift are described in Section 6.7.1.1, and results of the analysis are provided in Section 6.7.1.2. Inputs for the modeling of the reaction of seepage water with cooled basalt are described in Section 6.8, and results are described in Section 6.8.3.

The outputs of the dike/drift interactions model provide descriptions of physical and chemical conditions associated with migration of magmatic gases, thermal effects, and seepage water chemistry (Section 8.2) and the uncertainties associated with those outputs (Section 8.3) for application in the TSPA-LA in-drift submodels.

2. Sufficient data have been collected on the geology of the natural system, engineering materials, and initial manufacturing defects, to establish initial and boundary conditions for the TSPA abstraction of mechanical disruption of engineered barriers.

   This report describes the models and analysis that support the modeling of dike/drift interactions. The response to the previous criterion identifies the locations in this report where the inputs for the various models and analyses are described. The response also identifies where model results and analysis results are described. Evaluation of the descriptions of formulations of the analyses and models provides the basis to determine the sufficiency of data used as input or to establish boundary and initial conditions.

   The outputs of the dike/drift interactions model provide descriptions of physical and chemical conditions associated with migration of magmatic gases, thermal effects, and seepage water chemistry (Section 8.2) and the uncertainties associated with those outputs (Section 8.3) for application in the TSPA-LA in-drift submodels.

3. Data on geology of the natural system, engineering materials, and initial manufacturing defects used in the TSPA abstraction, are based on appropriate techniques. These techniques may include laboratory experiments, site-specific field measurements, natural analogue research, and process-level modeling studies. As appropriate, sensitivity or uncertainty analyses used to support the U.S. Department of Energy TSPA abstraction are adequate to determine the possible need for additional data.

   The models and analyses that support the model of dike drift interactions use input information about the geology of the natural system and engineering materials, but the analyses and models do not consider initial manufacturing defects. Parameters used in the analysis of dike/drift interactions are summarized in Table 4.1. The suitability of methods used to develop the information is established in the model reports and analysis reports that provide the information (e.g. BSC 2004 [DIRS 169989] and BSC 2004 [DIRS 169980]). Natural analog research unique to this report is described in Sections 6.3.8, 6.5.2.2, 7.3.1.1.1. Comparisons with field observations and associated mathematical models used to increase post-development confidence in the dike intrusion submodel are described in Section 7.3.1.

   Inputs for the modeling of dike propagation are described in Section 6.3.5, and the use of the information is described in Section 6.3.3. Model results are described in Section 6.3.7. Inputs for the analysis of effusive flow of magma into drifts are described in Section 6.4.3; the use of the information is described in Section 6.4.2, and results are provided in Section 6.4.5. Magma-waste package interactions are described in Section 6.4.8. Inputs for the analysis of secondary dike propagation are described in Section 6.5.1.1. The analysis examines the potential for development of secondary dikes under effusive flow conditions (Section 6.5.1) and for two-phase flow conditions Section 6.5.2). A synthesis describing the likelihood of the dog-leg scenario for effusive flow is presented in Section 6.5.1.5. Conclusions are presented in Section 6.5.4. Inputs for the analysis of gas flow between drifts are described in Section 6.6.3, and the use of the information is described in the numerical formulation in Section 6.6.2. Results are presented in Section 6.6.5. Inputs and the use of the information for the analysis of the effects of magma cooling and solidification on neighboring drift are described in Section 6.7.1.1, and results of the analysis are provided in Section 6.7.1.2. Inputs for the modeling of the reaction of seepage water with cooled basalt are described in Section 6.8, and results are described in Section 6.8.3.

   Effects of pressure inside the tip cavity and thermally induced increased horizontal stress on dike propagation are described in Sections 6.3.7.2 and 6.3.7.3. The effect of expanding magma on dike extension to the surface is described in Section 6.3.8.2. Sensitivity of the effects of magma cooling to latent heat effects and saturation effects are described in Sections 6.7.2.1 and 6.7.2.2. Sensitivity of the reaction of seepage water with cooled basalt is described in Section 6.8.2.

   The outputs of the dike/drift interactions model provide descriptions of physical and chemical conditions associated with migration of magmatic gases, thermal effects, and

seepage water chemistry (Section 8.2) and the uncertainties associated with those outputs (Section 8.3) for application in the TSPA-LA in-drift submodels.

4. Engineered barrier mechanical failure models for disruption events are adequate. For example, these models may consider effects of prolonged exposure to the expected emplacement drift environment, material test results not specifically designed or performed for the Yucca Mountain site, and engineered barrier component fabrication flaws.

   The model of dike propagation from depth provides the inputs needed for the analysis of magma flow into drifts (Section 6.3.9). Magma-waste package interactions under effusive flow conditions are described in Section 6.4.8. Magma cooling rates and their effects on secondary dike propagation, including the potential for stoppage of a new dike because of cooling-induced viscosity changes are described in Section 6.5.1.4. Results of simulations of gas flow between drifts are described in Section 6.6.5 and the simulation of gas transport through backfill are described in Section 6.6.5.3. Effects on neighboring drifts of magma cooling and solidification are described in Section 6.7.1.1.2. Simulations of the reaction of the reaction of seepage water with cooled basalt using EQ6 are described in Section 6.8.3.

A1.3 Acceptance Criterion 3: Data Uncertainty is Characterized and Propagated Through the Model Abstraction

1. Models use parameter values, assumed ranges, probability distributions, and bounding assumptions that are technically defensible, reasonably account for uncertainties, and variabilities, and do not result in an under-representation of risk.

   Parameters used in the analysis of dike/drift interactions are summarized in Table 4.1. Inputs for the modeling of dike propagation are described in Section 6.3.5, and the use of the information is described in Section 6.3.3. Model results are described in Section 6.3.7. Inputs for the analysis of effusive flow of magma into drifts are described in Section 6.4.3; the use of the information is described in Section 6.4.2, and results are provided in Section 6.4.5. Magma-waste package interactions are described in Section 6.4.8. Inputs for the analysis of secondary dike propagation are described in Section 6.5.1.1. The analysis examines the potential for development of secondary dikes under effusive flow conditions (Section 6.5.1) and for two-phase flow conditions Section 6.5.2). A synthesis describing the likelihood of the dog-leg scenario for effusive flow is presented in Section 6.5.1.5. Conclusions are presented in Section 6.5.4. Inputs for the analysis of gas flow between drifts are described in Section 6.6.3, and the use of the information is described in the numerical formulation in Section 6.6.2. Results are presented in Section 6.6.5. Inputs and the use of the information for the analysis of the effects of magma cooling and solidification on neighboring drift are described in Section 6.7.1.1, and results of the analysis are provided in Section 6.7.1.2. Inputs for the modeling of the reaction of seepage water with cooled basalt are described in Section 6.8, and results are described in Section 6.8.3.

Boundary and initial conditions used in the modeling of dike propagation are described in Section 6.3.6. Boundary and initial conditions used in the analysis of magma flow are described in Section 6.4.4, and initial and boundary conditions used in the analysis of gas flow between drifts are described in Section 6.6.4. Propagation of the boundary and initial conditions into the dike propagation model is described in the mathematical description of the dike propagation model in Section 6.3.6.

Effects of pressure inside the tip cavity and thermally induced increased horizontal stress on dike propagation are described in Sections 6.3.7.2 and 6.3.7.3. The effect of expanding magma on dike extension to the surface is described in Section 6.3.8.2. Sensitivity of the effects of magma cooling to latent heat effects and saturation effects are described in Sections 6.7.2.2 and 6.7.2.3. Sensitivity of the reaction of seepage water with cooled basalt is described in Section 6.8.2.

The outputs of the dike/drift interactions model provide descriptions of physical and chemical conditions associated with migration of magmatic gases, thermal effects, and seepage water chemistry (Section 8.2) and the uncertainties associated with those outputs (Section 8.3) for application in the TSPA-LA in-drift submodels.

The representation of risk is a TSPA-LA responsibility. This report describes no results that could be used to evaluate the representation of risk from magma-drift and magma-waste package interactions, but the review of magma-waste package interactions and recommendations for TSPA-LA are summarized in Section 6.4.8. It is important to note that no parameters are passed from these models directly to the TSPA-LA. Rather, parameter time histories developed in this report could be used by the waste form and waste package groups to determine possible damage states, which then are passed to TSPA-LA.

2. Process-level models used to represent mechanically disruptive events, within the emplacement drifts at the proposed Yucca Mountain repository, are adequate. Parameter values are adequately constrained by Yucca Mountain site data, such that the estimates of mechanically disruptive events on engineered barrier integrity are not underestimated. Parameters within conceptual models for mechanically disruptive events are consistent with the range of characteristics observed at Yucca Mountain.

   Three models and four analyses describe the processes that could occur if an igneous intrusion were to intersect the repository. The first model describes dike propagation from depth (Section 6.3.1), and the mathematical description of the model (Section 6.3.3). Assumptions related to the model are described in Section 6.3.2, and uncertainties associated with the model are described in Section 6.3.4. Alternative models of dike propagation are described in Section 6.3.8. Results from exercise of the base-case model are described in Section 6.3.7, and the inputs for the analysis of magma flow into drifts are provided in Section 6.3.5.

   The second model describes heating of neighboring drifts from cooling of the emplaced magma (Section 6.7). The conceptual model is described in Section 6.7.1, and the results are described in Section 6.7.1.2. Sensitivity to latent heat effects is

described in Section 6.7.2.1, and sensitivity to saturation is described in Section 6.7.2.2.

The third model describes seepage water alteration by reaction with intruded basalt in drifts (Section 6.8). The EQ6 modeling of basalt-water interactions is described in Section 6.8.1, and the results are described in Section 6.8.3. Sensitivity cases are described in Section 6.8.2, and modeling uncertainties, including uncertainties associated with EQ6 are described in Section 6.8.4.1. Alternate models for water/basalt interactions are described in Section 6.8.5.

The analyses documented in this report are natural and thermal stresses (Section 6.2), magma flow into drifts at dike/drift intersections (Section 6.4). Alternative models for dike propagation are described in Section 6.3.8. The effects of expanding magma on dike extension to the surface are described in Section 6.3.8.2. Magma flow to the surface along a secondary pathway developed at some distance from the intersection is described in Section 6.5. Gas flow between drifts is described in Section 6.6. Magma-waste package interactions are described in Section 6.4.8. Results support the TSPA-LA assumption that waste packages in intersected drifts provide no protection for the waste. For waste packages in Zone 2, results described in Sections 6.6.5 and 6.7.1.2 indicate that exposure to magmatic products would produce only limited damage because the repository host rock is expected to limit migration of volatile components and heat conduction to Zone 2. Radionuclide mobility associated with magma-waste form interactions is described in Section 6.8.5. Magma-waste form interactions are expected to form silicate and oxide minerals.

Parameters used in the analysis of dike/drift interactions are summarized in Table 4.1. Constraints on parameters and consistency of parameter values with the range of characteristics observed at Yucca Mountain is established in the model reports and analysis reports that provide the information (e.g. BSC 2004 [DIRS 169989] and BSC 2004 [DIRS 169980]). Natural analog research unique to this report is described in Sections 6.3.8, 6.5.2.2, and 7.3.1.1.1. Comparisons with field observations and associated mathematical models used to increase post-development confidence in the dike intrusion submodel are described in Section 7.3.1.1.2. Model uncertainties associated with the dike propagation model are described in Section 6.3.4, and alternative models are described in Section 6.3.8. Uncertainties associated with the modeling of the reaction between seepage water and cooled basalt are described in Section 6.8.4. Output uncertainties for the gas flow calculation are summarized in Section 8.3.1; output uncertainties associated with the heat flow calculation are described in Section 8.3.2, and output uncertainties associated with the EQ6 calculations for seepage water chemistry are described in Section 8.3.3.

3. Uncertainty is adequately represented in parameter development for conceptual models, process-level models, and alternative conceptual models considered in developing the TSPA abstraction of mechanical disruption of engineered barriers. This may be done through either sensitivity analyses or use of conservative limits.

Parameters used in the analysis of dike/drift interactions are summarized in Table 4.1. Uncertainties associated with the dike propagation model are described in Section 6.3.4, and alternative models are described in Section 6.3.8. Alternatives for the magma flow in drifts analysis are described in Sections 6.4.7. Uncertainties associated with the analysis of gas flow between drifts are described in Section 6.6. Uncertainties associated with the analysis of effects on neighboring drifts of magma cooling and solidification are described in Section 6.7.1.1. Boundary and initial conditions for the dike propagation model are described in Section 6.3.6. Boundary and initial conditions for the magma flow analysis are described in Section 6.4.4. Inputs for the analysis of gas flow between drifts are described in Section 6.6.3. Sensitivity of the model for effects of magma cooling and solidification on neighboring drifts to the latent heat effects is described in Section 6.7.2.1, and sensitivity to saturation effects is described in Section 6.7.2.2. Uncertainties associated with the model for reaction of seepage water with cooled basalt are described in Section 6.8.4. Model outputs for TSPA-LA for migration of magmatic gases, thermal effects, and seepage water chemistry are described in Sections 8.2.2, 8.2.3, and 8.2.4, respectively. Uncertainties associated with the gas flow calculation, the heat flow calculation, and EQ6 calculations are described in Sections 8.3.1, 8.3.2, and 8.3.3, respectively.

4. Where sufficient data do not exist, the definitions of parameter values and conceptual models are based on appropriate use of expert elicitation, conducted in accordance with NUREG-1563 (Kotra et al. 1996 [DIRS 100909]). If other approaches are used, the U.S. Department of Energy adequately justifies their use.

   Expert elicitation was not used in the development of the models of dike propagation, magma flow, gas flow between drift or magma cooling and solidification. However, results of the *Final Report of the Igneous Consequences Peer Review Panel* (Detournay et al. 2003 [DIRS 169660]) were used in the development of the dike propagation and magma flow models. Use of the peer review results is described in Section 7.3.1.1.2.

A1.4 Acceptance Criterion 4: Model Uncertainty is Characterized and Propagated Through the Model Abstraction

1. Alternative modeling approaches of features, events, and processes are considered and are consistent with available data and current scientific understanding, and the results and limitations are appropriately considered in the abstraction.

   Alternative conceptual models that were considered in the development of the model of dike propagation are discussed in Section 6.3.8. Alternatives for the analysis of magma flow into drifts are described in Section 6.4.7. Alternatives for secondary dike propagation are described in Sections 6.5.2 and 6.5.3. Features, events and processes that were considered in developing these models were identified in Section 6.1 and described in Table 6-1. Confidence building conducted during model development is described for the dike intrusion model in Section 7.2.1 and for the post intrusion submodel in Section 7.2.2. Post-development confidence building activities for the

dike propagation model are described in Section 7.3.1. Post-development confidence building for the model of drift-scale gas flow between drifts is summarized in Section 7.3.2.1. Confidence building for the model for magma cooling and solidification is summarized in Section 7.3.2.2, and similar work for the model of reactions between cooled basalt and seepage water is summarized in Section 7.3.2.3. Uncertainties associated with the outputs from these models are described in Section 8.3.

Limitations associated with the analysis of natural and thermal stresses are described in Section 1.4.1. Limitations associated with the dike propagation model are described in Section 1.4.2. Limitations associated with the analysis of magma flow in drifts are described in Section 1.4.3. Limitations associated with the analysis of the development of secondary dikes (dog-leg scenario) are described in Section 1.4.4. Limitations associated with the modeling of drift-scale gas flow are described in Section 1.4.5. Limitations associated with the modeling of basalt cooling and solidification are described in Section 1.4.6. Limitations associated with the modeling of reactions between cooled basalt and seepage water are described in Section 1.4.7.

2. Consideration of conceptual model uncertainty is consistent with available site characterization data, laboratory experiments, field measurements, natural analog information and process-level modeling studies; and the treatment of conceptual model uncertainty does not result in an under-representation of the risk estimate.

   Model uncertainties associated with the dike propagation model are described in Section 6.3.4. Sensitivity of the modeling of effects of magma cooling and solidification on neighboring drifts to latent heat effects is described in Section 6.7.2.1 and to saturation in Section 6.7.2.2. Uncertainties associated with the reaction of seepage water with basalt after return to pre-intrusion conditions are described in Section 6.8.4.

   Uncertainties associated with the gas flow calculation output are described in Section 8.3.1. Uncertainties associated with the heat flow calculation output are described in Section 8.3.2. Uncertainties associated with the EQ6 calculation output are described in Section 8.3.3.

   The representation of risk is a TSPA-LA responsibility, but the review of magma-waste package interactions and recommendations for TSPA-LA are summarized in Section 6.4.8. This report describes no results that could be used to evaluate the representation of risk from magma-drift and magma-waste package interactions.

3. Appropriate alternative modeling approaches are investigated that are consistent with available data and current scientific knowledge and that appropriately consider their results and limitations using tests and analyses that are sensitive to the processes modeled.

Alternative conceptual models that were considered in the development of the model of dike propagation are discussed in Section 6.3.8. Alternatives for the analysis of magma flow into drifts are described in Section 6.4.7. Alternatives for secondary dike propagation are described in Section 6.5.3. Features, events and processes that were considered in developing these models were identified in Section 6.1 and described in Table 6-1. Confidence building conducted during model development is described for the dike intrusion model in Section 7.2.1 and for the post intrusion submodel in Section 7.2.2. Post-development confidence building activities for the dike propagation model are described in Section 7.3.1. Post-development confidence building for the model of drift-scale gas flow between drifts is summarized in Section 7.3.2.1. Confidence building for the model for magma cooling and solidification is summarized in Section 7.3.2.2, and similar work for the model of reactions between cooled basalt and seepage water is summarized in Section 7.3.2.3.

Effects on dike propagation of pressure inside the tip cavity are described in Section 6.3.7.2, and effects of thermally induced increased horizontal stress are described in Section 6.3.7.3. Effects of expanding magma on dike extension to the surface are described in Section 6.3.8.2. Sensitivity of magma cooling and solidification effects on neighboring drifts to latent hear are described in Section 6.7.2.1, and effects from saturation are described in Section 6.7.2.2. Sensitivity cases related to reactions between seepage water and cooled basalt are described in Section 6.8.2.

Limitations associated with the analysis of natural and thermal stresses are described in Section 1.4.1. Limitations associated with the dike propagation model are described in Section 1.4.2. Limitations associated with the analysis of magma flow in drifts are described in Section 1.4.3. Limitations associated with the analysis of the development of secondary dikes (dog-leg scenario) are described in Section 1.4.4. Limitations associated with the modeling of drift-scale gas flow are described in Section 1.4.5. Limitations associated with the modeling of basalt cooling and solidification are described in Section 1.4.6. Limitations associated with the modeling of reactions between cooled basalt and seepage water are described in Section 1.4.7.

A1.5 Acceptance Criterion 5: Model Abstraction Output is Supported by Objective Comparisons

1. Models implemented in this TSPA abstraction provide results consistent with output from detailed process-level models and/or empirical observations (laboratory and field testings and/or natural analogues).

   Model outputs for the migration of magmatic gases are described in Section 8.2.2; outputs for thermal effects are described in Section 8.2.3, and outputs for seepage water chemistry are described in Section 8.2.4. Uncertainties associated with gas flow calculations are described in Section 8.3.1; uncertainties associated with the heat flow calculation are described in Section 8.3.2, and uncertainties associated with the EQ6 calculation are described in Section 8.3.3.

Magma-waste package interactions are described in Section 6.4.8. Results support the TSPA-LA assumption that waste packages in intersected drifts provide no protection for the waste. For waste packages in Zone 2, results described in Sections 6.6.5 and 6.7.1.2 indicate that exposure to magmatic products would produce only limited damage because the repository host rock is expected to limit migration of volatile components and heat conduction to Zone 2. Radionuclide mobility associated with magma-waste form interactions is described in Section 6.8.5. Magma-waste form interactions are expected to form silicate and oxide minerals.

2. Outputs of mechanical disruption of engineered barrier abstractions reasonably produce or bound the results of corresponding process-level models, empirical observations, or both.

   Model outputs for the migration of magmatic gases are described in Section 8.2.2; outputs for thermal effects are described in Section 8.2.3, and outputs for seepage water chemistry are described in Section 8.2.4. Uncertainties associated with gas flow calculations are described in Section 8.3.1; uncertainties associated with the heat flow calculation are described in Section 8.3.2, and uncertainties associated with the EQ6 calculation are described in Section 8.3.3. Confidence building conducted during model development is described for the dike intrusion model in Section 7.2.1 and for the post intrusion submodel in Section 7.2.2. Post-development confidence building activities for the dike propagation model are described in Section 7.3.1. Post-development confidence building for the model of drift-scale gas flow between drifts is summarized in Section 7.3.2.1. Confidence building for the model for magma cooling and solidification is summarized in Section 7.3.2.2, and similar work for the model of reactions between cooled basalt and seepage water is summarized in Section 7.3.2.3.

3. Well-documented procedures that have been accepted by the scientific community to construct and test the mathematical and numerical models, are used to simulate mechanical disruption of engineered barriers.

   The computer codes used in the modeling activities documented in this report are described in Table 3-1. Confidence building conducted during model development is described for the dike intrusion model in Section 7.2.1 and for the post intrusion submodel in Section 7.2.2. Post-development confidence building activities for the dike propagation model are described in Section 7.3.1. Post-development confidence building for the model of drift-scale gas flow between drifts is summarized in Section 7.3.2.1. Confidence building for the model for magma cooling and solidification is summarized in Section 7.3.2.2, and similar work for the model of reactions between cooled basalt and seepage water is summarized in Section 7.3.2.3.

4. Sensitivity analyses or bounding analyses are provided to support the TSPA abstraction of mechanical disruption of engineered barriers that cover ranges consistent with site data, field or laboratory experiments and tests, and natural analogue research.

Model outputs for the migration of magmatic gases are described in Section 8.2.2; outputs for thermal effects are described in Section 8.2.3, and outputs for seepage water chemistry are described in Section 8.2.4. Uncertainties associated with gas flow calculations are described in Section 8.3.1; uncertainties associated with the heat flow calculation are described in Section 8.3.2, and uncertainties associated with the EQ6 calculation are described in Section 8.3.3.

Effects of pressure inside the tip cavity and thermally induced increased horizontal stress on dike propagation are described in Sections 6.3.7.2 and 6.3.7.3. The effect of expanding magma on dike extension to the surface is described in Section 6.3.8.2. Sensitivity of the effects of magma cooling to latent heat effects and saturation effects are described in Sections 6.7.2.1 and 6.7.2.2. Sensitivity of the reaction of seepage water with cooled basalt is described in Section 6.8.2. Boundary and initial conditions for the dike propagation model are described in Section 6.3.6. Boundary and initial conditions for the magma flow analysis are described in Section 6.4.7.1.4. Boundary and initial conditions for the analysis of gas flow between drifts are described in Section 6.6.4.

A2. VOLCANIC DISRUPTION OF WASTE PACKAGES

A2.1 Acceptance Criterion 1: System Description and Model Integration are Adequate

1. TSPA adequately incorporates important design features, physical phenomena, and couplings, and uses consistent and appropriate assumptions throughout the volcanic disruption of the waste package abstraction process.

   Dike Drift/Interactions addresses propagation of a magma filled fracture (dike) and the characteristics of magma for the intrusive case and not for the eruptive case. The number of waste packages contacted by magma in the igneous intrusion-groundwater transport modeling case is considered in *Number of Waste Packages Hit by Igneous Intrusion* (BSC 2004 ([DIRS 170001]).

2. Models used to assess volcanic disruption of waste packages are consistent with physical processes generally interpreted from igneous features in the Yucca Mountain region and/or observed at active igneous systems.

   This report discusses models that provide some of the initial conditions needed to evaluate volcanic disruption of waste packages. The first model describes dike propagation from depth (Section 6.3.1), and the mathematical description of the model (Section 6.3.3). Assumptions related to the model are described in Section 6.3.2, and uncertainties associated with the model are described in Section 6.3.4. Alternative models of dike propagation are described in Section 6.3.8. Results from exercise of the base-case model are described in Section 6.3.7, and the inputs for the analysis of magma flow into drifts are provided in Section 6.3.5.

   The second model describes heating of neighboring drifts from cooling of the emplaced magma (Section 6.7). The conceptual model is described in Section 6.7.1,

and the results are described in Section 6.7.1.2. Sensitivity to latent heat effects is described in Section 6.7.2, and sensitivity to saturation is described in Section 6.7.2.2.

The third model describes seepage water alteration by reaction with intruded basalt in drifts (Section 6.8). The EQ6 modeling of basalt-water interactions is described in Section 6.8.1, and the results are described in Section 6.8.3. Sensitivity cases are described in Section 6.8.2, and modeling uncertainties, including uncertainties associated with EQ6 are described in Section 6.8.4.1.

3. Models account for changes in igneous processes that may occur from interactions with engineered repository systems.

   Not applicable

4. Guidance in NUREG-1297 (Altman et al. 1988 [DIRS 103597]) and NUREG-1298 (Altman et al. 1988 [DIRS 103750], or other acceptable approaches is followed.

   NUREG-1297 describes the generic technical position with respect to the use of peer reviews on high-level waste repository programs. The use of information from the *Final Report of the Igneous Consequences Peer Review Panel* (Detournay et al. 2003 [DIRS 169660]) is summarized in Section 7.2.1. The *Final Report of the Igneous Consequences Peer Review Panel* (Detournay et al. 2003 [DIRS 169660], pp. 44 and 45) addressed the limitations of modeling dike propagation, when assuming that the magma is an incompressible fluid (whereas real magma would be compressible). Use of peer review in the development of the model for *Atmospheric Dispersal and Deposition of Tephra from a Potential Volcanic Eruption at Yucca Mountain, Nevada* is described in BSC 2004 ([DIRS 170026], Section 7.4).

   NUREG-1298 describes the generic technical position with respect to qualification of existing data. External sources have provided unqualified data that have been used as direct input to this document. The inputs from these sources are qualified for intended use within the document using the criteria found in AP-SIII.9Q, *Scientific Analyses*. These criteria represent a subset of the methods and attributes required for qualification of data per AP-SIII.2Q, *Qualification of Unqualified Data.* These methods and attributes are based on those that are presented in NUREG-1298, which are meant to provide "the level of confidence in the data … commensurate with their intended use.

A3. AIRBORNE TRANSPORT OF RADIONUCLIDES

The models of dike propagation near drifts, magma and gas flow in drifts, and drift-scale gas flow constrain the conceptual models that support generation of the source term for the analysis of airborne transport of radionuclides.

The outputs from this report provide no direct parameter inputs to the analysis and modeling of airborne transport of radionuclides. The description of the modeling of airborne transport of radionuclides is provided in *Atmospheric Dispersal and Deposition of Tephra from a Potential Volcanic Eruption at Yucca Mountain, Nevada* BSC 2004 [DIRS 170026]).

INTENTIONALLY LEFT BLANK

APPENDIX B

EQ6 MINERAL DISSOLUTION RATES

APPENDIX B
EQ6 MINERAL DISSOLUTION RATES

This appendix contains figures that show input values to, calculation of, and EQ6 rate comparisons of the rates for the dissolution of minerals in the EQ6 simulation of basalt/water interaction. EQ6 is qualified software (CRWMS-M&O 1999 [DIRS 153964]) as discussed in Section 3.1. Calculation of the mineral dissolution rates for EQ6 is as follows:

- Using Microsoft Excel, a trendline was added (linear) to each of the pH legs (i.e., low pH values were fit with one trendline and high pH values were fit with a different trendline). These linear fits are shown by the black trendlines in the figures. The linear equation for these lines is also presented as well as the rounded values used for the calculation of the rate for EQ6.

- EQ6 calculates the rate of dissolution at any pH by the following formula

$$\text{Total Dissolution Rate} = k_1[H^+]^{S1} + k_2[H^+]^{S2} \text{ (moles/cm}^2\cdot\text{s)} \qquad \text{(Eq. B-1)}$$

  where k_1 and k_2 represent the exponential of the intercept and S1 and S2 values represent the slope of the trendlines.

- The EQ6 curve (pH dependent dissolution rate) is calculated by using the above stated values to calculate the dissolution rate for each pH leg. These values are then combined to create one dissolution rate by the model.

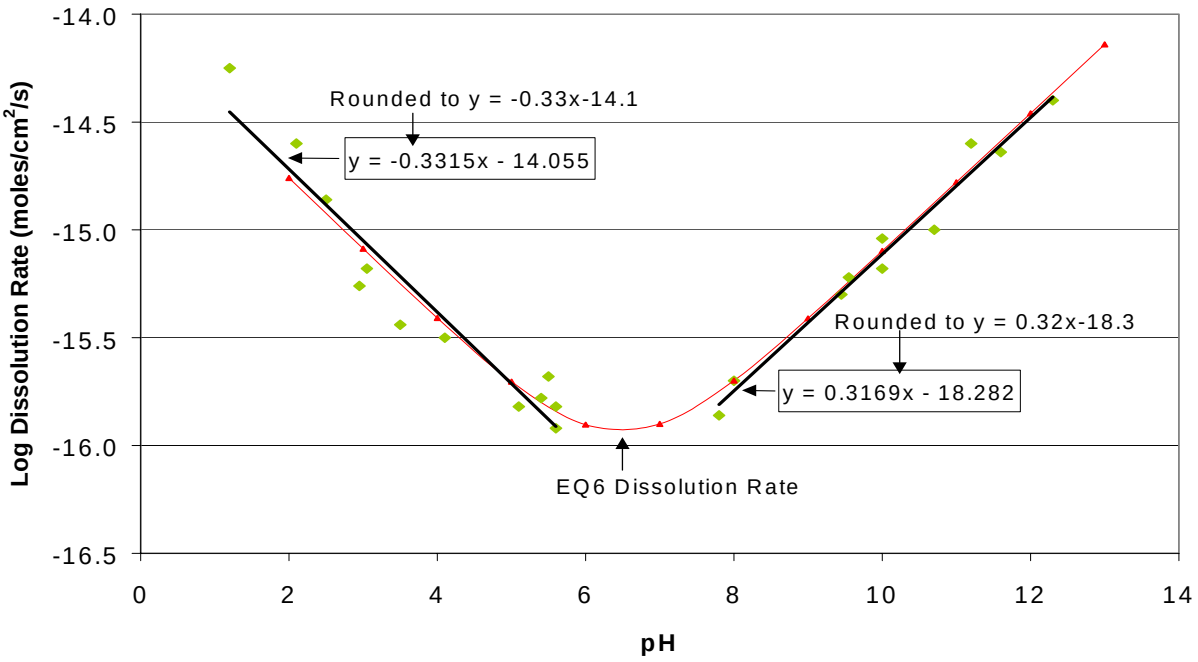

NOTE: Calculated in Spreadsheet *Aluminosilicate rates.xls* (see Appendix E).

Figure B-1. EQ6 Dissolution Rate of Albite (also used for Sanidine)

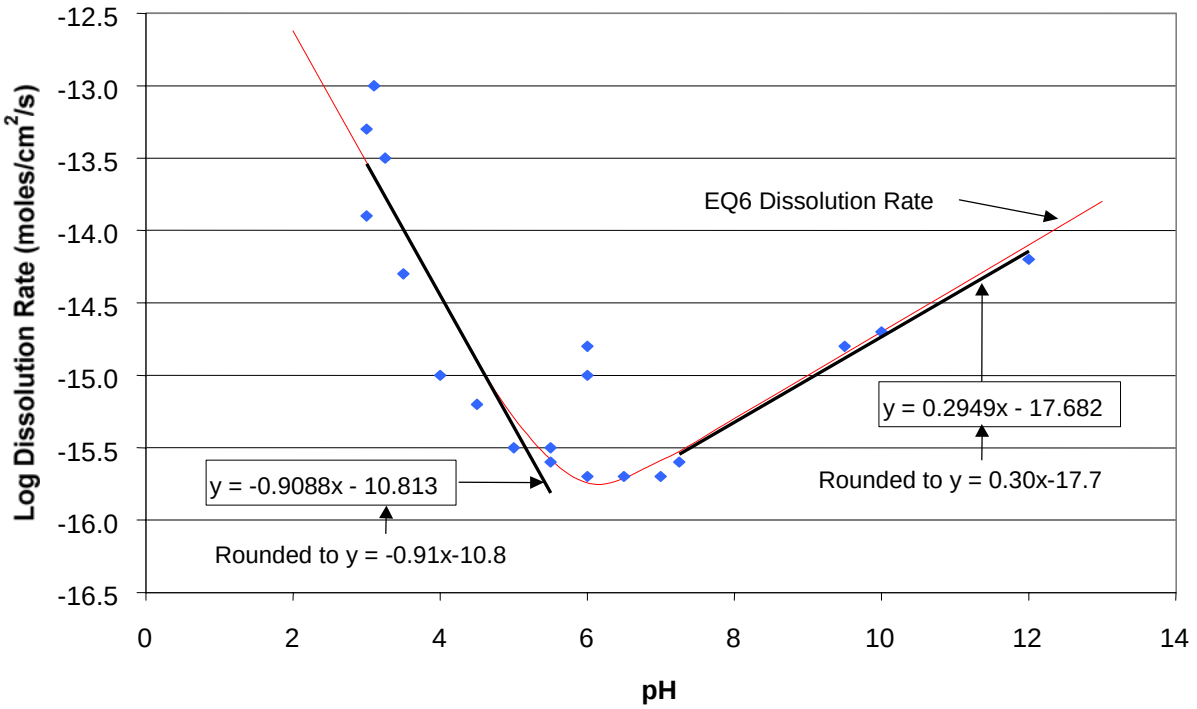

NOTE: Calculated in Spreadsheet *Aluminosilicate rates.xls* (see Appendix E).

Figure B-2. EQ6 Dissolution Rate of Anorthite

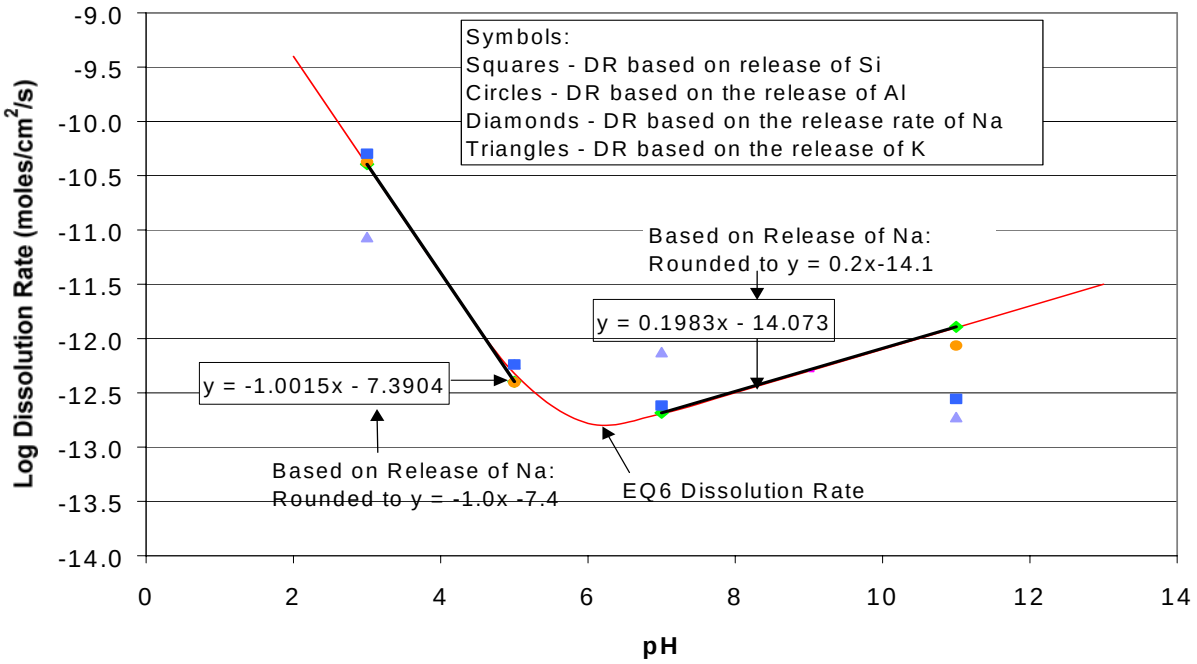

NOTE: Calculated in Spreadsheet *Aluminosilicate rates.xls* (see Appendix E) from Na release data found in Table 4-7.

Figure B-3. EQ6 Dissolution Rate of Nepheline

Table B-1. Additional Nepheline Dissolution Rates Shown on Figure B-3

	Based on release of Si		Based on release of Al		Based on release of K	
pH	DR (mole/cm^2 s)	Log DR	DR (mole/cm^2 s)	Log DR	DR (mole/cm^2 s)	Log DR
3	5.03E-11	-10.30	4.22E-11	-10.37	8.61E-12	-11.06
5	5.78E-13	-12.24	3.94E-13	-12.40	5.81E-13	-12.24
7	2.42E-13	-12.62	-------	--------	7.50E-13	-12.12
11	2.78E-13	-12.56	8.61E-13	-12.06	1.89E-13	-12.72

NOTE: DR from Tole et al. 1986 [DIRS 163289], Table 2, Log DR calculated on *Aluminosilicate rates.xls* (see Appendix E).

DR = Dissolution Rate

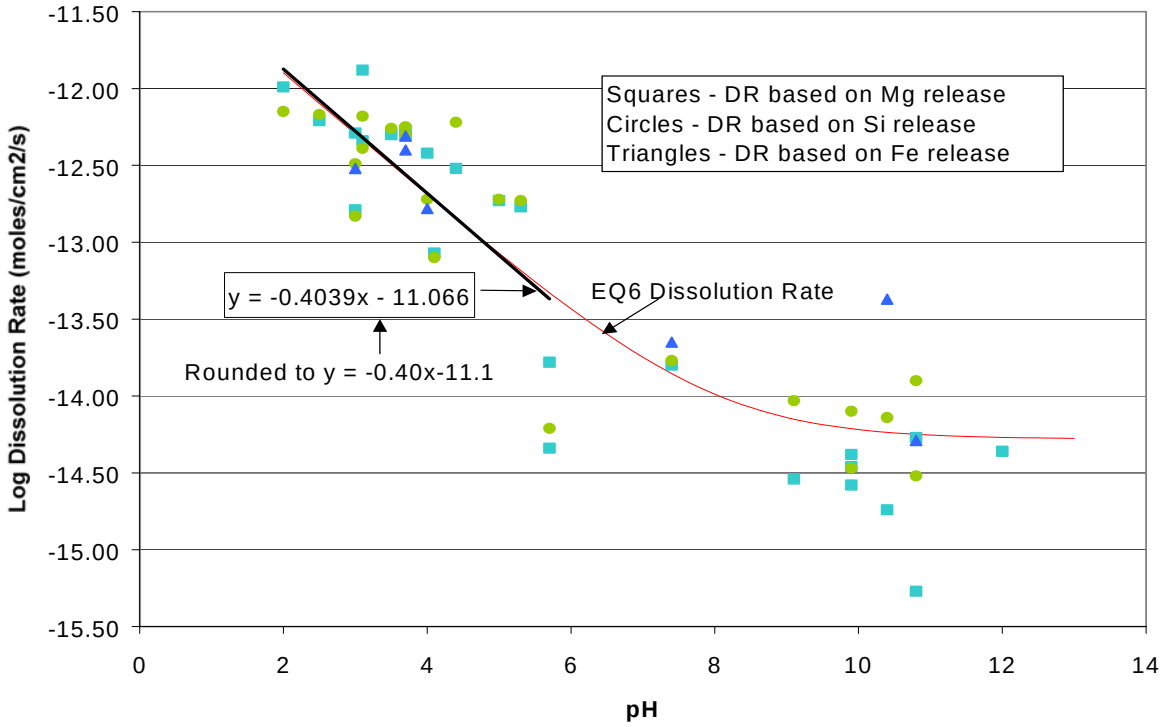

NOTE: Calculated in Spreadsheet *olivine rate.xls* (see Appendix E) from Mg release data found in Table 4-8. Release rates for Si and Fe can be found in Table B-3.

Figure B-4. EQ6 Dissolution Rate of Olivine (Used for Forsterite and Fayalite)

Table B-2. Additional Olivine Dissolution Rates Shown on Figure B-4

Based on release of Si					
pH	Log DR (mole/cm^2 s)	pH	Log DR (mole/cm^2 s)	pH	Log DR (mole/cm^2 s)
4.1	-13.10	5	-12.72	3.1	-12.18
10.4	-14.14	5.7	-14.21	4	-12.72
7.4	-13.77	2	-12.15	3	-12.49
9.9	-14.47	9.1	-14.03	3.5	-12.26
9.9	-14.10	3.7	-12.30	3.1	-12.39
3.7	-12.25	2.5	-12.17	5.3	-12.73
10.8	-14.52	4.4	-12.22	10.8	-13.90
3	-12.83				
Based on release of Fe					
pH	Log DR (mole/cm^2 s)	pH	Log DR (mole/cm^2 s)	pH	Log DR (mole/cm^2 s)
10.4	-13.37	3.7	-12.40	3	-12.52
7.4	-13.65	4	-12.78	10.8	-14.29
3.7	-12.31				

NOTE: Log DR from Wogelius and Walther [DIRS 163290], Table 2

DR = Dissolution Rate

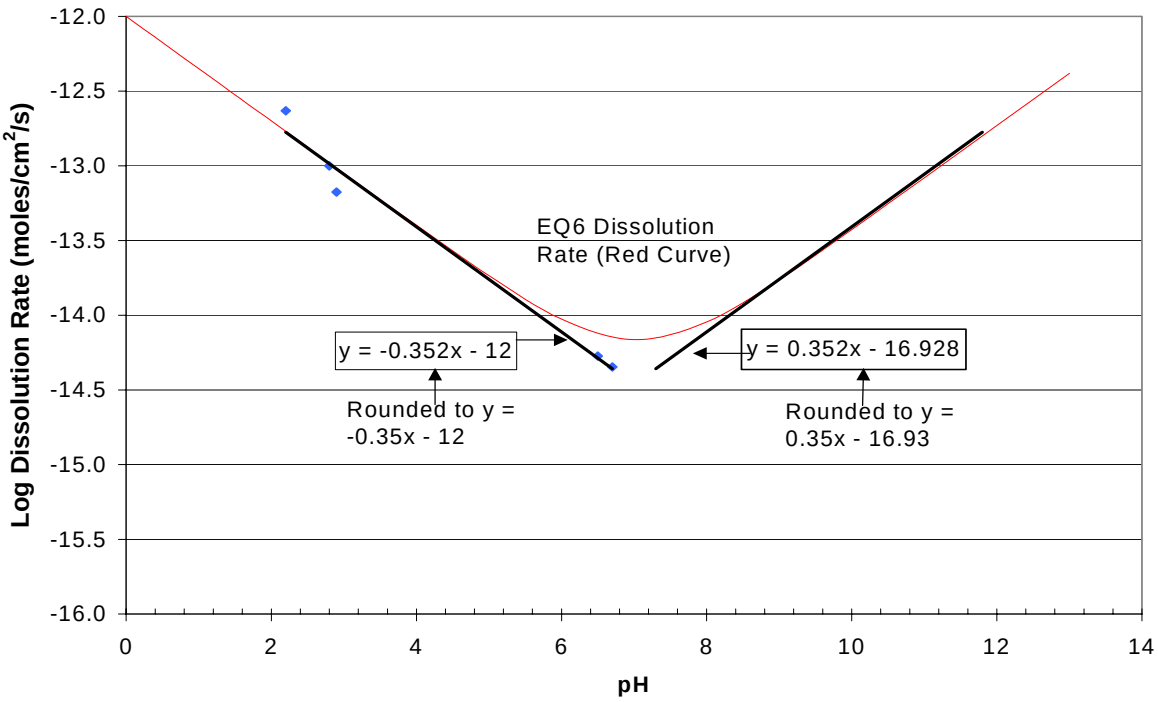

NOTE: Calculated in Spreadsheet *apatite rate.xls* (see Appendix E) Figure B-5. EQ6 Dissolution Rate of Hydroxylapatite.

Figure B-5. EQ6 Dissolution Rate of Hydroxylapatite

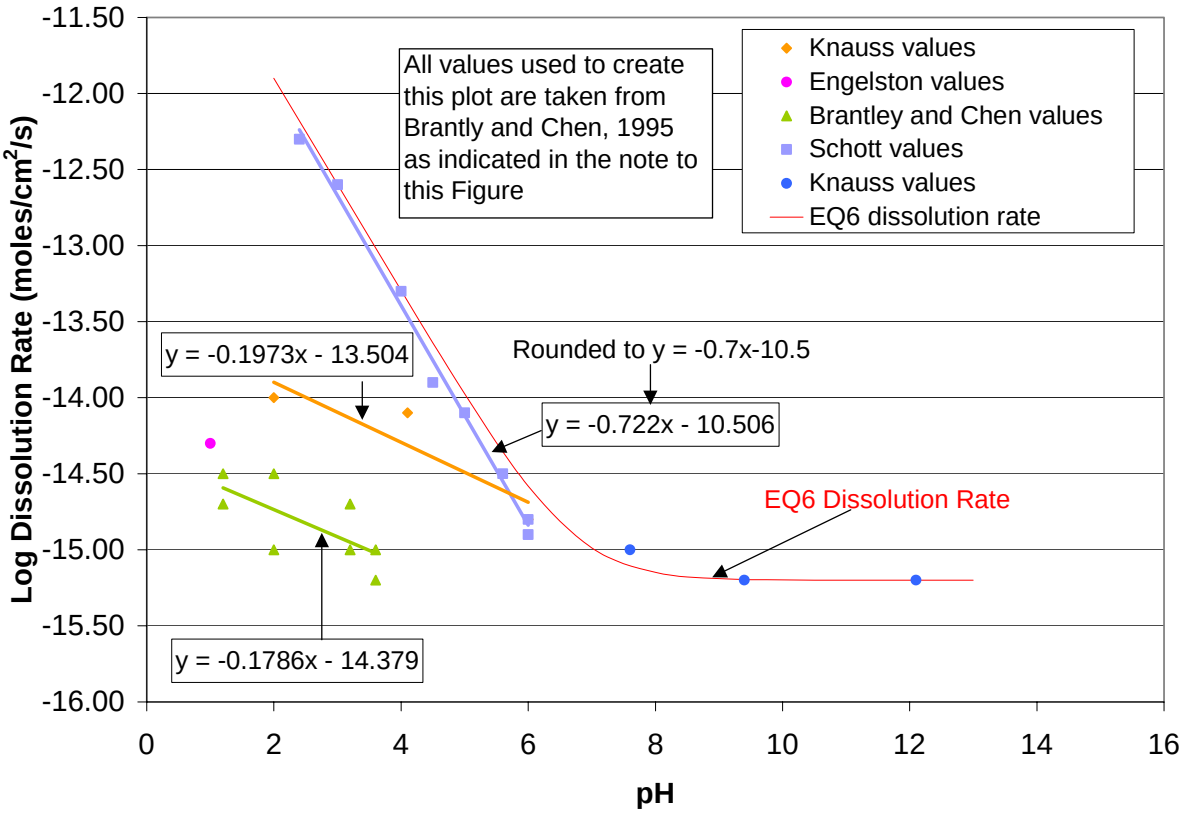

NOTE: All plotted data are from Table 1 of Brantley and Chen (1995 [DIRS 163275]), which is a compilation of dissolution data from different sources mentioned in the plot inset box. Calculated in Spreadsheet *pyroxene rates.xls* (see Appendix E) from Schott data found in Table 4-8. Other release rates shown on the plot can be found in Table B-3.

Figure B-6. EQ6 Dissolution Rate of Diopside (Used for Hedenbergite)

Table B-3. Additional Diopside Dissolution Rates Shown on Figure B-6

pH	Log DR (mole/cm^2 s)	pH	Log DR (mole/cm^2 s)	pH	Log DR (mole/cm^2 s)
Brantley and Chen 1995 [DIRS 163275]					
1.2	-14.50	3.6	-15.00	3.2	-15.00
2	-14.50	1.2	-14.70	3.6	-15.20
3.2	-14.70	2	-15.00		
Knauss data presented in Brantley and Chen 1995 [DIRS 163275]					
2	-14.00	4.1	-14.10	6	-14.80
Engelston data presented in Brantley and Chen 1995 [DIRS 163275]					
1	-14.30				

DR = dissolution rate

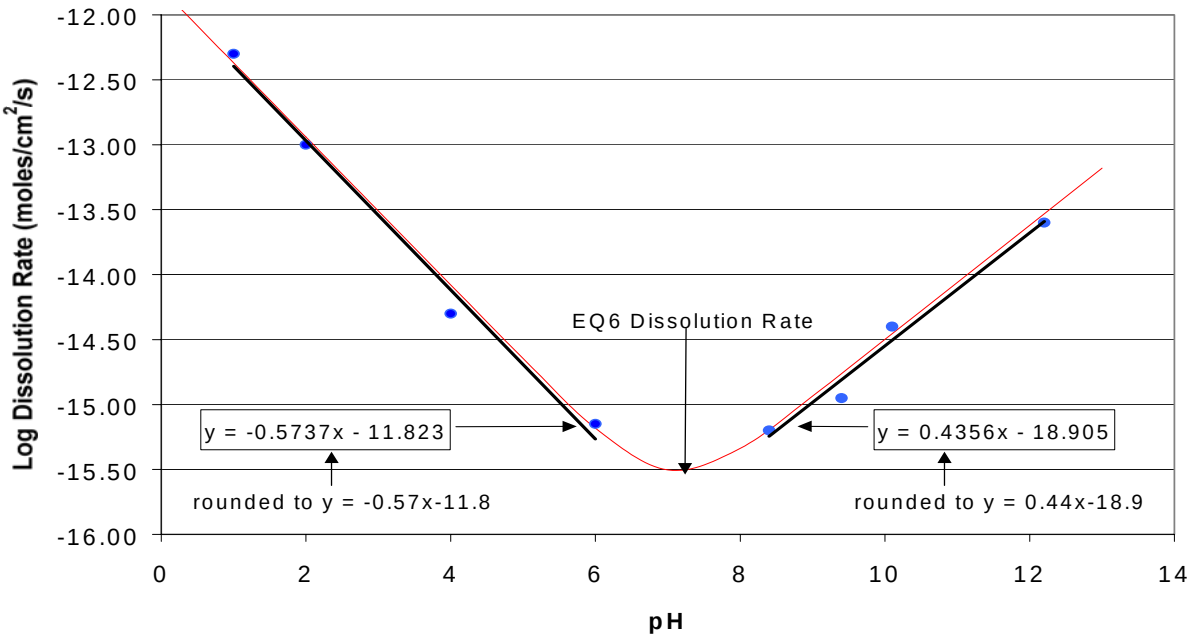

NOTE: Calculated in Spreadsheet *pyroxene rates.xls* (see Appendix E).

Figure B-7. EQ6 Dissolution Rate of Enstatite

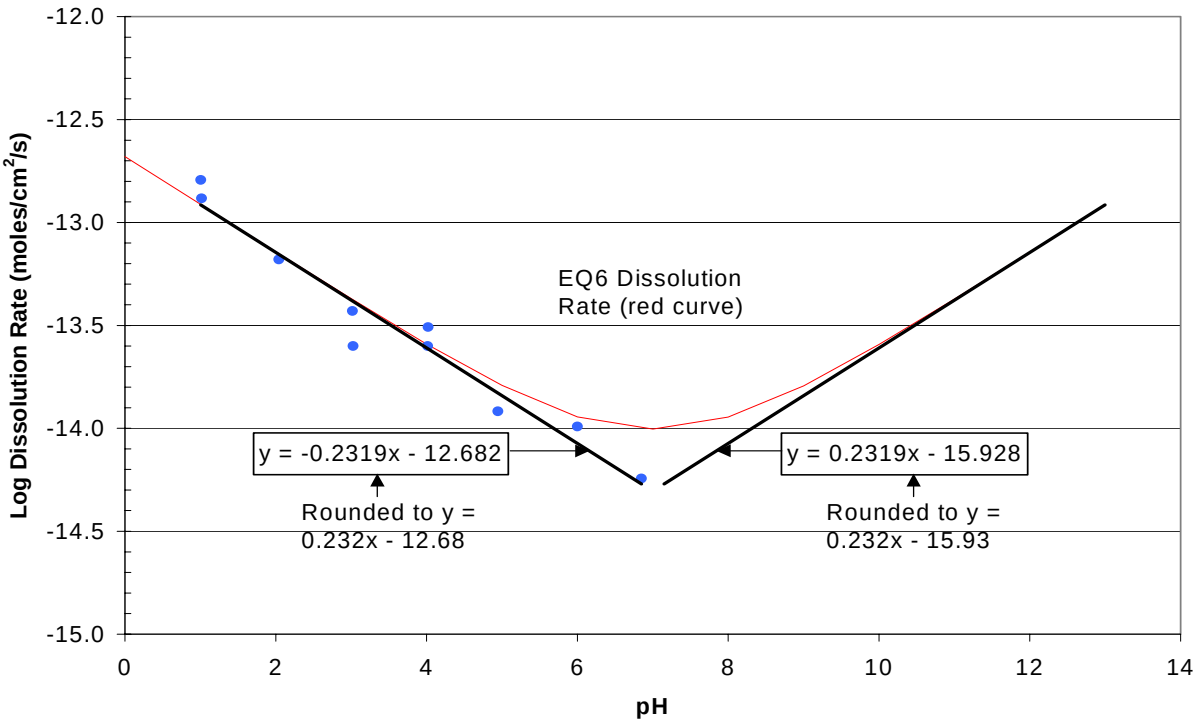

NOTE: Calculated in Spreadsheet *oxides rate.xls* (see Appendix E).

Figure B-8. EQ6 Dissolution Rate of Magnetite

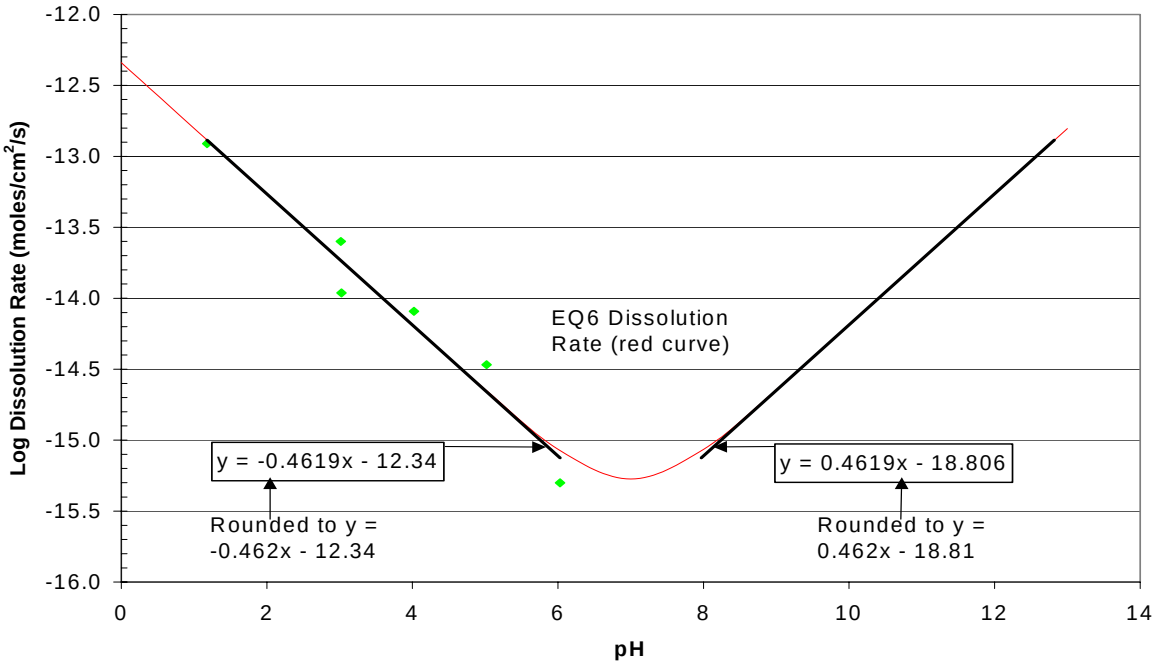

NOTE: Calculated in Spreadsheet *oxides rate.xls* (see Appendix E).

Figure B-9. EQ6 Dissolution Rate of Ilmenite

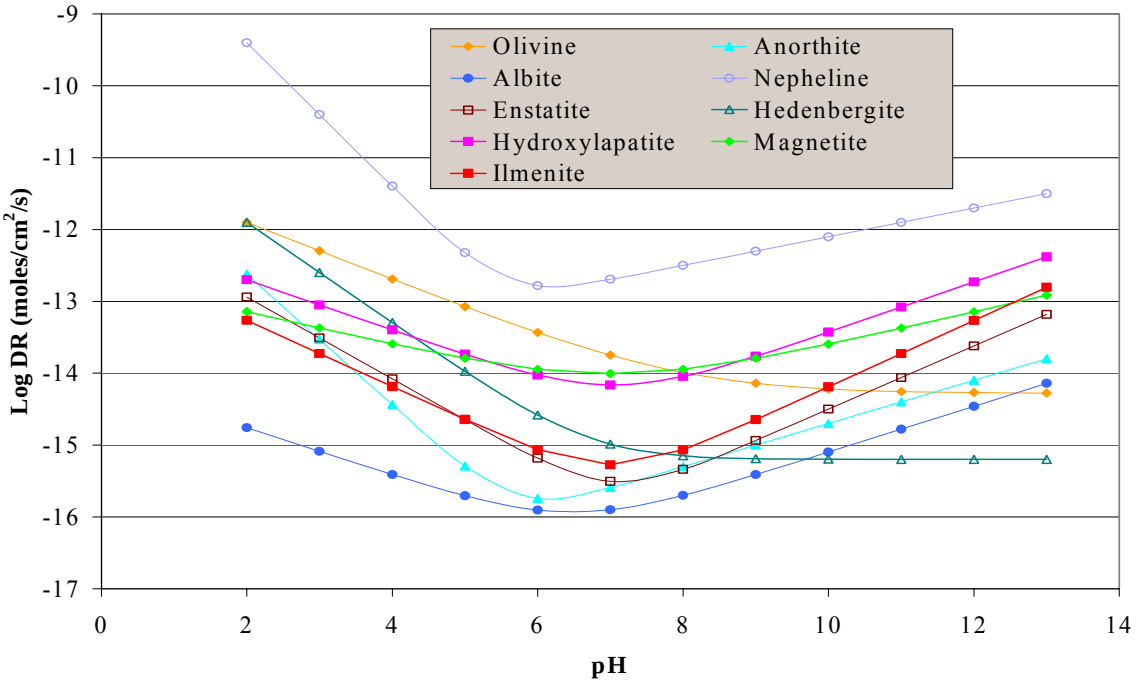

NOTE: Calculated in Spreadsheet *Diss-Rate Summary.xls* (see Appendix E).

Figure B-10. Comparison of Rates Used in EQ6 Calculations

INTENTIONALLY LEFT BLANK

APPENDIX C

VERIFICATION OF HEAT CONDUCTION MODEL SIMULATION CALCULATIONS

APPENDIX C
VERIFICATION OF HEAT CONDUCTION MODEL SIMULATION CALCULATIONS

C1. HEAT FLOW MODEL

A one-dimensional second order partial differential equation (Chapman 1974 [DIRS 152938], p. 137), subject to initial temperature (due to the constant heat content) and a far field temperature boundary condition applies to the problem of magma intrusion:

$$k\left[\frac{1}{r}\cdot\frac{\partial T}{\partial r}+\frac{\partial^2 T}{\partial r^2}\right]=\rho\cdot C_p\cdot\frac{\partial T}{\partial t} \qquad \text{(Eq. C-1)}$$

The temperature distribution for a magma flow filling a Zone 1 emplacement drift can be estimated using a one-dimensional unsteady radial heat conduction model, subject to constant heat content. The magma is considered to be at an initial intrusive temperature of 1150°C (DTN: LA0407DK831811.001 [DIRS 170768]). The magma fills the drift entirely and instantaneously, and then the temperature spatially and temporally dissipates. The temperature of the drift wall and the far-field is considered to be 25°C, and up to 200°C, at the time of the intrusion. The heat transfer thermal properties of the magma are considered to be the same as those for the densely welded tuff for a first order analysis.

Carnahan et al. (1990 [DIRS 163096], p. 462) provides finite difference expression approximations to first and second order derivatives for the radial heat conduction problem. The governing equation may be expressed as:

$$\frac{1}{r_i}\cdot\left(\frac{T'_{i+1}-T'_{i-1}}{2\cdot\Delta r}\right)+\frac{1}{\Delta r^2}\cdot\left[T'_{i+1}+T'_{i-1}-2\cdot T'_i\right]=\frac{1}{\alpha}\cdot\frac{T_i-T'_i}{\Delta t} \qquad \text{(Eq. C-2)}$$

Using the following definition of thermal diffusivity (Incropera and DeWitt 2002 [DIRS 163337], p. 59):

$$\alpha=\frac{k}{\rho C_p} \qquad \text{(Eq. C-3)}$$

where

- Δt is the change in time (time-step) in years
- r_i is the total distance to the center of the cylinder (units: m)
- Δr is the change in distance from the center of the cylinder in one time-step (units: m)
- T_i is the temperature at distance r_i from the center of the cylinder (°C)
- T'_i is the temperature from the previous time-step at a distance of r_i from the center of the cylinder
- T'_{i+1} is the temperature from the previous time-step at a distance of r_{i+1} from the center of the cylinder
- T'_{i-1} is the temperature from the previous time-step at a distance of r_{I-1} from the center of the cylinder
- α is the thermal diffusivity of the rock mass (and thus the magma) (m^2/year)
- k is the thermal conductivity of the rock mass (and thus the magma) (W/m·K)

ρ is the density (kg/m^3)
C_p is the specific heat (J/kg·K)

Factoring the expression to express T_i in terms of $T`_i$, $T`_{i-1}$, and $T`_{i+1}$ in an explicit finite difference calculation:

$$T_i = \alpha \cdot \Delta t \cdot \left[\frac{1}{r_i \cdot 2 \cdot \Delta r} + \frac{1}{\Delta r^2} \right] \cdot T'_{i+1} + \alpha \cdot \Delta t \cdot \left[\frac{-1}{r_i \cdot 2 \cdot \Delta r} + \frac{1}{\Delta r^2} \right] \cdot T'_{i-1} - \frac{2\alpha \cdot \Delta t \cdot T'_i}{\Delta r^2} + T'_i \qquad \text{(Eq. C-4)}$$

Radial Equation ($r_i > 0$)

A simple explicit finite difference calculation was set up in Microsoft Excel based upon the second order finite difference expression for radial flow. The stability of the calculation was confirmed by using an energy balance check within the spreadsheet. The explicit finite difference calculation can be simplified by defining the coefficients for T'_{i+1}, T'_{i-1}, and T'_i as α', β', and γ', respectively:

$$\alpha' = \left[\frac{1}{r_i \cdot 2 \cdot \Delta r} + \frac{1}{\Delta r^2} \right] \qquad \text{(Eq. C-4a)}$$

$$\beta' = \left[\frac{-1}{r_i \cdot 2 \cdot \Delta r} + \frac{1}{\Delta r^2} \right] \qquad \text{(Eq. C-4b)}$$

$$\gamma' = \left(-\frac{2}{\Delta r^2} \right) \qquad \text{(Eq. C-4c)}$$

The explicit finite difference expression (Equation I-4) then becomes:

$$T_i = \alpha \cdot \Delta t \cdot \left[\alpha' \cdot T'_{i+1} + \beta' \cdot T'_{i-1} + \gamma' \cdot T'_i \right] + T'_i \qquad \text{(Eq. C-5)}$$

The far-field temperature boundary condition at a distance of 150 meters (approximately 10 m less than twice the drift spacing) is set to a constant ambient temperature of 25°C. Additional calculations look at ambient temperatures up to 200°C.

Centerline Equation ($r_i = 0$)

To obtain an equation for the centerline temperature, a finite difference expression at the center of the model sets the insulated temperature boundary condition equal to the centerline temperature ($T`_{i-1} = T`_{i+1}$).

$$T_i = \alpha \cdot \Delta t \cdot \left[\frac{1}{r_i \cdot 2 \cdot \Delta r} + \frac{1}{\Delta r^2} \right] \cdot T'_{i+1} + \alpha \cdot \Delta t \cdot \left[\frac{-1}{r_i \cdot 2 \cdot \Delta r} + \frac{1}{\Delta r^2} \right] \cdot T'_{i+1} - \frac{2\alpha \cdot \Delta t \cdot T'_i}{\Delta r^2} + T'_i \qquad \text{(Eq. C-6)}$$

Simplifying this equation:

$$T_i = \left[\frac{2\alpha \cdot \Delta t}{\Delta r^2}\right] \cdot [T'_{i+1} - T'_i] + T'_i \qquad \text{(Eq. C-7)}$$

The model was implemented by entering Equations C-4 and C-7 into Microsoft Excel spreadsheets (see Appendix E). The required thermal diffusivity (α) was calculated using the method discussed below.

Thermal Diffusivity

Assessment of the effects of temperatures of intruded magma (intruded into Zone 1 drifts) on Zone 2 waste packages requires the rock mass thermal diffusivity, which in turn requires an estimate of the rock mass volumetric heat capacity and thermal conductivity of the welded tuff at the repository horizon.

The volumetric heat capacity was calculated using an equation derived in *Ventilation Model and Analysis Report* (BSC 2004 [DIRS 169862], Equation II-15).

$$C_{rock} = \frac{S \cdot \frac{\phi_m}{1-\phi_m} C_{vw} + \rho_g \cdot C_p}{\left(1 + \frac{\phi_m}{1-\phi_m} + \frac{\phi_l}{1-\phi_l} \cdot \left(1 + \frac{\phi_m}{1-\phi_m}\right)\right)} \qquad \text{(Eq. C-8)}$$

Simplifying this equation:

$$C_{rock} = \frac{S \cdot \frac{\phi_m}{1-\phi_m} C_{vw} + \rho_g \cdot C_p}{\left(1 + \frac{\phi_l}{1-\phi_l}\right) \cdot \left(1 + \frac{\phi_m}{1-\phi_m}\right)} \qquad \text{(Eq. C-9)}$$

where

- C_{rock} volumetric heat capacity of the rock mass (J/m^3·K)
- S saturation (S = 0: dry; S = 1: wet)
- ϕ_m matrix porosity
- ϕ_l lithophysal porosity
- C_{vw} volumetric heat capacity of water (J/m^3·K)
- ρ_g grain density of solids (kg/m^3)
- C_p specific heat capacity of solids (J/kg·K)

The saturation in this heat flow calculation is either completely dry (no water; S = 0), or completely wet (matrix is completely filled with water; S = 1). Real conditions of saturation are not so absolute; unsaturated conditions really lie between 10 and 20 percent saturation (DTN: LB0207REVUZPRP.002 [DIRS 159672]), and fully saturated conditions do not consider the lithophysae to be filled with water.

The Yucca Mountain Project assessed the thermal conductivity of the potential repository horizon for spatial variability and uncertainty of thermal conductivity in the host horizon (BSC 2004 [DIRS 169854], Table 7-10). Table C-1 presents the properties taken from that report for the rock units near the repository horizon.

Table C-1. Summary of Primary Thermal Conductivity Statistics

Stratigraphic Unit	Bulk Dry Rock Mass Thermal Conductivity (W/m·K)	Bulk Wet Rock Mass Thermal Conductivity (W/m·K)	Matrix Porosity	Lithophysal Porosity	Dry Bulk Density (kg/m^3)	Specific Heat Capacity of Solids J/(kg·K)[2]
	k_{rm}[1]	k_{rm}[1]	ϕ_m[1]	ϕ_l[1]	ρ_{bd}[1]	C_p
Tptpul	1.18	1.77	0.17	0.12	1830	934
Tptpmn	1.42	2.07	0.13	0.03	2150	932
Tptpll	1.28	1.89	0.15	0.09	1980	933
Tptpln	1.49	2.13	0.11	0.03	2210	933

Sources: [1]BSC 2004 [DIRS 169854], Table 7-10.
[2]DTN:SN0307T0510902.003 [DIRS 164196].

NOTE: Porosity is the ratio of void volume to total rock volume, and has units of m^3 void/m^3 rock.

The volume heat capacity of water (C_{vw}) is calculated for saturated water at 62°C by multiplying the density of water (kg/m^3) to the specific heat of water (J/kg·K) (Incropera and DeWitt 2002 [DIRS 163337], pp. 58 and 59). Such that:

$$C_{vw} = C_P \cdot \rho \qquad \text{(Eq. C-10)}$$

where

ρ density of water ($1/v_f$) 982.3 (kg/m^3)
C_p specific heat capacity 4186 J/kg·K
(Incropera and DeWitt 2002 [DIRS 163337], p. 924, Table A.6)

The grain density of solids can be calculated from the dry bulk density (ρ_{bd}) and the porosities of the matrix and lithophysae using the following equation from *Thermal Conductivity of the Potential Repository Horizon Model Report* (BSC 2004 [DIRS 169854], p. 41, Equation 6-4):

$$\rho_{bd} = (1-\phi_l)(1-\phi_m)\rho_g \qquad \text{(Eq. C-11)}$$

Solving for the grain density of solids:

$$\rho_g = \frac{\rho_{bd}}{(1-\phi_l)(1-\phi_m)} \qquad \text{(Eq. C-12)}$$

After plugging in the required values into Equation C-9 and solving for C_{rock}, the thermal diffusivity can be calculated by combining Equation C-3 with Equation C-10:

$$\alpha = \frac{k}{C_{rock}} \quad \text{(Eq. C-13)}$$

Note: The units of watts are converted to joules (W=J/s), and then seconds converted to years, since Δt is in terms of years.

Table C-2 contains all of the values calculated using the values presented in Table C-1, and Equation C-10 through Equation C-13, which were then used in the heat transfer explicit finite difference calculation.

Table C-2. Summary of Volumetric Heat Capacity and Thermal Diffusivity Calculations

Stratigraphic Unit	Grain Density of Solids (kg/m^3)	Dry Volumetric Heat Capacity (J/(m^3·K)	Wet Volumetric Heat Capacity (J/(m^3·K)	Dry Thermal Diffusivity (m^2/yr)	Wet Thermal Diffusivity (m^2/yr)
	ρ_g	C_{rock}	C_{rock}	α	α
Tptpul	2504	1709220.0	2335595.2	21.84	23.98
Tptpmn	2532	2003800	2528980	22.35	25.88
Tptpll	2551	1847340	2414589	21.84	24.69
Tptpln	2548	2061930	2491536	22.80	26.98

NOTE: Calculated in various spreadsheets (see Appendix E).

C2. HEAT FLOW MODEL UNCERTAINTY ANALYSIS OF PEAK TEMPERATURE IN THE ROCK MASS AT A DISTANCE OF 10 M

The generation of system moments allows a determination of the relative importance of each component variable by examining the magnitude of its partial derivative. Hahn and Shapiro (1967 [DIRS 146529], p. 229) provide an expression for the mean system performance (for example the maximum temperature at a radius of 10 m from the drift with magma) through the expression under the assumption that the parameters are independent for the composite model:

$$E(z) = h((E(x_1), E(x_2), ...E(x_n)) + \frac{1}{2} \cdot \sum_{i=1}^{n} \frac{\partial^2 h}{\partial x_i^2} \cdot Var(x_i) \quad \text{(Eq. C-14)}$$

where

- $E(z)$ = Expectation for the System Performance
- $E(x_i)$ = Expectation of the Component Variables
- $x_i ... x_n$ = Component Variables
- $h()$ = Functional relationship between the component variables and the system performance

Hahn and Shapiro (1967 [DIRS 146529], p. 231) present the following relationship for the variance in which the higher order moments are not used:

$$Var(z) = \sum_{i=1}^{n} \left(\frac{\partial h}{\partial x_i} \right)^2 \cdot Var(x_i) \qquad \text{(Eq. C-15)}$$

This relation is frequently a satisfactory approximation to calculating the variance for independent parameters.

The peak temperature at a radius of 10 m for the constant heat content process depends on the rock mass thermal conductivity and thermal diffusivity that in turn depend on the solids thermal conductivity; the solids specific heat capacity; the solids grain density; the matrix porosity; the matrix saturation; and the lithophysal porosity. This set of parameters is taken as the independent set of parameters.

Table C-3 presents the evaluation of the system variance. The values for mean and standard deviation were obtained from *Ventilation Model and Analysis Report* (BSC 2004 [DIRS 169862], Section 6.11).

Table C-3. Sensitivity of Uncertainty in Input Parameters (with Standard Deviation for Use in Delta Method)

Input/Design Parameter	Mean Value	Standard Deviation	Rock Mass Thermal Conductivity[a]		Rock Mass Thermal Diffusivity[a]		Peak Temperature[a]			Percent Contribution[a]
			Plus	Minus	Plus	Minus	Plus	Minus	Variance	
Solids Thermal Conductivity (W/(m·K)	2.603	0.3413	2.02	1.62	26.68	21.48	78.17	78.12	5.55E-04	0%
Solids Grain Density (kg/m^3)	2593	138	1.82	1.82	23.14	25.16	78.13	78.15	8.54E-05	0%
Solids Specific Heat Capacity (J/(kg·K)	930	170	1.82	1.82	21.09	28.15	78.11	78.16	4.50E-04	0%
Matrix Porosity	14.86%	3.40%	1.74	1.91	22.59	25.79	78.13	78.16	2.08E-04	0%
Matrix Saturation	90.50%	10%	1.89	1.76	24.39	23.82	78.14	78.14	5.91E-06	0%
Lithophysal Porosity	8.83%	5.40%	1.72	1.93	24.13	24.09	78.14	78.14	1.92E-08	0%
Initial Temperature*	1150	35.51	1.82	1.82	24.11	24.11	73.23	79.04	2.81	100%
								Sum	2.81	100%
								Standard Deviation	1.68	

[a] Calculated in *Heat Conduction – Uncertainty Analysis.xls* in "heat.zip" (see Appendix E).

The Method of Moments provides information as to the source of uncertainty from the individual variables. In Equation C-13, the variance of each individual variable x_i is multiplied by the square of the derivative of the system function for that parameter. The square of the derivative represents the sensitivity of the system variance to the individual parameter. If the sensitivity, and the variance to an individual parameter are large, then the system variance is dominated by this contribution. Conversely, if the sensitivity, and the variance to an individual parameter are small, then the system variance is not influenced by this individual contribution.

Table C-3 represents the results of the analysis using the method of generating system moments. The analysis is performed by calculating the first order partial derivatives of temperature to the solids thermal conductivity (k_s); the solids specific heat capacity (C_p); the solids grain density (ρ_g); matrix porosity (ϕ_m); the matrix saturation (S_m); and the lithophysal porosity (ϕ_l). Each component is perturbed from its mean value by plus or minus one standard deviation while the other components are evaluated at their mean value. The rock mass thermal conductivity and the thermal diffusivity are then calculated based upon the relations for thermal conductivity and thermal diffusivity presented previously. The finite difference calculations are then performed and the peak temperature at a radius of 10 m is evaluated for the parameters. The first order partial derivatives are approximated for the mean values plus or minus one standard deviation for each component and then substituted into Equations C-14.

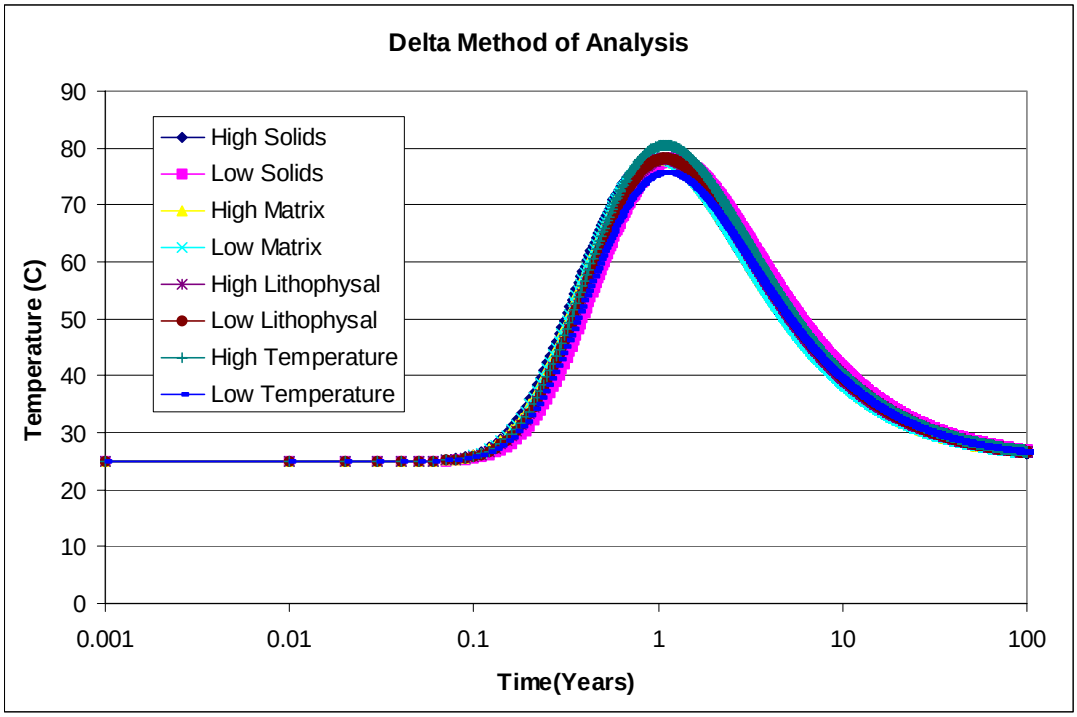

Figure C-1. Peak Temperatures for Variations in Key Inputs

Figure C-1 shows that variations in key inputs other than initial temperature result in a shift in the time when the peak temperature occurs, but the actual peak temperature remains the same.

The contributions to variance are then calculated for each component as the product of the sensitivity time the variance. The contributions are then summed. The analysis provides information on the percent contributions to system variance from each of the component variables. The analysis suggests that the principal source of uncertainty is the initial temperature (100 percent of the uncertainty). The variance caused by the uncertainty of the initial temperature should be used as the uncertainty of the output temperatures, which is ±3°C.

INTENTIONALLY LEFT BLANK

APPENDIX D

ALTERNATIVE ANALYTICAL SOLUTION TO HEAT FLOW

APPENDIX D
ALTERNATIVE ANALYTICAL SOLUTION TO HEAT FLOW

D1. DEFINITION OF THE PROBLEM

Consider a drift 5.5 m in diameter and 637-m long created in tuff at a depth of 300 m below the surface and where the ambient tuff temperature is 30°C. If that drift were to be instantaneously filled with basaltic magma at a temperature of 1150°C, the tuff surrounding the drift would begin to heat up as the magma cooled. The temperature profile through the drift and surrounding rock evolves with time.

Analysis of energy conservation can only provide exact solutions for thermal evolution when simplifying assumptions are made about the effects of dimensionality, latent heat, and contrasting thermal properties. These simplifying assumptions are necessary to make analytical solutions bear any resemblance to the problem, but the results must be regarded as approximate.

The analytical theory described below derives a solution first in Cartesian coordinates, treating the drift as a slab, and then in cylindrical coordinates, treating the drift as an infinitely long cylinder. Because solutions for the effects of latent heat are only valid for cooling times up to the point of complete solidification of the magma, late-time solutions must employ an approximate solution mated to the early time solution. To these results are added the effects of contrasting thermal properties between the magma and tuff.

Calculations based on these solutions were performed in the Microsoft Excel™ 2000 (SP 3) spreadsheet file: *Analytical Solutions of Heat Flow.xls*, which is documented in Scientific Notebook SN-LANL-SCI-279-V1 (Gaffney 2003 [DIRS 163631], pp. 17-30) and in DTN: LA0307EG831811.001 [DIRS 166942]. These results are shown for radial distances from the drift to 40.5 m (half of the nominal spacing between parallel drifts) and are discussed and shown in Figure D-1 through Figure D-6.

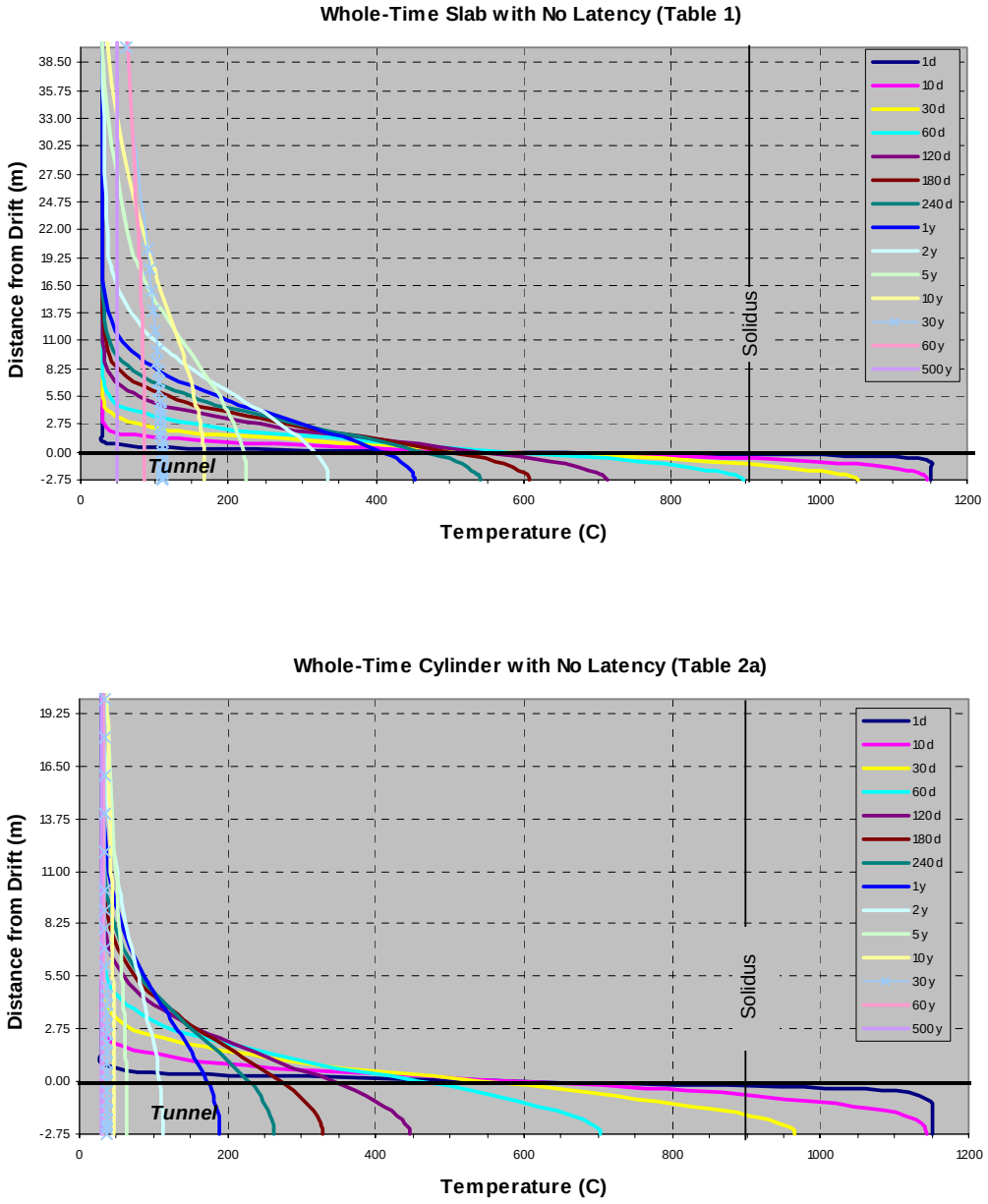

DTN: LA0307EG831811.001 [DIRS 166942], Tables 1 and 2a, Charts 1 and 2.

Source: Output Data Plots.

NOTES: Calculations are for a drift in tuff at an initial temperature of 30°C and filled with basaltic magma at an initial temperature of 1150°C. This whole-time solution does not account for thermal property contrasts and the effects of latent heat.

Figure D-1. Plot of Calculated Temperature Profiles for Various Cooling Times Comparing Results for a 1-D Slab-Like Geometry (upper plot) With Results for a 2-D Cylindrical Drift Geometry (lower plot)

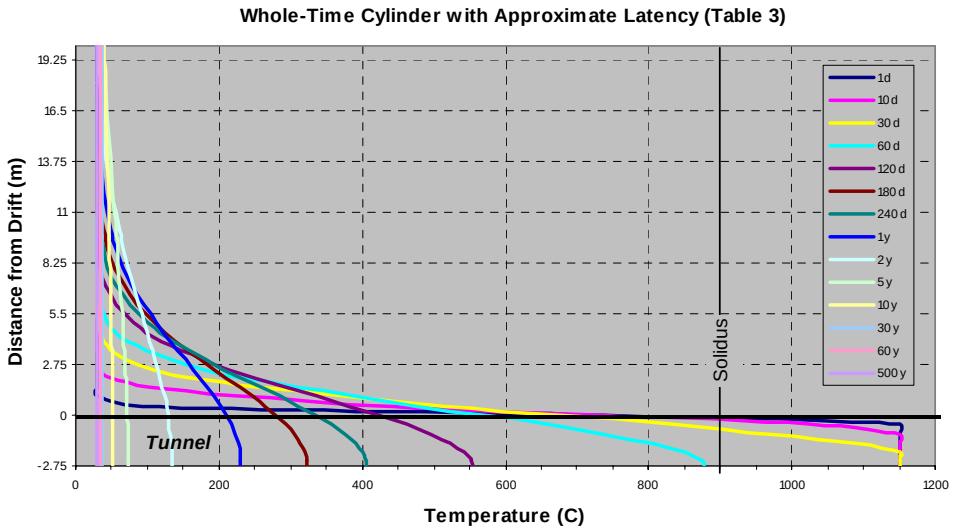

DTN: LA0307EG831811.001 [DIRS 166942], Table 3, Chart 3.

Source: Output Data Plots.

Figure D-2. Plot of Calculated Whole-Time Temperature Profiles for Various Cooling Times Assuming a Cylindrical Drift Geometry and Showing the Approximate Effect of Latent Heat

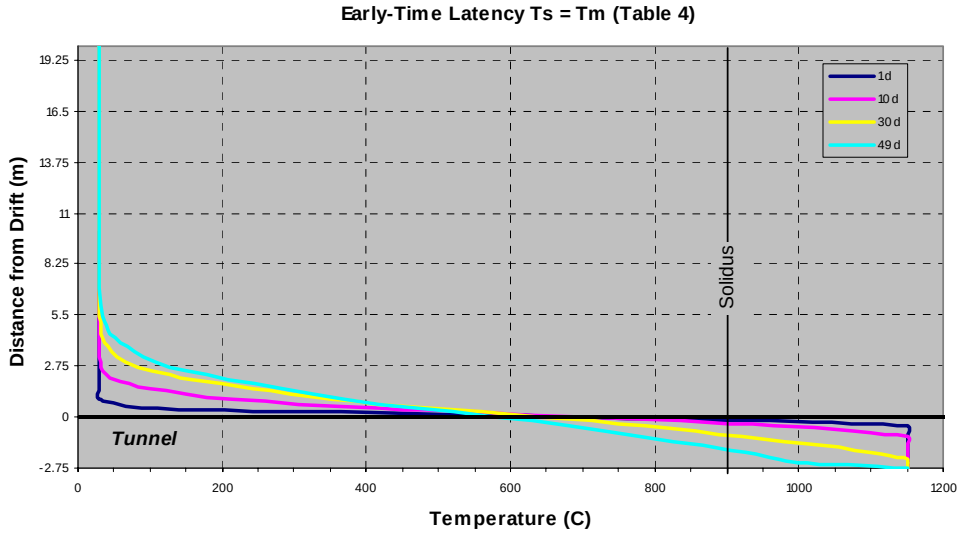

DTN: LA0307EG831811.001 [DIRS 166942], Table 4, Chart 4.

Source: Output Data Plots.

NOTES: These calculations are valid only for early times when the temperature of the magma at the drift center is above the assumed solidus at 900°C.

Figure D-3. Plot of Calculated Temperature Profiles for Various Cooling Times with Latency Modeled as Occurring at a Specific Temperature (Ts = Tm)

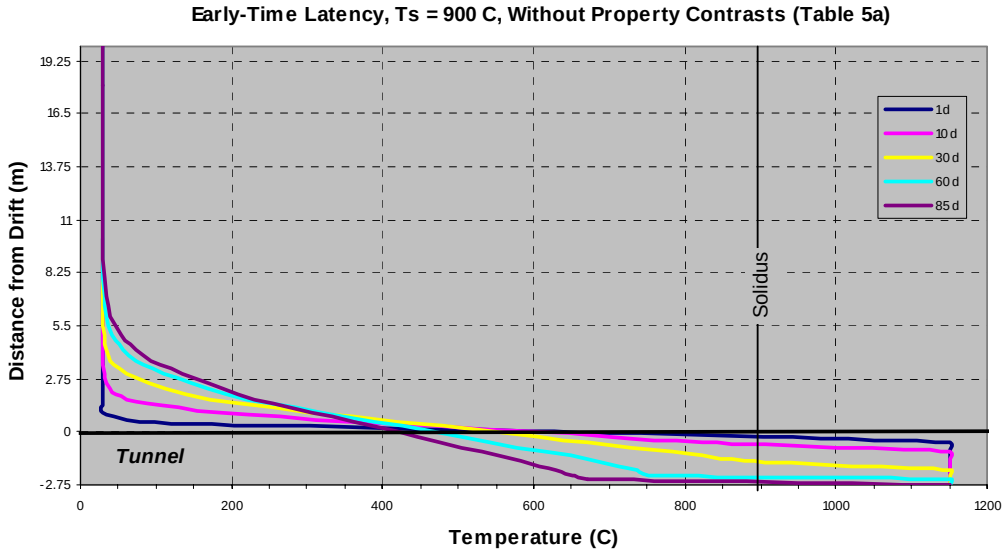

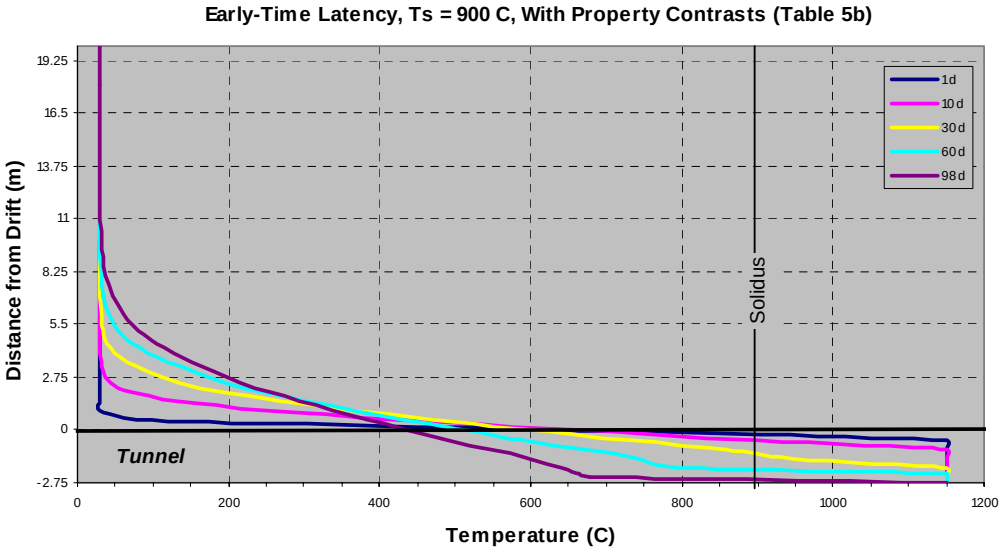

DTN: LA0307EG831811.001 [DIRS 166942], Tables 5a and 5b, Charts 5 and 6.

Source: Output Data Plots.

NOTES: These calculations are valid only for early times when the temperature of the magma at the drift center is above the assumed solidus at 900°C.

Figure D-4. Plot of Calculated Temperature Profiles for Various Cooling Times With Latent Heat, Calculated for T_s = 900°C and for the Cases With (lower panel) and Without (upper panel) Property Contrasts Between Magma and Tuff

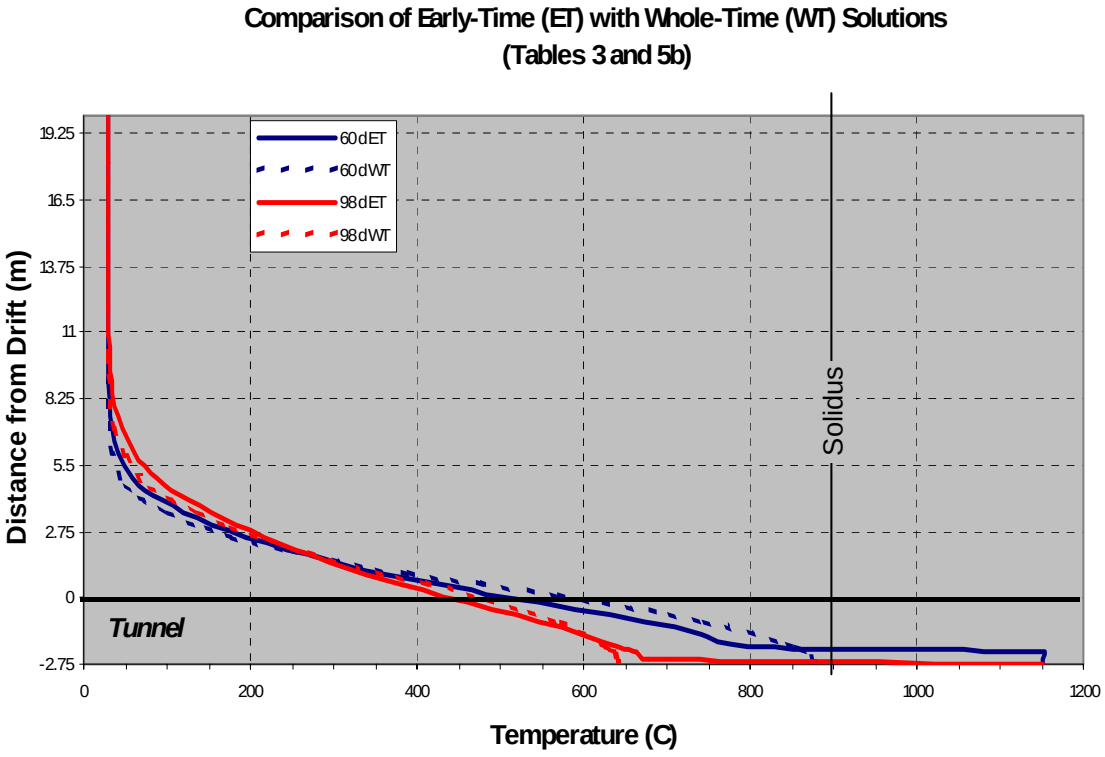

DTN: LA0307EG831811.001 [DIRS 166942], Tables 3 and 5b, Chart 7.

Source: Output Data Plots.

NOTE: Dashed curves are the whole-time solutions from Figure D-2; solid curves are early-time solutions from Figure D-4.

Figure D-5. Plot of Calculated Temperature Profiles at 60 and 99 Days Comparing the Whole-Time Solutions with Early-Time Solutions

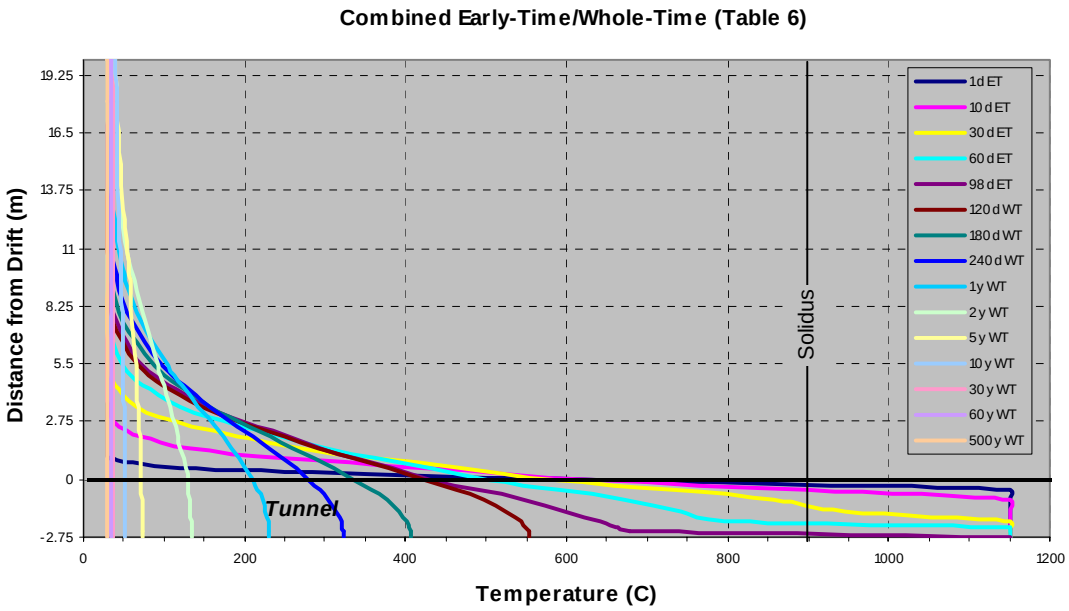

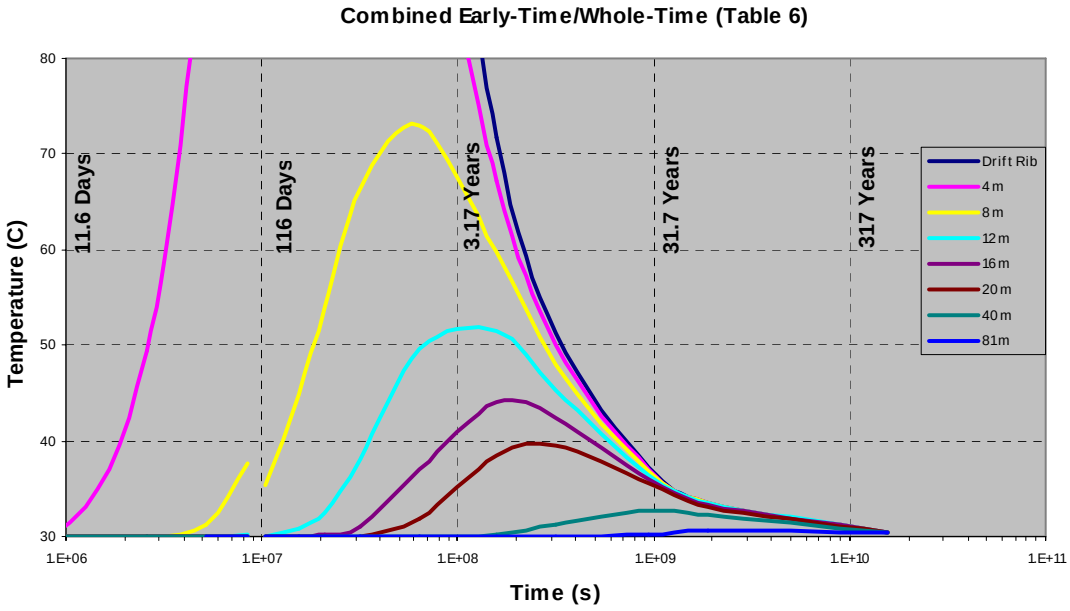

DTN: LA0307EG831811.001 [DIRS 166942], Table 6, Chart 8.

Source: Output data plots.

Figure D-6. Whole-Time Solution Combining the Results for Early-Time Latency (Turcotte and Schubert (1982 [DIRS 139651, pp. 168 to 170]) With Those Late-Time Results Calculated by the Modified Method of Delaney (1987 [DIRS 102776])

D2. MATERIAL PROPERTY INPUTS

For the Yucca Mountain Project problem, the thermal properties shown in Table D-1 are applied, and an initial tuff temperature of 30°C without any thermal gradient is assumed. Although values are given for density (ρ), specific heat (c), and thermal conductivity (k), those properties always appear in the solutions in combination in the form of the thermal diffusivity ($\kappa = k/\rho c$). Further, for the simplest solutions presented, it is assumed that the diffusivities of the magma and the host rock are equal with a value of the mean diffusivity of the two rocks used by the Igneous Consequences Peer Review Panel in their final report (Detournay et al. 2003 [DIRS 169660]). The Panel's sources for these numbers are given in Table 4-1. For more detailed solutions presented, thermal property contrasts between the magma and the tuff are included, and these set the diffusivities of the magma and tuff to 0.3×10^{-6} m^2 s^{-1} and 0.7×10^{-6} m^2 s^{-1}, respectively.

The other property inputs affecting the results of this section are the temperatures of the magma and the host rock and the latent heat of solidification of the magma. The magma temperature used is a round number that is about 0.3 percent above the value listed for a magma with 0.5 percent water in *Characterize Eruptive Processes at Yucca Mountain, Nevada* (BSC 2004 [DIRS 169980]. The host rock temperature is a round number close to room temperature. The net result of these two round-number approximations will be less than 2 percent at early times, and the percentage error will decrease with time. The latent heat of solidification is the value used by the Igneous Consequences Peer Review Panel, their source is listed in Table 4-1.

Table D-1. Thermal Properties of Magma and Tuff

Property	Value
Magma	
Temperature, T_m	1150°C
Latent heat, Λ	350 kJ/kg
Tuff	
Temperature, T	30°C
Average	
Thermal diffusivity, κ	0.5×10^{-6} m^2 s^{-1}

Source: Detournay et al. 2003 [DIRS 169660], Table 1-2 (latent heat and thermal diffusivity).

The solutions given below are sensitive to magma temperature; an approximately 10 percent variation in T_m produces a 10 percent variation in T near the magma-tuff contact for cooling times up to 1 year but falling to ~3 percent after 30 years. The solutions are less sensitive to diffusivity, with a 10 percent variation in κ producing only ~1 to ~6 percent change in T near the magma-tuff contact during the first year or so of cooling.

D3. DERIVATION OF EQUATIONS

One-Dimensional Cartesian Equations–Assuming that the magma is emplaced in the drift instantaneously and that it experiences no further movement nor loss or gain of mass, the cooling and heat transfer is governed by the conservation of energy:

$$\frac{\partial T}{\partial t} = \nabla \cdot (\kappa \nabla T) - \mathbf{u} \cdot \nabla T + q \qquad \text{(Eq. D-1)}$$

where:

T = temperature
t = time
κ = thermal diffusivity
u = the magma convective velocity vector
q = represents heat sources and sinks.

This equation describes the change of temperature with time (left-hand side), with the right-hand side summing the effects of thermal conductivity (first term) and thermal convection (second term) with heat sources and sinks (third term). Given the height of the drift as 5.5 m, one may show by consideration of the magnitude of the thermal Rayleigh number that magma convection will not occur within the drift. No heat sinks or sources other than the latent heat of magma crystallization are considered.

To start the analysis, any latent heat released during magma crystallization is ignored and there are no thermal property contrasts between the magma and tuff. First, consider the case for 1-D Cartesian coordinates, such that the drift is represented by a slab of a finite thickness but of infinite length and width. These simplifications allow a 1-D expression of Equation D-1 as:

$$\frac{\partial T}{\partial t} = \kappa \frac{\partial^2 T}{\partial x^2} \qquad \text{(Eq. D-2)}$$

for which x represents distance measured perpendicular to the surface of the slab. An analytical solution of Equation D-2 for geological systems has most commonly been achieved by using self-similarity solutions (Carslaw and Jaeger 1959 [DIRS 100968]) in which temperature is expressed non-dimensionally as θ:

$$\theta = \frac{T - T_0}{T_m - T_0} \qquad \text{(Eq. D-3)}$$

for which subscripts m and 0 refer to the initial temperature of the magma and tuff, respectively. A single similarity variable, η, that combines both temporal and spatial effects can be defined as the ratio of distance to twice the characteristic thermal diffusion distance:

$$\eta = \frac{x}{2\sqrt{\kappa t}} \qquad \text{(Eq. D-4)}$$

Rewriting Equation D-2 using non-dimensional temperature, θ, and the similarity variable, η, requires the derivation of θ with respect to t and x in terms of η and reduces Equation D-2 from a partial differential equation to an ordinary differential equation:

$$-\eta\left[\frac{d\theta}{d\eta}\right]=\frac{1}{2}\frac{d^2\theta}{d\eta^2} \qquad \text{(Eq. D-5)}$$

To solve Equation D-5, one may define a variable $\varphi = d\theta/d\eta$ so that the equation becomes:

$$-\eta d\eta=\frac{1}{2}\frac{d\varphi}{\varphi} \qquad \text{(Eq. D-6)}$$

With integration and exponentiation of Equation D-6, one can show:

$$\frac{d\theta}{d\eta}=ce^{-\eta^2} \qquad \text{(Eq. D-7)}$$

in which c is a constant of integration. Considering the boundary between a magma and rock where $\eta = 0$ and $\theta(0) \equiv 1/2$, integration of Equation D-7 yields:

$$\theta=c\int_0^{\eta}e^{-n^2}dn+1/2 \quad \text{and} \quad \theta=c\int_{-\eta}^{0}e^{-n^2}dn-1/2, \qquad \text{(Eq. D-8)}$$

for which n is an arbitrary integration variable. For the boundary condition $\theta(\infty) = 0$:

$$0=c\int_0^{\infty}e^{-n^2}dn+1/2 \qquad \text{(Eq. D-9a)}$$

and for $\theta(-\infty) = 0$:

$$0=c\int_{-\infty}^{0}e^{-n^2}dn-1/2\,. \qquad \text{(Eq. D-9b)}$$

For $n \geq 0$, the definite integral in Equation D-9a is equal to $\pi^{1/2}/2$, and the constant $c = -(2/\pi^{1/2})/2$, so that:

$$\theta=1/2-\left(\frac{1}{2}\right)\frac{2}{\sqrt{\pi}}\int_0^{\eta}e^{-z^2}dz=1/2-\left(\frac{1}{2}\right)\mathrm{erf}(\eta)=\left(\frac{1}{2}\right)\left[1-\mathrm{erf}\left(\frac{x}{2\sqrt{\kappa t}}\right)\right] \qquad \text{(Eq. D-10a)}$$

For $n \leq 0$, $c = (2/\pi^{1/2})/2$ and recalling that $\mathrm{erf}(-\eta) = -\mathrm{erf}(\eta)$, the solution is:

$$\theta=-1/2+\left(\frac{1}{2}\right)\frac{2}{\sqrt{\pi}}\int_{-\eta}^{0}e^{-n^2}dz=-1/2-\left(\frac{1}{2}\right)\mathrm{erf}(-\eta)=\left(\frac{1}{2}\right)\left[\mathrm{erf}\left(\frac{x}{2\sqrt{\kappa t}}\right)-1\right] \qquad \text{(Eq. D-10b)}$$

Jaeger (1968 [DIRS 163630], p. 54) defines a problem for cooling of a sheet-like magma body of thickness 2*a*, intruded beneath deep cover, for which the *x*-axis origin is defined at the center of the sheet. For this problem, θ must be evaluated away from both surfaces of the sheet (*x*-*a* and *x*+*a*), and because the solution of Equations D-10a and D-10b are linear, they can be summed:

$$\theta = \frac{1}{2}\left[1 - \operatorname{erf}\left(\frac{x-a}{2\sqrt{\kappa t}}\right)\right] + \frac{1}{2}\left[\operatorname{erf}\left(\frac{x+a}{2\sqrt{\kappa t}}\right) - 1\right] = \frac{1}{2}\left[\operatorname{erf}\left(\frac{x+a}{2\sqrt{\kappa t}}\right) - \operatorname{erf}\left(\frac{x-a}{2\sqrt{\kappa t}}\right)\right] \quad \text{(Eq. D-11)}$$

The above equations are valid only in a one-dimensional Cartesian system, which will provide a good temperature solution for the case of a sill, but which is not adequate for the roughly cylindrical geometry of a magma-filled drift.

One-Dimensional Cylindrical Equations--This section derives the analysis for a drift of circular cross-section and finite length. Consider the 3-D form of Equation D-2, expressed in Cartesian coordinates:

$$\frac{\partial T}{\partial t} = \kappa\left(\frac{\partial^2 T}{\partial x^2} + \frac{\partial^2 T}{\partial y^2} + \frac{\partial^2 T}{\partial z^2}\right). \quad \text{(Eq. D-12)}$$

Carslaw and Jaeger (1959 [DIRS 100968], p. 56, Section 2.2(10)) show that the solution to Equation D-12 is similar to Equation D-11, but with added terms for the extra dimensions:

$$\theta = \left[\frac{1}{2}\left(\operatorname{erf}\frac{x+a}{2\sqrt{\kappa t}} - \operatorname{erf}\frac{x-a}{2\sqrt{\kappa t}}\right)\right]\left[\frac{1}{2}\left(\operatorname{erf}\frac{y+b}{2\sqrt{\kappa t}} - \operatorname{erf}\frac{y-b}{2\sqrt{\kappa t}}\right)\right]\left[\frac{1}{2}\left(\operatorname{erf}\frac{z+c}{2\sqrt{\kappa t}} - \operatorname{erf}\frac{z-c}{2\sqrt{\kappa t}}\right)\right] \quad \text{(Eq. D-13)}$$

for which

a = the half-height
b = the half-width
c = the half-length of the drift.

The drift cross-section is best represented as a circle. Because in 3-D the drift is a cylinder, Equation D-12 can be simplified by using cylindrical coordinates with radial distance, *r*, azimuth ϕ, and length, *z*:

$$\frac{\partial T}{\partial t} = \kappa\left(\frac{\partial^2 T}{\partial r^2} + \frac{1}{r}\frac{\partial T}{\partial r} + \frac{1}{r^2}\frac{\partial^2 T}{\partial \phi^2} + \frac{\partial^2 T}{\partial z^2}\right) \quad \text{(Eq. D-14)}$$

Assuming that magma temperature within the drift is homogeneous with azimuth then $\partial^2 T/\partial \phi^2 = 0$. Because the drift half-length *c* is more than 100 times greater than its radius *a*, $\partial^2 T/\partial z^2$ vanishes for radial solutions midway through the drift, where *z* = 0 at all times earlier than the *z*-coordinate diffusive time. This time can be easily determined for the value of the last term of Equation D-13, which is within 0.001 percent of unity for erf(*n*), where $n \geq \pi$. Letting $n \geq c/(2(\kappa t)^{1/2}) \geq \pi$, then $t \leq c^2/4\pi^2\kappa$ or ~200 years for *c* = 318.5 m and κ = 0.0000004 m^2/s. In

fact, even after 500 years of cooling, the z-component accounts for less than a half of percent. With this consideration, Equation D-14 is suitably expressed as:

$$\frac{\partial T}{\partial t} = \kappa\left(\frac{\partial^2 T}{\partial r^2} + \frac{\partial T}{r\partial r}\right). \quad \text{(Eq. D-15)}$$

From Carslaw and Jaeger (1959 [DIRS 100968], Section 2.2(9)), the solution of Equation D-15 is that of an infinite cylinder where ω = the cylinder radius and Carslaw and Jaeger's x-coordinate is replaced by r and their y-coordinate is set to zero ($z = 0$):

$$\theta = \frac{1}{2}\left(\operatorname{erf}\frac{r+\omega}{2\sqrt{\kappa t}} - \operatorname{erf}\frac{r-\omega}{2\sqrt{\kappa t}}\right)\left(\operatorname{erf}\frac{\omega}{2\sqrt{\kappa t}}\right) \quad \text{(Eq. D-16)}$$

The above solutions assume that no latent heat is released during magma cooling and that the magma and tuff do not display thermal property contrasts (i.e., $\kappa_m/\kappa_r = k_m/k_r = 1$), where k is thermal conductivity ($k = \rho c \kappa$), ρ is density, c is heat capacity, and subscript m and r refer to magma and tuff, respectively.

The average diffusivity, κ, is applied to the following calculations based on Equations D-11 and D-16. Results using values from Tables 1 and 2a of the spreadsheet *Analytical Solutions of Heat Flow.xls* are shown in plots of T versus x at various times (Figure D-1) for both slab-like and cylindrical geometries. The former is appropriate for dike or sill geometries; the latter is appropriate for application to drift geometry.

D4. THERMAL PROPERTY CONTRASTS AND LATENT HEAT

Addressing the issue of contrasting thermal properties between the magma and host rock, Delaney (1987 [DIRS 102776]) shows the initial contact temperature θ_{ci} as:

$$\theta_{ci} = \frac{k_m / k_t}{k_m / k_t + \sqrt{\kappa_m / \kappa_t}} \quad \text{(Eq. D-17)}$$

where the subscripts m and t refer to the magma and tuff, respectively. Using the values listed under the heading "Assumed Thermal Properties" in Gaffney (2003 [DIRS 163631], p. 17) and in DTN: LA0307EG831811.001 [DIRS 166942], then $\theta_{ci} \approx 0.54$ and the initial contact temperature is ~630°C, which is ~10°C (~7 percent) higher than that predicted by no thermal-property contrasts. One must recognize that conductivities generally rise with falling temperature; for example, at 30°C, k_m may reach 2 W m^{-1} K^{-1} or more. However, Delaney (1987 [DIRS 102776]) finds that, although thermal-property contrasts affect the maximum temperature achieved in the host rock (tuff in this case), they do not have large influence over solutions at late times. In fact, Delaney (1987 [DIRS 102776]) points out that most workers do not consider thermal-property contrasts.

The effect of latent heat (Λ) production is not negligible, but, as Delaney (1987 [DIRS 102776]) points out, there is no analytically exact method to include its effects. Assuming $\Lambda = 350$ kJ/kg,

a first approximation of its effect is to find an effective initial magma temperature T^*_m by adding to the temperature of the magma the amount Λ/c_m (Λ/c_m = 350 kJ kg^{-1}/1.2 kJ kg^{-1} K^{-1} = 292°C). Delaney (1987 [DIRS 102776]) finds that setting $T^*_m = T_m + \Lambda/c_m$ provides for adequate solutions for temperatures in host rocks at a distance of more than a quarter of a dike thickness away from the contact. Results for this consideration, documented in DTN: LA0307EG831811.001 [DIRS 166942], Table 3, are shown in Figure D-2, for which T_c is 736°C.

In Figure D-6, the upper plot shows temperatures at specific times as a function of distance from the drift, whereas the lower plot shows temperatures at specific locations as a function of time. The discontinuity at ~120 days in the curve at 8 m from the drift (yellow) is a result of combining calculation methods.

The main problem with this approximate approach for including the effect of latent heat is that temperature profiles within and near the magma-filled drift are not realistic and are too high. A more physically accurate method to account for latent heat is discussed by Turcotte and Schubert (1982 [DIRS 139651], pp. 168 to 170]). They follow the classical Stefan problem in which the cooling of a body of magma has a definite solidification temperature $T_s = T_m$. Considering a 1-D case (slab-like geometry) with magma intruded at $x < 0$, the solidification surface occurs at X_s:

$$X_s = -2\lambda\sqrt{\kappa t} \qquad \text{(Eq. D-18)}$$

for which λ is a constant to be determined. With this approach, one needs a solution that fits the conditions that $\theta = 1$ ($T = T_m = T_s$), where $x = X_s$. The solution implies that the temperature at any point, defined by η (from Equation D-12), is proportional to the position of the solidification surface defined by λ:

$$\theta = \frac{\operatorname{erfc}(\eta)}{\operatorname{erfc}(-\lambda)} \qquad \text{(Eq. D-19)}$$

For $x \le X_s$, $T = T_m$, and for $X_s < x < 0$, $T_m > T > T_t$. This solution is valid only for times at which latent heat is being released in the magma (i.e., the temperature at the hottest part of the magma, the center of the drift, is above the magma's solidus temperature).

Because $T_s = T_m$, solidification occurs immediately during cooling from T_m, releasing latent heat at a rate $\rho\Lambda(dx_m/dt)\delta_t$. Equating this rate with the rate of heat conduction by Fourier's law gives:

$$\rho\Lambda\left(\frac{dX_s}{dt}\right) = k\left(\frac{\partial T}{\partial x}\right)_{X=X_s} \qquad \text{(Eq. D-20)}$$

The derivative on the left-hand side of Equation D-28 can be found by differentiating Equation D-18:

$$\frac{dX_s}{dt} = \frac{-\lambda\sqrt{\kappa}}{\sqrt{t}}. \qquad \text{(Eq. D-21)}$$

The derivative on the right-hand side of Equation D-20 can be found by differentiating Equation D-1980:

$$\left(\frac{\partial T}{\partial x}\right)_{x=X_s} = \left(\frac{d\theta}{d\eta}\right)_{\eta=-\lambda}\left(\frac{\partial \eta}{\partial x}\right)(T_m - T_0) = \frac{-(T_m - T_0)}{2\sqrt{\kappa t}}\frac{2}{\sqrt{\pi}}\frac{e^{-\lambda^2}}{[1+erf(\lambda)]} \qquad \text{(Eq. D-22)}$$

A transcendental equation of λ is derived by substituting Equations D-21 and D-22 into Equation D-20 and recalling that $k = \rho c \kappa$:

$$\frac{\Lambda\sqrt{\pi}}{c(T_m - T_0)} = \frac{e^{-\lambda^2}}{\lambda[1+erf(\lambda)]} \qquad \text{(Eq. D-23)}$$

With Equations D-19 and D-23, temperatures in time and space can be calculated for 1-D problems that involve release of latent heat. Furthermore, Equation D-18 can be used to calculate the time for all the magma to solidify (i.e., when the solidification surface reaches the center of the slab and $X_s^2 = a^2$, where a is the slab half-thickness). The solidification time is a function of one-quarter of the area a^2:

$$t_s = \frac{a^2}{4\kappa\lambda^2} \qquad \text{(Eq. D-24)}$$

Considering cylindrical geometry, the area expressed by the term a^2 in Equation D-24 becomes $\pi a^2/4$. Replacing the Cartesian position of the solidification surface by its cylindrical equivalent, R_s, Equation D-18 becomes:

$$R_s = -4\lambda\sqrt{\kappa t/\pi} \qquad \text{(Eq. D-25)}$$

and the transcendental equation for λ is:

$$\frac{2\Lambda}{c(T_m - T_0)} = \frac{e^{-\lambda^2}}{\lambda[1+erf(\lambda)]} \qquad \text{(Eq. D-26)}$$

For given values of Λ, c, T_m, and T_0, λ can be found by iteratively calculating the right-hand side of Equation D-26 until it equals the left-hand side. For a system for which r is 0 at the contact between magma and host rock and increases towards the center of the magma body, the following solutions depend upon the value of R_s, which is a function of λ:

$$T = T_m \quad (r \geq R_s) \qquad \text{(Eq. D-27)}$$

$$T = T_c\left(1 + erf\,\frac{r}{2\sqrt{\kappa t}}\right)\left(erf\,\frac{\omega}{2\sqrt{\kappa t}}\right) \quad (R_s > r) \qquad \text{(Eq. D-28)}$$

where:

$$T_c = T_0 + \frac{(T_s - T_0)}{1 + erf\,(\lambda)} \qquad \text{(Eq. D-29)}$$

As Carslaw and Jaeger (1959 [DIRS 100968]) point out, there is no exact solution for a cylinder beyond its radius. Equation D-28 takes into account the cylindrical geometry in the same fashion as Equation D-16. As such, this solution is approximate, but comparisons of its calculated results shown in Figure D-3 (DTN: LA0307EG831811.001 [DIRS 166942]) with those shown in Figure D-2, show remarkable similarity, as will be shown later. The solutions are valid for early times when liquid magma (above its solidus) exists: T_c = 664°C and λ = 0.84. The full solidification time occurs when the solidification surface, R_s, reaches the center of the drift ($R_s(\lambda, \kappa, t)$ = 2.75 m, t_s = 49 days). This time is shorter than the ~81 days that would be predicted for a 1-D slab, using Eq. 87, which is not unexpected because of the smaller cooling surface involved with cylindrical geometry. It is interesting to note that calculated drift-center magma temperatures at this point in time are at 900°C, which is the assumed solidus temperature to be considered in the following discussions.

Because magma solidifies over a range of temperatures ($T_s < T_m$) and displays a small but finite contrast in thermal properties with tuff, one can follow the more complicated analysis of Carslaw and Jaeger (1959 [DIRS 100968]). For conditions for which the conductivity of liquid and solid magma are equal ($k_m = k_s$), the transcendental equation in λ from Carslaw and Jaeger (1959 [DIRS 100968]) can be modified for cylindrical geometry and property contrasts (Carslaw and Jaeger 1959 [DIRS 100968], Section 2.16 and Section 11.2[42]):

$$p\frac{\sqrt{\pi}(T_m - T_s)}{4T_s} = \frac{[1 - erf\,(p\lambda)]\exp[(p^2 - 1)\lambda^2]}{\zeta + erf\,(\lambda)} \qquad \text{(Eq. D-30)}$$

Equation D-30 accounts for the effects of latent heat by the variable p, which is the square-root of the ratio of diffusivities (κ) of the solid (subscript s) and liquid (subscript m). The magma diffusivity reflects the effect of a higher effective heat capacity from the addition of latent heat:

$$p = \left[\frac{\kappa_s}{k_m / \rho_m[c_m + \Lambda/(T_m - T_s)]}\right]^{1/2} \qquad \text{(Eq. D-31)}$$

The effect of property contrasts between the magma and tuff in Equation D-30 are accounted for by the variable ζ,

$$\zeta = \frac{k_m\sqrt{\kappa_r}}{k_r\sqrt{\kappa_m}} \qquad \text{(Eq. D-32)}$$

The solution temperatures are like those in Equations D-27 to D-29 and depend upon the temporal radial position of the cooling surface R_s.

$$T_c = T_0 + \frac{\zeta(T_s - T_0)}{[\zeta + erf(\lambda)]} \quad \text{(Eq. D-33)}$$

$$T = T_m \quad (r \geq R_s) \quad \text{(Eq. D-34)}$$

$$T = T_c\left(1 + \frac{1}{\zeta} erf\left(\frac{r}{2\sqrt{\kappa_m t}}\right)\right) \bullet \left(erf\left(\frac{\omega}{2\sqrt{\kappa t}}\right)\right) \quad (0 < r < R_s) \quad \text{(Eq. D-35)}$$

$$T = T_c\left(1 + erf\left(\frac{r}{2\sqrt{\kappa_t t}}\right)\right) \bullet \left(erf\left(\frac{\omega}{2\sqrt{\kappa t}}\right)\right) \quad (r < 0) \quad \text{(Eq. D-36)}$$

Again, the effect of cylindrical divergence is accounted for, as in Equation D-28. Equations D-30 to D-36 take into account latent heat being released between T_m and T_s (solidus temperature) as well as property contrasts between the magma (subscript *m*) and tuff (subscript *t*).

Assuming a solidus temperature of 900°C, the effect of $T_s < T_m$ (without property contrasts) results in a lower predicted contact temperature, T_c = 563°C, as well as a lower value of λ (0.64). If the effect of property contrasts is also calculated, then T_c rises to 600°C and λ falls to a value of 0.60. In both cases, a 50°C change in solidus temperature results in a ~16°C change in T_c.

Compared to the calculation for latent heat in which $T_s = T_m$, the effect of $T_s < T_m$ increases the length of time for complete solidification from 49 days to 85 days (without property contrasts) to 98 days (with property contrasts). Figure D-4 shows results from DTN: LA0307EG831811.001 [DIRS 166942], Table 5, for the cases in which ζ = 1 (no property contrast) and ζ = 1.19.

D5. WHOLE-TIME SOLUTIONS

Because the analytical results for latency are only valid at early times, a plot of whole-time solutions requires a combination. The whole-time calculations for approximated latency (Figure D-6 and DTN: LA0307EG831811.001 [DIRS 166942], Table 3) are valid for all times, with the caveat that they are inaccurate for temperatures in or near the magma while it is still molten. On the other hand, the early-time results shown in Figure D-4 (DTN: LA0307EG831811.001 [DIRS 166942], Table 5b are believed to be analytically more accurate. Figure D-6 shows a comparison of results for 60 and 99 days for these whole-time and early-time solutions. The comparison demonstrates that temperatures are within ~10°C for the two methods at the time when solidification is complete (99 days).

Accordingly, results as documented in DTN: LA0307EG831811.001 [DIRS 166942], Table 5b, through 99 days of calculated time are combined with those of DTN: LA0307EG831811.001 [DIRS 166942], Table 3 (120 days to 500 years) in the upper panel of Figure D-6. The lower

panel of Figure D-6 shows the evolution of temperature at specific points in space as a function of time.

D6. CONCLUSIONS

Analytical solutions for heat flow within and around a drift filled with magma and that use cylindrical symmetry, the effects of latent heat, and property contrasts, can only be approximate and, thus, must be viewed as analysis results only (Figure D-6).

Several variations of analytical solutions show slight variations in predicted thermal profiles at different cooling times for a drift filled with magma. The approximate effects of thermal properties contrasts between the magma and tuff host rock are shown to be small. In contrast, latent heat of crystallization, which cannot be exactly accounted for by analytical means, does have a significant effect; it prolongs the cooling times within the magma and causes early-time temperatures within the magma and tuff near the contact to be ~100°C hotter.

The values for the thermal properties of the magma and tuff may vary from those of newer measurements, which might differ by up to 10 percent. Calculations based on varying these properties by 10 percent (with the exception of the initial magma temperature) shows that each property varied accounts for only ~3 percent of the change in calculated temperatures.

With respect to the thermal effects on neighbor drifts (~81 m distant), a slight thermal pulse (~1°C) might be felt after 60 years of cooling. After 500 years of cooling, the magma-filled drift and surrounding tuff has cooled to within 0.5°C of the initial temperature (30°C).

APPENDIX E

INFORMATION REGARDING INPUT/OUTPUT FILES AND SPREADSHEET FILES

APPENDIX E
INFORMATION REGARDING INPUT/OUTPUT FILES AND SPREADSHEET FILES

Please note that references to this appendix (Appendix E) in the body of the report are in regard to:

- Input and output computer files for program approved software
- Spreadsheets in support of this model report and associated output DTNs (as appropriate).

These files are used, without changes, from two CDs that are contained in Attachment III of *Igneous Intrusion Impacts on Waste Packages and Waste Forms* (BSC 2004 [DIRS 168960]). The complete file listing for these CDs is contained in Attachment IV of *Igneous Intrusion Impacts on Waste Packages and Waste Forms*.

NOTE: These data have been generated under the guidance of AP-SIII.10Q during the development of *Igneous Intrusion Impacts on Waste Packages and Waste Forms* (BSC 2004 [DIRS 168960]), and were technically reviewed as an integral part of that model report.

The data have been re-evaluated for their appropriateness for use as inputs to Section 6.8, Section 8.2, Appendix B, and Appendix C of this model report.

Per the requirements of AP-SIII.10Q, the following discussion provides the justification for the use of output of a cancelled document. As discussed above, results of calculations that were performed in *Igneous Impacts on Waste packages and Waste Forms* (BSC 2004 [DIRS 168960]) were documented on two CDs that were submitted to records under accession number DOC.20040421.0002. The Responsible Manager of the Regulatory Integration - Igneous Team, canceled the document described above. Upon evaluation of the document, the decision was made that the content duplicated much of the technical scope of this model report. In addition, the technical bases and alternative models that are documented in this model report provided a more complete and in-depth discussion of the model and related consequences. One technical area that was covered in *Igneous Intrusion Impacts on Waste Packages and Waste Forms* that was not covered sufficiently in REV 00 of this model report, was the effect of interactions between the drift seepage water and the cooled basalt after intrusion. The decision was made to bring the geochemical calculations forward from *Igneous Impacts on Waste packages and Waste Forms*, and include those results as apart of the current model development presented in this document. The results of these calculations are presented in Section 6.8, in Appendix B, and in Appendix C. These calculations were evaluated to ensure that they met the requirements of the modeling that are presented in this report. The original calculations were augmented where necessary to ensure that potential geochemical conditions were addressed. These calculations were then subject to additional checking and reviews during the development process of this model report, and were deemed to be appropriate for the intended use within this document.

INTENTIONALLY LEFT BLANK

APPENDIX F
INDEPENDENT TECHNICAL REVIEW OF DIKE PROPAGATION SUBMODEL

This appendix includes the letter, with review criteria, requesting independent technical review of Dike Propagation Submodels, and the response to it by Dr. Allan Rubin. The attached letter contains an error in the designation of the version of the document that Dr. Rubin reviewed. The correct version was REV 00 ICN 01 Draft B.

BECHTEL SAIC COMPANY, LLC

JUL 02 2004

QA:N/A

RECEIVED BY BSC CCU
DATE: 07/02/2004

Allen Rubin, Professor
Department of Geosciences
Princeton University
Princeton, NJ 08544

RE: Independent Review for Model Validation of the Dike Propagation Model

Dear Dr. Rubin:

You are requested to perform a technical review of the dike propagation model as a part of the validation process to enhance confidence in the model. Model validation, as stated in the model validation procedure (AP-SIII.10Q), is the process used to establish confidence that the mathematical model (if applicable) and its technical bases adequately represent the conceptual model, system processes, and/or the phenomenon being investigated.

The models developed to represent the various aspects of repository performance or consequences of potential disruptive events are required as part of the OCRWM Quality Assurance program to have post model development validation to ensure they are applicable for their intended use. In general these models will be an integral part of demonstrating system performance and compliance with the regulatory requirements set forth by the Nuclear Regulatory Commission for licensing a repository at Yucca Mountain. Model validation can be done in a number of ways. The Administrative Procedure on models (AP-SIII.10Q) identifies a number of methods for validating models that range from simple documentation to peer review. For the dike propagation model, the *Technical Work Plan -- Igneous Activity Analysis for Disruptive Events* (TWP-WIS-MD-0000071), Rev 05 (draft) identifies the post development method to achieve the desired level of model validation (Level II):

1. "Technical review, planned in the applicable TWP, by reviewers independent of the development, checking, and interdisciplinary review of the model documentation (the Originator, Responsible Manager/Lead, Checker, QER, and interdisciplinary reviewers assigned to the model document/activity may not serve as an independent post-development model validation technical reviewer) (Section 5.4.1(c)(5))."

The TWP states that the conceptual model, developed specifically for the Yucca Mountain Project, will be validated under SIII.10Q to develop confidence in its intended use. The draft model report (*Dike Drift Interactions*, Rev 02) describes the conceptual and mathematical model for dike propagation. You are requested to perform an independent review on the application of this model to modeling the dike propagation processes for the Yucca Mountain Project. The intended use of the model is to describe the propagation of a dike through rhyolitic tuff in the vicinity of Yucca Mountain assuming an igneous event occurs.

JUL 02 2004

Log# 0701042226
Page 2

The criteria for your independent review are as follows:

1. Is the conceptual model reasonable and appropriate for its intended use
2. Are the mathematical relationships appropriate and representative of the scientific understanding of fracture/dike propagation
3. Are the outputs of the model reasonable and representative
4. Are limitations of the model adequately described
5. Are there other alternative models or approaches that should be considered.

Your response (memo or letter report) should explicitly address these criteria.

The relevant parts of the *Dike Drift Interactions* Rev. 02 model report will be sent to you separately. Please initiate your review upon receipt of that material. Your response is expected to be available no later than July 8, 2004, so that we may incorporate your comments and the originator's response into the model report prior to its scheduled Project review.

Your independent technical review is an important component to the validation process for developing confidence in the use of the ash redistribution conceptual model. Your Comments (letter reports or memos) from this review will become a part of the validation process consistent with SIII.10Q.

Should you have any questions, please direct your comments me (mike_cline@ymp.gov or 702 295-4899) or Ed Gaffney (edgaffney@earthlink.net, or 712 527-4527).

Your support is greatly appreciated

Sincerely,

K. Michael Cline, Team Lead
Igneous Regulatory Integration Team

July 2, 2004
Date Signed

MC:glm - 0701042226

cc. Edward Gaffney, Las Vegas
William Hackett, Las Vegas

Technical Review of "Dike/Drift Interactions", MDL-MGR-GS-000005 REV 00B ICN 01

Allan Rubin

July 9, 2004

Some general comments:

The draft was well-written and easy to read. Thank you.

I found the boundaries between some of the five "criteria for independent review" to be somewhat subjective. I have chosen a particular breakdown in this review, but mostly I aimed for completeness without worrying too much about which comments fell under which category.

1. *Is the conceptual model reasonable and appropriate for its intended use?* Section 6.1 states: "The development of a comprehensive list of features, events, and processes, potentially relevant to postclosure performance of the potential Yucca Mountain repository is an ongoing, iterative process based on site-specific information, design, and regulations". To "site-specific information, design, and regulations" I would add something to the effect of "the collective imagination of the people thinking about such processes". At least for Igneous Events, for example, it is not feasible to generate an all-encompassing model based on first principles that would produce all classes of possible outcomes if it were run with a wide enough range of initial conditions. Therefore the mode of operation is to imagine the event first and only then then to design software, with suitable approximations, to investigate it. Because the approximations are usually very specific to the event under consideration, it is unlikely that a new "potential event" will first attract attention as a result of model calculations. They must be imagined first. This means that a conceptual model that appears to be "comprehensive" must be understood as "comprehensive" in the limited sense of pertaining to all those processes that have been imagined thus far.

With the above caveat, I find the conceptual model here to be reasonable and appropriate for its intended use. By "conceptual model" I mean the combination of the particular model of dike propagation discussed at length in this document, and the idea that dike/drift interaction can be understood by first modeling dike propagation in the absence of a repository and then using the output of those models as input into a first generation of dike/drift

interacton models. One other caveat: By necessity many simplifications are made in the specific dike propagation calculation, some of them possibly rather severe (neglect of magma compressibility, magma freezing, inelastic deformation of the host rock, etc.). This is required to make the models tractable numerically and because our understanding of some of these processes is quite limited. Nonetheless, enough approximations are made that I think one could legitimately ask what the point of the calculations is. The proper response, I think, is that the goal is not the faithful numerical reproduction of dike propagation in the pre-repository environment, but to understand in a general sense what would happen if a dike intersected the repository. But the dike/drift interaction models that will be used to develop this understanding were not discussed in this document. So I find myself reviewing a model of dike propagation whose main purpose is to be used as input into a model that I cannot evaluate. In a strict sense that makes it difficult to evaluate the assumptions made in the dike propagation model. I have to imagine how the output will be used.

Details:

TSPA-LA FEP 1.2.04.03 in Table 6-1 would be more complete if it included the possibility of intrusion along a bedding plane that cuts the drifts. From analog examples this strikes me as more likely than a horizontal sill in the plane of the drifts.

In describing the dike propagation model it is stated (Table 6-1): "The output of this model provides the support for a conceptual dike propagation model that precludes development of a conduit extending from the original point of intersection to encompass the entire length of the drift (forming a "dog-leg"),...". I did not see this claim ("dog-leg is precluded") justified anywhere in the document.

2. *Are the mathematical relationships appropriate and representative of the scientific understanding of fracture/dike propagation?* I have chosen to put my evaluation of the main model assumptions here. In general I would answer "yes" to this question. Many of the comments below provide an alternate or in my view more accurate justification for the adopted assumptions, without calling into question the suitableness of that assumption. One exception might be the neglect of inelastic deformation as it pertains to the dike tip reaching the surface before the magma reaches the repository (again, whether this is important depends upon the dike/drift interaction model, which I have not seen).

The numbers below correspond to those used in: 6.3.2 Assumptions and Simplifications.

1) It is true that from the standpoint of the fluid flow the 2-D elasticity/1-D flow model becomes more appropriate as the along-strike length of the dike decreases. But from the standpoint of elasticity this model becomes *less* appropriate as the strike length decreases, because the plane of the model cross-section is vertical. From the standpoint of elasticity the 2-D elasticity/1-D flow model should be appropriate provided the along-strike length is greater than the length scale l^* defined in this document. This is discussed briefly in Appendix 4.1 of the Final Report of the Igneous Consequences Peer Review Panel (ICPRPFR).

Also, I know of no field observations supporting the claim that the limited lateral extent of dikes in this environment is "probably due to cumulative inelastic effects as the dike intersects more joints, faults, and other discontinuities and inhomogeneities" (see also the last paragraph of section 6.3). If the magma is everywhere "effectively" buoyant ($\rho_m g < dS_h/dz$), the lateral extent can be much less than the vertical extent because the pressure gradient for vertical flow exceeds that for lateral flow (provided the lateral extent is at least as large as l^*). But this explanation is not feasible if you think the least horizontal stress S_h is controlled by the frictional strength of normal faults down to depths of 10 or more kilometers, where volatile exsolution is unlikely to reduce the magma density significantly.

2) Adding magma compressibility would change the pressure profiles in the dikes noticeably, but if the ultimate goal is a qualitative statement along the lines of "the maximum magma pressure is at most 1 MPa larger [I might say 'a few MPa larger'] than the horizontal far-field stress at the given depth" (Section 6-3, p. 30), then neglecting compressibility is probably justifiable. Compressibility might be most important in how it contributes to the statement that the pressure in the tip cavity is near atmospheric (Section 60-3, p. 33), a claim that is repeated here from the ICPRPFR.

3) (see also Section 6 p. 2 PP 2, and 5.1 p. 5-10. Assumption 3): "Linear-elastic behavior would be a conservative assumption because anelastic behavior would serve to increase dike widths and reduce pressures at the repository". I think this statement is untrue, or at least an oversimplification. The actual outcome very likely depends upon the assumed boundary conditions, but take the case of a constant flux from a deep source and accept the notion that anelasticity at the repository level acts to increase the dike thickness locally. If the dike source is deep enough, the excess pressure is tied to the local confining pressure over most of the dike height and changes in thickness at shallow depth don't affect the flux significantly. Under these conditions, widening at shallow depth leads to lower flow velocities and smaller pressure drops. Because the magma pressure is tied to the host rock stress at greater depth, a smaller viscous pressure drop leads to larger pressures at the repository. Of course, I base this scenario only on my intuition, and the story is more complicated because of the coupling between elasticity and fluid flow (l^* would likely decrease somewhat, for example). But I'm guessing that the net effect would still be a pressure increase.

If it were deemed important, this question could be explored numerically (in an approximate way) by adding some arbitrary inelastic thickness to the computed elastic dike thickness over some depth interval. This approach (or a reduced confining pressure over some interval) might also be used to mimic the expected increase in host rock elastic modulus with depth. In the end this may not be an important enough question to warrant the effort. I understand the motivation for making the claim quoted above – Given that so many simplifications are required to make the problem tractable, it is nice to be able to label some of them as "conservative" and move on. But I don't think it has been established that neglecting anelasticity is conservative, and for this reason it is probably safest to just say that the pressure differences it would induce are likely to be small compared to the expected uncertainty in dike parameters. I put it in the same category as neglect of magma compressibility, turbulent flow, or magma freezing – Until you build models that

include these parameters it is difficult to quantify their effects, but perhaps we have gained enough intuition using the simpler model to state with some confidence that their effects would be small compared to natural variability from dike to dike. Therefore a better justification might be that for assumption 5 ("this is the only possible assumption for analyzing the behavior of a deep-source dike.")

(Even the statement "anelastic behavior would serve to increase dike widths ... at the repository" is questionable. The most likely form of large-scale inelastic deformation in this environment, at least more than 200 m below the repository or in the post-thermal period, is induced normal faulting because the existing normal faults are near a state of failure. If a normal fault cut by the dike had more slip on the updip than downdip extension of the fault, which seems reasonable, this would widen the dike below the intersection but narrow the dike above.)

There is one aspect of this model where neglecting inelastic deformation may be both significant and not conservative. It is stated in Section 6, p, 6-1 that "If the dike does reach the surface prior to the drifts being filled the probability of a dog-leg through the repository will be greatly reduced". Figure 3-2 of the ICPRPFR, with no free surface, shows that when the dike tip is just about to run to the surface the cavity is a very small fraction of the dike thickness (much less than 10%). A zero-pressure crack centimeters or less in thickness and hundreds of meters high would seem to be very susceptible to closure by normal faulting along in the Basin and Range environment. Normal faults intersecting the dike cavity can sometimes be seen to prevent eruption where dikes cut cinder cones. Thus, inelastic deformation makes it more difficult for the dike tip to breach the surface (deformation is diffuse, rather than being concentrated along a single plane), which in turn decreases the chance that the dike would breach the surface before the drifts fill with magma.

4) See the above comment concerning the "conservative" nature of neglecting inelastic deformation. If you really want to make this claim, support it with a few model calculations where (as an approximation) the dike thickness is artificially altered. Otherwise just state that it is neglected to make the problem tractable.

6) "The dike is a single fracture." Combine this with the statement in 6.2.3, p 6-9: "Stress changes from the drift excavation are of limited spatial extent and decay quickly as a function of distance from the drift wall... They will have insignificant effect on dike propagation." Perhaps this is true on a large scale, but on a small scale the stresses could deflect the dike near a dike-drift intersection, and cause an otherwise planar dike to intersect a drift as two en-echelon segments separated by perhaps a drift diameter (or more?), depending upon the drift orientation relative to the principal stresses. Probably this would reduce the magma flux into the drift, as the flux is so sensitive to thickness and the thickness of each overlapping tip should be less than that of the unaffected dike, so ignoring it is likely conservative. On the other hand, this might increase mechanical erosion near the dike/drift intersection and increase the likelihood that a conduit to the surface ultimately forms from that point, as opposed to elsewhere along the dike (in a 1981 USGS Professional Paper [1202] Delaney and Pollard suggested that conduits sometimes localize where dike segments

overlap). Without a dike/drift interaction model it is hard to comment on the significance of these scenarios.

8) I am not much bothered by the neglect of turbulence, but I would feel more comfortable if there were a (justifiable) qualitative description of how it would affect the solution. If this were a constant-thickness slot with a pressurized source at depth, turbulence would just uniformly slow the flow for the available pressure gradient. But the dike narrows toward the tip, and in the steady solution the average cross-sectional flow velocity is everywhere the same, so the Reynolds number decreases linearly with decreasing thickness near the tip. Probably flow would be laminar to thicknesses of several tens of centimeters, even if it were turbulent (smaller velocity for the available pressure gradient) at greater depth. How the resulting solution would compare qualitatively to the purely laminar case I don't know. Any guesses?

11) "This approach is a conservative assumption because the additional load of the mountain could serve to deflect any dike away from the mountain. However, analysis of in situ stresses in Section 6.2.2 demonstrates that topography has negligible effect on the dike path". I find the second statement here, in conjunction with figure 6-22, quite convincing. But I would throw out the first. Muller, Ito and Martel (JGR, June 2001) showed that linear loads on the surface of a half-space act to *attract* dikes by adding a quasi-radial greatest compressive stress to the existing stress distribution. Unless you have information from your simulations that contradicts this, I would throw out the conservative assumption claim.

Other:

Section 6-3, p. 2: I find it odd to justify the neglect of leak-off into the surrounding medium but never mention the neglect of magma freezing, which could have a greater influence on propagation than many of the items listed in 6.3.2. I would put it in the same category as the laminar flow or homogeneous linear elasticity assumptions. Some references to dike models that include freezing can be found on p. 46 of the ICPRPFR.

6-3, p. 4: I get ascent velocities of about 10^{-3} m/s for 1-mm bubbles (for a viscosity of 10 Pa s), which (unless I've made an error) seems small enough compared to the 1-10 m/s flow velocity that I'm surprised by the statement that they effectively separate.

Section 6.3.7.3 Effect of Thermally Induced Increased Horizontal Stress. There are several aspects of this model that I think I do not understand. The main goal seems to be the computation of the dike path and ascent velocity in the face of an increased horizontal stress, using a model that allows for non-planar propagation on a pre-defined, somewhat random network of existing cracks. I presume the fluid flow equations are being solved rigorously, as in the planar dike model described earlier. Is the discretization for those equations just more coarse (that is, on the scale of the distinct elements)? Why do the dike thickness and pressure profiles appear to be asymmetric in Figures 8 and 9? Is this just an artifact of the plotting? And what is meant by "saturation of the dike" on p. 6-14?

I guess my biggest question has to do with the ability of the code to accurately predict propagation paths in the face of variable principal stress orientations. On p. 6-21 it is stated "because of the change in stress due to the presence of the dike itself, the tip will not necessarily deviate even if the in-situ principal stresses rotate. The deviation will depend on the strength of the stress difference." But in a homogeneous elastic body the tip *will* rotate even in the face of arbitrarily small changes in the ambient principal stress orientations. I interpret the quoted statement as really meaning that, given the limited range of pre-defined orientations available to the dike tip, for small enough variability in stress the dike might propagate more-or-less straight ahead. It is true that in a homogeneous continuum the path of a propagating crack can develop a large radius of curvature if the magnitude of the resolved shear stress on the crack is small. So if it would take the dike more than 200 m to rotate I suppose it is reasonable to state that it propagates mostly straight ahead. But how has the distinct element model with a limited network of existing cracks been validated as a means of predicting crack propagation paths? The fourth conclusion on p. 6-25, that the dike "is not expected to turn and create a sill if rock mass properties are homogeneous and isotropic", strikes me as difficult to justify on the basis of what has been presented (is "homogeneous and isotropic" here intended to imply a 'random" grid of the form of Figure 3, or a continuum?). I think a useful calculation would be to put in a representation of the *expected* anisotropy, for example the existing subhorizontal bedding and any known joint set orientations. Then, if a sill does not form along the existing bedding in the presence of large thermal stresses, perhaps a meaningful conclusion can be drawn.

The conclusion that a near-vertical dike with an increased confining pressure of 13 MPa has a maximum excess pressure at the repository depth of only 6 MPa (that is, well below the confining pressure; p. 6-26) is significant. This means that the dike walls are held open at this depth by the excess pressure at greater depth or shallower depth. It would be nice to reproduce this result with the numerical planar dike code described previously, just to make sure that it is not an artifact of the limited vertical extent of the model. It also reinforces the point made in the paragraph below that the uniformly increased load may not be the most instructive case to consider.

Section 6.3.9.4 Effect of Expanding magma on Dike Extension to the Surface. I think I understand what is going on here, although more from the figure caption than the text. Of course, the more relevant point is not how much sooner the tip breaches the surface in the low-density case, but where the magma front is when the tip breaches the surface, and I'm not sure what generalizations can be made concerning this from Figure 6.3.9.4-1. The philosophy underlying this approximate approach to compressibility is hard for me to evaluate. It is clear that the pressure-time history at the repository depth would be identical to a particular case of an incompressible magma, because that is how it is computed. It is just that given some range of likely source parameters (density and flux at depth), matching the fluxes when the density goes down will shift the region of parameter space thought of as "likely". If this shift is small compared to the size of the likely parameter space, it is not terribly significant. If it is large, then the limitations of the approximation need to be considered, and this is difficult to evaluate. For example, q^{∞} is proportional to $w^{\infty}\delta'^{1/3}$, while l^{*} is proportional to $(w^{\infty}/\delta')^{1/2}$. This means that maintaining a constant flux in the manner

adopted here implies a"hidden" change in l^*, which is not accounted for when jumping from one solution to the next.

3. *Are the outputs of the model reasonable and representative?* Yes, with a few qualifications given below. I think it may be a useful result (for the dike/drift interaction model) that the pressure-time history at the repository depth can be well-approximated by "convecting" a single prior snapshot of the time-dependent calculation past the repository depth (section 6.3.7.1, p. 30). It is useful to investigate different tip cavity pressures (6.3.7.2). It is also useful to investigate the effect of an increased horizontal stress (6.3.7.3), designed to address intersection during a time of high thermal loading. But why is this load applied uniformly over the full model height? This is not necessarily a "bounding" case, as is claimed. For a uniform pressure increase, the only effect is to produce in a shorter cavity at a given depth (the source pressure just goes up in lock-step with the remote load, as does the magma pressure everywhere "far" from the cavity). But for a locally increased confining pressure, the thickness is reduced locally while the source flux remains largely unaffected (see the earlier discussion regarding the effect of inelastic deformation or elastic modulus variation). I can see that it might be more difficult to handle the localized stress increase numerically, but this is the numerical experiment that is relevant. If it can't be done for numerical reasons then this should be stated.

If I take the broadest view, the statement "the maximum magma pressure is at most 1 MPa larger than the horizontal far-field stress at the given depth" (Section 6-3, p. 30), seems to be the sort of "bottom-line" result that that one would hope to get out of simulations like this (or that statement plus a qualitative description of the variation of pressure as a function of depth below the dike tip, that might be translated into an approximate pressure-vs-time history at the repository depth). How representative is this result? The dimensional estimate of the maximum excess pressure is $\delta' \equiv (\kappa\rho_r - \rho_f)g$ times the length scale $l^* \equiv (w_* E'/\delta')^{1/2}$, or $(w_* E' \delta')^{1/2}$. For $w_* = 1$ m, $E' = 15$ GPa, and $\delta' = 10^3$ Pa/m, this yields an estimated maximum excess pressure of ~ 3 MPa. My recollection is that this dimensional estimate overestimates the actual excess pressure in a "base case" calculation by a factor of ~ 3 (ICPRPFR, Fig. 3-5). So a refined estimate is very close to the number of 1 MPa cited in this document as a maximum. On the other hand, in Figure 6M-11 a pressure of 1 MPa is reached for a dike thickness of 0.16 m. If a thick dike was assumed, say 4 m (as I believe is representative of some of the thicker dikes in the region), this would increase the maximum excess pressure by a factor of 5 (that is, $(4/0.16)^{1/2}$). This is what prompted my earlier comment that "a few MPa" may be a more robust maximum value than "1 MPa". On the other hand, an excess pressure this large will give rise to a much taller tip cavity at the same depth of the magma front.

In a practical sense, the question of the validity of the neglect of magma freezing, turbulence, inelastic deformation, etc, can be reduced to the two questions of (1) Do these additional processes introduce any qualitatively new behavior?, and (2) Do they alter the estimate of the maximum excess pressure from $\sim 0.3(w_* E' \delta')^{1/2}$ by an amount that begins to approach the variation expected from natural variations in w_*, E', and δ'? To this second question might be added a question (2a), Do these processes significantly change the

pressure-vs-depth profile (press-vs-time at the repository)? I am mostly comfortable with the neglect of these additional processes because I think the answer to questions (2) and (2a) is "no". To the extent that I have remaining doubts it is because of the difficulty in answering question (1) with certainty (e.g., does inelastic deformation greatly reduce the tip cavity length; might freezing cause the magma front to halt a short distance above the repository, etc.).

A detail:

Fig 6M-16, p 34: I am surprised that the dike tip does not appear to have gone unstable (no equilibrium position) before reaching the surface for (for example) V=1m/s. Numerical simulations and an analytic solution in Appendix 3.2 of the ICPRPFR suggest that it would do so. Admittedly this is for no free surface, which might change things. But with a constant cavity pressure, I find it hard to believe that the free surface could stabilize the tip when the cavity pressure exceeds the confining pressure, which it does in this case at 40 m depth. The analytic (no free surface) approximate solution would have it going unstable at closer to 120 m depth, for a magma front at 200 m depth as in Fig. 6M-16.

6.4.8 Summary (Should this be 6.3.8?): If 1 m/s is the "expected" velocity, perhaps this should be achieved with a larger viscosity, because 0.12-0.25 m sounds small for eroded dikes in this region. On the other hand, I am not sure of the basis upon which this is "expected". 1 m/s is a good upper-bound velocity for dikes in Iceland and Hawaii, but the viscosities there are probably 100 Pa s or somewhat larger, and if 10 Pa s is a good number, then perhaps 10 m/s should be the "expectation".

Less of a detail, perhaps, but not necessarily important:

On p. 19 of Section 6.3, it appears that a κ of 0.5, which may be appropriate throughout the brittle crust, requires very low magma densities of 751 kg/m^3. This in turn requires unreasonably large bubble fractions at depths below a few km. I bring this up because it is related to the problem of the limited lateral extent of these dikes mentioned in assumption (1) of 6.3.2. If the magma is to be locally buoyant and if the magma density is constrained by reasonable bubble fractions, κ can be significantly less than 1 only in the upper few kilometers of the crust. I am not concerned here with the possibility that a depth-variable κ is being modeled as constant; I am pointing out that there is a significant gap in our understanding of how these dikes make it up through most of the upper crust (until gas exsolution makes the magma buoyant even for a low κ). If they do it by being bounded laterally by faults, as was suggested in this document, then δ' must change sign over most of the upper crust. The flux from below can continue to drive the dike tip upward in this case, but the elastic stresses should be far different from that computed in these models, even perhaps at the depth of the repository (the dike thickness in the middle crust might be ten times that computed here). On the other hand, if κ is increased to near 1 over most of the upper crust by earlier dikes that froze, then seeing one cone at the surface implies many more non-eruptive dikes at depth, with perhaps significant implications for the probability of a future igneous event.

Model validation, Section 7.3:

I think the comparison to Lister's more analytic solution demonstrates that the code NPHF2D is perfectly adequate for its advertised task. The deviation from the Lister solution probably has more to do with the presence of the free surface than any numerical approximations made (although one should check the depth of the tip against l^* to bolster this claim). The comparison with Paricutin is an important qualitative test, although admittedly the quantitative constraints are few. Perhaps most important is just the validation of the concept that a "tip cavity" can breach the surface long before magma gets there. One question related to my earlier comment on the possibility that inelastic deformation could "short-circuit" this cavity: What is known of the stress state near Paricutin? Are there active normal faults, as at Yucca Mountain, that would allow one to infer that the least horizontal stress is quite low? Or might the least horizontal stress be much closer to the vertical stress? (As a possible erratum, I have no doubt that the numerical model can adequately reproduce the stress intensity factor and thickness for a uniformly pressurized crack, as it has passed more stringent tests. But Section 7.3.1.1.2 doesn't say this, and it looks like the wrong paragraph might have been inserted here.)

4. *Are limitations of the model adequately described?* Yes. Any concerns I might have about this have already been stated in response to question (2).

5. *Are there alternative models or approaches that should be considered?* Not really, except insofar as the more analytic ones provide some "reasonableness" checks on the calculations presented here. This is adequately discussed in the document. Some of the published dike propagation models that include freezing might be looked at, just to develop an intuition for how they might change the flow. And, as I stated earlier, it might be instructive to run some additional models where the dike thickness or confining pressure is varied only over a limited depth interval.

Errata:

5.3 Assumption 21: 88 MPa should be 8 MPa?

Section 6.2.2, p. 6-6: Figure 10, 11 should be 6-21, 6-22?

Section 6-3, p. 23, check the end of the first sentence, 2nd paragraph.

Section 6-3, p. 30, line 4: "remains invariant" should be changed to "is approximated as remaining invariant", I think.

Section 6-3, p. 30: $D = 20.28$ (Figure 6M-11) should be (Figure 6M-13).

APPENDIX G

QUALIFICATION OF EXTERNAL SOURCES

APPENDIX G
QUALIFICATION OF EXTERNAL SOURCES

External sources have provided unqualified data that have been used as direct input to this document. The inputs from these sources are qualified for intended use within the document using the criteria found in AP-SIII.10Q, Models. These criteria represent a subset of the methods and attributes required for qualification of data per AP-SIII.2Q, Qualification of Unqualified Data. The following information is provided for each source: The full reference citation, a description of the data that were used from the source, and the extent to which the data demonstrate the properties of interest. In addition, one or more of the following criteria is also addressed:

- Reliability of data source
- Qualifications of personnel or organizations generating the data
- Prior uses of the data
- Availability of corroborating data.

The criteria described above meet the requirements of AP-SIII.10Q and are provided as justification that the data that have been used from these sources are considered to be qualified for intended use.

G1. BRADY AND WALTHER 1989

Reference–Brady, P.V. and Walther, J.V. 1989. "Controls on Silicate Dissolution Rates in Neutral and Basic pH Solutions at 25°C." *Geochimica et Cosmochimica Acta, 53*, 2823-2830. New York, New York: Pergamon Press. TIC: 235216. [DIRS 110748]

Description of Use–Brady and Walther (1989) are cited in Section 4.0 as the source of dissolution rates of olivine and pyroxene minerals and aluminosilicate minerals. Specifically, data presented in Figure 4 and Figure 5 of Brady and Walther (1991) are used to establish the dissolution rate of enstatite and anorthite, respectively. Brady and Walther (1989) data are plotted as a function of the log dissolution rate (mols/cm2/s) versus pH to establish the dissolution rate of enstatite and anorthite for use in EQ3/6 calculations. The output from the EQ3/6 calculations is abstracted as an input to the TSPA igneous intrusion groundwater model.

Extent to which the Data Demonstrate the Properties of Interest–After post-intrusive magma cooling and reversion to normal in-drift environmental conditions, the seepage water is expected to flow through the contact metamorphic aureole and react first with the basalt in the intruded emplacement drifts, resulting in basalt-equilibrated seepage water. The geochemical interaction of seepage water with the basalt and the resulting hydrochemistry are simulated using EQ3/6.

For EQ3/6 calculations, mineral dissolution rates are a required input. This journal source presents dissolution rate data at 25°C directly plotting log dissolution rate (mols/cm2/s) versus pH. The data are consistent with the expected seepage composition during post-igneous in-drift environmental conditions.

Reliability of Data Source–Brady and Walther (1989) published their experimental results in the journal Geochimica et Cosmochimica Acta. Published for over 100 years, the Geochimica et Cosmochimica Acta (GCA) is a professional scientific research journal for geochemistry and cosmochemistry. It is sponsored by The Geochemical Society and The Meteoritical Society and is published by Elsevier Science Ltd. Contributions to the journal are evaluated for scientific merit by thorough professional review. Peer review is an essential and integral aspect of Geochimica et Cosmochimica Acta. The fundamental role of the reviewer is to advise the Associate Editor and the Executive Editor on the virtues, or lack thereof, of a manuscript submitted for publication. Normally the journal requires three "external" reviews. The Associate Editor writes a report summarizing reviewer opinion, presenting his/her overall evaluation based on his/her own reading of the manuscript and the advice of the reviewers.

G2. BRANTLEY AND CHEN 1995

Reference–Brantley, S.L. and Chen, Y. 1995. "Chemical Weathering Rates of Pyroxenes and Amphiboles." Chapter 4 of *Chemical Weathering Rates of Silicate Minerals*. White, A.F. and Brantley, S.L., eds. Reviews in Mineralogy Volume 31. Washington, D.C.: Mineralogical Society of America. TIC: 222496. [DIRS 163275]

Description of Use–Brantley and Chen (1995) are cited in Section 4.0 as the source of dissolution rates of olivine and pyroxyene minerals. Specifically, data presented in Table 1 of Brantley and Chen (1995) are used to establish the dissolution rate of diopside (used for hedenbergite). Data from several sources compiled in Table 1 of Brantley and Chen (1995) are plotted as a function of the log dissolution rate (mols/cm2/s) versus pH to establish the dissolution rate of diopside for use in EQ3/6 calculations. The output from the EQ3/6 calculations is abstracted as an input to the TSPA igneous intrusion groundwater model.

Extent to which the Data Demonstrate the Properties of Interest–After post-intrusive magma cooling and reversion to normal in-drift environmental conditions, the seepage water is expected to flow through the contact metamorphic aureole and react first with the basalt in the intruded emplacement drifts, resulting in basalt-equilibrated seepage water. The geochemical interaction of seepage water with the basalt and the resulting hydrochemistry are simulated using EQ3/6.

For EQ3/6 calculations, the incoming water composition is run through EQ3NR, which requires mineral dissolution rates. This journal source provides peer-reviewed mineral dissolution rates for inosilicates under ambient conditions and over a range of pH, consistent with predicting the seepage composition during post-igneous in-drift environmental conditions.

Reliability of Data Source–Brantley and Chen (1995) appear as Chapter 4 in Chemical Weathering Rates of Silicate Minerals (White and Brantley, 1995). Chemical Weathering Rates of Silicate Minerals is the 31st volume of a collection of journal articles and monographs published in conjunction with a series of short courses sponsored by the Mineralogical Society of America. Referred to as the Reviews in Mineralogy Series, volume 31 represents the twenty-second year of published material accompanying courses in the subjects of mineralogy, petrology, crystallography, and geochemistry. The courses are conducted in conjunction with annual meetings of professional organizations such as the Geological Society of America and the American Geophysical Union. This 31st volume was edited by Art White (U.S. Geological

Survey, Menlo Park) and Sue Brantley (Penn State University) who, in addition to their own feedback to authors, managed the peer review process.

Founded in 1919, the Mineralogical Society of America has a worldwide reputation, through education and research, for promoting the understanding and application of mineralogy by industry, universities, government, and the public. The Mineralogical Society of America is a non-profit corporation organized under the laws of the District of Columbia. The enormously successful "Reviews in Mineralogy" series has changed its name to "Reviews in Mineralogy and Geochemistry" (ISSN 1529-6466), starting with Volume 39, and is now published jointly by the Mineralogical Society of America and the Geochemical Society (1015 Eighteenth Street, NW, Suite 601, Washington, DC 20036).

G3. CHOU AND WOLLAST 1985

Reference–Chou, L. and Wollast, R. 1985. "Steady-State Kinetics and Dissolution Mechanisms of Albite." *American Journal of Science, 285*, 963-993. [New Haven, Connecticut: Yale University, Kline Geology Laboratory]. TIC: 223169. [DIRS 160182]

Description of Use–Chou and Wollast (1985) are cited in Section 4.0 as the source of the dissolution rate of aluminosilicate minerals. Specifically, data presented in Figure 5 of Chou and Wollast (1985) are used to establish the dissolution rate of albite. Chou and Wollast (1985) data are plotted as a function of the log dissolution rate (mols/cm2/s) versus pH to establish the dissolution rate of albite for use in EQ3/6 calculations. The output from the EQ3/6 calculations is abstracted as an input to the TSPA igneous intrusion groundwater model.

Extent to which the Data Demonstrate the Properties of Interest–After post-intrusive magma cooling and reversion to normal in-drift environmental conditions, the seepage water is expected to flow through the contact metamorphic aureole and react first with the basalt in the intruded emplacement drifts, resulting in basalt-equilibrated seepage water. The geochemical interaction of seepage water with the basalt and the resulting hydrochemistry are simulated using EQ3/6.

For EQ3/6 calculations, mineral dissolution rates are a required input. This journal source plots the log dissolution rate (mols/cm2/s) versus pH. The dissolution of albite was studied at room temperature under a broad range of experimental conditions, including pH. The data are consistent with the expected seepage composition during post-igneous in-drift environmental conditions.

Reliability of Data Source–Chou and Wollast (1985) published their experimental results in the American Journal of Science. Founded in 1818, the American Journal of Science (AJS) is the oldest scientific journal in the United States that has been published continuously. The Journal is devoted to geology and related sciences and publishes articles from around the world presenting results of major research from all earth sciences. Readers are primarily earth scientists in academia and government institutions. The American Journal of Science is published by Yale University, Department of Geology and Geophysics: AMERICAN JOURNAL OF SCIENCE 217 Kline Geology Laboratory PO Box 208109 New Haven, Connecticut 06520-8109

G4. TOLE, LASAGA, PANTANO, AND WHITE 1986

Reference–Tole, M.P.; Lasaga, A.C.; Pantano, C.; and White, W.B. 1986. "The Kinetics of Dissolution of Nepheline ($NaAlSiO_4$)." *Geochimica et Cosmochimica Acta, 50*, (3), 379-392. New York, New York: Pergamon Press. TIC: 253992. [DIRS 163289]

Description of Use–Tole et al (1986) are cited in Section 4.0 as the source of the dissolution rate of aluminosilicate minerals. Specifically, data presented in Table 2 of Tole et al (1986) are used to establish the dissolution rate of nepheline. Tole et al (1986) data are plotted as a function of the log dissolution rate (mols/cm2/s) versus pH to establish the dissolution rate of nepheline for use in EQ3/6 calculations. The output from the EQ3/6 calculations is abstracted as an input to the TSPA igneous intrusion groundwater model.

Extent to which the Data Demonstrate the Properties of Interest–After post-intrusive magma cooling and reversion to normal in-drift environmental conditions, the seepage water is expected to flow through the contact metamorphic aureole and react first with the basalt in the intruded emplacement drifts, resulting in basalt-equilibrated seepage water. The geochemical interaction of seepage water with the basalt and the resulting hydrochemistry are simulated using EQ3/6.

For EQ3/6 calculations, mineral dissolution rates are a required input. This journal source tabulates the experimental dissolution rate (mols/cm2/s) data for nepheline. Dissolution experiments were carried out at 25, 60, and 80°C within aqueous solutions at variable pH. These conditions are consistent with the expected seepage conditions within the post-igneous in-drift environment.

Reliability of Data Source–Tole et al (1986) published their experimental results in the journal Geochimica et Cosmochimica Acta. Published for over 100 years, the Geochimica et Cosmochimica Acta (GCA) is a professional scientific research journal for geochemistry and cosmochemistry. It is sponsored by The Geochemical Society and The Meteoritical Society and is published by Elsevier Science Ltd. Contributions to the journal are evaluated for scientific merit by thorough professional review. Peer review is an essential and integral aspect of Geochimica et Cosmochimica Acta. The fundamental role of the reviewer is to advise the Associate Editor and the Executive Editor on the virtues, or lack thereof, of a manuscript submitted for publication. Normally the journal requires three "external" reviews. The Associate Editor writes a report summarizing reviewer opinion, presenting his/her overall evaluation based on his/her own reading of the manuscript and the advice of the reviewers.

G5. VALSAMI-JONES, RAGNARSDOTTIR, PUTNIS, BOSBACH, KEMP, AND CRESSEY 1998

Reference–Valsami-Jones, E.; Ragnarsdottir, K.V.; Putnis, A.; Bosbach, D.; Kemp, A.J.; and Cressey, G. 1998. "The Dissolution of Apatite in the Presence of Aqueous Metal Cations at pH 2-7." Chemical Geology, 151, ([1-4]), 215-233. [New York, New York]: Elsevier. TIC: 255204. [DIRS 166412]

Description of Use–Valsami-Jones et al. (1998) is cited in Section 4.0 as the source of the dissolution rate of the mineral hydroxylapatite. Valsami-Jones et al. (1998) data are plotted as a

function of the log dissolution rate (mols/cm2/s) versus pH to establish the dissolution rate of hydroxylapatite albite for use in EQ3/6 calculations. The output from the EQ3/6 calculations is abstracted as an input to the TSPA igneous intrusion groundwater model.

Extent to which the Data Demonstrate the Properties of Interest–After post-intrusive magma cooling and reversion to normal in-drift environmental conditions, the seepage water is expected to flow through the contact metamorphic aureole and react first with the basalt in the intruded emplacement drifts, resulting in basalt-equilibrated seepage water. The geochemical interaction of seepage water with the basalt and the resulting hydrochemistry are simulated using EQ3/6.

For EQ3/6 calculations, mineral dissolution rates are a required input. This journal source tabulates in Table 2, the experimental dissolution rate (mols/m2/min) data for hydroxylapatite. Dissolution experiments were carried out at 25°C + 0.1°C using low-density polyethylene batch reactors at variable pH. These conditions are consistent with the expected seepage conditions within the post-igneous in-drift environment.

Reliability of Data Source–Valsami-Jones et al. (1998) published their experimental results in the journal Chemical Geology. Chemical Geology (including Isotope Geoscience) is the official journal of the European Association for Geochemistry. This international journal publishes original research papers on the isotopic and elemental geochemistry and geochronology of the Earth. The editorial board is a worldwide group representing academia, business and government that ensures the scientific pedigree of published articles. The journal is published by Elsevier Publishing, a world -leading, multiple-media publisher of scientific, technical and health information products and services.

G6. WHITE, PETERSON, AND HOCHELLS 1994

Reference–White, A.F.; Peterson, M.L.; and Hochells, M.F., Jr. 1994. "Electrochemistry and Dissolution Kinetics of Magnetite and Ilmenite." Geochimica et Cosmochimica Acta, 58, (8), 1859-1875. Oxford, United Kingdom: Elsevier. TIC: 246373. [DIRS 131014]

Description of Use–White et al. (1994) are cited in Section 4.0 as the source of the dissolution rate of the minerals magnetite and ilmenite. White et al. (1994) data are plotted as a function of the log dissolution rate (mols/cm2/s) versus pH to establish the dissolution rate for these minerals for use in EQ3/6 calculations. The output from the EQ3/6 calculations is abstracted as an input to the TSPA igneous intrusion groundwater model.

Extent to which the Data Demonstrate the Properties of Interest–After post-intrusive magma cooling and reversion to normal in-drift environmental conditions, the seepage water is expected to flow through the contact metamorphic aureole and react first with the basalt in the intruded emplacement drifts, resulting in basalt-equilibrated seepage water. The geochemical interaction of seepage water with the basalt and the resulting hydrochemistry are simulated using EQ3/6.

For EQ3/6 calculations, mineral dissolution rates are a required input. This journal source tabulates in Table 2 the pH ranges, experimental duration, rate constants for Fe2+ release (mols/cm2/s) and correlation coefficients for short-term Fe-oxide experiments at 25°C. Rates used for magnetite and ilmenite are from anoxic tests. Since the Fe and Ti released by these

minerals are quickly taken up into minerals and are not important to the aqueous parameters of interest, these rates are considered adequate for use.

Reliability of Data Source–White et al. (1994) published their experimental results in the journal Geochimica et Cosmochimica Acta. Published for over 100 years, the Geochimica et Cosmochimica Acta (GCA) is a professional scientific research journal for geochemistry and cosmochemistry. It is sponsored by The Geochemical Society and The Meteoritical Society and is published by Elsevier Science Ltd. Contributions to the journal are evaluated for scientific merit by thorough professional review. Peer review is an essential and integral aspect of Geochimica et Cosmochimica Acta. The fundamental role of the reviewer is to advise the Associate Editor and the Executive Editor on the virtues, or lack thereof, of a manuscript submitted for publication. Normally the journal requires three "external" reviews. The Associate Editor writes a report summarizing reviewer opinion, presenting his/her overall evaluation based on his/her own reading of the manuscript and the advice of the reviewers.

G7. WOGELIUS AND WALTHER 1991

Reference–Wogelius, R.A. and Walther, J.V. 1991. "Olivine Dissolution at 25°C: Effects of pH, CO2, and Organic Acids." Geochimica et Cosmochimica Acta, 55, (4), 943-954. New York, New York: Pergamon Press. TIC: 236732. [DIRS 163290]

Description of Use–Wogelius and Walther (1995) are cited in Section 4.0 as the source of dissolution rates of olivine and pyroxyene minerals. Specifically, data presented in Table 2 of Wogelius and Walther (1991) are used to establish the dissolution rate of olivine. Wogelius and Walther (1991) data are plotted as a function of the log dissolution rate (mols/cm2/s) versus pH to establish the dissolution rate of olivine for use in EQ3/6 calculations. The output from the EQ3/6 calculations is abstracted as an input to the TSPA igneous intrusion groundwater model.

Extent to which the Data Demonstrate the Properties of Interest–After post-intrusive magma cooling and reversion to normal in-drift environmental conditions, the seepage water is expected to flow through the contact metamorphic aureole and react first with the basalt in the intruded emplacement drifts, resulting in basalt-equilibrated seepage water. The geochemical interaction of seepage water with the basalt and the resulting hydrochemistry are simulated using EQ3/6.

For EQ3/6 calculations, mineral dissolution rates are a required input. This journal source presents experimental dissolution data for olivine collected at atmospheric equilibrium and for solvents of variable pH, consistent with predicting the seepage composition during post-igneous in-drift environmental conditions.

Reliability of Data Source–Wogelius and Walther (1991) published their experimental results in the journal Geochimica et Cosmochimica Acta. Published for over 100 years, the Geochimica et Cosmochimica Acta (GCA) is a professional scientific research journal for geochemistry and cosmochemistry. It is sponsored by The Geochemical Society and The Meteoritical Society and is published by Elsevier Science Ltd. Contributions to the journal are evaluated for scientific merit by thorough professional review. Peer review is an essential and integral aspect of Geochimica et Cosmochimica Acta. The fundamental role of the reviewer is to advise the Associate Editor and the Executive Editor on the virtues, or lack thereof, of a manuscript

submitted for publication. Normally the journal requires three "external" reviews. The Associate Editor writes a report summarizing reviewer opinion, presenting his/her overall evaluation based on his/her own reading of the manuscript and the advice of the reviewers.

G8. LASAGA 1998

Reference–Lasaga, A.C. 1998. *Kinetic Theory in the Earth Sciences.* Princeton, New Jersey: Princeton University Press. TIC: 246279. [DIRS 117091]

Description of Use–The reference, Lasaga 1998 [DIRS 117091], p. 322 is the source for the equation (Eq6-94) that is used to calculate the binary diffusion of water vapor and air. These calculations are run simultaneously with the flow calculations in TOUGHREACT. Diffusion of HCl, HF, SO_2, and CO_2 in the gas phase is based on a model presented in this reference for tracer diffusion in an ideal gas as a function of temperature and pressure.

Extent to which the Data Demonstrate the Properties of Interest–Section 6.6 of this document discusses the potential impact of an intersection of a basaltic dike with one or more drifts. The pressure, volume, composition, and temperature history of volcanic gas potentially entering a repository drift depends on several factors, including the volume of magma emplaced in a drift, its rate of ascent, and its composition. The conceptual models consider a volcanic gas source inside the drift that allows gas species to migrate via advection and diffusion either through the fractured tuff around the drift, or alternatively, through a backfilled access drift. Gaseous components include air, H_2O, CO_2, HCl, HF, and SO_2. The equation that is presented in the Lasaga reference evaluates diffusion of these gases at the varying temperatures and pressures that could occur during the potential intrusion.

Qualifications of Personnel or Organizations Generating the Data–The source is an advanced textbook on kinetic processes including diffusion, fluid flow, and isotope exchange processes. The preface identifies nine persons who were involved in reviewing or editing the book. Dr. A.C. Lasaga, the author of the text, is a recognized expert in his field and he was a professor of Geochemistry at Yale University at time of publication.

G9. WHITE, D.E.; HEM, J.D.; AND WARING, G.A. 1980; HEARN, P.P.; STEINKAMPF, W.C.; BORTLESON, G.C.; AND DROST, B.W. 1985; HEM, J.D. 1985

References–White, D.E.; Hem, J.D.; and Waring, G.A. 1980. "Chemical Composition of Subsurface Waters." Chapter F of *Data of Geochemistry*. 6th Edition. Geological Survey Professional Paper 440-F. Washington, D.C.: U.S. Government Printing Office. TIC: 249975. [DIRS 163752]

Hearn, P.P.; Steinkampf, W.C.; Bortleson, G.C.; and Drost, B.W. 1985. *Geochemical Controls on Dissolved Sodium in Basalt Aquifers of the Columbia Plateau, Washington.* Water-Resources Investigations Report 84-4304. Tacoma, Washington: U.S. Geological Survey. TIC: 230835. [DIRS 166893]

Hem, J.D. 1985. *Study and Interpretation of the Chemical Characteristics of Natural Water.* 3rd Edition. Geological Survey Water-Supply Paper 2254. Washington, D.C.: U.S. Government Printing Office. ACC: NNA.19940427.0181. [DIRS 115670]

Description of Use–The White et al. 1980; Hearn et al. 1985; and Hem 1985 references were used as the sources of values for fluoride concentrations taken from waters sampled from basaltic aquifers. These data are used for comparison with modeled fluoride concentrations developed through the EQ6 simulations of crown seepage water reaction with cooled basalt in an emplacement drift, discussed in Sec. 6.8.3. These data are used to establish the range for fluoride concentrations in basaltic waters by incorporating both natural and modeled values.

Extent to which the Data Demonstrate the Properties of Interest–After post-intrusive magma cooling and reversion to normal in-drift environmental conditions, the seepage water is expected to flow through the contact metamorphic aureole and react first with the basalt in the intruded emplacement drifts, resulting in basalt-equilibrated seepage water. The geochemical interaction of seepage water with the basalt and the resulting hydrochemistry are simulated using EQ6. Many EQ6 simulations of basalt/water interactions show no change in fluoride content, resulting in the final fluoride content largely reflecting the starting water composition. In comparison with fluoride concentrations of natural basaltic acquires, such as those reported by White, et al., the concentrations that were modeled by EQ6 were found to be generally higher. The result of White et al, and others were used to set the lower bounding value for the range of fluoride compositions.

Reliability of Data Source–The White et al., 1980, reference was published as a chapter in the 6th edition of *Data of Geochemistry,* a Geological Survey Professional Paper. This Geological Survey Professional Paper is one of series of reports published by the United Stated Geological Survey, the leading research organization in the geological sciences. This series is considered by the international geoscience community to be one of the most highly respected publications in the field. This publication series has long been used as a standard for technical quality and substance, and are considered to be the definitive source in their field. The Hearn et al 1985, and Hem 1985, references are published in two other publication series put out by the U.S. Geological Survey; the Water-Resources Investigations Reports and the Geological Survey Water-Supply Papers, respectively. The review process within the USGS is stringent and the Professional Papers are subject to intensive internal peer review prior to final approval by the Director of the USGS.

Corroborative Data–The three references discussed above provide a range of fluoride concentrations from basaltic aquifers in Washington and Oregon. Data for 32 waters from these basalt aquifers are taken from these references: Hearn et al. 1985, page 28, Table 2 [DIRS 166893]; White et al. 1980, page F-16, Table 2, column 8 [DIRS 163752]; and Hem 1985, pages 70-71, samples 4 and 5 [DIRS 115670]). The values are used to corroborate each other and provide the basis for the value that is, in turn, used as the lower boundary for fluoride concentrations in basaltic aquifers. The range of values varied from 0.01 to 4.1 mg/L, with a mean F^-content of 0.8±0.8 1σ mg/L. The median value is 0.5 mg/L, reflective of the fact that the mean is skewed upward on the basis of a few analyses with F^- compositions in the range of a few mg/L.

G10. HEIKEN, G.; WOHLETZ, K.; AND EICHELBERGER, J. 1988

Reference–Heiken, G.; Wohletz, K.; and Eichelberger, J. 1988. "Fracture Fillings and Intrusive Pyroclasts, Inyo Domes, California." *Journal of Geophysical Research, 93,* (B5), 4335-4350. Washington, D.C.: American Geophysical Union. TIC: 252109. [DIRS 165566]

Description of Use–Heiken et al. (1988, p. 4346 and Figure 10) is the source for the magma overburden pressure and the selected center range of magma viscosity respectively, as discussed in Section 6.5.2.1. These magma properties are inputs to single-phase simulations that have been conducted to simulate pyroclastic magma flow into a pre-existing crack. The analysis is used to determine the feasibility of a similar phenomenon occurring at Yucca Mountain.

Extent to which the Data Demonstrate the Properties of Interest–Heiken et al. 1988, reported the results of studies of intrusive pyroclastics and the resulting fracture fill at Inyo Canyon, California. The investigations at Inyo Canyon included detailed mapping and analysis of the process of the intrusive fracture fill. A portion of the research included formulating an analytical approach to describing the fracturing process during such intrusions. The analysis presented in Section 6.5.2.1 of this document, is based on a similar approach to that presented by the Heiken study, which is used to corroborate the results from the single-phase simulations presented in this analysis.

Qualifications of Personnel or Organizations Generating the Data–Dr. Grant Heiken is a volcanologist with the Las Alamos National Laboratory in Energy, Geosciences, Earth and Space Sciences, and Earth and Environmental Science Divisions. He has over 40 years of work and research experience. He received his B.A. in Geology from the University of California, Berkeley, 1964, his M.A. in Geology from the University of Texas, Austin, 1966 and his Ph.D. in Geology from the University of California, Santa Barbara, 1972.

His professional associations and honors include: President, International Association of Volcanology and Chemistry of the Earth's Interior, 1995-1999. Past-President, 1999-2003, Fulbright Research Scholar, University of Rome-TRE, 1999, Member of the National Academy of Sciences/National Research Council committee on "Future Roles, Challenges, and Opportunities for the US Geological Survey," 1998-1999, Best Geoscience Reference Book Award, for Lunar Sourcebook—A User's Guide to the Moon, from Geosciences Information Society (Geological Society of America), October, 1992, Liaison between the International Union of Geodesy and Geophysics (IUGG) and the International Civil Aviation Organization (ICAO), 1983-Present. Member, organizing committee for the First International Symposium on Volcanic Ash and Aviation Safety, 1991. Chair, Megacities Committee, IUGG, 1999-2003.

Dr. Kenneth Wohletz received his PhD degree in 1980 in geology from Arizona State University, covering geophysical fluid dynamics, mathematical modeling, petrologic thermodynamics, and experimental physics. He received his M.S. also from Arizona State University, 1977, and his B.A. from the University of California, Santa Barbara, 1974. From 1980 to 1981, he did postdoctoral research in planetary cratering mechanics at NASA and was a guest scientist of the Italian National Research Council. In 1981, he was awarded a Director's Postdoctoral Fellowship at Los Alamos National Laboratory for shockwave studies in volcanism. A technical

staff-member at Los Alamos National Laboratory since 1983, his recent research efforts have been directed toward several problems:

- Monitoring technologies for nuclear test sites
- Numerical simulation of volcanic eruptions
- Mathematical analysis of particle mass distributions of dynamic fragmentation and transport phenomena.

Dr. Woletz has authored and co-authored numerous books and articles published in professional journals.

Dr. John Eichelberger is currently Department Chair and Professor, Volcanology and Igneous Petrology at the University of Alaska, Fairbanks. Dr. Eichelberger has over 30 years research and work experience. His research interests are in physical and chemical aspects of magmatic behavior, with emphases on field and drilling observations and interdisciplinary collaborations. Much of his current research is concerned with volatiles in magmas and their control of eruptive processes. An earlier focus, but continuing interest, is the interaction of chemically and thermally contrasting magmas in magma reservoirs and volcanic conduits. He has a long-term interest in research drilling and has led or participated in drilling into a number of volcanic systems. His now-completed drilling project at Inyo Domes, California led to new models for lava eruptions and for segregation of magmas during flow. Dr. Eichelberger is also the Coordinating Scientist for the Alaska Volcano Observatory (AVO), which monitors and conducts supporting research on Alaska's active volcanoes. Dr. Eichelberger has authored and co-authored numerous books and articles published in professional journals.

APPENDIX H

VALIDATION CALCULATIONS

APPENDIX H
VALIDATION CALCULATIONS

H1. INITIAL SOLUTION

The initial solution is according to Pulvirenti et al. (2004 [DIRS 169631], Table 1, Column UZ×1243).

H1.1 Recipe

The initial solution in the Catholic University's experiment was prepared using the recipe given in Table H-1 (according to Pulvirenti et al. (2004 [DIRS 169631], Table 1, Column UZ×1243):

Table H-1. Recipe

Solute:	Molecular Weight	Concentration (mg/L)	Concentration (moles/L)
$CaCl_2 \cdot 2H_2O$	147.0164	57767	0.3929289
$MgSO4 \cdot 7H_2O$	246.469	5382	0.021836417
KNO_3	101.1032	4205	0.04159
NaF	41.98817	1198	0.028532
$NaHCO_3$	84.00687	61	0.0007261
$SiO_2 \cdot xH_2O$ (84% SiO_2)	60.0843/0.84=71.52893	644	0.00900335
$MgCl_2 \cdot 6H_2O$	203.3238	42264	0.2078654
NaCl	58.44277	14211	0.24316095
KCl	74.5513	1975	0.0264918
0.001 M NaOH	39.99887	0.12 (g/L)=120mg/L =0.000479987mg/L of pure NaOH	0.00012 (0.00000012 of pure NaOH)

H1.2 Concentration of aqueous species:

In this recipe, the species concentration are calculated as:

$[Ca^{++}] = [CaCl_2 \cdot 2H_2O] = 0.3929289$ (moles/L)

$[Cl^-] = 2[CaCl_2 \cdot 2H_2O]+2[MgCl_2 \cdot 6H_2O]+[NaCl]+[KCl]$
$= 2* 0.3929289+2*0.2078654+0.24316095+0.0264918$
$= 0.7858578+0.4157308+0.24316095+0.0264918$
$= 1.47124135$(moles/L)

$[Mg^{++}] = [MgSO4 \cdot 7H_2O]+[MgCl_2 \cdot 6H_2O]$
$= 0.021836417+0.2078654$
$= 0.229701817$(moles/L)

$[K^+]=[KNO_3]+[KCl]$
$= 0.04159+0.0264918$
$= 0.0680818$ (moles/L)

$[Na^+]=[NaF]+[NaHCO_3]+[NaCl]+[NaOH]$
$=0.028532+0.0007261+0.24316095+0.00000012$
$=0.27241917$ (moles/L)
$[F^-]=[NaF]= 0.028532$ (moles)

$[NO_3^-]=[KNO_3]= 0.04159$ (moles/L)

$[HCO_3^-]=[NaHCO_3]= 0.0007261$ (moles/L)

$[SO4^{--}]=[MgSO4\cdot 7H_2O]= 0.021836417$(moles/L)

$[SiO_2]=[SiO_2\cdot xH_2O$ (84% $SiO_2)]=0.00900335$

$[OH^-]=[NaOH]= 0.00012$

H1.3 Solution density

As one of the dominant components, the solution contains 5.776 g $CaCl_2\cdot 2H_2O$ /100g, according to the *CRC Handbook of Chemistry and Physics* (Weast and Astle 1981 [DIRS 100833], p. D-204) the density is between 1.0443 and 1.0486.

As another dominant component, the solution contains 4.2264 g $MgCl_2\cdot 6H_2O$ /100ml solution, according to the same handbook, the density is between 1.0309 and 1.0394 (Weast and Astle 1981 [DIRS 100833], p. D-215).

The solution used in this experiment is a multi-component solution and there is not a handbook value. We consider that the solution is dominant by 5.776 g $CaCl_2\cdot 2H_2O$ /100 ml and 4.2264 g $MgCl_2\cdot 6H_2O$ /100 ml and both contribute to the density change of the solution and the solution density is not linearly combined from both components. However, the solution density ranges between 1.0443 and 1.0870 (1.0486+1.0394). Here we assume the solution density is at the middle of this range, 1.06565.

H1.4 Conversion of concentration unit from moles/L of solution into moles/kg of water

Per liter of solution weights 1.06565 kg and contains:

$40.078\times[Ca^{++}]+39.0983\times[K^+]+ 24.305\times[Mg^{++}]+22.98977\times[Na^+]+35.453\times[Cl^-]+18.9984\times[F^-]$
$61.0168\times[HCO_3^-]+62.0046\times[NO_3^-]+96.0626\times[SO4^{--}]+60.0843\times[SiO_2]$

$=40.078\times0.3929289+39.0983\times0.0680818+24.305\times0.229701817+22.98977\times0.27241917+35.453$
$\times1.47124135+18.9984\times0.028532+61.0168\times0.0007261+62.0046\times0.04159+96.0626\times0.02183641$
$7+60.0843\times0.00900335$

$=15.7478044542+2.66188264094+5.582902662185+6.2628540618909+52.15991958155+$

$0.5420623488+0.04430429848+2.578771314+2.0976629917042+0.540959982405$

$=88.2191243361551$ g of solutes.

Per liter of solution contains 1065.65 (g) –88.219124 (g) =977.430876 g of water.

Then, the concentrations of solutes as moles per kg of water are:

[Ca++] =0.3929289/0.977430876 = 0.4020017 (moles/kg of water)
[K+] =0.0680818/0.977430876 = 6.965383E-2 (moles/kg of water)
[Mg++] =0.229701817/0.977430876 = 0.2350057 (moles/kg of water)
[Na+] =0.27241917/0.977430876 = 0.2787094 (moles/kg of water)
[Cl-] =1.47124135/0.977430876 = 1.505213 (moles/kg of water)
[F-] =0.028532/0.977430876 = 2.919081E-2 (moles/kg of water)
[HCO3-] =0.0007261/0.977430876 = 7.428658E-4 (moles/kg of water)
[NO3-] =0.04159/0.977430876 = 4.255033E-2 (moles/kg of water)
[SO4- -] =0.021836417/0.977430876 = 2.234063E-2 (moles/kg of water)
[SiO2] =0.00900335/0.977430876 = 9.211239E-3 (moles/kg of water)

In summary, the solution concentration, in moles/L and moles/Kg of water are listed in Table H-2.

Table H-2. Solution Concentration in Moles/L and Moles/Kg of Water

Components	Concentration (Moles/L)	Concentration (Moles/Kg of Water)
Ca^{++}	0.3929289	0.4020017
K^{+}	0.0680818	6.965383E-2
Mg^{++}	0.229701817	0.2350057
Na^{+}	0.27241917	0.2787094
Cl^{-}	1.47124135	1.505213
F^{-}	0.028532	2.919081E-2
HCO_3^{-}	0.0007261	7.428658E-4
NO_3^{-}	0.04159	4.255033E-2
$SO4^{--}$	0.021836417	2.234063E-2
SiO_2	0.00900335	9.211239E-3

H1.5 Estimate of pH of the solution

$[OH^{-}]$=0.00012 Moles/liter=0.0001228moles/liter of water

Log K_{eq}=–12.2551 at 100 $^{\circ}$C, and 11.6308 at 150 $^{\circ}$C (TOUGHREACT database)

Using linear interpolation we calculate the Log K_{eq} at 144 $^{\circ}$C that is 11.69323.

$[H^{+}]=K_{eq}/[OH^{-}]=10^{-11.69323}/0.0001228$= 1.65E-8
pH= –log$[H^{+}]$=7.7825

INTENTIONALLY LEFT BLANK